

**Structure Activity Study of a Family of Functional
Pyrene-Isoxazole-Calix[4]arene Fluorescent Chemosensors
for Metal Ion Detection**

A thesis submitted to Maynooth University in fulfilment of the
requirements for the degree of

Doctor of Philosophy

by

Justine O'Sullivan, B.Sc.



**Maynooth
University**
National University
of Ireland Maynooth

Department of Chemistry,

Maynooth University,

Maynooth,

Co. Kildare,

Ireland.

December 2016

Research Supervisor: Dr. Frances Heaney

Head of Department: Dr. John Stephens

Table of Contents

Acknowledgements.....	ix
Declaration.....	xi
Abstract.....	xii
Abbreviations.....	xiii
Chapter 1 - Introduction	1
1.1 Calixarene Chemistry	2
1.1.1 Overview	2
1.1.2 History of Calixarenes	2
1.1.3 General Applications of Functionalised Calixarenes	4
1.1.4 Synthetic Approaches to Functional Calixarenes	8
1.1.4.1 1,3-Disubstitution of the Lower Rim	8
1.1.4.2 Tetrasubstitution of the Lower Rim	10
1.2 Metal Ion Sensors	11
1.2.1 General Design of Metal Ion Sensors	11
1.2.2 Non-Calixarene Based Metal Ion Sensors	12
1.2.3 Calixarene Based Metal Ion Sensors	14
1.3 Fluorescence Spectroscopy Overview	16
1.3.1 Basic Principles of Fluorescence Spectroscopy	16
1.3.2 Fluorophore Overview	18
1.3.2.1 Common Fluorophores	18
1.3.2.2 Pyrene	21
1.3.3 Detection of Analytes using Fluorescence Spectroscopy	21
1.3.4 Energy Transfer	22

1.3.5 Excimer Formation	23
1.3.6 Photoinduced Electron Transfer	24
1.4 Analysis of Host:Guest Binding Events.....	25
1.4.1 Determination of Host:Guest binding Stoichiometry: Job's Method (Method of Continuous Variation)	25
1.4.2 Stern-Volmer Analysis	27
1.4.3 Benesi-Hildebrand Analysis.....	29
1.5 Sensing Applications Involving Pyrene Fluorophores	30
1.6 Click Chemistry Overview.....	32
1.6.1 1,3-Dipolar Cycloadditions	32
1.6.2 Copper-Catalysed Azide-Alkyne Cycloaddition (CuAAC).....	33
1.6.3 Nitrile Oxides.....	33
1.6.4 Generation of Nitrile Oxides	34
1.6.5 1,3-Dipolar Cycloaddition of Nitrile Oxides	35
1.6.6 Isoxazole Heterocyclic Ring	36
1.7 Isoxazoles as Metal Binding Sites.....	36
1.8 Aims of the Research	38
Chapter 2 - Pyrene Isoxazole Calixarene (PIC)	39
2.1 Overview	40
2.2 Isoxazole Functionalised Calixarenes.....	40
2.3 Synthesis and Applications of Lower Rim Pyrene Functionalised Calixarenes	41
2.4 Novel Pyrene Isoxazole Functionalised Calixarene.....	45
2.4.1 Design of PIC	45
2.4.2 Synthesis and Characterisation of PIC	46
2.4.3 Solid State Structure of PIC	48
2.4.4 Host:Guest Studies of PIC and the Model Compound.....	50

2.4.4.1	Determination of the Stoichiometry of association between PIC and Cu ²⁺	52
2.4.5	EPR Spectroscopic Investigation of the Geometry of the PIC:Cu ²⁺ Complex.....	52
2.4.6	Computational Study	53
2.5	Further Analysis of PIC and its Copper Complexation	54
2.5.1	UV-Vis Spectroscopic Investigation of Cu ²⁺ → Cu ⁺ Reduction by PIC in MeCN.....	54
2.5.2	Experiments in Search of a Solid Sample of the PIC:Cu ²⁺ Complex.....	55
2.5.1.1	Vapour Diffusion Crystallisation Technique.....	60
2.5.3	¹ H NMR Spectroscopic Investigation of the Effect of the Cu ²⁺ Ion on PIC.....	61
2.5.4	Analysis of the Fluorescence Quenching Mechanism of PIC by Copper Perchlorate	65
2.5.5	Binding Constant Determination of the PIC:Cu ²⁺ Complex Formation	67
2.5.6	Detection Limit of PIC for the Cu ²⁺ Ion	68
2.6	Conclusions	70
2.7	Future Work	71
Chapter 3 - PIC Analogues: Design, Synthesis and Characterisation ...		72
3.1	Overview	73
3.2	Ethylene Pyrene Isoxazole Calixarene (EPIC).....	73
3.2.1	Synthesis of EPIC	73
3.2.2	Characterisation of EPIC.....	76
3.2.2.1	¹ H and ¹³ C NMR Spectroscopic Characterisation of EPIC.....	76
3.2.2.2	Solid State Structure of EPIC.....	79
3.2.2.3	UV and Fluorescence Spectroscopy of EPIC.....	82

3.3 Propyl Pyrene Isoxazole Calixarene (PPIC)	84
3.3.1 Synthesis of PPIC	85
3.3.2 Characterisation of 1-Pyrenebutanenitrile	87
3.3.3 Characterisation of 1-Pyrenebutanaloxime	89
3.3.4 Characterisation of PPIC	95
3.3.4.1 ¹H and ¹³C NMR Characterisation of PPIC	95
3.3.4.2 UV and Fluorescence Spectroscopy of PPIC	96
3.4 Methoxy Pyrene Isoxazole Calixarene (MPIC)	98
3.4.1 Synthesis of MPIC	100
3.4.1.1 Characterisation of MPIC	104
3.4.1.2 Variable Temperature ¹H NMR Spectroscopic Study of MPIC	105
3.4.1.3 ¹H NMR and ¹³C NMR Characterisation of MPIC	106
3.4.1.4 Solid State Structure of MPIC	115
3.4.1.5 UV and Fluorescence Spectroscopy of MPIC	117
3.5 Conclusions	121
Chapter 4 - Sensing Potential of EPIC, PPIC and MPIC	123
4.1 Overview	124
4.1.1 Linearity of the Fluorescence Response vs. Concentration of the Hosts	125
4.1.2 Fluorescence Response of Calixarene Hosts to Metal Perchlorates	130
4.1.3 Competitive Metal Ion Study	135
4.1.4 Counterion Study	142
4.1.5 Determination of the Stoichiometry of Association between the Calixarene Hosts and the Cu²⁺ Ion	147

4.1.6	Analysis of the Fluorescence Quenching Mechanism by Stern-Volmer Approach	150
4.1.7	Calculation of Binding Constants (K_a) using Benesi-Hildebrand Analysis.....	153
4.1.8	Detection Limit of the Calixarene Hosts for the Cu^{2+} Ion	156
4.2	An NMR Spectroscopic Study of the Interactions between the Calixarene Hosts and the Cu^{2+} Ion	157
4.3	Conclusions	163
Chapter 5 - Aqueous and Solid State Fluorescence Study of PIC.....		166
5.1	Overview	167
5.2	PIC Aqueous Fluorescence Study.....	167
5.2.1	SEM Investigation of the Morphology of the PIC Aggregates	176
5.2.2	UV Investigation of the Formation of Aggregates of PIC	178
5.3	Fluorescence Sensing in an Aqueous MeCN Environment	179
5.3.1	Detection of Copper Ions in Aqueous MeCN Solutions – Optimisation of Experimental Design	180
5.3.2	Detection of Copper Ions in Aqueous MeCN Solutions	182
5.3.3	Counterion Study	184
5.3.4	Metal Ion Selectivity Study – Metal Perchlorates Presented as Solutions in MeCN.....	186
5.3.5	Study of Ability of PIC to Sense Cu^{2+} Ions from an Aqueous Source	188
5.3.6	Competitive Metal Study – Metal Perchlorates Presented as Solutions in Water.....	191
5.3.7	Investigation of Potential Aggregate Formation in Copper Containing aq. MeCN solution of PIC	192
5.4	Fluorescence Study of PIC in Aqueous MeCN - Conclusions	194

5.5 Solid Supported PIC Overview	196
5.5.1 Drop-casting: PIC Coated Glass Slides.....	196
5.5.2 Introduction to Nanofibers and Electrospinning	199
5.5.2.1 Electrospinning of Polycaprolactone (PCL).....	201
5.5.2.2 Electrospinning of Polysulfone (PSF).....	208
5.6 Solid Supports Study - Conclusions	217
Chapter 6 - Conclusions and Future Work	218
Chapter 7	224
Experimental.....	224
7.1 Instrumentation and Reagents	225
7.2 5,11,17,23- <i>tetra-tert</i> -Butyl-25,27-bis(but-3-ynyloxy)-26,28-dihydroxycalix [4]arene, 12 ¹⁰⁴	226
7.3 1-Pyrenecarbaldoxime, 12 ⁸⁸	227
7.4 5,11,17,23- <i>tetra-tert</i> -Butyl-25,27-bis[(3-(pyren-1-yl)isoxazol-5-yl)ethyl]- 26,28- dihydroxycalix[4]arene (EPIC), 14	228
7.5 5,11,17,23- <i>tetra-tert</i> -Butyl-25,27-dipropargyloxy-26,28-dihydroxycalix[4] arene, 15 ¹⁸	229
7.6 1-Pyrenebutanol, 16 ²²⁵	230
7.7 1-Pyrenebutanal, 17 ¹²¹	230
7.8 1-Pyrenebutanaldoxime, 18	231
7.9 5,11,17,23- <i>tetra-tert</i> -Butyl-25,27-bis[(3-(3-(pyren-1-yl)propyl) isoxazol-5-yl) methyl]-26,28-dihydroxycalix[4]arene (PPIC), 21.....	233
7.10 5,11,17,23- <i>tetra-tert</i> -Butyl-25,27-bis[(3-(pyren-1-yl)isoxazol-5-yl)methyl]- 26,28-dihydroxycalix[4]arene (PIC), 25 ⁸⁸	235
7.11 5,11,17,23- <i>tetra-tert</i> -Butyl-25,27-bis[(3-(pyren-1-yl)isoxazol-5-yl)methyl]- 26,28-dimethoxycalix[4]arene (MPIC), 27	235

Bibliography	xvi
Appendix	xvi
Publication List	xvii
Oral Presentations.....	xvii
Poster Presentations	xvii
Graduate Modules	xviii
Crystal Structure Report for PIC.2DCM	xvi
Crystal Structure Report for EPIC.2DCM	xxxix
Crystal Structure Report for MPIC.2DCM	lxvi

To my family, John, Betty, Laura, Yvonne and John.

Thanks for everything.

Acknowledgements

I would like to thank my supervisor Dr. Frances Heaney for entrusting this project to me, and for her constant support, encouragement, enthusiasm and generosity with her time. I really could not have asked for a better supervisor. I would also like to thank the Irish Research Council for providing the funding to complete this project and to Dr. John Stephens for allowing me to complete my research at Maynooth.

To all members of the research group past and present, Colin, Vickie and Haowen - thanks for showing me the ropes when I first joined the group – and to the newest member of the group, Jack – I don't know how the glove/pipette/filter paper fairy will manage without me.

Thanks to all the academic and technical staff in the department, to Ria, Ollie, Barbara, Walter, for all their help, advice and mass spec samples. Thanks also to Donna and Carol for being so helpful with everything I ever needed. Special thanks are due to Dr. Ken Maddock for giving up a few long days to help me with the variable temperature NMR experiments.

Noel, I don't think this department would function without you, thank you for fixing everything I ever broke, for keeping all our computers running perfectly and especially for making sure the foyer is perfectly decorated every Halloween.

Outside of Maynooth, thanks to Dr. Brendan Twamley and Dr. John Gallagher for solving the x-ray crystal structures and to Dr. John O'Brien for the initial help with the NMR titration experiments.

Thanks to all the postgrads, past and present, for making this department one of the most enjoyable and entertaining places to work, and for all the nights out and movie nights in, the Christmas, Halloween and summer parties. I will miss the craic and random chats in the coffee room that could never be repeated anywhere else. Never have I worked anywhere where I've been called so many different names, Jacinta, Christine, Jessica are just a few....I think for the rest of my life I will always answer to the name Jacinta. Thanks to my write up room buddies, Chiggy, hAndrew, Michelle D., Ross and Matt, for the good chats and banter, I don't think any of us will ever

leave our computers unlocked again. To the rest of the postgrads I haven't mentioned, upstairs and downstairs, Muhib, Anthony, Xiang, Nan, Sam, (new) Michelle K., Mark K., Harlei, Jessica, Mark G., Alice, Michelle Q., Lucy, Karen, Aoife and Caroline, thanks for the friendship and best of luck with your research.

Thanks to Aisling and Chris (even though you broke my thesis) for taking the time to proofread and for the helpful pointers. Special thanks to Jessica (my Spanish twin) for giving up her time to help me with the electrospinning experiments and the SEM analysis.

To all the girls from home, Ais, Grá, Fi, Kee, Andi, Laura and Nic – Thanks for your constant encouragement over the last few years, someday soon we will all be in the one country or at least the one continent at the same time.

Kean, I can't even begin to thank you for the love and support you've shown me over the last few years, thanks for listening to me tell you all about my calixarenes and my fluorescence experiments, and especially for making sure I was never hungry, I promise I will learn how to cook...someday...soon!! Love always.

A huge thank you to my family for their continued love and support, especially to Mam and Dad. I'll always remember telling Daddy about my first reaction working and him asking did that mean I was nearly finished my Ph.D., almost 4 years later I'm nearly there!!

Declaration

I hereby certify that this thesis has not been submitted before, in whole or in part, to this or any other university for any degree and is, except where otherwise stated, the original work of the author.

Signed: _____

Date: _____

Abstract

This thesis reports on the design, synthesis and structural characterisation of a novel family of pyrene-isoxazole-calix[4]arenes. An investigation of their metal cation sensing abilities using techniques including absorbance, fluorescence and ^1H NMR spectroscopies follows.

The novel work begins by developing a pyrene-isoxazole appended calix[4]arene, **PIC** that could selectively detect and report, *via* fluorescence spectroscopy, on the presence of Cu^{2+} ions in MeCN. The host:guest binding interaction was investigated by ^1H NMR spectroscopy. Stern-Volmer analysis of the quenching mechanism, Benesi-Hildebrand analysis of the binding constant and detection limit calculations were performed in characterisation of the binding properties of this host.

The relationship between the modular building blocks and the conformational presentation of the host structures and their metal cation sensing abilities was probed by design of three new members of this family, structurally related to **PIC**. Each member differed at just one key position. **EPIC**, introduced an ethylene linker between the lower rim of the calixarene and the isoxazole heterocycle, **PPIC** introduced an alkyl chain between the isoxazole rings and the pyrene units and **MPIC** incorporated methoxy groups in place of the hydroxyl groups of **PIC**. Each host was successfully synthesised using catalyst-free click cycloaddition and were structurally characterised using the full suite of analytical techniques including solid state structures of **EPIC** and **MPIC**.

Fluorescence spectroscopic studies indicated that whilst **EPIC**, **PPIC** and **MPIC**, like **PIC**, had affinities for Cu^{2+} binding, there were subtle differences in the binding association of the H:G complexes (K_a values varied between 33,000 – 6,000 M^{-1}) and in the information that could be extracted from the NMR spectroscopic study of their binding.

In order to probe real-world applications such as waste water analysis, studies involving **PIC** in aqueous MeCN were conducted. A tendency for the host to self-assemble and form supramolecular structures in the aqueous media was hypothesised on the basis of emission and absorbance data and supported by SEM images.

PIC was shown to be fluorescent in drop-casted solid state samples and subsequently in electrospun **PIC** doped polymeric microfibers. The fluorescent microfibers responded spectrofluorometrically to the presence of Cu^{2+} cations in water.

Abbreviations

ACQ	aggregation-caused quenching
ADP	Adenosine Diphosphate
AIE	aggregation-induced emission
AMP	Adenosine Monophosphate
anh	anhydrous
aq.	aqueous
Ar	aromatic
ArH	aromatic proton
ArC	aromatic carbon
ATP	Adenosine Triphosphate
a.u.	arbitrary units
br s	broad singlet
Ch-T	Chloramine-T
COSY	Correlation Spectroscopy
CuAAC	Copper-Catalysed Azide-Alkyne Cycloaddition
DEPT	Distortionless Enhancement by Polarisation Transfer
DFT	Density Functional Theory
DIPEA	<i>N,N</i> -Diisopropylethylamine
DL	Detection Limit
Δ	Reflux Temperature
δ	Chemical Shift
EPIC	Ethylene Pyrene Isoxazole Calixarene
ESI	Electrospray Ionisation
EPR	Electron Paramagnetic Resonance
eqs	equivalents
ESR	Electron Spin Resonance
FITC	fluorescein isothiocyanate
Fl.	Fluorescence
FRET	Fluorescence/Förster Resonance Energy Transfer
G	guest

H	host
HRMS	High-Resolution Mass Spectrometry
hrs	hours
HSQC	Heteronuclear Single Quantum Correlation
Hz	Hertz
IPNS	Isopenicillin <i>N</i> -synthase
ISE	Ion Selective Electrode
K	Kelvin
kV	kilovolt
LAH	lithium aluminium hydride
L-His	L-Histidine
L-Trp	L-Tryptophan
mbar	millibar
mg	milligram
μL	microlitre
μM	micromolar
mmol	millimole
MPIC	Methoxy Pyrene Isoxazole Calixarene
MW	microwave/molecular weight as appropriate
NBS	<i>N</i> -bromosuccinimide
NCS	<i>N</i> -chlorosuccinimide
MFs	microfibers
nm	nanometre
NMR	Nuclear Magnetic Resonance
NOAC	Nitrile Oxide/Alkyne Cycloaddition
ns	nanosecond
OLED	Organic Light Emitting Diode
P'	Polarity Index
P _A	peak-to-valley ratio
paco	partial cone
PAH	polycyclic aromatic hydrocarbon
PCC	pyridinium chlorochromate

PCL	polycaprolactone
PCT	photoinduced charge transfer
PET	photoinduced electron transfer
PIC	Pyrene Isoxazole Calixarene
PIC/PCL MFs	PIC doped PCL microfibers
PIC/PSF MFs	PIC doped PSF microfibers
PIM	Pyrene Isoxazole Monomer
PPIC	Propyl Pyrene Isoxazole Calixarene
ppt	precipitate
PSF	polysulfone
qC	quaternary carbon
rt	room temperature
SEM	Scanning Electron Microscopy
Soln	solution
STP	Standard Temperature and Pressure
THF	tetrahydrofuran
TLC	Thin Layer Chromatography
TMS-CN	trimethylsilyl cyanide
TNT	trinitrotoluene
Vol.	volume
vt	variable temperature
v/v	volume per volume
W	Watt

Chapter 1

Introduction

1.1 Calixarene Chemistry

1.1.1 Overview

Calixarenes are a class of versatile macrocycles. Their popularity stems from their ease of synthesis, their functionalisable upper and lower rims and their wide range of applications. This section will provide an overview of the history of calixarenes, their general applications and synthetic methods for lower rim functionalisation.

1.1.2 History of Calixarenes

Calixarenes were first synthesised in Germany by Adolph von Baeyer in 1872. He observed that mixing formaldehyde and phenol in the presence of a strong acid resulted in the formation of a resinous mixture.¹ At the time, isolation of pure products from this material was not possible. Even though Baeyer was unsuccessful at characterisation of the mixture, his work was pivotal in the beginning of phenol-formaldehyde chemistry which paved the way for calixarene chemistry.

In 1902, in the United States, Leo Baekeland began an investigation into base-catalysed phenol-formaldehyde reactions. After several years of research he demonstrated that by using a defined amount of base the reaction could be controlled resulting in polymeric products of reproducible rigidity. He patented this process in 1907 and his material became known as Bakelite, which was one of the first commercially available synthetic plastics.²

Depending on their substitution pattern, phenols have the possibility of reacting with formaldehyde at the *ortho*- and/or *para*-positions. Thus the formation of a wide variety of crosslinked polymers where each phenolic unit can be attached to up to three other phenolic units can result. This potential lack of regioselectivity was a problem in the initial phenol-formaldehyde chemistry. In 1942, seventy years after Baeyer's formaldehyde experiments, Alois Zinke and Erich Ziegler "simplified" the reaction using a *para*-substituted phenol in a condensation reaction with formaldehyde.³ A *para*-substituted phenol can only react at the *ortho*- positions thereby reducing the possible number of polymeric products. Zinke and Ziegler proposed that the product of their reaction had the cyclic tetrameric structure shown

in **Figure 1.1**. Concomitantly, Joseph Niederl and his colleague Heinz Vogel in New York University proposed a cyclic tetrameric structure for the product of their acid catalysed reactions between aldehydes and resorcinols.⁴

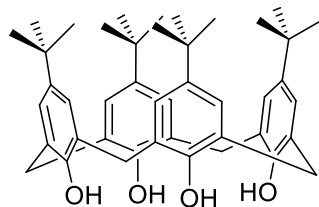


Figure 1.1: Tetrameric structure proposed by Zinke and Ziegler as the product of base catalysed reaction between *p-tert*-butylphenol and formaldehyde.³

David Gutsche coined the term “calixarene” in 1975 and this name first appeared in print in 1978.⁵ The name is derived from the Greek word calix meaning “vase” or “chalice”; and arene which indicates the presence of aryl residues in the macrocyclic array, **Figure 1.2**. A calix[n]arene contains “n” aryl residues in the macrocycle; calix[4]arenes, calix[6]arenes and calix[8]arenes are the most heavily represented in the literature. Calix[4]arenes can present as four distinct conformers: cone, partial cone (paco), 1,3-alternate and 1,2-alternate, **Figure 1.3**.

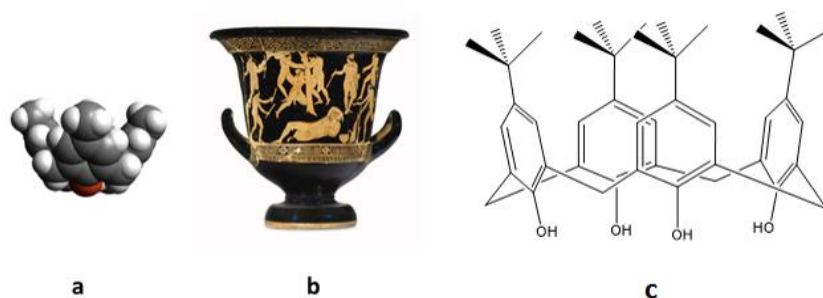


Figure 1.2: **a)** Space filling diagram of a calix[4]arene, **b)** Greek vase and **c)** calix[4]arene with upper rim *p-tert*-butyl substituents.

Gutsche saw the potential of calixarenes as molecular baskets capable of functioning as enzyme mimics. Cyclodextrins⁶ and crown ethers⁷ had previously been utilised for this purpose, but he noted that calixarenes had two distinct advantages: **(i)** they were easy to synthesise, whereas cyclodextrins were only available by isolation from natural sources; and **(ii)** they had a true basket-like shape, whereas crown ethers had

a more disc like shape. Gutsche's seminal work on calixarenes spanned three decades and included: the establishment of the structures of the parent cyclic tetramer, hexamer and octamer, a study of their conformational properties and the development of methods for the functionalisation of the upper and lower rims of the calixarene skeleton.

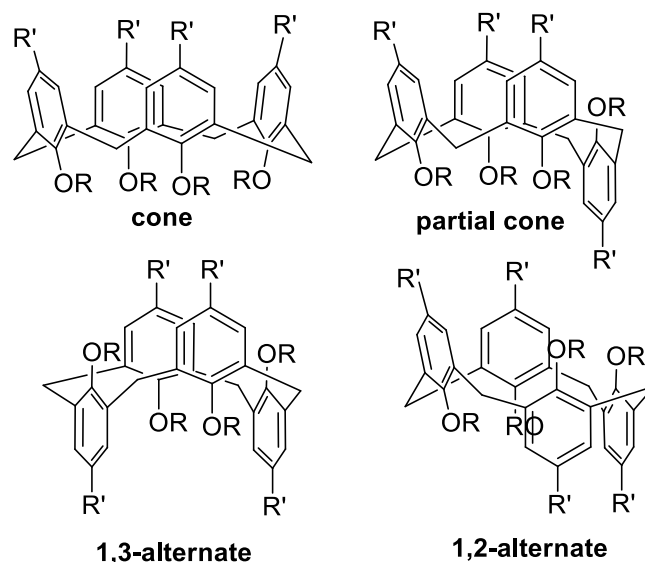


Figure 1.3: Common conformations of substituted calix[4]arenes.

1.1.3 General Applications of Functionalised Calixarenes

Calixarenes have unique three dimensional structures with hollow inner cavities. This characteristic, taken together with the ease of functionalisation of the upper and lower rims, gives rise to many applications within supramolecular chemistry, including molecular recognition, sensing and self-assembly, catalysis, nanotechnology and drug delivery.⁸

In a recent publication, Rao *et al.* reported a drug storage and release application of a lower rim monocholesteryl derivatised calix[4]arene, **Figure 1.4.**⁹ This functionalised calix[4]arene showed instantaneous gelation in THF:MeCN (1:1, v/v) at a minimum gelator concentration of 0.6%. Gelation was also achieved in the presence of three different drugs, doxorubicin, curcumin and tocopherol, >90% release of the drugs was subsequently demonstrated in water. The guest-entrapped gels exhibited the same microstructures as the guest-free gels. Fluorescence

spectroscopy and molecular mechanics studies suggested that the drug molecules occupied the hydrophobic pockets of the calixarene.

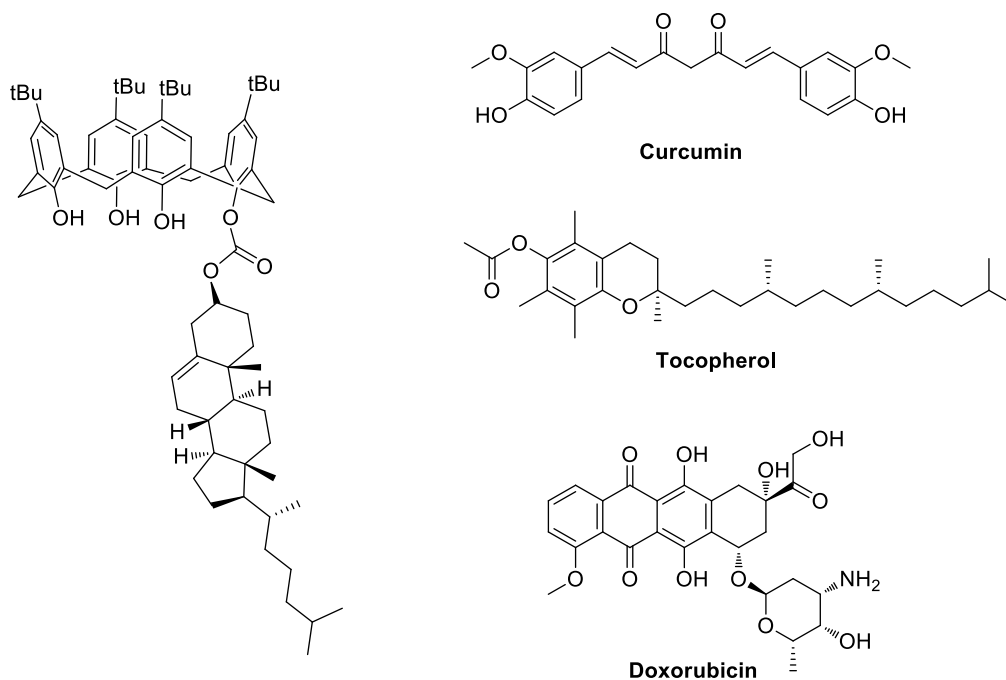


Figure 1.4: Cholesteryl derivatised calix[4]arene capable of gel formation, storage and release of the three drug molecules shown.⁹

Vigalok *et al.* have reported catalytic activity of lower rim heterocycle functionalised calix[4]arenes.¹⁰ A three-step synthesis led to a triazole derivative which, upon exposure to TiCl_4 and *N,N*-diisopropylethylamine (DIPEA), formed a Ti^{4+} complex capable of catalysing TMS-CN addition to benzaldehyde. No catalytic activity was observed when control reactions were carried out with the Ti^{4+} complex of 1,3-dimethylcalixarene, confirming the role of the heterocyclic ring in the catalytic cycle.

A more recent publication cites a copper-catalysed, one-step lower rim amination reaction which produced pyrazole functionalised calixarenes which also formed complexes with some main group and transition metal ions.¹¹ The pyrazole Ti^{4+} complex, shown in **Figure 1.5**, had superior catalytic activity to its triazole analogue in promoting TMS-CN addition to benzaldehyde.

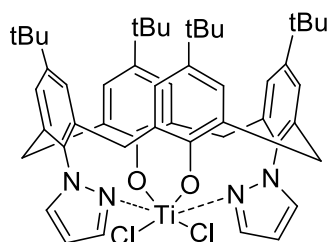


Figure 1.5: Ti^{4+} complex of a pyrazole functionalised calix[4]arene used to catalyse TMS-CN addition to benzaldehyde and cyclohexene epoxidation reactions.¹¹

Environmental and human health have suffered due to the widespread use of pesticides. The potential binding of a naphthol-appended calix[4]arene to six common pesticides was investigated using fluorescence spectroscopy. Enhancement of the intensity of the fluorescence emission signal of the functionalised calixarene occurred when exposed to only one of this group: metolcarb. No such change occurred in the case of the five other pesticides examined in the same study.¹² To facilitate exploitation of the sensor in the field, the calix[4]arenes were immobilised onto gold nanoparticles using a triazole forming click cycloaddition reaction. Contact angle measurements were used as a simple and visual method to determine if metolcarb was present, **Figure 1.6**. This easily executed technique consists of a stage, a syringe, a light source and an optical aid with a reticule for angle measurement. A droplet of a metolcarb containing solution was shown to form a specific contact angle of $20.6 \pm 2.0^\circ$ on the gold nanoparticle surface, while solution samples of the five other pesticides tested had contact angles $>113^\circ$. Therefore, the calixarene functionalised gold nanoparticles were suitable for the rapid detection of metolcarb in an environmental setting.

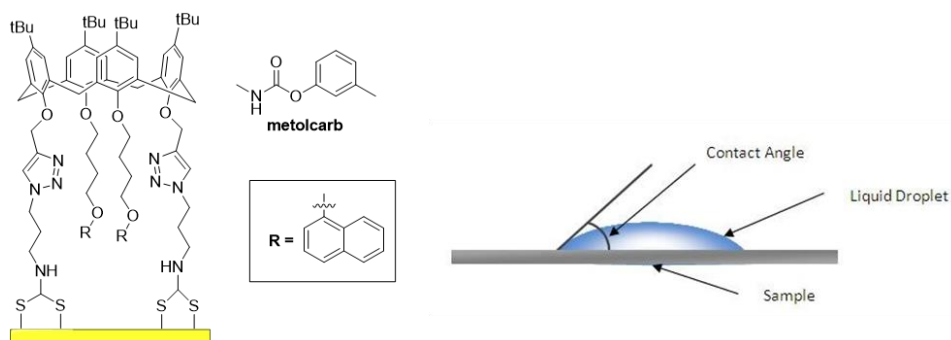


Figure 1.6: Left: Naphthol-appended calix[4]arene immobilised onto gold nanoparticles used for the detection of the pesticide metolcarb.¹² Right: General diagram showing a contact angle measurement.¹³

Calix[4]arenes modified on the upper rim with arylacetylene units, **Figure 1.7**, have been utilised in selective spectrofluorometric sensing of the common explosive trinitrotoluene (TNT) from an aqueous medium. Arylacetylene substituents are known to widen the calixarene cavity and this increased size combined with the hydrophobicity of the cavity provides selectivity for TNT.¹⁴ In a more robust application it has been noted that fluorescence emission resulting from filter paper coated with the modified calixarene was quenched upon exposure to TNT vapour as visualised under a UV lamp at 365 nm, thus environmental on-site detection of TNT was possible.

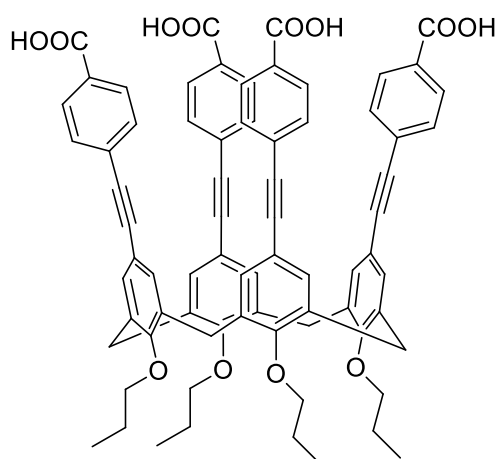


Figure 1.7: Arylacetylene modified calix[4]arene used in TNT detection.¹⁴

Iodide is an essential nutrient for healthy development of the human body and is of particular importance for pregnant women and children. Therefore, sensors capable of selective and sensitive iodide detection at low concentrations remain highly sought after. Maity *et al.* have designed and synthesised a water soluble 1,3-alternate *p*-sulphonatocalix[4]arene capable of detecting iodide to a remarkable limit of 2.5 μM .¹⁵ They anchored this calixarene onto the surface of gold nanoparticles, **Figure 1.8**. In aqueous solutions these nanoparticles show a vivid colour change from pink to blue in the presence of iodide. It is understood that the iodide is oxidised to iodine at the exposed surface of the nanoparticle which results in a change of the size and morphology of the particles causing the colour change of the solution.

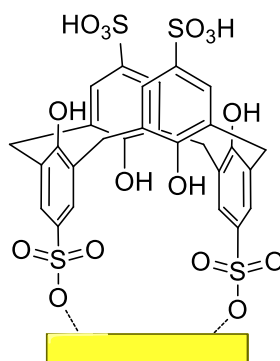


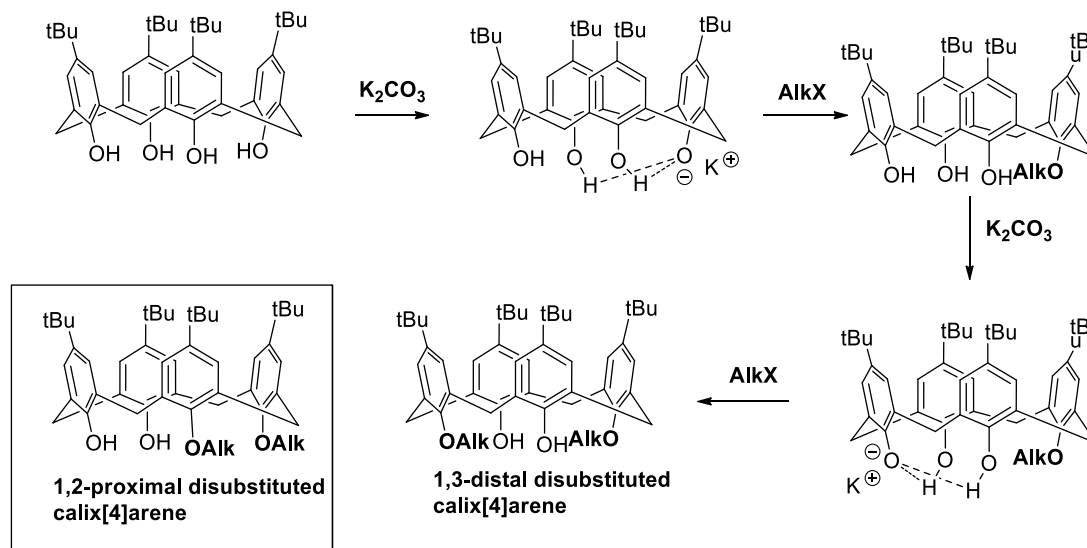
Figure 1.8: Gold nanoparticles with anchored *p*-sulphonatocalix[4]arene used for the colourimetric detection of the iodide ion.¹⁵

1.1.4 Synthetic Approaches to Functional Calixarenes

The upper and lower rims of calixarenes have been modified with an extensive range of functional groups including carboxylic acids, amides, crown ethers and azacrown ethers.¹⁶ However, as the novel calixarenes studied in this author's work all fall in the category of lower rim functionalised molecules, this section will give a brief overview of the range of chemistries employed for functionalisation at the lower rim, a topic which has been the subject of an attractive review by Creaven *et al.*¹⁷

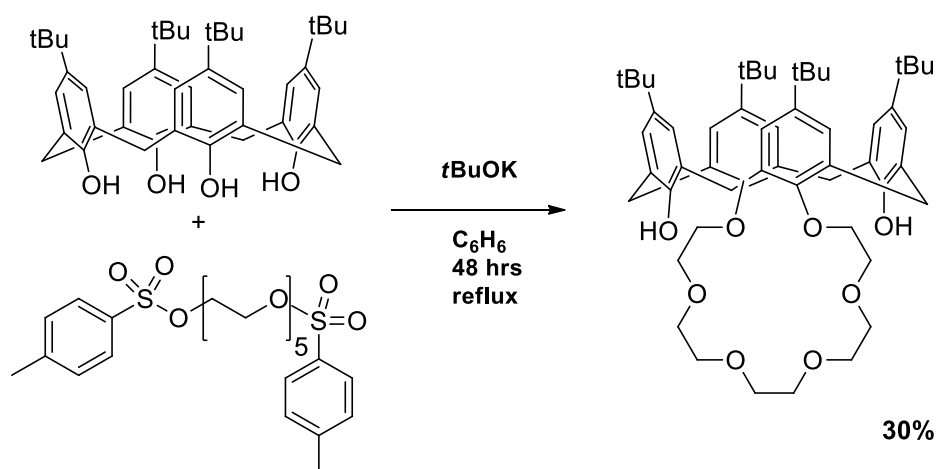
1.1.4.1 1,3-Disubstitution of the Lower Rim

The hydroxyl groups of the lower rim of calixarenes are useful handles to introduce various functional groups and Williamson ether syntheses have been a popular synthetic tool.¹⁸ Typically a base, often potassium carbonate, is used to generate the calixarene alkali salt and an alkyl halide is introduced to the resulting alkoxide, culminating in the formation of a mono-substituted phenoxy-ether. This can then be selectively deprotonated at the distal position and further alkylated to give 1,3-disubstituted products. The regioselectivity of the second alkylation reaction can be explained by the relative stability of the intermediate alkoxides leading to 1,2- and 1,3-disubstituted products. 1,3-Distal are favoured over 1,2-proximal products due to the availability of proximal hydroxyl moieties to stabilise the intermediate alkoxide leading to the 1,3-disubstituted product, **Scheme 1.1**.



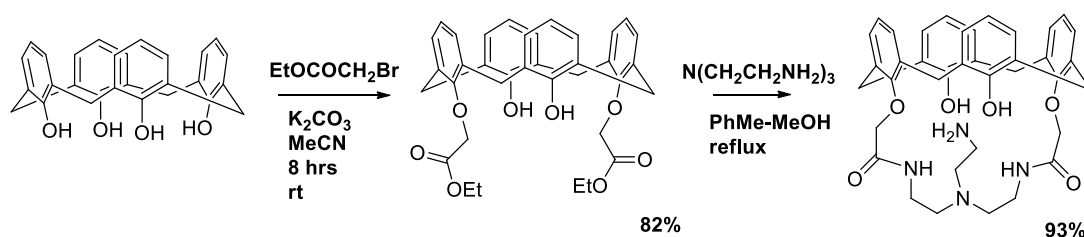
Scheme 1.1: General synthetic scheme for formation of 1,3-distal disubstituted calix[4]arenes by ether formation; stabilising hydrogen bonds of the intermediate alkoxides are shown with dashed lines. Inset: Structure of a 1,2-proximal disubstituted calix[4]arene.

Lower rim functionalisation of calixarenes with crown ethers has been popular due to the potential of the crown as a metal binding site. Ungaro and co-workers were the first to report the synthesis of a member of this family.¹⁹ Their method involved treating the parent calix[4]arene with two equivalents of potassium *tert*-butoxide and one equivalent of pentaethylene glycol ditoluene-*p*-sulphonate. Following heating at reflux in benzene for 48 hrs the crown ether functionalised calix[4]arene shown in **Scheme 1.2** was formed in 30% yield.



Scheme 1.2: Synthesis of the first calix-crown from Ungaro and co-workers.¹⁹

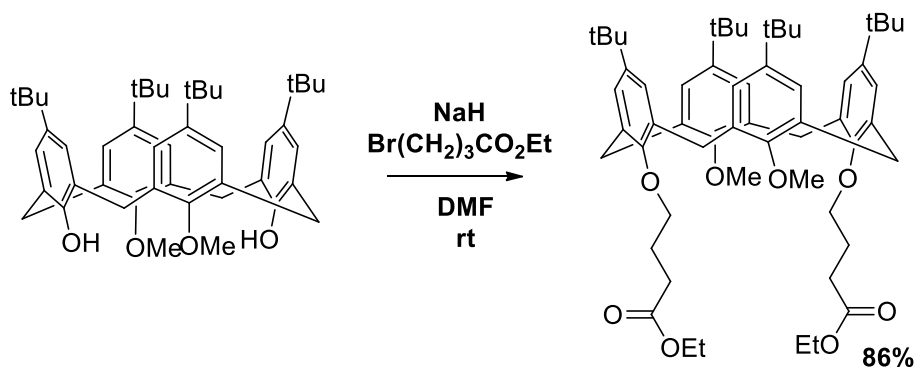
Calixarenes with pendant amide or ester groups have been synthesised in a manner analogous to the Williamson ether synthesis. Following deprotonation, ester or amide functional groups have been introduced using appropriate halogenated esters²⁰ or isocyanates.²¹ If desired these groups can be used as handles for further derivatisation. In one example, Bitter *et al.* cycloamidated a lower rim diester functionalised calix[4]arene using a polyamine, to produce in 93% yield the capped calix[4]arene shown in **Scheme 1.3**.²² This derivative showed potential as a chromogenic optical sensor for alkali and alkaline earth metal ions.



Scheme 1.3: Synthesis of a lower rim carboxamide capped calix[4]arene from a 1,3-diester calix[4]arene.²²

1.1.4.2 Tetrasubstitution of the Lower Rim

Tetrasubstitution is usually achieved by functionalisation of a 1,3-distal disubstituted calix[4]arene. It requires a strong base such as sodium hydride due to the difficulty in forming the alkoxide ion when there are no proximal hydroxyl groups present for stabilisation by intramolecular hydrogen bond formation. In one example Shen *et al.* formed a fully substituted calixarene by reaction of a distally methylated precursor with ethyl 4-bromobutanoate in the presence of sodium hydride, **Scheme 1.4**.²³



Scheme 1.4: Synthesis of a tetrasubstituted calix[4]arene from reaction of a distally methylated precursor and ethyl 4-bromobutanoate using NaH as a base.²³

1.2 Metal Ion Sensors

Metal ions are ubiquitous in biological systems and in the environment. They are present in very precise amounts and any deviation from the concentration norm can have drastic effects on ecosystems and human health. For this reason, chemosensors that can selectively and sensitively detect and report on the presence of metal ions in solution are widely desired. This section will give details on the general design of metal ion sensors, beginning with examples of non-calixarene based metal ion sensors before discussing calixarene based metal ion sensors.

1.2.1 General Design of Metal Ion Sensors

An excellent review by de Silva *et al.* highlights the importance of the involvement of synthetic organic chemists in sensor design and manufacture. Their review highlights examples of “simple” and more intricate metal ion sensors.²⁴ The design of any sensor, whether it is to be used to detect a cation, anion or neutral species must deliver the same three criteria:

i) a receptor,

The receptor or binding site is the location where the analyte of interest interacts with the sensor.

ii) a reporter group

The reporter group is a functionality that must undergo a measurable change upon analyte binding such as absorbance or emission, **Figure 1.9.**²⁵

iii) a linker group.

The linker group or molecular scaffold is the framework that must hold the binding site and reporter unit in the desired orientation; it can take various forms, from a simple linker, as in the pictorial representation below, to a complex framework.

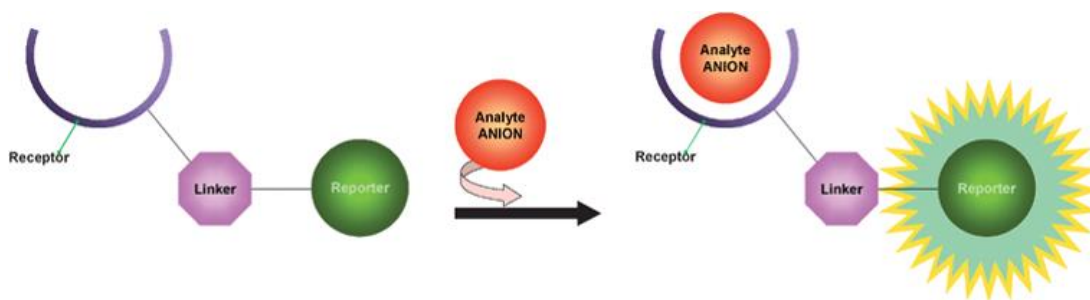


Figure 1.9: Schematic showing the recognition of an analyte by a chemosensor.²⁵

1.2.2 Non-Calixarene Based Metal Ion Sensors

Sensitive and inexpensive methods that give real-time results are essential for the detection of heavy metal ions from aqueous samples in environmental and biological fields. In one such example Suresh *et al.* designed and synthesised a cyclodextrin based probe for Fe^{3+} and Ru^{3+} detection, **Figure 1.10**.²⁶ When *p*-nitrophenol is added to a solution containing *per*-6-amino- β -cyclodextrin, an inclusion complex is formed and the solution changes from colourless to an intense yellow. The colour change occurs due to the presence of the *p*-nitrophenolate anion, formed by abstraction of the phenolic proton by an amino group of the cyclodextrin. It was hypothesised that in the presence of a suitable cation the protonation/deprotonation process may be reversed and *p*-nitrophenol regenerated, thereby creating a colourimetric cation sensor. Aqueous solutions of fourteen mono-, di- and trivalent metal ions were examined and the change from yellow to colourless was observed only with Fe^{3+} and Ru^{3+} . Thus the presence of Fe^{3+} and Ru^{3+} can be determined colourimetrically and spectrophotometrically.

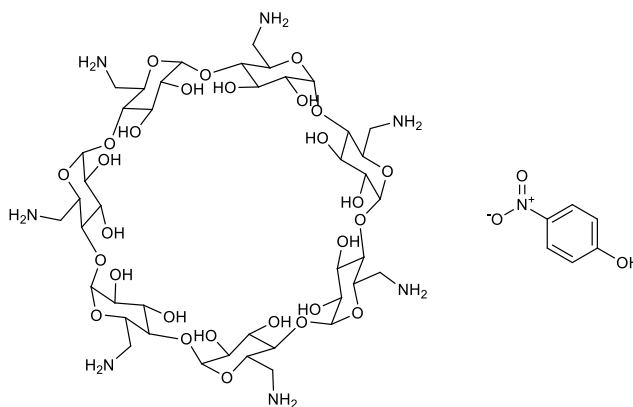


Figure 1.10: *Per*-6-Amino- β -cyclodextrin and 4-nitrophenol used for the naked eye detection of Fe^{3+} and Ru^{3+} .²⁶

Cryptands are another well-known sub-group of macrocyclic ligands. They have hollow inner cavities along with nitrogen and oxygen donor atoms available to act as efficient binding sites. In the late 1990s Ghosh *et al.* designed and synthesised three heteroditopic cryptands with different cavity sizes which were capable of detecting and reporting on the presence of the lanthanide ions Eu^{3+} and Tb^{3+} , as well as transition metal and Pb^{2+} ions.²⁷ The supramolecular structures were designed with anthracene reporter units attached to the three secondary amino groups of each cryptand, **Figure 1.11**. The anthracene moieties of the hosts showed no fluorescence emission due to a photoinduced intramolecular electron transfer (PET) between them and the lone pairs on the amino nitrogen atoms. However, in the presence of an analytical quantity of a suitable transition metal ion, such as Cu^{2+} or Ni^{2+} , a fluorescence signal emerged. The signal arose since the nitrogen lone pairs, formerly involved in PET, became involved in metal ion complexation. In the absence of a PET mechanism the anthracene units fluoresce. Of the three trianthryl derivatised cryptands investigated, the one with the smallest cavity size, **Figure 1.11a**, was capable of distinguishing between Eu^{3+} and Tb^{3+} in solution.

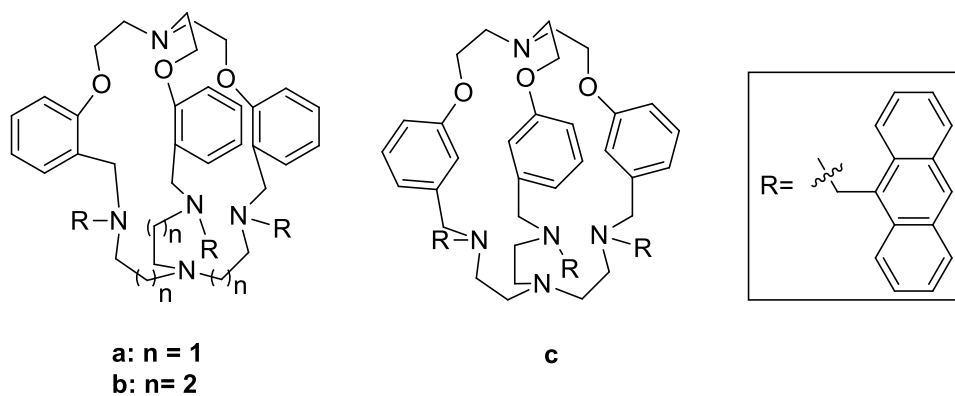


Figure 1.11: Three trianthryl derivatised cryptands of various cavity sizes designed by Ghosh *et al.* for lanthanide and transition metal ion detection.²⁷

An interesting class of crown ether platinum(II) alkynyl terpyridine complexes were designed and synthesised by Tang *et al.*, **Figure 1.12**.²⁸ They investigated their complexation abilities with alkali, alkaline earth and transition metal ions using fluorescence spectroscopy. Complex **1** shows an enhancement of the fluorescence emission on binding with Mg^{2+} and Ca^{2+} , while complex **2** which shows a purple colour in MeCN in the absence of metal ions, changes to various distinct shades of orange,

yellowish-brown or yellow when introduced to the triflate salts of Li^+ , Na^+ , Mg^{2+} , Ca^{2+} , Cd^{2+} and Zn^{2+} .

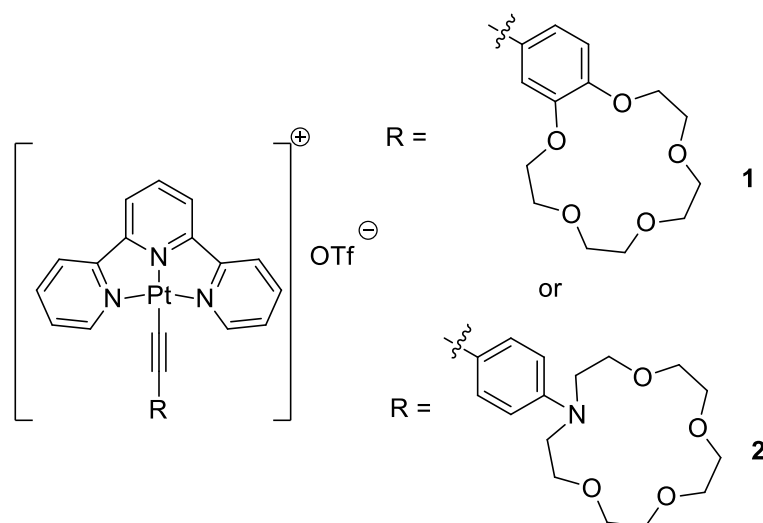


Figure 1.12: Crown ether platinum(II) alkynyl terpyridine triflate salt complexes used for the detection of alkali, alkaline earth and transition metal ions.²⁸

1.2.3 Calixarene Based Metal Ion Sensors

There is a plethora of excellent literature on calixarenes as metal ion sensing agents.²⁹⁻³¹ Beer *et al.* have demonstrated that a calix[4]arene functionalised with lower rim acid and amide groups can be used to extract toxic metal ions, including lanthanide ions, from aqueous solutions containing low levels of nuclear waste.³² They hypothesised that the introduction of an electroactive ferrocene moiety to the framework could provide an electrochemical sensing handle.³³ The monomeric ferrocene derivative, **Figure 1.13**, showed anodic potential shifts of up to 60 mV upon the addition of one equivalent of lanthanide ions, while ferrocene-bridged calixarene dimers underwent much larger shifts of up to 200 mV in the presence of the same relative amount of lanthanide ions.

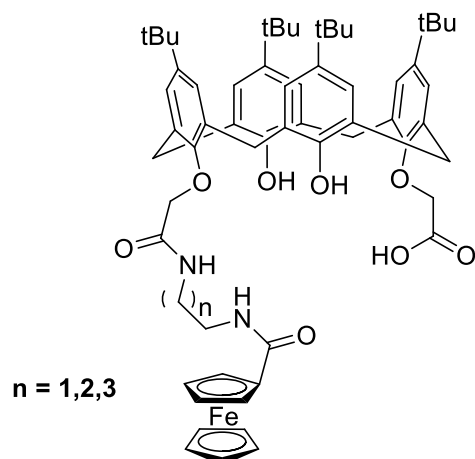


Figure 1.13: Monomeric ferrocene derivatised calix[4]arenes used for the detection of trivalent lanthanide ions.³³

Dublin based researchers Nolan and Diamond were amongst the first to design analytical sensors for soft metal ions utilising coordinating nitrile functional groups, **Figure 1.14**.³⁴ Host:guest interactions were monitored by Ion Selective Electrode (ISE) based potentiometry and selectivity with sensor **a** was observed for Hg^{2+} and Ag^+ cations amongst a range of thirteen cations studied. In order to tune the cation coordination abilities of their sensors, electron delocalising aromatic groups were positioned proximal to the nitrile groups, **Figure 1.14b**. This structural modification resulted in suppression of the Hg^{2+} cation complexation and thus produced a selective and sensitive sensor for Ag^+ cations.

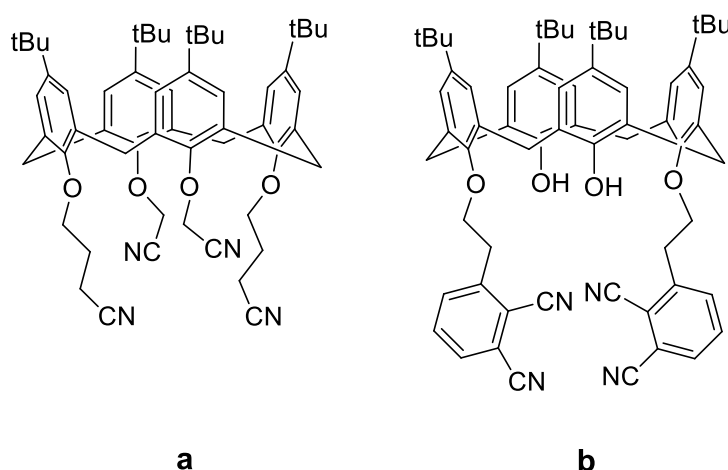


Figure 1.14: Nitrile functionalised calixarenes used for the electrochemical detection of **a)** Hg^{2+} and Ag^+ and **b)** Ag^+ ions.³⁴

An optical sensor for heavy metal ion detection based on a fiber coated with an immobilised azo-bearing chromogenic calix[4]arene has been designed by Benounis *et al.*, **Figure 1.15**.³⁵ The calixarene functions as a complexing agent *via* the nitrogen atoms of the amide groups. It was found that the light intensity output from the optical fiber increased in proportion to the concentration of metal ions present. The system was suitable for the detection of Cu^{2+} , Co^{2+} and Cd^{2+} to limits of $1\ \mu\text{M}$, $1 \times 10^{-3}\ \mu\text{M}$ and $1 \times 10^{-4}\ \mu\text{M}$ respectively. The lifetime of the sensor was shown to be greater than eight months.

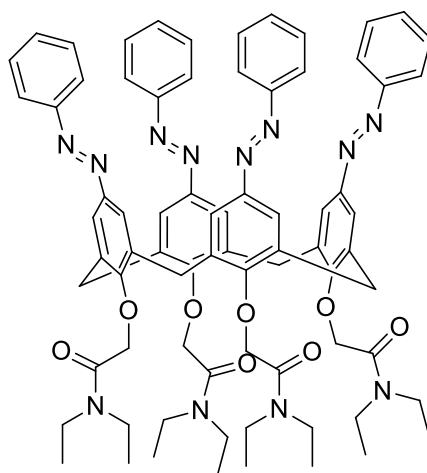


Figure 1.15: Chromogenic *p*-tetrakisphenylazocalix[4]arene *tetra*-amide derivative used for sensing Cu^{2+} , Co^{2+} and Cd^{2+} ions.³⁵

1.3 Fluorescence Spectroscopy Overview

This section will give a brief overview of the principles behind fluorescence spectroscopy, the structure of fluorophores and the detection of analytes by fluorescence spectroscopy.

1.3.1 Basic Principles of Fluorescence Spectroscopy

Luminescence is the emission of light from a substance in an electronically excited state occurring independently of temperature. Fluorescence and phosphorescence are specific forms of luminescence.

At standard temperature and pressure (STP) conditions most molecules will occupy the lowest vibrational level (ν_0) of their ground electronic state (S_0). When a photon of light energy is absorbed, the absorbing species is elevated to produce excited

electronic states (S_n , $n > 0$). For each excited state there are a number of vibrational levels. Excited species relax through a number of processes including intramolecular charge transfer, conformational change, energy transfer, excimer formation and internal conversion. Excited state molecular collisions cause the molecule to lose energy and relax to the lowest vibrational level of the excited state (vibrational relaxation). From there the molecule can return to the ground electronic state, emitting light energy in the form of fluorescence. Intersystem crossing involves a “forbidden” transition from a singlet excited state to a triplet excited state ($S_n \rightarrow T_n$, $n > 0$). Relaxation of the molecule from the triplet excited state to the ground state results in the emission of light as phosphorescence. These various processes are represented in the Jablonski diagram shown in **Figure 1.16**.

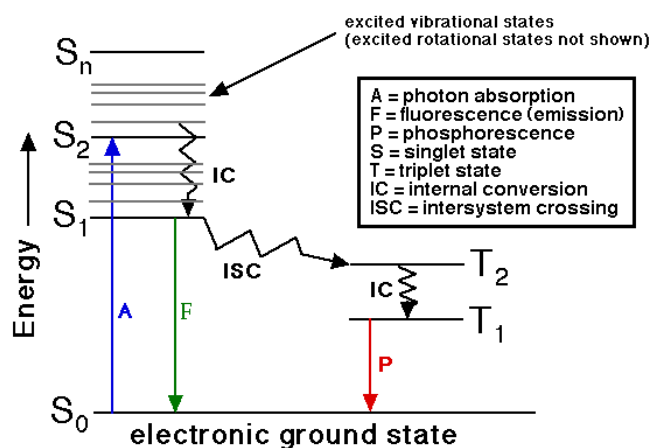


Figure 1.16: Jablonski diagram showing the transitions giving rise to absorption (A), fluorescence (F) and phosphorescence (P) emission spectra.³⁶

As is apparent in the Jablonski diagram, the energy of the emission is typically less than that of absorption and thus fluorescence typically occurs at lower energies, or longer wavelengths, than the excitation light. Thus, the difference in energy between the absorbed and emitted photons allows them to be distinguished from each other. Irish physicist George Stokes was one of the first to observe the difference between the band maxima of the absorption and emission spectra of the same electronic transition which subsequently became known as the Stokes shift, **Figure 1.17**.³⁷

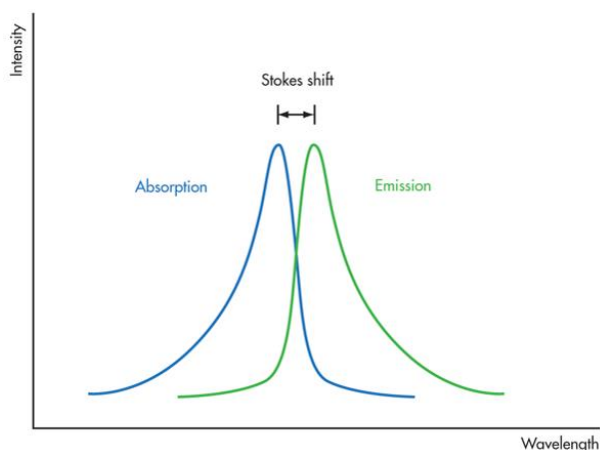


Figure 1.17: Generic absorption and emission spectra showing the Stokes shift between their band maxima.³⁷

1.3.2 Fluorophore Overview

A fluorophore is a molecule, or a unit within a molecule, that can emit fluorescent light following excitation from light of a particular wavelength. A fluorophore typically contains several fused aromatic rings. The efficiency of a fluorophore is measured by a number of characteristics including the fluorescence quantum yield (Φ), fluorescence lifetime (τ) and Stokes shift.

The fluorescence quantum yield (Φ) measures the ratio of photons emitted to photons absorbed to a maximum value of 1, this value can be used to compare the fluorescence efficiency of a fluorophore. The fluorescence lifetime (τ) refers to the duration that a fluorophore remains in the excited state before returning to the ground state, this can vary from picoseconds to hundreds of nanoseconds (10^{-12} – 10^{-9} s). A large Stokes shift can indicate the efficiency of a fluorophore as it allows for differentiation between absorbed and emitted photons.

The following section will give a brief overview of some commonly encountered fluorophores.

1.3.2.1 Common Fluorophores

Naphthalene, anthracene, coumarin, fluorescein and pyrene are among the most commonly encountered fluorophores, **Figure 1.18**.

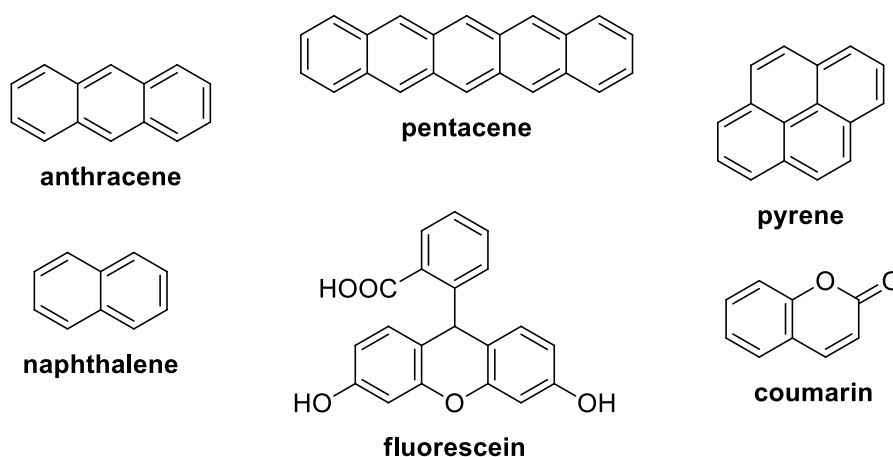


Figure 1.18: Structures of commonly encountered fluorophores.

Naphthalene, mostly obtained from coal tar, consists of two fused rings. It is classed as a polycyclic aromatic hydrocarbon (PAH). Generally as the degree of conjugation increases, the wavelengths of absorption and fluorescence also increase. Thus, pentacene, with five linearly fused rings, emits in the red region, while naphthalene emits in the UV region of the electromagnetic spectrum, **Figure 1.19**.³⁸

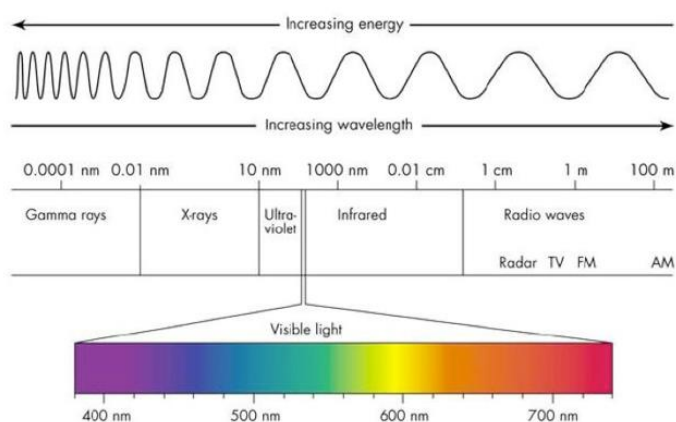


Figure 1.19: Diagram of the electromagnetic spectrum showing the colours making up the visible light region.³⁹

Anthracene comprises three linearly fused aromatic rings and, like naphthalene, it is most commonly extracted from coal tar. Anthracene is colourless but when excited with ultraviolet light it emits fluorescence in the blue region of the electromagnetic spectrum. An extensive range of substituents have been introduced to the anthracene framework and the fluorescence emission of the resulting derivatives

cover the entire visible spectrum. For example, 9,10-bis(*p*-dibutylaminostyryl)-2,6-bis(*p*-*t*-butylstyryl)anthracene emits red light (632 nm), **Figure 1.20a**,⁴⁰ while a series of 1,8-diaryl substituted anthracenes emit in the blue region, **Figure 1.20b**.⁴¹ Substituted anthracenes are recognised as highly efficient light emitting materials and have been incorporated in organic light emitting diodes (OLED)⁴² which find application in a variety of devices, for example mobile phones, car stereos, digital cameras and white solid state lighting.

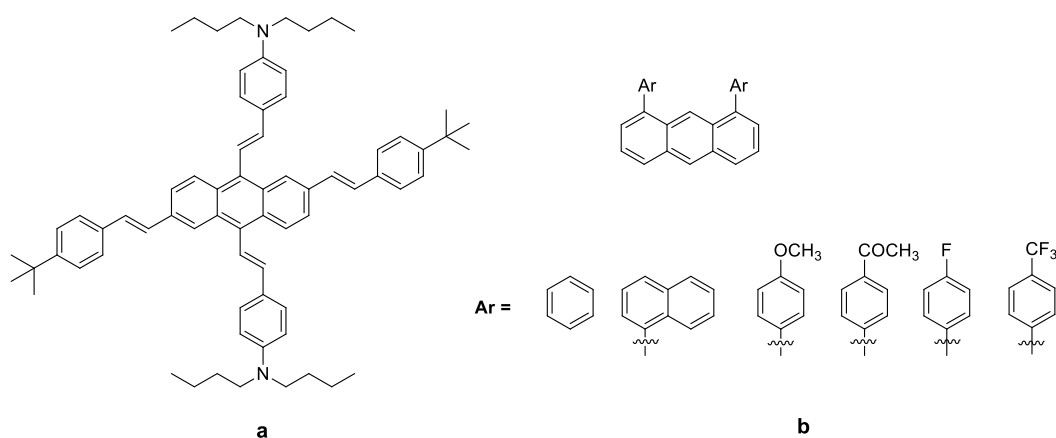


Figure 1.20: **a)** 9,10-Bis(*p*-dibutylaminostyryl)-2,6-bis(*p*-*t*-butylstyryl)anthracene capable of emitting red light⁴⁰ and **b)** 1,8-diaryl anthracene derivatives capable of emitting blue light.⁴¹

Coumarin is a member of the benzopyrone family, it is fluorescent but with low quantum yield. Efficiency can be improved by appropriate substitution. Fluorescence emission in the blue-green visible light region is produced by substituted coumarins. A number of methyl derivatives have been utilised as efficient pH indicators showing a large variation in fluorescence intensity with respect to pH, **Figure 1.21**.³⁸

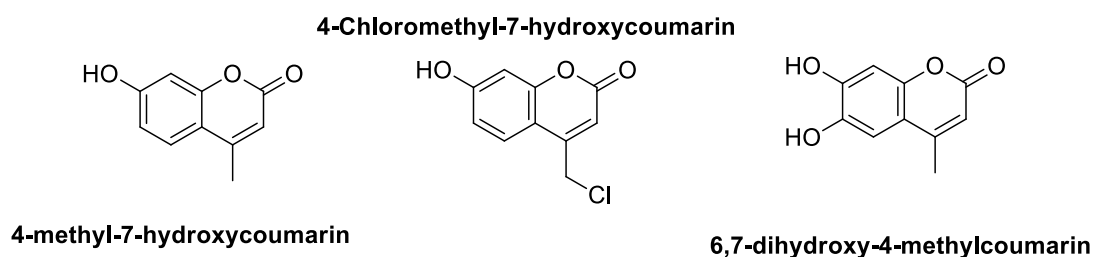
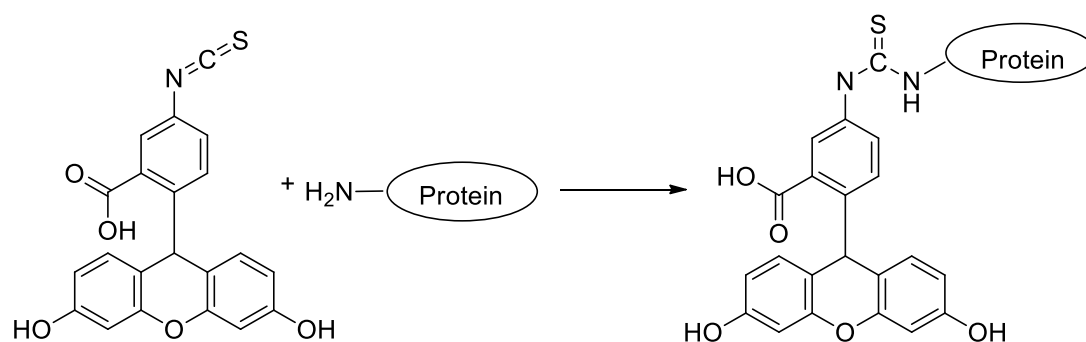


Figure 1.21: Structures of substituted coumarins used as fluorescent pH probes.³⁸

Fluorescein was first prepared by reacting phthalic acid and resorcinol over a zinc catalyst. It is red in colour and emits fluorescent light in the green region of the electromagnetic spectrum. It is one of the most commonly used fluorescent dyes with recent applications in neurosurgery, dermatology and endomicroscopy.⁴³ The isothiocyanate derivative is commonly used to attach fluorescein to molecules of biological interest such as antibodies or proteins by nucleophilic attack on the central electrophilic carbon of the isothiocyanate group, **Scheme 1.5**. This allows for fluorescence microscopy imaging techniques to be used in disease diagnosis.



Scheme 1.5: General scheme for a protein labelling reaction using fluorescein isothiocyanate (FITC).

1.3.2.2 Pyrene

Pyrene is a planar molecule with four fused rings, it makes up approximately 2% of coal tar. Upon excitation at an appropriate wavelength it displays monomer emissions between 380 to 420 nm; if two pyrenes are in close contact such as in a concentrated solution, excimer emission will be observed in the range 410 to 500 nm. The potential to form inter- or intramolecular pyrene excimers is due to the relatively long fluorescence lifetime, ~410 ns for excited state pyrene units.

1.3.3 Detection of Analytes using Fluorescence Spectroscopy

Fluorescence spectroscopy is a popular method for analyte detection due to the intrinsic sensitivity, selectivity, rapid response time, low cost and the possibility of *in situ* monitoring. Using an appropriate hosting molecule the detection of cations, anions and neutral species is possible, if a reporting fluorophore is built into the sensor. In analyte sensing by fluorescence spectrometer, the recognition event can

involve a number of photoinduced processes including energy transfer, excimer formation or electron transfer.

1.3.4 Energy Transfer

Fluorescence resonance energy transfer (FRET), also known as Förster resonance energy transfer (FRET) is a mechanism of energy transfer between chromophores either intermolecularly, *i.e.* between separate light sensitive units or intramolecularly, *i.e.* between two light sensitive functional groups within one molecule. One molecule, or functional group, acts as a donor (transfers energy) and the other as an acceptor, or quencher (accepts energy). If the emission spectrum of the donor overlaps with the absorption spectrum of the acceptor, energy transfer will occur. The efficiency of the energy transfer depends on the distance between the donor and the acceptor, the relative orientation of the dipole moments and the degree of spectral overlap. Ono *et al.* designed a FRET based sensor for mercury ions in aqueous solutions. An oligonucleotide chain with two Hg^{2+} binding sequences separated by a linker, with a fluorescein fluorophore at the 3'-terminus and a non-fluorescent dabcyI quencher moiety at the 5'-terminus, **D-ODN-F**, **Figure 1.22**.⁴⁴ On binding with Hg^{2+} ions the oligonucleotide forms a hairpin structure and FRET occurs between the fluorescein and dabcyI moieties. No fluorescence quenching occurs with a range of ten other metal ions, thus the sensor is selective for Hg^{2+} ion detection.

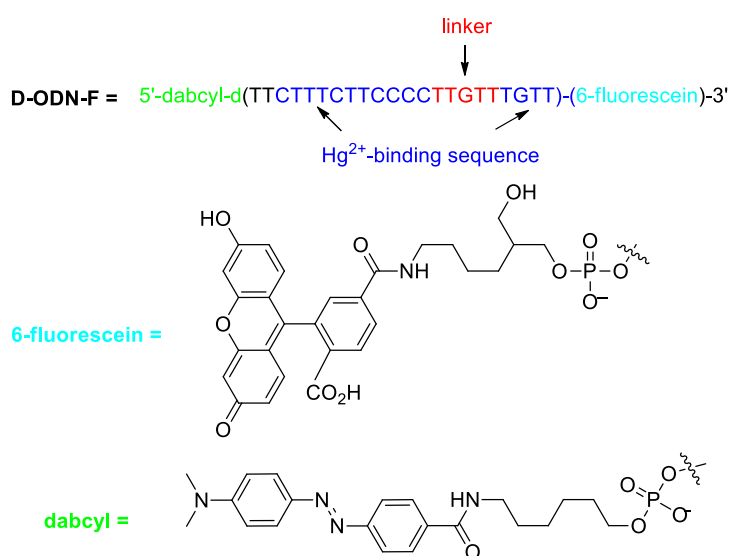


Figure 1.22: FRET based oligonucleotide sensor for Hg^{2+} with fluorescein donor and dabcyI acceptor moieties.⁴⁴

1.3.5 Excimer Formation

Birks has defined an excimer as a “dimer which is associated in an electronic excited state and which is dissociated in its ground state”.⁴⁵ Excimer emission results when one molecule/fluorophore in the excited state interacts with a second molecule/fluorophore in the ground state. The general equation for the formation of an excimer (E^*) is shown in **Equation 1.1**.



M is the fluorophore in the ground state.

M^* is the fluorophore in the first excited singlet state.

The ability of a fluorophore to form excimers is related to its fluorescence lifetime as this determines the time available for the excited fluorophore to interact with a second fluorophore in the ground state. This type of excimer is classified as a dynamic excimer.

For a given fluorophore the energy change associated with excimer emission is smaller than that for the monomer emission and thus excimer bands will occur at longer wavelengths than the monomer bands.

A fluoroionophore can be designed to contain two intramolecular fluorophores capable of excimer formation. If a binding event, such as metal cation complexation, affects the separation of the fluorophores, then changes to the intensity of the excimer emission signal can be used to monitor the presence and quantity of metal ions present. Ghosh *et al.* designed and synthesised a simple anthracene-ligated benzimidazole diamide fluorescent sensor capable of excimer emission due to the closely spaced anthracene fluorophores, **Figure 1.23**.⁴⁶ A binding induced destruction of the excimer signal was observed in the presence of organic sulphonic acids and Cu^{2+} cations.

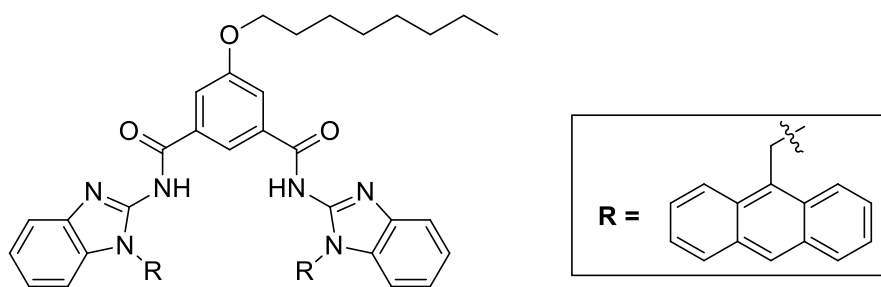


Figure 1.23: Anthracene-ligated benzimidazole diamide fluorescence sensor for Cu^{2+} cations and sulphonic acids.⁴⁶

1.3.6 Photoinduced Electron Transfer

Photoinduced electron transfer (PET) involves an electron transfer from a donor, in the ground or excited electronic state, to an acceptor in the opposite state. Either the donor or the acceptor can be the fluorophore. The general equations for PET processes are shown in **Equations 1.2** and **1.3**. Generally PET sensors do not fluoresce. However, in the presence of an analyte of interest PET can be shut down and the excited state energy emitted as fluorescence.



A is an acceptor molecule or functional group, D is a donor molecule or functional group and * denotes an excited state.

An effective acid sensor that exploits PET was designed and utilised by de Silva *et al.*, **Figure 1.24**.⁴⁷ In the host molecule the diethylamino functionality transfers an electron to the excited state aminonaphthalimide eliminating the possibility for fluorescence emission. In the presence of H^+ ions the diethylamino group is protonated, blocking the PET pathway allowing for fluorescence emission.

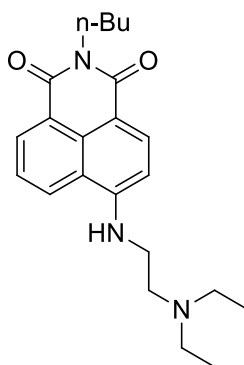


Figure 1.24: PET based proton sensor developed by de Silva *et al.* with a naphthalene acceptor and a diethylamino donor group.⁴⁷

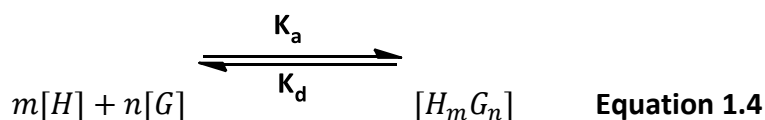
1.4 Analysis of Host:Guest Binding Events

This section will give an overview of the various techniques available for the analysis of host:guest binding events, such as determination of the stoichiometry of a binding event using Job's method, analysis of the quenching mechanism of a host:guest system using Stern-Volmer analysis and determination of the association constant, K_a of a binding event using the Benesi-Hildebrand method.

1.4.1 Determination of Host:Guest binding Stoichiometry: Job's Method (Method of Continuous Variation)

Job's Method of Continuous Variation, also known as a Job's Plot, is an easy and common method for the determination of the reactant stoichiometry of chemical equilibria such as host:guest interactions.⁴⁸ This method is named after Paul Job's 1928 approach to the characterisation of host:guest associations.⁴⁹

Host:Guest equilibria is shown in **Equation 1.4**.



$[H]$, $[G]$ and $[HG]$ are the concentration of the host and guest species and host:guest complex respectively, where m and n are whole numbers. K_a and K_d are the association and dissociation constants respectively, given in **Equation 1.5** and **Equation 1.6**.

$$K_a = \frac{[HG]}{[H][G]} \quad \text{Equation 1.5}$$

$$K_d = \frac{[H][G]}{[HG]} \quad \text{Equation 1.6}$$

Job showed that a plot of the intensity of the UV absorption of the host species (H) at a given wavelength, against the mole fraction, χ_a , of the additive [a, or guest, (G)], can be used to determine the stoichiometry of the binding event. At the point of maximum change of the Job's plot, the mole fraction reflects the value of the stoichiometric ratio of the binding event. In order to construct a Job's plot, the total molar concentration of the binding partners is kept constant, whilst their mole fraction is varied. An observable change that occurs following complex formation, typically absorbance or fluorescence emission intensity, is plotted against the mole fraction of either of the binding components. The mole fraction of the host species, χ_H , in a host:guest sample is given in **Equation 1.7**:

$$\chi_H = \frac{[H]}{[H]+[G]} \quad \text{Equation 1.7}$$

Job's original study involved varying the mole fraction of $\text{Tl}(\text{NO}_3)$ in a $\text{Tl}(\text{NO}_3)/\text{NH}_3$ solution and plotting the change in UV absorbance against the mole fraction, χ_H . This gave a symmetrical, $-x^2$ shaped plot with a maximum at $\chi_a = 0.5$. Examination of the equation for the mole fraction (**Equation 1.7**) reveals that a value of 0.5 occurs when equal concentrations of host and guest are present, thus Job concluded that a 1:1 complex had formed. Higher order complexes such as 2:2 or n:n, also produce symmetrical curves with the maximum or minimum at $\chi_H = 0.5$, but they have a subtle bell shape.⁵⁰

If the Job's plot shows a maximum change at $\chi_H = 0.33$, there is double the amount of guest w.r.t. host present in solution indicating a complex of the form HG_2 formed in solution. These plots have been shown experimentally to display a sigmoidal curvature on the right side of the graph.⁵¹ While complexes of the form HG_2 have been verified by the Job's plot method,⁵² they can be difficult to view experimentally and may need computer aided fitting programs.⁵¹

Conversely, a Job's plot which shows a maximum change at $\chi_H = 0.66$, this indicates that double the amount of host w.r.t. guest was present in solution, indicating a complex of the form H_2G formed in solution.

1.4.2 Stern-Volmer Analysis

The Stern-Volmer relationship, first derived and published by Otto Stern and Max Volmer in 1919,⁵³ can be used to analyse fluorescence quenching and study molecular interactions of a host:guest system. Quenching is any process which decreases the fluorescence intensity and it can occur by a number of methods, of which dynamic and static quenching are predominant. Dynamic quenching, also called collisional quenching, occurs when the fluorescent species collides with a quencher without the formation of a complex. Static quenching occurs when a fluorescent unit and a quencher form a complex in the ground state which prevents fluorescence emission from occurring. Only static quenching is significant for supramolecular binding studies.

Dynamic quenching follows the Stern-Volmer equation, **Equation 1.8**.

$$\frac{I_0}{I} = 1 + K_{SV}[Q] \quad \text{Equation 1.8}$$

I_0 is the fluorescence intensity in the absence of a quencher, I is the fluorescence intensity upon the addition of a quencher, $[Q]$ is the concentration of quencher present in the solution and K_{SV} is the Stern-Volmer quenching constant.

The magnitude of Stern-Volmer constants (K_{SV}) for a given host:guest system can be used to provide information on the association. When all other variables are held constant, high K_{SV} values are associated with guests that can cause quenching at low concentrations.⁵⁴

The magnitude of Stern-Volmer constants vary significantly. Khoumeri *et al.* reported a K_{SV} of $9.9 \times 10^4 \text{ M}^{-1}$ for the interaction of 1,4-dimethoxy-2,3-dibromomethyl anthracene-9,10-dione with silver nanoparticles in MeOH, **Figure 1.25a**,⁵⁵ while Rao *et al.* reported a significantly larger K_{SV} , $4.76 \times 10^5 \text{ M}^{-1}$, for the interaction of their triazole anthracene functionalised calix[4]arene with Co^{2+} perchlorate ions in EtOH, **Figure 1.25b**.¹⁸

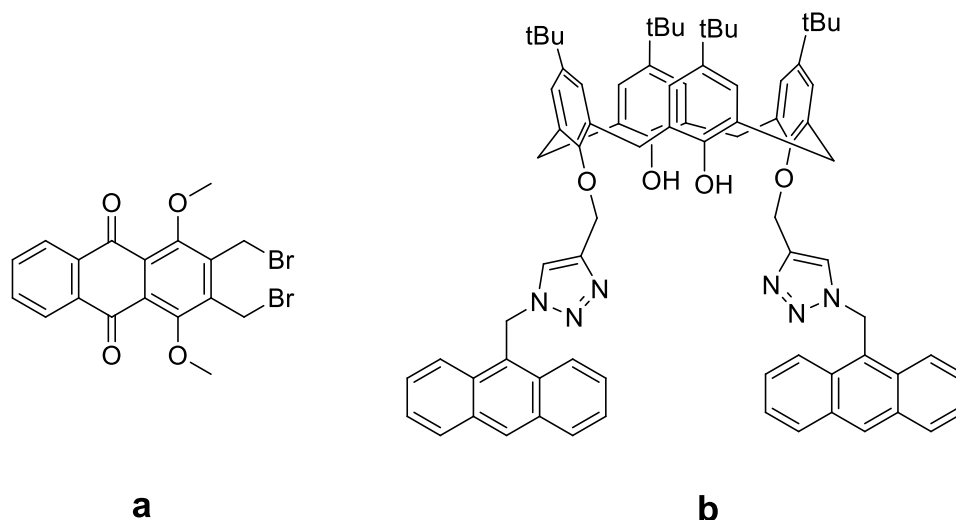


Figure 1.25: Structures of **a)** 1,4-dimethoxy-2,3-dibromomethylanthracene-9,10-dione⁵⁵ and **b)** triazole-linked anthracenyl-appended calix[4]arene.¹⁸

If quenching occurs purely by a dynamic process, then a plot of $\frac{I_0}{I}$ vs. $[Q]$ will produce a linear graph with K_{SV} equal to the slope of the line.

Unfortunately, pure 1:1 static quenching follows a nearly identical relationship as dynamic quenching, **Equation 1.9**.

$$\frac{I_0}{I} = 1 + K_a[Q] \quad \text{Equation 1.9}$$

Where K_a is the association or binding constant between the host and guest. Therefore the slope of a Stern-Volmer plot that follows pure static quenching corresponds to the binding constant for complex formation, **Equation 1.5**. The size of K_a indicates the equilibrium between the concentrations of the host:guest complex and individual host and guest moieties in solution. Larger values indicate that the equilibrium lies to the right, *i.e.* in favour of the complex.

Unfortunately, a linear graph of $[Q]$ against $\frac{I_0}{I}$ does not discriminate between purely dynamic or purely static quenching. In such cases analysis of the fluorescence lifetimes or temperature dependant fluorescence studies must be used to discriminate between the possible quenching modes.

In the case of pure static quenching the fluorescence lifetime of the sample will remain unchanged, under variable temperature conditions, since those fluorophores

which are not complexed, are able to emit after excitation and have normal excited state properties.

In contrast, a rise in temperature would theoretically increase dynamic quenching, while having little or no effect on static quenching. This is due to the increase in the random motion of the molecules in solution due to the temperature rise which would increase the occurrence of random collisions between the fluorophore and quencher moieties.

A Stern-Volmer plot that displays an upwards curvature indicates that the quenching mechanism is a combination of dynamic and static quenching.

1.4.3 Benesi-Hildebrand Analysis

The Benesi-Hildebrand method, introduced in 1949, can be used to determine the binding or association constant, K_a , of host:guest interactions.⁵⁶ Benesi and Hildebrand used the absorption changes observed upon the interaction of iodine with various aromatic hydrocarbons to calculate the K_a for the interactions.

The concentration of the free host, $[H]$, at any given time in a host and guest containing solution is the difference between the initial concentration of the host, $[H]_0$, and the concentration of the host:guest complex, $[HG]$, **Equation 1.10**.

$$[H] = [H]_0 - [HG] \quad \text{Equation 1.10}$$

Combining **Equations 1.5** and **1.10** gives **Equation 1.11**.

$$K_a = \frac{[HG]}{[H][G]} = \frac{[HG]}{[G]([H]_0 - [HG])} \quad \text{Equation 1.11}$$

Rearranging **Equation 1.11** gives **Equation 1.12**.

$$K_a([G]([H]_0 - [HG])) - [HG] = 0 \quad \text{Equation 1.12}$$

Rearranging **Equation 1.12** for $[HG]$ gives **Equation 1.13**.

$$[HG] = \frac{[H]_0 K_a [G]}{1 + K_a [G]} \quad \text{Equation 1.13}$$

The Beer-Lambert law is given in **Equation 1.14**.

$$F = \epsilon l c \quad \text{Equation 1.14}$$

F is the fluorescence intensity, ϵ and c are the molar absorption coefficient and concentration of the species under investigation respectively, and l is the pathlength of the light. The Beer-Lambert law can be rewritten to give **Equation 1.15**, where b is a constant.

$$\Delta F = \Delta\epsilon[HG]b \quad \text{Equation 1.15}$$

Combination of **Equations 1.13** and **1.15** gives **Equation 1.16**.

$$\Delta F = \frac{b\Delta\epsilon[H]_0K_a[G]}{1+K_a[G]} \quad \text{Equation 1.16}$$

Rearrangement of **Equation 1.16** gives the Benesi-Hildebrand equation, **Equation 1.17**.

$$\frac{1}{\Delta F} = \frac{1}{b\Delta\epsilon[H]_0K_a[G]} + \frac{1}{b\Delta\epsilon[H]_0} \quad \text{Equation 1.17}$$

A Benesi-Hildebrand graph is constructed by plotting $\frac{1}{\Delta F}$ vs. $\frac{1}{[G]}$. From this plot, the K_a can be determined by dividing the intercept of the resulting line by the slope. Thus Benesi-Hildebrand analysis can be used for direct calculation of the K_a of a host:guest binding event and the Stern-Volmer approach can be used for the analysis of the quenching mechanism and determination of the quenching constant, K_{SV} .

1.5 Sensing Applications Involving Pyrene Fluorophores

A pyrene based adenosine triphosphate (ATP) fluorescent sensor was designed by Yoon *et al.*, **Figure 1.26**.⁵⁷ The water-soluble sensor contains four imidazole groups as phosphate anion receptors. The sensor undergoes excimer quenching and monomer enhancement in the presence of ATP. The measured quenching/enhancement ratio was significantly larger than that observed for the other biologically relevant nucleosides adenosine diphosphate (ADP) and adenosine monophosphate (AMP), thus creating a fluorescent sensor for investigations of ATP-relevant biological processes.

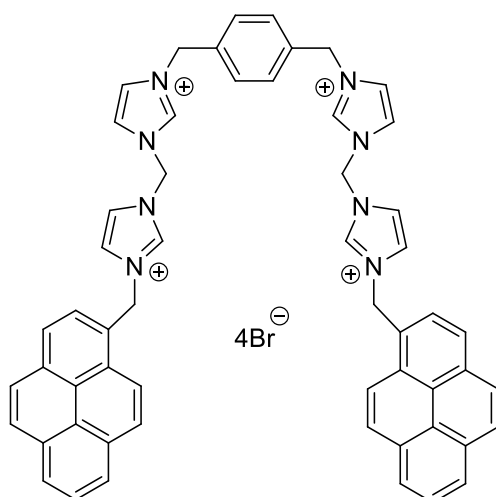


Figure 1.26: Pyrene imidazolium based fluorescent sensor for ATP.⁵⁷

The Ag^+ ion is highly toxic to aquatic organisms and can inactivate sulphhydryl enzymes and accumulate in the body.⁵⁸ Yoon *et al.* designed and synthesised a pyridine based sensor with two pendant pyrene moieties.⁵⁹ A strong excimer emission noted for the host-alone was significantly quenched in the presence of Ag^+ ions. The proposed binding site, **Figure 1.27**, suggests that the pyrene units are splayed apart upon Ag^+ binding preventing excimer formation. The Ag^+ binding event was investigated at a physiological pH (7.4), which means that this system can be utilised for biological applications.

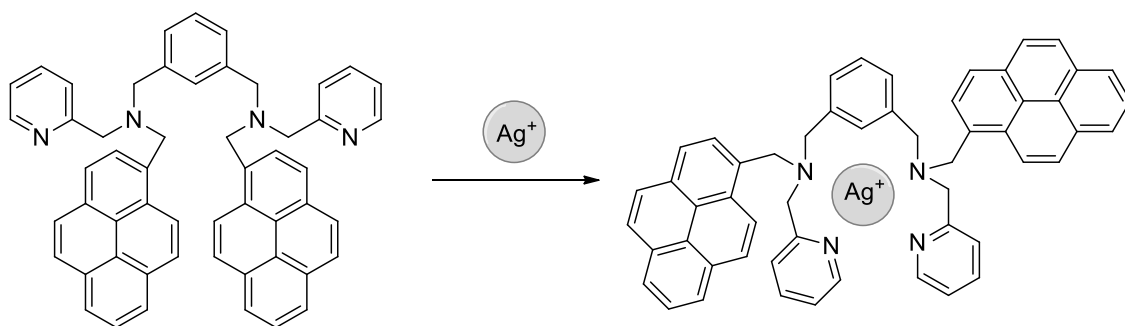


Figure 1.27: Proposed Ag^+ binding site of the pyridine-pyrene based fluorescent chemosensor designed by Yoon and co-workers.⁵⁹

Molecular recognition of substrates involved in biological processes is an important issue within supramolecular and analytical chemistry. Tryptophan (L-Trp) and histidine (L-His) are amino acids used for the biosynthesis of proteins which are not synthesised within the human body so they are a dietary essential. Abnormal levels

of either amino acid can have devastating effects, for example, chronic kidney disease is attributed to a deficiency of L-His.⁶⁰ Menon *et al.* designed and synthesised a calix[4]arene functionalised on the lower rim with two aminopyrene pendants which could be used for the selective and sensitive detection of L-His or L-Trp in blood serum samples, **Figure 1.28**. It was found that L-Trp enhances the fluorescence of the pyrene units by the PET mechanism whilst L-His causes quenching.

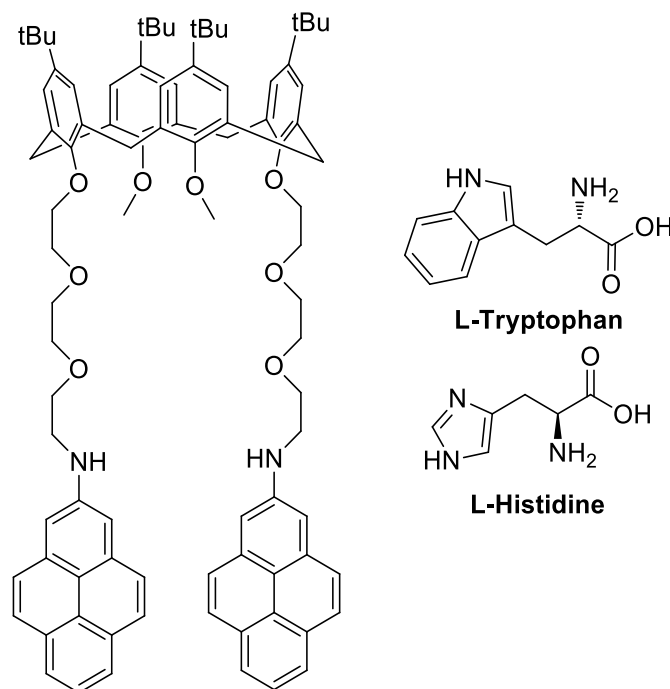


Figure 1.28: Bis-pyrene functionalised calix[4]arene fluorescent chemosensor for selective detection of the amino acids L-Histidine and L-Tryptophan.⁶¹

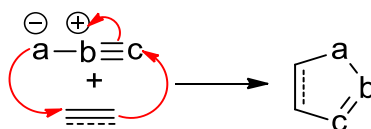
1.6 Click Chemistry Overview

Click chemistry, a term first introduced by Sharpless *et al.* in 2001, claims the ability to diversify chemical function through a few good reactions.⁶² Reactions must be modular, stereospecific, wide in scope and have simple experimental conditions in order to fall into this category. These criteria place an emphasis on green chemistry principles. This section will discuss 1,3-dipolar cycloadditions, copper-catalysed azide-alkyne cycloadditions (CuAAC), and formation and reactivity of nitrile oxides.

1.6.1 1,3-Dipolar Cycloadditions

The 1,3-dipolar cycloaddition reaction is popular in organic chemistry. It involves a combination of a 1,3-dipole and a dipolarophile to form a five-membered

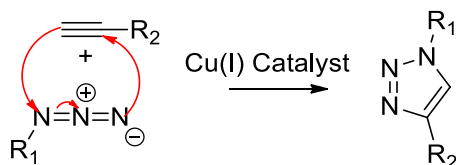
heterocycle, **Scheme 1.6**. A 1,3-dipole shares 4 electrons in a π system over 3 atoms. The first reported 1,3-dipolar cycloaddition was carried out between diazoacetic ester and α,β -unsaturated esters,⁶³ and in 1963 Huisgen published a systematic study of the 1,3-dipolar cycloaddition class⁶⁴ which subsequently became known as Huisgen cycloadditions.



Scheme 1.6: General scheme and mechanism of a 1,3-dipolar cycloaddition reaction.

1.6.2 Copper-Catalysed Azide-Alkyne Cycloaddition (CuAAC)

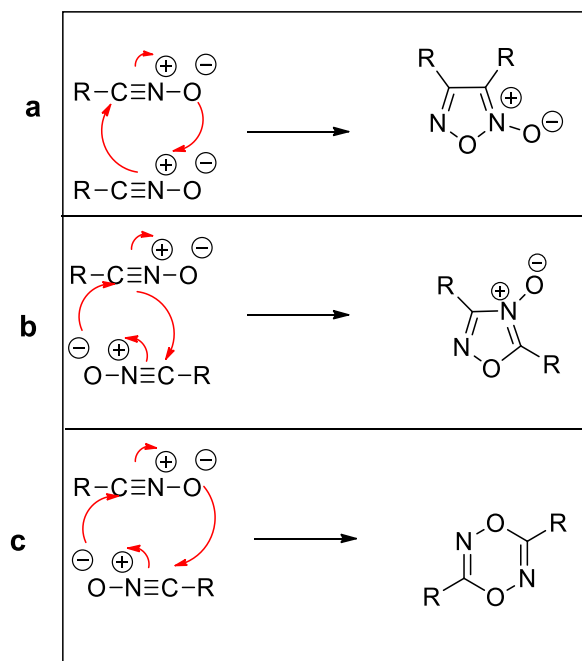
The classic click chemistry reaction is the copper-catalysed azide-alkyne cycloaddition (CuAAC) forming five-membered, 1,4-disubstituted, triazole rings, **Scheme 1.7**. While CuAAC reactions fulfil the definitions of click chemistry set out by Sharpless *et al.*, the reliance on a metal based catalyst can render them unsuitable for certain applications.



Scheme 1.7: Generic scheme and mechanism for a CuAAC reaction forming 1,4-disubstituted triazoles.

1.6.3 Nitrile Oxides

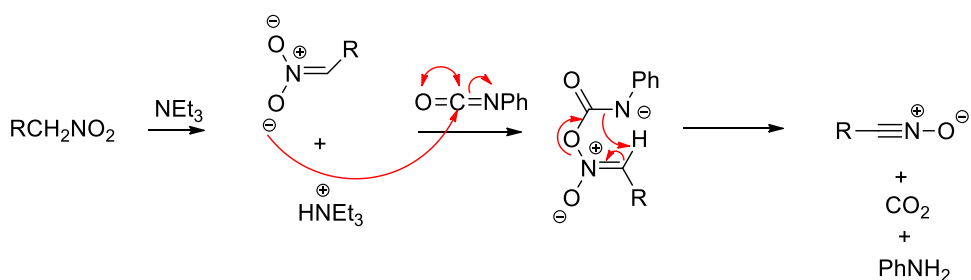
Most nitrile oxides are highly reactive and in the absence of a reacting partner they will undergo rapid self-reaction to give furoxans and dioxadiazines, **Scheme 1.8**.^{65,66} For this reason nitrile oxides required for cycloaddition chemistry are usually prepared with a trapping agent, such as an alkyne, *in situ*.



Scheme 1.8: Self-reaction of nitrile oxides to form furoxans (**a** and **b**) and dioxadiazines (**c**).^{65,66}

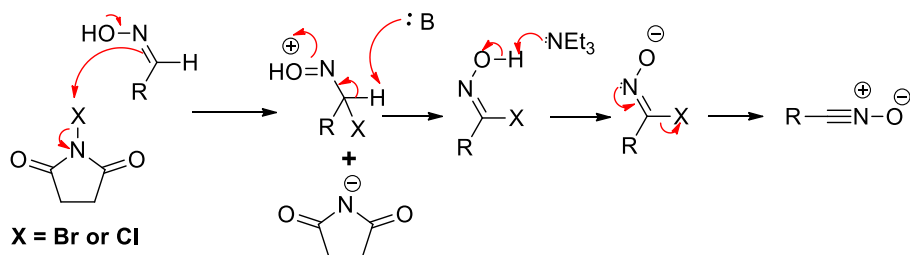
1.6.4 Generation of Nitrile Oxides

Nitrile oxides can be formed by a number of methods. The Mukaiyama procedure⁶⁷ involves the dehydration of a nitroalkane with an aryl isocyanate in the presence of a base, **Scheme 1.9**.



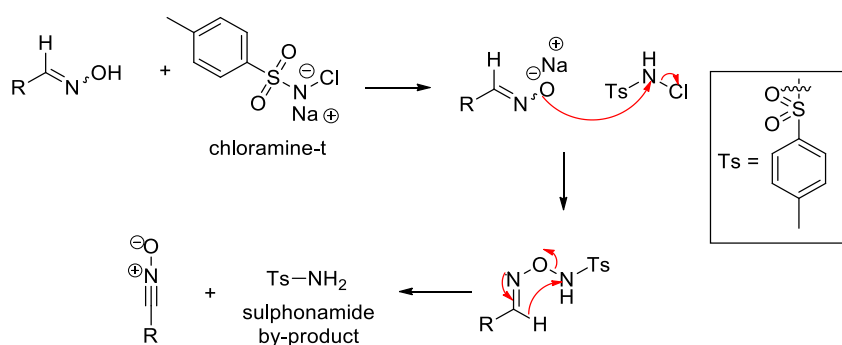
Scheme 1.9: Proposed mechanism for the Mukaiyama procedure for the generation of nitrile oxides from nitroalkanes.^{67,68}

Nitrile oxides can also be accessed from halooximes following treatment with a suitable base, often triethylamine. Halooximes are themselves formed from oximes using appropriate halogenating agents such as *N*-chlorosuccinimide (NCS) or *N*-bromosuccinimide (NBS), **Scheme 1.10**.⁶⁹



Scheme 1.10: Mechanism for the formation of nitrile oxides, starting with the conversion of an oxime to a halooxime.⁷⁰

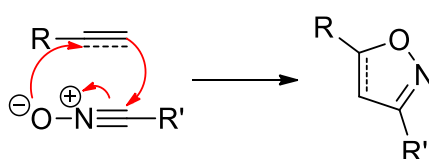
Nitrile oxides can also be formed by the reaction of the appropriate aldoxime with chloramine-T (Ch-T). Padmavathi *et al.* suggest this mechanism involves oxidative dehydrogenation initiated by deprotonation of the oxime OH proton, followed by nucleophilic substitution and finally elimination of a stoichiometric amount of tosyl amine, **Scheme 1.11**.⁷¹



Scheme 1.11: Mechanism proposed by Padmavathi *et al.* for Ch-T induced formation of nitrile oxides.⁷¹

1.6.5 1,3-Dipolar Cycloaddition of Nitrile Oxides

Addition of nitrile oxides to alkenes or alkynes leads to the formation of isoxazolines or isoxazoles respectively, **Scheme 1.12**. A recent review by Heaney highlights the importance of the nitrile oxide/alkyne cycloaddition (NOAC) as a catalyst-free synthetic route to heterocyclic rings.⁷²



Scheme 1.12: General mechanism for a 1,3-Huisgen click cycloaddition leading to formation of isoxazolines or isoxazoles.

1.6.6 Isoxazole Heterocyclic Ring

The isoxazole ring is a five membered aromatic heterocyclic ring containing adjacent oxygen and nitrogen atoms, **Figure 1.29a**. It can be found in natural products; *e.g.* ibotenic acid, **Figure 1.29b**. A number of amino functionalised derivatives show anti-tumour activity, *e.g.* **Figure 1.29c**.⁷³

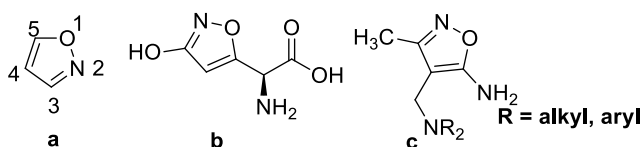


Figure 1.29: a) Heterocyclic isoxazole ring with numbering system, b) structure of ibotenic acid and c) general structure of amino functionalised isoxazole family shown to be effective antitumour agents.⁷³

1.7 Isoxazoles as Metal Binding Sites

Isoxazole rings are considered to be relatively weak electron donors, however complexes with numerous metal ions, predominantly M^{2+} , have been described.⁷⁴⁻⁷⁶ The nitrogen, and to a lesser extent the oxygen atoms, provide potential metal complexation sites.

Ponticelli *et al.* found the parent isoxazole and 3,5-dimethylisoxazole capable of forming complexes of the form ML_2X_2 , involving N-donation to Pd^{2+} and Pt^{2+} ions. Complexes of the form MLX_2 involved both N- and O-donation, where $X = Cl$ or Br .⁷⁷ Metal complexes of Cu^{2+} , Ag^+ , Zn^{2+} , Cd^{2+} , Hg^{2+} , Cr^{3+} , Mn^{2+} , Fe^{2+} , Co^{2+} and Ni^{2+} ions have also been reported.⁷⁴ A series of ML_2 hydrazone complexes were formed with an isoxazole functionalised dimethyl barbituric acid ligand and investigated as optical recording materials for the recordable blu-ray disc system, **Figure 1.30**.⁷⁸ ML_2 complexes were formed with Ni^{2+} , Co^{2+} , Cu^{2+} and Zn^{2+} metal cations using the appropriate metal acetate salt.

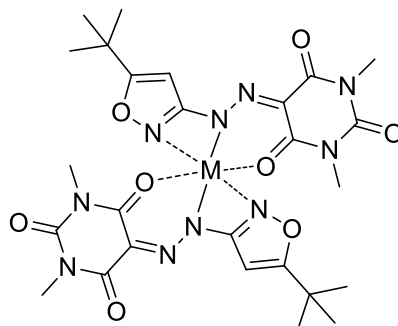


Figure 1.30: ML_2 complexes with an isoxazole functionalised dimethyl barbituric acid as the ligand, L, where $M^{2+} = Ni^{2+}, Co^{2+}, Cu^{2+}$ or Zn^{2+} .⁷⁸

A square-planar *trans*-dichloropalladium(II) complex, formed from 5-(*p*-tolyl)isoxazol-3-amine ligands, was structurally characterised by IR and NMR spectroscopies and by single crystal x-ray diffraction. The complex was prepared by refluxing the isoxazole ligands in MeCN in the presence of bis(acetonitrile)dichloropalladium(II). Replacement of the MeCN ligands occurred in under 10 mins to form the Pd^{2+} complex. X-ray crystallography revealed that the complex was of the form ML_2Cl_2 and the Pd^{2+} was coordinated by the isoxazole N atoms, **Figure 1.31**. The hydrogen atoms of the amino groups were involved in H-bonding to two chlorine atoms. This complex was air and water stable and proved effective as a new catalyst for the Suzuki-Miyaura cross-coupling reaction.⁷⁹

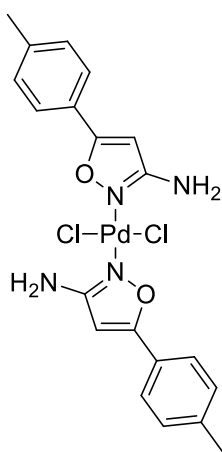


Figure 1.31: 5-(*p*-Tolyl)isoxazol-3-amine Pd^{2+} complex capable of catalysing the Suzuki-Miyaura cross-coupling reaction.⁷⁹

1.8 Aims of the Research

- Our particular research interest lies in the development of new sensors incorporating an isoxazole heterocycle as a potential metal binding site and a pyrene fluorophore as a reporter unit. As our research group has extensive experience in the use of click cycloaddition as a conjugation tool, nitrile oxide/alkyne cycloaddition chemistry will be utilised to link pyrene moieties to the lower rim of calix[4]arenes so synthesising a family of calix[4]arenes with a scaffold-receptor-reporter modular design.
- The work reported in this thesis will focus on the synthesis, purification and characterisation of a range of lower rim isoxazole-pyrene functionalised calix[4]arenes.
- The detection and sensing abilities of this family for metal ions will be explored using UV-Vis absorbance, fluorescence and NMR spectroscopies.
- Following analysis of the spectroscopic data, the best performing sensor in the series will be brought forward as a candidate for sensing in aqueous media. This research will explore the possibility of real-world metal ion sensing applications, such as waste water analysis.
- Finally, following result collation and analysis a hypothesis on the metal ion sensing abilities of the pyrene-isoxazole calixarenes will be constructed.

Chapter 2

Pyrene Isoxazole

Calixarene (PIC)

2.1 Overview

As outlined in Chapter 1, the aims of this research are to design, synthesise and investigate the metal ion sensing potential of a novel family of pyrene functionalised calixarenes, while also developing a hypothesis on the mechanism of the host:guest interactions. Prior to discussing the author's own research this chapter begins with an overview of isoxazole functionalised calixarenes. It also discusses synthetic routes to lower rim pyrene functionalised calix[4]arenes along with an overview of their application as fluorescent probes. This chapter will also detail the work conducted on **Pyrene Isoxazole Calixarene (PIC)** at Maynooth in a collaboration between the groups of Heaney and McGinley prior to the author taking up this research project. This will be followed by a discussion on the author's contributions to the characterisation and sensing potential of **PIC**.

2.2 Isoxazole Functionalised Calixarenes

Isoxazole forming nitrile oxide/alkyne cycloadditions (NOAC) are useful reactions for conjugation chemistry (Section 1.6.5). Chang *et al.* used this chemistry to attach two 9-chloroanthracen-10-yl moieties to the lower rim of a calix[4]arene in a distal substitution pattern.⁸⁰ Similarly, Senthilvelan and co-workers introduced 1-naphthyl moieties using the same approach,⁸¹ **Figure 2.1**. Both the 9-chloroanthracen-10-yl derivative **3** and the 1-naphthyl derivative **4**, showed selectivity towards copper perchlorate over all other metal perchlorates examined. The presence of the Cu²⁺ ion in solution induced a quenching of the excimer emission of **3** and **4**. In contrast, **5**, the ring opened derivative of **4** showed a strong enhancement of the monomer emission, at 343 nm, and a small increase in the excimer emission at 450 nm in the presence of Cu(ClO₄)₂. The enhancement is believed to be due to the rigidity of the **5**:Cu²⁺ complex and diminished PCT.

It was hypothesised that a pyrene-isoxazole appended calixarene would prove a more effective chemosensor; due to the long fluorescence lifetime and high quantum yield of the pyrene fluorophore. This novel pyrene-isoxazole calixarene may show superior sensitivity to transition metal ions with respect to the related 9-chloroanthracen-10-yl⁸⁰ and 1-naphthyl analogues,⁸¹ **3**, **4** and **5** described above.

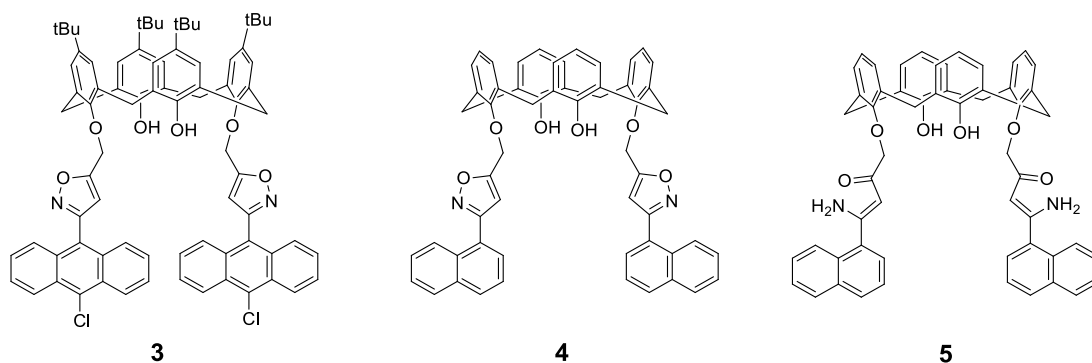
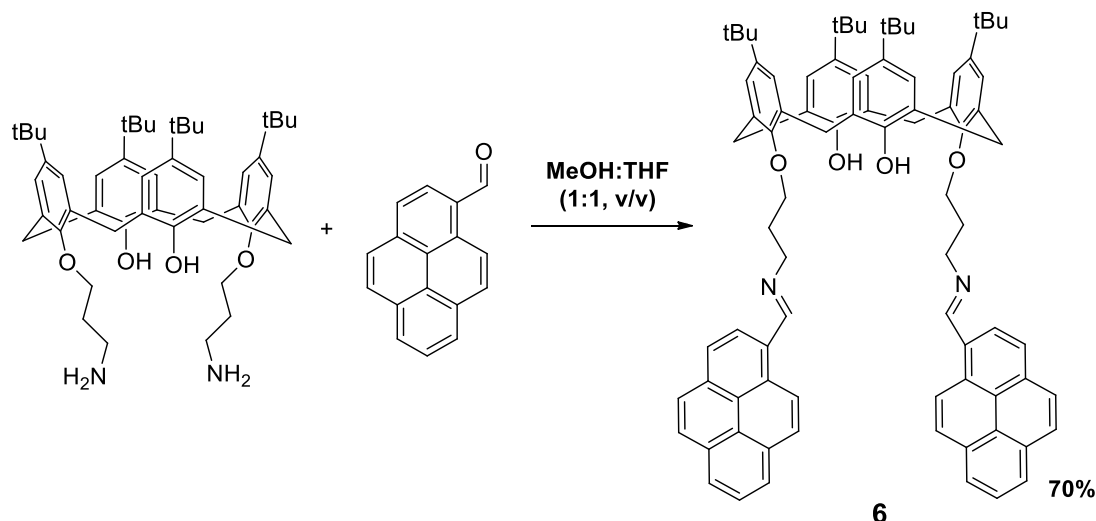


Figure 2.1: Structures of 9-chloroanthracen-10-yl, **3** and 1-naphthyl, **4** and 5 isoxazole functionalised calix[4]arenes used as fluorescent chemosensors for the Cu²⁺ ion.^{80,81}

2.3 Synthesis and Applications of Lower Rim Pyrene Functionalised Calixarenes

The pyrene moiety has been introduced to the lower rim of calix[4]arenes using a number of methodologies including, but not limited to, Schiff base formation,⁸² click cycloaddition chemistry,⁸³ and amide⁸⁴ and ester⁸⁵ condensation chemistries.

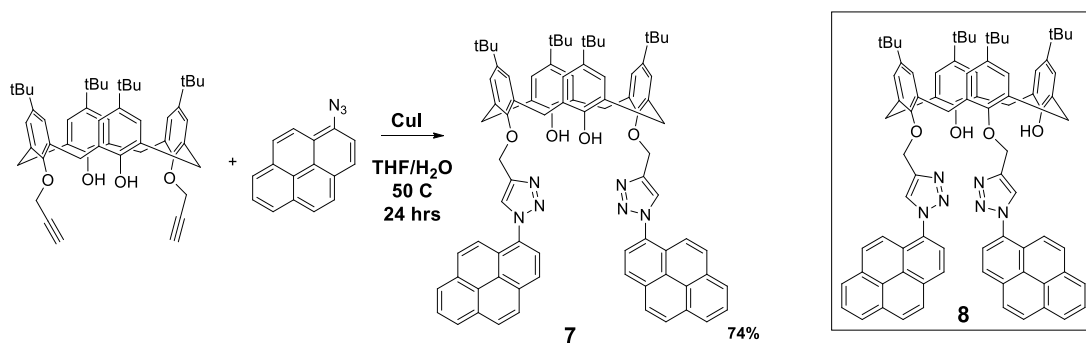
A lower rim Schiff base pyrene functionalised calix[4]arene, reported by Yilmaz *et al.*, was formed from the reaction between bis(3-aminopropoxy)calix[4]arene and 1-pyrene carboxaldehyde following 6 hrs heating at reflux in MeOH:THF (1:1, v/v), **Scheme 2.1**.⁸² Upon excitation at 350 nm a solution of **6** (1 μM, DCM:MeCN, 1:1, v/v) showed monomer and excimer fluorescence emissions at 370–450 nm and 503 nm respectively. In the presence of 10 eqs of Pb²⁺, Cu²⁺ and Zn²⁺ ions, introduced as perchlorate salts, more extensive quenching was observed than for the same relative amount of Ca²⁺, Li⁺, Mg²⁺, Ba²⁺, Na⁺ or Ni²⁺ ions. The observed quenching was explained by PET from the pyrene units to the nitrogen atoms which had become electron deficient upon metal complexation. The heavy metal effect and conformational changes were also considered a factor in fluorescence quenching.



Scheme 2.1: Schiff base chemistry for the introduction of pendant pyrene rings to the lower rim of a calix[4]arene; fluorescent sensor **6** developed by Yilmaz *et al.* for detection of Pb^{2+} , Cu^{2+} and Zn^{2+} ions.⁸²

Triazole forming copper-catalysed azide-alkyne click cycloaddition (CuAAC) chemistry is a powerful tool for conjugation of molecules including peptides, nucleotides or carbohydrates (Section 1.6.2).⁶² In one example of its application to calixarene modification, Chung *et al.* introduced two pyrene moieties to the lower rim of a calix[4]arene. Both proximal and distal isomers were formed.⁸³ 1-Azidopyrene and the required bis-alkyne functionalised calix[4]arene were heated at 50°C , in $\text{THF}:\text{H}_2\text{O}$ (2:1, v/v), in the presence of a catalytic amount of CuI . After 24 hrs reaction and purification by flash column chromatography, **7** and **8** were formed in 74 and 72% yield respectively, **Scheme 2.2**. Both were found to be highly selective and sensitive fluorescent chemosensors for Ag^+ , over Li^+ , Na^+ , K^+ , Mg^{2+} , Ca^{2+} , Ba^{2+} , Cu^{2+} , Ni^{2+} , Cd^{2+} , Hg^{2+} , Zn^{2+} , Mn^{2+} , Pb^{2+} and Cr^{3+} ions, introduced as perchlorate salts, in $\text{MeOH}:\text{CHCl}_3$ (98:2, v/v, $\lambda_{\text{ex}} = 342 \text{ nm}$). Upon the addition of 10 eqs of Ag^+ ions, the excimer emission of **8** decreased with the concomitant enhancement of its monomer emission, while the monomer and excimer emissions of **7** were both enhanced by Ag^+ . The distinctly different fluorescent responses of ligands **7** and **8** toward Ag^+ ions implied that the orientation of the lower rim triazolylpyrenes played an important role in sensing. The selectivity of the host **8** for the Ag^+ ion was retained in an aqueous environment ($\text{MeOH}:\text{CHCl}_3:\text{H}_2\text{O}$, 88:2:10, v/v), however, the enhancement factor of

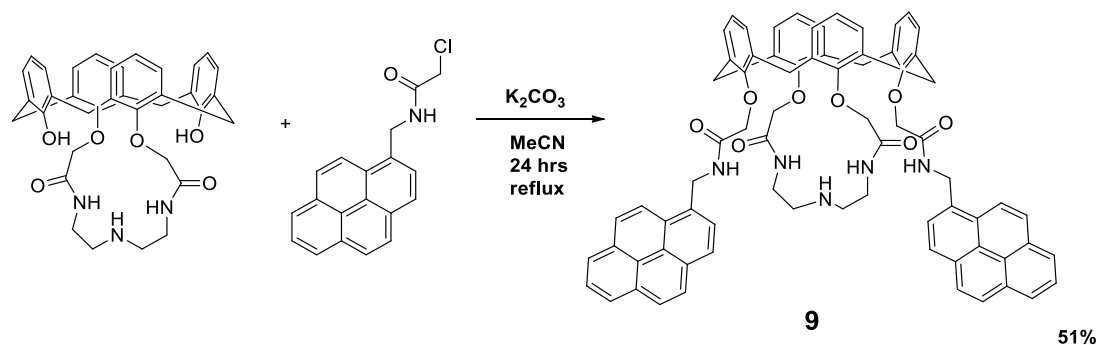
the monomer emission of H to H:G dropped from 9.2 in MeOH:CHCl₃ (98:2, v/v) to 3.1 in the 10% aqueous solution on the addition of 10 eqs of Ag⁺ guest ions.



Scheme 2.2: Copper-catalysed azide-alkyne cycloaddition (CuAAC) chemistry for the introduction of distal, pendant pyrene moieties to the lower rim of a calix[4]arene, **7** developed by Chung *et al.* as an Ag⁺ fluorescent sensor.⁸³ Inset: Proximal substituted analogue, **8**.

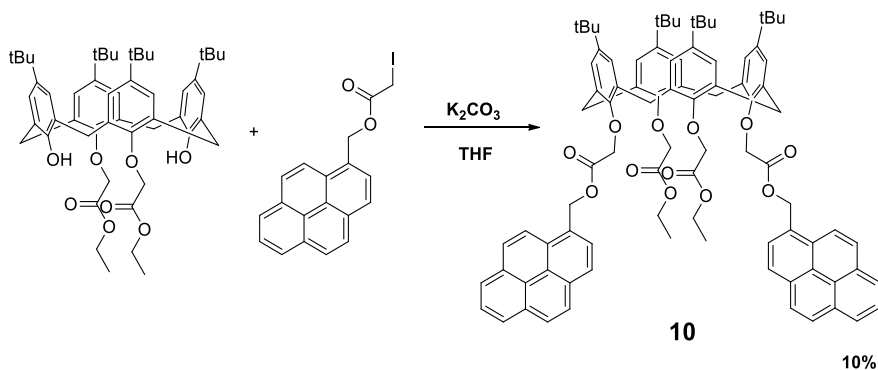
An ether forming reaction between *N*-(1-pyrenylmethyl)chloroacetamide and a triazacrown functionalised calix[4]arene in MeCN in the presence of potassium carbonate has been reported by Kim *et al.*, **Scheme 2.3**.⁸⁴ Quenching of the fluorescence spectrum of **9** in MeCN (6 μM, λ_{ex} = 343 nm) occurred in the presence of Pb²⁺ and Co²⁺ ions, introduced as perchlorate salts, whilst no effect was observed in the presence of Na⁺, Li⁺, K⁺ or Cs⁺ ions under the same conditions. The Pb²⁺ and Co²⁺ induced quenching of **9** was attributed to conformational changes, reverse PET and the heavy metal ion effect.

The selectivity of **9** towards anions of tetrabutylammonium salts was also explored revealing a selectivity for F⁻ anions. The **9**:F⁻ complex is believed to involve H-bonding from the amide groups of the triazacrown to the guest, causing fluorescence quenching due to a PET effect. Thus, **9** could be used as a cation sensor for Co²⁺ or Pb²⁺ and as an anion sensor for F⁻.



Scheme 2.3: Etherification chemistry for the introduction of pendant pyrene rings to the lower rim of an azacrown calix[4]arene giving **9**, developed by Kim *et al.* as a cation (Pb^{2+} and Co^{2+}) and anion (F^-) sensor.⁸⁴

Koyama *et al.* reported the first example of a calix[4]arene based fluorescence sensor for Na^+ ions. A pyrene functionality was introduced to the lower rim of a bis-ethoxycarbonylmethyl functionalised calixarene using potassium carbonate as a base and 1-pyrenemethyl iodoacetate as the pyrene containing reagent, **Scheme 2.4**.⁸⁵ Calix[4]arene **10** was formed in 10% yield and the fluorescence spectrum ($4.8 \mu\text{M}$, $\lambda_{\text{ex}} = 330 \text{ nm}$, $\text{MeOH}:\text{THF}$, 15:1, v/v), showed both monomer and excimer emissions, at 390 and 480 nm respectively. Upon gradual addition of Na^+ ions, in the form of the thiocyanate salt, the monomer emission increased whilst the excimer emission decreased concomitantly. The utility of **10** as a selective Na^+ sensor was verified by competitive titration of other alkali metal cations (K^+ , Li^+ , Rb^+ and Cs^+). Only slight perturbations in the fluorescence intensity of **10** were observed in the presence of competitive metal ions, indicating that **10** could function as a selective detector for Na^+ .



Scheme 2.4: Etherification reaction forming bis-pyrene functionalised calix[4]arene **10** developed by Koyama *et al.* as a Na^+ sensor.⁸⁵

2.4 Novel Pyrene Isoxazole Functionalised Calixarene

This section will give an overview of the stage of the development of **Pyrene Isoxazole Calix[4]arene (PIC)** as a metal ion sensor at Maynooth University, prior to the author setting out on her PhD research programme. The discussion over the next pages, follow the results of Diao⁸⁶ and Maher,⁸⁷ which include:

- design and synthesis
- x-ray crystallographic analysis
- fluorescence spectroscopic studies
- electron paramagnetic resonance (EPR) spectroscopic studies
- a theoretical Density Functional Theory (DFT) study.

The work of Diao and Maher combined with that for this thesis forms the subject of a Tetrahedron publication.⁸⁸

2.4.1 Design of PIC

In designing a new fluorescent sensor particular care was taken in choosing the combination of fluorophore, binding site, molecular scaffold and linker.

The isoxazole ring was chosen due to its potential, at one and the same time, to function as the linking unit between the fluorophore and the calix[4]arene scaffold, and as a metal binding site. The isoxazole ring (Section 1.7) has shown potential as a transition metal binding ligand, although it remains relatively unexplored as a binding site within a chemosensor or fluoroionophore.

Pyrene was chosen as an effective and versatile fluorophore. It is particularly attractive due to its relatively long fluorescence lifetime and high quantum yield as outlined in Section 1.3.2.2.

A calix[4]arene was chosen as a versatile molecular scaffold for hosting the pyrene units in a flexible manner capable of adopting the required orientation for excimer formation.

Typically calix[4]arene based fluorescence sensors contain a methylene spacer between the fluorophore and the binding site.⁸⁹⁻⁹¹ In contrast, **Pyrene Isoxazole**

Calixarene, **PIC**, was designed with direct linkage between the pyrene unit and the binding site to introduce the possibility for modified sensitivities and binding affinities for metal ions, **Figure 2.2**.

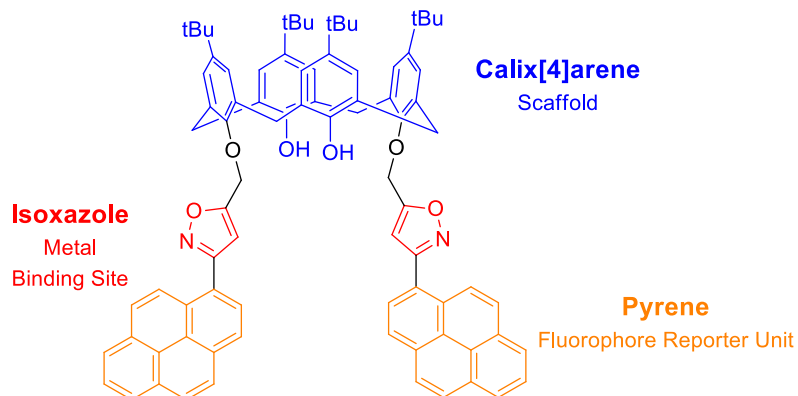
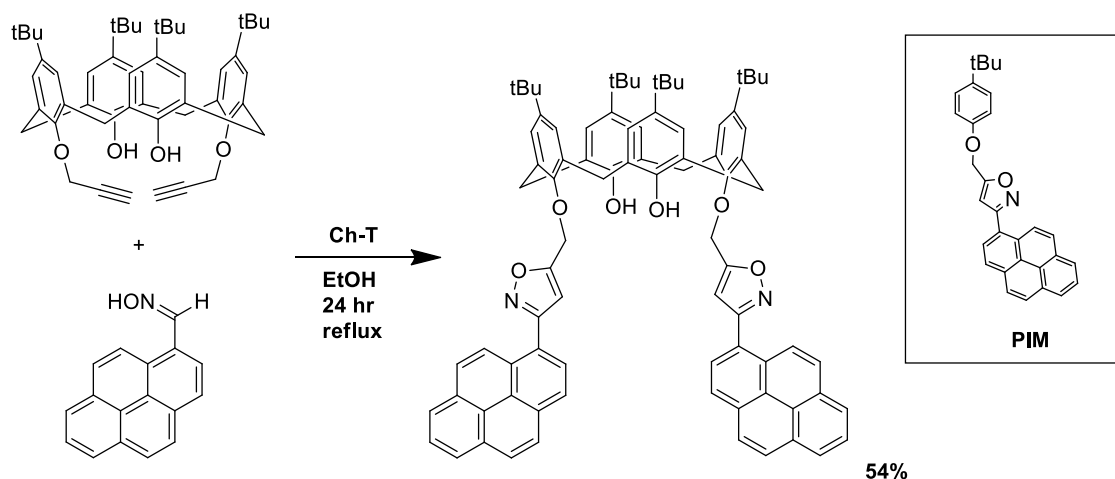


Figure 2.2: Structure of Pyrene Isoxazole Calixarene (**PIC**).

2.4.2 Synthesis and Characterisation of PIC

Nitrile oxide/alkyne cycloaddition (NOAC) was the method of choice for the formation of **PIC**. Chloramine-T (Ch-T) was chosen as the reagent for nitrile oxide formation from the parent pyrene oxime. The *in situ* generated nitrile oxide was allowed to react with a bis-alkylated calix[4]arene in refluxing EtOH, **Scheme 2.5**.

A model compound, desired to ascertain if the calixarene moiety was required for metal detection, **Pyrene Isoxazole Monomer (PIM)**, inset **Scheme 2.5**, was synthesised in a similar manner. If **PIC** showed a fluorescence response to the presence of a metal cation and if **PIM** failed to respond spectrofluorometrically to the same metal cation it would indicate that the conformational confines of the calixarene scaffold were necessary for the system to deliver the twin requirements of efficient ion complexation and effective reporting of the binding event.



Scheme 2.5: Synthesis of Pyrene Isoxazole Calixarene (**PIC**), Inset: Structure of Pyrene Isoxazole Monomer (**PIM**).

The targeted compounds **PIM** and **PIC** were successfully synthesised and their characterisation was completed using the normal range of spectroscopic techniques. Of particular relevance for this project was the ^1H NMR and fluorescence spectroscopic data. A pair of AB doublets at 4.37 and 3.40 ppm in the ^1H NMR spectrum indicated that **PIC** presented in the cone conformation, **Figure 2.3**.

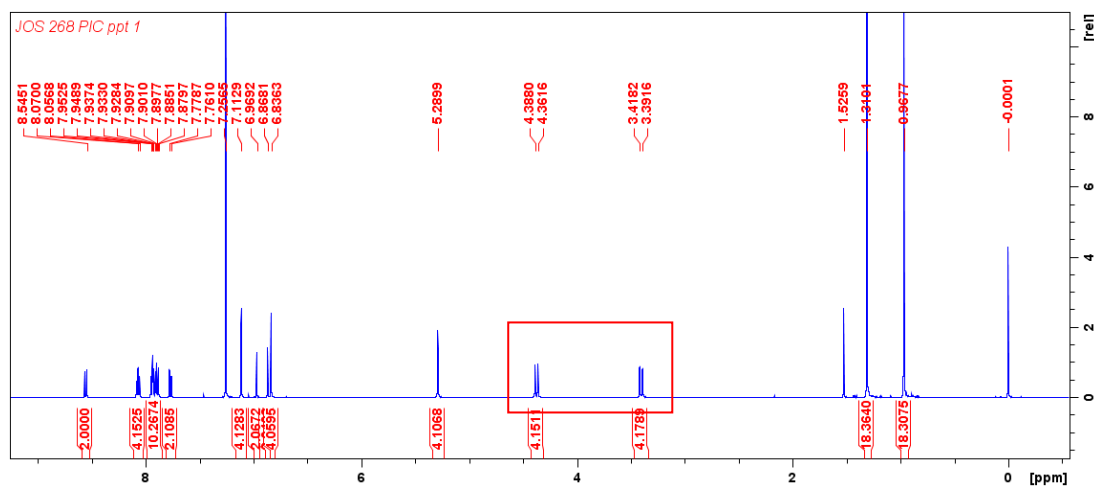


Figure 2.3: ^1H NMR (500 MHz) spectrum of **PIC** in CDCl_3 at 25°C , AB doublets of the methylene bridges of the calixarene core are indicated by the red box.

A fluorescence emission spectrum of **PIC** ($6\ \mu\text{M}$) was obtained in MeCN, **Figure 2.4**. The λ_{max} (343 nm) of the absorption band of longest wavelength of **PIC** was chosen as the excitation wavelength for the measurement of the emission spectrum. Pyrene is known to display monomer emissions between 380 to 420 nm and if excimer formation is possible it will occur between 410 to 500 nm, Section 1.3.2.2. In the

fluorescence emission spectrum of **PIC**, small monomer emission bands appear at 386 and 407 nm and a large excimer emission band appears at 498 nm.

Following excitation at 274 nm, **PIM** (6 μM , MeCN) showed strong monomer emissions at 386 and 406 nm, with a slight shoulder at 428 nm. The absence of an excimer emission suggested that intermolecular interactions of the pyrene units of **PIM** did not occur in MeCN at the given concentration.

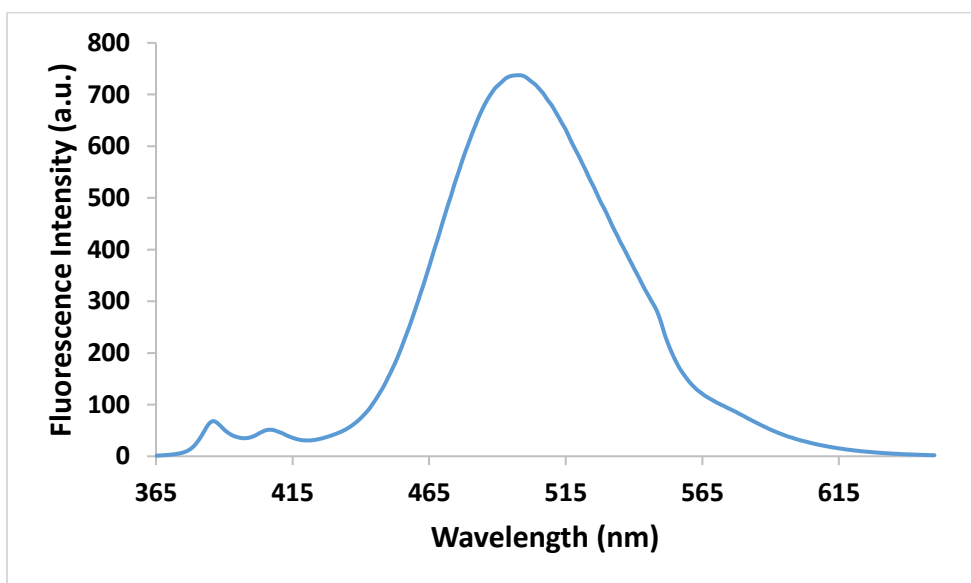


Figure 2.4: Emission spectrum of **PIC** (6 μM , $\lambda_{\text{ex}} = 343 \text{ nm}$) in MeCN showing monomer emission bands at 386 and 407 nm and an excimer band at 498 nm.

2.4.3 Solid State Structure of PIC

Crystalline needles of **PIC**, grown in MeCN were analysed by x-ray crystallography by Dr. John Gallagher of Dublin City University. In the solid state the calix[4]arene core presented in the cone conformation, lower rim intra-annular H-bonding between the phenolic OH and the neighbouring ether atoms stabilised this conformation at an average O...O distance of 2.83 Å, **Figure 2.5a**.

Intramolecularly the pendant pyrene units do not align in a face-to-face manner, rather the planes created by the pyrene units are at 47.70° to each other, **Figure 2.5b**.

The isoxazole and pyrene moieties of the pendant arms are not coplanar and angles of 45.31° and 44.12° were measured between the planes of the pyrene and isoxazole moieties of the pendant arms.⁸⁸

“Short contacts”, which reveal inter- and intramolecular interactions, between neighbouring pyrene units, are indicated by the blue lines in the diagram, **Figure 2.5c**. Whilst each pyrene moiety is parallel to a pyrene moiety from a neighbouring unit of **PIC**, the fluorophores are almost fully slipped from each other.

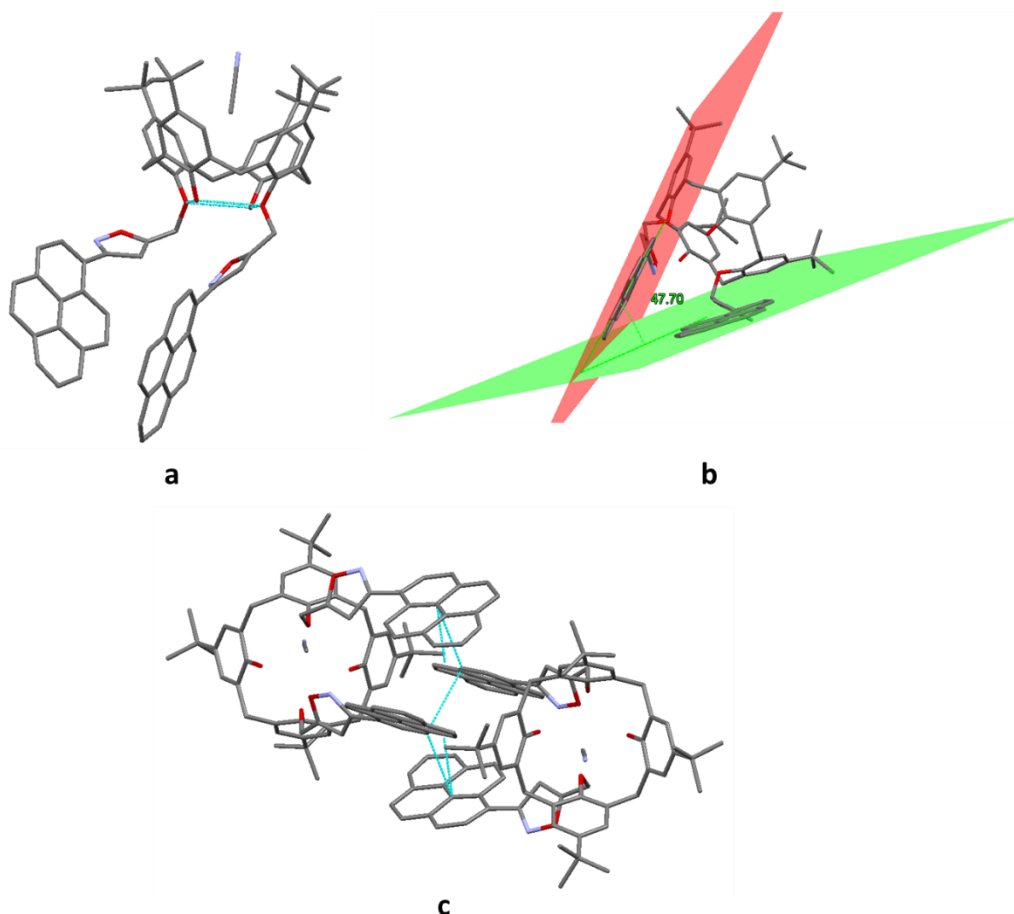


Figure 2.5: **a)** Molecular structure of **PIC.MeCN** showing intramolecular hydrogen-bonding (blue lines), a molecule of MeCN is shown encapsulated in the upper rim, **b)** diagram of **PIC** showing the 47.70° angle between the planes of the pyrene moieties and **c)** tail-to-tail *dimer* of **PIC** showing intermolecular short contact between neighbouring pyrene units (blue lines).⁸⁸

Examination of the extended network created by the units of **PIC** in the solid state structure revealed a tail-to-tail arrangement of the calixarene units, creating a channel between the interlocking pyrene units from neighbouring calixarene moieties, **Figure 2.6**. A summary of the interesting characteristics of the **PIC.MeCN** crystal is given in **Table 2.1**.

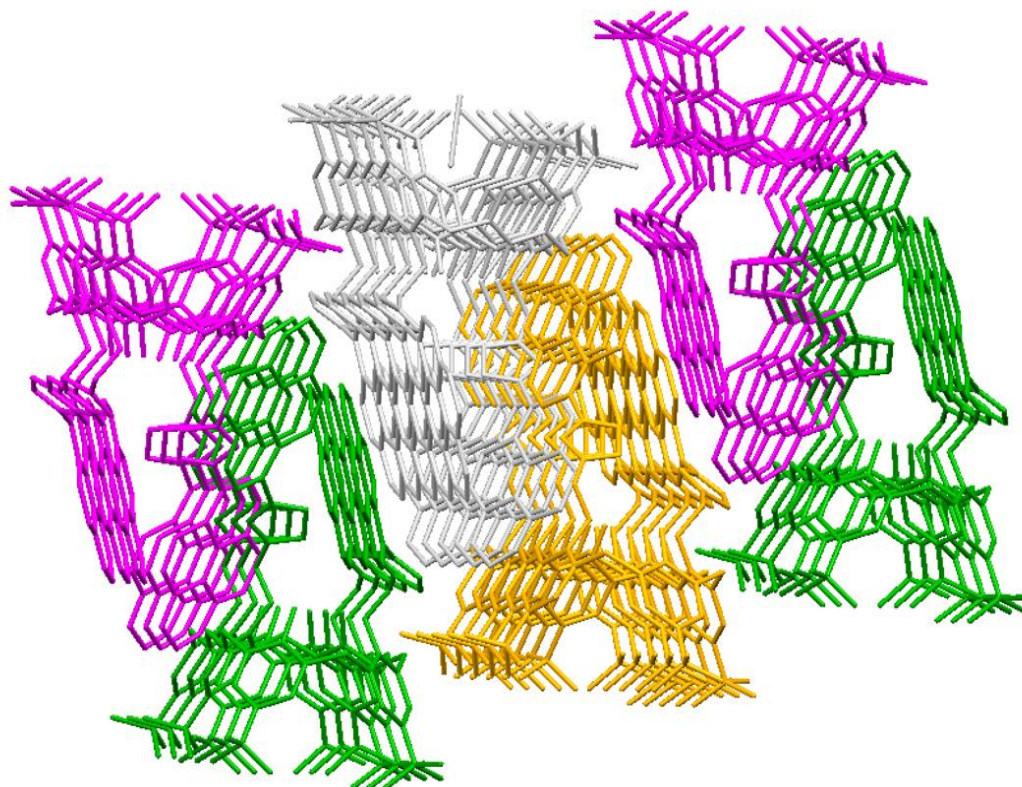


Figure 2.6: Extended network of the **PIC.MeCN** solid state structure showing the tail-to-tail arrangement of the calixarene units.

Table 2.1: Summary of the characteristics of the **PIC.MeCN** crystal structure.

Py-Py Plane Angle	Py-Isox Plane Angles		Lower-Rim Hydrogen Bonding	Solvent Interaction	Other Interesting Features
47.70°	45.31°	44.12°	Present at an average O...O distance of 2.83 Å.	One molecule of MeCN in upper cavity of calixarene.	Tail-to-tail interlocking arrangement between units of PIC . Channel between interlocking pyrene units in extended network.

2.4.4 Host:Guest Studies of **PIC** and the Model Compound

Fluorescence spectroscopy was used to investigate the potential of **PIC**, and the model compound **PIM**, to selectively detect and report on the presence of metal ions in MeCN. All fluorescence spectra presented in this thesis were recorded at room

temperature (rt). Salts tested included Hg^{2+} , Ni^{2+} , Zn^{2+} , Co^{2+} , Fe^{2+} , Pb^{2+} , Cd^{2+} and Cu^{2+} perchlorates. **PIM**, containing only one isoxazole ring and one pyrene moiety, showed no perceptible response to any of the metal perchlorates tested. Contrastingly, the calix[4]arene based **PIC** showed a dramatic excimer quenching when exposed to copper perchlorate only, **Figure 2.7**. These results suggested that the calixarene scaffold of **PIC** was necessary for the twin requirements of efficient Cu^{2+} ion complexation and effective reporting of the binding event.

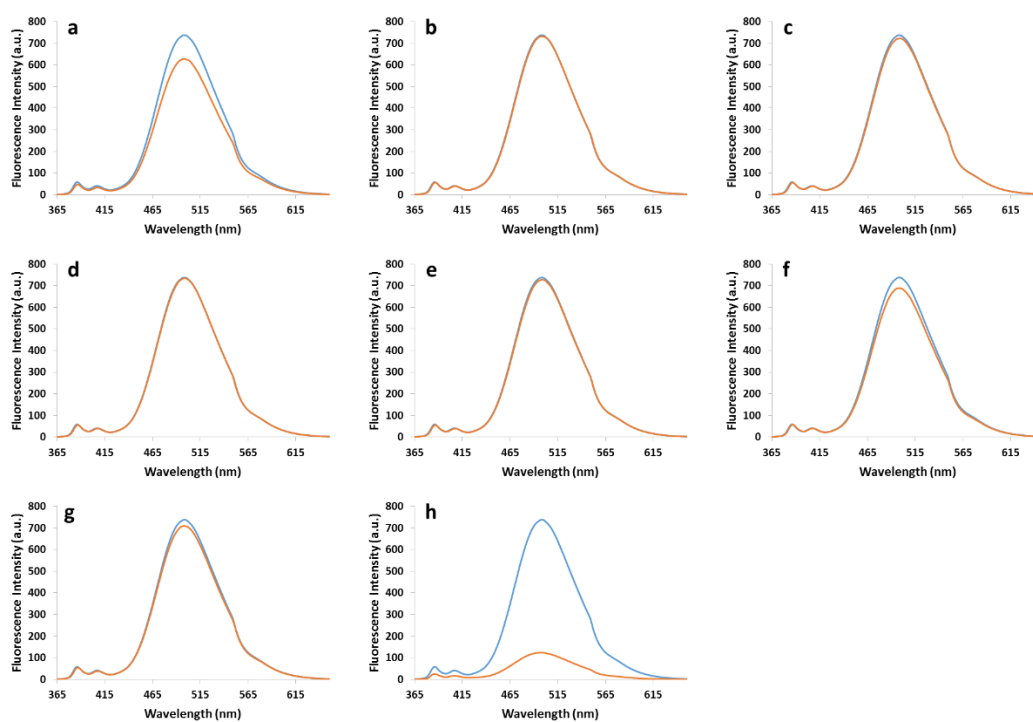


Figure 2.7: Emission spectra of **PIC** (6 μM , $\lambda_{\text{ex}} = 343 \text{ nm}$) in MeCN with 0 (blue) and 10 (orange) eqs of $\text{M}^{\text{n}+}(\text{ClO}_4^-)_n$; where $\text{M}^{\text{n}+} = \text{a) Hg}^{2+}$, **b) Ni}^{2+}**, **c) Zn}^{2+}**, **d) Co}^{2+}**, **e) Fe}^{2+}**, **f) Pb}^{2+}**, **g) Cd}^{2+}** and **h) Cu}^{2+}**.

The effect of the counterion was explored by comparing the impact of copper perchlorate, chloride, nitrate and acetate salts (100 eqs) on the extent of fluorescence quenching of **PIC**. A decrease in the following order $\text{Cu}(\text{ClO}_4)_2 > \text{CuCl}_2 > \text{Cu}(\text{NO}_3)_2 > \text{Cu}(\text{CO}_2\text{CH}_3)_2$ was observed, **Figure 2.8**. This suggested that the degree of dissociation of the metal salt in MeCN may be important for successful detection and reporting of the binding event.

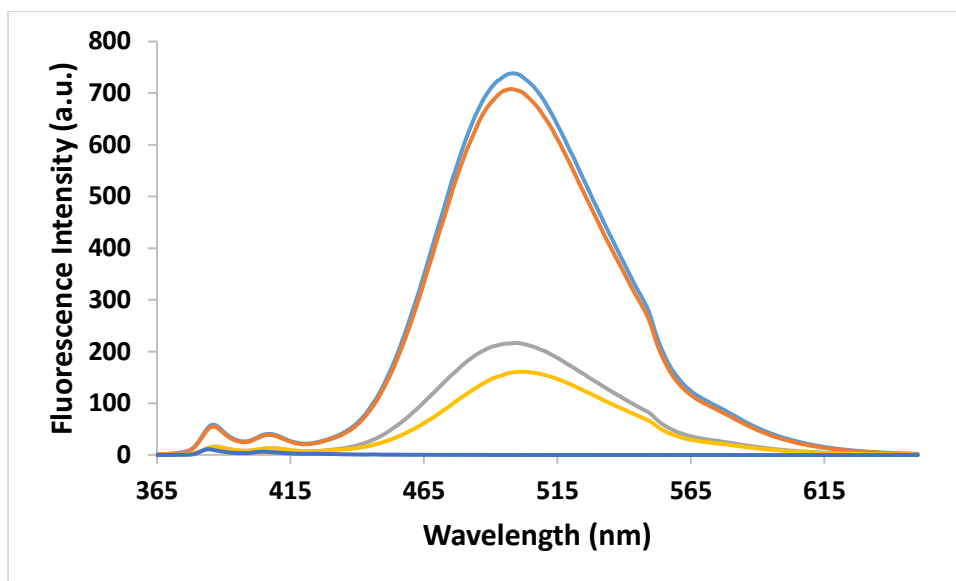


Figure 2.8: Emission spectra of **PIC** (6 μM , $\lambda_{\text{ex}} = 343 \text{ nm}$) in MeCN (blue) with 100 eqs of: $\text{Cu}(\text{CO}_2\text{CH}_3)_2$ (orange), $\text{Cu}(\text{NO}_3)_2$ (grey), CuCl_2 (yellow) and $\text{Cu}(\text{ClO}_4)_2$ (navy).

The potential for application of **PIC** as a sensor was further probed by conducting a competitive metal ion study. The fluorescence emission spectrum of **PIC** (6 μM) in MeCN showed little or no quenching when exposed to 20 eqs of Hg^{2+} , Ni^{2+} , Zn^{2+} , Co^{2+} , Fe^{2+} , Pb^{2+} or Cd^{2+} perchlorates. However, the subsequent addition of a further 20 eqs of $\text{Cu}(\text{ClO}_4)_2$ caused a dramatic quenching of the fluorescence signal. Thus indicating the potential of **PIC** to detect copper in the presence of contaminating metal ions.

2.4.4.1 Determination of the Stoichiometry of association between **PIC** and Cu^{2+}

The stoichiometry of the complex formed between **PIC** and Cu^{2+} was determined using the Job's Method (Section 1.4.1). The total molar concentration of **PIC** and Cu^{2+} was held at 6 μM . The Job's plot that was constructed displayed a symmetrical $-x^2$ shaped curve, with the maximum fluorescence change observed when the molar fraction of **PIC** was 0.5, showing that 1:1 **PIC**: Cu^{2+} metal complexes were formed in MeCN.

2.4.5 EPR Spectroscopic Investigation of the Geometry of the **PIC**: Cu^{2+} Complex

Electron paramagnetic resonance (EPR) or electron spin resonance (ESR) spectroscopy is a non-destructive technique for the analysis of species with one or more unpaired electrons, such as free radicals or transition metal ions. Autoreduction of Cu^{2+} to Cu^+ by the phenolic moieties of the calix[4]arene scaffold of

PIC was considered a possibility and thus the nature of the complex formed between **PIC** and Cu^{2+} was investigated by EPR spectroscopy. In parallel to Rao and co-workers' investigation of a lower rim triazole-benzimidazole functionalised calix[4]arene,⁹² **PIC** (10 mM, MeCN:CHCl₃, 3:1, v/v) was added to a $\text{Cu}(\text{ClO}_4)_2$ solution until a 1:1 (**PIC**: Cu^{2+}) solution was reached. This was then repeated in the reverse approach, increasing volumes of the $\text{Cu}(\text{ClO}_4)_2$ solution was added to the **PIC** solution until a 1:1 solution was reached. It was observed that the final pattern of signals in the EPR spectra was independent of the direction of the titration experiment. No obvious change in the signal of the EPR spectrum was observed on going from a $\text{Cu}(\text{ClO}_4)_2$ solution to a **PIC**: $\text{Cu}(\text{ClO}_4)_2$ solution, slight signal broadening occurs in the 1:1 solution. This data suggests that there is no change to the geometry around the Cu^{2+} ion when going from a MeCN solution of the perchlorate salt to the solution of the complex. Thus the autoreduction of Cu^{2+} to Cu^+ by **PIC** was not considered a possibility in MeCN at room temperature.

2.4.6 Computational Study

Molecular modelling studies, carried out by Dr. Elisa Fadda of Maynooth University, considered three possibilities for the **PIC**: Cu^{2+} complex: **i)** a 1:1 **PIC**: Cu^{2+} complex independent of solvent molecules; **ii)** a 1:1 π -cation interaction between the Cu^{2+} ion and the pyrene rings of **PIC** and **iii)** a 1:1 **PIC**: Cu^{2+} complex involving solvent molecules.

These are discussed in more detail below:

- i)** The minimum energy structure found for the **PIC**: Cu^{2+} complex with no coordinating solvent molecules shows the metal ion in a penta-coordinate, distorted square-pyramidal geometry with one of the isoxazole *O*-atoms acting as the apical ligand and the base of the pyramid made up of the four oxygen atoms on the lower rim of **PIC**. Relative to the structure of the unbound **PIC**, there was significant rotation of the pyrenyl moieties to involve the isoxazole *O*-atom in metal binding. Opportunity for solution phase intramolecular π - π stacking of the pyrene moieties

would be hindered by this conformation and this would explain the significant excimer quenching observed in the fluorescence study.

- ii) Calculations failed to identify a minimum structure with π -cation interactions between the pyrene moieties and the Cu^{2+} ion, which suggested that if such an interaction exists it was unstable in the gas phase.
- iii) Modelling in the presence of solvent molecules identified a tetrahedral **PIC**: Cu^{2+} :MeCN complex, where two MeCN molecules and the isoxazole nitrogen atoms are involved in the coordination sphere. This structure would be expected to disrupt solution phase intramolecular π - π stacking of the parent **PIC** which is also consistent with the fluorescence study.

2.5 Further Analysis of PIC and its Copper Complexation

At the outset of the author's research, it was known that **PIC** could selectively detect Cu^{2+} ions over a range of other metal ions. However, despite EPR spectroscopic and DFT theoretical studies details of the geometry of the **PIC**: Cu^{2+} complex remained unclear. The remainder of this chapter will discuss the contributions of the author to an understanding of the binding event between **PIC** and Cu^{2+} including a attempts to form crystals of the **PIC**: Cu^{2+} complex, an advanced ^1H NMR spectroscopic study, an investigation of the mechanism of Cu^{2+} induced quenching of **PIC** using Stern-Volmer analysis, calculation of the binding constant using Benesi-Hildebrand analysis and calculation of the detection limit of **PIC** for Cu^{2+} in MeCN.

2.5.1 UV-Vis Spectroscopic Investigation of $\text{Cu}^{2+} \rightarrow \text{Cu}^+$ Reduction by PIC in MeCN

The autoreduction of Cu^{2+} to Cu^+ by **PIC** was not considered a possibility in MeCN at room temperature following an EPR spectroscopic study (Section 2.4.5). Numerous reports within the literature attribute the presence of an absorbance band at ~430 nm to the MLCT band between Cu^+ and calixarene lower rim phenolic OH moieties.^{81,92}

Thus a UV-Vis spectroscopic investigation was desired in order to rule out the formation of Cu^+ in the presence of Cu^{2+} and **PIC** in MeCN. The absorbance spectra of **PIC** (6 μM) in MeCN in the presence of 0, 1, 10 and 100 eqs of $\text{Cu}(\text{ClO}_4)_2$ were

recorded, which did not show any evidence of a charge transfer band in the 430 nm region, **Figure 2.9**, further suggesting that the autoreduction of Cu^{2+} to Cu^+ by the phenolic moieties of **PIC** was not likely in MeCN at room temperature.

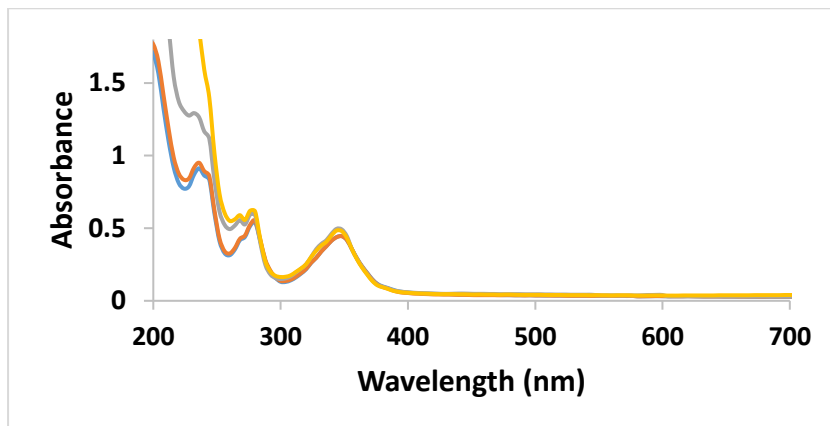


Figure 2.9: UV-Vis absorbance spectrum of **PIC** (6 μM) in MeCN with 0 (blue), 1 (orange), 10 (grey) and 100 (yellow) eqs of $\text{Cu}(\text{ClO}_4)_2$.

2.5.2 Experiments in Search of a Solid Sample of the **PIC**: Cu^{2+} Complex

To unambiguously identify the binding site of **PIC** for Cu^{2+} , crystals of the complex of suitable quality for x-ray structure determination were desired. A number of attempts to form a solid sample of the **PIC**: Cu^{2+} complex were conducted.

Heating a solution of a metal salt and ligand to reflux, followed by cooling to room temperature is a common technique for the formation of solid samples of metal-ligand complexes.⁹³⁻⁹⁵ This strategy was employed in an attempt to form a solid sample of the **PIC**: Cu^{2+} complex. Initially **PIC** and copper perchlorate, in a 1:1 (40 μM :40 μM) ratio, were dissolved in 100% MeCN, 100% EtOH or EtOH:DCM (2:1, v/v), **Table 2.2**. All solutions were heated to reflux for three hours and then allowed to cool slowly to rt. Small off-white crystals formed from the MeCN solution, however, IR and NMR spectroscopic data identified these as the parent **PIC**. Similarly, an amorphous off-white solid which precipitated from the EtOH solution was also shown by IR and NMR spectroscopy to be the uncomplexed calixarene **PIC**. Small yellowish needle shaped crystals fell from the EtOH:DCM (2:1, v/v) solution, these were also revealed to be **PIC**.

Table 2.2: Summary of experiments carried to form a solid sample of the **PIC:Cu²⁺** complex using a 3 hour reflux of a solution containing **PIC** and copper perchlorate.

PIC : Cu²⁺ Eqs	PIC : Cu²⁺ Concentration (μM)	Solvent	Solid Formed	Result*
1:1	40:40	MeCN	Small Off-White Crystals	PIC Returned
1:1	40:40	EtOH	Amorphous Off-White Solid	PIC Returned
1:1	40:40	EtOH:DCM (2:1, v/v)	Small Light Yellow Needle-Like Crystals	PIC Returned

* Verified by IR and NMR spectroscopy.

A further attempt to form a solid sample of the **PIC:Cu²⁺** complex involved dissolving **PIC** in EtOH:DCM (20 mL, 2mM, 2:1, v/v) in the presence of 20 eqs of Cu(ClO₄)₂. The solution was allowed to stir at rt for 3 hrs and then allowed to stand. After 2 weeks small needle like colourless crystals formed. In spite of the expectation that a copper complex of **PIC** would be green-blue in colour⁹³ the crystals were solved by Dr. Brendan Twamley of Trinity College Dublin. Unfortunately, the crystals were shown to be the calixarene, free of copper ions but containing two molecules of DCM. One solvent molecule was present in the upper cavity of the calix[4]arene. The second DCM molecule was involved in a short contact to a nitrogen atom (2.65 Å) of one isoxazole unit and in close contact with the upper rim of the calixarene of a neighbouring molecule.

PIC.2DCM presented in the cone conformation, lower rim intra-annular H-bonding between the phenolic OH and the neighbouring ether atoms stabilised this conformation at an average O...O distance of 2.79 Å, blue lines in **Figure 2.10a**.

Intramolecularly, the pyrene units were orientated away from each other with an interplanar angle of 45.57°, **Figure 2.10b**.

The isoxazole and pyrene moieties of the pendant arms were not coplanar, angles of 39.28° and 31.49° were measured between the planes of the rings. These are significantly smaller than the angles observed for the **PIC.MeCN** crystal (45.31° and

44.12°). It is possible that crystallisation with the second DCM molecule causes a twist in the orientation of the isoxazole unit.

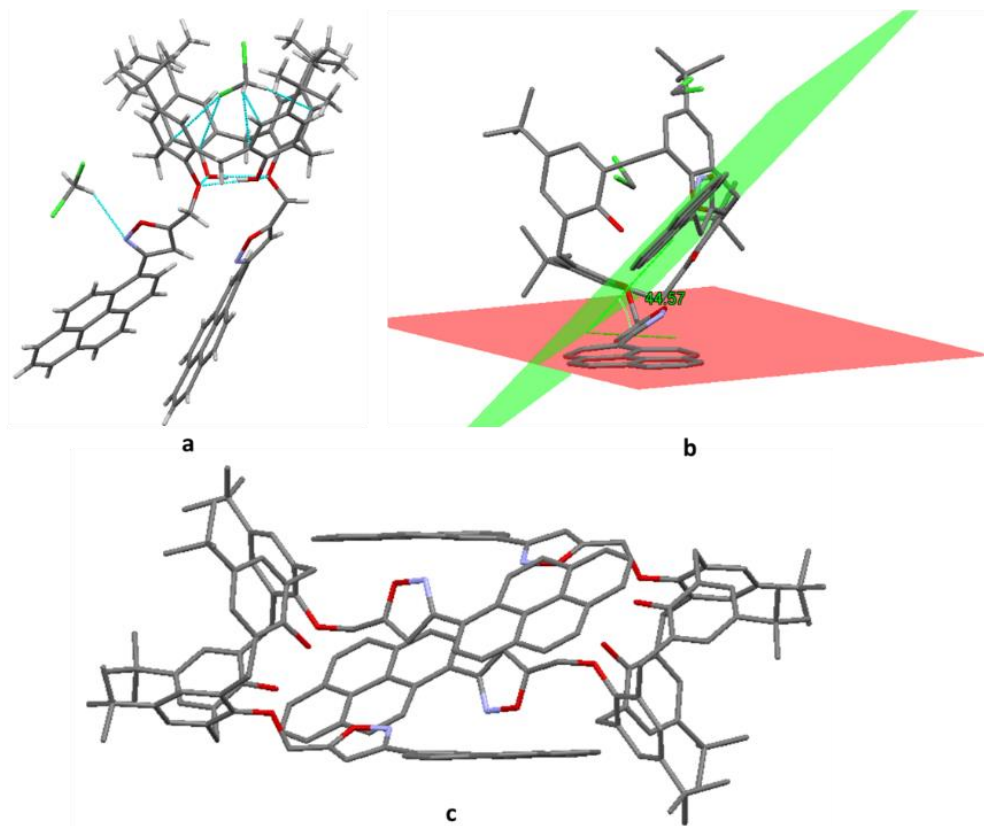


Figure 2.10: a) Solid state structure of **PIC.2DCM**, crystal grown from EtOH:DCM (2:1, v/v); one molecule of DCM is in the upper cavity and a second in close contact with the isoxazole ring, **b)** diagram of **PIC** showing the 45.57° angle between the planes of the pyrene moieties and **c)** tail-to-tail “sandwich” *dimer* of **PIC** showing that no intermolecular π - π interactions are evident between neighbouring pyrene units.

Tail-to-tail “sandwich” *dimers* were observed, a pyrene moiety of one **PIC** was parallel to a pyrene from another molecule of **PIC**. The second pyrene moieties of each **PIC** molecule were also parallel. However, the parallel fluorophores were fully slipped from each other leading to no intermolecular interactions in the *dimeric* structure, as shown in **Figure 2.10c**.

Examination of the extended network created by the units of **PIC** in the solid state structure revealed a tail-to-tail arrangement of the calixarene units, creating a

channel, occupied by the DCM molecule, between the interlocking pyrene units from neighbouring calixarene moieties, **Figure 2.11**.

A summary of the interesting characteristics of the **PIC.2DCM** crystal is given in **Table 2.3**.

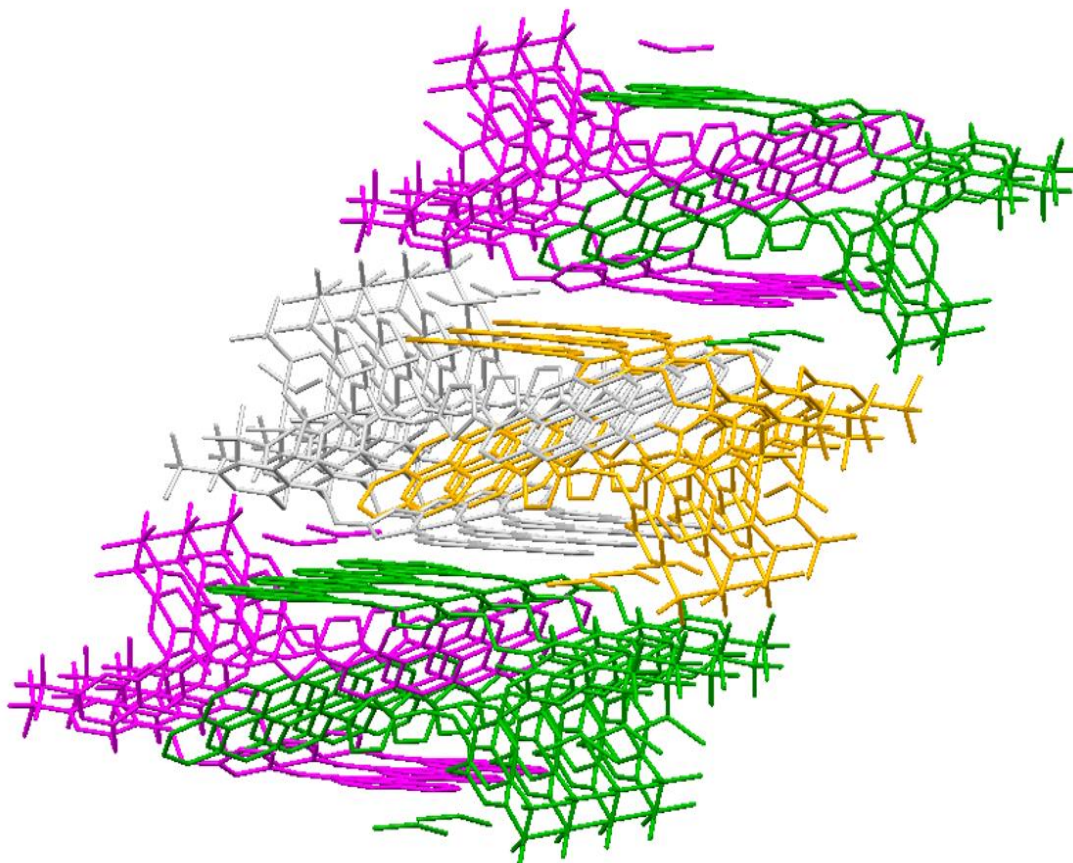


Figure 2.11: Extended network of the **PIC.2DCM** solid state structure showing the tail-to-tail arrangement of the calixarene units.

Table 2.3: Summary of the characteristics of the **PIC.2DCM** crystal structure.

Py-Py Plane Angle	Py-Isox Plane Angles		Lower-Rim Hydrogen Bonding	Solvent Interaction	Other Interesting Features
45.57°	39.28°	31.49°	Present at an average O...O distance of 2.79 Å.	One unit of DCM in upper cavity and second molecule in short contact with one of the isoxazole rings.	No intermolecular π - π interactions are evident between neighbouring pyrene units. Tail-to-tail interlocking arrangement between units of PIC . Channel observed between interlocking pyrene units in extended network.

The influence of the nature of the solvent of crystallisation on x-ray crystal structures of calixarenes is well reported in the literature,^{96,97} and it is not surprising that crystallisation of **PIC** from two different solvent systems led to polymorphic structures.

Dupont *et al.* report three different molecular structures for their *para*-azidomethyltetrahydroxy-calix[4]arene, **Figure 2.12**, crystallised from **i)** a CHCl_3 -MeOH mixture, **ii)** a CHCl_3 -hexane mixture and **iii)** 100% toluene.⁹⁷ No solvent molecules were present in the first two crystal structures, whilst toluene co-crystallised in the third, where it provided a π - π stacking network that connected dimers of the calixarene to six other dimers and two solvent molecules in all directions. These results indicated that solvents for crystallisation can influence the packing with or without being present in the crystal.

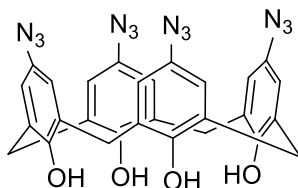


Figure 2.12: *Para*-azidomethyltetrahydroxy-calix[4]arene used to study the influence of the nature of the solvent of crystallisation on x-ray crystal structures of calixarenes by Dupont *et al.*⁹⁷

2.5.1.1 Vapour Diffusion Crystallisation Technique

A hanging drop vapour diffusion technique was used to crystallise a complex of isopenicillin *N*-synthase (IPNS) with Fe^{2+} sulphate and δ -(*L*- α -amino adipoyl)-*L*-cysteinyl-*D*-valine (Aad-Cys-Val) by Roach and co-workers.⁹⁸ They prepared stock solutions of ferrous sulphate, IPNS and Aad-Cys-Val and placed 6 μL drops of this solution over a container of solvent. Three crystalline forms were obtained using this technique, while analogous crystallisation attempts in the absence of Aad-Cys-Val were unsuccessful.

A vapour diffusion technique⁹⁹ can also be useful to form solid samples of a compound or crystal. This technique involves placement of a solution of the analyte to be crystallised into an open vial, no more than half full, inside a larger sealed container containing a solvent that is more volatile than that used in the inner vial, **Figure 2.13.**³⁹ It is important that the analyte for crystallisation be either insoluble or only sparingly soluble in the more volatile solvent. Over time the vapour of the more volatile solvent will diffuse into the head space in the larger sealed container and subsequently into the solution of the compound resulting in a decrease in solubility of the compound and thus forcing it out of solution, ideally in crystalline form.

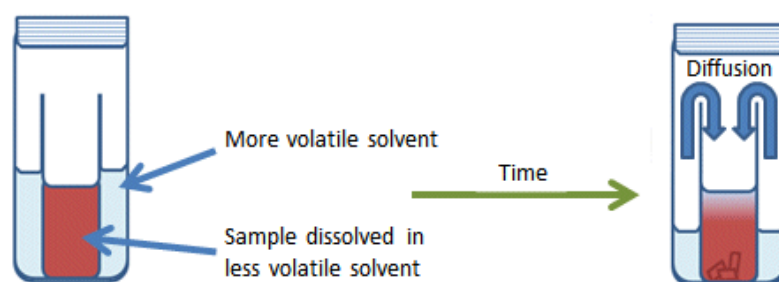


Figure 2.13: General set-up of a vapour diffusion crystallisation approach.³⁹

The vapour diffusion technique was pursued in search of *in situ* formation of a crystalline **PIC**:Cu²⁺ complex. Four separate vapour diffusion experiments were set up; **PIC** (37 μM, MeCN:CHCl₃, 10:1, v/v) was placed inside a 2 cm diameter glass vial, Cu(ClO₄)₂ (37 or 74 μM) was added to the vial which was placed inside a 5 cm diameter screw top jar containing either EtOAc or diethyl ether as the volatile solvents, **Table 2.4**. Unfortunately, despite several months, neither a crystalline nor an amorphous solid formed in any of the four inner vials.

Table 2.4: Summary of vapour diffusion experiments carried out for *in situ* **PIC**:Cu²⁺ complex (MeCN:CHCl₃, 10:1, v/v) formation and precipitation.

PIC : Cu²⁺	PIC : Cu²⁺ Concentration (μM)	Volatile Solvent	Result
1:1	37:37	EtOAc	No Solid Formed
1:2	37:74	EtOAc	No Solid Formed
1:1	37:37	Diethyl Ether	No Solid Formed
1:2	37:74	Diethyl Ether	No Solid Formed

2.5.3 ¹H NMR Spectroscopic Investigation of the Effect of the Cu²⁺ Ion on PIC

A ¹H NMR spectroscopic study was undertaken to investigate the mode of complexation between **PIC** and Cu²⁺ ions. A mix of CD₃CN:CDCl₃ (4:1, v/v) was chosen as the best mimic of the fluorescence experiments (conducted in MeCN), the 20% v/v CDCl₃ was required to reach a sufficient concentration of **PIC** for the ¹H NMR spectroscopy measurements. A stock solution of **PIC** at 0.65 mM was prepared in a CD₃CN:CDCl₃ (3:1, v/v) mixed solvent system. A stock solution of Cu(ClO₄)₂ at 6.77 mM was prepared in CD₃CN. Samples with varying ratios of host to metal salt were prepared (1:0 through 1:2 eqs) according to the volumes shown in **Table 2.5**. Each sample was allowed to equilibrate for 20 mins prior to recording its ¹H NMR spectrum.

Table 2.5: Summary of the volume of reagents employed for the ^1H NMR spectroscopic study of **PIC**: Cu^{2+} (1:0 to 1:2 eqs) complexation in $\text{CD}_3\text{CN}:\text{CDCl}_3$ (4:1, v/v).

PIC : $\text{Cu}(\text{ClO}_4)_2$	PIC - 0.65 mM (μL) ($\text{CD}_3\text{CN}:\text{CDCl}_3$, 3:1, v/v)	$\text{Cu}(\text{ClO}_4)_2$ - 6.77 mM (μL) (CD_3CN)	CD_3CN (μL)
1 : 0	500	0	100
1 : 1	500	48	52
1 : 2	500	96	4

Following exposure of **PIC** to increasing amounts of $\text{Cu}(\text{ClO}_4)_2$, significant concentration dependant changes became evident as shown in **Figure 2.14**. A significant broadening of the pyrene proton signals is observed in the presence of the Cu^{2+} ion in solution which suggests that the pyrene moieties are in close proximity to the paramagnetic Cu^{2+} metal ion during host:guest binding. In contrast, the peaks in the rest of the spectra remain relatively sharp and well resolved.

A number of significant new signals appeared at 6.80, 6.38, 6.04 and 4.54 ppm in the copper containing samples. The new singlets at 6.80 and 6.38 ppm showed identical integrations and were assigned to the ArH of the upper rim of the calixarene of the host:guest complex. These signals were more intense in the presence of 2 eqs of Cu^{2+} w.r.t. 1 eq of Cu^{2+} . These relative intensities were ascertained by comparison to a spiked DCM peak at 5.12 ppm and by comparison the peaks of the host alone. The new peak at 4.54 ppm was assigned to the ArOCH_2 of the host:guest complex in a similar manner.

A number of new signals appeared in the *t*-butyl range of **PIC** in the presence of $\text{Cu}(\text{ClO}_4)_2$, **Figure 2.14b**. These new signals were deemed indicative of conformational changes induced to the calixarene scaffold upon guest binding which altered the resonance positions of the *t*-butyl moieties of the host:guest complex.

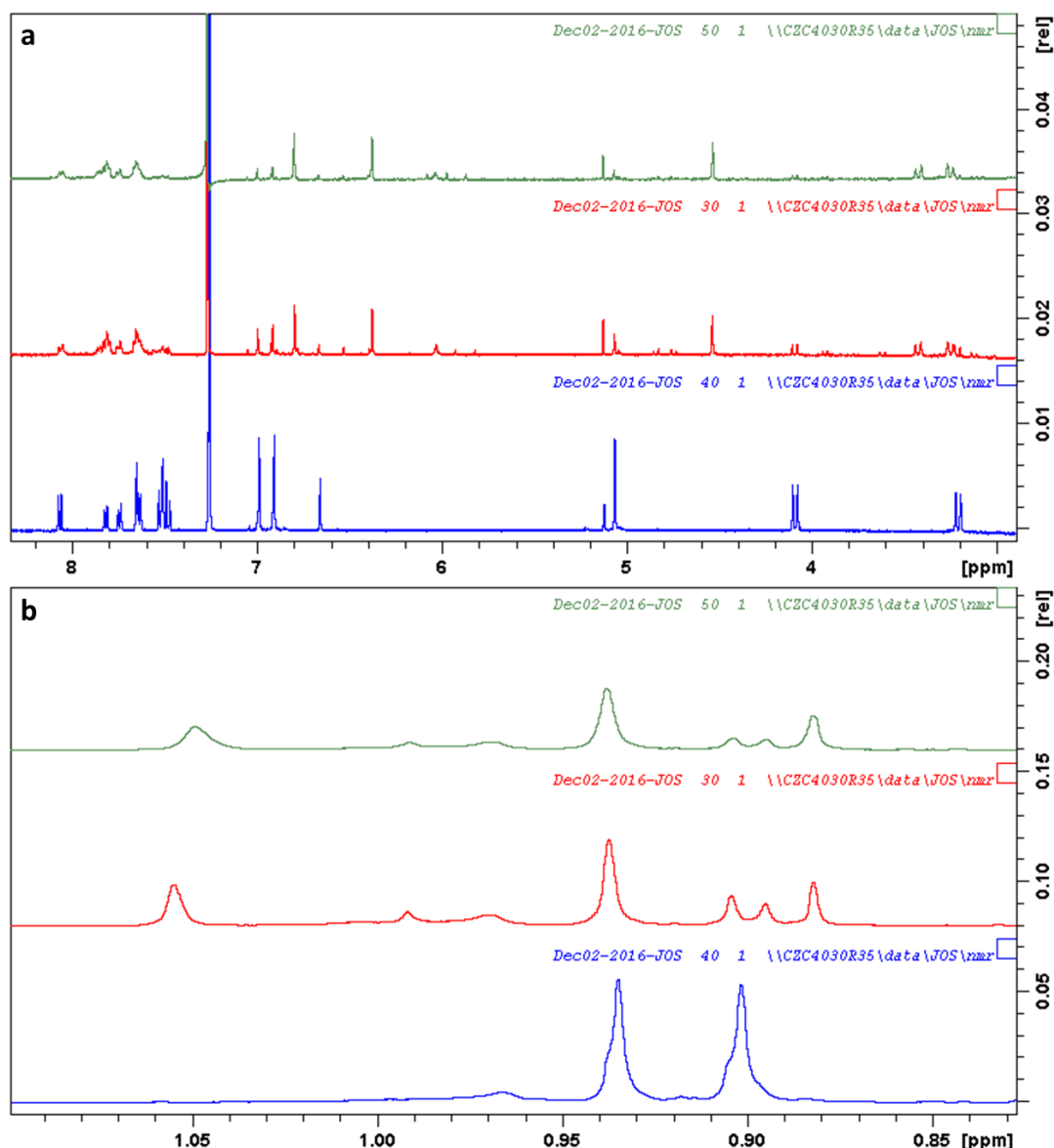


Figure 2.14: ^1H NMR (500 MHz) spectra of **PIC** (0.54 mM, $\text{CD}_3\text{CN}:\text{CDCl}_3$, 4:1, v/v) at 25°C in the region between: **a)** 8.30 and 3.00 ppm and **b)** 1.10 and 0.83 ppm; with increasing numbers of equivalents of $\text{Cu}(\text{ClO}_4)_2$: 0 (blue), 1 (red) and 2 (green).

Copper perchlorate in MeCN can act as an oxidising agent or in the presence of adventitious water as a Brønsted acid.^{100,101} The potential increase in acidity of the NMR sample was considered a possible contributor to the guest induced effects on the isoxazole proton observed in the ^1H NMR titration experiments. This phenomenon was investigated by exposing **PIC** to perchloric acid and recording the ^1H NMR spectra. Stock solutions of **PIC** at 0.65 mM and HClO_4 at 65 mM in $\text{CD}_3\text{CN}:\text{CDCl}_3$ (3:1, v/v) were prepared, and ^1H NMR spectra were recorded, according

to the volumes shown in **Table 2.6**. Each sample was allowed to equilibrate for 20 mins prior to recording its ^1H NMR spectrum.

Table 2.6: Summary of the volume of reagents required for a ^1H NMR spectroscopic study of the interactions between **PIC** and perchloric acid (1:0 to 1:5 eqs) in $\text{CD}_3\text{CN}:\text{CDCl}_3$ (3:1, v/v).

PIC : HClO_4	PIC - 0.65 mM (μL)	HClO_4 - 65 mM (μL)
1 : 0	500	0
1 : 2	500	10
1 : 5	500	25

PIC (0.65 mM, $\text{CD}_3\text{CN}:\text{CDCl}_3$, 3:1, v/v) was titrated against 0, 2 and 5 eqs of perchloric acid, **Figure 2.15**. A slight broadening of all proton signals was observed, with no significant effect to the isoxazole proton at 6.67 ppm. The ^1H NMR titrations of **PIC** with $\text{Cu}(\text{ClO}_4)_2$ indicated the emergence of several new signals both up and down field from the isoxazole proton signal. This was not the case in the perchloric acid titrations suggesting that the effects of the Cu^{2+} ion on the ^1H NMR spectra of **PIC** were not due to changes in the acidity of the NMR sample.

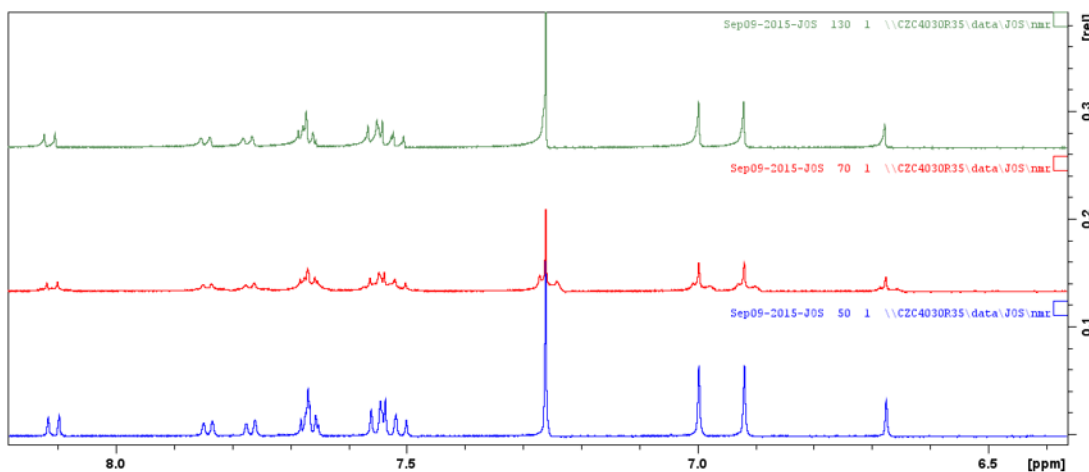


Figure 2.15: ^1H NMR (500 MHz) spectra of **PIC** (0.65 mM, $\text{CD}_3\text{CN}:\text{CDCl}_3$, 3:1, v/v) at 25°C in the region between 8.20 and 6.40 ppm with increasing amounts of HClO_4 : 0 (blue), 2 (red) and 5 (green) eqs.

In order to lend support to the suggestion that the spectroscopic changes to **PIC** on exposure to copper perchlorate were not due to the acidity of Cu^{2+} ions, a fluorescence spectrum of **PIC** in the presence of 30 eqs of perchloric acid was

compared to that recorded for the host-alone, **Figure 2.16**. No difference was observed between these; the shape and the intensity of both the monomer and excimer peaks were unchanged from the host **PIC** (6 μM) in the absence of perchloric acid, indicating that the fluorescence emission of **PIC** is unaffected by the induced acidity of the MeCN solution of $\text{Cu}(\text{ClO}_4)_2$.

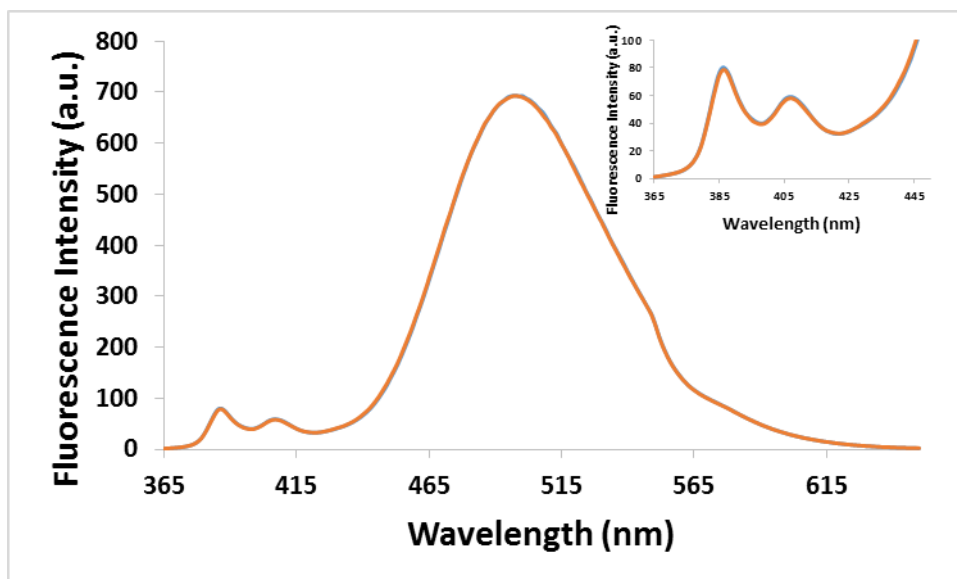


Figure 2.16: Emission spectra of **PIC** (6 μM , $\lambda_{\text{ex}} = 343 \text{ nm}$) in MeCN with 0 (blue) and 30 (orange) eqs of HClO_4 . Inset: Expansion of monomer region from 365 to 450 nm.

2.5.4 Analysis of the Fluorescence Quenching Mechanism of **PIC** by Copper Perchlorate

The method of fluorescence quenching of **PIC** by copper perchlorate was investigated by Stern-Volmer analysis (Section 1.4.2). The host **PIC** was prepared at 12 μM in MeCN and a solution of $\text{Cu}(\text{ClO}_4)_2$ in the same solvent was prepared at 24 μM . Appropriate quantities were drawn from these stock solutions to prepare the samples as indicated in **Table 2.7**.

Fluorescence emission spectra were recorded for **PIC** (6 μM) in MeCN in the presence of 0-2 equivalents of $\text{Cu}(\text{ClO}_4)_2$, **Figure 2.17**. As larger quantities of Cu^{2+} ions were added, the quenching of excimer fluorescence became more apparent, reaching 35% in the presence of 2 eqs of $\text{Cu}(\text{ClO}_4)_2$ (12 μM).

Table 2.7: Summary of the volume of reagents and solvent required in order to construct a Stern-Volmer plot for **PIC** and $\text{Cu}(\text{ClO}_4)$ (1:0 to 1:2 eqs).

PIC : Cu^{2+}	PIC - 12 μM (μL)	$\text{Cu}(\text{ClO}_4)_2$ - 24 μM (μL)	MeCN (μL)
6 : 0	1500	0	1500
6 : 1.2	1500	150	1350
6 : 2.4	1500	300	1200
6 : 3.6	1500	450	1050
6 : 4.8	1500	600	900
6 : 6	1500	750	750
6 : 9	1500	1125	375
6 : 12	1500	1500	0

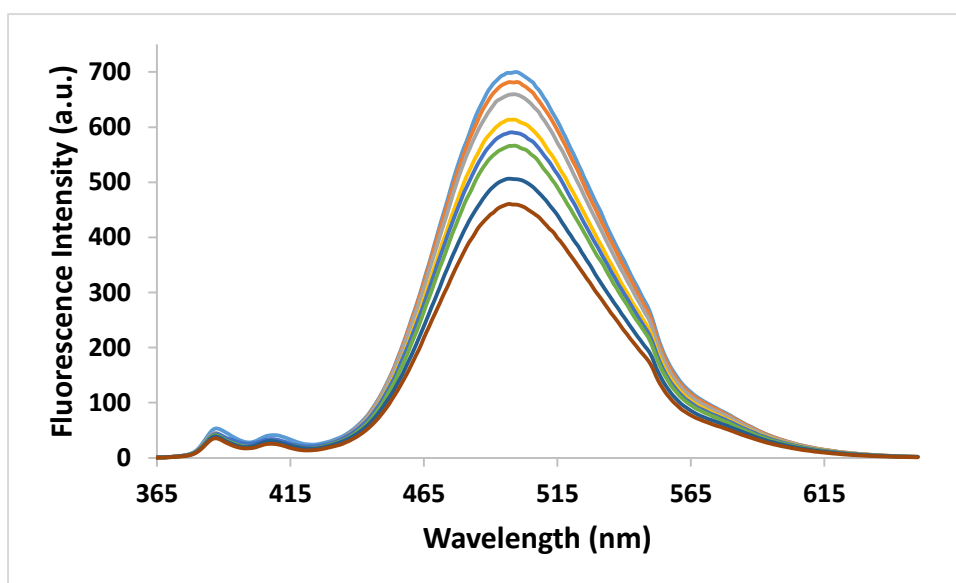


Figure 2.17: Emission spectra of **PIC** (6 μM , MeCN, $\lambda_{\text{ex}} = 343 \text{ nm}$) with 0-2 eqs of $\text{Cu}(\text{ClO}_4)_2$.

Using the data shown in **Figure 2.17** a Stern-Volmer plot was constructed by graphing $\frac{I_0}{I}$ on the y-axis and $[\text{Cu}^{2+}]$ on the x-axis. It showed a linear relationship ($R^2 = 0.9941$), **Figure 2.18**. The linearity was consistent with either purely static or purely dynamic quenching of the fluorescence emission of **PIC** by up to 2 equivalents of Cu^{2+} ions in MeCN at rt. The slope of the plot indicated that the Stern-Volmer quenching constant, K_{SV} , was $45,000 \text{ M}^{-1}$, which is in the same range as the K_{SV} ($47,600 \text{ M}^{-1}$) determined by Rao *et al.*, for the interaction of their triazole anthracene functionalised calix[4]arene with Co^{2+} perchlorate ions in EtOH, **Figure 1.25b**.¹⁸

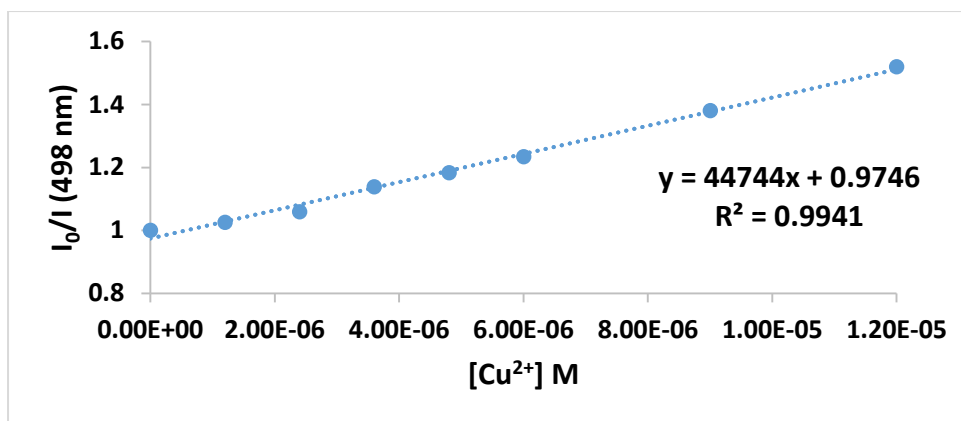


Figure 2.18: Stern–Volmer plot of **PIC** (6 μM) with $\text{Cu}(\text{ClO}_4)_2$ (0-2 eqs), in MeCN in which the fluorescence intensity ($\frac{I_0}{I}$) at 498 nm was plotted against the concentration of Cu^{2+} (Slope = 44744, $R^2 = 0.9941$).

2.5.5 Binding Constant Determination of the **PIC**: Cu^{2+} Complex Formation

The Benesi-Hildebrand method (Section 1.4.3) was used to determine the binding constant, K_a , for the **PIC**: Cu^{2+} complex formation reaction in MeCN at rt. The data used to construct the plot corresponded to that used to construct the Stern-Volmer plot, **Table 2.7**. Thus, the concentration of **PIC** was kept at 6 μM while varying the concentration of the Cu^{2+} from 0 μM to 12 μM . The plot was constructed by plotting $\frac{1}{\Delta F}$ on the y-axis and $\frac{1}{[G]}$ on the x-axis, **Figure 2.19**. This plot showed a linear relationship ($R^2 = 0.9928$). According to the Benesi-Hildebrand equation the intercept divided by the slope gives the K_a , the binding constant. Therefore $K_a = 0.0033/(7 \times 10^{-8}) = 47,000 \text{ M}^{-1}$, which is higher than that calculated for the 9-chloroanthracen-10-yl isoxazole analogue, **3** ($15,800 \text{ M}^{-1}$)⁸¹ and approximately 20 times greater than the K_a calculated for the 1-naphthyl isoxazole functionalised calix[4]arene, **4** (2080 M^{-1})⁸¹ indicating that the pyrene-isoxazole-calixarene combination may be an attractive design for a calix[4]arene based Cu^{2+} sensor.

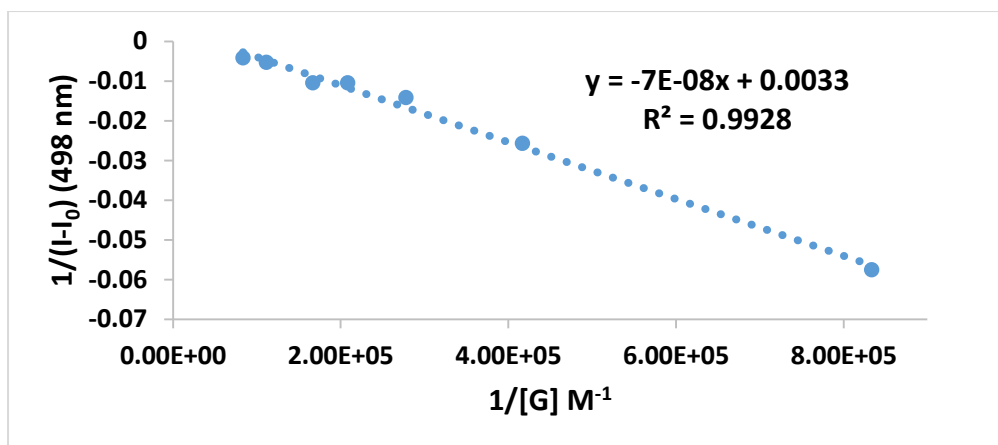


Figure 2.19: Benesi-Hildebrand plot of **PIC** with $Cu(ClO_4)_2$ (0-2 eqs) in MeCN (6 μM). ($R^2 = 0.9928$, intercept = 0.0033, slope = -7×10^{-8}).

2.5.6 Detection Limit of PIC for the Cu^{2+} Ion

The detection limit (DL), “the smallest concentration of a substance that can be reliably measured by an analytical procedure”¹⁰² was determined using the following formula:^{29,30}

$$Detection\ Limit = \frac{K \cdot SB1}{S} \quad \text{Equation 2.1}$$

K is an arbitrary unit equal to 2 or 3, SB1 is the standard deviation of the fluorescence intensity of host solutions, S is the slope of the calibration curve of the fluorescence intensity of the host with varying eqs of guest.

The required calibration curve was constructed by plotting the fluorescence intensity of **PIC** (6 μM , MeCN, $\lambda_{ex} = 343$ nm) at 498 nm against the concentration of $Cu(ClO_4)_2$ (0-2 eqs), **Figure 2.20**. The data used to construct the calibration curve corresponded to the data used for the Stern-Volmer analysis (Section 2.5.4).

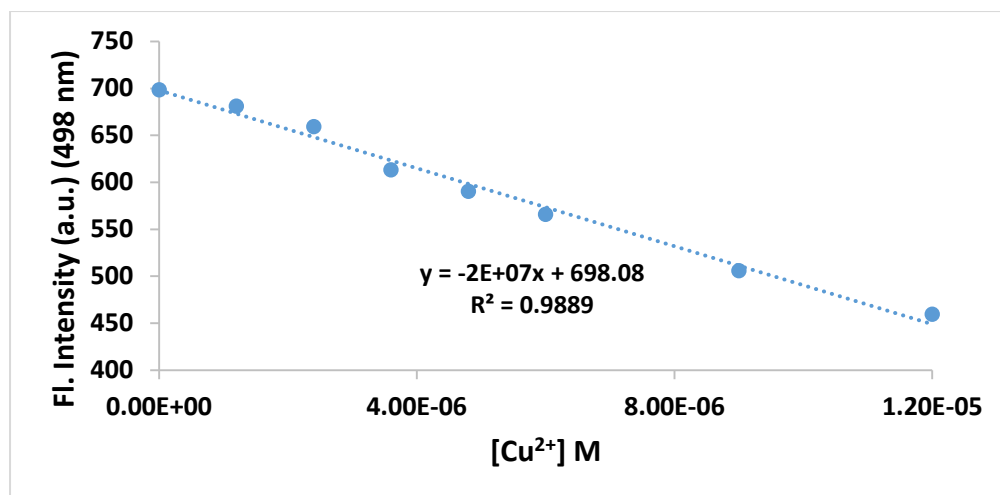


Figure 2.20: Calibration Curve of **PIC** (6 μM , MeCN, $\lambda_{\text{ex}} = 343 \text{ nm}$) with 0-2 eqs of $\text{Cu}(\text{ClO}_4)_2$, $R^2 = 0.9889$.

The detection limit was thus calculated as follows:

$$\begin{aligned}
 \text{DL} &= \text{KSB1/S} \\
 &= (2 \times 2.90)/(2 \times 10^7) \\
 &= 2.90 \times 10^{-7} \text{ M} \\
 &= 0.3 \mu\text{M}.
 \end{aligned}$$

This indicates that **PIC** can accurately detect Cu^{2+} ions from a MeCN solution of copper perchlorate to the lowest concentration of 0.3 μM . This compares favourably with the detection limit of 0.60 μM ascertained by Shukla and co-workers for their coumarin functionalised calixarene fluorescent Cu^{2+} sensor, **Figure 2.21**.

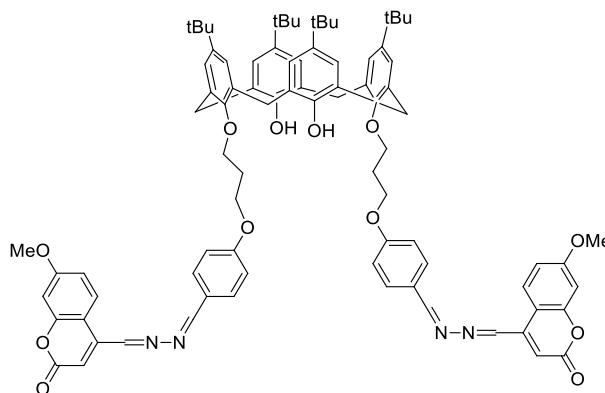


Figure 2.21: Coumarin functionalised calixarene designed by Shukla *et al.* as a fluorescent chemosensor for Cu^{2+} ions in MeCN with a detection limit of 0.6 μM .¹⁰³

2.6 Conclusions

At the outset of the author's research, it was known that **PIC** could selectively detect the Cu^{2+} ion over a range of other metal ions, however, despite EPR spectroscopic and DFT theoretical studies, details of the geometry of the **PIC**: Cu^{2+} complex remained unclear.

- (i) **PIC**, equipped with distal isoxazole units as potential metal binding sites and pyrene moieties as fluorophoric reporter units was synthesised by catalyst-free nitrile oxide/alkyne cycloaddition (NOAC).
- (ii) **PIC** presented in the cone conformation in the solid state structure obtained from a crystal grown in MeCN with no interactions evident between pendant pyrene moieties. The packing diagram showed intermolecular short contacts between pyrene moieties in neighbouring **PIC** molecules.
- (iii) Excimer signals in the fluorescence emission spectra indicated an intramolecular π - π interaction of the pyrene rings in the solution state. Fluorescence quenching occurred in the presence of Cu^{2+} ions over a range of other divalent transition metal cations, all introduced as perchlorate salts.

The contributions of the author to an understanding of the binding event between **PIC** and Cu^{2+} are summarised below.

- Attempts were made to prepare a solid sample or to grow crystals of the **PIC**: Cu^{2+} complex suitable for x-ray analysis, however all were unsuccessful.
- An advanced ^1H NMR spectroscopic study of the effect of the Cu^{2+} ion on **PIC** indicated binding influenced the protons pyrene regions of **PIC** most significantly. Thus the Cu^{2+} binding site is likely to be in the pyrene region.
- Stern-Volmer analysis indicated that the quenching of **PIC** by up to two eqs of copper perchlorate occurred either purely by a static or a dynamic mechanism.
- The binding constant of **PIC** with copper perchlorate in MeCN, was calculated using the Benesi-Hildebrand method; $K_a = 47,000 \text{ M}^{-1}$.

- The detection limit for **PIC** to sense Cu^{2+} ions in MeCN solution was found to be $0.3 \mu\text{M}$.

2.7 Future Work

Following on from the initial success of **PIC** as a Cu^{2+} fluorescent sensor, a sequential investigation of the relationship between molecular structure, and selectivity and sensitivity to detection of metal ions was designed.

The proposed studies included an examination of the importance of:

- i) the length of the linker between the lower rim ether O atoms and the heterocyclic isoxazole rings
- ii) direct conjugation between the pyrene fluorophore and the isoxazole ring
- iii) the phenolic hydroxyl moieties on the lower rim of the calix[4]arene;

Chapter 3 will report on the design, synthesis and characterisation of three novel lower rim pyrene functionalised calix[4]arenes structurally related to **PIC**, intended to investigate the three structural features mentioned above.

Chapter 3

PIC Analogues: Design, Synthesis and Characterisation

3.1 Overview

This chapter gives a description of the design, synthesis and characterisation of a number of novel pyrene functionalised calixarenes structurally related to **PIC**. Each new compound was designed to differ from **PIC** at only one position, these variations included **(i)** extension of the linker group between the lower rim of the calixarene and the isoxazole rings, **(ii)** introduction of a spacer between the pyrene fluorophore and the isoxazole ring and **(iii)** alkylation of the lower rim hydroxyl groups.

3.2 Ethylene Pyrene Isoxazole Calixarene (EPIC)

EPIC, Ethylene Pyrene Isoxazole Calixarene, shown in **Figure 3.1**, was designed with an ethylene linkage separating the isoxazole ring from the lower rim of the calixarene, whilst retaining the hydroxyl groups and having no spacer between the isoxazole and pyrene rings.

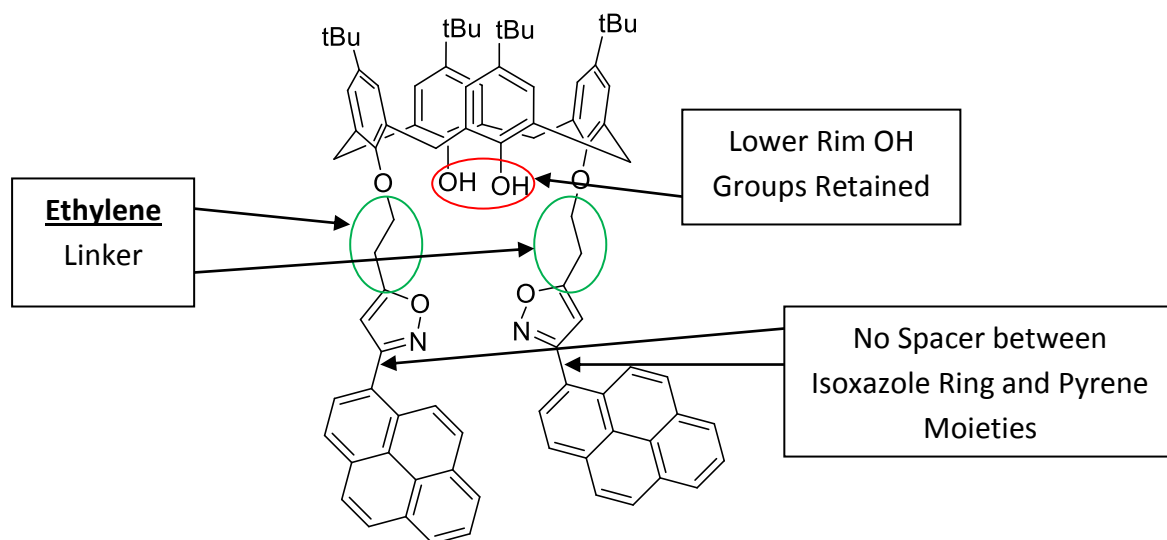
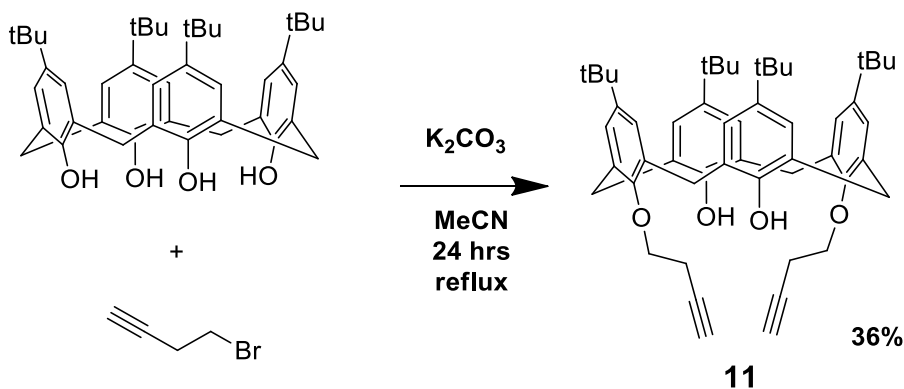


Figure 3.1: Structure of Ethylene Pyrene Isoxazole Calixarene (**EPIC**).

3.2.1 Synthesis of EPIC

To access **EPIC** by nitrile oxide/alkyne cycloaddition chemistry the distally functionalised calix[4]arene **11** was required to act as the dipolarophile and 1-pyrenecarbaldoxime, **12** as the dipole precursor. The bis-alkylated calix[4]arene 5,11,17,23-*tetra-tert*-butyl-25,27-bis(but-3-ynyloxy)-26,28-dihydroxy calix[4]arene, **11**, was synthesised by the method of Bonnamour *et al.*, **Scheme 3.1**.¹⁰⁴

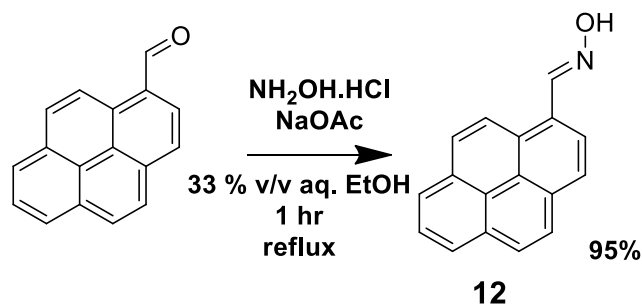
Commercially available 4-*tert*-butylcalix[4]arene was initially exposed to 5 eqs of potassium carbonate in anhydrous MeCN for 1 hour at rt. 4-Bromo-1-butyne (4.2 eqs) was added dropwise over 30 mins and the solution was heated to reflux for 24 hrs. Following filtration over celite, an acidic work-up and flash column chromatography, **11** was obtained as a bright white amorphous solid in 36% yield. ^1H NMR spectroscopic data corresponded to that reported in the literature.¹⁰⁴



Scheme 3.1: Synthesis of 5,11,17,23-*tert*-butyl-25,27-bis(but-3-ynoxy)-26,28-dihydroxycalix[4]arene, **11**.¹⁰⁴

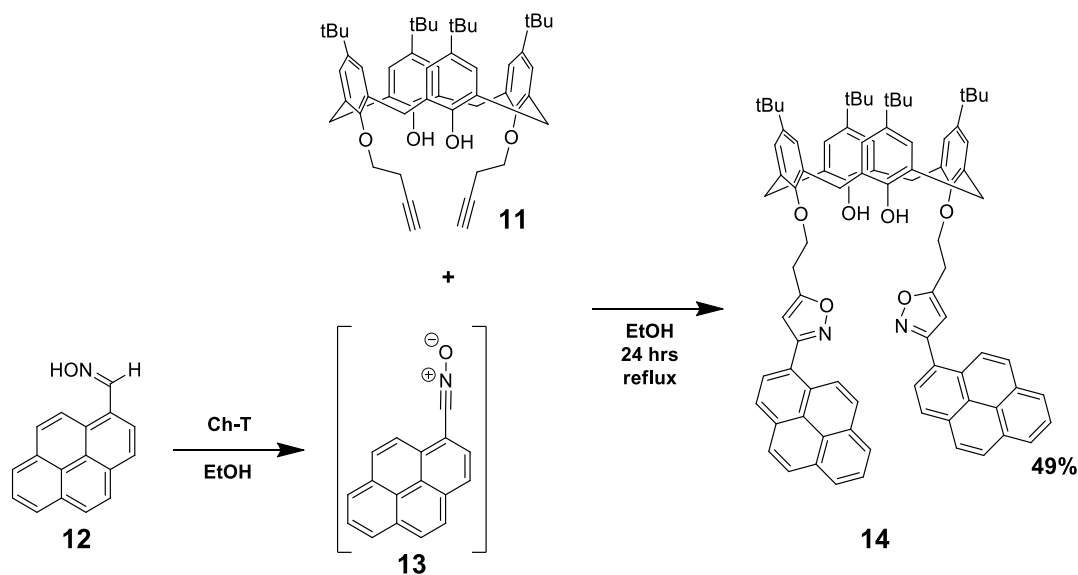
The modest yield of **11** is in keeping with, as evidenced in the ^1H NMR spectrum, the presence of both the monoalkylated calixarene and unreacted starting material in the crude mixture. The presence of these species led to difficulty in purification of **11**. The moderate yield may also be due to the tendency of the haloalkyne to undergo base induced dehydrohalogenation,¹⁰⁵ thus two new peaks at 3.03 (m) and 2.16 (t) ppm in the ^1H NMR spectrum of the crude mixture may be attributed to alkene elimination products.

1-Pyrenecarbaldoxime, **12** was prepared from 1-pyrenecarbaldehyde by optimisation of a known method, **Scheme 3.2**.¹⁰⁶ Hydroxylamine hydrochloride (3 eqs) and sodium acetate trihydrate (4 eqs) were added to commercially available 1-pyrenecarbaldehyde in 33% v/v aq. EtOH and the resulting solution was heated to reflux for 1 hr. Following an EtOAc extraction, **12** was obtained as a bright yellow solid in 95% yield, a 28% improvement in the reported yield. ^1H NMR spectroscopic data corresponded to that reported.¹⁰⁷



Scheme 3.2: Synthesis of 1-pyrenecarbaldoxime, **12**.¹⁰⁶

EPIC was synthesised following a 1,3-Huisgen cycloaddition between the *in situ* generated 1,3-dipole **13** and the calixarene dipolarophile **11**. One eq of **11** was dissolved in EtOH and 4 eqs of 1-pyrenecarbaldoxime, **12** were added to the solution which was heated to reflux. Three portions, each of 2 eqs of Ch-T, were added at 0, 3 and 6 hrs from the commencement of the reaction, this allowed for generation of the putative nitrile oxide **13** and *in situ* reaction with the alkyne. The portion-wise addition of Ch-T was also designed to help avoid self-reaction of the nitrile oxide, which could result in the formation of furoxan and dioxadiazine by-products, (see discussion in Section 1.6.3). When addition of Ch-T was complete, the reaction mixture was allowed to stir for a further 18 hrs at reflux, cooled, and the product extracted with chloroform and washed with 5% aq. NaOH to remove sulphonamide by-products. The solvent was removed under reduced pressure and the crude material purified by flash column chromatography and finally recrystallised from EtOH:DCM (2:1, v/v) to yield **EPIC** as a white crystalline solid in 49% yield, **Scheme 3.3**.



Scheme 3.3: Synthesis of Ethylene Pyrene Isoxazole Calixarene (**EPIC**), **14**.

3.2.2 Characterisation of EPIC

Characteristic ^1H NMR signals expected following the successful synthesis of the isoxazole ligated pyrene-calixarene **14** from reaction between **11** and **12** include the emergence of a singlet peak between 6.25 and 7.25 ppm (in CDCl_3) for the CH of the isoxazole ring,¹⁰⁸ and the disappearance of the terminal alkyne triplet signal of the starting material at ~ 2 ppm.

The ^1H NMR spectra of isolated **EPIC** and alkyne **11** were compared, the triplet signal at 2.08 ppm of the alkyne proton was not present in the ^1H NMR spectrum of **EPIC**, while a number of singlets between 6.90 and 6.71 ppm in the spectrum of **EPIC** strongly suggested that the heterocyclic isoxazole ring had been formed.

3.2.2.1 ^1H and ^{13}C NMR Spectroscopic Characterisation of EPIC

The ^1H NMR spectrum of **EPIC**, **Figure 3.2** showed a pair of sharp AB doublets at 4.03 and 3.25 ppm with reciprocal coupling constants of 13.0 Hz which indicated that **EPIC** presented in the cone conformation.¹⁰⁹ The conformational assignment was further supported by two *t*-butyl singlets, each with a relative integration of 18H at 1.38 and 0.90 ppm.¹⁰⁹

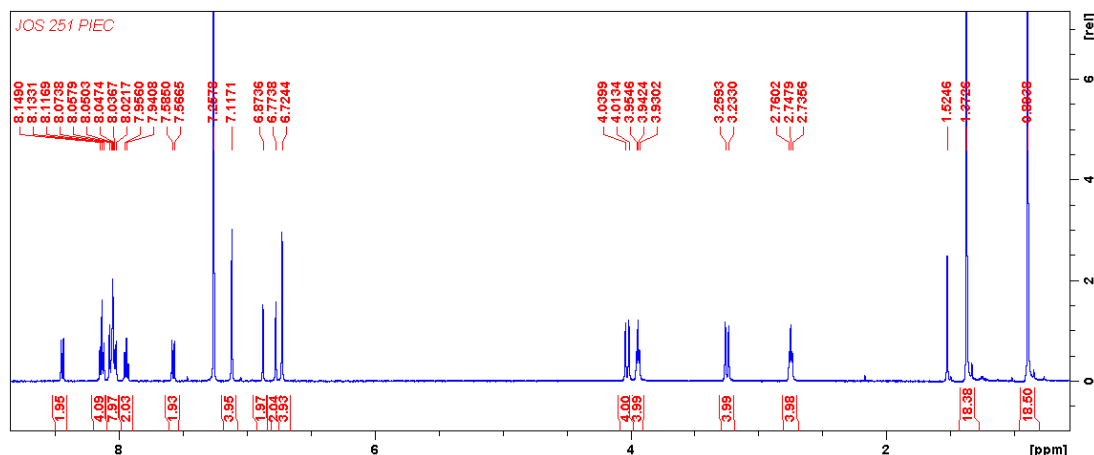


Figure 3.2: ^1H NMR spectrum (500 MHz) of **EPIC** in CDCl_3 at 25°C .

Triplet resonances at 3.95 and 2.76 ppm were assigned as the methylene protons of the ethylene linker. The more downfield signal was intuitively assigned as the OCH_2 group, as the O -atom is expected to have a stronger deshielding effect than the isoxazole ring. The assignment is supported by comparing the ^1H NMR spectra of the starting alkyne and the cycloadduct, **Figure 3.3**. In the starting material **11**, the methylene group adjacent to the alkyne appears as a triplet of doublets due to coupling to both the neighbouring CH_2 and CH protons whilst the signal of the corresponding protons appears as a triplet in the spectrum of **EPIC**. Thus, the upfield triplet, at 2.76 ppm was assigned as the CH_2 -isoxazole group.

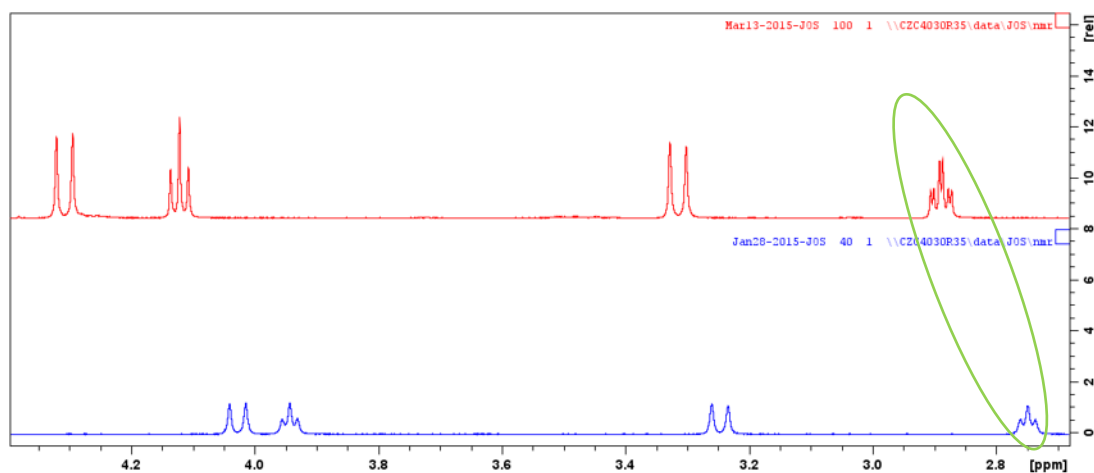


Figure 3.3: ^1H NMR spectra (500 MHz) of bis-alkylated calixarene **11** (red) and **EPIC** (blue) in CDCl_3 at 25°C showing the change in multiplicity of the OCH_2CH_2 methylene groups on converting from the alkyne **11** (td) to **EPIC**, **14**, (t).

Sharp singlets, with the same relative intensities at 6.88 and 6.78 ppm, were tentatively assigned as the OH and the isoxazole CH protons. The disappearance of the signal at 6.78 ppm following a D₂O shake identified it as representing the lower rim OH protons. It followed intuitively that the singlet at 6.88 ppm arose from the isoxazole protons. The assignment was supported by a HSQC spectrum, **Figure 3.4**. Isoxazole CH carbon atoms resonate at approximately 105 ppm in ¹³C NMR spectra¹¹⁰ and the singlet peak at 6.88 ppm in the ¹H NMR spectrum showed a correlation with a ¹³C NMR signal at 105.1 ppm. Singlets at 7.13 and 6.73 ppm were assigned as the ArH protons of the upper rim of the calixarene based on their chemical shift, multiplicity and relative integrations. The aromatic signals between 8.45 and 7.58 ppm showed a relative integration of 18H and were assigned as the pyrene protons; individual signals were not assigned due to severe resonance overlap.

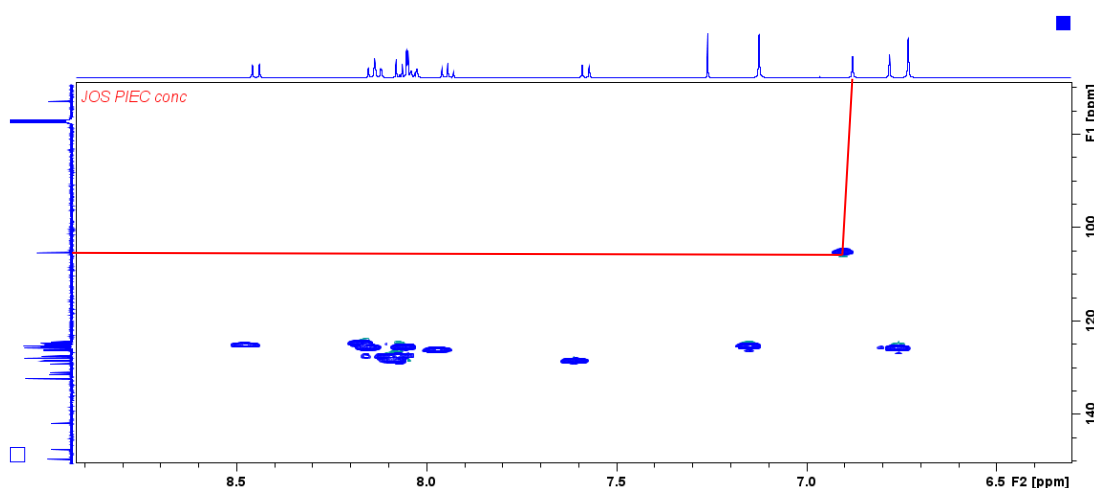


Figure 3.4: Section of the HSQC NMR spectrum of **EPIC** in CDCl₃ at 25°C showing the isoxazole CH correlation with red lines.

ESI HR mass spectrometry supported the structure of **EPIC**. The mass spectrum showed a peak at 1261.6039 corresponding to the [M+Na]⁺ ion of **EPIC** with a -2.06 ppm difference between the calculated and observed values.*

* The calculation of the difference (in ppm) between the observed and calculated value of the mass to charge ratio of a molecular ion is explained in Section 7.1.

3.2.2.2 Solid State Structure of EPIC

Small white needle like crystals formed following slow evaporation of an EtOH:DCM (2:1, v/v) solution of **EPIC**. These were solved by x-ray diffraction crystallography by Dr. Brendan Twamley at Trinity College Dublin, **Figure 3.5**. Two encapsulated DCM molecules form part of the structure. One in the upper annulus of the calix[4]arene is shown with short contacts, at an average distance of 2.87 Å, between two distal aromatic rings of the calixarene cavity and the methylene protons of DCM. The second DCM molecule showed short contacts to the nitrogen atoms of both of the isoxazole nuclei and to the oxygen atom of one heterocycle, at an average distance of 2.69 Å, **Figure 3.5a**.

In keeping with the solution state structure suggested by ¹H NMR data **EPIC** presented in the cone conformation. The crystal structure showed that the lower rim phenolic OH and the neighbouring ether oxygen atoms were involved in intramolecular hydrogen bonding which helps to stabilise the cone conformation, **Figure 3.5a**. The O...O distances, spanned from 2.75 to 2.86 Å, which compares favourably with the distance range of 2.75 to 2.93 Å previously reported for the crystals of **PIC** grown from MeCN⁸⁸ or DCM and other related systems published in the literature.¹¹¹⁻¹¹³

Intramolecularly the pendant pyrene units do not align in a face-to-face manner, rather the planes created by the pyrene units are at an angle of 70.56° which is considerably larger than the angles of 47.70° and 45.57° calculated for the **PIC.MeCN** and **PIC.2DCM** crystals respectively. This larger angle may be due to the rotation of the pendant arms to allow both heterocycles to interact with the DCM molecule and/or to facilitate intermolecular π-π stacking of the pyrene moieties, which was not evident in the two crystalline forms of **PIC**.

Intermolecular π-π stacking between neighbouring pyrene units of **EPIC** was evident. Face-to-face overlap at an average distance of 3.38 Å was observed between one pyrene unit of each molecule with a neighbouring pyrene moiety, with the centroids of each pyrene moiety creating a slip angle of 66.12°, **Figure 3.5c**. The second pendant pyrene molecule was not involved in inter- or intramolecular π-π stacking.

Comparison of the lack of π - π stacking within the solid state structure of **PIC.2DCM** and the face-to-face π - π stacking observed in the solid state structure of **EPIC.2DCM** suggested that the extra methylene group on the lower rim of **EPIC** provided the opportunity for overlap of the π orbitals of one pyrene moiety of **EPIC** with a pyrene moiety from a neighbouring **EPIC** moiety, possibly facilitated by the complexation of the isoxazole nuclei to DCM.

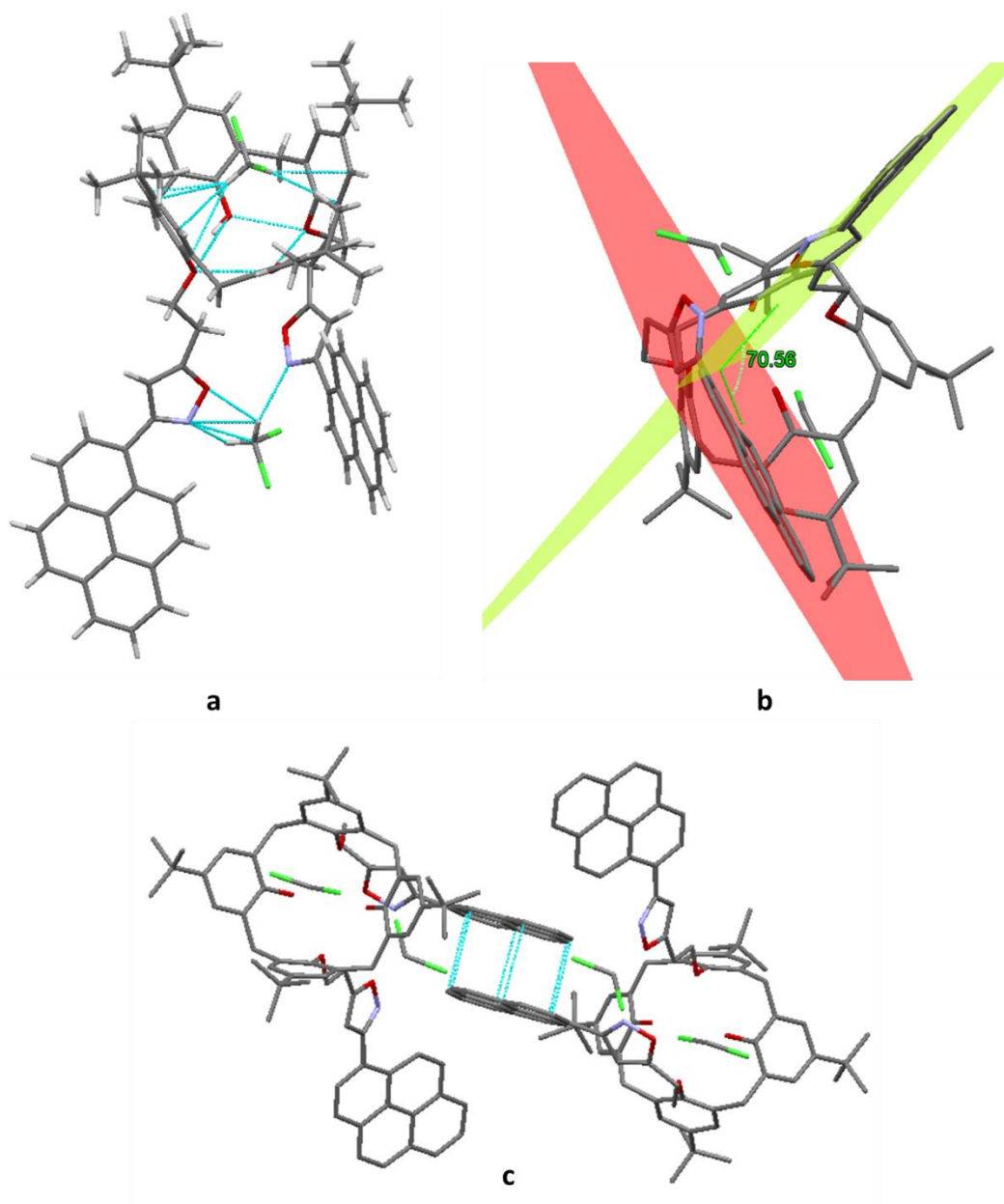


Figure 3.5: a) Single x-ray crystal structure of **EPIC.2DCM**, b) diagram of **EPIC** showing the 70.56° angle between the planes of the pyrene moieties and c) two neighbouring units of **EPIC** showing the intermolecular π - π stacking between adjacent pyrene units (blue lines).

As observed for **PIC**, the isoxazole and pyrene moieties of the pendant arms are not coplanar and the dihedral angles between those rings on the pendant arms of **EPIC** are: 42.73° between the moieties on the pendant arm involved in π - π stacking and 26.08° on the opposite arm.

Examination of the extended network created by the units of **EPIC** in the solid state structure revealed a tail-to-tail arrangement of the calixarene units, creating a channel between the pyrene units from neighbouring calixarene moieties, **Figure 3.6**.

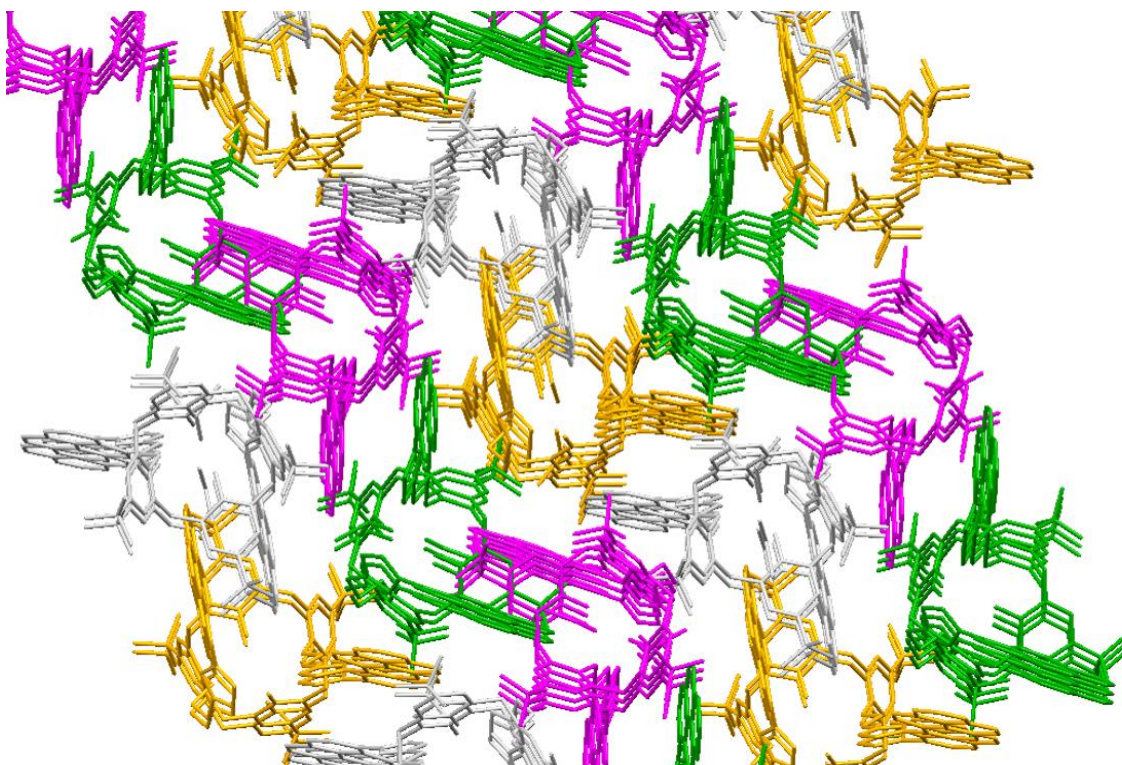


Figure 3.6: Extended network of the **EPIC.2DCM** solid state structure showing the tail-to-tail arrangement of the calixarene units

A summary of the interesting characteristics of the **EPIC.2DCM** crystal is given in **Table 3.1**.

Table 3.1: Summary of the characteristics of the **EPIC.2DCM** crystal structure.

Py-Py Plane Angle	Py-Isox Plane Angles		Lower-Rim Hydrogen Bonding	Solvent Interaction	Other Interesting Features
70.56°	42.73°	26.08°	Present at an average O...O distance of 2.79 Å.	One unit of DCM in upper cavity and second molecule in short contact with both of the isoxazole rings.	Tail-to-tail arrangement between units of EPIC . Channel created between pyrene units in extended network.

3.2.2.3 UV and Fluorescence Spectroscopy of EPIC

Although the pyrene moieties of **EPIC** may dominate the UV-Vis spectrum, it is known that absorption bands for the *t*-butyl substituted calixarene core are also expected, at ~240 and 301 nm in acetone¹¹⁴ and at 280 and 288 nm in chloroform.¹⁰⁹ Pyrene exhibits three well-structured absorption bands from 213 to 385 nm, when recorded in either hexane or MeCN by Morel *et al.*¹¹⁵ and in a Ne matrix by Salama *et al.*¹¹⁶ These absorption bands have been assigned to the $S_4 \leftarrow S_0$, $S_3 \leftarrow S_0$ and $S_2 \leftarrow S_0$ transitions.^{116,117}

In their investigation of the absorption spectra of PAHs (parent, substituted and charged), Salama *et al.* observed that the band positions in the absorption spectra of the aliphatically substituted pyrenes, **Figure 3.7**, were relatively unchanged w.r.t. the parent pyrene. They attributed this to the fact that the molecular orbitals that comprise the aromatic nature of the pyrene chromophore were not perturbed to a great extent by the aliphatic side chains. In contrast, the absorption spectra of the naphthalene and phenanthrene chromophores and their aliphatic substituted derivatives differed significantly.

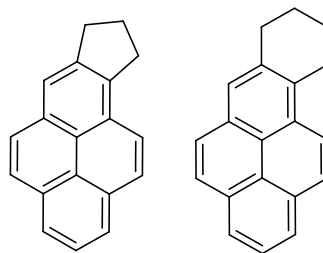


Figure 3.7: Aliphatic substituted pyrenes studied by Salama *et al.*¹¹⁶

In contrast, Morel *et al.* observed that the introduction of an electron withdrawing nitro group to the 1-, 2- and 4-positions of the pyrene chromophore resulted in three broad, structureless absorption bands, in MeCN and hexane w.r.t. the fine structure of the absorption spectra of the parent pyrene in the same solvents.¹¹⁵

A UV absorbance spectrum of **EPIC** at 6 μM in MeCN, **Figure 3.8** shows three absorption bands at 240, 280 and 348 nm, which correspond to the positions expected for the pyrene moieties. Whilst, the absorbance bands are broad with limited vibronic structure, the band at 240 nm appears suggestive of a double peak and there are small shoulders at lower wavelengths of the bands at 280 and 348 nm.

The lack of structure in the absorbance spectrum of **EPIC** was attributed to the direct attachment of the isoxazole heterocycles to the 1-position of the pyrene moieties in **EPIC** which induces differences in the photochemistry of the pyrene functionalised calixarene w.r.t. the parent pyrene moiety.

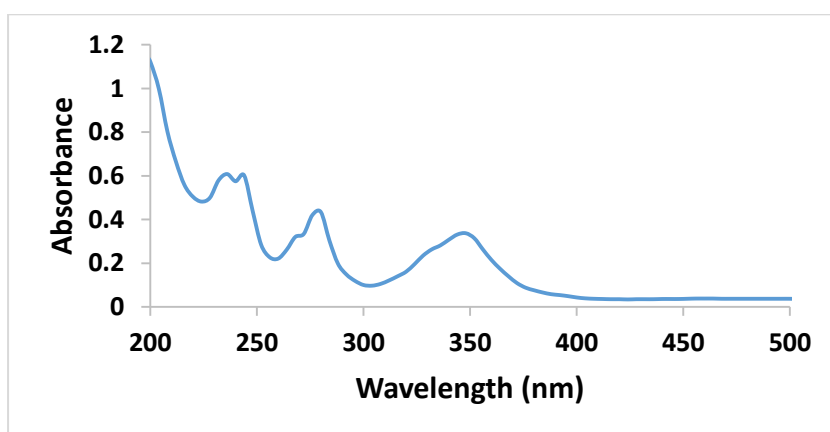


Figure 3.8: UV-Vis absorbance spectrum of **EPIC** (6 μM) in MeCN showing absorption bands at 240, 280 and 348 nm.

The λ_{max} (348 nm) of the absorption band of longest wavelength of **EPIC** was chosen as the excitation wavelength (λ_{ex}) for the measurement of the emission spectrum of **EPIC** (6 μM , MeCN), **Figure 3.9**. As recorded in Section 1.3.2.2 pyrene units are expected to display a monomer emission between 380 to 420 nm, and, if excimer formation is possible, it will present as a band between 410 and 500 nm.

The fluorescence emission spectrum of **EPIC**, displayed low intensity monomer emission bands at 386 and 407 nm and an intense, featureless, excimer emission band with a maximum at 494 nm. The ratio of the fluorescence intensity at the first monomer emission band (94 a.u.) to the λ_{max} of the excimer (551 a.u.), was calculated to be 1:5.9, thus the excimer signal was approximately six fold higher than the maximum monomer intensity.

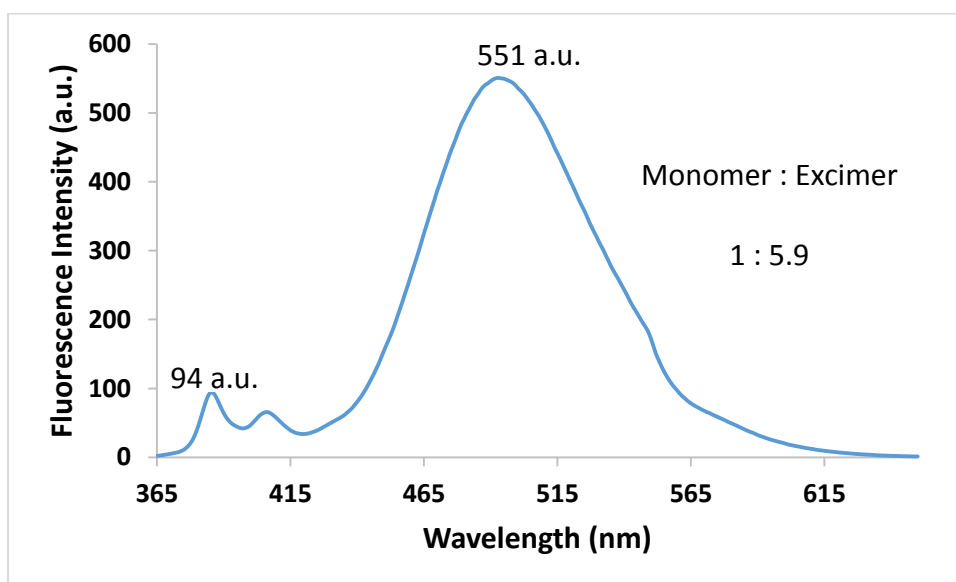


Figure 3.9: Emission spectrum of **EPIC** (6 μM , $\lambda_{\text{ex}} = 348 \text{ nm}$) in MeCN showing monomer emission bands at 386 and 407 nm and an excimer band at 494 nm.

3.3 Propyl Pyrene Isoxazole Calixarene (PPIC)

The degree of conjugation, if any, between the fluorophore and binding site of a chemosensor is quite variable.^{118,119} It was hypothesised that the direct attachment of the pyrene moieties and the isoxazole rings of **PIC** may have played an important role in the detection and selectivity for Cu^{2+} ions, and that breaking this direct linkage may help inform on the optimal structural features of isoxazole-calixarene derived copper sensors. Thus a new calix[4]arene was designed with a propyl linker between

the isoxazole and the pyrene moieties, and denoted **Propyl Pyrene Isoxazole Calixarene (PPIC)**, **Figure 3.10**.

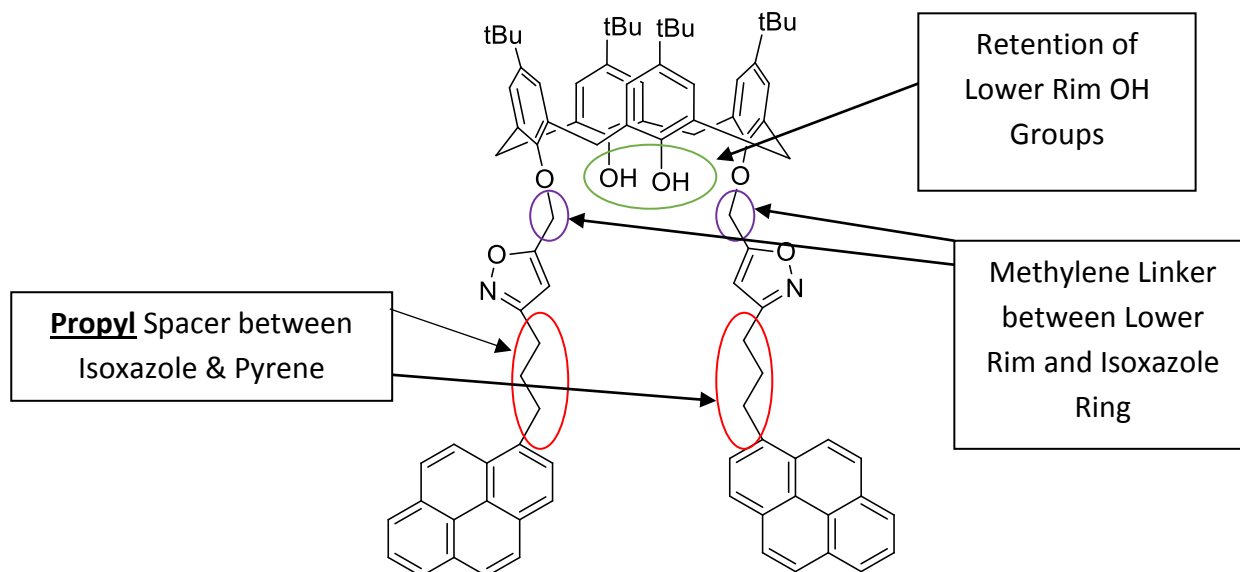
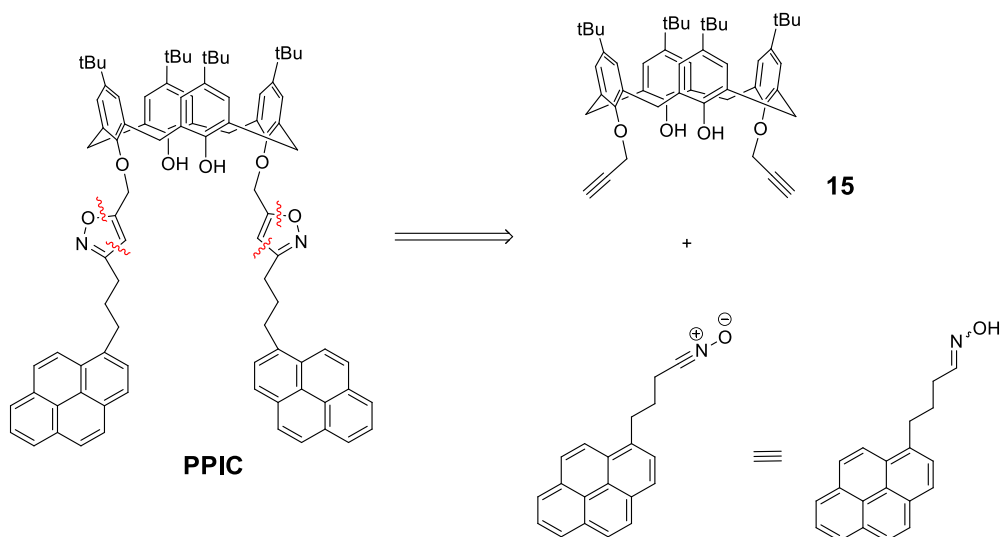


Figure 3.10: Structure of **Propyl Pyrene Isoxazole Calixarene (PPIC)**.

3.3.1 Synthesis of PPIC

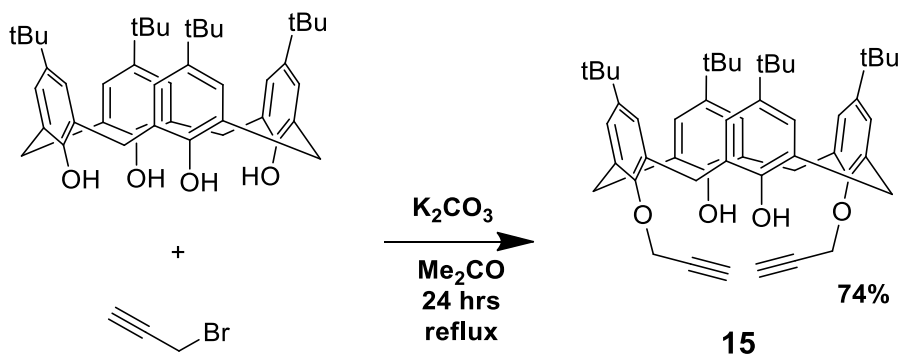
A retrosynthetic approach to **PPIC** is laid out in **Scheme 3.4**. The proposed synthesis involved a 1,3-dipolar cycloaddition between an *in situ* generated pyrene nitrile oxide, and the known alkyne functionalised calixarene **15**.



Scheme 3.4: Proposed retrosynthetic scheme for the synthesis of **PPIC**.

The known bis-alkylated calix[4]arene, 5,11,17,23-*tetra-tert*-butyl-25,27-dipropargyloxy-26,28-dihydroxycalix[4]arene, **15**, was synthesised using a method

reported by Rao *et al.*, **Scheme 3.5**.¹⁸ Commercially available 4-*tert*-butylcalix[4]arene was exposed to 2.4 eqs of potassium carbonate in anhydrous acetone for 1 hour at rt prior to dropwise addition of propargyl bromide (2.4 eqs) over 30 mins and heating to reflux for 24 hrs. Following filtration over celite, an acidic work-up and crystallisation, **15** was obtained as a white crystalline solid in 74% yield. ¹H NMR spectroscopic data corresponded to that reported by Rao *et al.*¹⁸



Scheme 3.5: Synthesis of 5,11,17,23-*tetra-tert*-butyl-25,27-dipropargyloxy-26,28-dihydroxycalix[4]arene, **15**.¹⁸

1-Pyrenebutanaloxime, **18**, precursor to the desired dipole, was not commercially available. The proposed synthetic approach to **18** involved initial reduction of the available acid to the alcohol, then oxidation to the aldehyde and finally oximation as outlined in **Scheme 3.6**. Commercially available 1-pyrenebutyric acid was reduced using LiAlH₄ (LAH) to form 1-pyrenebutanol, **16** as a yellow oil in 95% yield. ¹H NMR spectroscopic data corresponded to that reported.¹²⁰ The alcohol was oxidised using pyridinium chlorochromate (PCC); 1-pyrenebutanal, **17** was isolated as a pale yellow solid in 85% yield. ¹H NMR spectroscopic data corresponded to that reported.¹²¹ 1-Pyrenebutanal was oximated by a method developed within the group.¹⁰⁸ The aldehyde was allowed to react with 1.5 eqs of hydroxylamine hydrochloride and 1.5 eqs of pyridine in EtOH in a scientific microwave (125°C, 1 hour, P_{max} = 300 W). Following a chloroform extraction and purification by flash column chromatography, 1-pyrenebutanaloxime **18** and 1-pyrenebutanenitrile **19** were obtained in 46 and 43% yields, both compounds were pale yellow solids with R_f = 0.6 and 0.8 respectively (SiO₂, DCM). Both the oxime **18** and the nitrile **19** were novel compounds and thus were fully characterised.

A ^{13}C NMR spectrum revealed twenty unique signals. Three signals appeared between 32.0 and 16.8 ppm. HSQC and DEPT-135 spectra confirmed these signals as representative of three methylene groups. The remaining signals appeared between 133.7 and 119.6 ppm. A DEPT-90 spectrum distinguished the quaternary from the CH carbon atoms. The furthest downfield carbon signal at 133.7 ppm showed a HMBC correlation to the two methylene groups adjacent to the 1-position of the pyrene and was assigned as the quaternary carbon (qC) at the 1-position of the pyrene moiety, **Figure 3.12** (green lines). A second HMBC correlation between the carbon signal at 119.6 ppm and the two methylene groups adjacent to the nitrile functionality, confirmed this signal as the nitrile carbon atom, **Figure 3.12** (orange lines).

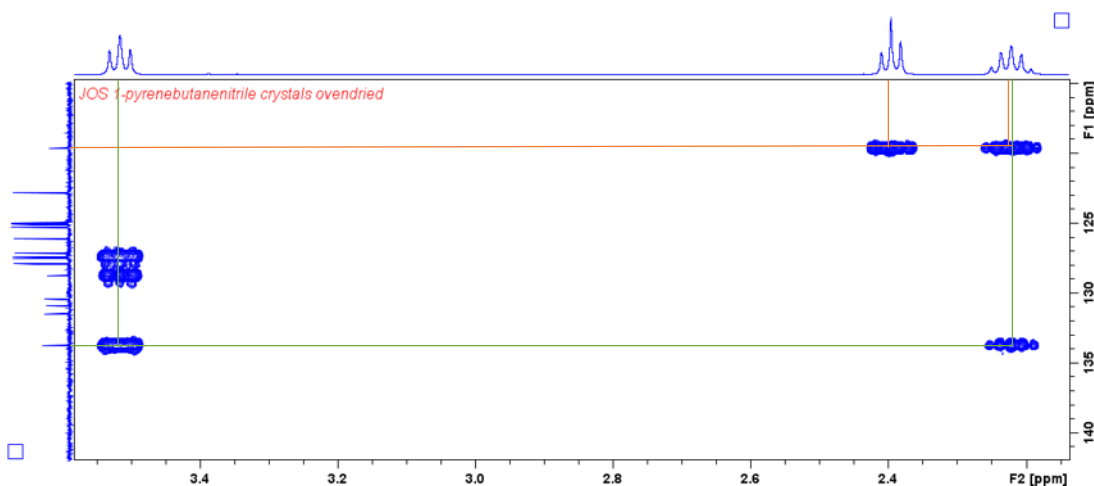


Figure 3.12: Portion of the HMBC spectrum of 1-pyrenebutanenitrile **19** showing correlations between the nitrile carbon atom and the protons of the two adjacent methylene groups (orange lines), and between the quaternary carbon at the 1-position of the pyrene moiety and the protons of the two adjacent methylene groups (green lines).

Nitrile functional groups typically appear as medium intensity stretching bands between 2260 and 2220 cm^{-1} in an IR spectrum.⁷⁰ A band at 2246.4 cm^{-1} , present in the IR spectrum of a sample prepared as a KBr disc, supports the presence of a nitrile functional group in **19**.

The yellow solid was analysed by ESI HR mass spectrometry. The mass spectrum showed a molecular ion peak at 292.1102 which corresponded to the $[\text{M}+\text{Na}]^+$ ion of 1-pyrenebutanenitrile with a -1.73 ppm difference between the calculated and

observed values supporting the formation of 1-pyrenebutanenitrile as a by-product during oximation of **17**, **Scheme 3.6**.

3.3.3 Characterisation of 1-Pyrenebutanaloxime

The second yellow product, lower R_f , was assigned as 1-pyrenebutanaloxime, **Figure 3.13**. Severe overlapping and an almost doubling of the expected number of signals in the ^{13}C NMR spectrum suggested that the product may have presented as a mixture of geometrical isomers. Further analysis of the NMR spectra completed assignment of the structures.

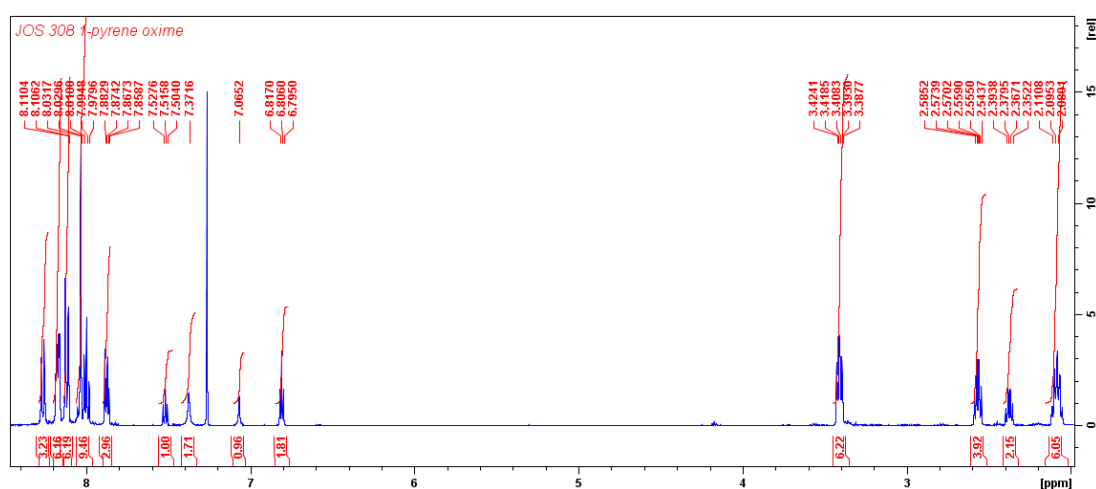


Figure 3.13: ^1H NMR spectrum (500 MHz) of 1-pyrenebutanaloxime **18** in CDCl_3 at 25°C .

^1H NMR signals between 8.29 and 7.85 ppm were assigned as the 9 pyrene CH protons, **Figure 3.13**. Two multiplet signals at 3.44-3.38 and 2.12-2.04 ppm were assigned as the pyr- CH_2 and pyr- CH_2CH_2 respectively on the basis of their chemical shift, relative integration, DEPT-135 and HSQC spectra. Six signals remained in the ^1H NMR spectrum, two broad singlets, two triplets and two multiplets. They did not show whole number integrations relative to the aromatic region or the previously assigned methylene groups. The three pairs of matching signals instead showed an approximate integration ratio, relative to the aforementioned signals, of 0.6:0.4, suggesting the presence of geometrical oxime isomers in a 3:2 ratio. The disappearance of the two broad singlets at 7.37 and 7.07 ppm following a D_2O shake supported their assignment as hydroxyl proton signals. $^1\text{H}^1\text{H}$ COSY showed that the two remaining multiplets arose from the CH_2 group adjacent to the oxime

functionality. Both multiplets showed a correlation to the CH₂ group in the middle of the propyl chain but no correlation to each other, **Figure 3.14**. This indicated that the signals arose from the CH₂ group adjacent to the oxime functionality in both isomers.

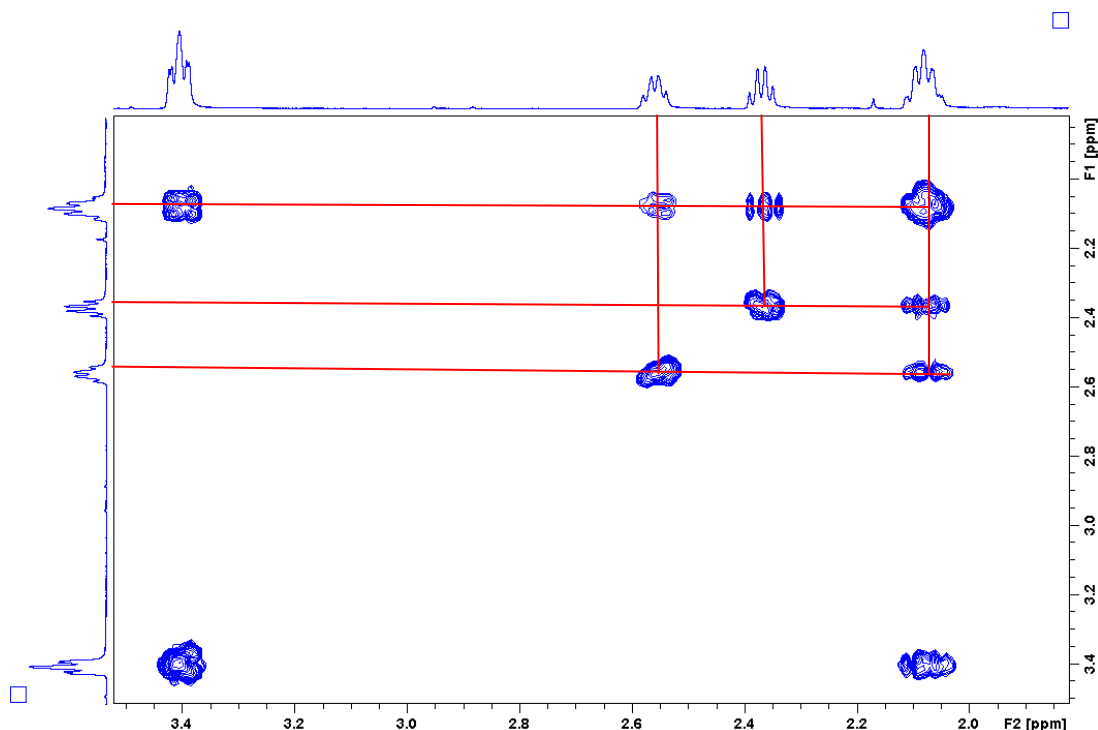


Figure 3.14: ¹H¹H COSY of 1-pyrenebutanaloxime **18** at 25°C showing the correlation between the middle CH₂ group of the propyl chain and the multiplets representing the CH₂ groups adjacent to the oxime functionality of the *E*- and *Z*-isomers.

The two remaining triplets at 7.52 and 6.81 ppm, based on their multiplicity, chemical shift and relative integration, were intuitively assigned as representing the imine N=CH protons of the isomers of **18**. The tentative assignment of signals as representing either the *E*- or the *Z*-oxime isomers was aided by examination of literature data. Crandall and Reix separated and characterised *E*- and *Z*-isomers of butanal oxime, decanal oxime and 5-methyl-3,4-hexadienal oxime, **Figure 3.15**.¹²² In each case the ¹H NMR signal of the imine proton of the *E*-oxime appeared as a triplet at ~0.6 ppm downfield to the corresponding signal of the *Z*-isomer. The imine triplet at 7.52 ppm was thus assigned as the *E*-isomer and that at 6.81 ppm as the *Z*-isomer. 1-Pyrenebutanaloxime presented, in solution in CDCl₃ as a 2:3 ratio of *E*-:*Z*-isomers.

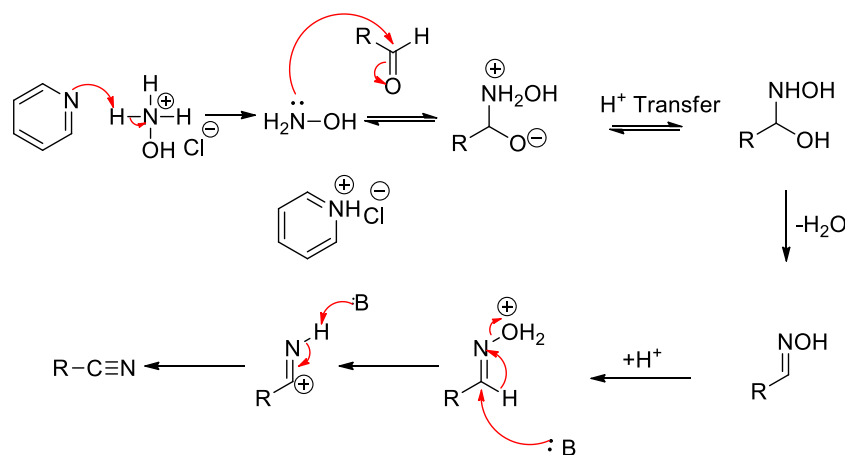
Analysis by ESI HR mass spectrometry showed a molecular ion peak at 310.1207 which corresponded to the [M+Na]⁺ ion of 1-pyrenebutanaloxime with a -1.61 ppm

difference between the calculated and observed values. This along with the ^1H and ^{13}C NMR analyses support the characterisation of 1-pyrenebutanaloxime.

	Butanal Oxime	Decanal Oxime	5-Methyl-3,4-hexadienal Oxime
<i>E</i> -isomer: δ imine proton (ppm)	7.41	7.41	7.40
<i>Z</i> -isomer: δ imine proton (ppm)	6.71	6.71	6.80

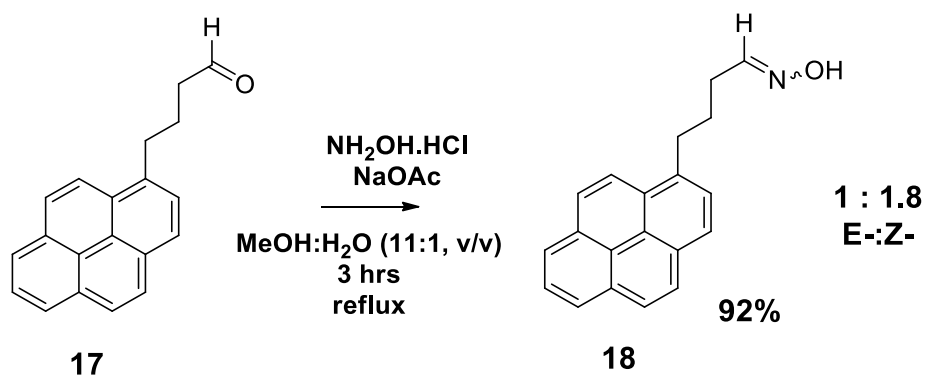
Figure 3.15: Structures of butanal oxime, decanal oxime and 5-methyl-3,4-hexadienal oxime with the ^1H NMR chemical shifts in CDCl_3 of the imine protons of the *E*- and *Z*-isomers shown underneath.¹²²

In order to minimise formation of 1-pyrenebutanenitrile, **19** as a by-product of oxime formation, an alternative synthetic approach to **18** was desirable. The experience within the group indicated that, under the conditions employed, $\text{NH}_2\text{OH}\cdot\text{HCl}$ and pyridine in EtOH, the conversion of aryl aldehydes to oximes was not complicated by formation of nitrile side products. However, there is literature precedent for pyridine acting as a catalyst in a hydroxylamine hydrochloride promoted aldehyde to nitrile conversion.¹²³ It may be the case that the by-product of the oximation step, pyridinium hydrochloride, is sufficiently acidic to facilitate oxime dehydration so generating the nitrile, **Scheme 3.7**.



Scheme 3.7: Mechanism for the conversion of an aldehyde to a nitrile using hydroxylamine hydrochloride in the presence of catalytic pyridine suggested by Zhu *et al.*¹²³

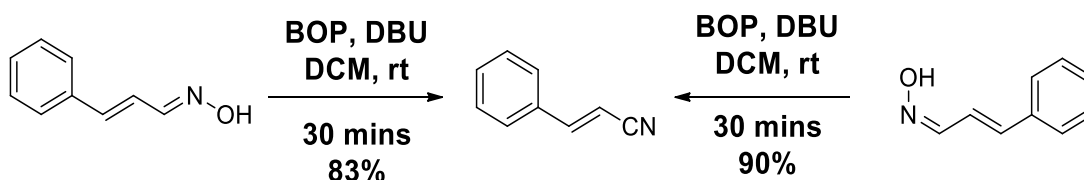
The “oximation” of **17** was repeated using sodium acetate as the base as utilised by Parghi and co-workers for formation of both aliphatic and aryl aldoximes.¹²⁴ 1-Pyrenebutanal was allowed to heat at reflux for 3 hrs in MeOH:H₂O (11:1, v/v) in the presence of 2 eqs of hydroxylamine hydrochloride and 2 eqs of sodium acetate, **Scheme 3.8**. Following cooling, water was added to aid the precipitation of the pure oximes as a pale yellow solid in 92% yield, in a 1:1.8 (*E*-:*Z*-) ratio.



Scheme 3.8: Synthesis of 1-pyrenebutanal oximes, **18**.

Unlike imines which rapidly isomerise between inseparable *E*- and *Z*- forms, geometrical oxime isomers can be rather stable, they may be isolated as discrete species¹²⁵ and their reactivity may or may not be influenced by their geometry. *E*- and *Z*-cinnamaloximes were found to be almost equally susceptible to dehydration with 1*H*-benzotriazol-1-yl-oxyltris(dimethylamino)phosphoniumhexafluorophosphate (BOP) and 1,8-Diazabicyclo[5.4.0]undec-7-ene (DBU) in DCM at rt, **Scheme 3.9**,

yielding, after 30 mins, cinnamitrile in 83 and 90% yield respectively. Conversely, Boucher *et al.* report the *E*-isomers of benzaldoxime and 4-(hexyloxy)benzaldoxime failed to dehydrate with catalytic rat liver microsomes and NADPH or dithionite whilst the *Z*-isomers readily dehydrated under the same conditions.¹²⁶



Scheme 3.9: Reactions of *E*- and *Z*-cinnamaldoximes to independently form cinnamitrile.¹²⁷

As oxime isomers are often used without separation,^{128,129} a mixed sample of *E*- and *Z*-**18** was used for the formation of **PPIC**. As described previously, the dimerisation of nitrile oxides, Section 1.6.3, is faster for aliphatic than for aromatic nitrile oxides⁶⁵ as such extra care was taken with the experimental conditions selected for nitrile oxide formation and subsequent cycloaddition. A literature search of isoxazole forming reactions from aliphatic oximes revealed a preference for the NCS/NBS halooxime approach to dipole formation (Section 1.6.4).¹³⁰⁻¹³²

1-Pyrenebutanaloxime, **18** was allowed to react with 1.5 eqs of NCS for 1 hr in DCM at rt resulting in formation of the chlorooxime, **20**. The success of the transformation was supported by the disappearance of the triplet signals for the imine protons of the *E*- and *Z*-oximes, **Figure 3.16**.

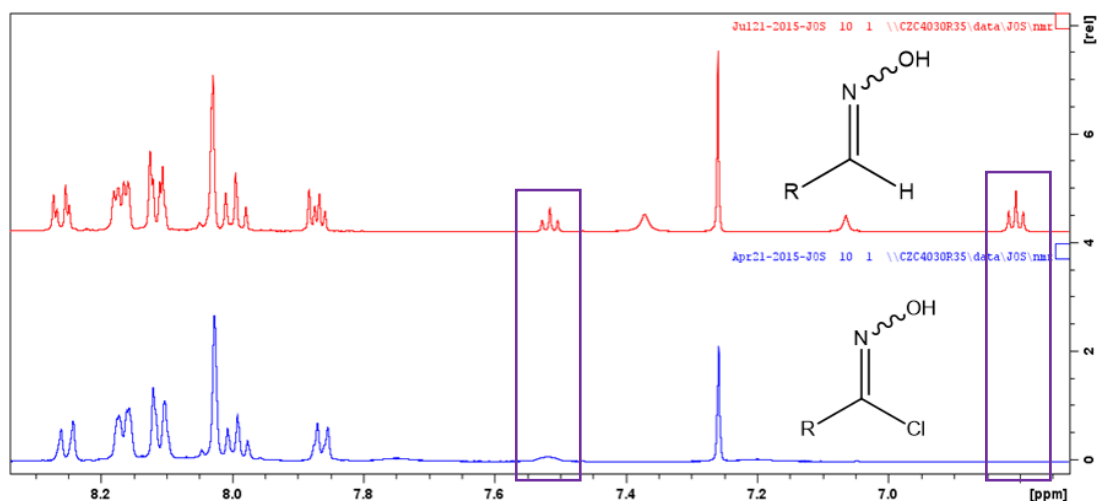
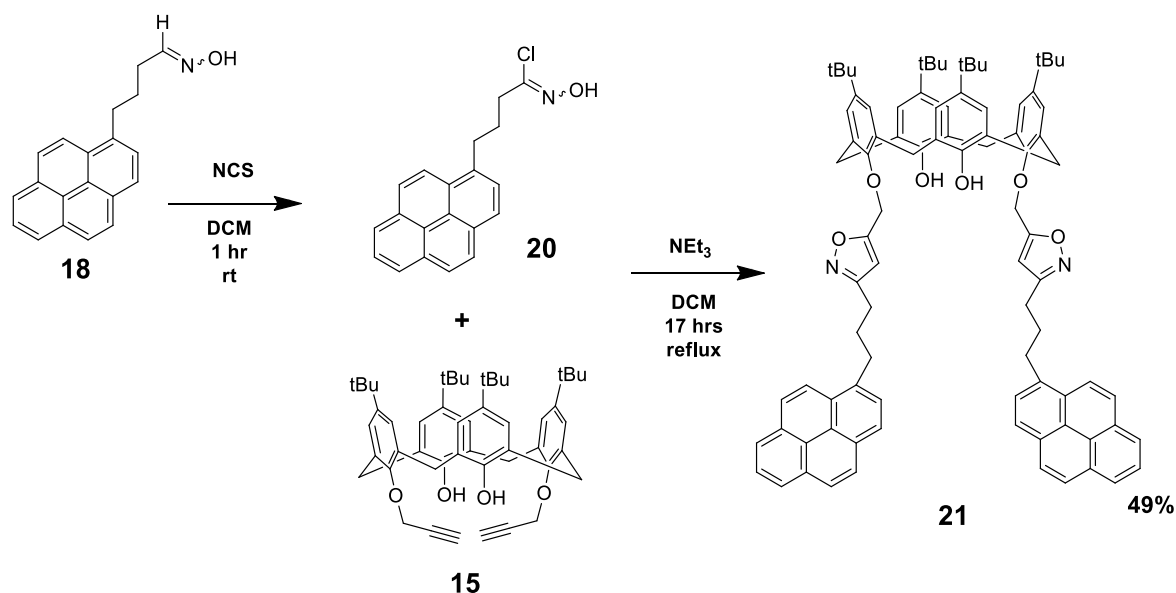


Figure 3.16: ^1H NMR spectra (500 MHz) of 1-pyrenebutanaloxime **18** isomers (red) and the chlorooxime derivative **20** (blue) in CDCl_3 at 25°C , showing the disappearance of the imine proton signals (purple boxes).

The alkylated calixarene **15** was added to a refluxing DCM solution of the chlorooxime, 3 eqs of NEt_3 were added at a rate of $4.96 \mu\text{mol}/\text{min}$ using a syringe pump. This particularly slow rate was used to ensure optimal time for the alkyne to trap the *in situ* generated nitrile oxide, **Scheme 3.10**. The crude reaction mixture was cooled, washed with water and purified by flash column chromatography to give **PPIC** as an off-white solid in 49% yield.



Scheme 3.10: Synthesis of Propyl Pyrene Isoxazole Calixarene (**PPIC**), **21**.

3.3.4 Characterisation of PPIC

The successful synthesis of **PPIC** was supported by initial inspection of the ^1H NMR spectrum, which showed the disappearance of the triplet signal of the alkyne proton of **15**, the disappearance of a doublet signal at 4.74 ppm and the appearance of a new singlet at 4.97 ppm representing the OCH_2CC protons of the starting material and product respectively; finally a new signal observed at 6.32 ppm, was deemed typical of the isoxazole CH proton.

3.3.4.1 ^1H and ^{13}C NMR Characterisation of PPIC

The ^1H NMR spectrum of a pure sample of **PPIC**, **Figure 3.17** showed a pair of sharp AB doublets at 4.15 and 3.24 ppm with reciprocal coupling constants of 13.3 Hz indicating that **PPIC** presented in the cone conformation.¹⁰⁹ This was further confirmed by two large *t*-butyl singlets, each with a relative integration of 18H at 1.27 and 0.89 ppm.¹⁰⁹

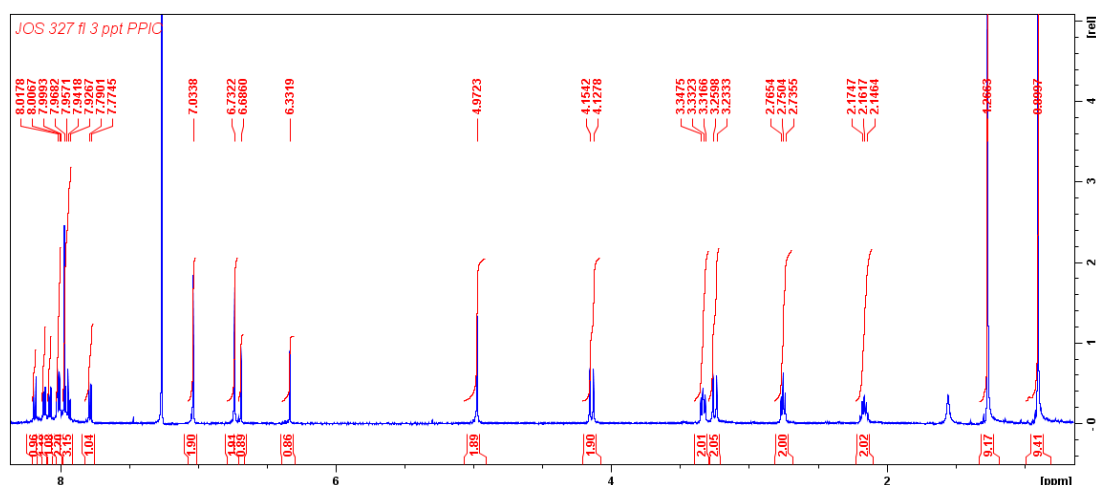


Figure 3.17: ^1H NMR spectrum (500 MHz) of **PPIC** in CDCl_3 at 25°C .

Triplets at 3.34 and 2.75 ppm and a multiplet at 2.22–2.12 were intuitively assigned as the CH_2 groups of the propyl chain of **PPIC** based on HMBC correlations and through comparison with the data from 1-pyrenebutanenitrile and 1-pyrenebutanaloxime. Analysis of DEPT-135 and HSQC spectra confirmed that the singlet at 4.97 ppm represented the methylene group adjacent to the *O*-atom on the lower rim of the calixarene. A HSQC correlation between the singlet at 6.32 ppm and a carbon signal at 103.5 ppm permitted assignment of the former as the signal for

the isoxazole CH proton. Interestingly, the isoxazole proton of **PPIC** appears ~0.60 ppm upfield of the isoxazole protons of **PIC** and **EPIC** whilst the isoxazole CH carbon signal appears ~1.80 ppm upfield of the corresponding carbons of **PIC** and **EPIC**. This is in keeping with the fact that the isoxazole rings of **PPIC** are less influenced by the deshielding zone of the pyrene nuclei than is the case for **PIC** and **EPIC**, where the heterocycle and pyrene ring are directly connected. The upfield shifts may also be due to loss of the degree of conjugation between the pyrene and isoxazole moieties w.r.t. **PIC** and **EPIC**.

The remaining 2H singlet at 6.62 ppm was assigned as the phenolic OH protons and the two 4H singlets at 7.03 and 6.72 ppm as the upper rim aromatic protons of the calixarene. Aromatic proton signals between 8.18 and 7.78 ppm showed a relative integration of 18H and were assigned as the pyrene protons, they were not individually assigned due to severe resonance overlap.

ESI HR mass spectrometry also supported the structure of **PPIC**. The mass spectrum showed a molecular ion peak at 1333.6435 which corresponded to the $[M+K]^+$ ion of **PPIC** with a -0.37 ppm difference between the calculated and observed values.

3.3.4.2 UV and Fluorescence Spectroscopy of **PPIC**

A UV absorbance spectrum of **PPIC** at 6 μ M in MeCN is shown in **Figure 3.18** with three main absorption regions at 244, 276 and 348 nm. The spectrum of **PPIC** shows more fine structure than that which was observed for **EPIC**. The first absorption band, at 244 nm, displays a shoulder at a shorter wavelength of 232 nm. The remaining two absorption regions each comprise three discernible peaks with, in each case, deep troughs between the second and third.

The presence of well-defined vibronic structure in the absorbance profile of **PPIC**, w.r.t. **EPIC** and **PIC** was expected due to the aliphatic chain at the 1-position of the pyrene moieties instead of directly connected isoxazole rings. The UV profile of **PPIC** was similar to that of the parent pyrene in MeCN,¹¹⁵ which is in keeping with Salama *et al.*s. observations that aliphatic substitution of pyrene does not affect the aromatic nature of the molecule and in turn the absorption spectrum appears similar to the parent pyrene.¹¹⁶

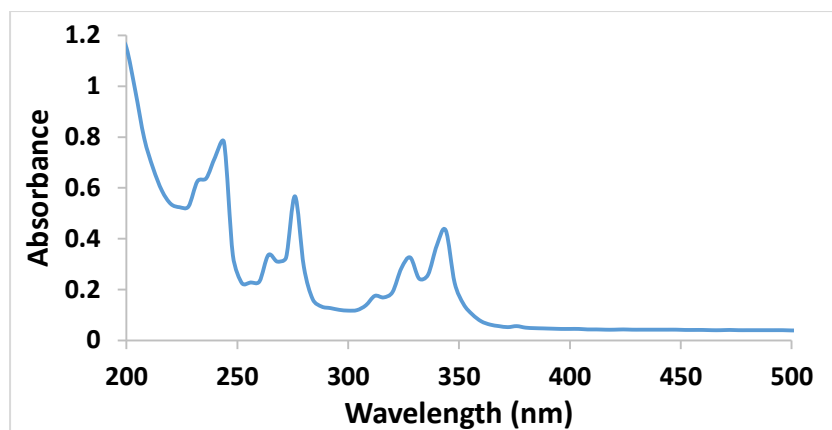


Figure 3.18: UV-Vis absorbance spectrum of **PPIC** (6 μM) in MeCN.

The absorption spectrum of Yilmaz and Sahin's pyrene functionalised calixarene **22**, **Figure 3.19**, which bears a flexible alkyl linker chain in the 1-position of the pyrene moieties, in MeCN:DCM (1:1, v/v) is similar to that of **PPIC** in MeCN in terms of vibronic structure and band positions.⁸² Thus, the propyl chain does not significantly influence the electronic properties of the pyrene moieties of **PPIC**.

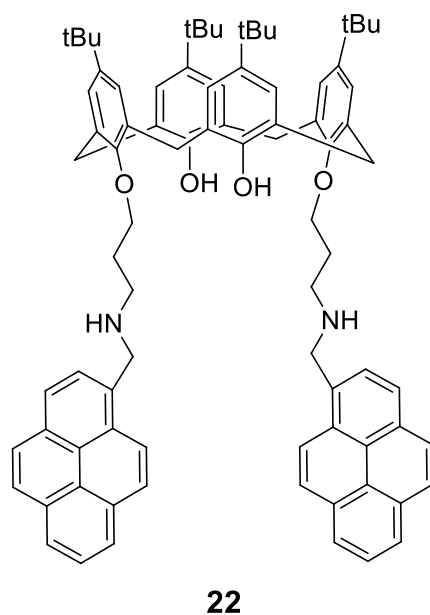


Figure 3.19: Propyl amino pyrene functionalised calix[4]arene **22**.⁸²

A fluorescence emission spectrum of **PPIC** (6 μM) was recorded in MeCN, **Figure 3.20**. The λ_{max} (348 nm) of the absorption band of longest wavelength was chosen as the excitation wavelength (λ_{ex}) for the measurement of the emission spectrum which displayed monomer emission bands at 384 (shoulder at 379 nm) and 403 nm and an excimer emission band at 480 nm. The ratio of the emission intensity at the first

monomer band (87 a.u.) to the intensity at the λ_{\max} of the excimer band (243 a.u.) was calculated to be 1:2.8, which was significantly smaller than the values of 1:10.8 and 1:5.9 determined, under the same conditions, for **PIC** and **EPIC** respectively. The reduced significance of the excimer band for **PPIC** suggested that the propyl chain between the isoxazole heterocycle and the pyrene moieties of the pendant arms of **PPIC** sufficiently increased the flexibility of the molecule so making intramolecular excimer formation less likely than in **EPIC** and **PIC**.

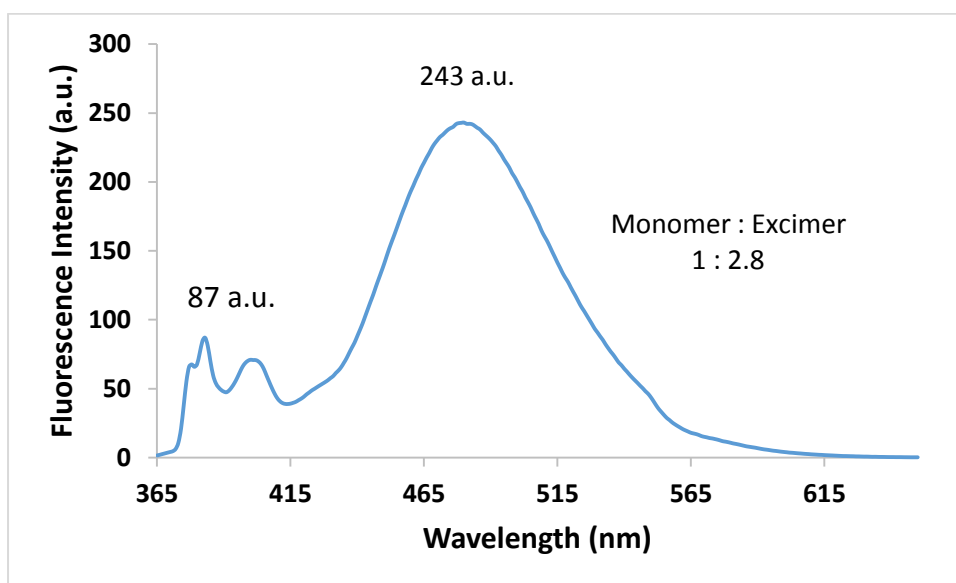


Figure 3.20: Emission spectrum of **PPIC** (6 μM , $\lambda_{\text{ex}} = 348 \text{ nm}$) showing monomer emission bands at 384 (shoulder at 379 nm) and 403 nm and an excimer band at 480 nm.

Numerous attempts were made to grow **PPIC** crystals of suitable quality for a solid state structure determination, these attempts involved slow evaporation of solutions of **PPIC** in different solvent systems, including EtOH:DCM (2:1, v/v), MeCN:CHCl₃ (2:1, v/v) and DCM:petroleum ether (1:2, v/v). In all cases an amorphous off white solid formed over time, no crystals suitable for x-ray crystallographic studies could be obtained suggesting irregular packing of the molecule in the solid state.

3.4 Methoxy Pyrene Isoxazole Calixarene (MPIC)

There is a plethora of literature reports on calix[4]arenes as analyte binding ligands with one or more of the lower rim phenolic hydroxyl groups forming part of the

proposed binding site^{18,20,81,90,92,133} and also numerous reports detailing calixarene sensors with no free phenolic hydroxyl groups on the lower rim.¹³⁴⁻¹³⁸ A novel calix[4]arene with methoxy groups in place of the free OH groups of **PIC**, denoted **Methoxy Pyrene Isoxazole Calixarene (MPIC)**, **Figure 3.21**, was designed with the objective of investigating the necessity, if any, of the hydroxyl groups of **PIC** for effective Cu²⁺ binding.

In selecting the group for alkylation of the lower rim, two main issues were considered:

- i) the influence of conformational mobility
- ii) the influence of steric factors on analyte binding.

The origins of the concerns are discussed below:

- i) A methoxy group is the smallest possible functional group suitable for replacement of a phenolic hydroxyl with a group incapable of functioning as a H-bond donor. However, the choice presents its own difficulties in that the methoxy group is small enough to fit through the inner annulus of a calix[4]arene and with no hydrogen bonding opportunities to hold the calix[4]arene in the cone conformation, the emergence of a conformationally mobile calix[4]arene was deemed likely, Section 1.1.2.
- ii) The steric requirements of the replacing group may interfere with the guest binding if the group chosen to replace the hydroxyl groups is large. Thus, if the new calix[4]arene was not a good sensor for Cu²⁺, possible explanations could include the following **(a)** the hydroxyl groups may be a necessary part of the Cu²⁺ binding site or **(b)** the Cu²⁺ cation may not be a suitable size for the new binding site proportions.

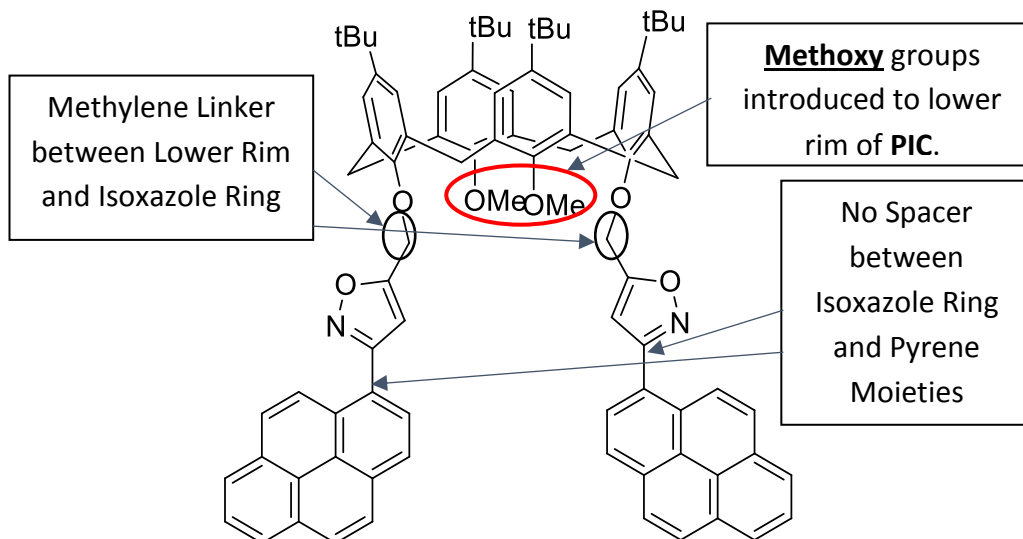
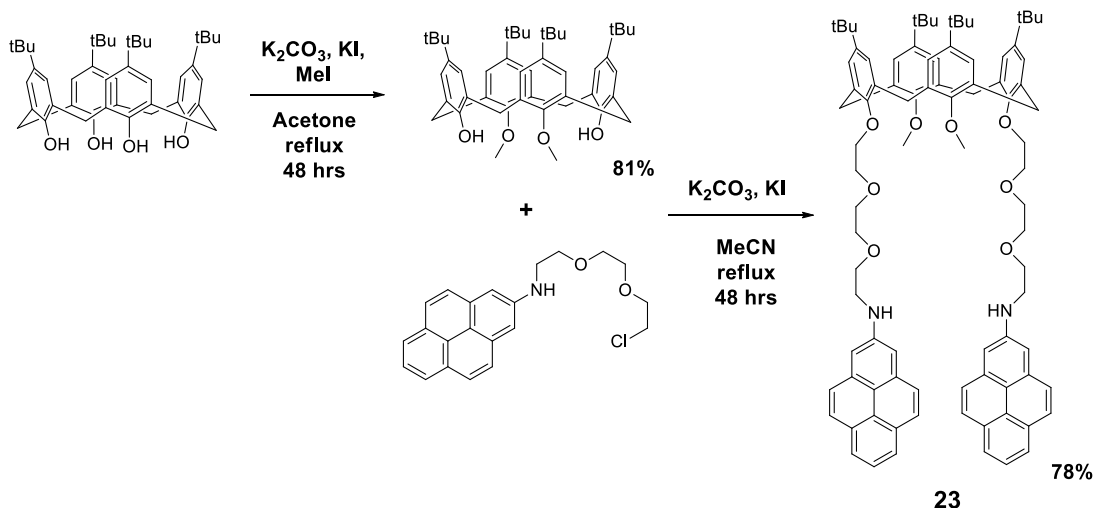


Figure 3.21: Structure of **Methoxy Pyrene Isoxazole Calixarene (MPIC)**.

3.4.1 Synthesis of MPIC

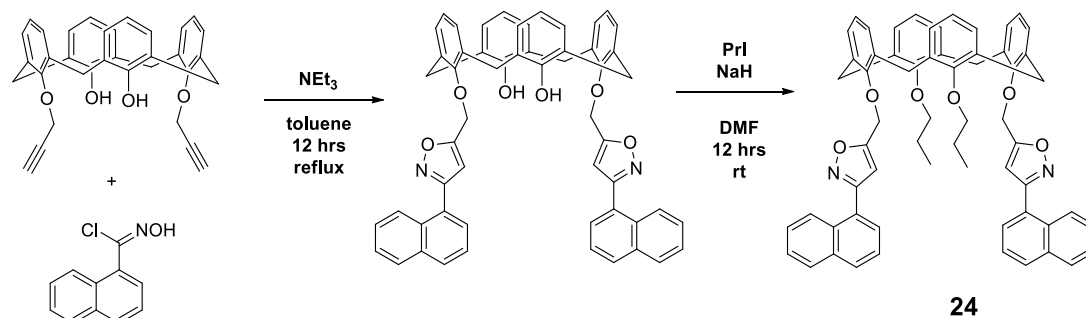
Synthesis of tetrasubstituted calix[4]arenes has been achieved in a number of ways. Menon *et al.* synthesised the bis-pyrene bis-methoxy functionalised calixarene, **23**, **Scheme 3.11** by reaction of 4-*tert*-butylcalix[4]arene with methyl iodide in the presence of a base followed by reaction with *N*-(2-(2-(2-chloroethoxy)ethoxy)ethyl)pyren-2-amine in the presence of potassium carbonate and potassium iodide.⁶¹



Scheme 3.11: Synthesis of the bis-pyrene bis-methoxy functionalised calixarene, **23** by Menon and co-workers.⁶¹

Chung *et al.* in accessing a bis-propoxy, bis-naphthalene functionalised calix[4]arene **24** utilised the reverse approach, introducing the naphthalene moieties by a 1,3-

dipolar cycloaddition prior to replacing the remaining hydroxyl groups with propyl groups using sodium hydride and propyl iodide, **Scheme 3.12**.⁸¹ During a subsequent fluorometric study, they observed that the naphthalene functionalised calixarene with free phenolic hydroxyl groups was selective for the Cu^{2+} ion.



Scheme 3.12: Synthesis of a tetrasubstituted calix[4]arene **24** by Chung *et al.*⁸¹

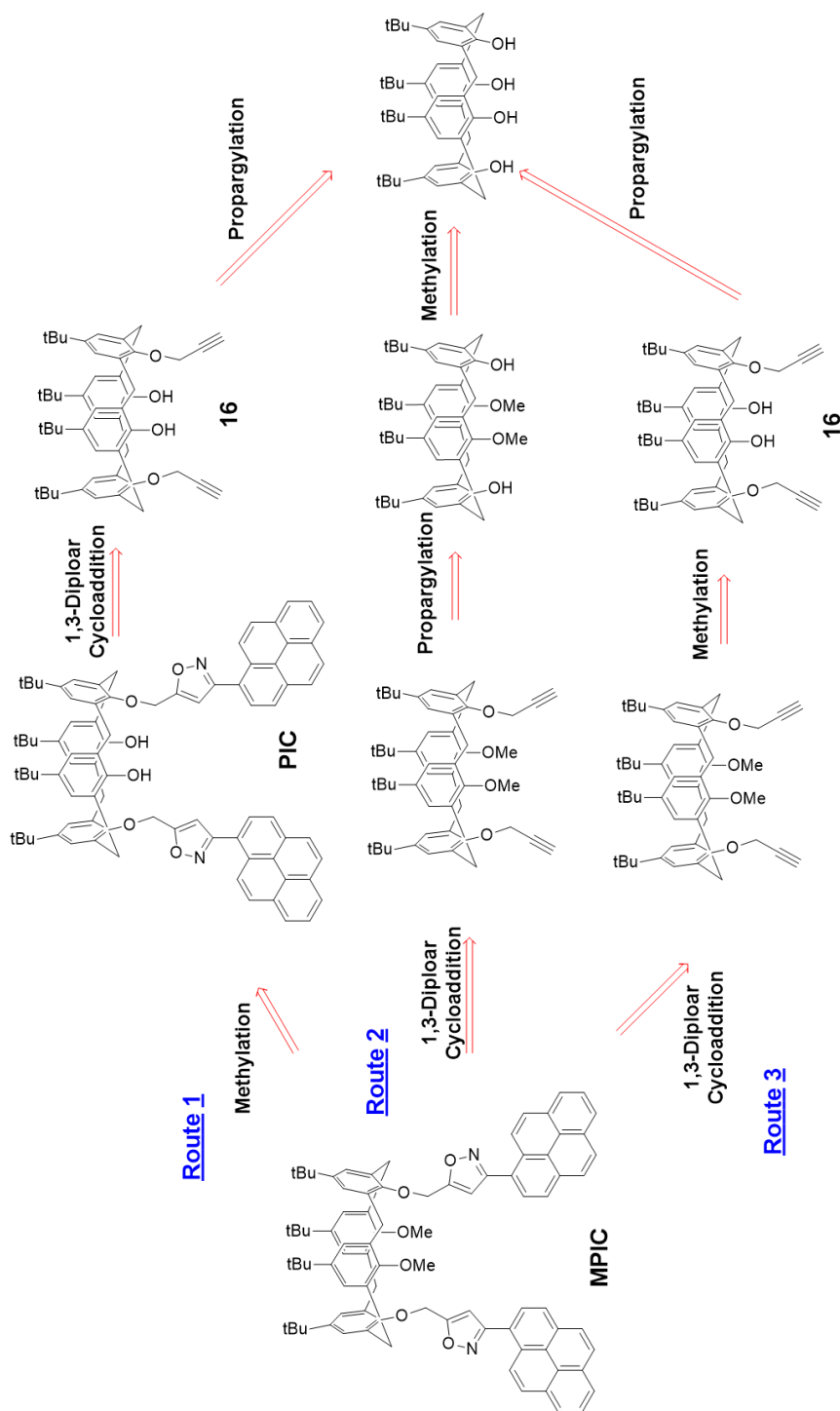
Thus, three routes were considered for the synthesis of **MPIC**, **Scheme 3.13**:

Route 1 Distal propargylation, bis-cycloaddition, bis-methylation – *i.e.* initial formation of **PIC** followed by methylation.

Route 2 Distal methylation, bis-propargylation, bis-cycloaddition.

Route 3 Distal propargylation, bis-methylation, bis-cycloaddition.

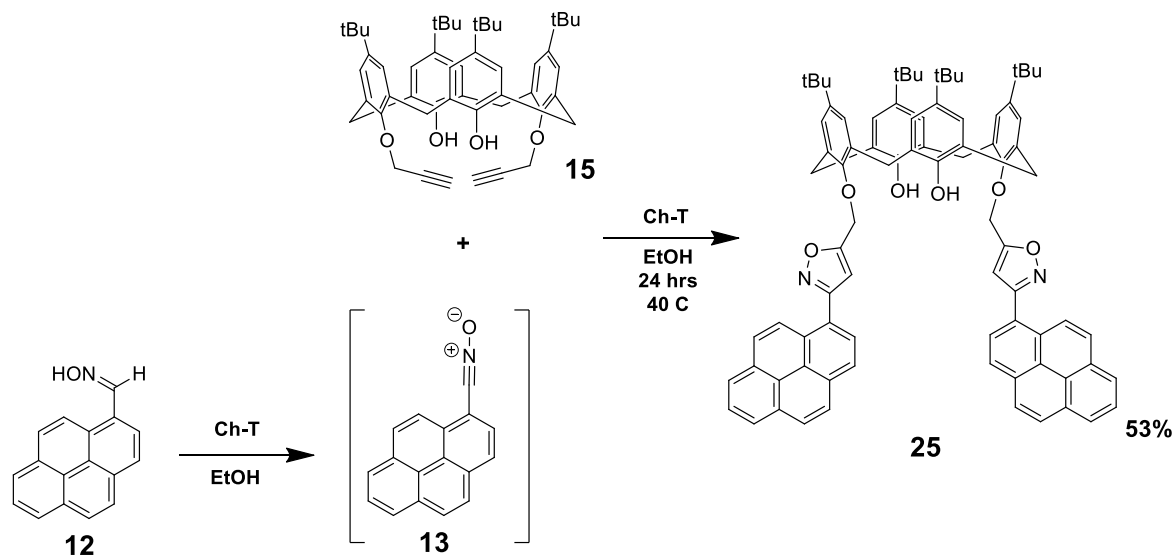
Route 1 involving initial synthesis of **PIC** followed by methylation of the free hydroxyl groups was the first choice route for exploring the synthesis of **MPIC**.



Scheme 3.13: Three retrosynthetic routes proposed for the synthesis of MPIC.

PIC was prepared by a modification of the route previously developed by co-workers in the laboratory, thus one eq of the bis-alkyne **15** was dissolved in EtOH and 4 eqs of 1-pyrenecarbaldoxime, **12** were added and the solution was heated to 40°C. Three portions of 2 eqs of Ch-T were added at 0, 3 and 6 hrs from the commencement of the reaction. The reaction was allowed to stir for a further 18 hrs at 40°C, cooled, extracted with chloroform, washed with 5% aq. NaOH to remove the sulphonamide

by-products, purified by flash column chromatography and finally recrystallised from EtOH:DCM (2:1, v/v) to yield **PIC, 25**, as a white crystalline solid in 53% yield, **Scheme 3.14**. ^1H NMR spectroscopic data corresponded to that previously recorded.⁸⁸



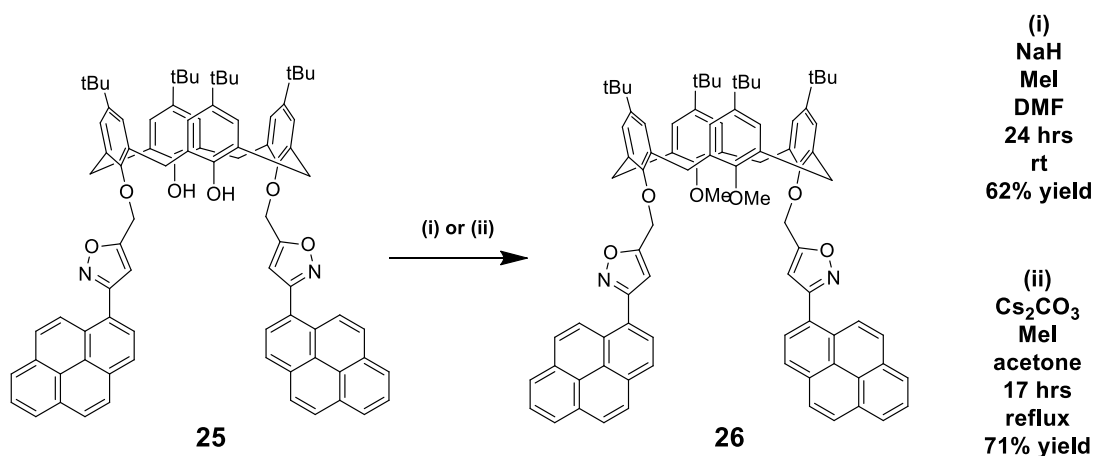
Scheme 3.14: Synthesis of Pyrene Isoxazole Calixarene (**PIC**), **25**.

A strong base such as NaH can be required to deprotonate the hydroxyl groups of a 1,3-disubstituted calix[4]arene (Section 1.1.4.2), accordingly, one eq of **PIC** in DMF was exposed to 30 eqs of stripped NaH.[†] Methyl iodide (20 eqs) was then added and the resulting solution was allowed to stir at rt for 12 hrs. The reaction mixture was quenched with distilled water and extracted with DCM. Following solvent evaporation the crude residue was triturated with hot MeOH to yield **MPIC** as a bright white solid in 62% yield, **Scheme 3.15**.

Whilst the reaction was successful, the fact that sodium hydride is extremely flammable when exposed to air or moisture led to a search for alternative reaction conditions and it was subsequently established that Cs_2CO_3 was a suitable base for the reaction, accordingly it became the reagent of choice in subsequent **MPIC** formation reactions. The latter reaction conditions were also attractive due to the use of acetone as the solvent medium in place of DMF. Repeated exposure to DMF

[†]Procedure for stripping sodium hydride in Section 7.1.

has serious health and safety issues that are avoidable with acetone, a further attraction of acetone is its low boiling point of 56°C.



Scheme 3.15: Synthesis of **Methoxy Pyrene Isoxazole Calixarene (MPIC), 26**.

3.4.1.1 Characterisation of MPIC

Full structural characterisation of **MPIC**, a white crystalline solid obtained following flash column chromatography, began with an analysis of its thin layer chromatography profile (SiO₂, DCM:petroleum ether; 4:1, v/v) followed by mass spectrometry and NMR spectroscopic analyses.

The molecular formula of **MPIC** was supported by HRMS. An electrospray ionisation (ESI) high-resolution mass spectrum showed a molecular ion peak at 1261.6105 which corresponded to the [M+Na]⁺ ion of **MPIC** with a -3.17 ppm difference between the calculated and observed values.

One fluorescent spot was observed under a UV lamp ($\lambda_{\text{ex}} = 254 \text{ nm}$) following TLC analysis of **MPIC** in a number of DCM:petroleum ether based elution systems which did not correspond to the R_f value of the starting **PIC**.

A ¹H NMR spectrum, recorded at rt in CDCl₃, was poorly resolved, **Figure 3.22**, suggesting **MPIC** had conformational mobility under the conditions of the experiment.

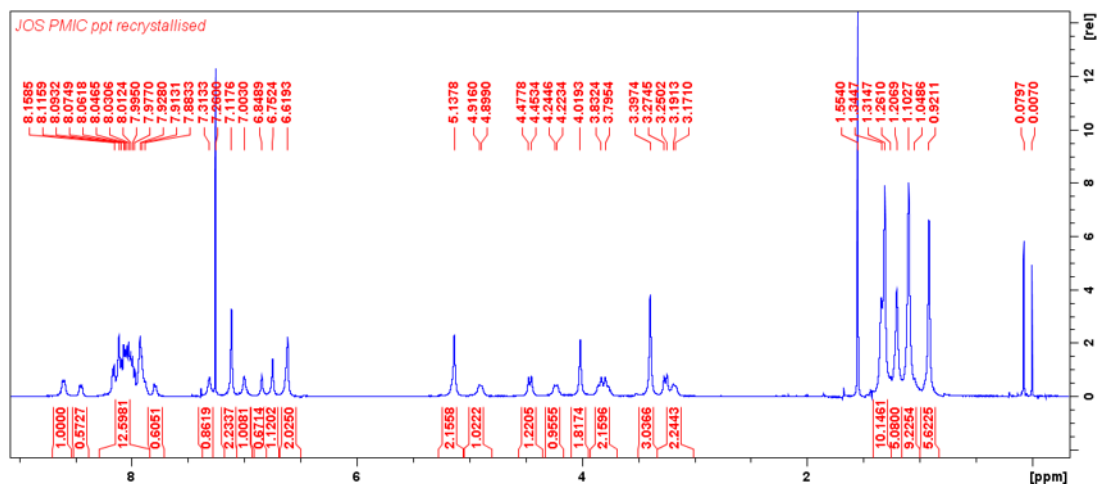


Figure 3.22: ^1H NMR spectrum (500 MHz) of **MPIC** in CDCl_3 at 25°C .

3.4.1.2 Variable Temperature ^1H NMR Spectroscopic Study of **MPIC**

The broad appearance of the ^1H NMR spectrum of **MPIC** was not unexpected due to the lack of hydrogen bonding opportunities on the lower rim of the calixarene along with the small size of the methoxy group facilitating intra-annular movement. A variable temperature (vt) ^1H NMR spectroscopic study of **MPIC** was carried out to assess the structural presentation over a range of temperatures. A study carried out on a 300 MHz Bruker instrument recorded spectra at 25, 30, 35, 40 and 45°C in CDCl_3 . As shown in **Figure 3.23**, as the probe temperature increased the resolution of the peaks continued to deteriorate suggesting an increase in conformational mobility of **MPIC** over the temperature range ($25 - 45^\circ\text{C}$).

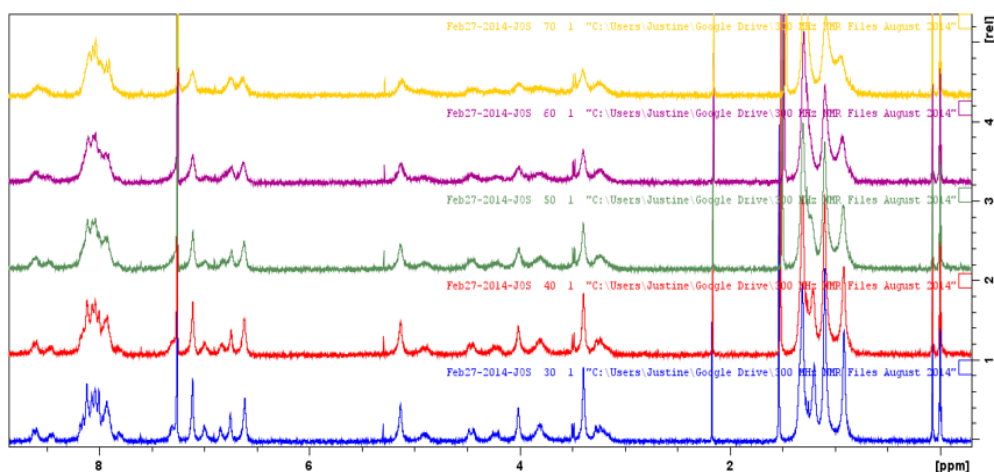


Figure 3.23: ^1H NMR spectra (300 MHz) of **MPIC** in CDCl_3 at 25°C (blue), 30°C (red), 35°C (green), 40°C (purple) and 45°C (yellow).

A second series of spectra recorded at and below rt, (25, 10, 0, -10, -20, -30, -40 and -50°C), **Figure 3.24**, show that as the probe temperature decreased, the resolution of the spectra improved. This observation is in keeping with a reduction in mobility at lower temperatures as the energy barrier for conformational switching becomes less attainable.

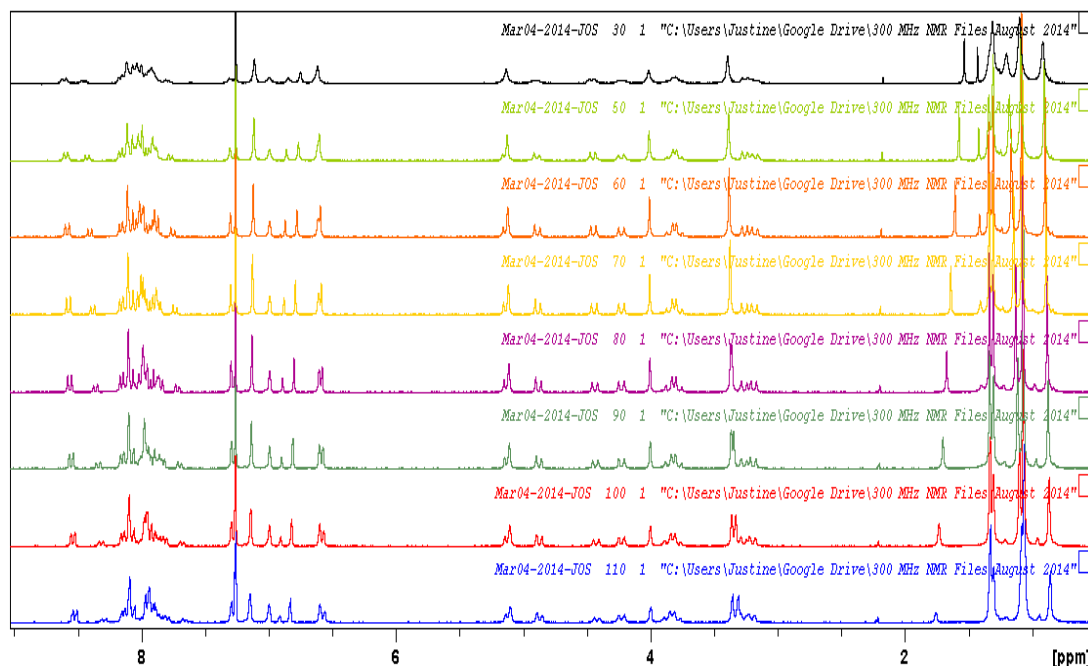


Figure 3.24: ^1H NMR spectra (300 MHz) of **MPIC** in CDCl_3 at -50°C (blue), -40°C (red), -30°C (green), -20°C (purple), -10°C (yellow), 0°C (orange), 10°C (light green) and 25°C (black).

3.4.1.3 ^1H NMR and ^{13}C NMR Characterisation of **MPIC**

The four main conformers of substituted calix[4]arenes are the cone, paco, 1,2- and 1,3-alternate conformers as shown for a generic example in **Figure 1.3**. Each of these conformers were considered possible for **MPIC**, **Figure 3.25**. The 1,2-alternate conformer was easily ruled out as it involves two proximal lower rim groups rotating through the inner annulus of the calix[4]arene and the pendant isoxazole-pyrene group is too bulky to pass through the core. Thus, the presenting forms to be considered for **MPIC** included the cone, the partial cone and the 1,3-alternate conformers.

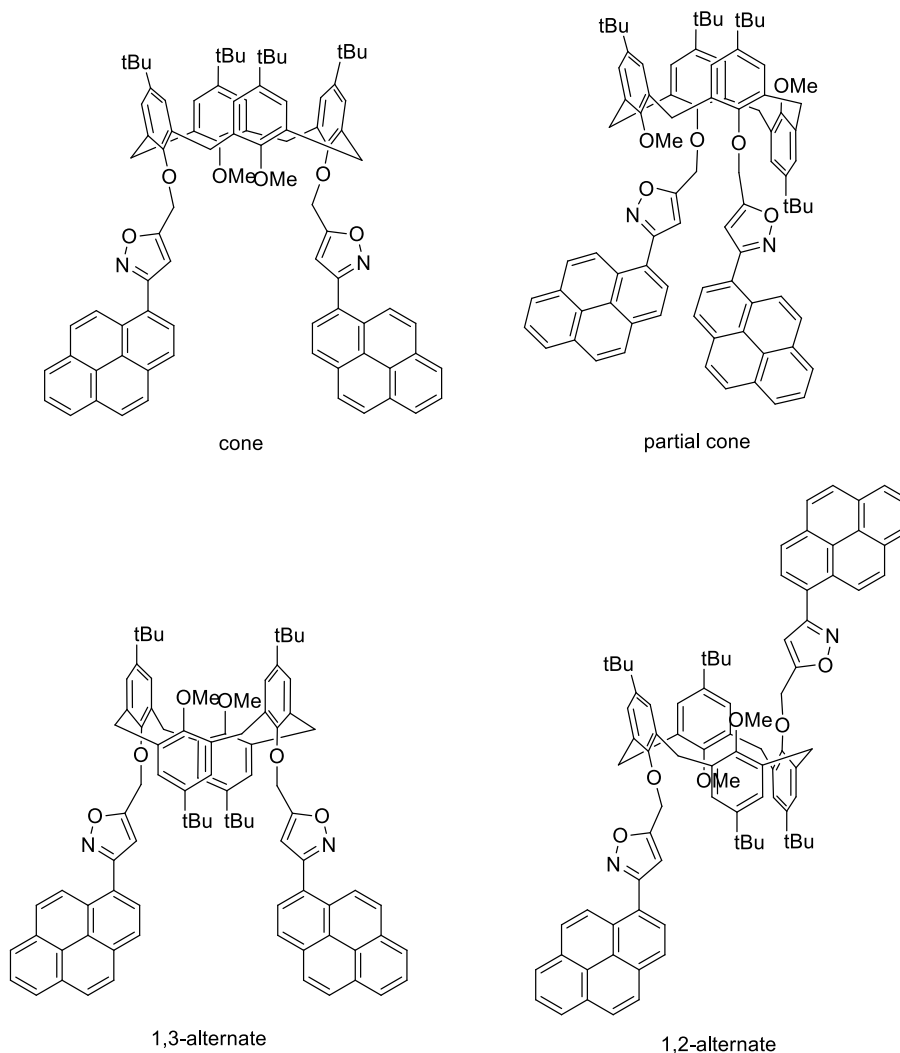


Figure 3.25: Cone, partial cone, 1,2- and 1,3-alternate conformations of **MPIC**.

A full NMR characterisation of **MPIC** was carried out in CDCl_3 at -30°C on a 500 MHz Bruker Avance NMR spectrometer. This temperature was selected due to limited conformational inversion of **MPIC** and because the instrument can hold this temperature with limited fluctuation. ^{13}C , ^1H , COSY, DEPT-135 and HSQC NMR spectra were recorded at -30°C .

It was shown by de Mendoza *et al.* that the resonance position of the methylene bridge carbon atoms is diagnostic of the conformation of calix[4]arene derivatives.¹³⁹ If the aryl groups around the methylene bridge are *syn* (both facing upwards or downwards) the methylene carbon atoms resonate at approximately 31 ppm and if they are *anti* (one facing upwards and one downwards) the resonance will be further downfield at approximately 37 ppm. The proposed number of ArCH_2 signals, and the

approximate chemical shift in ppm for each of the conformers of **MPIC** were considered and are summarised in **Table 3.2**.

Table 3.2: Proposed number of ArCH₂ signals and approximate chemical shift expected in the ¹³C NMR spectra of cone, partial cone and 1,3-alternate conformers of **MPIC**.

MPIC Conformer	Expected No. of ArCH₂ signals	Expected Approximate Chemical Shift (ppm)
Cone	1	31
Partial Cone	2	31 and 37
1,3-Alternate	1	37

The ¹³C NMR spectrum of **MPIC** at -30 °C showed eight carbon signals between 30 and 40 ppm, of which three were at approximately 31 ppm and one was at approximately 37 ppm. A DEPT-135 spectrum was used to ascertain which, if any of these four signals arose from CH₂ carbon atoms. A DEPT-135 spectrum shows positive signals for CH₃ and CH C-atoms, and negative intensity signals for CH₂ C-atoms while quaternary carbon signals are suppressed. A DEPT-135 spectrum of **MPIC** at -30°C (CDCl₃) revealed three CH₂ signals in the 31-37 ppm range at 37.8, 31.22 and 31.16 ppm, **Figure 3.26**. This suggested that **MPIC** presented as two conformers in solution: as the partial cone, with two distinct methylene C-atoms (resonating at ~37 and 31 ppm) and as the fully symmetrical cone where all the bridging methylene C-atoms are in identical environments (resonating at ~31 ppm), **Table 3.2**. Two further CH₂ signals downfield at 67.3 and 65.7 ppm represent the OCH₂-isoxazole carbon atoms.

The presence of both the cone and partial cone conformers of **MPIC** was further supported by the presence of five signals in the *t*-butyl range of the ¹H NMR spectrum, **Figure 3.27**. Three of these signals at 1.34, 1.11 and 1.07 ppm showed a relative integration of 1:1:2 which correlated with that expected for the *t*-butyl groups of a partial cone conformer of **MPIC**. Two further signals at 1.31 and 0.87 ppm, in a 1:1 ratio, were typical of that which was to be expected for the *t*-butyl signals of a cone conformer of **MPIC**. In order to ascertain the ratio of cone to partial cone at -30°C the relative intensities of the peaks at 1.07 (18 H of paco) and 0.87 ppm (18 H of cone) were compared. This gave a cone:paco ratio of 1:2.78 which indicated

that the paco conformer represented close to 75% of the material in solution at -30°C in CDCl_3 .

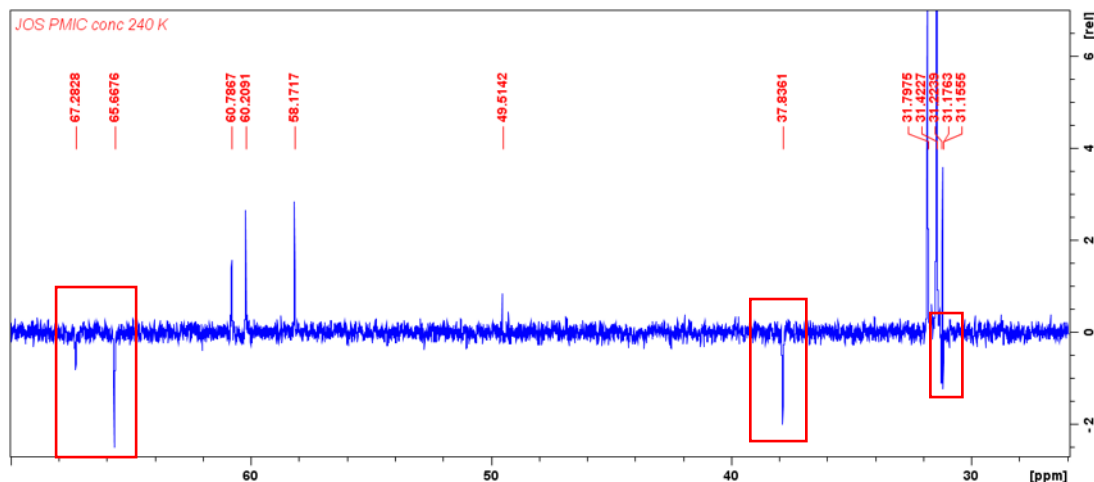


Figure 3.26: DEPT-135 (125 MHz) spectrum of **MPIC** in CDCl_3 at -30°C showing 5 CH_2 signals (red boxes) at 67.3, 65.7, 37.6, 31.22 and 31.16 ppm.

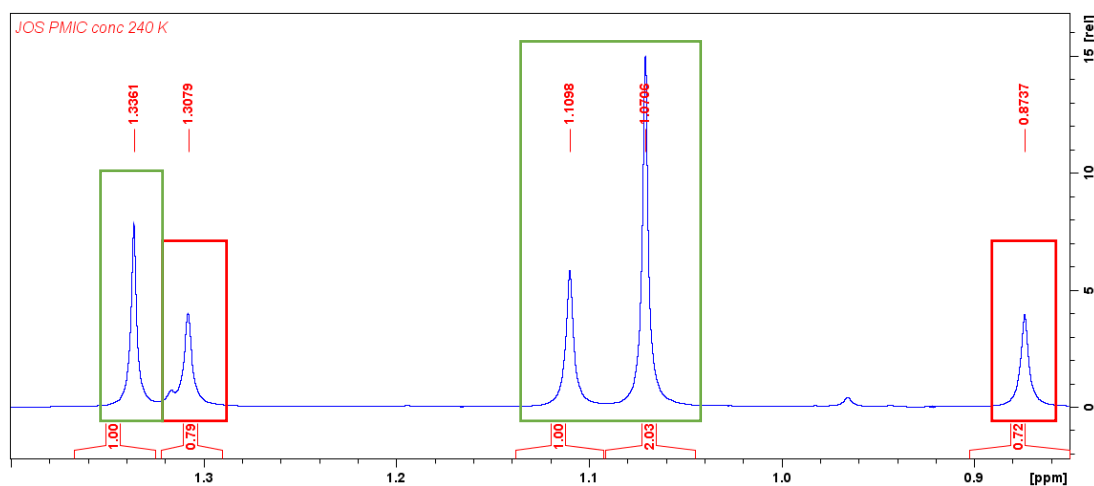


Figure 3.27: Section of the ^1H NMR spectrum (500 MHz) of **MPIC** in CDCl_3 at -30°C in the region between 1.40 and 0.85 ppm with the signals from the different conformers highlighted in coloured boxes: paco *t*-butyl signals (green boxes) and cone *t*-butyl signals (red boxes).

A conformationally mobile bis-pyrenyl bis-hydroxamate calix[4]arene **27**, **Figure 3.28**, that bears strong structural similarities to **MPIC**, including methoxy groups on the lower rim, was fully characterised by Laguerre *et al.*¹³⁴ They reported the methoxy protons of the paco and cone conformations of **27** at 3.93 (cone) and 3.80 and 2.02 (paco) ppm (CDCl_3). A 1.3:1, paco:cone ratio of the conformers of **27** at rt was observed in CDCl_3 .

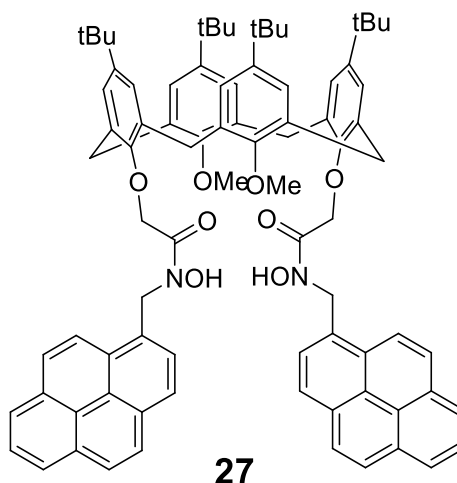


Figure 3.28: Conformationally mobile bis-pyrenyl bis-hydroxamate calix[4]arene **27** characterised in CDCl_3 by Laguerre and co-workers.¹³⁴

One singlet signal was expected for the OCH_3 protons of **MPIC** in the cone conformation while two signals were expected for the non-equivalent OCH_3 protons of the paco conformer. Three singlets at 4.00, 3.37 and 3.34 ppm in the ^1H NMR spectrum of **MPIC** (CDCl_3 , -30°C) were tentatively assigned as the OCH_3 protons, **Figure 3.29**.

During the low temperature study of **MPIC** in CDCl_3 on the 500 MHz Avance instrument, the singlets at 3.37 and 3.34 merged to one broad signal at temperatures above -10°C , red spectra **Figure 3.29**. Whilst baseline resolution was almost reached at -50°C as inversion of the conformers became limited.

Comparison of the relative integrals of the assigned *t*-butyl signals with those for the singlets at 4.00, 3.67 and 3.34 ppm led to the assignment of the signal at 4.00 ppm as the OCH_3 protons of the cone conformer and the two signals at 3.37 and 3.34 ppm, present in a 1:1 ratio, as representing the OCH_3 protons of the partial cone. The relative integration of these signals was used to calculate the ratio of cone to partial cone conformers at -30°C as 1:2.8 cone:paco; this figure agrees very well with that concluded from analysis of the relative integrals of the *t*-butyl signals.

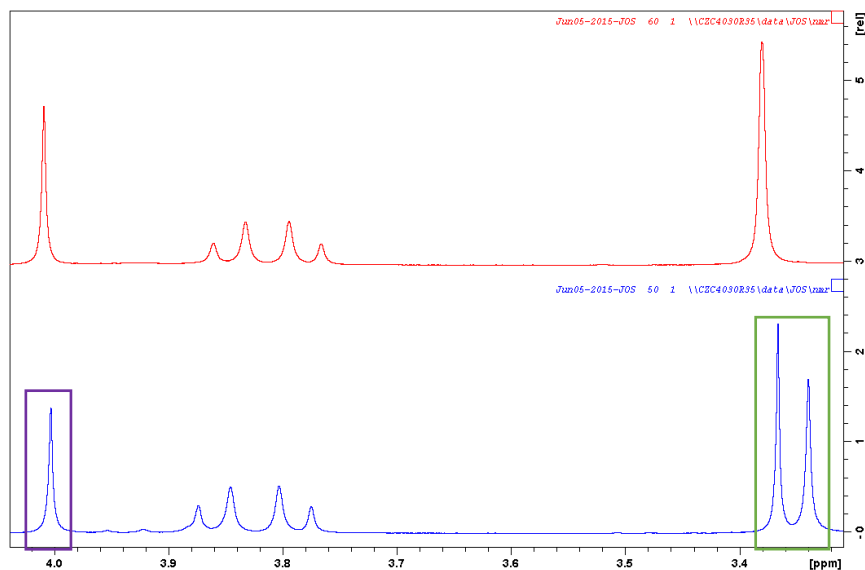


Figure 3.29: Section of the ^1H NMR spectra (500 MHz) of **MPIC** in CDCl_3 at -30°C (blue) and 0°C (red) in the region between 4.05 and 3.30 ppm with paco OCH_3 signals (green box) and cone OCH_3 signal (purple box).

The region of the spectrum (CDCl_3 , -30°C) between 4.44 and 3.19 ppm displayed six doublets. A $^1\text{H}^1\text{H}$ COSY spectrum of **MPIC** at -30°C was analysed to establish the correlation, if any, between these signals, **Figure 3.30**. Three strong correlations between the doublets revealed three pairs of methylene protons.

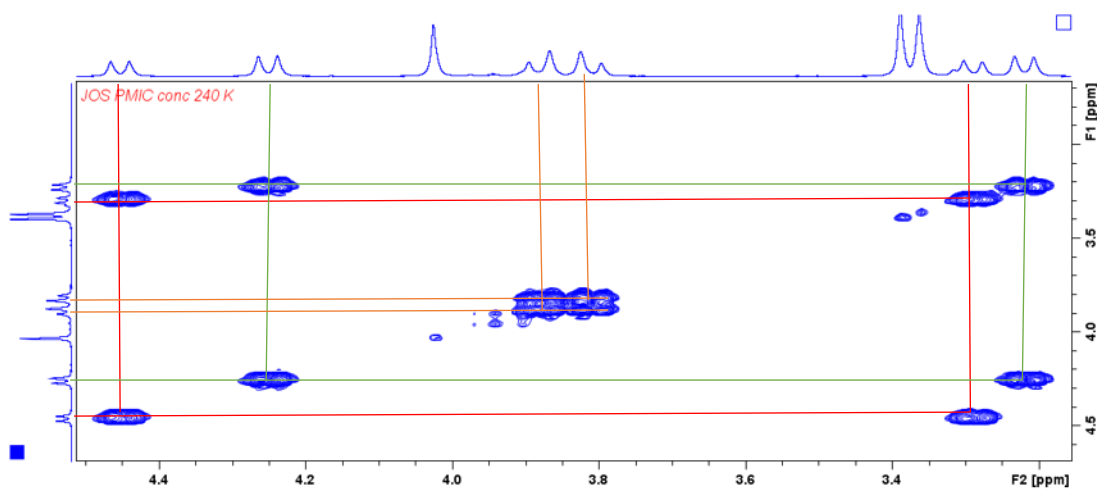


Figure 3.30: $^1\text{H}^1\text{H}$ COSY spectrum (500 MHz) of **MPIC** in CDCl_3 at -30°C showing three strong sets of correlations (green, red and brown lines) suggesting three pairs of methylene protons.

The relative integration values of the six doublets between 4.44 and 3.19 ppm, **Table 3.3**, combined with the correlations observed in the COSY spectrum and the reciprocity of the coupling constants were used to assign them as three pairs of

diastereotopic CH₂ protons, these were assigned as the methylene bridges of the calixarene core of the paco and cone conformations.

Table 3.3: Chemical shift, coupling constants, conformer assignments and relative integration of six doublets appearing between 4.44 and 3.19 ppm of the ¹H NMR spectrum of **MPIC** at -30°C.

Chemical Shifts (ppm), (J values)	Conformer	Relative Integration
4.43 (12.6 Hz) and 3.27 (12.7 Hz)	Cone	8H
4.23 (12.9 Hz) and 3.20 (13.2 Hz)	Partial Cone	4H
3.86 (14.1 Hz) and 3.79 (14.1 Hz)	Partial Cone	4H

A HSQC spectrum established that the two doublet signals at 5.12 and 4.88 ppm arose from a pair of methylene protons on a carbon atom with a resonance position at 65.7 ppm. A singlet at 5.11 ppm which overlapped with the doublet was shown to arise from a proton(s) directly attached to a carbon atom resonating at 67.3 ppm, **Figure 3.31**. The carbon signals at 65.7 and 67.3 ppm were previously shown by DEPT-135 analysis to be CH₂ signals, **Figure 3.26**. The doublets were assigned as the diastereotopic OCH₂ protons of the partial cone, while the singlet was assigned as the OCH₂ group of the cone conformer. These assignments were also supported by the relative integration values of the signals compared to those of the OCH₃ and *t*-butyl groups.

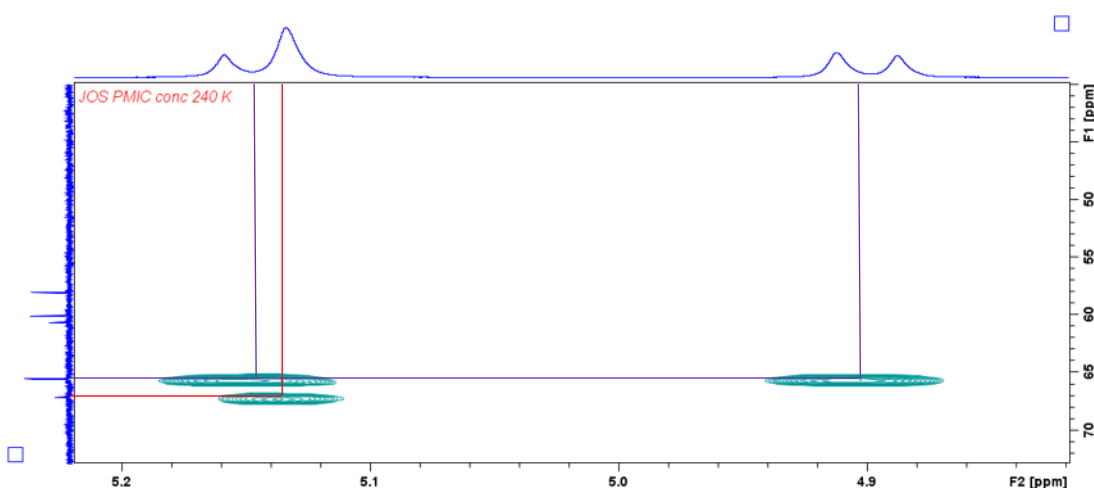


Figure 3.31: HSQC spectrum of **MPIC** in CDCl₃ at -30°C showing two OCH₂-isoxazole correlations with purple (paco) and red lines (cone).

Seven peaks appeared between 7.30 and 6.57 ppm in the ^1H NMR spectrum of **MPIC** at -30°C . These peaks were tentatively assigned as the isoxazole $\underline{\text{C}}\text{H}$ protons and the upper rim aromatic protons of both conformers of the calixarene. Isoxazole $\underline{\text{C}}\text{H}$ signals appear at approximately 100-105 ppm.¹⁰⁸ In the ^{13}C NMR spectrum of **MPIC** only two carbon signals were observed in this range, at 105.2 and 105.7 ppm; these were assigned as the isoxazole $\underline{\text{C}}\text{H}$ resonances. The HSQC spectrum of **MPIC** showed correlations between the singlet at 6.82 ppm in the ^1H NMR spectrum and the carbon at 105.7 ppm in the ^{13}C NMR spectrum; and between the singlet at 6.90 ppm and the carbon at 105.2 ppm, **Figure 3.32**. The relative integrals of the singlets in this region compared to those previously assigned as the *t*-butyl, OCH_3 and OCH_2 -isoxazole protons were then used to assign the signal at 6.90 ppm as the isoxazole protons of the cone conformer and the signal at 6.82 ppm as the corresponding signal of the partial cone conformer.

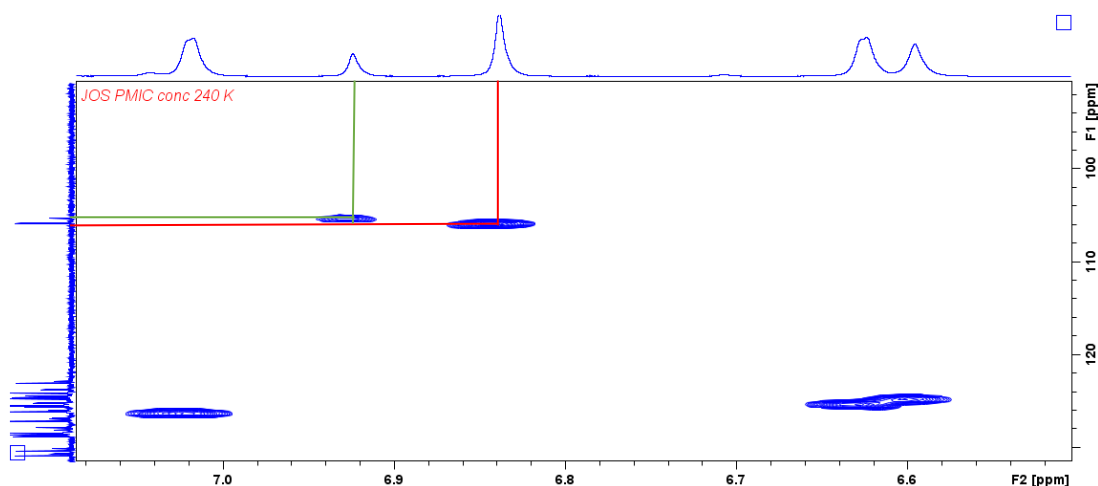


Figure 3.32: HSQC spectrum of **MPIC** in CDCl_3 at -30°C showing two isoxazole $\underline{\text{C}}\text{H}$ correlations with green (cone) and red (paco) lines.

The remaining five peaks in the range 7.30 to 6.57 ppm, on the basis of their integration values, multiplicity and relative chemical shift were assigned as the upper rim aromatic protons of the calixarene, **Table 3.4**.

Table 3.4: Chemical shift, multiplicity, relative integration and conformer assignments of five singlets appearing between 7.30 and 6.57 ppm of the ^1H NMR spectrum of **MPIC** at -30°C .

Chemical Shift (ppm)	Multiplicity	Relative Integration	Conformer Assignment
7.30	s	2H	paco calix-ArH
7.14	br s	6H	2 x paco calix-ArH 4 x cone calix-ArH
7.00	br d	2H	paco calix-ArH
6.60	br d	2H	paco calix-ArH
6.57	s	4H	cone calix-ArH

The ^1H and ^{13}C NMR resonances of the pyrene nuclei were not fully assigned due to severe resonance overlap. However, in the ^1H NMR spectrum three distinct doublet signals were discernible, these were assigned based on their chemical shift and relative integration values, **Table 3.5**. The remaining overlapping resonances between 8.17 and 7.80 ppm were assigned, based on their total integration values, as 16 and 14 pyrene protons of the partial cone and the cone conformer of **MPIC** respectively.

Table 3.5: Chemical shift, multiplicity, relative integration and conformer assignments of three doublets appearing between 8.55 and 7.69 ppm of the ^1H NMR spectrum of **MPIC** at -30°C .

Chemical Shift (ppm)	Multiplicity	Relative Integration	Conformer Assignment
8.55	d	2H	paco pyrene-H
8.33	d	2H	cone pyrene-H
7.69	d	2H	cone pyrene-H

The ratio of the cone and partial cone conformers of **MPIC** over the temperature range studied was determined at -20°C , -10°C and 25°C by reviewing the relative integrals of the methoxy proton signals at 4.00 ppm (representing 6H of the cone conformer) and 3.37 and 3.34 ppm (each representing 3H of the paco conformer), **Figure 3.33**. The paco conformer of **MPIC** dominated at all temperatures analysed,

however, the contribution of cone conformer increased with temperature, rising from 26% cone at -30°C to 38% at 25°C .

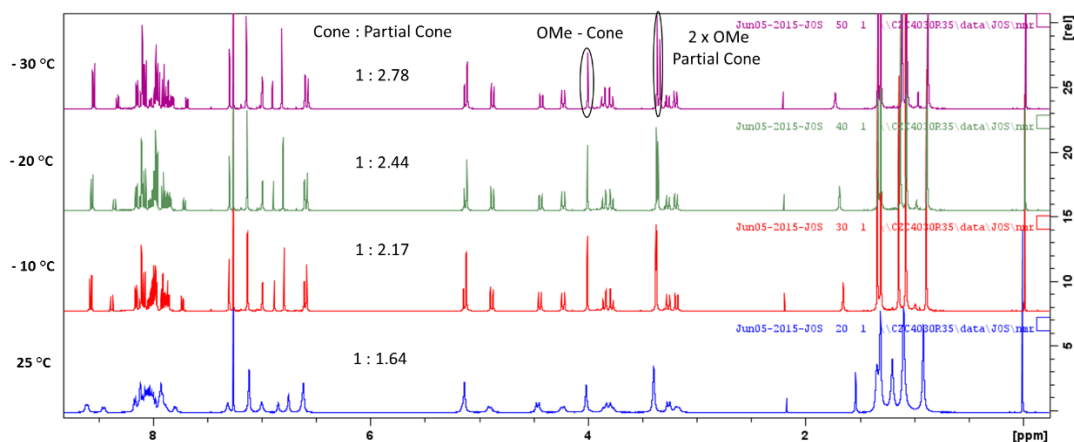


Figure 3.33: ^1H NMR spectra (500 MHz) of **MPIC** in CDCl_3 at 25°C (blue), -10°C (red), -20°C (green) and -30°C (purple), ratio of cone:paco conformers of **MPIC** are indicated on each spectrum.

3.4.1.4 Solid State Structure of **MPIC**

Small white needle like crystals of **MPIC** formed following slow evaporation of an EtOH:DCM (2:1, v/v) solution. These were solved by x-ray diffraction crystallography by Dr. Brendan Twamley of Trinity College Dublin, **Figure 3.34**. In the solid state **MPIC** presented as the partial cone conformer, the same conformer as dominated the solution state as judged by NMR analysis (Section 3.4.1.3). In the paco conformer one methoxy group of **MPIC** had moved through the inner annulus of the calix[4]arene and faced upwards while the aryl residue distal to this methoxy group was in a “pinched” or “flattened” calix[4]arene orientation, **Figure 3.34a**.

As in the crystalline forms of **PIC** and **EPIC**, the pyrene and isoxazole units of the pendant arms were not coplanar, dihedral angles of 50.29° and 39.12° were measured between the moieties in the pendant arms of **MPIC**. A summary of the interesting characteristics of the **MPIC** crystal is given in **Table 3.6**.

Intramolecularly the pendant pyrene units do not align in a face-to-face manner, rather the planes created by the pyrene units are at an angle of 42.25° , **Figure 3.34b**, which is similar to the angles of 47.70° and 45.57° calculated for the **PIC.MeCN** and **PIC.2DCM** crystals respectively, whilst a larger angle, 70.56° , was measured for **EPIC**.

Examination of the extended packing network of **MPIC** gave no indication of any inter- or intramolecular π - π stacking between the pyrene units, however, a small number of short contacts were observed between the pyrene protons of one molecule and the pyrene ring of an adjacent molecule with separations ranging from 2.70 to 3.31 Å, **Figure 3.34c**. A head-to-tail extended network of the **MPIC** units was observed in the solid state, unlike the tail-to-tail arrangements of the crystalline forms of **PIC** and **EPIC**.

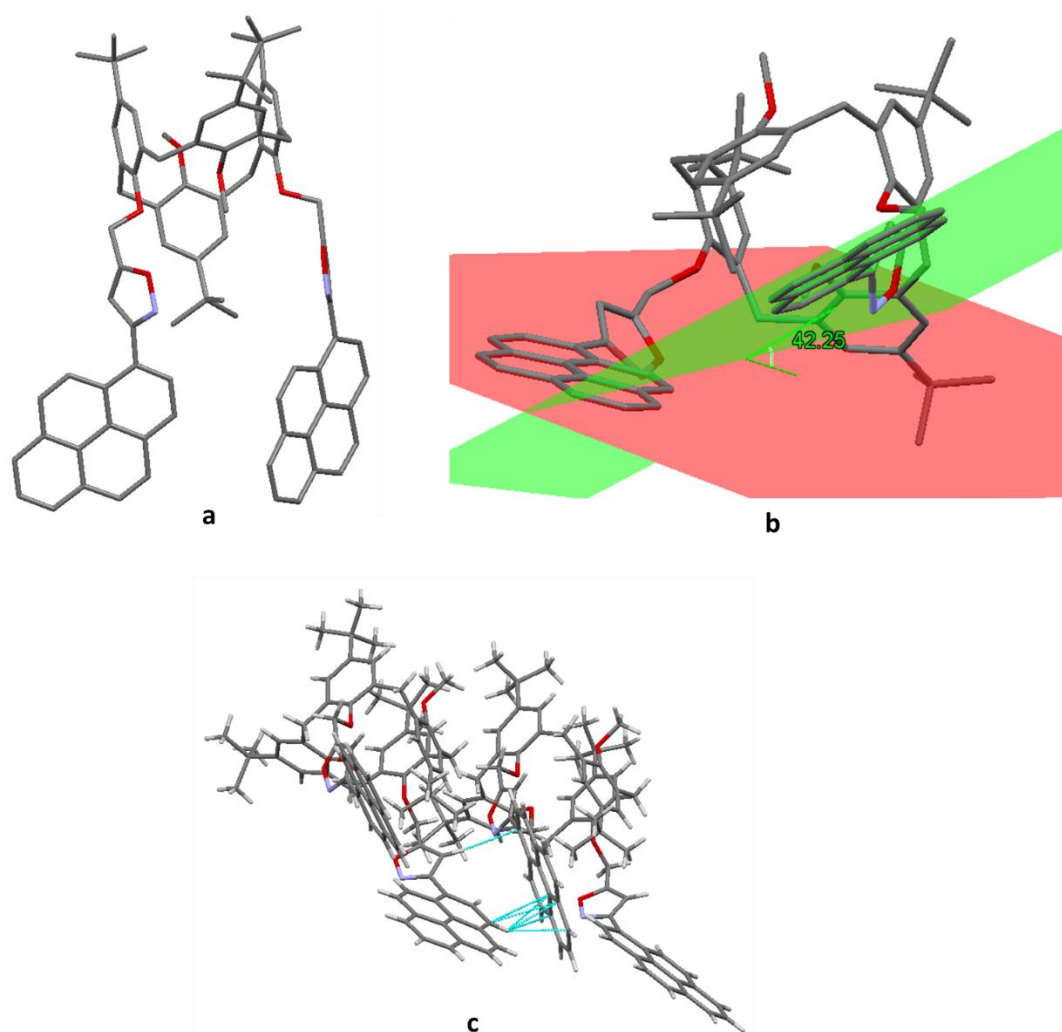


Figure 3.34: **a)** Solid state structure of **MPIC**; crystal grown from EtOH:DCM (2:1, v/v), showing **MPIC** in the partial cone conformation, **b)** diagram of **MPIC** showing the 42.25° angle between the planes of the pyrene moieties and **c)** two neighbouring units of **MPIC** showing “short contacts” between pyrene units and between an isoxazole CH and an adjacent pyrene in a neighbouring molecule (blue lines).

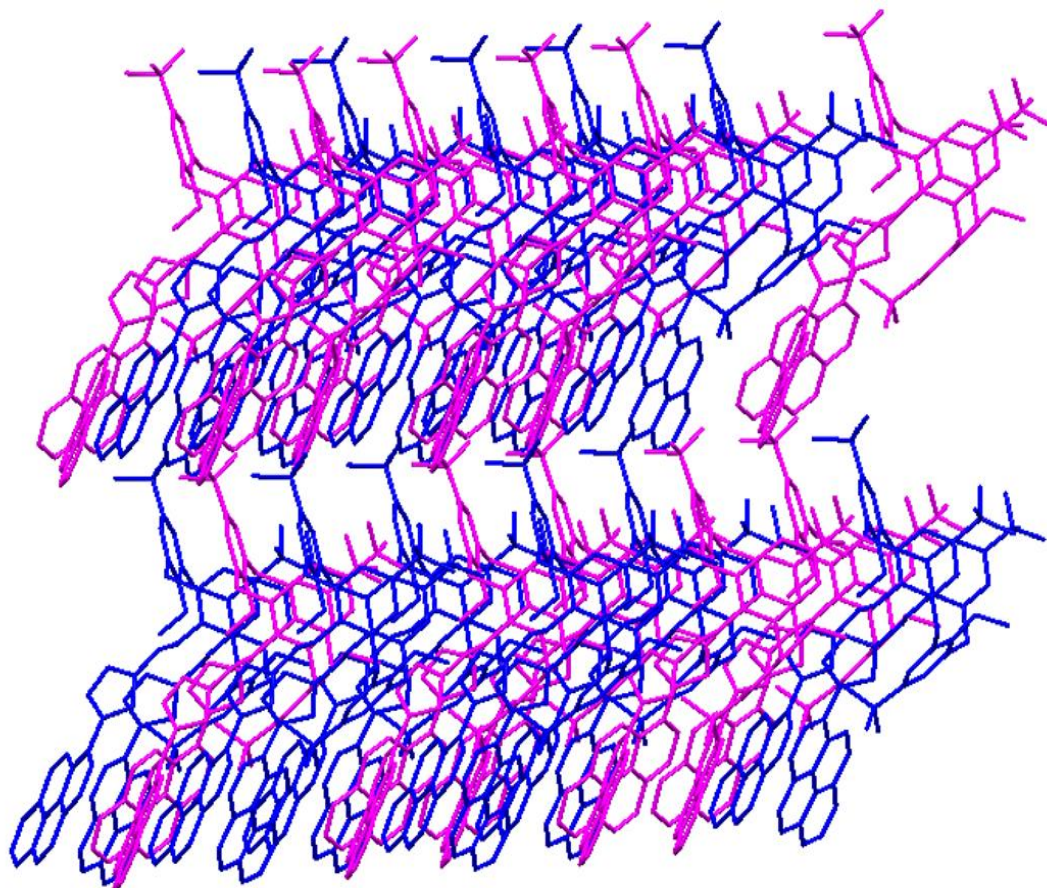


Figure 3.35: Extended packing network of the **MPIC** solid state structure showing the head-to-tail arrangement of the calixarene units.

Table 3.6: Summary of the characteristics of the **MPIC** crystal structure.

Py-Py Plane Angle	Py-Isox Plane Angles		Lower-Rim Hydrogen Bonding	Solvent Interaction	Other Interesting Features
42.25°	50.29°	39.12°	Not evident.	No solvent of crystallisation evident.	Head-to-tail arrangement between units of MPIC .

3.4.1.5 UV and Fluorescence Spectroscopy of MPIC

A UV absorbance spectrum of **MPIC** at 6 μM in MeCN, shown in **Figure 3.36** displays three broad absorption bands, each with shoulders, at 240, 280 and 348 nm similar to that observed for **EPIC** (Section 3.2.2.3). As expected, the UV profile of **MPIC** does not show the same fine vibronic structure as observed for the parent pyrene or **PPIC**

in MeCN, which again suggests that the direct linkage of the isoxazole ring at the 1-position of the pyrene moieties alters the electronics and photophysical properties of the fluorophores.

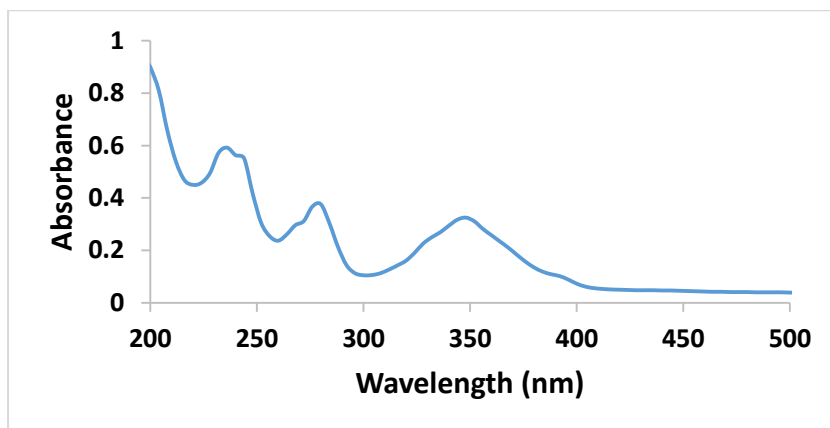


Figure 3.36: UV-Vis absorbance spectrum of **MPIC** (6 μM) in MeCN showing absorption bands at 240, 280 and 348 nm.

A fluorescence emission spectrum of **MPIC**, 6 μM in MeCN, is shown in **Figure 3.37**. The λ_{max} of the absorption band of longest wavelength, 348 nm, was chosen as the excitation wavelength (λ_{ex}) for the measurement of the emission spectrum. **MPIC** exhibited low intensity monomer emission bands at 387 and 409 nm and a relatively intense excimer emission band at 494 nm. The ratio of the emission of the first monomer band (44 a.u.) to the intensity at the λ_{max} of the excimer (328 a.u.) band was calculated to be 1:7.5. This suggests that the equilibrium between the cone and paco conformers in MeCN solution does not prohibit pyrene-pyrene excimer formation. Whilst the profile is similar to **PIC**, the relative intensity of both the monomer and excimer bands is reduced.

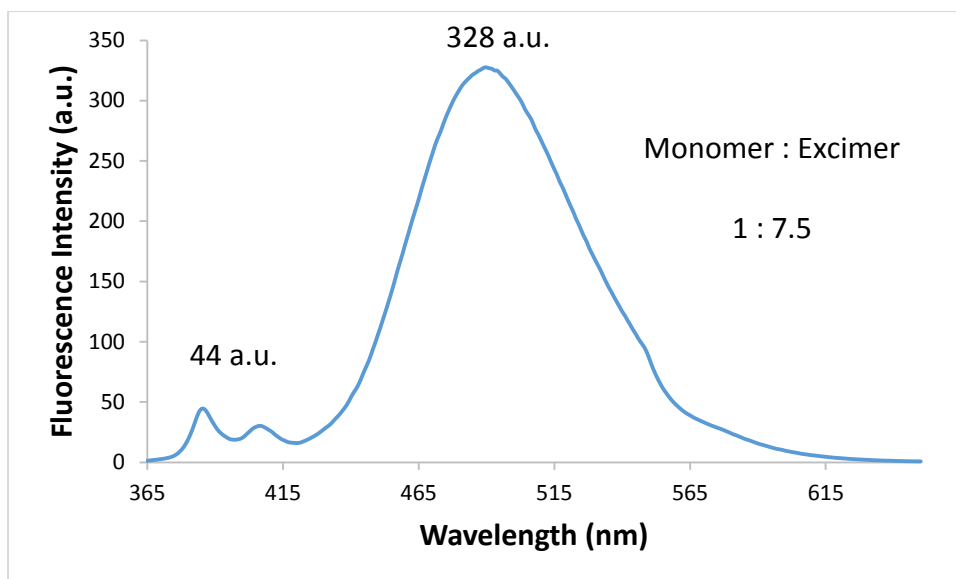


Figure 3.37: Emission spectrum of **MPIC** (6 μM , $\lambda_{\text{ex}} = 348 \text{ nm}$) in MeCN showing monomer emission bands at 387 and 409 nm and an excimer band at 494 nm.

The suggestion that the existence of a combination of cone and paco conformers in solution produces a more intense excimer emission band relative to a solution of the pure cone conformer of the same calixarene, was reported by Shinkai *et al.* for the pyrene functionalised conformationally mobile calixarene, **28**, shown in **Figure 3.38**.¹⁴⁰ They suggested that, as the lower rim of the calixarene is less sterically crowded in the paco conformer, excimer formation occurs more easily in this conformation.

They also observed a reduced intensity excimer emission in more polar solvents, *e.g.* methanol, where the cone conformer dominates, w.r.t. spectra recorded in less polar solvents. They measured the relative peak intensity of the monomer emission, which they defined as $I_m (\%) = I_m / (I_m + I_e)$, where I_m and I_e are the emission intensities at the monomer and emission bands, respectively. The value of $I_m (\%)$ was larger in solvents with larger cone:paco ratios, which supported the view that the interaction of the two pyrene moieties to form an excimer occurred more easily in paco-**28** than in cone-**28**.

The intensity of the monomer emission of **MPIC**, 44 a.u., was approximately half that recorded for **PIC**, **EPIC** and **PPIC**, 80-94 a.u. Thus, it may be the case that, similar to conformationally mobile calixarene **28**, the dominance of the paco conformer of

MPIC in solution allows for enhanced excimer formation, leading to a reduced monomer intensity w.r.t. **PIC**, **EPIC** and **PPIC**.

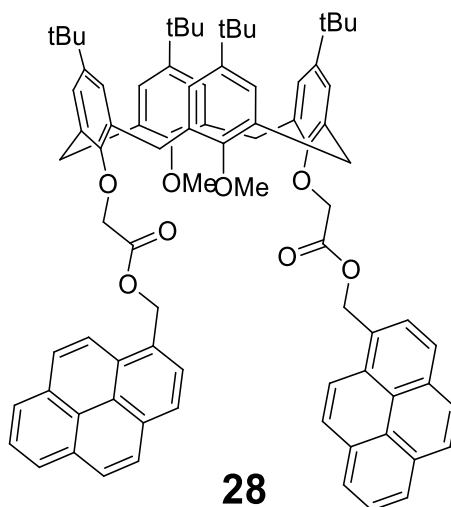


Figure 3.38: Pyrene functionalised conformationally mobile calixarene, **28**, shown by Shinkai and co-workers to have reduced excimer emission in polar solvents as the cone conformer becomes more predominant relative to less polar solvents with predominant pacoc conformer.¹⁴⁰

The intensities of the signals (a.u.) at the λ_{\max} of the excimer and first monomer emission along with the ratio of the former to the latter for all four pyrene functionalised calixarenes studied in this thesis (MeCN, 6 μ M) are summarised in **Table 3.7**. Comparison of the purely cone conformers (**PIC**, **EPIC** and **PPIC**) reveals that **PPIC** differs most from the others in the series w.r.t. the excimer intensity. The maximum intensity of the monomer emissions of **PIC**, **EPIC** and **PPIC** remained within a narrow range of 80-94 a.u. while that of the excimer bands varied through 243 a.u., 551 a.u. and 737 a.u. for **PPIC**, **EPIC** and **PIC** respectively. It can be seen that excimer emission from **PIC** was both more intense and more dominant than was the case for **EPIC** and **PPIC**. Thus, an attractive design for excimer emission involves (i) limiting the linker between the lower rim of the calixarene and the isoxazole ring to a single methylene group and (ii) making a direct linkage between the isoxazole and the pyrene moieties.

Table 3.7: Comparison of the intensity at the λ_{\max} of the first monomer peak and the excimer peak of **PIC**, **EPIC**, **PPIC** and **MPIC** all at 6 μM in MeCN, and the ratios of the excimer to the monomer intensity.

	λ_{ex} (nm)	Absorbance Intensity at λ_{ex} (a.u.)	Intensity at λ_{\max} of First Monomer Emission (a.u.) (wavelength)	Intensity at λ_{\max} of Excimer Emission (a.u.) (wavelength)	Monomer : Excimer Intensity Ratio
PIC	343	0.358	68 (386 nm)	737 (498 nm)	1 : 10.8
EPIC	348	0.337	94 (386 nm)	551 (494 nm)	1 : 5.9
PPIC	348	0.227	87 (384 nm)	243 (480 nm)	1 : 2.8
MPIC	348	0.325	44 (387 nm)	328 (494 nm)	1 : 7.5

3.5 Conclusions

- Three novel lower rim pyrene functionalised calixarenes structurally related to **PIC**; **EPIC**, **PPIC** and **MPIC**, were designed to study the relationship between host structure and ion sensing ability.
- **EPIC**, with an ethylene linker between the lower rim of the calixarene and the isoxazole heterocycle was successfully prepared. It presented in the cone conformer in solution and in the solid state. One pyrene unit of **EPIC** showed “slipped” face-to-face intermolecular π - π interactions to a pyrene moiety of a neighbouring **EPIC** unit in the solid state structure. No such interaction was observed with the second pyrene unit of each molecule.
- **PPIC** with an alkyl chain between the isoxazole rings and the pyrene units was successfully prepared. It presented as the cone conformer in solution. Crystals suitable for determination of a solid state structure could not be grown.
- **MPIC**, was formed by methylation of the hydroxyl groups of **PIC**. It was found to be conformationally mobile in solution over the temperature range - 50 to 45°C. NMR spectroscopic data, showed it to present at -30°C as a mixture of cone and paco conformers in a 1:2.8 ratio. The paco conformer was dominant at all temperatures in the range - 30 to 25°C. An x-ray crystal structure showed **MPIC** presented as the paco conformer in the solid state structure,

with no evidence of inter- or intramolecular π - π stacking between pyrene moieties.

- All three novel calixarenes displayed monomer and excimer bands in their fluorescence emission spectra. The ratio of the intensity of emission at the λ_{max} of the excimer band to the first monomer bands at 1:10.8 was greatest for **PIC** and smallest at 1:2.8 for **PPIC** suggesting that the propyl chain between the isoxazole heterocycles and the pyrene moieties of the pendant arms of **PPIC** made excimer formation less likely than in **PIC**, **EPIC** and **MPIC**.
- The $I_m:I_e$ ratio calculated for **MPIC**, 1:7.5, was larger than the ratios calculated for **EPIC** and **PPIC**.

Chapter 4

Sensing Potential of EPIC, PPIC and MPIC

4.1 Overview

This chapter reports on investigations of the metal ion sensing potential of the pyrene functionalised calixarenes, **EPIC**, **PPIC** and **MPIC**, using fluorescence and ^1H NMR spectroscopy. An analysis of the results, together with those found for **PIC** is provided, in an effort to formulate a hypothesis regarding the structural components of a pyrene appended isoxazole-calixarene necessary for guest detection.

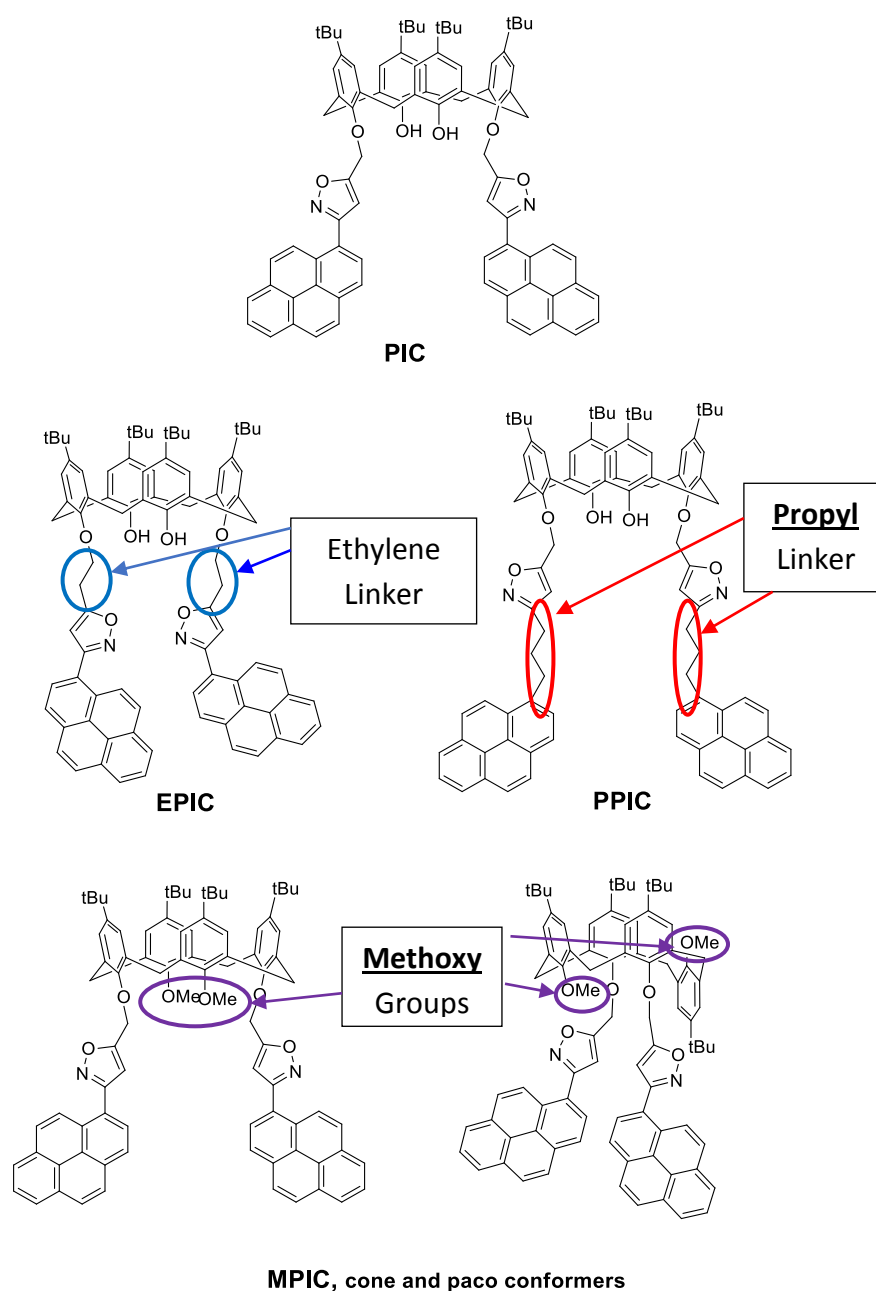


Figure 4.1: Structures of **PIC**, **EPIC**, **PPIC** and **MPIC**.

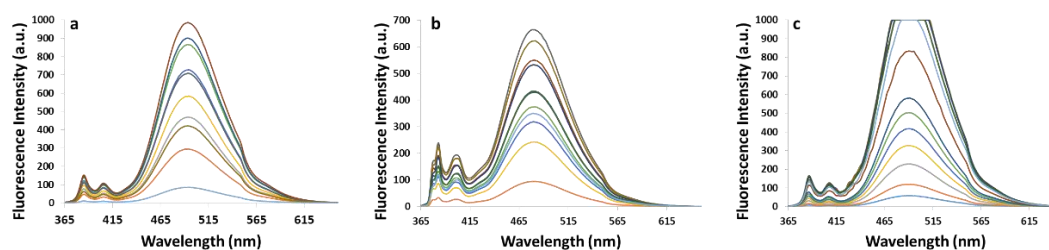
4.1.1 Linearity of the Fluorescence Response vs. Concentration of the Hosts

To be of analytical value, over the range of the investigation, the fluorescence emission intensity and concentration of a particular sample should be directly proportional.³⁸ Certain factors, such as the pathlength of the light (*i.e.* the dimensions of the cuvette), the excitation and emission wavelengths; the composition and optical density of the solvent medium can affect this linearity. If the concentration of a sample is high then excitation light may not pass completely through the sample; consequently all the molecules may not be excited. Therefore, samples at high concentrations can display a lower fluorescence emission intensity than samples at a lower concentration. This process, known as the inner filter effect or concentration dependant quenching, can cause inaccuracy during analytical experiments. Thus, it is important to verify the linearity of the host fluorescence response within the operational concentration range of subsequent studies.

As all analytical measurements concerning **PIC** were carried out at 6 μM in MeCN, it was deemed preferable to maintain this parameter for studies with **EPIC**, **PPIC** and **MPIC**. Accordingly calibration plots were constructed for each host around this window. Stock solutions of the calixarene hosts were prepared in MeCN at concentrations of 12 and 120 μM . A quartz cuvette with an internal volume of 3000 μL was used for all fluorescence emission measurements, and thus appropriate volumes of the host solutions were combined with MeCN, **Table 4.1**. For each potential host, **EPIC**, **PPIC** and **MPIC**, spectra were recorded over the range 1-120 μM , **Figure 4.2**, and the intensity of the absorption at the λ_{max} was plotted against sample concentration, data shown in **Figure 4.3**.

Table 4.1: Summary of the volumes of the calixarene host stock solutions and MeCN required to prepare samples in the concentration range: 1 – 120 μM .

Sample No.	Concentration of Calibration Sample (μM)	Vol. of Stock Solution μL (conc)	Vol. Of MeCN (μL)
1	1	250 (12 μM)	2750
2	2	500 (12 μM)	2500
3	4	1000 (12 μM)	2000
4	6	1500 (12 μM)	1500
5	8	2000 (12 μM)	1000
6	10	2500 (12 μM)	500
7	12	3000 (12 μM)	0
8	20	500 (120 μM)	2500
9	40	1000 (120 μM)	2000
10	60	1500 (120 μM)	1500
11	80	2000 (120 μM)	1000
12	100	2500 (120 μM)	500
13	120	3000 (120 μM)	0

**Figure 4.2:** Emission spectra of **a) EPIC**, **b) PPIC** and **c) MPIC** in MeCN ($\lambda_{\text{ex}} = 348$ nm in all cases) at 1 μM (light blue), 2 μM (orange), 4 μM (grey), 6 μM (yellow), 8 μM (dark blue), 10 μM (green), 12 μM (navy), 20 μM (brown), 40 μM (dark grey), 60 μM (beige), 80 μM (dark navy), 100 μM (dark green) and 120 μM (light blue).

Calibration plots for **EPIC** ($\lambda_{\text{max}} = 494$ nm) are shown in **Figure 4.3Ia** (0-10 μM) and **Ib** (0-120 μM). In the range 0-10 μM the plot was linear ($R^2 = 0.9869$), indicating that over this range the fluorescence emission intensity was directly proportional to the concentration. Whilst the intensity of the fluorescence emission continued to increase up to 20 μM , the linear relationship was lost between 10-20 μM . Significantly, beyond 20 μM a sharp decrease in the fluorescence intensity was noted, reducing from 986 a.u. at 20 μM to 86 a.u. at 120 μM , **Figure 4.3Ib**. This suggested

that at concentrations beyond 10 μM an inner filter effect or concentration dependent quenching was operational and therefore analytical studies ought to be restricted to samples at concentrations lower than 10 μM .

The calibration plot for **PPIC** involved plotting fluorescence intensity at the λ_{max} (480 nm) against concentration. The plots over a narrow and wider concentration range are shown in **Figure 4.3IIa** (0-12 μM) and **IIb** (0-120 μM). In the range 0-12 μM , the plot was linear ($R^2 = 0.9909$). However, as observed for **EPIC**, the intensity of the emission continued to increase with sample concentration, this time up to 40 μM (664 a.u.), before falling off significantly, to 350 a.u. for the 120 μM sample.

The fluorescence intensity ($\lambda_{\text{max}} = 494$ nm) of **MPIC**, bearing methoxy groups in place of the lower rim hydroxyl groups of **PIC**, was plotted against sample concentration, as shown in **Figure 4.3IIIa** (0-12 μM) and **IIIb** (0-120 μM). In the range 0-12 μM a linear relationship was observed ($R^2 = 0.9945$). Beyond 12 μM the intensity of the fluorescence emission continued to increase reaching the instrument maximum, 1000 a.u., and giving the appearance of "plateauing" between 40 and 120 μM .

PIC exhibited a similar profile with the intensity of fluorescence emission reaching the instrument maximum of 1000 a.u. from 12 to 60 μM and then dipping to 943 a.u. at 120 μM , **Figure 4.3IVb**.

The extended calibration profiles of **MPIC** and **PIC** (**Figure 4.3IIIb** and **IVb**) appear to differ from those for **EPIC** (**Ib**) and **PPIC** (**IIb**), which show significant falling off in fluorescence intensity at high concentrations. However, examination of the relative peak widths for the excimer bands of the **MPIC** samples reaching the maximum intensity revealed that the band widths varied with sample concentration. The excimer band of the 60 μM sample spanned 38 nm at 1000 a.u. whilst the span of the 120 μM sample at the same intensity was just 14 nm, **Figure 4.4**. This band narrowing can be extrapolated to indicate that the fluorescence intensity of **MPIC**, whilst still beyond the instrument maximum, peaks somewhere between 40-80 μM before decreasing. Thus, the fluorescence response of **MPIC** to increasing sample concentration is more in line with that of **EPIC** and **PPIC** than it appears on initial inspection.

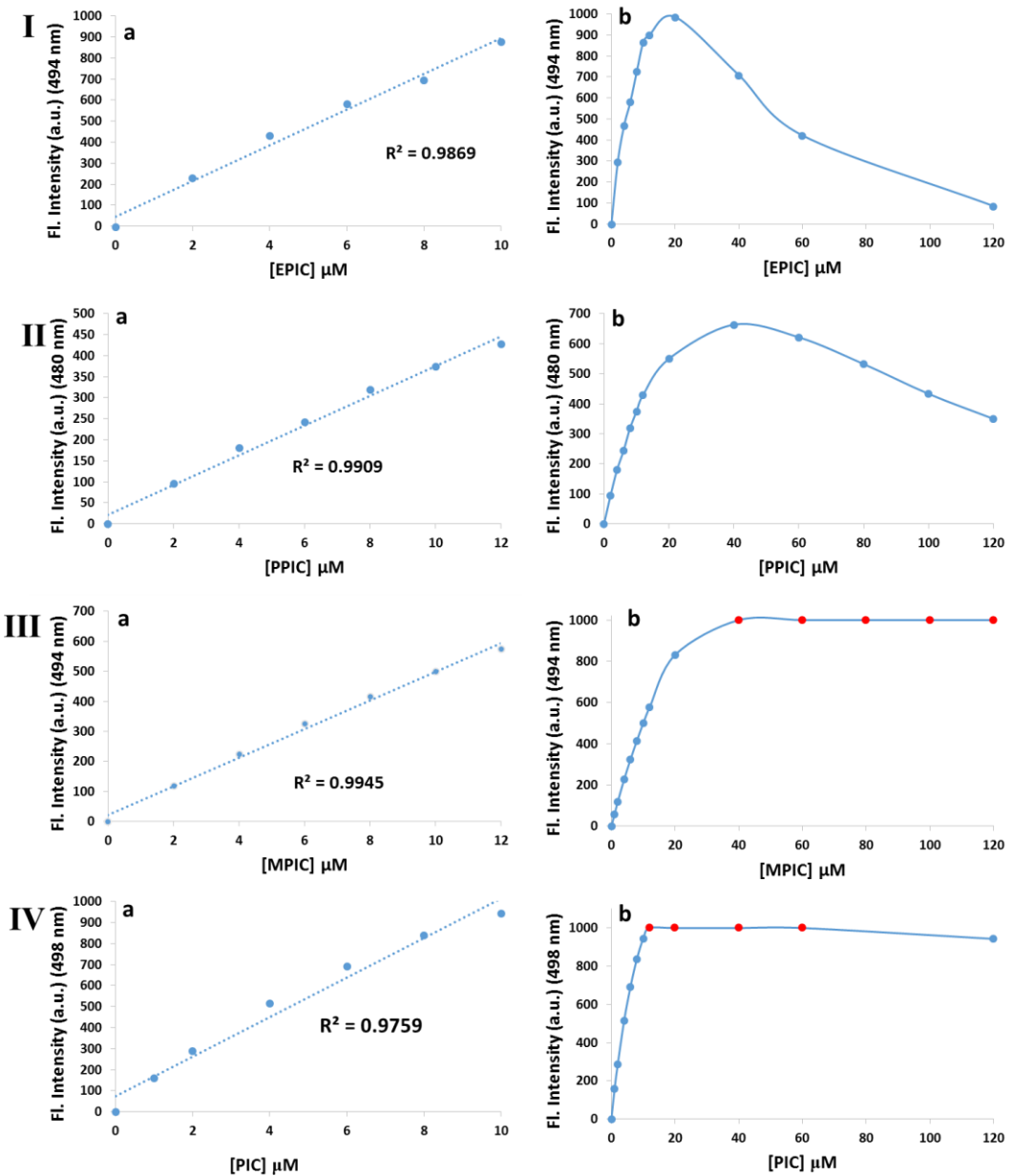


Figure 4.3: Calibration plots for **I) EPIC**, **II) PPIC**, **III) MPIC** and **IV) PIC** in which the fluorescence intensity at the λ_{max} was plotted against concentration in the ranges: **a)** 0-10/12 μM (Fitted to lines) and **b)** 0-120 μM . Red data points indicate instrument detector saturation.

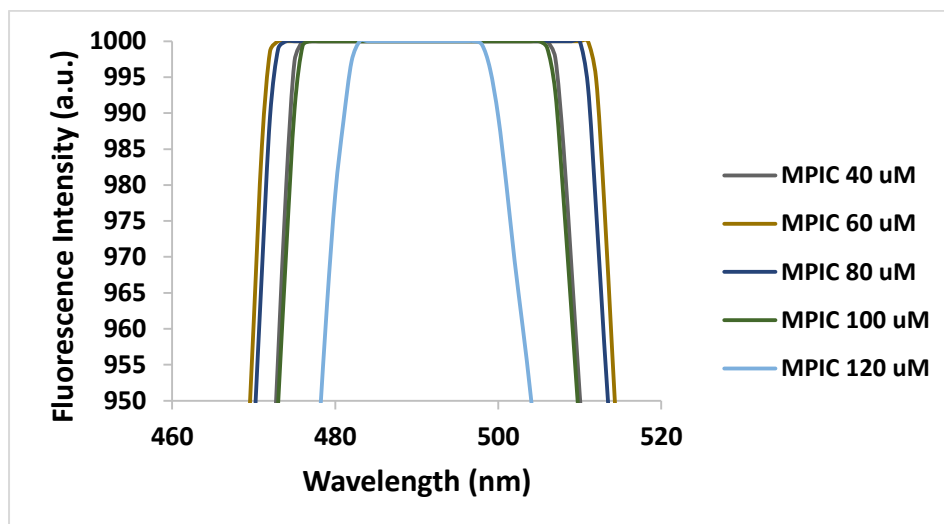


Figure 4.4: Region of the emission spectra of **MPIC** ($\lambda_{\text{ex}} = 348 \text{ nm}$) showing the apparent “plateau” at 1000 a.u. of the 40 – 120 μM samples.

The structures of the pendant arms of **PIC**, **EPIC**, **PPIC** and **MPIC** and the number of carbon atoms between the calixarene lower rim ether oxygen atoms and the 1-position of the pyrene moieties are shown in **Figure 4.5**. **EPIC** and **PPIC** have greater separation between these units, and thus may have a greater degree of mobility of the pendant pyrene moieties in comparison to **PIC** and **MPIC**.

One hypothesis for the variance in the intensities of the excimer bands and the concentration at which the intensity begins to decrease in the extended calibration plots of the four compounds, is that **EPIC** and **PPIC** may be more likely than **PIC** and **MPIC** to form intermolecular excimers at high concentrations due to the greater number of flexion points between their calixarene scaffolds and their pyrene moieties. This opportunity for facile intermolecular excimer formation could result in complete absorption of the incident excitation light to such an extent that the concentration dependant quenching is reached earlier in concentrated samples of **EPIC** and **PPIC**.

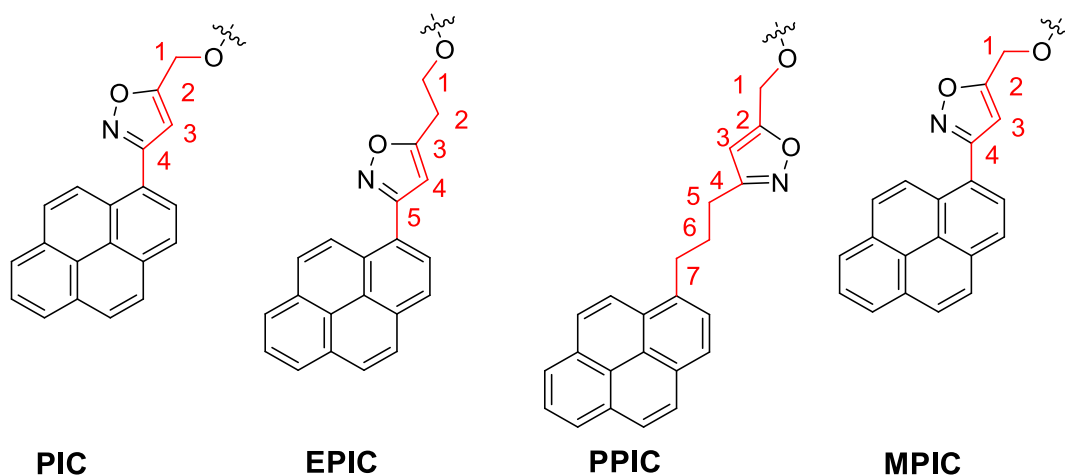


Figure 4.5: Structures of the pendant arms of **PIC**, **EPIC**, **PPIC** and **MPIC**, showing the number of carbon atoms between the lower rim ether oxygen and the 1-position of the pyrene moieties.

4.1.2 Fluorescence Response of Calixarene Hosts to Metal Perchlorates

The potential of the new calixarene hosts to selectively detect and report on the presence of metal ions in MeCN was investigated by fluorescence spectroscopy. The species tested included the Hg^{2+} , Ni^{2+} , Zn^{2+} , Co^{2+} , Pb^{2+} , Mn^{2+} , Ca^{2+} , Ag^+ and Cu^{2+} perchlorate salts. Samples containing the potential host and guest in a 1:100 ratio were prepared using stock solutions of the calixarenes at 12 μM in MeCN and the 9 metal salts at 1200 μM in the same solvent. Appropriate volumes of the host and guest solutions were combined with pure MeCN giving samples with a final volume of 3000 μL , **Table 4.2**.

Table 4.2: Summary of the volumes of solutions and solvent required to prepare samples exposing the calixarenes to 0 and 100 eqs of $\text{M}^{n+}(\text{ClO}_4^-)_n$, where $n = 1$ or 2.

Sample No.	Host : M^{n+}	Vol. of Host Stock Solution 12 μM in MeCN (μL)	Vol. of $\text{M}^{n+}(\text{ClO}_4^-)_n$ Stock Solution 1200 μM in MeCN (μL)	Vol. of MeCN (μL)
1	1:0	1500	0	1500
2	1:100	1500	1500	0

The fluorescence spectra for each sample were recorded in turn and are presented in **Figure 4.6**, **4.7** and **4.9** for **EPIC**, **PPIC** and **MPIC** respectively. Total quenching of

the excimer peak of **EPIC** was observed upon exposure to 100 eqs of $\text{Cu}(\text{ClO}_4)_2$, **Figure 4.6i**, significant quenching, at approximately 21%, occurred in the presence of $\text{Hg}(\text{ClO}_4)_2$, **Figure 4.6e**, whilst quenching levels of ~7 and 9% occurred in the presence of Pb^{2+} and Co^{2+} respectively. Little or no change to the fluorescence profile of **EPIC** occurred following exposure to the remaining salts. Thus, **EPIC**, with an ethylene chain between the isoxazole and the calixarene lower rim, was an effective host for the Cu^{2+} cation.

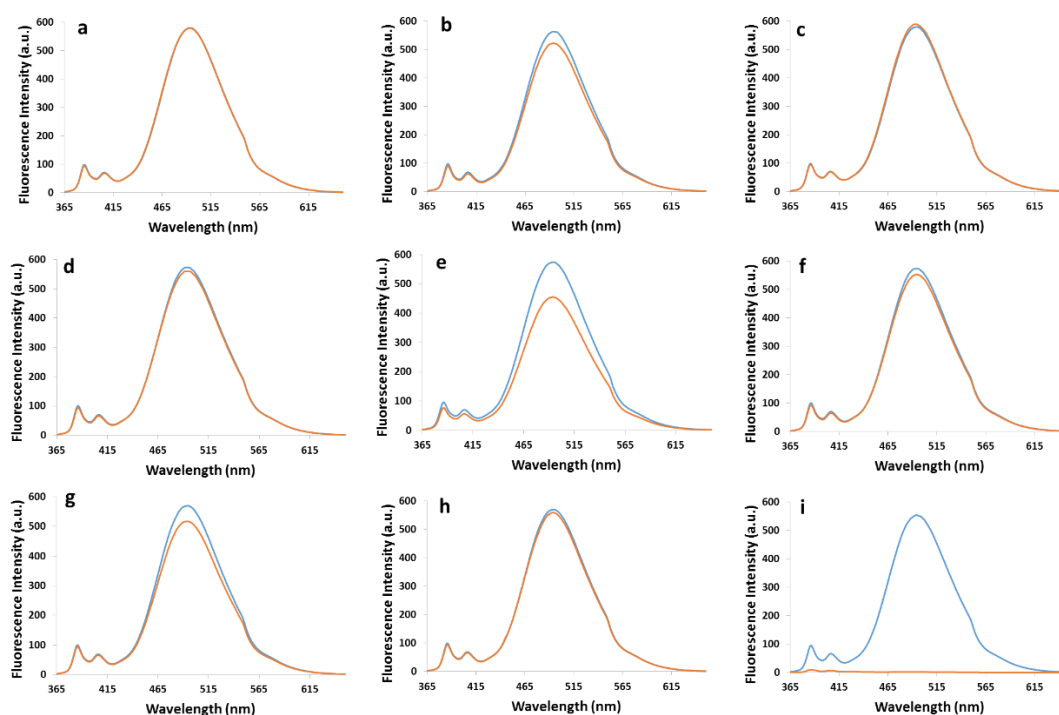


Figure 4.6: Emission spectra of **EPIC** (6 μM , $\lambda_{\text{ex}} = 348 \text{ nm}$) in MeCN with 0 (blue) and 100 (orange) eqs of $\text{M}^{n+}(\text{ClO}_4^-)_n$; where $\text{M}^{n+} = \text{a) Ca}^{2+}$, **b) Pb^{2+}** , **c) Mn^{2+}** , **d) Zn^{2+}** , **e) Hg^{2+}** , **f) Ni^{2+}** , **g) Co^{2+}** , **h) Ag^+** and **i) Cu^{2+}** .

Very limited quenching, ~4%, of the excimer peak of **PPIC** was observed in the presence of $\text{Hg}(\text{ClO}_4)_2$ and $\text{Co}(\text{ClO}_4)_2$, **Figure 4.7e**. Little or no effect was observed following exposure to any of the other metal perchlorate salts, **Figure 4.7**, with the exception of copper when approximately 83% quenching, band broadening and a blue-shift (10 nm or 445 cm^{-1}) of the λ_{max} was noted, **Figure 4.7i**. Thus **PPIC**, with the flexible propyl chain between the pyrene and the heterocyclic units, discriminates more selectively between the Cu^{2+} cation and the other mono- and divalent metal cations studied than **EPIC**.

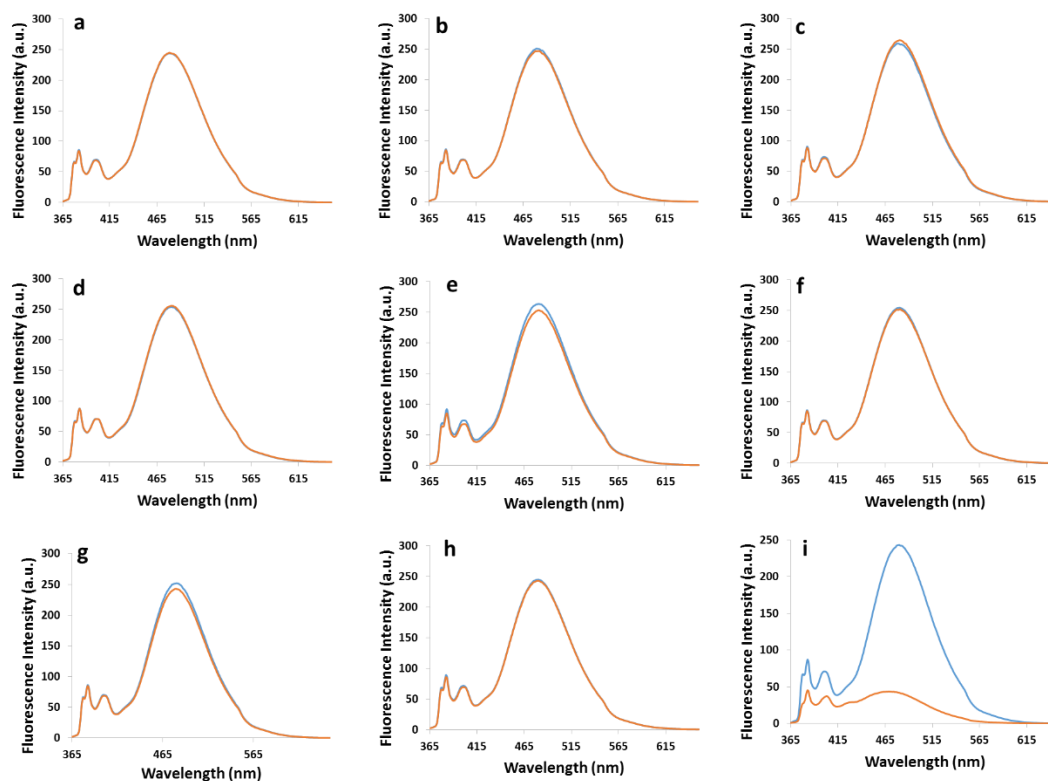


Figure 4.7: Emission spectra of PPIC (6 μM , $\lambda_{\text{ex}} = 348 \text{ nm}$) in MeCN with 0 (blue) and 100 (orange) eqs of $\text{M}^{\text{n}+}(\text{ClO}_4^-)_n$; where $\text{M}^{\text{n}+} = \text{a) Ca}^{2+}$, **b) Pb**²⁺, **c) Mn**²⁺, **d) Zn**²⁺, **e) Hg**²⁺, **f) Ni**²⁺, **g) Co**²⁺, **h) Ag**⁺ and **i) Cu**²⁺.

Hypsochromic (blue) and bathochromic (red) shifts of absorption or emission bands of host solutions can indicate the occurrence of a particular binding event, as has been reported for calixarene and non-calixarene based fluorescence sensors.^{81,141-146} Leray *et al.* observed hypsochromic shifts, of 3-8 nm, in the absorption and emission spectra of their bis crown ether-BODIPY functionalised calixarene **29**, **Figure 4.8**, upon binding with Cs⁺ or K⁺ cations. This shift was attributed to a reduction in electron-donating character of the oxygen atoms conjugated to the BODIPY fluorophore following cation binding.¹⁴⁷

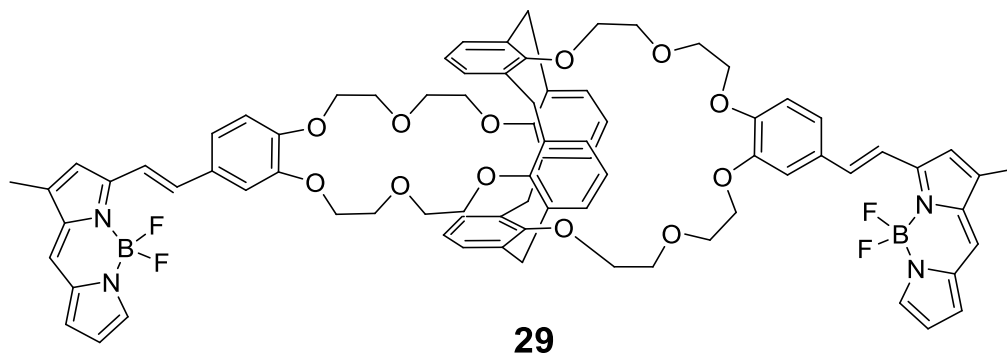


Figure 4.8: Structure of a BODIPY functionalised 1,3-alternate calix[4]arene, **29**, that displays a hypsochromic shift upon binding with the K^+ or Cs^+ cations.¹⁴⁷

The 10 nm blue-shift of the emission band of **PPIC** following exposure to 100 eqs of $Cu(ClO_4)_2$ was attributed to a consequence of reduced electron density of the fluorophore following a possible reduction in electron density of the isoxazole heterocycle following guest binding.

Quenching (27%) of the excimer signal of **MPIC**, with the lower rim methoxy groups, was noted upon exposure to $Cu(ClO_4)_2$, **Figure 4.9i**. Significantly the extent of quenching is lower than that observed with **EPIC** or **PPIC** of >99% and 83% respectively. The reduced effectiveness of copper induced quenching may be due to the presence of equilibrating cone and paco conformers of **MPIC** in solution. There was no detectable response to any of the other metal ions except for $Hg(ClO_4)_2$ which showed ~3% excimer band quenching, **Figure 4.9e**.

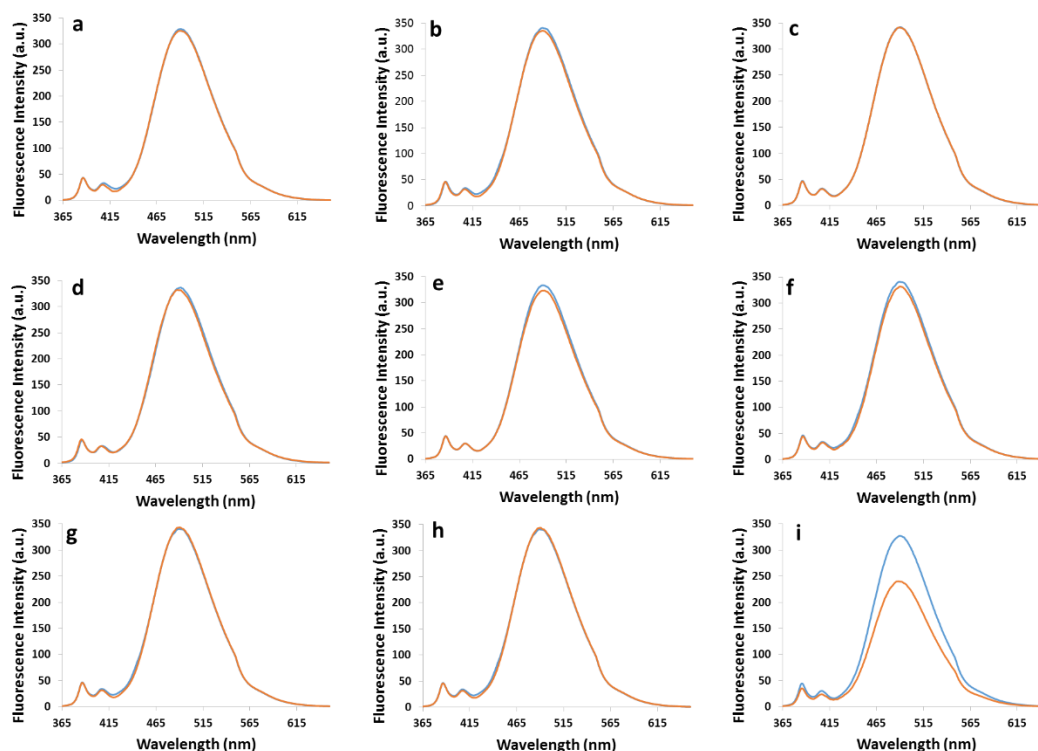


Figure 4.9: Emission spectra of **MPIC** (6 μM , $\lambda_{\text{ex}} = 348 \text{ nm}$) in MeCN with 0 (blue) and 100 (orange) eqs of $\text{M}^{n+}(\text{ClO}_4^-)_n$; where $\text{M}^{n+} = \text{a) Ca}^{2+}$, **b) Pb²⁺**, **c) Mn²⁺**, **d) Zn²⁺**, **e) Hg²⁺**, **f) Ni²⁺**, **g) Co²⁺**, **h) Ag⁺** and **i) Cu²⁺**.

The effectiveness of quenching at the λ_{max} of the excimer band of each calixarene host upon exposure to 100 eqs of $\text{Cu}(\text{ClO}_4)_2$, $\text{Pb}(\text{ClO}_4)_2$, $\text{Hg}(\text{ClO}_4)_2$ and $\text{Co}(\text{ClO}_4)_2$ is summarised in **Table 4.3**. This clearly shows that all four hosts have an affinity for Cu^{2+} ions, reduced affinities for the Hg^{2+} , Pb^{2+} and Co^{2+} cations may be due to the heavy metal ion effect and the inherent quenching nature of the Hg^{2+} and Pb^{2+} cations.^{148,149}

Table 4.3: Comparison of the degree of quenching of the excimer bands observed upon exposure of each calixarene host to 100 eqs of a given metal perchlorate.

	Cu²⁺	Pb²⁺	Hg²⁺	Co²⁺
PIC	>99%	0%	0%	0%
EPIC	>99%	7%	21%	9%
PPIC	83%	0%	4%	4%
MPIC	27%	0%	3%	0%

4.1.3 Competitive Metal Ion Study

The potential for the real-life application of **EPIC**, **PPIC** and **MPIC** as metal ion sensors was further probed by conducting a competitive metal ion study. This study was carried out by comparing the fluorescence response of each host to that for the host in the presence of 10 eqs of the range of metal perchlorates, and finally to that when the hosts were exposed to 10 eqs of both the competitive metal salts and $\text{Cu}(\text{ClO}_4)_2$. If quenching occurred in the latter, but not the former, samples it could be concluded that the hosts can detect Cu^{2+} in the presence of contaminating metal ions.

Stock solutions of the hosts at $12 \mu\text{M}$ and of the 9 metal perchlorates at $1200 \mu\text{M}$ were prepared in MeCN. Appropriate volumes were drawn from these stock solutions to prepare the samples indicated in **Table 4.4**.

Table 4.4: Summary of the volumes of solutions and solvent required to prepare samples exposing the calixarene hosts to (i) 0 and (ii) 10 eqs of $\text{M}^{n+}(\text{ClO}_4^-)_n$ salts (other than copper), to (iii) 10 eqs of $\text{M}^{n+}(\text{ClO}_4^-)_n$ followed by a subsequent addition of 10 eqs of $\text{Cu}(\text{ClO}_4)_2$ and to (iv) 10 eqs $\text{Cu}(\text{ClO}_4)_2$.

Sample No.	H:M ⁿ⁺ :Cu ²⁺	Vol. of Host Stock Solution 12 μM MeCN (μL)	Vol. of M ⁿ⁺ (ClO ₄ ⁻) _n Stock Solution 1200 μM MeCN (μL)	Vol. of Cu(ClO ₄) ₂ Stock Solution 1200 μM MeCN (μL)	Vol. of MeCN (μL)
(i)	1:0:0	1500	0	0	1500
(ii)	1:10:0	1500	150	0	1350
(iii)	1:10:10	1500	150	150	1200
(iv)	1:0:10	1500	0	150	1350

Fluorescence spectra for each host were recorded for each of the samples indicated in **Table 4.4**. Initially **EPIC** ($6 \mu\text{M}$) in MeCN was exposed to 10 eqs of a given metal perchlorate salt and the fluorescence emission spectra were recorded. In a subsequent experiment **EPIC** ($6 \mu\text{M}$) was exposed to 10 eqs of contaminating metal perchlorate ions as well as 10 eqs of copper perchlorate. The data is summarised in **Figure 4.10**, blue plots are for the host-alone, orange plots are for the host with metal

salts other than copper and grey plots are for the host plus a contaminating metal perchlorate as well as copper.

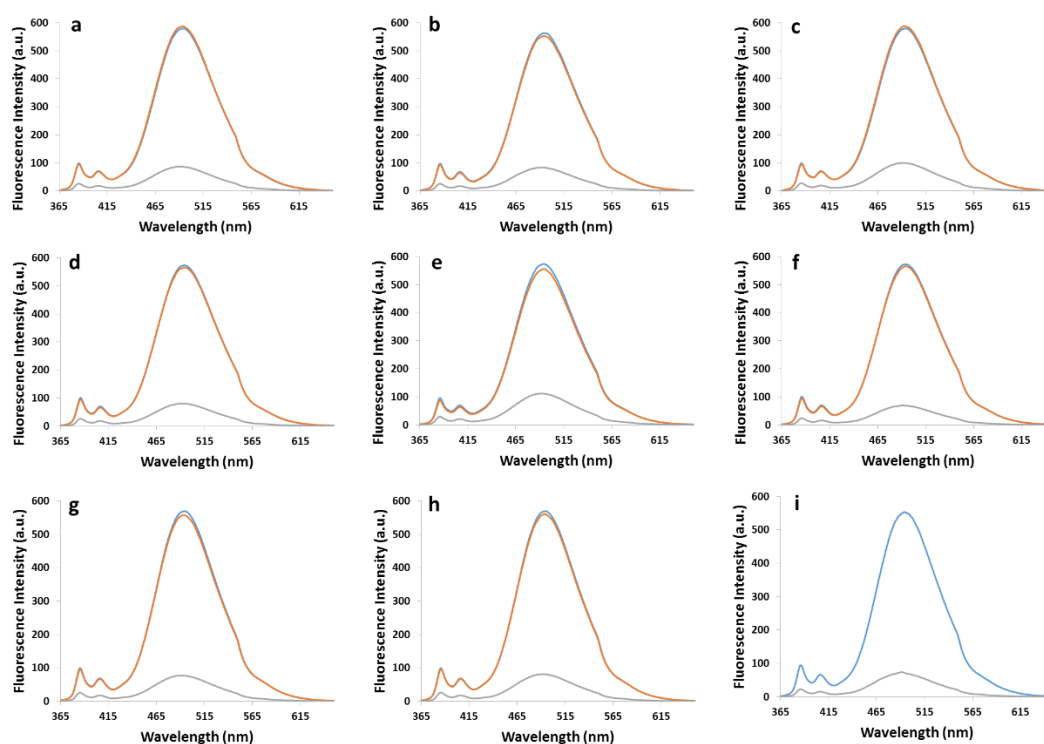


Figure 4.10: Emission spectra of **EPIC** (6 μM , $\lambda_{\text{ex}} = 348 \text{ nm}$) in MeCN with Host-alone (blue) and Host + 10 eqs of $\text{M}^{\text{n}+}(\text{ClO}_4^-)_n$ (orange); and Host + 10 eqs of $\text{M}^{\text{n}+}(\text{ClO}_4^-)_n$ + 10 eqs of $\text{Cu}(\text{ClO}_4)_2$ (grey); where $\text{M}^{\text{n}+} = \text{a) Ca}^{2+}$, **b) Pb}^{2+}**, **c) Mn}^{2+}**, **d) Zn}^{2+}**, **e) Hg}^{2+}**, **f) Ni}^{2+}**, **g) Co}^{2+}** and **h) Ag}^{+}**; **i) Host-alone** (blue) and Host + 10 eqs $\text{Cu}(\text{ClO}_4)_2$ (grey).

The results indicate that **EPIC** retained the ability to sense Cu^{2+} ions in the presence of other contaminating metal perchlorate salts in MeCN. The initial fluorescence intensity of **EPIC** ($\lambda_{\text{max}} = 494 \text{ nm}$) following the addition of 10 eqs of Hg^{2+} , Ni^{2+} , Zn^{2+} , Co^{2+} , Ca^{2+} , Pb^{2+} , Mn^{2+} or Ag^{+} metal perchlorate salts remained relatively unchanged, whilst samples containing 10 eqs of the same metal salts and 10 eqs of copper perchlorate displayed quenching, ranging from 81-88%, **Figure 4.11**. These figures compare favourably with the 87% quenching of the excimer band of **EPIC** observed following addition of 10 eqs of Cu^{2+} ions in the absence of contaminating metal ions, **Figure 4.6i**.

A blue-shift of 3 nm (124 cm^{-1}) of the λ_{max} of the excimer signal of **EPIC** was noted in the presence of 10 eqs of copper ions, regardless of whether the solution also contained contaminating metal ions. In the earlier experiments with 100 eqs of Cu^{2+} ,

blue-shifts were observed with **PPIC** and **MPIC**, but no such judgement could be made for **EPIC** since it was fully quenched. This 3 nm blue-shift was again considered a consequence of the formation of a host:guest complex.

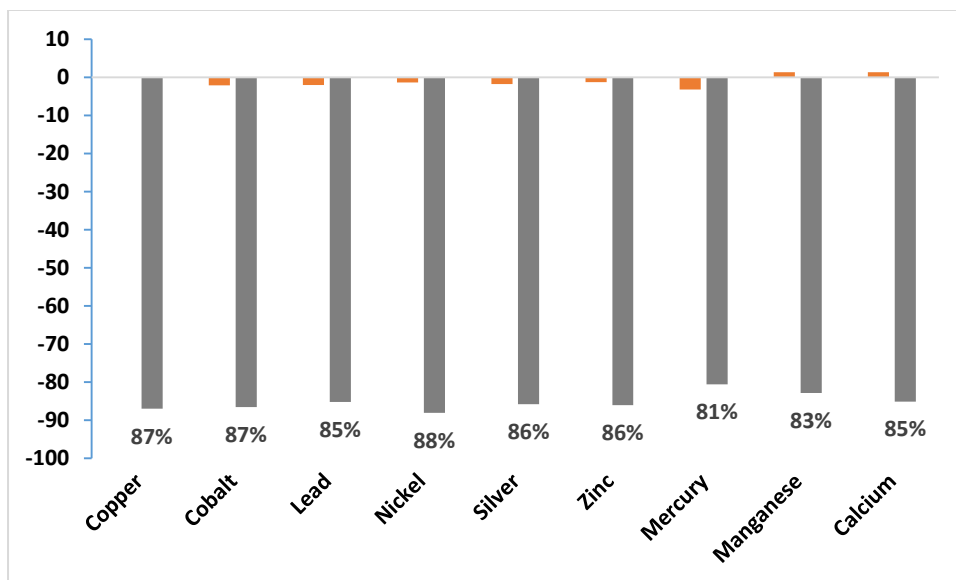


Figure 4.11: Percentage change in the intensity of maximum fluorescence emission of **EPIC** (6 μ M, λ_{ex} =348 nm) at λ_{max} (494 nm) upon the addition of 10 eqs of metal perchlorates (orange) and upon the addition of 10 eqs of metal perchlorate and copper perchlorate (grey).

A parallel selectivity study was conducted with **PPIC** and the resulting spectra are displayed in **Figure 4.12**, again, blue plots are for the host-alone, orange plots are for the host with metal salts other than copper and grey plots are for the host plus a contaminating metal perchlorate as well as copper.

PPIC, like **EPIC** retained the ability to sense Cu^{2+} ions in the presence of other contaminating metal perchlorate salts in MeCN. The initial fluorescence intensity of **PPIC** (λ_{max} = 480 nm) was not decreased upon addition of 10 eqs of Hg^{2+} , Ni^{2+} , Zn^{2+} , Co^{2+} , Ca^{2+} , Pb^{2+} , Mn^{2+} or Ag^{+} perchlorate salts, whilst samples containing 10 eqs of both metal perchlorate and copper perchlorate showed similar extents of quenching, 83-87%, as occurred in the presence of 10 eqs of Cu^{2+} ions only, **Figure 4.13**.

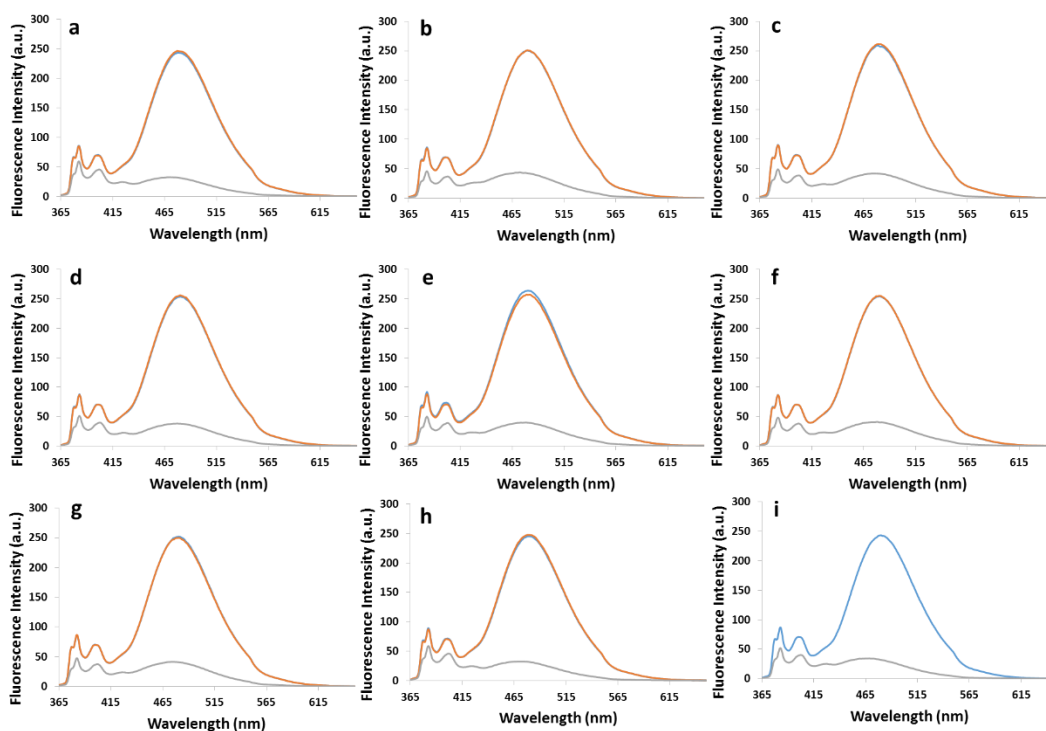


Figure 4.12: Emission spectra of **PPIC** (6 μM, λ_{ex} = 348 nm) in MeCN with Host-alone (blue) and Host + 10 eqs of Mⁿ⁺(ClO₄⁻)_n (orange); and Host + 10 eqs of Mⁿ⁺(ClO₄⁻)_n + 10 eqs of Cu(ClO₄)₂ (grey); where Mⁿ⁺ = **a**) Ca²⁺, **b**) Pb²⁺, **c**) Mn²⁺, **d**) Zn²⁺, **e**) Hg²⁺, **f**) Ni²⁺, **g**) Co²⁺, **h**) Ag⁺; and **i**) Host-alone (blue) and Host + 10 eqs Cu(ClO₄)₂ (grey).

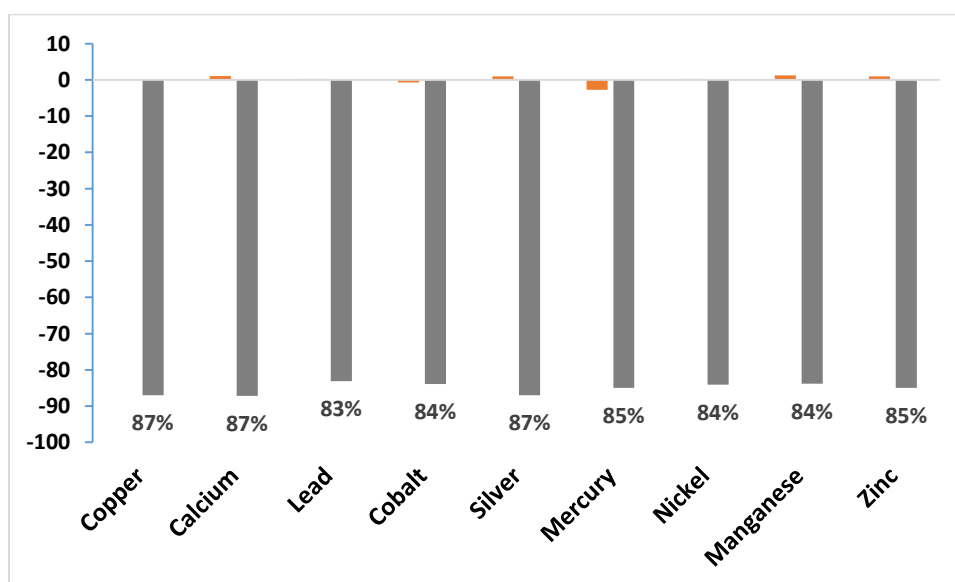


Figure 4.13: Percentage change in the intensity of maximum fluorescence emission of **PPIC** (6 μM, λ_{ex} = 348 nm) at λ_{max} (480 nm) upon the addition of 10 eqs of metal perchlorates (orange) and upon the addition of 10 eqs of both metal perchlorate and copper perchlorate (grey).

The third host in the series, **MPIC** was studied in the same manner and the data shown in **Figure 4.14**. The extent of copper induced fluorescence quenching was broadly similar in the presence (14-22%) or absence (16%) of contaminating metal ions, **Figure 4.15**.

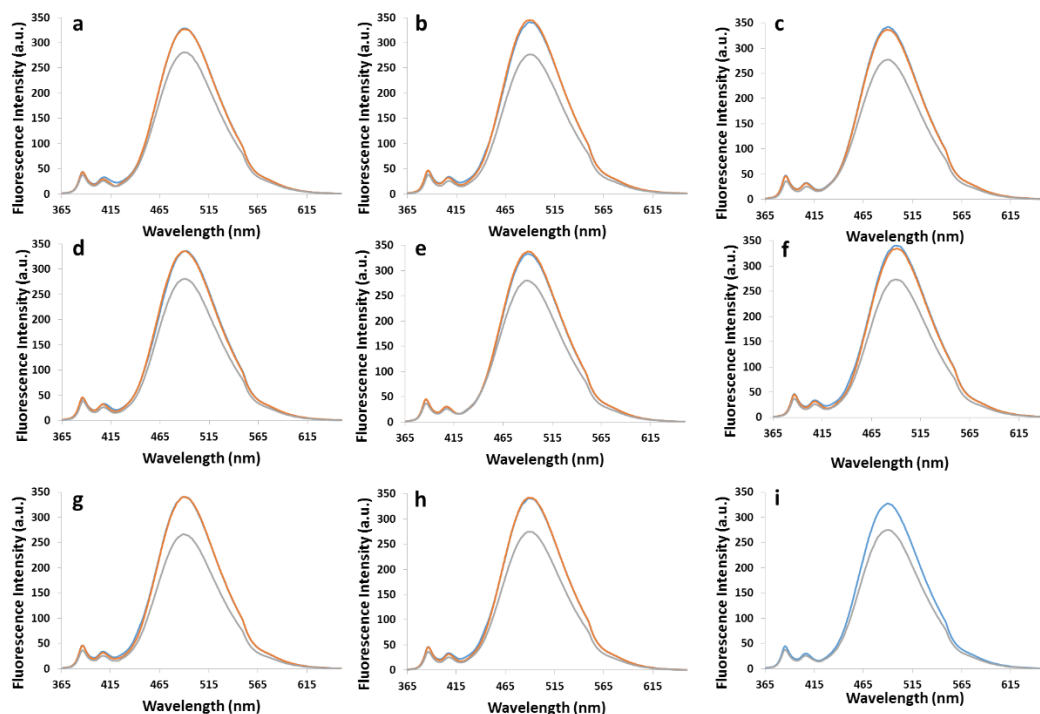


Figure 4.14: Emission spectra of **MPIC** ($6 \mu\text{M}$, $\lambda_{\text{ex}} = 348 \text{ nm}$) in MeCN with Host-alone (blue) and Host + 10 eqs of $\text{M}^{\text{n}+}(\text{ClO}_4^-)_n$ (orange); and Host + 10 eqs of $\text{M}^{\text{n}+}(\text{ClO}_4^-)_n$ + 10 eqs of $\text{Cu}(\text{ClO}_4)_2$ (grey); where $\text{M}^{\text{n}+} =$ **a)** Ca^{2+} , **b)** Pb^{2+} , **c)** Mn^{2+} , **d)** Zn^{2+} , **e)** Hg^{2+} , **f)** Ni^{2+} , **g)** Co^{2+} , **h)** Ag^+ ; and **i)** Host-alone (blue) and Host + 10 eqs $\text{Cu}(\text{ClO}_4)_2$ (grey).

The response of each calixarene host to 10 eqs of Cu^{2+} ions in the presence and absence of competitive metal ions is summarised in **Table 4.5**. The extent of copper induced excimer quenching was found to be in the same range irrespective of the presence or absence of a second metal ion. Thus, it was evident that, like **PIC**, the three calixarene hosts **EPIC**, **PPIC** and **MPIC** could all detect copper ions in MeCN in the presence of contaminating metal perchlorate salts.

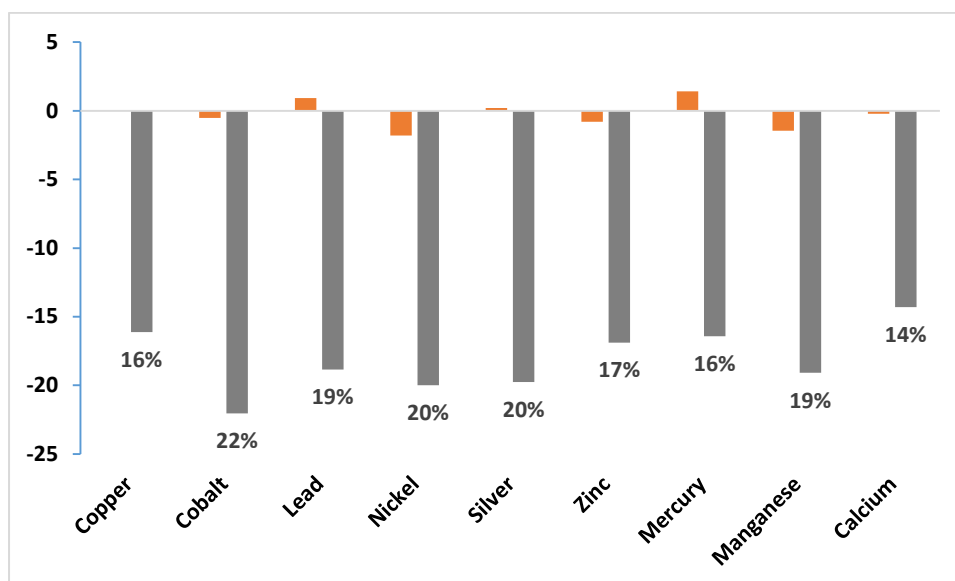


Figure 4.15: Percentage change in the intensity of maximum fluorescence emission of **MPIC** (6 μM , $\lambda_{\text{ex}}=348$ nm) at λ_{max} (494 nm) upon the addition of 10 eqs of metal perchlorates (orange) and upon the addition of 10 eqs of both metal perchlorate and copper perchlorate (grey).

Table 4.5: Comparison of the % quenching at λ_{max} of the excimer signals of **EPIC** ($\lambda_{\text{max}} = 494$ nm), **PPIC** ($\lambda_{\text{max}} = 480$ nm) and **MPIC** ($\lambda_{\text{max}} = 494$ nm) in the presence of 10 eqs of $\text{Cu}(\text{ClO}_4)_2$ and in the presence of 10 eqs of $\text{Cu}(\text{ClO}_4)_2$ plus 10 eqs of a competitive metal perchlorate.

Host	EPIC	PPIC	MPIC
10 eqs Cu^{2+}	87%	87%	16%
10 eqs Cu^{2+} and 10 eqs $\text{M}^{n+}(\text{ClO}_4^-)_n$	81-88%	83-87%	14-22%

A metal complex, or coordination complex, consists of a central metallic ion bound by molecules or ions known as ligands. Donor atoms are atoms within the ligands which are involved in bonding to the central metal ion. Typically, a metal ion will be bonded to several donor atoms which may be the same or different. The coordination number of a complex refers to the number of donor atoms attached to a metal. Different structural arrangements of the coordinated ligands result in different geometries, the most common geometries and their coordination numbers are shown in **Figure 4.16**.

Coordination Number

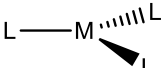
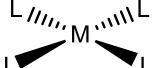
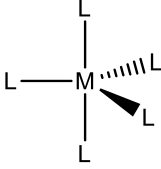
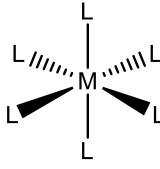
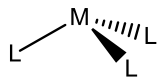
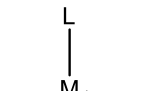
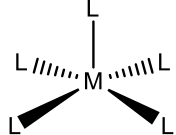
3	4	5	6
 <p>trigonal planar</p>	 <p>square planar</p>	 <p>trigonal bipyramidal</p>	 <p>octahedral</p>
 <p>pyramidal</p>	 <p>tetrahedral</p>	 <p>square pyramidal</p>	

Figure 4.16: Common geometries of metal-ligand complexes and their coordination numbers.

The observed selectivity of **PIC**, **EPIC**, **PPIC** and **MPIC** for the Cu^{2+} ion over all other first row transition metal ions tested can be analysed by reference to the Irving-Williams series. This series refers to the relative stability of transition metal ion complexes, which follows the order $\text{Mn}^{2+} < \text{Fe}^{2+} < \text{Co}^{2+} < \text{Ni}^{2+} < \text{Cu}^{2+} > \text{Zn}^{2+}$, regardless of the nature of the ligand or coordination number of the metal complex formed.¹⁵⁰

Metal-ligand complexes involving copper perchlorate in MeCN are reported in a range of geometries including square pyramidal,¹⁵¹ square planar¹⁵² and octahedral.¹⁵³

A square pyramidal Cu^{2+} complex was reported by Akbarsha *et al.*, **Figure 4.17a**.¹⁵¹ The base of the pyramid was composed of a nitrogen and oxygen atom from a tyrosine ligand and two nitrogen atoms of a dimethyl phenanthroline ligand, while the apical ligand was occupied by an oxygen atom of a water molecule.

Sánchez and co-workers report a square planar Cu^{2+} complex, formed from stirring a solution of their *N,N'*-bis-propyl-phenylenediamine ligand and copper perchlorate in MeCN at rt for 3 hours, the tetradentate square planar complex is made up of two amine nitrogen and two amide nitrogen atoms, **Figure 4.17b**.¹⁵²

A Cu^{2+} complex was reported by Hu *et al.* comprising of six coordinating nitrogen atoms, from four 2,2'-(methylenedithio)bis(1,3,4-thiadiazole) ligands and two acetonitrile solvent molecules forming a slightly distorted octahedral complex, **Figure 4.17c**.¹⁵³

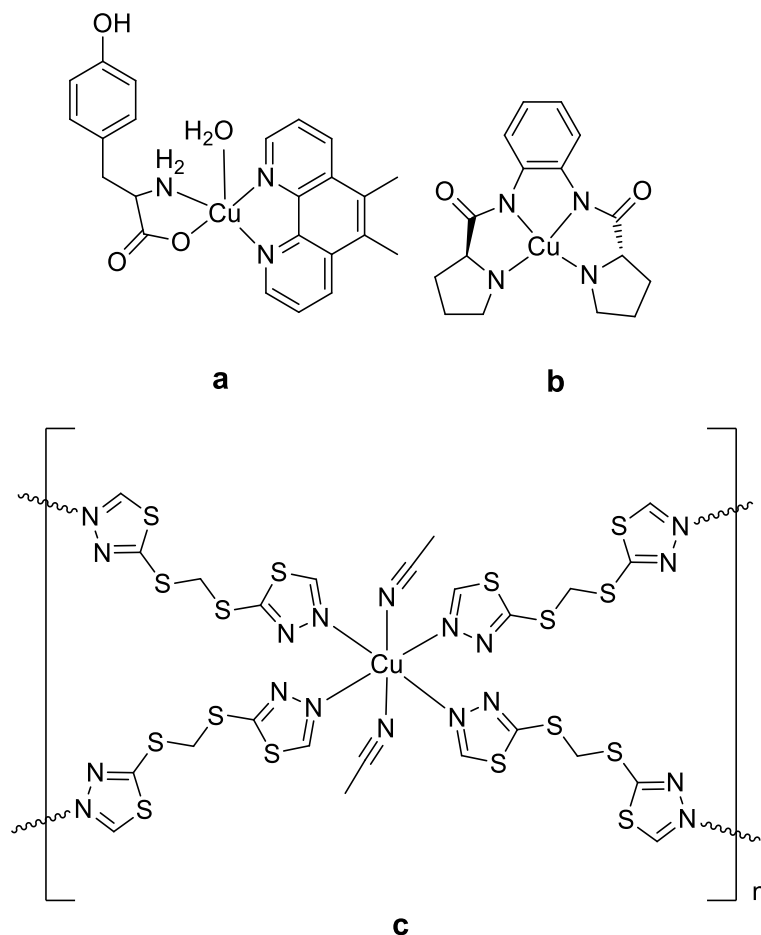


Figure 4.17: Structures of Cu^{2+} complexes in **a)** square pyramidal,¹⁵¹ **b)** square planar¹⁵² and **c)** octahedral¹⁵³ geometries.

4.1.4 Counterion Study

The effect of the counterion of the copper salt on the fluorescence behaviour of the hosts was investigated by comparing the effect of the copper chloride, nitrate and acetate salts with the findings for copper perchlorate. Host solutions were prepared at 12 μM in MeCN and solutions of the copper salts were prepared at 1200 μM in the same solvent. Appropriate volumes of the host and salt solutions were combined with MeCN to final volumes of 3000 μL in order to expose the hosts to 1, 10 and 100 eqs of each of the Cu^{2+} salts, **Table 4.6**.

Table 4.6: Summary of the volumes of solutions and solvent required to prepare samples with Host:Guest ratios of 1:0, 1:1, 1:10 and 1:100.

Sample No.	Host : Cu ²⁺	Vol. of Host Stock Solution 12 μ M in MeCN (μ L)	Vol. of Cu ²⁺ Salt Stock Solution 1200 μ M in MeCN (μ L)	Vol. of MeCN (μ L)
1	1:0	1500	0	1500
2	1:1	1500	15	1485
3	1:10	1500	150	1350
4	1:100	1500	1500	0

Fluorescence spectra of the samples indicated in **Table 4.6** were recorded, in turn, for each calixarene host. When **EPIC** (6 μ M) was exposed to the copper salts, fluorescence quenching occurred in all cases, as shown in **Figure 4.18**, decreasing in the same order as had been observed for **PIC**, *i.e.* $\text{Cu}(\text{ClO}_4)_2 > \text{CuCl}_2 > \text{Cu}(\text{NO}_3)_2 > \text{Cu}(\text{CO}_2\text{CH}_3)_2$, with 99%, 71%, 62% and 10% quenching for **EPIC** respectively.

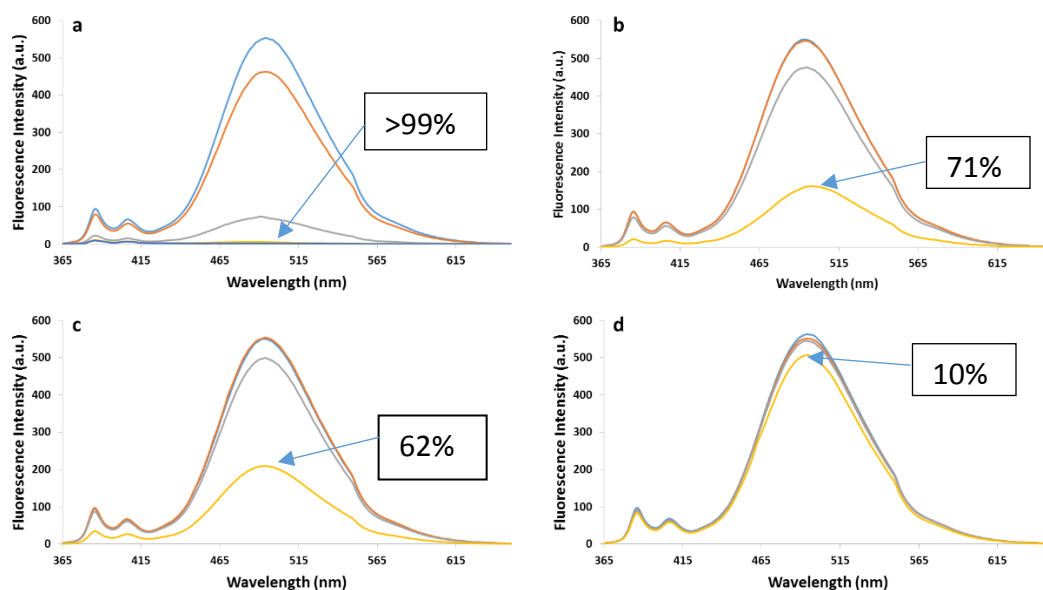


Figure 4.18: Emission spectra of **EPIC** (6 μ M, $\lambda_{\text{ex}} = 348$ nm) in MeCN with 0 (blue), 1 (orange), 10 (grey) and 100 (yellow) eqs of **a)** $\text{Cu}(\text{ClO}_4)_2$, **b)** CuCl_2 , **c)** $\text{Cu}(\text{NO}_3)_2$ and **d)** $\text{Cu}(\text{CO}_2\text{CH}_3)_2$. The % of fluorescence quenching at the λ_{max} upon exposure to 100 eqs of each copper salt is indicated on the spectra.

In a parallel experiment with **PPIC**, **Figure 4.19**, the effectiveness of quenching remained in the same order with 83%, 57%, 50% and 12% quenching observed upon exposure to the perchlorate, chloride, nitrate and acetate salts, respectively.

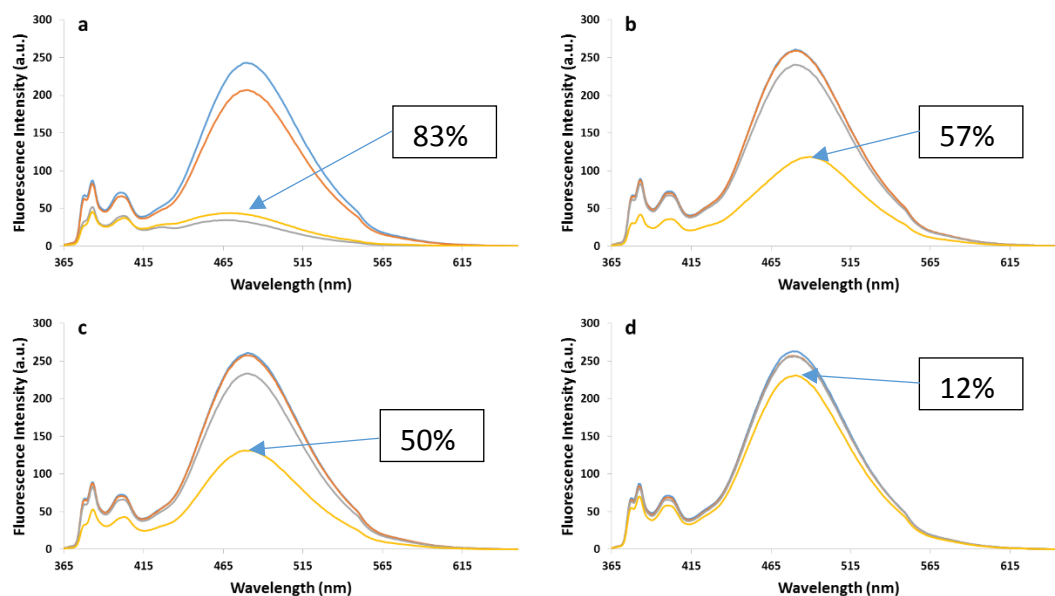


Figure 4.19: Emission spectra of PPIC (6 μM, $\lambda_{\text{ex}} = 348$ nm) in MeCN with 0 (blue), 1 (orange), 10 (grey) and 100 (yellow) eqs of **a)** Cu(ClO₄)₂, **b)** CuCl₂, **c)** Cu(NO₃)₂ and **d)** Cu(CO₂CH₃)₂. The % of fluorescence quenching at the λ_{max} upon exposure to 100 eqs of each copper salt is indicated on each spectrum.

With **MPIC** the effectiveness of excimer quenching with the salts decreased in the order CuCl₂ (69%) > Cu(NO₃)₂ (59%) > Cu(ClO₄)₂ (27%) > Cu(CO₂CH₃)₂ (10%), **Figure 4.20**. Thus whilst **MPIC** responds to the chloride, nitrate and acetate salts similarly to the other hosts in the series, it's response to copper perchlorate is quite different.

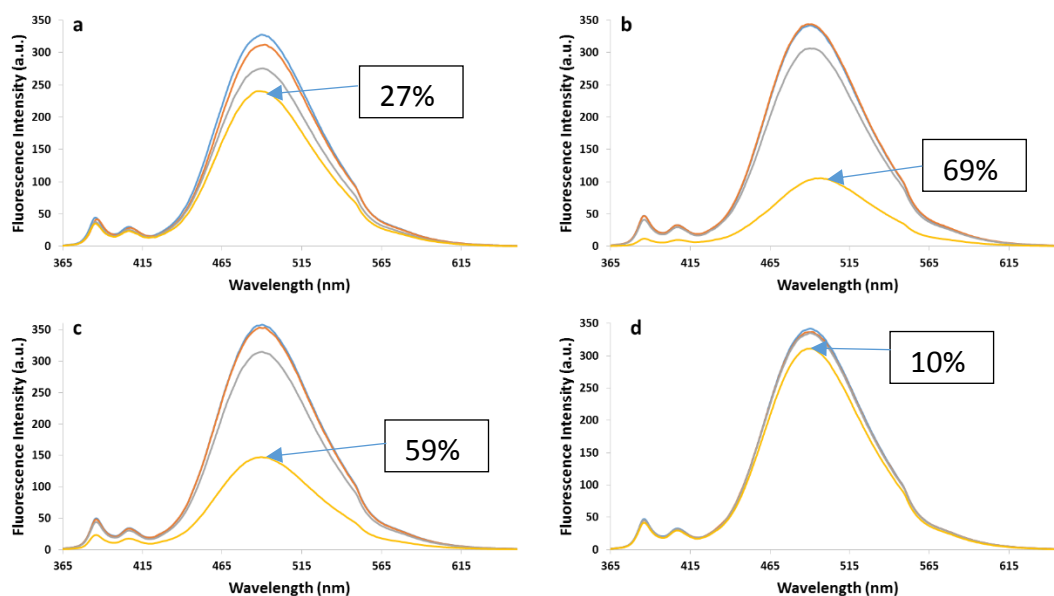
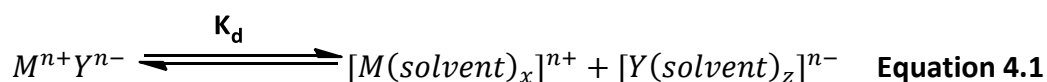


Figure 4.20: Emission spectra of **MPIC** (6 μM, $\lambda_{\text{ex}} = 348$ nm) in MeCN with 0 (blue), 1 (orange), 10 (grey) and 100 (yellow) eqs of **a)** $\text{Cu}(\text{ClO}_4)_2$, **b)** CuCl_2 , **c)** $\text{Cu}(\text{NO}_3)_2$ and **d)** $\text{Cu}(\text{CO}_2\text{CH}_3)_2$. The % of fluorescence quenching at the λ_{max} upon exposure to 100 eqs of Cu^{2+} is indicated on each spectra.

As metal salts dissolve, the component ions become surrounded by solvent molecules in a process called solvation, **Equation 4.1**. H:G complex formation in solution can involve desolvation of both the host and guest metal ions. In order to form a host:guest complex, these processes must be energetically favourable.



The degree of fluorescence quenching of the excimer peaks of the calixarene hosts in the presence of 100 eqs of the copper salts is summarised in **Table 4.7**, and an attempt is made to explain the relative quenching by consideration of the presentation of each copper salt in MeCN.

Table 4.7: Comparison of the % quenching of the intensity of the excimer bands of **EPIC**, **PPIC** and **MPIC** in the presence of 100 eqs of each of the Cu^{2+} salts.

	EPIC $\lambda_{\text{max}} = 494 \text{ nm}$	PPIC $\lambda_{\text{max}} = 480 \text{ nm}$	MPIC $\lambda_{\text{max}} = 494 \text{ nm}$
Cu(ClO₄)₂	>99%	83%	27%
CuCl₂	71%	57%	69%
Cu(NO₃)₂	62%	50%	59%
Cu(CO₂CH₃)	10%	12%	10%

Copper acetate consistently effected the lowest degree of quenching. This may be attributed to the tendency of this salt to exist as a dimeric species in many solvents, leaving relatively few solvated ions, such as $[\text{Cu}(\text{CO}_2\text{CH}_3)(\text{solvent})_x]^+$ or $[\text{Cu}(\text{solvent})_y]^{2+}$, available to coordinate to the host molecules.¹⁵⁴

The weak association properties of the perchlorate anion as well as the high dielectric constant of MeCN leads to significant dissociation of copper perchlorate into ionic species.¹⁵⁵ Thus, copper perchlorate is expected to present as a solvent separated ion pair in MeCN, and the copper ion likely exists as a hexasolvated cation, $[\text{Cu}(\text{MeCN})_6]^{2+}$.¹⁵⁶ This species appears to be an attractive guest, eliciting a high degree of excimer quenching of the cone adopting calixarenes **PIC**, **EPIC** and **PPIC** but not for **MPIC**, which exists predominantly as the paco conformer in CDCl_3 solution.

Nitrate ions have stronger associating properties than perchlorate ions and thus $\text{Cu}(\text{NO}_3)_2$ is not expected to dissociate to the same extent in MeCN.¹⁵⁵ Copper chloride has recently been shown by Becker *et al.* to form solvent clusters in MeCN of the form $[\text{Cu}_n\text{Cl}_{2n}(\text{solvent})]_x$.¹⁵⁷ The limited dissociation and the solvent clustering properties of the nitrate and chloride salts in MeCN may explain their reduced ability to quench the cone configured calixarene hosts w.r.t. $\text{Cu}(\text{ClO}_4)_2$.

A number of red- and blue-shifts were observed in the λ_{max} of the excimer bands of the hosts during the counterion study, data summarised in **Table 4.8**.

Table 4.8: Summary of the red- and blue-shifts observed following exposure of EPIC, PPIC and MPIC to 10 and 100 eqs of each of the copper salts.

Copper Salt	No. of eqs of Cu ²⁺	EPIC	PPIC	MPIC
Copper Perchlorate	10	3 nm (83 cm ⁻¹) blue-shift	13 nm (580 cm ⁻¹) blue-shift	No shift
	100	Not observable [‡]	10 nm (443 cm ⁻¹) blue-shift	No shift
Copper Chloride	10	No shift	No shift	No shift
	100	5 nm (-202 cm ⁻¹) red-shift	9 nm (-384 cm ⁻¹) red-shift	7 nm (-282 cm ⁻¹) red-shift
Copper Nitrate	100	No shift	No shift	No shift
Copper Acetate	100	No shift	No shift	No shift

In sharp contrast to the blue-shifts observed previously upon exposure of the hosts to Cu(ClO₄)₂, bathochromic shifts (5-9 nm) occurred in all cases following exposure of the calixarene hosts to 100 eqs of CuCl₂; that no shifts were evident in the presence of 10 eqs of the same salt is likely in keeping with the low level of quenching, **Table 4.8**. That the shift is in the opposite direction to that observed with the perchlorate counterion indicates that the hosts interact differently with copper chloride. The stronger association properties of the chloride counterion w.r.t. the perchlorate anion may have led to a different geometry with the chloride counterions forming part of the coordination sphere.

4.1.5 Determination of the Stoichiometry of Association between the Calixarene Hosts and the Cu²⁺ Ion

Job's plots (Section 1.4.1) were constructed in order to ascertain the stoichiometry of the binding event between the calixarene hosts and Cu(ClO₄)₂. The total molar

[‡] 100 eqs of Cu(ClO₄)₂ caused >99% quenching so no blue- or red-shifts were observable.

concentration of the hosts and Cu^{2+} was held at 6 μM . Host (12 μM) and $\text{Cu}(\text{ClO}_4)_2$ (24 μM) solutions were prepared in MeCN and appropriate volumes were combined to prepare the samples indicated in **Table 4.9**.

Table 4.9: Summary of the volume of reagents and solvent required to prepare samples in order to construct Job's plots for the hosts and $\text{Cu}(\text{ClO}_4)_2$; Host:Guest ratios varied from 6:0 to 1:5.

Sample No.	Host (μM)	$\text{Cu}(\text{ClO}_4)_2$ (μM)	Vol. of Host (μL) Stock Solution 12 μM	Vol. of $\text{Cu}(\text{ClO}_4)_2$ (μL) Stock Solution 24 μM	Vol. of MeCN (μL)
1	6	0	1500	0	1500
2	5.6	0.4	1400	50	1550
3	5	1	1250	125	1625
4	4.4	1.6	1100	200	1700
5	4	2	1000	250	1750
6	3.6	2.4	900	300	1800
7	3	3	750	375	1875
8	2.4	3.6	625	450	1925
9	2	4	500	500	2000
10	1.6	4.4	400	550	2050
11	1	5	250	625	2125

For each of the calixarene hosts, fluorescence spectra of the samples indicated in **Table 4.9** were recorded and from these Job's plots were constructed by plotting $\Delta F \cdot \chi_{\text{H}}$ against χ_{H} , **Figure 4.21**, where ΔF is the change in fluorescence intensity ($I_0 - I$), where I_0 = the initial fluorescence intensity of the host at 6 μM and I = the fluorescence intensity of the host following addition of $\text{Cu}(\text{ClO}_4)_2$ at the λ_{max} and χ_{H} is the mole fraction of the host, *i.e.* the concentration of the host divided by the total concentration of the host and Cu^{2+} (**Equation 1.7**).

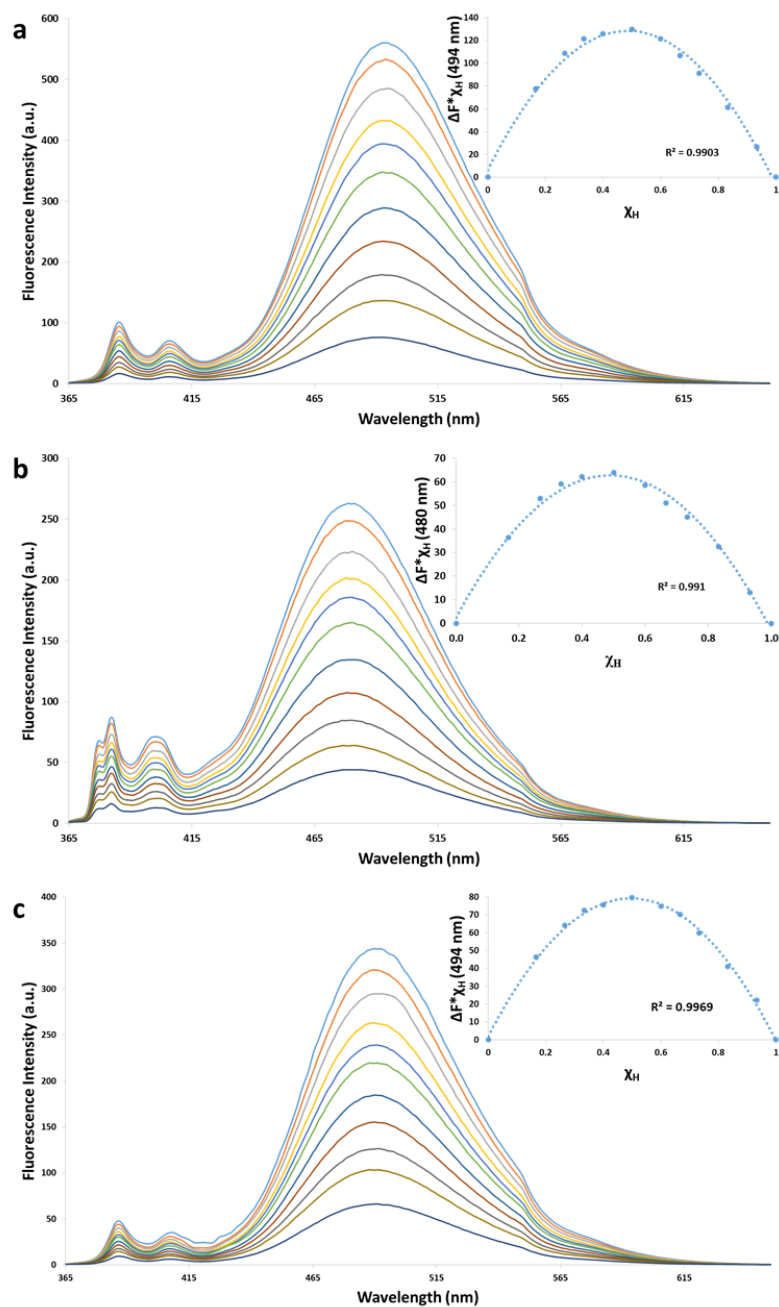


Figure 4.21: Emission spectra ($\lambda_{\text{ex}} = 348 \text{ nm}$) of **a) EPIC**, **b) PPIC** and **c) MPIC** (1-6 μM) in MeCN in the presence of 0-5 eqs of $\text{Cu}(\text{ClO}_4)_2$; The insets are Job's plots in which the difference in fluorescence intensity multiplied by the mole fraction of the host ($\Delta F^* \chi_H$) at the λ_{max} was plotted against the mole fraction of the host. (For **EPIC**, **PPIC**, **MPIC** R^2 , fitted to curves, = 0.9903, 0.991 and 0.9969 respectively).

The relevant spectra and the Job's plots for **EPIC**, **PPIC** and **MPIC** all show a maximum fluorescence change when the mole fraction of the host was 0.5, indicating that the stoichiometry of the host:guest binding event was 1:1, as previously determined for the **PIC**: Cu^{2+} complex (Section 2.4.4.1).

4.1.6 Analysis of the Fluorescence Quenching Mechanism by Stern-Volmer Approach

There are two main mechanisms by which quenching of a fluorophore occurs in solution; static and dynamic. Dynamic quenching, also called collisional quenching, occurs when an excited fluorophore collides with a quencher without the formation of a complex. Static quenching occurs when the fluorophore and a quencher form a complex in the ground state. It is important to differentiate between static and dynamic (collisional) quenching, as only the former is significant for supramolecular binding studies. The mechanism of copper perchlorate induced fluorescence quenching was investigated by Stern-Volmer analysis (Section 1.4.2). Solutions of the hosts at 12 μM and of $\text{Cu}(\text{ClO}_4)_2$ at 24 and 240 μM were prepared in MeCN. Appropriate volumes were drawn from these stock solutions to prepare the samples at the host:guest ratios indicated in **Table 4.10**.

Fluorescence spectra were recorded for all three hosts (6 μM) in MeCN in the presence of up to 14 equivalents of copper perchlorate. For each calixarene the data was analysed twice with guests in the range 0-2 eqs (samples no 1-8, **Table 4.10**) and in the range 0-12/14 eqs (samples no 1-13/14, **Table 4.10**).

Table 4.10: Summary of the volume of reagents and solvent required to prepare samples for Stern-Volmer analysis of the interaction between the calixarene hosts and $\text{Cu}(\text{ClO}_4)_2$.

Sample No.	Host : Cu^{2+}	Vol. of Host Stock Solution μL (12 μM)	Vol. of $\text{Cu}(\text{ClO}_4)_2$ Stock Solution μL (Conc)	Vol. of MeCN (μL)
1	1 : 0	1500	0 (24 μM)	1500
2	1 : 0.2	1500	150 (24 μM)	1350
3	1 : 0.4	1500	300 (24 μM)	1200
4	1 : 0.6	1500	450 (24 μM)	1050
5	1 : 0.8	1500	600 (24 μM)	900
6	1 : 1	1500	750 (24 μM)	750
7	1 : 1.5	1500	1125 (24 μM)	375
8	1 : 2	1500	1500 (24 μM)	0
9	1 : 4	1500	300 (240 μM)	1200
10	1 : 6	1500	450 (240 μM)	1050
11	1 : 8	1500	600 (240 μM)	900
12	1 : 10	1500	750 (240 μM)	750
13	1 : 12	1500	900 (240 μM)	600
14	1 : 14	1500	1050 (240 μM)	450

The extent of fluorescence quenching of the excimer peak of all hosts increased in line with added $\text{Cu}(\text{ClO}_4)_2$, reaching for **EPIC**, **PPIC** and **MPIC**, respectively 30, 38 and 10% quenching with 2 eqs of salt. For each host Stern-Volmer plots were constructed by plotting $\frac{I_0}{I}$ on the y-axis and $[\text{Cu}^{2+}]$ on the x-axis. For all three hosts linear relationships (R^2 varying between 0.9928 and 0.985) were observed over the concentration range, 0-12 μM *i.e.* 0-2 eqs of guest, supporting the mechanism of quenching in this range, in MeCN at rt, as either by a purely static or by a purely dynamic mechanism, **Figure 4.22Ia**, **IIa** and **IIIa**.

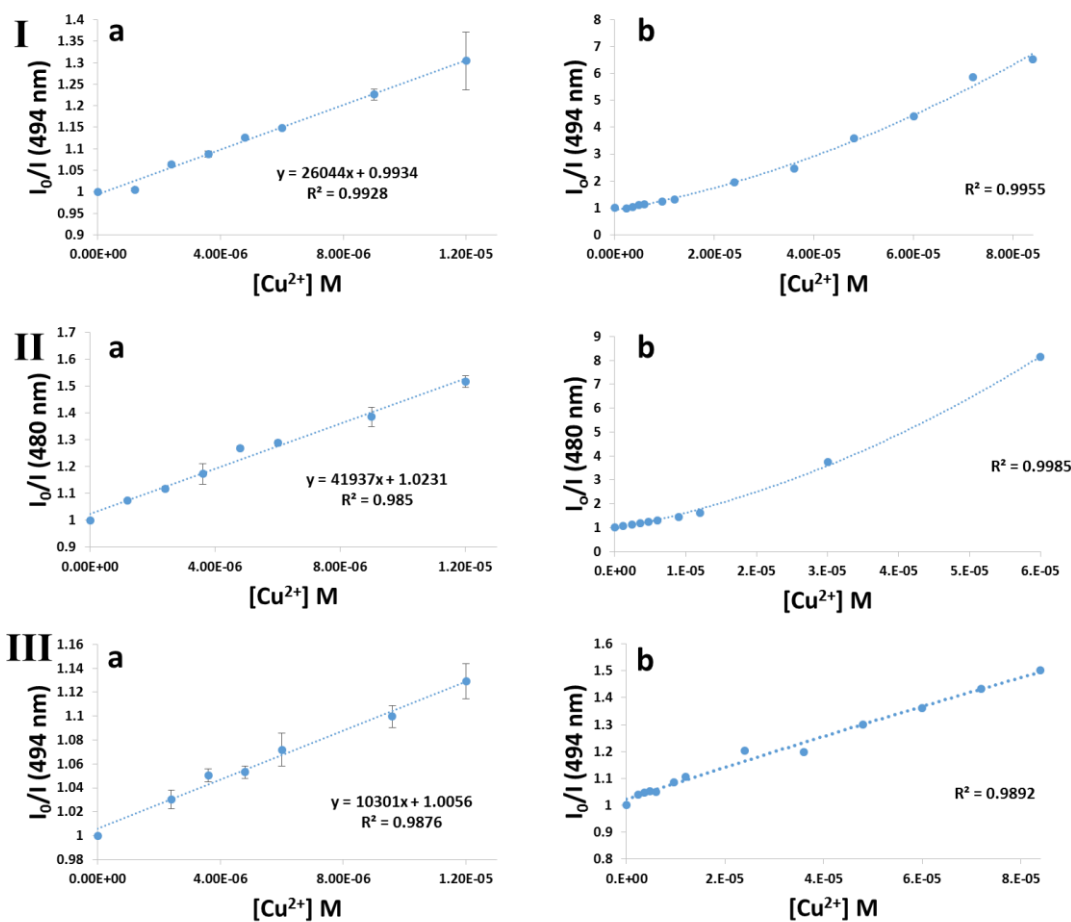


Figure 4.22: Stern-Volmer plots for **I) EPIC**, **II) PPIC** and **III) MPIC** in which the fluorescence intensity (I_0/I) at the λ_{max} was plotted against the concentration of Cu^{2+} in the ranges: **a)** 0-2 μ M (Fitted to lines) and **b)** 0-84 μ M (Fitted to curves).

The second set of Stern-Volmer plots with higher guest concentrations, up to 84 μ M (14 eqs), **Figure 4.22Ib**, **IIb** and **IIIb**, deviated from linearity. Instead the data fitted well to curves (R^2 varying from 0.9985 to 0.9892). The upwards curvature of the plots suggests quenching at high concentrations occurred by a combination of static and dynamic mechanisms in MeCN at rt. It follows intuitively that with increasing numbers of equivalents of quencher ions (Cu^{2+}) a combination of quenching mechanisms can emerge. This is because with higher ratios of quencher to host molecules a statistical increase is expected for both formation of a ground state complex between the host and guest (static), as well as for the chance of random collisional quenching between the host and the quencher (dynamic).

The magnitude of Stern-Volmer constants (K_{SV}) for a given host:guest system can be used to provide information on the association. When all other variables are held constant, high K_{SV} values are associated with guests that can cause quenching at low concentrations.⁵⁴

The K_{SV} for the H:G complex formed for the four calixarene hosts, determined in the presence of 0-2 eqs of $\text{Cu}(\text{ClO}_4)_2$ in MeCN, recorded in **Table 4.11**, reveal that, **PIC** and **PPIC** had the highest K_{SV} values, 45,000 and 42,000 M^{-1} respectively, approximately 4 times greater than that calculated for **MPIC**, ($\sim 10,000 \text{ M}^{-1}$) and also considerably larger than that calculated for **EPIC** (26,000 M^{-1}). The lower K_{SV} for **MPIC** suggests that the removal of the hydroxyl groups and/or the presentation of this host primarily in the *paco* conformer impacts negatively on its Cu^{2+} binding ability. The intermediate K_{SV} value recorded for **EPIC** suggests that the extension of the linker group between the calixarene scaffold and the isoxazole moieties to two methylene groups also negatively impacts on Cu^{2+} binding w.r.t. **PIC**.

It has also been noted by Lakowicz that K_{SV} values at or above $\sim 7 \times 10^3 \text{ M}^{-1}$ indicate purely static quenching as this value is too large to be due to pure collisional quenching.⁵⁴ Thus, it was deemed likely that Cu^{2+} induced quenching of all four hosts occurred by a purely static mechanism with 0-2 eqs of guest, as the K_{SV} values were all in excess of $7 \times 10^3 \text{ M}^{-1}$.

Table 4.11: Stern-Volmer constants (K_{SV}) calculated for pyrene functionalised calixarene hosts (6 μM) in the presence of 0-2 eqs of $\text{Cu}(\text{ClO}_4)_2$ in MeCN.

	PIC	EPIC	PPIC	MPIC
$K_{SV} (\text{M}^{-1})$	45,000	26,000	42,000	10,000

4.1.7 Calculation of Binding Constants (K_a) using Benesi-Hildebrand Analysis

The magnitude of the Stern-Volmer constants calculated for the four calixarene hosts in the presence of 0-2 eqs of $\text{Cu}(\text{ClO}_4)_2$ suggested pure static quenching, **Table 4.11**. If this is the case then the binding constants should equate to the slope of the Stern-Volmer plots, *i.e.* $K_{SV} = K_a$, **Equation 1.9**. However, in the absence of fluorescence

lifetime or temperature dependent studies unambiguous confirmation of the quenching mechanism cannot be made. Thus, the binding or association constants (K_a) of the 1:1 host: Cu^{2+} complexes in MeCN were calculated using Benesi-Hildebrand analyses, a popular method for related calixarene systems.^{12,81,103,133,158-160} The spectra used for the Benesi-Hildebrand analysis corresponded to the data collected from the samples prepared for Stern-Volmer analysis (Section 4.1.6), **Table 4.10**.

Benesi-Hildebrand plots are constructed by plotting $\frac{1}{\Delta F}$ on the y-axis and $\frac{1}{[G]}$ on the x-axis. According to the Benesi-Hildebrand equation the intercept of these plots divided by the slope gives the K_a of the binding reaction. The plot for **EPIC** showed a linear relationship ($R^2 = 0.9935$), **Figure 4.23a**, with $K_a = 0.002/(7 \times 10^{-8}) = 29,000 \text{ M}^{-1}$. Parallel studies for **PPIC** and **MPIC** also revealed linear Benesi-Hildebrand plots ($R^2 = 0.9887$ and 0.9836 respectively), **Figure 4.23b** and **c**, which gave K_a values of $33,000 \text{ M}^{-1}$ for **PPIC** and $6,000 \text{ M}^{-1}$ for **MPIC**.

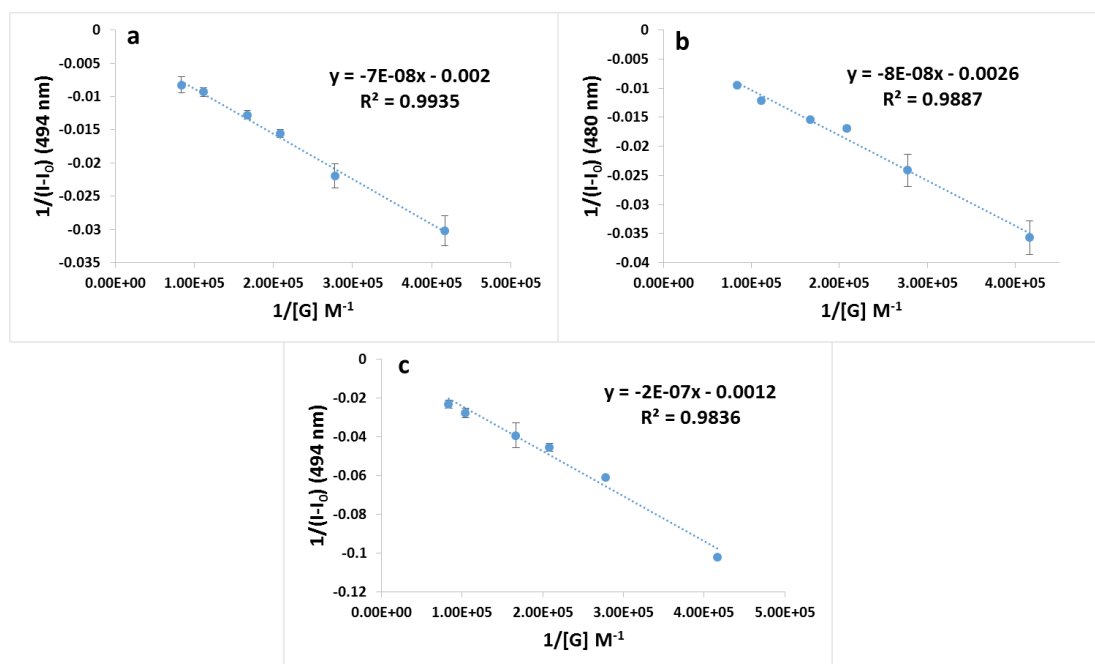


Figure 4.23: Benesi-Hildebrand plots of the hosts, $6 \mu\text{M}$ in MeCN with $\text{Cu}(\text{ClO}_4)_2$ (0-2 eqs). **a)** EPIC (intercept = 0.002 , slope = -7×10^{-8} , $R^2 = 0.9935$), **b)** PPIC (intercept = 0.0026 , slope = -8×10^{-8} , $R^2 = 0.9887$) and **c)** MPIC (intercept = 0.0012 , slope = -2×10^{-7} , $R^2 = 0.9836$).

The K_a and K_{sv} values calculated for the complexation between Cu^{2+} and the four pyrene functionalised calixarenes are summarised in **Table 4.12** together with key

structural features for each host. The higher values for **PIC** and **PPIC** suggest that restricting the distance between the lower rim of the calixarene and the isoxazole unit to one methylene group could be important for guest binding. Since the **PPIC** copper complex has a high K_a , it appears that direct linkage between the pyrene moieties and the isoxazole heterocycles is less important.

The sole structural difference between **PIC** and **MPIC** is the substitution of the hydroxyl groups on the lower rim with methoxy groups. It is apparent that this substitution has a significant impact on the magnitude of the binding constant. This may be attributed to **(i)** the removal of the H-bonding ability or **(ii)** the conformational mobility of **MPIC** and dominance of the *paco* conformer or **(iii)** a reduction in the size of the binding site.

Comparison of the data for **PIC** and **EPIC**, which differ only in the number of methylene groups between the isoxazole and calixarene framework shows that increasing the distance between the units has a negative impact on the K_a .

Table 4.12: Comparison of the functional groups present in the calixarenes, **PIC**, **EPIC**, **PPIC** and **MPIC**, the K_{SV} and the K_a values for their complexation reactions with Cu^{2+} (perchlorate) in MeCN at room temperature.

	Lower Rim Hydroxyl Groups	No. of CH ₂ Group Between Lower Rim of Calixarene and Isoxazole	Direct Linkage Between Isoxazole Ring and Pyrene	K_{SV} M ⁻¹	K_a M ⁻¹	Calixarene Sol ⁿ Phase Conformation (CDCl ₃)*
PIC	✓	1	✓	45,000	47,000	Cone
EPIC	✓	2	✓	26,000	29,000	Cone
PPIC	✓	1	×	42,000	33,000	Cone
MPIC	×	1	✓	10,000	6,000	Cone:Paco 1:1.64

*As determined by NMR spectroscopy.

4.1.8 Detection Limit of the Calixarene Hosts for the Cu²⁺ Ion

The detection limits of the hosts for Cu(ClO₄)₂ in MeCN was calculated in the manner outlined in Section 2.5.6, using the following formula: $Detection\ Limit = \frac{KSB1}{S}$,^{161,162} where K is an arbitrary unit equal to 2 or 3, SB1 is the standard deviation of the fluorescence intensity at the λ_{max} of 6 μ M solutions of each host (10 values were taken for each calculation) and S is the slope of the calibration curve of the fluorescence intensity of each host at 6 μ M in the presence of 0-2 eqs of Cu²⁺.

The data used to construct the calibration curves for **EPIC**, **PPIC** and **MPIC**, **Figure 4.24a, b and c**, correspond to the data gathered for the Stern-Volmer analysis (Section 4.1.6). The detection limits were thus calculated as shown in **Table 4.13**.

Table 4.13: Calculations for the detection limits of the pyrene functionalised calixarene hosts for the Cu²⁺ (perchlorate) ion in MeCN at rt using the formula $\frac{K*SB1}{S}$.

PIC	EPIC	PPIC	MPIC
KSB1/S	KSB1/S	KSB1/S	KSB1/S
= (2 x 2.90)/(2 x 10 ⁷)	= (2 x 4.49)/10 ⁷	= (2 x 8.89)/(8 x 10 ⁶)	= (2 x 7.22)/(4 x 10 ⁶)
= 2.90 x 10 ⁻⁷	= 8.98 x 10 ⁻⁷ M	= 2.22 x 10 ⁻⁶ M	= 3.61 x 10 ⁻⁶ M
= 0.3 μ M	= 0.9 μ M	= 2.2 μ M	= 3.6 μ M

It is apparent that **EPIC**, **PPIC** and **MPIC** can accurately detect Cu²⁺ (perchlorate) ions in MeCN solution to the lowest concentrations of 0.9, 2.2 and 3.6 μ M respectively. These values compared well to that of 0.3 μ M calculated for **PIC**.⁸⁸

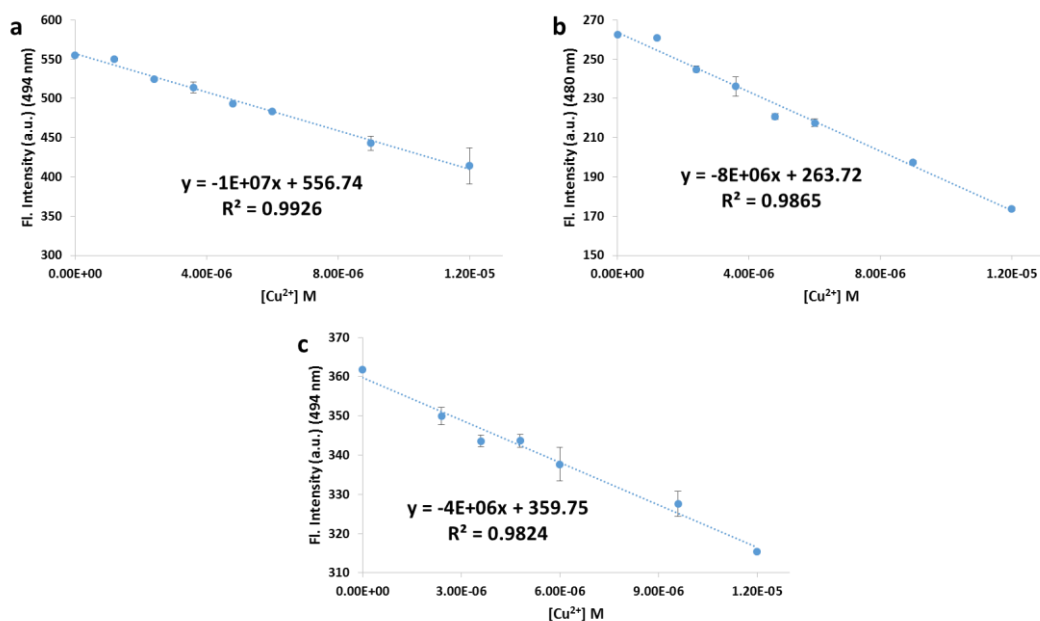


Figure 4.24: Calibration plots of the fluorescence intensity of the hosts **a) EPIC**, **b) PPIC** and **c) MPIC** (MeCN, 6 μ M, $\lambda_{\text{ex}} = 348$ nm) at λ_{max} with 0-2 eqs of $\text{Cu}(\text{ClO}_4)_2$.

4.2 An NMR Spectroscopic Study of the Interactions between the Calixarene Hosts and the Cu^{2+} Ion

^1H NMR spectroscopic studies were undertaken to inform on the key units within the hosts responsible for complexation with Cu^{2+} ions. As in the spectroscopic study of the complexation between **PIC** and Cu^{2+} (Section 2.5.3), a mix of $\text{CD}_3\text{CN}:\text{CDCl}_3$, (4:1, v/v) was chosen as the best compromise between the host solution at the required concentration and the solvent system used in the fluorescence experiments, MeCN.

Stock solutions of the hosts at 0.65 mM and were prepared in a $\text{CD}_3\text{CN}:\text{CDCl}_3$ mixed solvent system. A 3:1 v/v $\text{CD}_3\text{CN}:\text{CDCl}_3$ solution was used for **EPIC** and **PPIC** while a 1:1 v/v $\text{CD}_3\text{CN}:\text{CDCl}_3$ solution was used for **MPIC**. A stock solution of $\text{Cu}(\text{ClO}_4)_2$ at 6.77 mM was prepared in CD_3CN . Samples with varying ratios of host to metal salt were prepared (1:0 through 1:2 eqs) according to the volumes shown in **Table 4.14**. Each sample was agitated extensively to ensure homogeneity of the solution for 1 min and allowed to equilibrate by standing in the closed NMR tube for 20 mins at room temperature prior to recording the ^1H NMR spectrum.

Table 4.14: Summary of the volume of reagents required for a ^1H NMR spectroscopic study of the calixarene hosts and Cu^{2+} (1:0 to 1:2 eqs) complexation in $\text{CD}_3\text{CN}:\text{CDCl}_3$ (4:1, v/v). $x = 3$ for **EPIC** and **PPIC** and $x = 1$ for **MPIC**.

Sample No.	Host : $\text{Cu}(\text{ClO}_4)_2$	Host (μL) 0.65 mM $\text{CD}_3\text{CN}:\text{CDCl}_3$ (x:1, v/v)	$\text{Cu}(\text{ClO}_4)_2$ (μL) 6.77 mM (CD_3CN)	CD_3CN (μL)
1	1 : 0	500	0	100
2	1 : 1	500	48	52
3	1 : 2	500	96	4

Following exposure of **EPIC** to increasing amounts of $\text{Cu}(\text{ClO}_4)_2$, significant concentration dependant changes became evident as shown in **Figure 4.25**. A dramatic broadening of the pyrene proton signals is observed in the presence of the Cu^{2+} ion in solution which suggests that the pyrene moieties are in close proximity to the paramagnetic Cu^{2+} metal ion during host:guest binding. In contrast, the peaks in the rest of the spectra remain relatively sharp and well resolved.

A number of significant new signals appeared at 6.59, 6.63 and 6.34 ppm in the copper containing samples. The new singlets at 6.59 and 6.34 ppm showed identical integrations and were assigned to the ArH of the upper rim of the calixarene of the host:guest complex. These signals were more intense in the presence of 2 eqs of Cu^{2+} w.r.t. 1 eq of Cu^{2+} . These relative intensities were ascertained by comparison to the peaks of the host alone.

Whilst, the OH singlet of the host alone, at 7.61 ppm remained sharp and unaffected up to 2 eqs of Cu^{2+} , **Figure 4.25a**, it was deemed impossible to ascertain the position of the OH of the host:guest complex and subsequently if it also remained sharp. Thus, no conclusion was made concerning the participation of the phenolic OH moieties in the host:guest binding based on the ^1H NMR titration data.

Examination of the ^1H NMR spectra in the region that displays the ethylene chain protons and lower rim methylene groups (4.00 - 3.00 ppm) revealed the emergence

of a number of new signals in the presence of the Cu^{2+} ion indicative of the formation of a host guest complex, **Figure 4.25a**.

A multitude of new signals were observed in the region of the spectra where the *t*-butyl protons of **EPIC** appear, **Figure 4.25b**. These new signals were deemed indicative of conformational changes induced to the calixarene scaffold upon guest binding which altered the resonance positions of the *t*-butyl moieties of the host:guest complex.

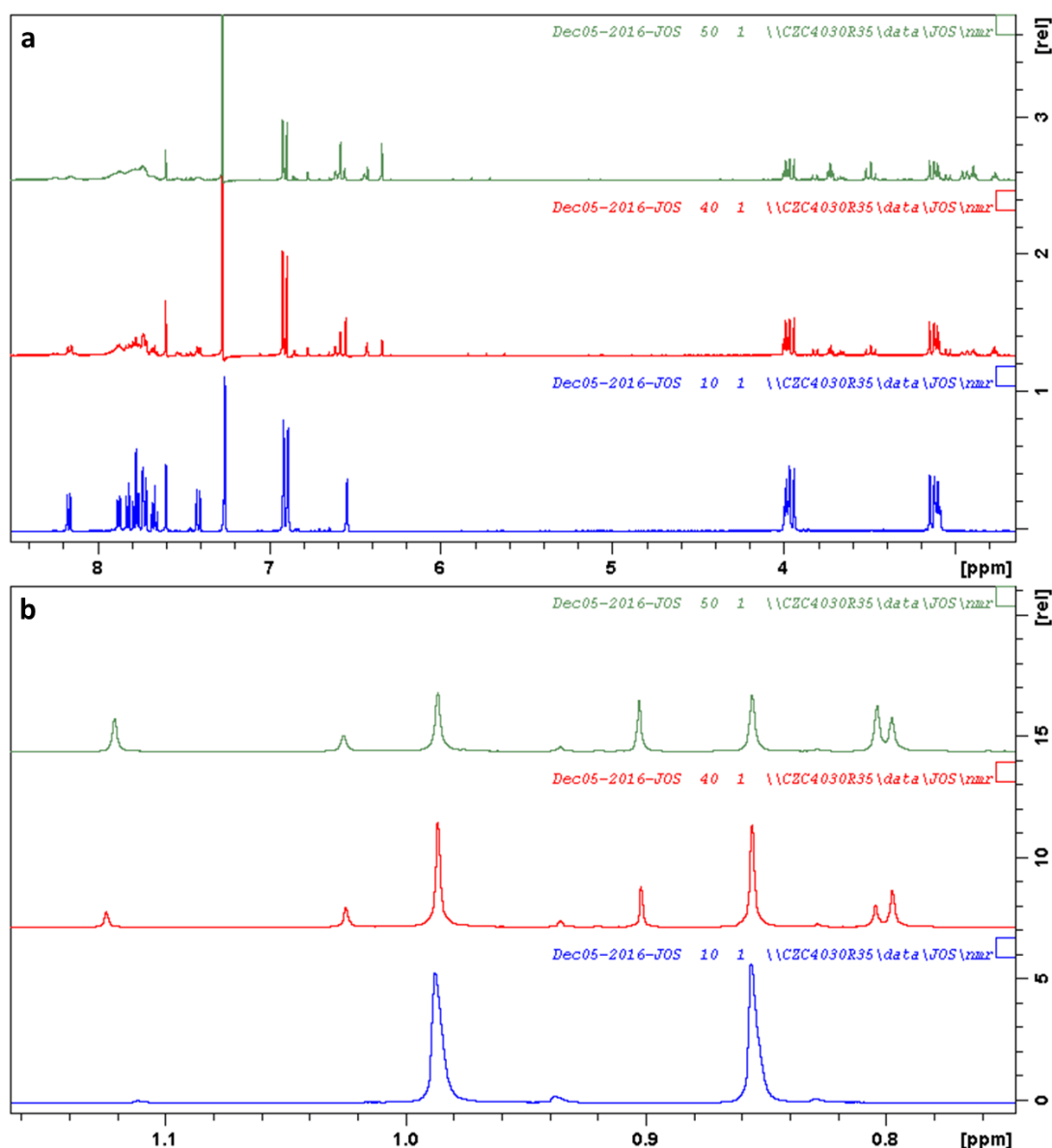


Figure 4.25: ^1H NMR (500 MHz) spectra of **EPIC** (0.54 mM, $\text{CD}_3\text{CN}:\text{CDCl}_3$, 4:1, v/v) at 25°C with increasing amounts of $\text{Cu}(\text{ClO}_4)_2$: 0 (blue), 1 (red) and 2 (green) eqs in the regions between: **a)** 8.50-2.60 and **b)** 1.16-0.74.

Following exposure of **PPIC** to increasing amounts of $\text{Cu}(\text{ClO}_4)_2$, significant concentration dependant changes became evident as shown in Figure 4.26. A dramatic broadening of the pyrene proton signals is observed in the presence of the Cu^{2+} ion in solution which suggests that the pyrene moieties are in close proximity to the paramagnetic Cu^{2+} metal ion during host:guest binding. In contrast, the peaks in the rest of the spectra remain relatively sharp and well resolved.

A number of significant new signals appeared at 6.64, 6.20 and 5.79 ppm in the copper containing samples. The new singlets at 6.64 and 6.20 ppm showed identical integrations and were assigned to the ArH of the upper rim of the calixarene of the host:guest complex. These signals were more intense in the presence of 2 eqs of Cu^{2+} w.r.t. 1 eq of Cu^{2+} , suggesting the increased conversion of the host to host:guest complex. These relative intensities were ascertained by comparison to the peaks of the host alone.

Similar to **EPIC**, the OH singlet of the host alone, at 7.41 ppm remained sharp and unaffected up to 2 eqs of Cu^{2+} , **Figure 4.26a**, it was deemed impossible to ascertain the position of the OH of the host:guest complex and subsequently if it also remained sharp. Thus, no conclusion was made concerning the participation of the phenolic OH moieties in the host:guest binding based on the ^1H NMR titration data.

A number of new signals were observed in the region of the spectra where the *t*-butyl protons of **PPIC** appear, **Figure 4.26b**. These new signals were deemed indicative of conformational changes induced to the calixarene scaffold upon guest binding which altered the resonance positions of the *t*-butyl moieties of the host:guest complex.

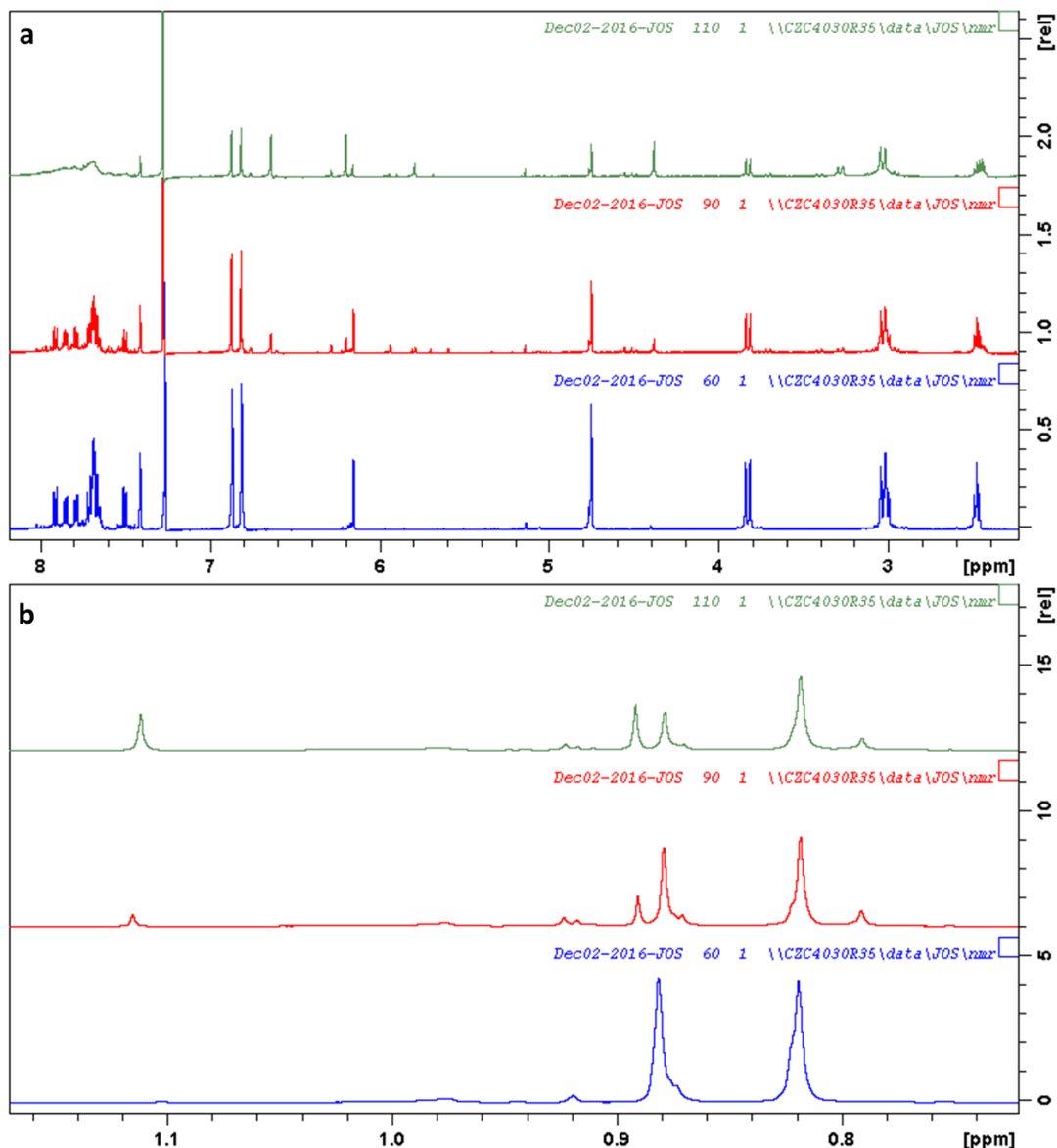


Figure 4.26: ^1H NMR (500 MHz) spectra of PPIC (0.54 mM, $\text{CD}_3\text{CN}:\text{CDCl}_3$, 4:1, v/v) at 25°C in the region between: **a)** 8.20 and 3.20 ppm and **b)** 1.18 and 0.72 ppm; with increasing numbers of equivalents of $\text{Cu}(\text{ClO}_4)_2$: 0 (blue), 1 (red) and 2 (green).

Numerous reports in the literature, supported by x-ray crystallography and NMR spectroscopy, describe the propensity of flexible or conformationally mobile calixarenes to adopt the conformation most suitable for inclusion of a particular guest.¹⁶³⁻¹⁷⁰ Talanova *et al.* used this idea to design efficient calix[4]arene based metal ion sensors.¹⁷¹ They synthesised a range of conformationally mobile calixarenes with the desired functional groups for metal binding, used NMR spectroscopy to determine the conformation of the preferred host (cone, paco or

1,3-alternate). They subsequently synthesised a rigid analogue of the identified calixarene in the preferred conformation.

This report prompted a hypothesis that **MPIC** may adopt its preferred conformation around the Cu^{2+} ion during the ^1H NMR titration study which could lead to a sharper more resolved spectrum.

The ^1H NMR spectrum of **MPIC** in $\text{CD}_3\text{CN}:\text{CDCl}_3$ (3:2, v/v) was broad, although this was not unexpected as the ^1H NMR spectrum of **MPIC** in pure CDCl_3 at rt was also poorly resolved (Section 3.4.1.1). The hypothesis that the resolution of the ^1H NMR spectrum of **MPIC** may improve upon guest binding to a preferred conformation was not apparent as the spectrum remained similar to that of the host-alone.

Similar to the ^1H NMR titrations involving **PIC**, **EPIC** and **PPIC**, all signals of the pyrene proton region became extremely broad and almost indiscernible from the baseline, strongly suggesting that the Cu^{2+} cation was close to the pyrene moieties upon complexation.

Although severely overlapping, the *t*-butyl signals between 1.34-0.87 ppm were visibly altered following exposure to 1 eq of Cu^{2+} , strongly suggestive of conformational changes following formation of a **MPIC**: Cu^{2+} complex, **Figure 4.27b**.

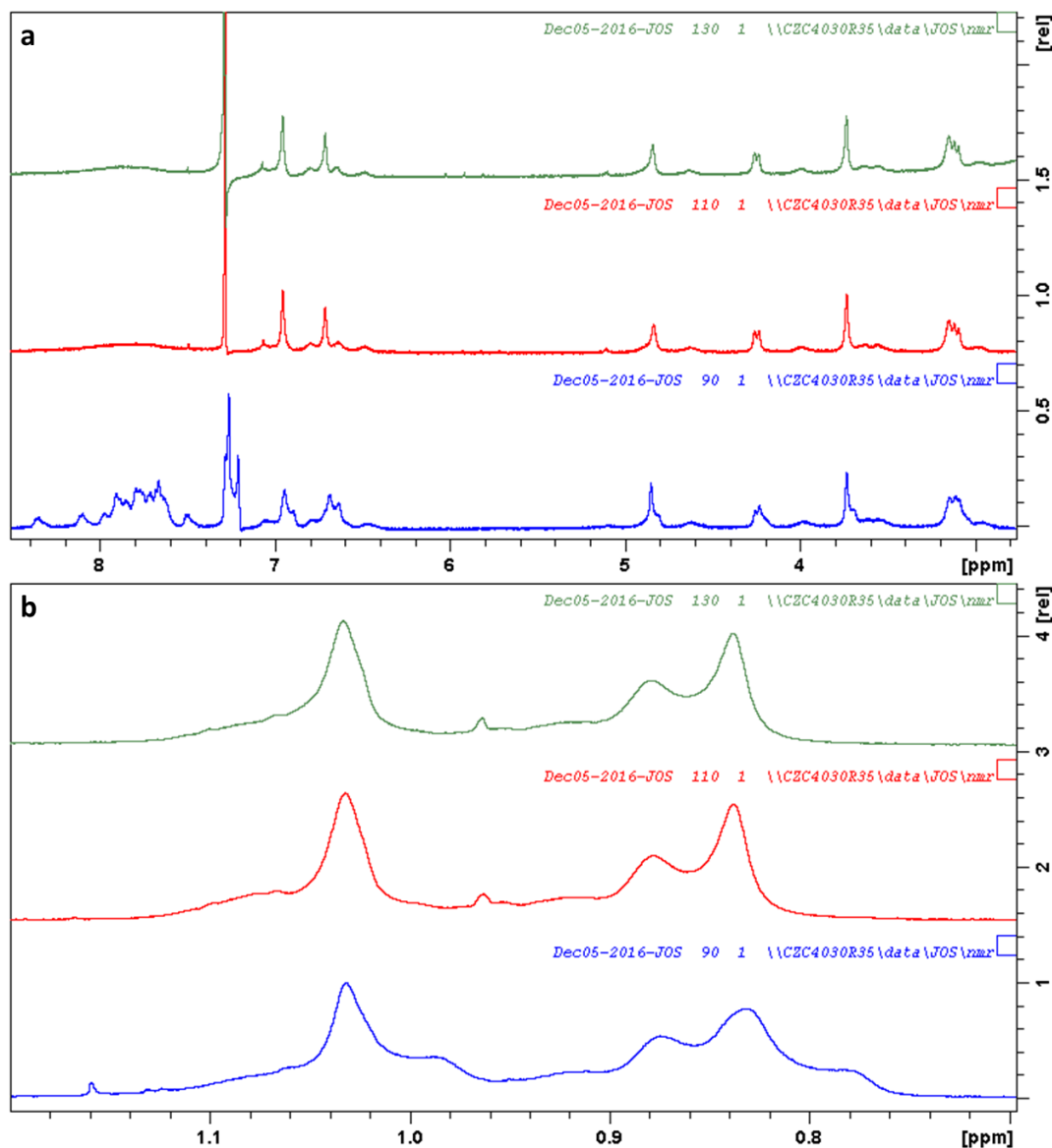


Figure 4.27: ^1H NMR (500 MHz) spectra of **MPIC** (0.54 mM, $\text{CD}_3\text{CN}:\text{CDCl}_3$, 3:2, v/v) at 25°C in the region between: **a)** 8.60 and 2.80 ppm and **b)** 2.00 and 0.70 ppm; with increasing numbers of equivalents of $\text{Cu}(\text{ClO}_4)_2$: 0 (blue), 1 (red) and 2 (green).

4.3 Conclusions

- The analogues of **PIC**; **EPIC**, **PPIC** and **MPIC** retained sensitivity to the Cu^{2+} ion. The extent of fluorescence quenching varied with the host structure and a fluorescence study of each host was conducted in order to ascertain further information on the Cu^{2+} binding.

- A competitive metal study indicated that **EPIC**, **PPIC** and **MPIC** like **PIC** were all capable of sensing and detecting Cu^{2+} perchlorate ions in the presence of other contaminating metal perchlorate cations in MeCN at rt.
- Job's method of continuous variation indicated that **EPIC**, **PPIC** and **MPIC** like **PIC** all formed 1:1 complexes with the Cu^{2+} perchlorate cation in MeCN at rt.
- Stern-Volmer analysis showed that the quenching mechanism of the three pyrene functionalised calixarenes by the Cu^{2+} cation was purely static up to two eqs of $\text{Cu}(\text{ClO}_4)_2$ in MeCN due to the magnitude of the K_{SV} constants being in excess of $7,000 \text{ M}^{-1}$. Addition of further eqs of the Cu^{2+} cation induced a combination of static and dynamic quenching.
- The binding constants (K_a) of **EPIC**, **PPIC** and **MPIC** for copper perchlorate in MeCN calculated using the Benesi-Hildebrand method to be 29,000, 33,000 and $6,000 \text{ M}^{-1}$, respectively, **Table 4.15**. These values are high and this suggested that the combination of an isoxazole heterocycle and pyrene moiety is an attractive design for a fluorescent calix[4]arene chemosensor for Cu^{2+} cation sensing in MeCN. However, they are lower than that calculated for **PIC** ($47,000 \text{ M}^{-1}$) (Section 2.5.5) which suggested that the new structural features built into **EPIC**, **PPIC** and **MPIC** had a negative impact on the host:guest complex formation reaction.
- The detection limits calculated indicated that **EPIC**, **PPIC** and **MPIC** can accurately detect Cu^{2+} ions in MeCN solution to the lowest concentrations of 0.9, 2.2 and $3.6 \mu\text{M}$ respectively, **Table 4.15**.

Table 4.15: Summary of the detection limits, binding constants and Stern-Volmer constants calculated for **PIC**, **EPIC**, **PPIC** and **MPIC** for the Cu^{2+} cation (perchlorate) in MeCN at rt.

	% quenching at λ_{max} with 10 eqs of $\text{Cu}(\text{ClO}_4)_2$	Detection Limit (μM)	Binding Constant - K_a (M^{-1})	Stern-Volmer Constant K_{SV}
PIC	85%	0.3	47,000	45,000
EPIC	87%	0.9	29,000	26,000
PPIC	87%	2.2	33,000	42,000
MPIC	16%	3.6	6,000	10,000

- A ^1H NMR spectroscopic study of the effect of the Cu^{2+} ion on each of the three pyrene functionalised calixarenes was carried out. In all three cases the pyrene aromatic region of the ^1H NMR spectra became broad and unresolved at high concentrations of $\text{Cu}(\text{ClO}_4)_2$ which indicated that the pyrene moiety was in close proximity to the Cu^{2+} cation during the binding event.

Chapter 5

Aqueous and Solid State Fluorescence Study of PIC

5.1 Overview

Copper is the third most abundant transition metal in the body. It is present as a trace element in all tissues, plays a role as a cofactor for numerous enzymes and is crucial for central nervous system development.¹⁷² However, cellular toxicity of copper has been connected to serious diseases in humans including Alzheimer's disease,¹⁷³ Indian childhood cirrhosis¹⁷⁴ and prion disease.¹⁷⁵ Copper ions are also significant heavy metal pollutants in waste water from industrial processes.¹⁷⁶

We have shown that **PIC**, **Figure 5.1**, and its analogues **EPIC**, **PPIC** and **MPIC** are all sensitive and selective fluorescent chemosensors for Cu^{2+} ions in MeCN⁸⁸ and it was desirable to explore their activity in aqueous environments. As **PIC** had the highest sensitivity and selectivity, it was chosen to evaluate real-world applications. This chapter reports initially on a study conducted in aqueous MeCN, followed by discussions on experiments designed to deposit **PIC** onto solid supports, alone or doped within a polymer, and an investigation of the Cu^{2+} sensing potential of the resultant materials.

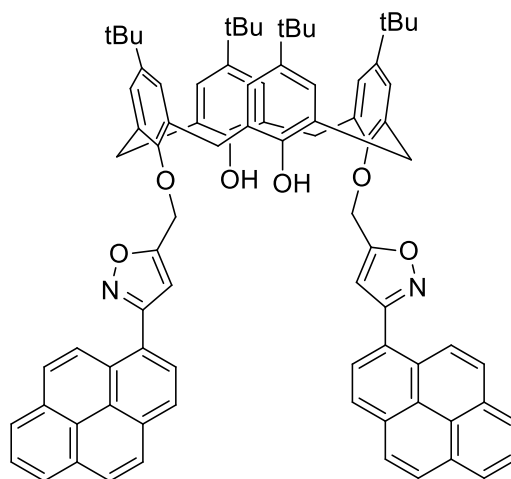


Figure 5.1: Structure of Pyrene Isoxazole Calixarene, **PIC**.

5.2 PIC Aqueous Fluorescence Study

The low solubility of pyrene in water (0.135 mg/L at 25°C)¹⁷⁷ as well as the high hydrocarbon content of **PIC** with regard to its polar components raised concerns about the solubility in water and for this reason, an initial study of the fluorescence emission of **PIC** in 0-60% v/v aq. MeCN was conducted. The polarity index (P'), a

relative measure of the degree of interaction of a solvent with polar test solutes, of water and MeCN are 10.2 and 5.8, respectively.¹⁷⁸ Thus, addition of water to MeCN increases the overall polarity of the solvent. To conduct the study, Millipore purified water and spectrophotometric grade, $\geq 99\%$ MeCN were used and background fluorescence readings of these solvents were recorded; λ_{ex} of 343 nm was chosen to match the study of **PIC** in pure MeCN. None of the three control solutions of 100% MeCN, 50% v/v aq. MeCN and 100% H₂O showed any evidence for the presence of fluorescent impurities under the experimental conditions employed, **Figure 5.2** and thus the solvents were deemed suitable for this study.

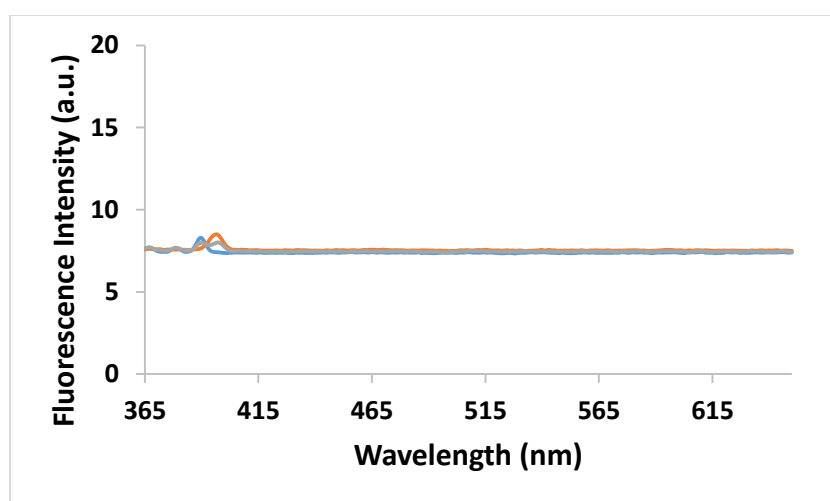


Figure 5.2: Emission spectra ($\lambda_{\text{ex}}=343$ nm) of the solvents used for copper sensing in aq. environments: 100% MeCN (blue), 50% v/v aq. MeCN (grey) and 100% H₂O (orange).

The concentration of **PIC** for the aq. studies was chosen as 6 μM , to correlate with the previous experiments in 100% MeCN⁸⁸ and fluorescence spectra were recorded for samples prepared in 0–60% v/v aq. MeCN as indicated in **Table 5.1**. Freshly prepared samples were allowed to stand at r.t. for 1 minute prior to recording the spectra, as in the case of the 100% MeCN studies.

Table 5.1: Summary of the volumes of the **PIC** stock solution, MeCN and water required to prepare samples of **PIC** at 6 μM in various 0-60% v/v aq. MeCN solvent systems.

Sample No.	Final Solvent % Water Content (v/v)	Vol. of PIC Stock Solution (20 μM in MeCN) μL	MeCN μL	Water μL
1	0	900	2100	0
2	5	900	1950	150
3	10	900	1800	300
4	20	900	1500	600
5	30	900	1200	900
6	40	900	900	1200
7	45	900	750	1350
8	50	900	600	1500
9	60	900	300	1800

The fluorescence spectra of the samples indicated in **Table 5.1** were recorded and the data plotted in **Figure 5.3**. The emission profile was expected to vary in line with the change in polarity and hydrogen bonding networks over the solvent range. It was also hypothesised that increasing the water content could cause **PIC** to precipitate from solution and thus cause the intensity of the fluorescence signal to dip. However, whilst inspection by the naked eye suggested that the host remained in solution despite water contents of up to 60% v/v aq. MeCN, subtle changes were observed in both the signal intensity and wavelength of maximum emission (λ_{max}).

- The emission intensity initially remained high; relative to the data recorded in 100% MeCN, the intensity of the excimer peak gradually increased reaching a maximum of 884 a.u. at 30% v/v aq. MeCN. At 40% v/v aq. MeCN the intensity of this band dropped to 774 a.u.
- For samples with greater than 40% v/v water content a blue-shift of the λ_{max} from 498 nm to 492 nm, and a decrease in the intensity of the excimer band (from 838 to 778 a.u.) was observed, **Table 5.2**.

- The excimer bands were slightly broadened as the water content increased, the peak-width at half-height ranged from 74 nm in 0-30% v/v aq. MeCN to 79 nm in 60% v/v aq. MeCN.

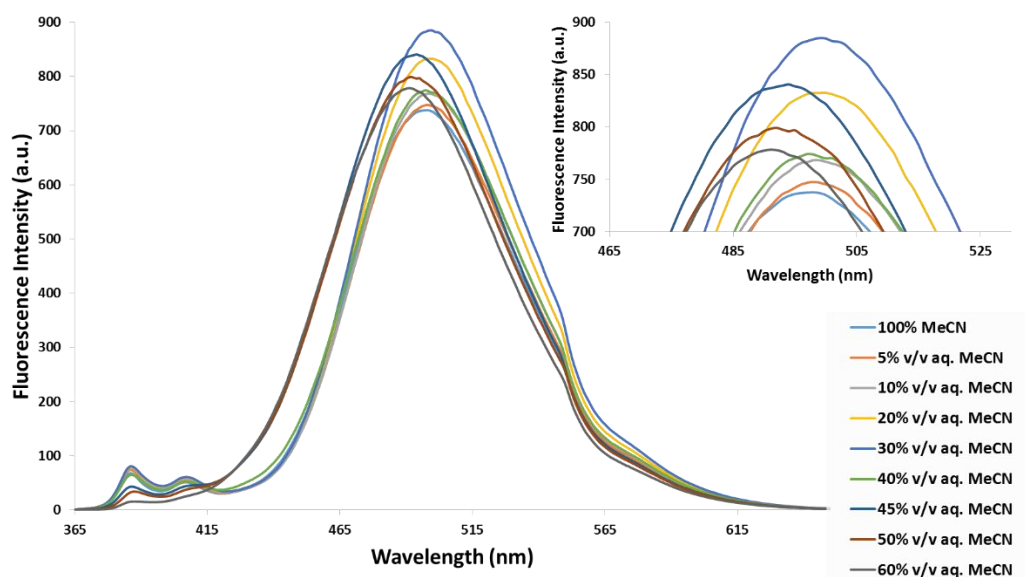


Figure 5.3: Emission spectra of **PIC** (6 μM , $\lambda_{\text{ex}} = 343 \text{ nm}$) in 0-60% v/v aq. MeCN following 1 minute *equilibration* time. Inset: Expansion of excimer region from 465 to 525 nm.

Table 5.2: Summary of the λ_{max} (nm) and fluorescence intensity (a.u.) of the excimer band for samples of **PIC** (6 μM) in 0-60% v/v aq. MeCN following 1 minute *equilibration* time.

Water Content	0%	5%	10%	20%	30%	40%	45%	50%	60%
λ_{max} of Excimer Band (nm)	498	498	498	498	498	498	492	492	492
Fluorescence Intensity at λ_{max} (a.u.)	737	747	768	832	884	774	838	799	778

To test the stability of **PIC** in aqueous solutions over an extended timeframe, spectra were re-recorded 5 mins after the initial spectrum was obtained. Significantly, in all cases after this interval, a drop in intensity of the emission signals was observed.

Thus, it was clear that **PIC** in aqueous MeCN needed an *equilibration* time in excess of the 1 minute period suitable for analysis in 100% MeCN, when the emission profiles recorded at 1, 5, 30 and 60 min time intervals were identical.

Fresh samples of **PIC** in aq. MeCN, **Table 5.1**, were prepared and fluorescence emission spectra were recorded at 5 minute intervals until overlapping data was obtained, **Figure 5.4**. The time period required to reach this point was termed the "*equilibration time*" and it is defined as the time point where the observed intensities of the last two spectra varied within ± 5 a.u. The *equilibration* time for each sample is summarised in **Table 5.3**. Thus, in 60% v/v aq. MeCN an *equilibration* time of 50 mins was required, whilst samples with 5 and 50% water content *equilibrated* rapidly, 15 mins.

The spectra of some of the *equilibrated* samples differed significantly from those recorded after just one minute, referred to as *non-equilibrated* samples.

- The sample in 30% v/v aq. MeCN showed a considerable drop in intensity of the excimer band from 884 a.u. for the *non-equilibrated* sample to 320 a.u. for the *equilibrated* sample.
- For samples in 45-60% v/v aq. MeCN the magnitude of the blue-shift of the excimer band increased from ~ 6 nm to 7-11 nm.
- The intensity of the excimer peak dipped to a minimum of 137 a.u. at 45% v/v aq. MeCN, however it increased again to 595 a.u. for the sample with 60% water content.
- As observed for the *non-equilibrated* samples, the excimer bands of the *equilibrated* spectra broadened as the water content increased.

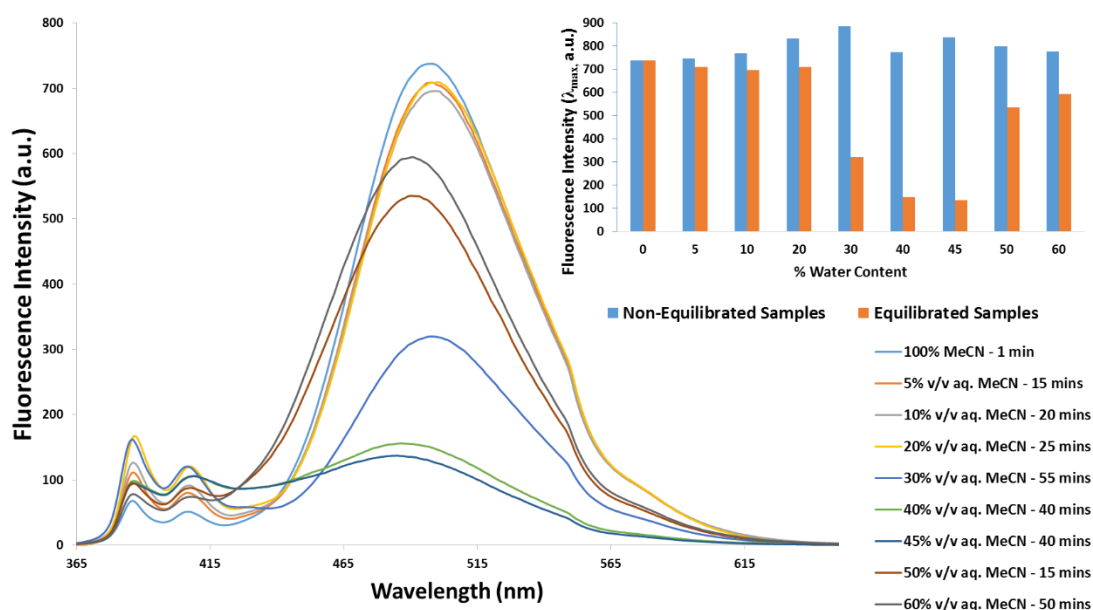


Figure 5.4: Emission spectra of *equilibrated* samples of **PIC** ($6 \mu\text{M}$, $\lambda_{\text{ex}} = 343 \text{ nm}$) in 0-60% v/v aq. MeCN – Spectra were recorded at 5 min intervals (for a period of up to 55 mins) until two spectra with comparable emission intensity were obtained. Inset: Bar chart showing the fluorescence intensity (a.u.) at the λ_{max} of the *non-equilibrated* (1 minute mixing time) (blue) and *equilibrated* (orange) samples of **PIC** ($6 \mu\text{M}$) in 0-60% v/v aq. MeCN.

Table 5.3: Summary of the times required for *equilibration* of samples of **PIC** ($6 \mu\text{M}$) in 0-60% v/v aq. MeCN and the λ_{max} and fluorescence intensity of the excimer band.

Water Content	0%	5%	10%	20%	30%	40%	45%	50%	60%
Equilibration Time (mins)	N/A	15	20	25	55	40	40	15	50
λ_{max} of Excimer Band (nm)	498	498	498	498	498	487	485	490	491
Fluorescence Intensity at λ_{max} (a.u.)	737	709	696	709	320	156	137	535	595

N/A indicates that the emission spectra of the solution of **PIC** ($6 \mu\text{M}$) in 100% MeCN remained unchanged over a 60 minute time interval.

Surface adherence of **PIC** to the walls of the quartz cuvette was considered a possible cause of reduction in signal intensity of the aq. samples. However this possibility was ruled out on the basis of the following experiment. A solution of **PIC** ($6 \mu\text{M}$) in 40% v/v aq. MeCN in a cuvette was allowed to stand for 40 minutes to *equilibrate*. The

spectrum was recorded, the cuvette was emptied but not rinsed with any solvents, and allowed to dry overnight under atmospheric conditions. It was then refilled with 3000 μL of MeCN and the emission spectrum measured. The data showed signals characteristic of **PIC** but with extremely low intensities (max. 6 a.u.), which suggested that no significant quantity of **PIC** adhered to the surfaces of the cuvette during the *equilibration* experiments.

Examples of how the emission profile varied over the *equilibration* period are shown for the samples in 30 and 60% v/v aq. MeCN in **Figure 5.5**. A continuous decrease in the intensity of the fluorescence signal was observed, reaching a minimum of 320 a.u. after 55 mins for **PIC** in 30% v/v aq. MeCN, **Figure 5.5a**. This profile was typical of all samples with one notable exception. The intensity of the excimer signal for the sample in 60% v/v aq. MeCN **Figure 5.5b**. decreased to a minimum of 312 a.u. after 20 mins (yellow plot) followed by a steady increase to 595 a.u. after a total of 50 mins.

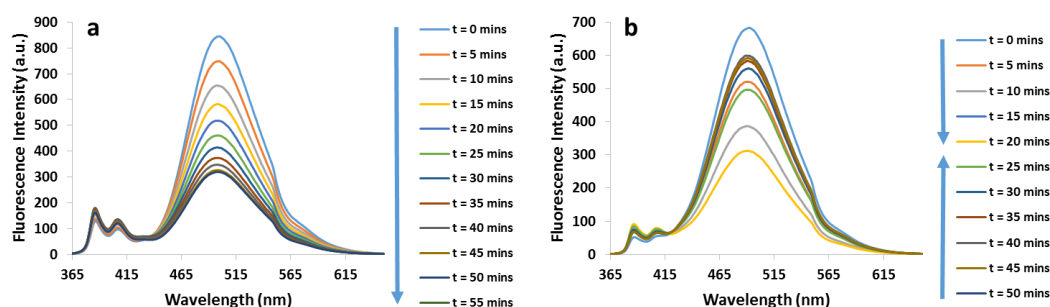


Figure 5.5: Emission spectra of **PIC** (6 μM) in **a)** 30% and **b)** 60% v/v aq. MeCN showing the fluorescence intensity over a time of 55 and 50 mins respectively; Blue arrows indicate the time intervals at which the intensity was increasing or decreasing.

The variation in fluorescence data for the *equilibrated* samples of **PIC** in aq. MeCN solutions was considered a consequence of self-association, or a change in *effective concentration* in the various media. Pyrene is an efficient fluorophore in dilute solutions, but it is known to aggregate under certain conditions, *e.g.* at high concentration or in polar solutions.^{179,180} The electron rich nature and high potential stacking area of pyrene leads to efficiency in forming π - π stacking units which can result in a phenomenon known as aggregation-caused quenching ACQ, resulting in a

reduction of the fluorescence emission due to relaxation of the excited states *via* non-radiative channels, which also occurs with other planar aromatic molecules.¹⁸¹

In direct contrast, a number of recent reports suggest aggregation-induced emission, AIE, is possible from molecules with suitably positioned pyrene moieties.¹⁸²⁻¹⁸⁴ In one particular report Diwan *et al.*, examining anthracene and pyrene-benzthiazolium fluorescence sensors, **Figure 5.6**, detail an ACQ trend upon increasing the water content in aq. MeCN solutions to explain a continuous decrease in emission intensity for the anthracene derivative, whilst an AIE trend was observed for the pyrene analogues up to 80% v/v aq. MeCN.¹⁸⁵

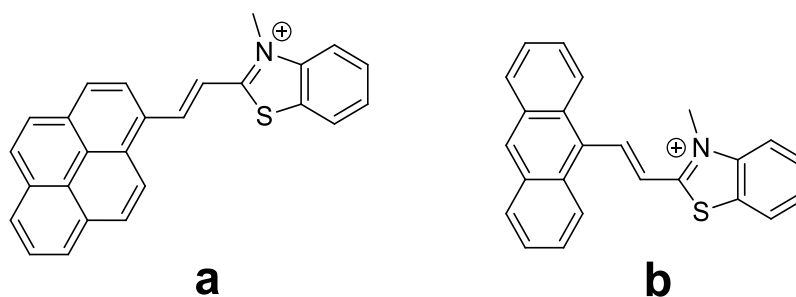


Figure 5.6: **a)** Pyrene-benzthiazolium sensor that displays AIE and **b)** an anthracene-benzthiazolium sensor that displays ACQ upon increasing the water content in H₂O:MeCN solutions.¹⁸⁵

Both ACQ and AIE phenomena can help explain the differences between the emission spectra of *equilibrated* and *non-equilibrated* aqueous samples of **PIC** (6 μ M).

The intensities and the λ_{\max} of the excimer band of **PIC** in 5-20% v/v aq. MeCN remained relatively unchanged compared to the data recorded in 100% MeCN, thus the calixarene host likely presents at the molecular level. In contrast, **PIC** self-assembly at 30 - 45% v/v aq. MeCN may lead to an ACQ effect resulting in the low intensity excimer signals (320, 156 and 137 a.u.).

In keeping with this hypothesis, an enhanced ACQ effect was expected as the water content increased beyond 45% v/v. However, a higher intensity excimer signal was observed at 50 v/v aq. MeCN, 535 a.u. This finding was interpreted to suggest that **PIC** might self-assemble differently at the higher water content leading to an AIE effect.

Interestingly, it was only in 60% v/v aq. MeCN that the emission profile of **PIC** (6 μ M) dipped to a minimum, ~312 a.u. after 20 mins, before increasing again, reaching *equilibrium*, after 50 mins, ~595 a.u. This behaviour was vastly different to that observed for the sample in 50% v/v aq. MeCN where the *equilibration* was reached following a steady dip to ~535 a.u. after only 15 mins. These observations suggest that in 60% water content, an initial self-assembly of the **PIC** moieties may have caused an ACQ effect after 20 mins, but a further realignment of the aggregate forms allows the excimer intensity to rise again, akin to an "AIE" after 50 mins.

It is known that solvents can have a significant effect on the emission profile of pyrene functionalised calixarenes. For example, an extremely low intensity excimer emission with high intensity monomer bands was observed in neat MeOH for Chang and co-workers' pyrenylacetamide diazacrown ether functionalised calix[4]arene, **Figure 5.7**, whereas the excimer emission dominated in MeOH:H₂O (1:1, v/v).¹⁸⁶ They attributed these observations to a change in molecular configuration as the water content increased and forced the hydrophobic pyrene moieties together so facilitating excimer emission. In the same way it can be hypothesised that at high water content the pyrene moieties of **PIC** compacted to minimise exposure to the hydrophilic water molecules so leading to a range of aggregates or supramolecular structures.

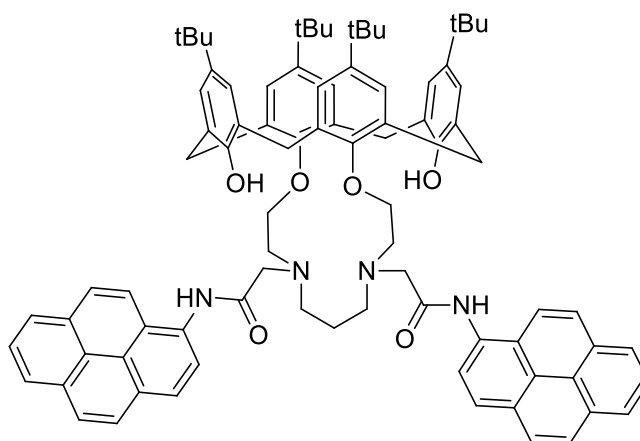


Figure 5.7: Pyrenylacetamide diazacrown ether functionalised calix[4]arene that shows low intensity excimer emission in MeOH and a strong excimer signal in MeOH:H₂O (1:1, v/v).¹⁸⁶

Sellinger *et al.* demonstrated the stark differences between the conformation of pyrene functionalised calix[4]arenes and their tendency to aggregate.¹⁸⁷ They suppressed the aggregation of pyrene moieties by attaching the fluorophore to a 1,3-alternate calix[4]arene, **Figure 5.8a**, they then successfully used this functionalised calixarene as an efficient blue light emitting diode. The related calixarene in the cone conformation, **Figure 5.8b**, showed less than 25% of the efficiency of the 1,3-alternate compound. The authors attributed these observations to the clustering of all pyrene units on the upper rim of the cone-calixarene scaffold which likely led to significant aggregation induced quenching. It could be postulated that the positioning of both pyrene units on the lower rim of **PIC** is likely to lead to significant aggregation of the calixarene units in aqueous solutions.

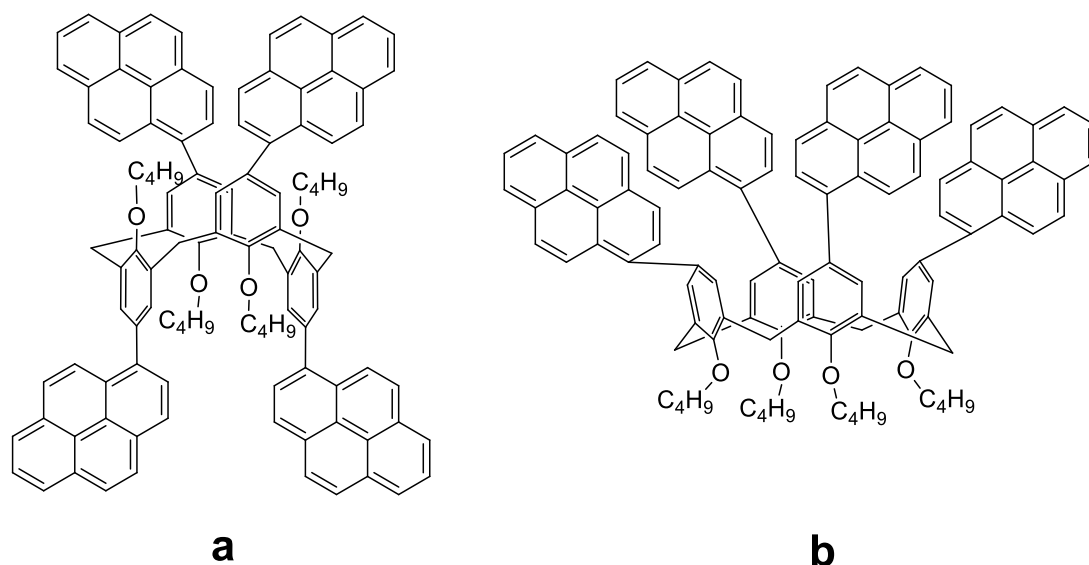


Figure 5.8: Pyrene functionalised **a)** 1,3-alternate and **b)** cone conformations calixarenes as organic light emitting diodes.¹⁸⁷

5.2.1 SEM Investigation of the Morphology of the PIC Aggregates

Diwan *et al.* attribute the formation of well-defined spherical aggregates, visualised using SEM analysis, to the amphiphilic nature of their sensor comprising a polar hydrophilic benzthiazolium head group and an apolar hydrophobic pyrene tail, **Figure 5.6a**. An examination of the structure of **PIC** shows the following moieties; a hydrophobic *t*-butylcalix[4]arene scaffold and two hydrophobic pyrene moieties at opposite ends of the molecule with a polar hydrophilic centre, comprising phenolic

hydroxyl groups, ether linkages and isoxazole heterocycles, **Figure 5.9**. The distribution of hydrophobic and hydrophilic groups as well as the tendency of both pyrene¹⁸⁸ and calixarene cores¹⁸⁹ to self-assemble in aqueous media suggests **PIC** may not form such well-defined aggregates in aqueous MeCN.

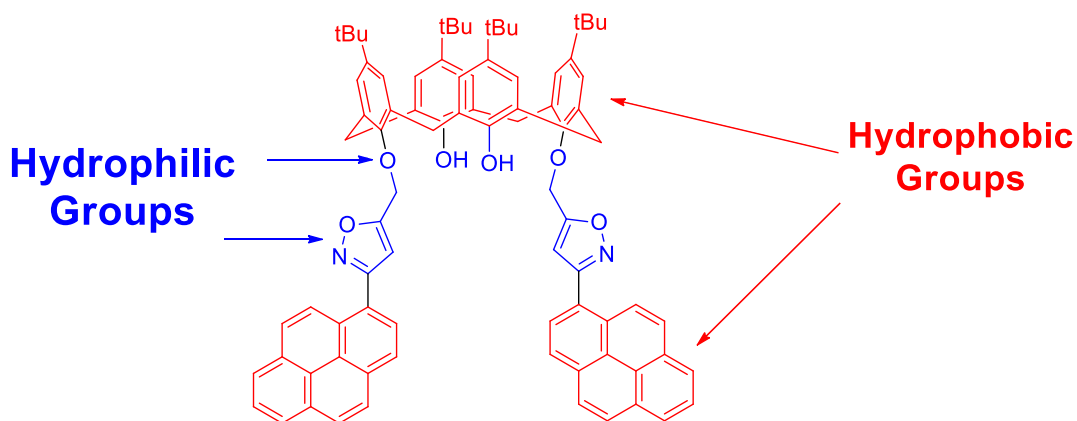


Figure 5.9: Structure of **PIC** with the hydrophobic and hydrophilic regions indicated.

To probe the structural presentation of **PIC** in aq. MeCN, scanning electron microscopy (SEM) images were acquired. Solutions of **PIC** (6 μM) were prepared in 0%, 30% and 50% v/v aq. MeCN and allowed to stand at rt for an *equilibration* time of 1 hour prior to drop-casting each solution onto carbon tape adhered to SEM stubs. Following solvent evaporation overnight at rt in a vacuum desiccator at 833.3 mbar the stubs were analysed. No discernible features were observed in any sample, possibly due to the low concentration of the drop-cast solutions, thus, a second batch of samples were prepared from 60 μM solutions of **PIC**. Data collected from the specimen prepared from 100% MeCN showed no evidence of aggregation at magnification settings in the range x35-150k, **Figure 5.10a-c**. This was not the case with the samples prepared from 30 and 50% v/v aq. MeCN, where aggregates were observed randomly distributed over the carbon tape, **Figure 5.10d-f** (30% v/v aq. MeCN) and **Figure 5.10g-i** (50% v/v aq. MeCN). Distinct cracks were observed on the carbon tape and aggregates were concentrated adjacent to these cracks, **Figure 5.10d** and **g**. The extent of aggregation was greatest in samples prepared from 50% v/v aq. MeCN. In both cases the aggregates were non-uniform in size or shape.

Presumably random association of the hydrophobic ends of the molecules, to minimise exposure to the water, accounts for their irregular appearance.

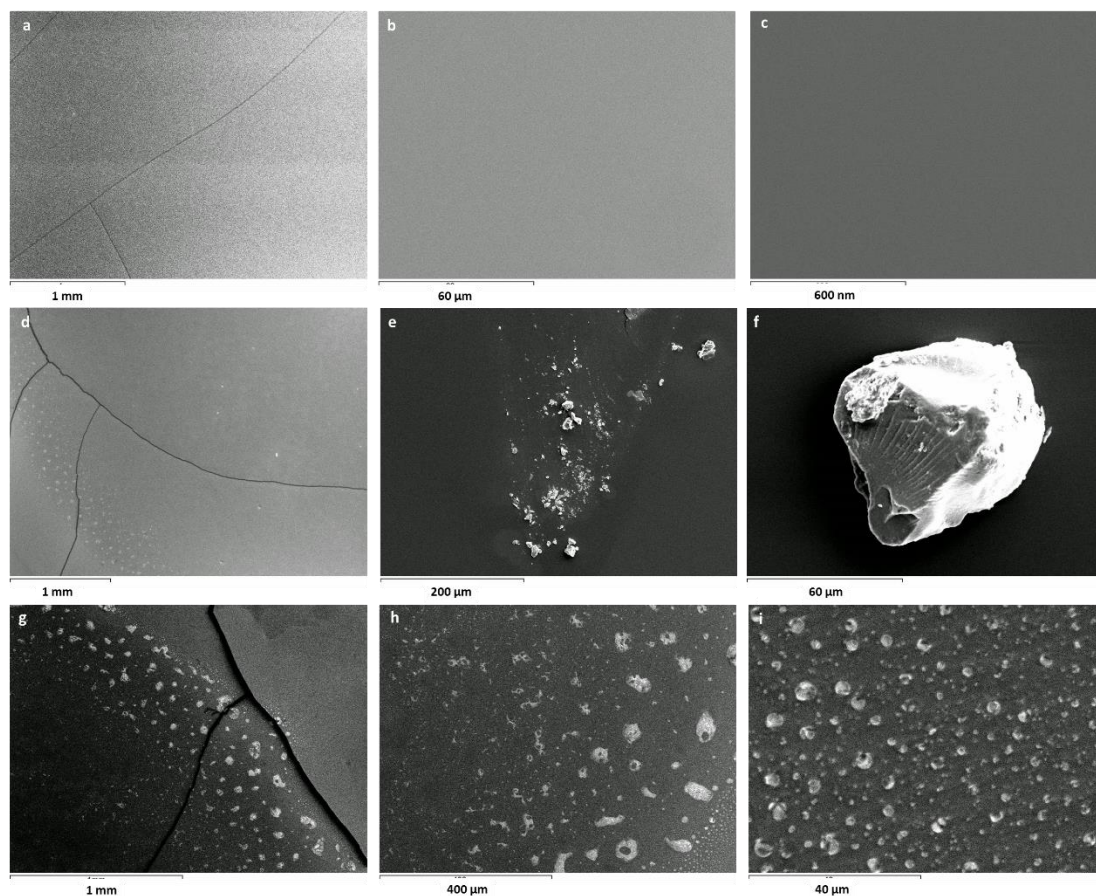


Figure 5.10: SEM images of drop-casted solutions of PIC (60 μM), dried overnight at rt in a vacuum desiccator at 833.3 mbar, samples prepared from; **a-c)** 100% MeCN, **d-f)** 30% v/v aq. MeCN and **g-i)** 50% v/v aq. MeCN.

5.2.2 UV Investigation of the Formation of Aggregates of PIC

Pyrene aggregation in solution is known to induce a broadening of the absorbance spectrum along with a red-shift of the λ_{max} of each absorbance band, with the magnitude of the shift directly proportional to the degree of aggregation.¹⁸⁸ The broadness of a UV profile can be characterised by the peak-to-valley ratio (P_A), with lower P_A values indicative of broader bands.¹⁹⁰ A P_A value greater or equal to 3.0 is expected for pyrene-labelled polymers that show no aggregation or pre-association.¹⁸⁸

To support the hypothesis that PIC aggregates were forming in the aqueous solutions, absorbance spectra of PIC over the range 4-8 μM were recorded in 0 and

60% v/v aq. MeCN. In 100% MeCN three bands peaking at 237, 280 and 343 nm were observed, while in 60% v/v aq. MeCN the bands are broadened and red-shifted to 238, 284 and 358 nm respectively, **Figure 5.11**. For each spectrum P_A values were calculated by taking the ratio of the intensity of the absorbance band at longest wavelength, 343 or 358 nm, to that of the adjacent trough, at 300 or 308 nm, **Table 5.4**. P_A values in the range 2.97-3.41 were determined for **PIC** (4-8 μM) in 100% MeCN. As these values were ~ 3.0 or greater it was concluded that no aggregation of **PIC** occurred in 100% MeCN, which has good solvating properties for both hydrophobic and hydrophilic moieties. In contrast, P_A values of ~ 2.0 were observed for **PIC** in 60% v/v aq. MeCN. Thus, it was deemed likely that as the water content increased to 60% v/v aq. MeCN aggregation minimising exposure of the pyrene units of **PIC** to water is likely to have resulted.

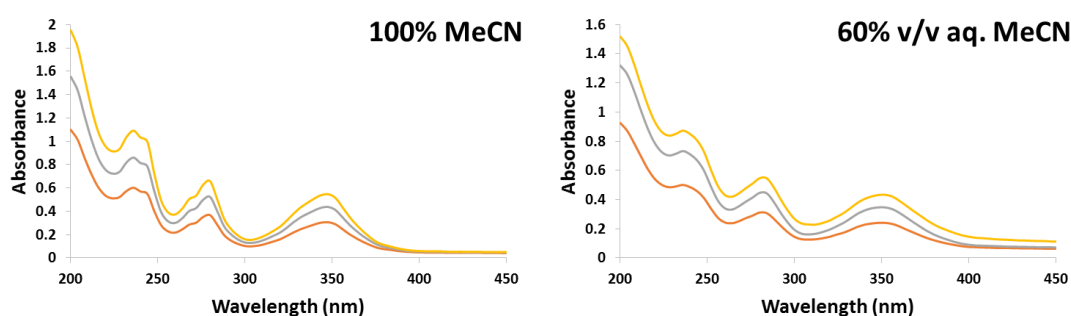


Figure 5.11: Absorbance spectra of **PIC** at 4 μM (orange), 6 μM (grey) and 8 μM (yellow) in 100% MeCN and in 60% v/v aq. MeCN.

Table 5.4: P_A values of **PIC** (4-8 μM) for the absorbance band at longest wavelength; 343 nm (100% MeCN) and at 358 nm (60% v/v aq. MeCN).

	100% MeCN (343 nm/300 nm)	60% v/v aq. MeCN (358 nm/308 nm)
4 μM	2.97	1.85
6 μM	3.28	2.07
8 μM	3.41	1.83

5.3 Fluorescence Sensing in an Aqueous MeCN Environment

This section describes the experiments conducted to assess the ability of **PIC** to detect copper from aqueous MeCN solutions.

5.3.1 Detection of Copper Ions in Aqueous MeCN Solutions – Optimisation of Experimental Design

(i) Order of Addition

The ability of **PIC** to detect $\text{Cu}(\text{ClO}_4)_2$ (10 eqs) in aqueous MeCN solutions was explored. Initial experiments indicated that the outcome was dependent on the detail of sample preparation; thus, fluorescence spectra of the samples indicated in **Table 5.5** were recorded, with two distinct orders of addition of the host, guest and solvents to the cuvette

a) 1) PIC, 2) MeCN, 3) Water, 4) $\text{Cu}(\text{ClO}_4)_2$ (orange plot);

i.e. the host in MeCN was combined with the required volume of MeCN and then exposed to water prior to addition of the MeCN solution of copper perchlorate and allowing to stand for 1 minute at rt.

b) 1) PIC, 2) MeCN, 3) $\text{Cu}(\text{ClO}_4)_2$, 4) Water (grey plot);

i.e. the host in MeCN was combined with the required volume of MeCN and then the MeCN solution of copper perchlorate was added followed by the required volume of water and allowing to stand for 1 minute at rt.

Table 5.5: Volume of stock solutions of **PIC** and $\text{Cu}(\text{ClO}_4)_2$ required to combine with MeCN and water, in order to introduce 0 and 10 eqs of $\text{Cu}(\text{ClO}_4)_2$ to **PIC** (6 μM) in 10 and 50% v/v aq. MeCN solutions.

Sample No.	Final Solvent % Water Content (v/v)	PIC:Cu ²⁺	Vol. of PIC Stock Solution (20 μM in MeCN) μL	MeCN μL	Vol. of $\text{Cu}(\text{ClO}_4)_2$ Stock Solution (1200 μM in MeCN) μL	Water μL
1	10	1:0	900	1800	0	300
2	10	1:10	900	1650	150	300
3	50	1:0	900	600	0	1500
4	50	1:10	900	450	150	1500

For the studies conducted in 10% v/v aq. MeCN the fluorescence spectra, recorded after 1 min of agitation, **Figure 5.12**, revealed that when the $\text{Cu}(\text{ClO}_4)_2$ solution was

added to **PIC** in MeCN before the water significant excimer quenching (~50%) occurred. However, if water was added to the host solution before the guest, no quenching was observed, **Figure 5.12a**.

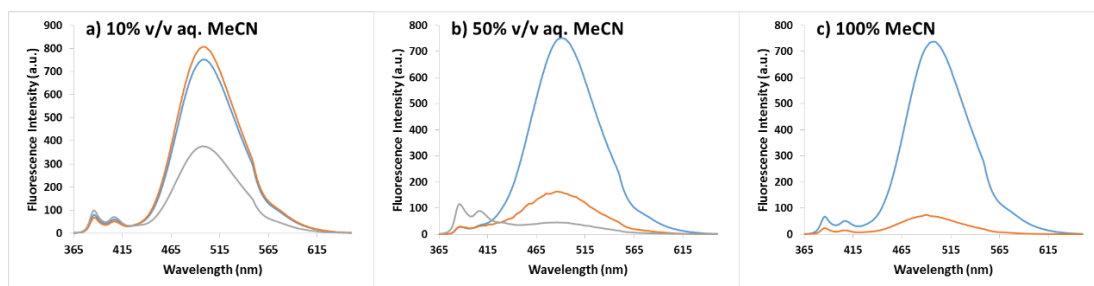


Figure 5.12: Emission spectra of **PIC** ($6 \mu\text{M}$, $\lambda_{\text{ex}}=343 \text{ nm}$, blue) in 10 and 50% v/v aq. MeCN and with 10 eqs of $\text{Cu}(\text{ClO}_4)_2$ with the water added before (orange) or after the copper (grey); spectra of **PIC** in 100% MeCN is shown for comparison.

In a parallel study with final solvent composition of 50% v/v water, significant excimer band quenching (79%) was observed if the water was added to the host solution before the copper ions. This improved to >90% if water was added to the cuvette after addition of the copper perchlorate solution, **Figure 5.12b**.

These results which are quite different to that for **PIC** in 100% MeCN, **Figure 5.12c**, make it clear that the presentation of **PIC** in aqueous solutions influences its ability to bind and report on the presence of the Cu^{2+} ion under the conditions of these experiments, as represented in **Figure 5.13**.

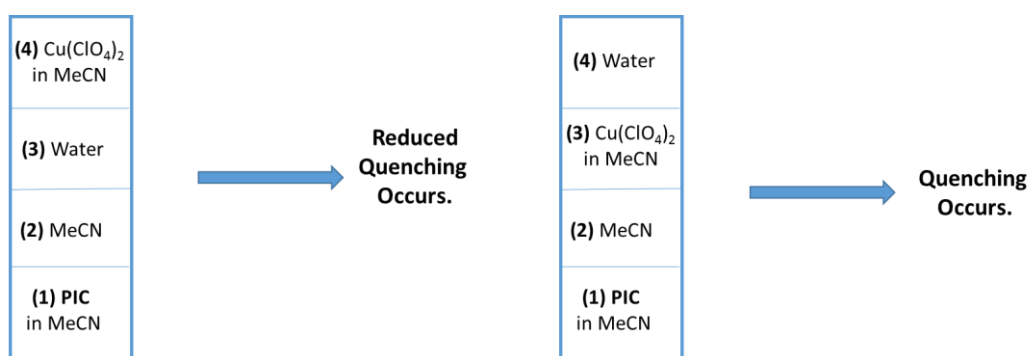


Figure 5.13: Schematic of the importance of the order of addition of the four solutions to the cuvette on the resultant fluorescence quenching observed.

Since the order of addition of water and metal ions to the MeCN solution of **PIC** were important parameters for sensitivity, all further analyses were conducted by adding solutions to the cuvette in the following order:

1. **PIC** in MeCN,
2. MeCN as required,
3. Metal Salt Solution, (in MeCN or H₂O),
4. Water as required.

(ii) Equilibration Time

Further, as it had been shown (Section 5.3) that aq. solutions of **PIC** required varying amounts of time to reach an *equilibrium* point, subsequent experiments designed to detect copper ions involved incorporation of an *equilibration* time.

5.3.2 Detection of Copper Ions in Aqueous MeCN Solutions

Individual samples of **PIC** (6 μ M) in the presence of 10 eqs of copper perchlorate were prepared in aq. MeCN according to the volumes shown in **Table 5.6**. Each sample was allowed to reach *equilibrium* as previously described, *i.e.* to the point where spectra recorded at 5 min intervals had overlapping emission profiles (\pm 5 a.u.).

Table 5.6: Volume of stock solutions of **PIC** and Cu(ClO₄)₂ required to combine with MeCN and water, in order to introduce 0 and 10 eqs of Cu(ClO₄)₂(in MeCN) to **PIC** (6 μ M) in a 5-60% v/v aq. MeCN solutions.

Sample No.	Final Solvent % Water Content (v/v)	Vol. of PIC Stock Solution (20 μ M in MeCN) μ L	MeCN μ L	Vol. of Cu(ClO ₄) ₂ Stock Solution (1200 μ M in MeCN) μ L	Water μ L	Equilibration Time (mins)
1	5	900	1800	150	150	80
2	10	900	1650	150	300	100
3	20	900	1350	150	600	70
4	30	900	1050	150	900	200
5	40	900	750	150	1200	90
6	45	900	600	150	1350	60
7	50	900	450	150	1500	30
8	60	900	150	150	1800	55

A comparison of the spectra of *equilibrated* samples in the presence and absence of Cu²⁺ showed fluorescence quenching of the excimer band occurred concomitantly

with an enhancement of the monomer bands for all samples containing Cu^{2+} , **Figure 5.14**. However, both the extent of the changes to the signal intensity, and the time required to reach *equilibrium* varied significantly. Graphs of the extent of monomer enhancement and excimer quenching versus the water content, plotted in **Figure 5.15a** and **b**, respectively, reveal that the highest level of quenching of the excimer band (94 and 92%) and lowest level of enhancement of the monomer band (23 and 31%) occurred with samples having 50 and 60% water content respectively. The almost complete quenching of the excimer band at high water content compared favourably to that observed in 100% MeCN.

Monomer enhancement, of the order of 1.5 fold, was greatest in the 10% v/v aq. MeCN sample. The lowest level of excimer quenching occurred in the 30% v/v aq. MeCN sample (18%). The same sample took the longest time to *equilibrate* (200 mins) whilst samples in 50 and 60% v/v aq. MeCN reached *equilibrium* more rapidly.

This data indicates that the % water content of the solvent plays an important role in the ability of **PIC** to detect copper ions, which may relate to the presence of different varieties of host supramolecular aggregates in the different media. It can be hypothesised that the copper ions may cause excimer quenching either **(i)** by virtue of disrupting the formation of aggregates and complexing to **PIC** at the molecular level, or **(ii)** by direct association with the supramolecular structures inducing a new association with reduced emission.

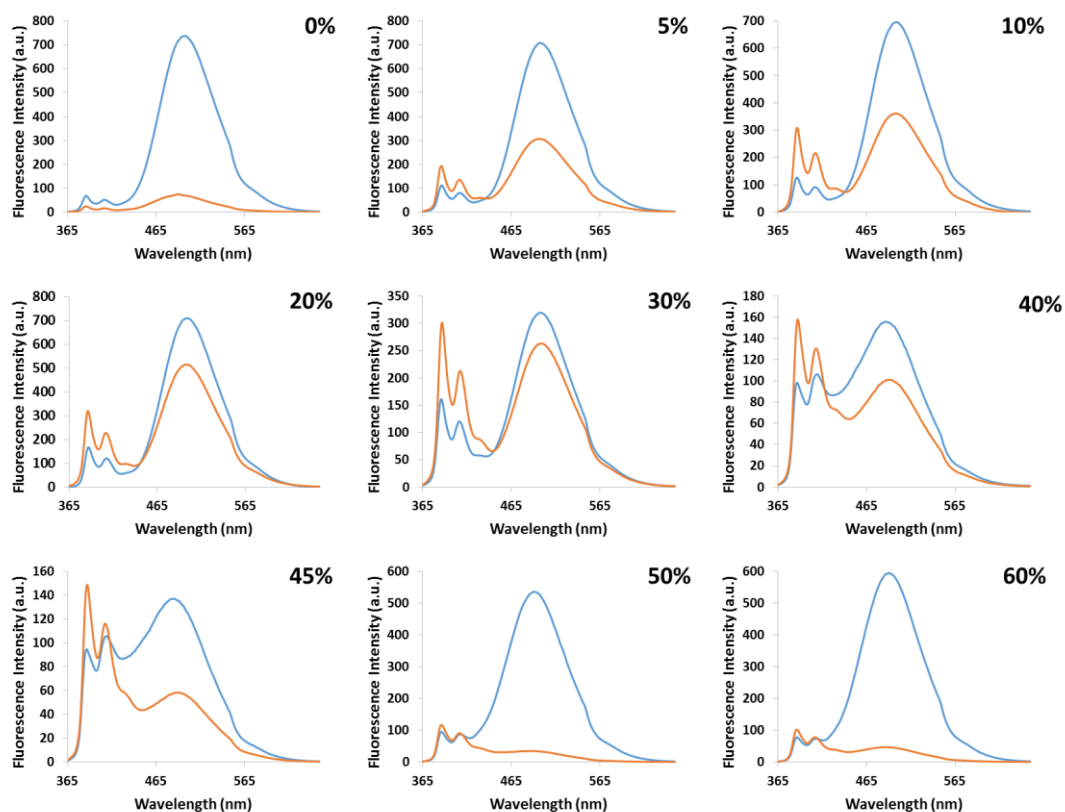


Figure 5.14: Emission spectra of *equilibrated* samples of **PIC** ($6 \mu\text{M}$, $\lambda_{\text{ex}} = 343 \text{ nm}$) with 0 (blue) and 10 (orange) eqs of $\text{Cu}(\text{ClO}_4)_2$ (in MeCN) in 0 - 60% v/v aq. MeCN.

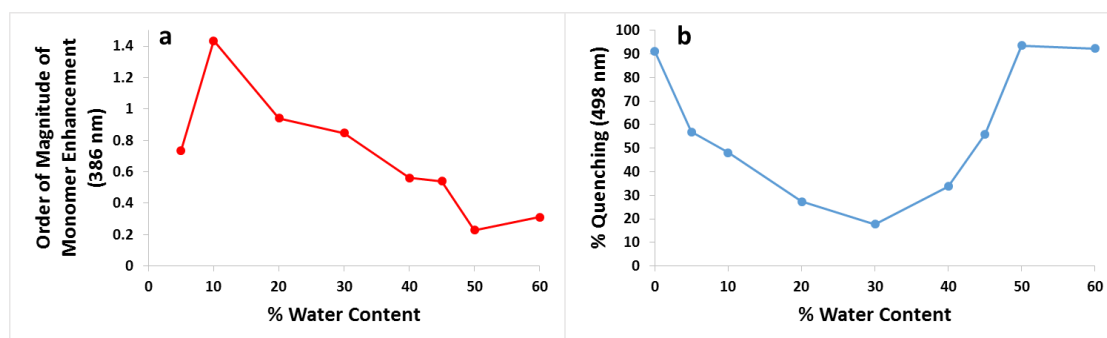


Figure 5.15: **a)** Order of magnitude of monomer enhancement (386 nm) and **b)** % of excimer quenching (λ_{max}) of the emission spectra of **PIC** ($6 \mu\text{M}$, $\lambda_{\text{ex}} = 343 \text{ nm}$) following addition of 10 eqs of $\text{Cu}(\text{ClO}_4)_2$ (in MeCN) versus the % water content.

5.3.3 Counterion Study

The influence of the counterion of the copper salt on the detection ability of **PIC** in 60% v/v aq. MeCN was studied by introducing 10 eqs of the perchlorate, nitrate, chloride and acetate salts, prepared in MeCN to **PIC** ($6 \mu\text{M}$). The samples were

prepared by addition of the required solutions and solvents in the order shown in

Table 5.7.

Table 5.7: Volume of stock solutions of **PIC** and Copper salt required to combine with MeCN and water, in order to introduce 10 eqs of each Cu^{2+} salt to **PIC** ($6 \mu\text{M}$) in a 60% v/v aq. MeCN solution.

Sample No.	Copper Salt	Vol. of PIC Stock Solution ($20 \mu\text{M}$ in MeCN) μL	MeCN μL	Vol. of Copper Salt Solution ($1200 \mu\text{M}$ in MeCN) μL	Water μL	Equilibration Time (mins)
1	$\text{Cu}(\text{CO}_2\text{CH}_3)_2$	900	150	150	1800	35
2	CuCl_2	900	150	150	1800	80
3	$\text{Cu}(\text{NO}_3)_2$	900	150	150	1800	30
4	$\text{Cu}(\text{ClO}_4)_2$	900	150	150	1800	55

Fluorescence spectra were recorded until the *equilibrium* point was reached and in all cases quenching of the host excimer band occurred, **Figure 5.16**. As outlined in Section 4.1.4, the degree of dissociation of the different copper salts in the various solutions was considered crucial to their ability to interact with the hosts. As previously observed in studies in 100% MeCN, the highest level of quenching, 92%, was observed for the perchlorate salt and the lowest, 31%, for the acetate salt. These figures correlate to the expected high¹⁹¹ and low¹⁵⁴ dissociation of the perchlorate and acetate salts in aqueous solutions, respectively.

In aq. MeCN the relative quenching efficiency abilities of the nitrate and chloride salts was inverted compared to the findings in neat MeCN. Copper chloride has a lower dissociation constant than copper nitrate in aqueous solutions,¹⁹² thus the effective concentration of $[\text{Cu}(\text{solvent})_n]^{2+}$ ions is likely to be higher in the copper nitrate than the copper chloride solutions, allowing for more effective quenching of the excimer band of **PIC**.

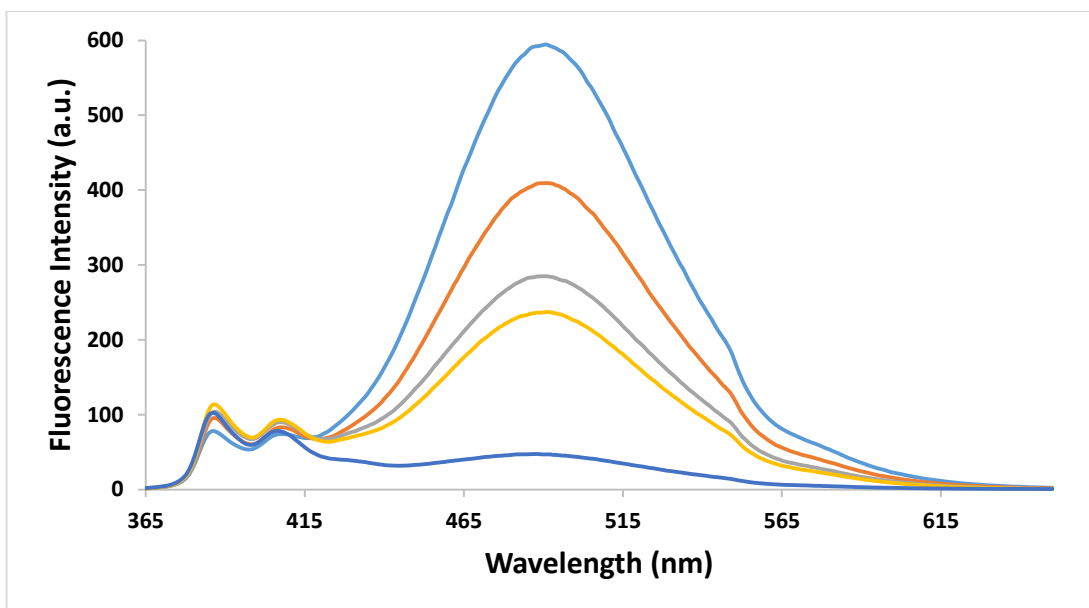


Figure 5.16: Emission spectra of *equilibrated* samples of PIC ($6 \mu\text{M}$, $\lambda_{\text{ex}} = 343 \text{ nm}$) in 60% v/v aq. MeCN (blue) with 10 eqs of: $\text{Cu}(\text{CO}_2\text{CH}_3)_2$ (orange), CuCl_2 (grey), $\text{Cu}(\text{NO}_3)_2$ (yellow) and $\text{Cu}(\text{ClO}_4)_2$ (navy).

5.3.4 Metal Ion Selectivity Study – Metal Perchlorates Presented as Solutions in MeCN

An examination of the selectivity for copper in aqueous media was carried out by introducing solutions of different metal perchlorates, in MeCN, to PIC ($6 \mu\text{M}$) in 60% v/v aq. MeCN. Samples were prepared by mixing solutions of host, guest and solvent media in the order shown in **Table 5.8**.

For each sample fluorescence spectra were recorded until the *equilibrium* point was reached. The data reveals that all of the metal ions have some effect on the excimer band of PIC; slight enhancements were noted in the presence of Zn^{2+} and Co^{2+} ions, (5 - 7%), whilst limited quenching occurred upon exposure to Mn^{2+} , Hg^{2+} and Ni^{2+} ions (2-9%), **Figure 5.17**. Greater degrees of quenching followed from exposure to Pb^{2+} (13%), Ca^{2+} (13%) and Ag^+ (22%) ions. However, no metal ion could compete with the 92% quenching observed in the presence of the Cu^{2+} ion.

Table 5.8: Volume of stock solutions of **PIC** and $M^{n+}(\text{ClO}_4^-)_n$ (in MeCN) required to combine with MeCN and water, in order to introduce 10 eqs of each metal salt to **PIC** (6 μM) in a 60% v/v aq. MeCN solution.

Sample No.	Metal Perchlorate	Vol. of PIC Stock Solution (20 μM in MeCN) μL	MeCN μL	Vol. of $M^{n+}(\text{ClO}_4^-)_n$ Stock Solution (1200 μM in MeCN) μL	Water μL	Equilibration Time (mins)
1	$\text{Ca}(\text{ClO}_4)_2$	900	150	150	1800	50
2	$\text{Pb}(\text{ClO}_4)_2$	900	150	150	1800	20
3	$\text{Mn}(\text{ClO}_4)_2$	900	150	150	1800	20
4	$\text{Zn}(\text{ClO}_4)_2$	900	150	150	1800	25
5	$\text{Hg}(\text{ClO}_4)_2$	900	150	150	1800	15
6	$\text{Ni}(\text{ClO}_4)_2$	900	150	150	1800	50
7	$\text{Co}(\text{ClO}_4)_2$	900	150	150	1800	70
8	AgClO_4	900	150	150	1800	30
9	$\text{Cu}(\text{ClO}_4)_2$	900	150	150	1800	55

Thus, it was evident that the selectivity of **PIC** for the Cu^{2+} ion previously observed in 100% MeCN, was reduced in 60% v/v aq. MeCN. In pure MeCN, **PIC** presents at the molecular level providing a binding site suitable for the Cu^{2+} ion, however, it is hypothesised that the dynamic range of aggregates formed in aq. MeCN allows for a range of binding sites that facilitate interactions with the other metal ions tested, namely Pb^{2+} , Ca^{2+} and Ag^+ ions.

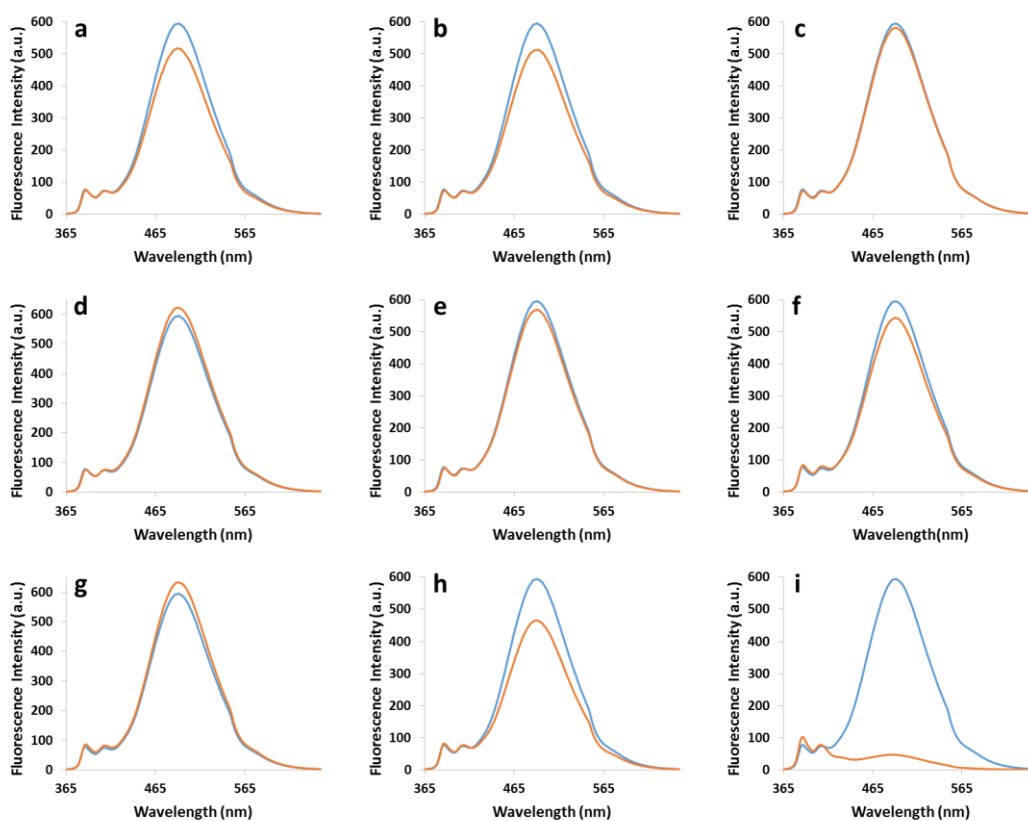


Figure 5.17: Emission spectra of *equilibrated* samples of aq. samples **PIC** ($6 \mu\text{M}$, $\lambda_{\text{ex}} = 343 \text{ nm}$) in 60% v/v aq. MeCN with 0 (blue) and 10 (orange) eqs of $\text{M}^{n+}(\text{ClO}_4^-)_n$ (in MeCN); where $\text{M}^{n+} = \text{a) Ca}^{2+}$, **b) Pb**²⁺, **c) Mn**²⁺, **d) Zn**²⁺, **e) Hg**²⁺, **f) Ni**²⁺, **g) Co**²⁺, **h) Ag**⁺ and **i) Cu**²⁺.

5.3.5 Study of Ability of PIC to Sense Cu²⁺ Ions from an Aqueous Source

The ability of **PIC** to detect copper ions from aqueous samples was explored to test potential for applications in waste water analysis. Thus, a $1200 \mu\text{M}$ solution of $\text{Cu}(\text{ClO}_4)_2$ in water was prepared. **PIC** was exposed to 10 eqs of aqueous $\text{Cu}(\text{ClO}_4)_2$ giving solutions with final solvent contents ranging from 5-60% v/v aq. MeCN, prepared according to the volumes shown in **Table 5.9**. The fluorescence spectra of the resulting solutions, recorded at 5 min intervals until overlapping spectra were obtained, are shown in **Figure 5.18**.

No significant changes to the monomer bands were observed over the solvent range. However, enhancement (11-31%) of the excimer band was observed in samples with up to 20% v/v aq. MeCN. Significant quenching occurred for host samples with 50-

60% water content (85 and 57% respectively), as had previously been noted in this medium when the Cu^{2+} salt was presented as a solution in MeCN, **Figure 5.14**.

Table 5.9: Volume of stock solutions of **PIC** and $\text{Cu}(\text{ClO}_4)_2$ required to combine with MeCN and water, in order to introduce 0 and 10 eqs of $\text{Cu}(\text{ClO}_4)_2$ (in H_2O) to **PIC** (6 μM) in 5-60% v/v aq. MeCN solutions.

Sample No.	Final Solvent % Water Content (v/v)	Vol. of PIC Stock Solution (20 μM in MeCN) μL	MeCN μL	Vol. of $\text{Cu}(\text{ClO}_4)_2$ Stock Solution (1200 μM in H_2O) μL	Water μL	Equilibration Time (mins)
1	5	900	1950	150	0	20
2	10	900	1800	150	150	20
3	20	900	1500	150	450	20
4	30	900	1200	150	750	90
5	40	900	900	150	1050	45
6	45	900	750	150	1200	40
7	50	900	600	150	1350	65
8	60	900	300	150	1650	165

The % quenching of the excimer band of **PIC** following exposure to 10 eqs of $\text{Cu}(\text{ClO}_4)_2$ from MeCN and H_2O solutions is represented in **Figure 5.19**. It clearly indicates that higher levels of quenching occurred at all water contents when the copper salt is introduced in MeCN. This data suggests that the energy required for desolvation of water ligands from the Cu^{2+} ion required to form a host:guest complex with **PIC**, may be less energetically favourable than the replacement of MeCN ligands from the same ion.

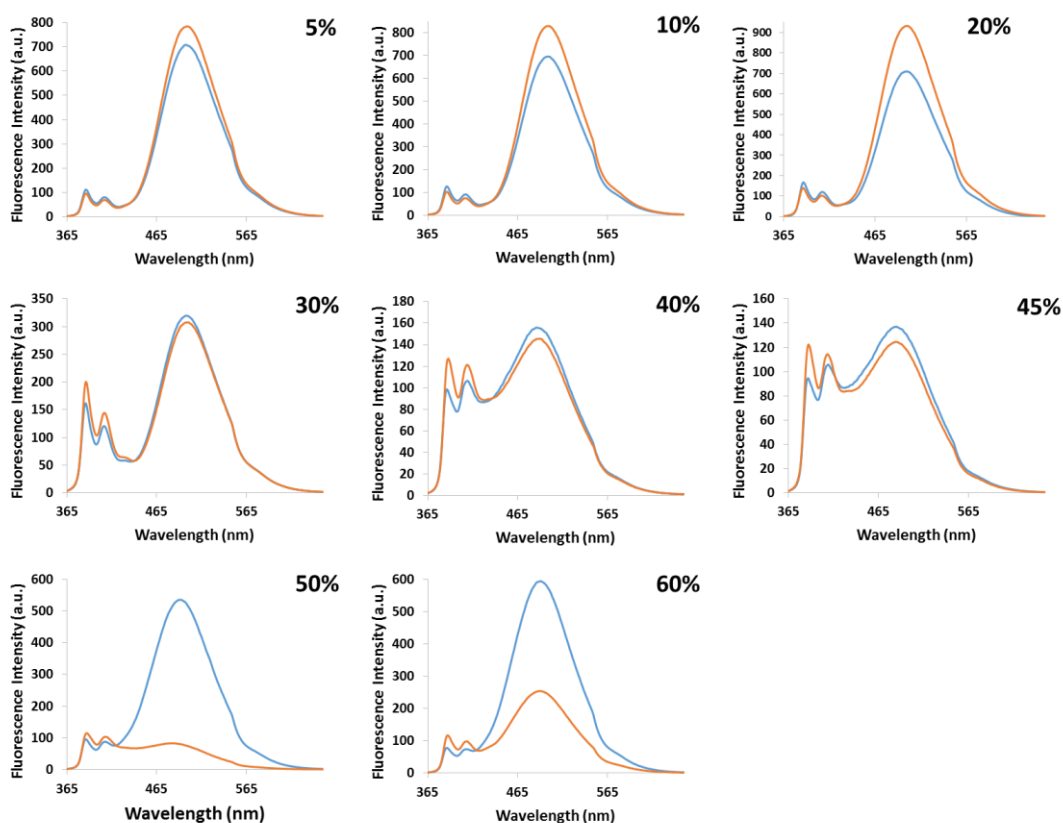


Figure 5.18: Emission spectra of *equilibrated* samples of PIC ($6 \mu\text{M}$, $\lambda_{\text{ex}} = 343 \text{ nm}$) with 0 (blue) and 10 (orange) eqs of $\text{Cu}(\text{ClO}_4)_2$ in 5-60% v/v aq. MeCN; $\text{Cu}(\text{ClO}_4)_2$ was presented as a solution in water.

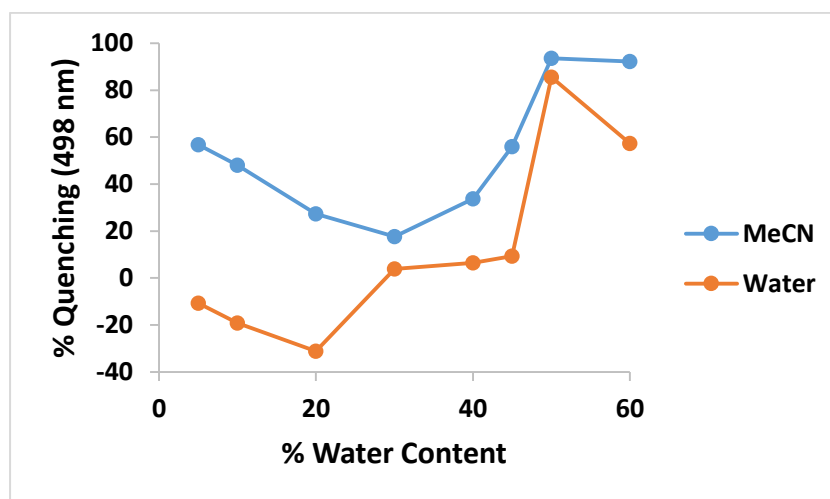


Figure 5.19: Graph of the % of excimer quenching (λ_{max}) of the emission spectra of PIC ($6 \mu\text{M}$, $\lambda_{\text{ex}} = 343 \text{ nm}$) following addition of 10 eqs of $\text{Cu}(\text{ClO}_4)_2$ versus the % water content; $\text{Cu}(\text{ClO}_4)_2$ in MeCN (Blue Line) or Water (Orange Line).

5.3.6 Competitive Metal Study – Metal Perchlorates Presented as Solutions in Water

Solutions of nine metal perchlorate salts were prepared in water (1200 μM). PIC (6 μM) was exposed to 50 eqs of the aqueous salt solutions, following addition of the host, guest and media in the order and according to the volumes shown in **Table 5.10**; the resulting fluorescence spectra are presented in **Figure 5.20**.

Fluorescence quenching of the host was noted in the presence of all metal perchlorates, with several salts causing greater than 25% quenching, **Table 5.11**. Significantly, Hg^{2+} ions were the most effective quenchers, (82%), while 50 eqs of Cu^{2+} ions induced only 45% quenching of the excimer band. Comparison of this data to that obtained following introduction of the metal perchlorates as MeCN solutions, **Figure 5.17** suggests that the water solvated metal ions may interact with PIC either on the molecular (low water content media) or supramolecular (high water content media) level. The availability of molecular as well as a dynamic range of PIC offers a range of binding sites and thus, a lower selectivity for copper ions is evident.

Table 5.10: Volume of stock solutions of PIC and $\text{M}^{n+}(\text{ClO}_4^-)_n$ (in H_2O) required to combine with MeCN and water, in order to introduce 50 eqs of each metal salt to PIC (6 μM) in a 60% v/v aq. MeCN solution.

Sample No.	Metal Perchlorate	Vol. of PIC Stock Solution (20 μM in MeCN) μL	MeCN μL	Vol. of $\text{M}^{n+}(\text{ClO}_4^-)_n$ Stock Solution (1200 μM in H_2O) μL	Water μL	Equilibration Time (mins)
1	$\text{Ca}(\text{ClO}_4)_2$	900	300	750	1050	65
2	$\text{Pb}(\text{ClO}_4)_2$	900	300	750	1050	40
3	$\text{Mn}(\text{ClO}_4)_2$	900	300	750	1050	40
4	$\text{Zn}(\text{ClO}_4)_2$	900	300	750	1050	65
5	$\text{Hg}(\text{ClO}_4)_2$	900	300	750	1050	55
6	$\text{Ni}(\text{ClO}_4)_2$	900	300	750	1050	30
7	$\text{Co}(\text{ClO}_4)_2$	900	300	750	1050	70
8	AgClO_4	900	300	750	1050	35
9	$\text{Cu}(\text{ClO}_4)_2$	900	300	750	1050	45

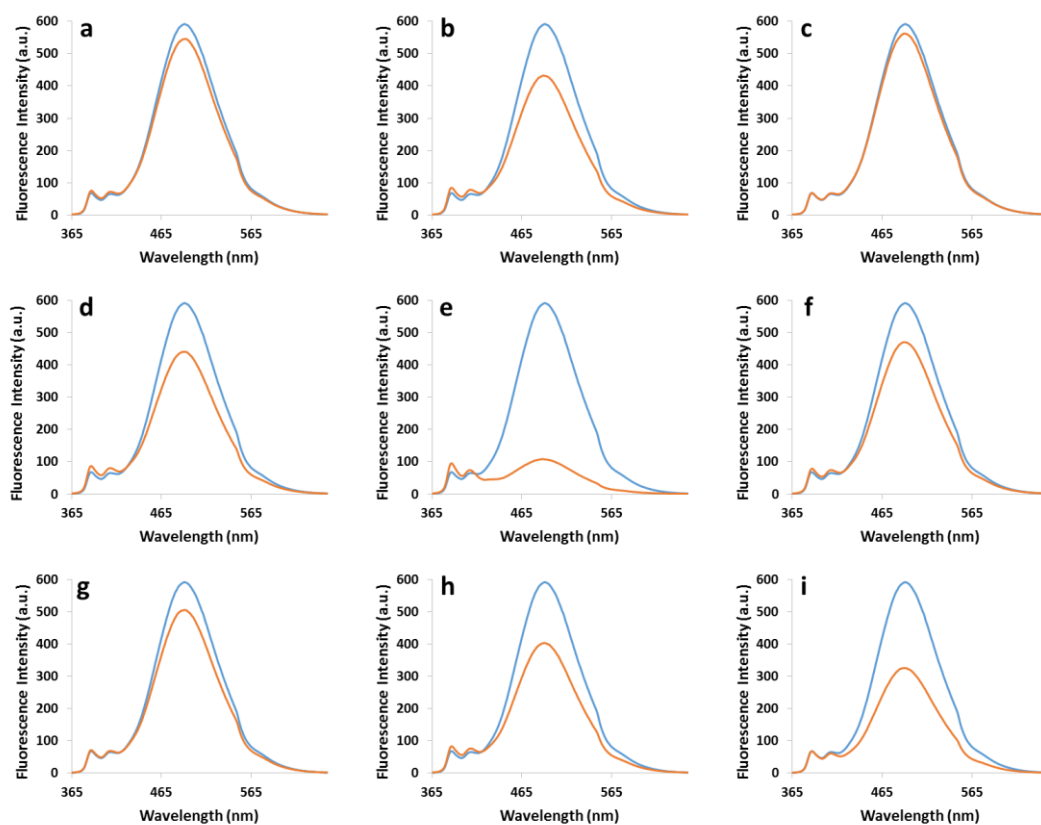


Figure 5.20: Emission spectra of *equilibrated* samples of **PIC** ($6 \mu\text{M}$, $\lambda_{\text{ex}} = 343 \text{ nm}$) in 60% v/v aq. MeCN with 0 (blue) and 50 (orange) eqs of $\text{M}^{\text{n}+}(\text{ClO}_4^-)_n$ (in H_2O); where $\text{M}^{\text{n}+} =$ **a)** Ca^{2+} , **b)** Pb^{2+} , **c)** Mn^{2+} , **d)** Zn^{2+} , **e)** Hg^{2+} , **f)** Ni^{2+} , **g)** Co^{2+} , **h)** Ag^+ and **i)** Cu^{2+} .

Table 5.11: Summary of the % quenching at the λ_{max} of the excimer band (491 nm) observed upon exposure of **PIC** ($6 \mu\text{M}$) in 60% v/v aq. MeCN to 50 eqs of $\text{M}^{\text{n}+}(\text{ClO}_4^-)_n$ (in H_2O), where $n = 1$ or 2.

$\text{M}^{\text{n}+}(\text{ClO}_4^-)_n$	Ca^{2+}	Pb^{2+}	Mn^{2+}	Zn^{2+}	Hg^{2+}	Ni^{2+}	Co^{2+}	Ag^+	Cu^{2+}
Quenching (492nm)	8%	27%	5%	25%	82%	20%	14%	32%	45%

5.3.7 Investigation of Potential Aggregate Formation in Copper Containing aq. MeCN solution of PIC

Fluorescence experiments had shown that aq. MeCN solutions of **PIC** were affected by the presence of metal ions, to greater or lesser extents depending on whether the metal ions were introduced as solutions in MeCN or water. SEM analysis had shown that **PIC** formed non-uniform aggregates in aq. MeCN solutions, **Figure 5.10d-i**, thus it was hypothesised that the metal ion guests may cause fluorescence

quenching/enhancement by either **(i)** disrupting the formation of aggregates or **(ii)** by complexation to an alternative binding site formed by the supramolecular structures present in aq. MeCN.

To investigate the potential formation of aggregate structures from **PIC** in copper containing aq. MeCN solutions, **PIC** (60 μM) in MeCN was exposed to the same relative concentration of an aqueous solution of $\text{Cu}(\text{ClO}_4)_2$. The $\text{Cu}(\text{ClO}_4)_2$ concentration was restricted to 60 μM to restrict on the use of large quantities of perchlorates under vacuum in the SEM chamber. The resulting 50% v/v aq. MeCN solution was allowed to stand at rt for an *equilibration* time of 90 mins. A sample for the SEM study was prepared by drop-casting this solution onto carbon tape adhered to an SEM stub, followed by solvent evaporation overnight at rt in a vacuum desiccator at 833.3 mbar.

SEM analysis revealed aggregate formation, **Figure 5.21a**, although in lower densities than previously observed from the sample of the host-alone, **Figure 5.10g-i**. One area of particularly dense aggregation was observed, **Figure 5.21b**. Expansion of this area revealed a highly ordered honeycomb like structure, **Figure 5.21c** and **d**. This showed that the sample containing 1 eq. of Cu^{2+} w.r.t. **PIC**, forms aggregates which differ in morphology from those formed by the host-alone, these changes help explain the differences between the fluorescence spectra of **PIC** in aq. MeCN and the host:guest samples in 50% v/v aq. MeCN.

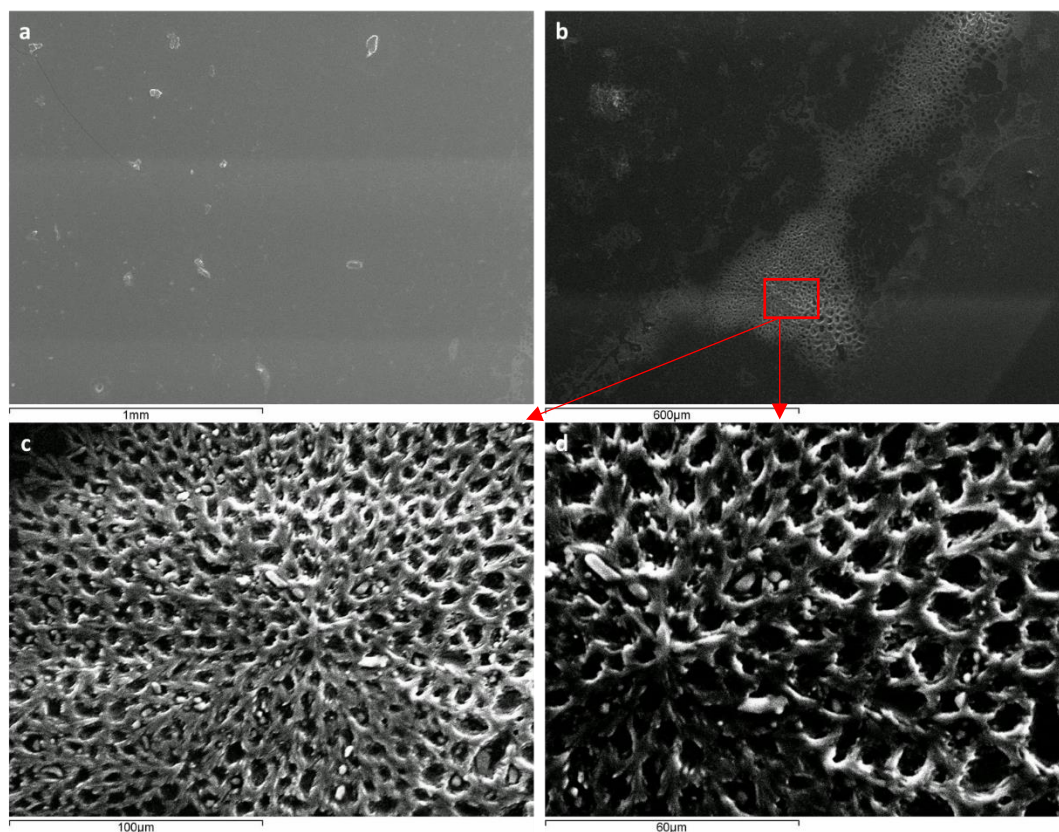


Figure 5.21: SEM images of a drop-casted solution of **PIC** (60 μM) and **Cu(ClO₄)₂** (60 μM) in a 50% v/v aq. MeCN medium, dried overnight at rt in a vacuum desiccator at 833.3 mbar.

5.4 Fluorescence Study of PIC in Aqueous MeCN - Conclusions

- To probe the ability of **PIC** to detect metal ions in real-world applications a study of the sensing ability of **PIC** for the Cu^{2+} ion was carried out in aqueous MeCN solutions.
- The emission profiles of **PIC** (6 μM) were recorded in 5-60% v/v aq. MeCN following 1 minute of mixing time; the host appeared to remain in solution.
- The intensity of the emission of **PIC** in aq. media was found to fluctuate with time until an *equilibration* point was reached. The variation was attributed to ACQ and AIE effects caused by the formation of a variety of supramolecular structures. Future experiments were carried out by analysis of *equilibrated* samples.
- The potential existence of **PIC** aggregates was investigated by SEM analysis. No evidence of aggregation was observed in samples prepared from 100%

MeCN. Irregular aggregates were observed in samples prepared from aq. media, (30 and 50% v/v aq. MeCN).

- Aggregate formation was supported by comparison of the absorbance spectra of **PIC** (4-8 μM) in 100% MeCN and in 60% v/v aq. MeCN. P_A values, ~ 3 were measured in the former and less than 2.07 in the latter. This data is in keeping with aggregation in the 60% v/v aqueous solution.
- Experimental design is crucial to the outcome of the experiments. For analyte samples in MeCN the guest must be added to the host in MeCN, before the required amount of water, otherwise no (or limited) fluorescence response is detected on addition of the guest. The formation of **PIC** aggregates following exposure to water is believed to account for this observation.
- The nature of the counterion of the copper salt was important in dictating the extent of fluorescence quenching by copper ions which was observed to decrease in the order $\text{Cu}(\text{ClO}_4)_2 > \text{Cu}(\text{NO}_3)_2 > \text{CuCl}_2 > \text{Cu}(\text{CO}_2\text{CH}_3)_2$. The trend was attributed to the preferred presentation of the copper salts in aqueous media and their abilities to interact with **PIC** at the molecular and supramolecular level.
- In 50% v/v aq. MeCN **PIC** showed selectivity for the Cu^{2+} ion, when the guests were introduced as MeCN solutions, 92% excimer quenching was observed with 10 eqs of guest, however, selectivity was limited and Ag^+ ions caused 22% quenching of the same signal.
- The intensity of the excimer band of **PIC** varied when exposed, in 5-60% v/v aq. MeCN, to aqueous samples of copper perchlorate. At 85% the most effective quenching by 10 eqs of guest was noted in 50% v/v aq. MeCN.
- Introduction of metal perchlorates from aqueous solutions resulted in a reduced selectivity of **PIC** for the Cu^{2+} ion. Significant quenching was noted with zinc, lead, silver, copper and mercury perchlorates, suggesting that these water solvated metal ions can all interact with **PIC** in 60% aq. MeCN.
- SEM analysis of a drop-casted and vacuum dried 50% v/v aq. MeCN samples containing **PIC** and $\text{Cu}(\text{ClO}_4)_2$ (1:1) revealed a lower density of non-uniform aggregates compared to those observed for host samples. An area of high

density well-structured honeycomb like aggregates formed, supporting the hypothesis that the metal ions can influence the formation of aggregates.

5.5 Solid Supported PIC Overview

Due to the limitations of **PIC** as a copper sensor in aqueous MeCN, a solid supported approach was explored. Molecules of interest can be covalently attached to a solid support *via* thiol,¹⁹³ ester,¹⁹⁴ heterocycle,¹² amide bonds,¹⁹⁵ *etc.* Non-covalent attachments are also possible, *e.g.* by direct drop-casting onto a solid support or by doping a polymer solution with the species of interest. The entrapped molecules generally retain their native chemical characteristics and thus doped polymeric solutions have been used in a range of applications including gel formation,¹⁹⁶ gas storage,¹⁹⁷ catalysis¹⁹⁸ and sensing.¹⁹⁹

This section will give an overview of experiments involving drop-casting **PIC** onto a solid support, followed by an outline of the technique of electrospinning and its potential to incorporate molecules of interest into polymeric solid supports and its application to the formation of electrospun fibers of polymeric systems with and without **PIC**. Finally an exploration of the potential of the **PIC** doped polymeric systems to act as Cu²⁺ sensors in real-world aqueous applications will be described.

5.5.1 Drop-casting: PIC Coated Glass Slides

Drop-casting a solution of a fluorescent material is a common technique for the investigation of the solid state emission properties of the compound of interest. The solution may be drop-cast directly to form films,²⁰⁰ onto electrodes²⁰¹ or onto a glass support.²⁰² The solid state emission properties of **PIC** were investigated in order to pursue aqueous copper sensing applications.

It was proposed to drop-cast **PIC** onto a glass slide and explore its potential to sense metal ions spectrofluorometrically. Whilst quantification of the host concentration and the judgement of the number of metal ions present in a given solution was not considered in these initial proof of concept studies, as controlling the quantity of **PIC** present on the glass slides is problematic.

As outlined in Chapter 2, two unique solid state structures followed from crystallisation of **PIC** from DCM and MeCN. The structures differed in the positioning and the number of solvent molecules of crystallisation; they displayed distinct intramolecular pyrene-pyrene planar angles and isoxazole-pyrene planar angles. Thus it was considered interesting to investigate the possibility that different emission profiles would result from drop-casted samples of **PIC**/DCM or **PIC**/MeCN.

As a control, the fluorescence spectra of a “blank” glass slide in a solvent free and aqueous environment was recorded; low level of background emission with a maximum of ~20 a.u. was observed for the solvent free sample, whilst the water sample showed no significant emission, **Figure 5.22**. Thus, it was deemed appropriate to measure the emission spectra of solid samples of **PIC** on the glass slides.

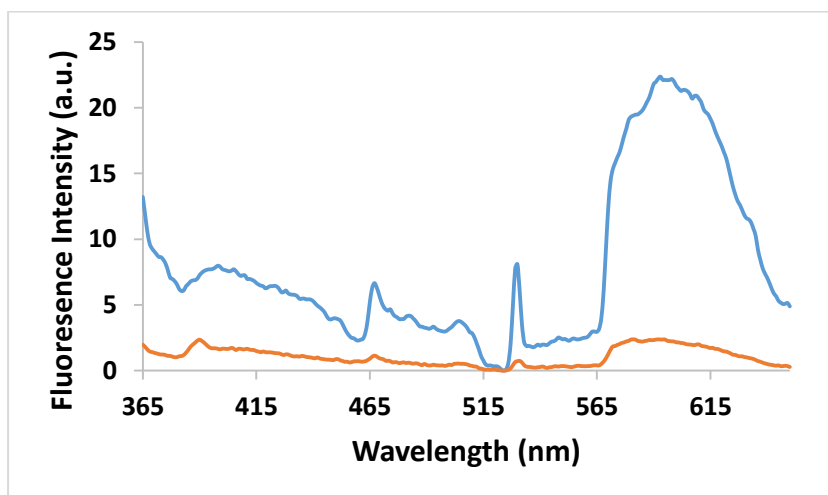


Figure 5.22: Emission spectra of the glass slide ($\lambda_{\text{ex}}=343$ nm) in a solvent free (blue) and water filled (orange) cuvette.

Two solutions of **PIC** were prepared at 0.5 mg/mL in DCM and in MeCN. Glass slides were covered with the solution, the solvent was allowed to evaporate under ambient conditions and the process repeated until four *layers* of the sample were introduced to each slide. The slides were dried overnight at rt in a vacuum desiccator at 833.3 mbar.

The samples prepared from the MeCN solution did not securely adhere to the glass slide; it gradually fell off when the slide was moved or placed into the cuvette, thus, this sample was not pursued further.

One glass slide coated from the solution of **PIC** in DCM was placed diagonally in an empty quartz cuvette (*i.e.* air filled, solvent free) with the coated side facing the excitation light source, **Figure 5.23**. The emission intensity, measured using $\lambda_{\text{ex}} = 343$ nm, exceeded the detector limit of 1000 a.u. with a band width of 111 nm at the maximum intensity, this band width reduced to 94 nm after 18 mins, **Figure 5.24a**. However, at this point it was concluded that the sample was too dense and a new sample with fewer layers of the **PIC**/DCM solution would be desirable for further work.

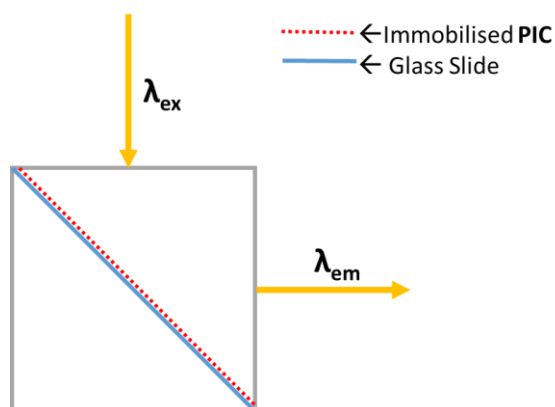


Figure 5.23: Schematic of the orientation of the glass slides containing **PIC** in the quartz cuvettes.

The stability of the fluorescence intensity of the glass supported drop-casted sample of **PIC**/DCM was investigated in pure water by placing a second glass slide, also coated with four layers of the **PIC**/DCM solution in a cuvette containing 3000 μL of water. The fluorescence spectra were recorded, however, the same trend of intense emission with a continual decrease over time was observed, **Figure 5.24b**.

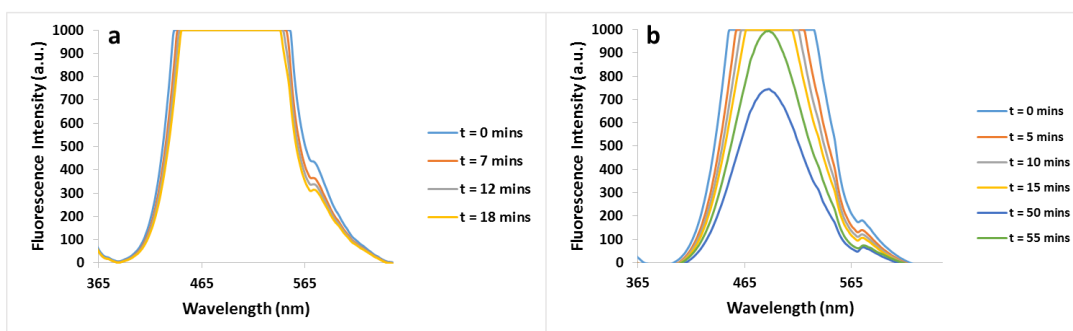


Figure 5.24: Emission spectra of a solid sample of **PIC** deposited on a glass slide from a DCM solution (four layers), $\lambda_{\text{ex}} = 343$ nm placed in a **a)** solvent free and **b)** water filled cuvette.

In order to avoid signal saturation a further set of glass slides were prepared as described above, but with the deposition of only a single layer of the DCM solution of **PIC**. Fluorescence spectra were recorded in a solvent free cuvette. However, initial emission intensity exceeding 1000 a.u. again, before decreasing over time, **Figure 5.25**.

This data could suggest that the drop-casted samples may have equilibrated on the solid support forming solid state inter- and intramolecular interactions, this aggregation could lead to an ACQ effect over time.

It was hypothesised that introducing a more *dilute*, polymer doped **PIC** sample would allay this issue. The introduction of a polymer support would also be helpful in ensuring adherence of **PIC** to the glass slide which was problematic for the MeCN drop-casted sample.

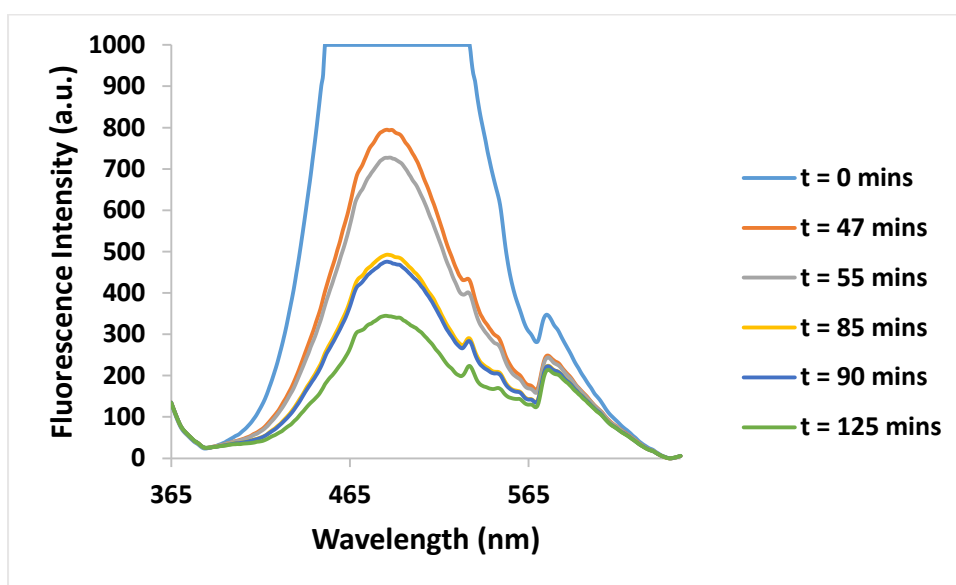


Figure 5.25: Emission spectra of a solid sample of **PIC** deposited on a glass slide from a DCM solution (one layer), $\lambda_{\text{ex}} = 343 \text{ nm}$ placed in a solvent-free cuvette.

5.5.2 Introduction to Nanofibers and Electrospinning

Electrospun nanofibers have become popular in recent years; their inherently smaller pores and higher surface area than regular nanofibers permit utility in applications including nanofiltration of various media,²⁰³ tissue engineering,²⁰⁴ biomedical and biosensor materials,²⁰⁵ protective clothing,²⁰⁶ drug delivery²⁰⁷ and affinity membranes.²⁰⁸ An unwoven mat of functional polymeric nanofibers can provide an

ideal scaffold for sensor applications.²⁰⁹ For these reasons electrospinning was chosen as an approach to incorporate **PIC** into a nanofibrous polymeric layer for metal ion sensor applications in aqueous media.

Electrospinning is a simple and versatile technique which can be used for generating continuous nanofibers from a number of materials, of which polymers are predominant. The technique involves utilising electrical forces to produce polymeric nanofibers with diameters ranging from 2 nm to several micrometres.

The general set-up of an electrospinning apparatus consists of three main components: a high voltage power supply, a spinneret (*i.e.* a metallic needle) and a grounded collector plate, **Figure 5.26**. A solution, typically of a polymer, is placed in a syringe connected to the spinneret *via* plastic tubing. A syringe pump is used to control the feeding rate of the solution. A high voltage (1 – 30 kV) is applied and the pendant drop at the tip of the metallic needle becomes highly electrified, with the induced charge evenly distributed over the surface of the droplet. This results in the drop experiencing two major electrostatic forces: the Coulombic force exerted by the external electrical field and the electrostatic repulsion between the surface charges on the droplet. These two forces result in the pendant drop becoming distorted into a conical shape known as a Taylor Cone, shown inset **Figure 5.26**. When the strength of the electric field surpasses a threshold value, the electrostatic forces can overcome the surface tension of the polymer solution and this results in a charged jet being ejected which travels to the grounded target, generating nanofibers typically in the form of a nonwoven mat.

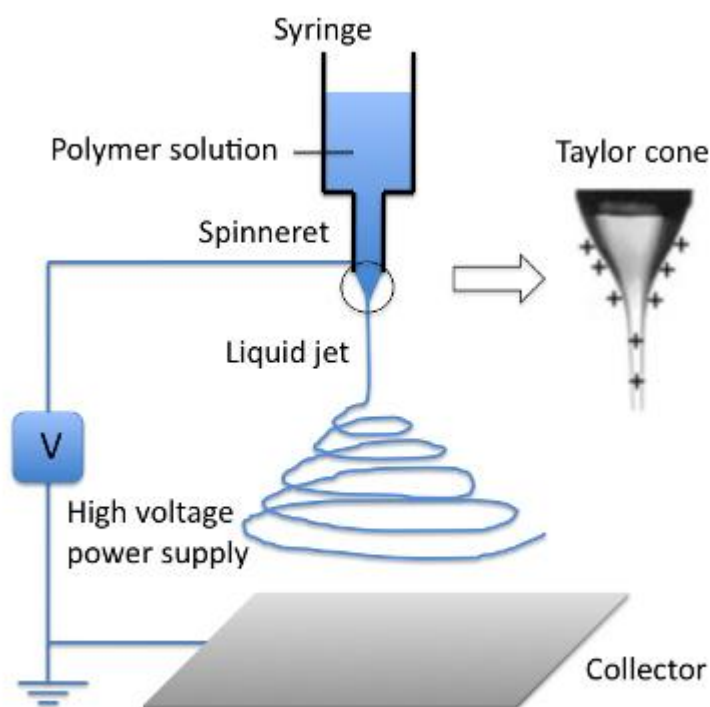


Figure 5.26: Schematic diagram of a general electrospinning set-up.²¹⁰

Although the fundamental theory of electrospinning is relatively simple, the process can prove quite complex due to the large number of parameters that can influence the size and morphology of the fibers that form. These include but are not limited to: **i)** the choice of polymer, **ii)** the solution viscosity, which relates to both the polymer concentration and the choice of solvent or solvent mixture, **iii)** the electrical conductivity and surface tension of the solution, **iv)** the applied voltage, **v)** the flow rate of the solution and **vi)** the distance between the needle tip (spinneret) and the collector plate. These parameters and their influence on the structure and morphology of nanofibers are discussed in a number of interesting literature reviews.²¹¹⁻²¹³

5.5.2.1 Electrospinning of Polycaprolactone (PCL)

Polycaprolactone (PCL), **Figure 5.27** is a biodegradable polyester which has been widely used in medical applications due to its inherent biocompatibility.²¹⁴ It is also commonly used in the electrospinning field with the resulting materials having applications including but not limited to nerve tissue engineering,²¹⁵ drug delivery,²⁰⁷ cell adhesion²¹⁶ and fluorescent sensors.²¹⁷ Due to the broad applicability of PCL as a

host polymer in electrospinning experiments, and its successful utilisation at Maynooth University within the group of Dr. Trinidad Velasco-Torrijos,²¹⁸ it was chosen as the supporting polymer for an examination of the synthesis and properties of electrospun **PIC** incorporating fibers.

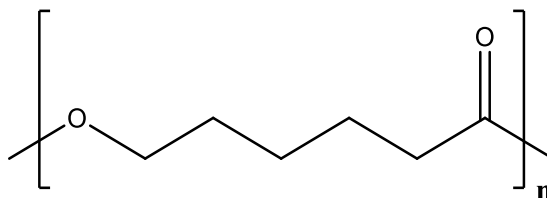


Figure 5.27: Structure of polycaprolactone (PCL).

A 10% w/v solution of PCL was prepared in CHCl_3 :EtOH (3:1, v/v) as follows; the polymer (1.00 g) was dissolved in CHCl_3 (7.5 mL) and the solution was stirred overnight. Addition of EtOH (2.5 mL) followed, and the mixed solvent solution stirred for a further 2 hours. Two samples of the PCL solution were electrospun according to the parameters shown in **Table 5.12** and allowed to dry at rt overnight in a vacuum desiccator at 833.3 mbar.

Table 5.12: Electrospinning parameters applied to a 10% w/v solution of PCL in CHCl_3 :EtOH (3:1, v/v).

Sample No.	Applied Voltage (kV)	Spinneret-Copper Plate Distance (cm)	Solution Feed Rate (mL/hr)
1	15	10	1
2	20	10	1

Both electrospun samples were examined by optical and scanning electron microscopy (SEM) and were shown to be pure microfibers with average diameters of 5.19 μM at 15 kV and 3.51 μM at 20 kV. The average diameter was calculated from a random sample of 10 fibers for each sample, **Figure 5.28**.

In electrospinning experiments, the voltage applied is known to influence the diameters of the resultant fibers, however, the level of significance varies with polymer concentration and the distance between the spinneret and the grounded collector plate.²¹⁹ The voltage parameter can have opposing effects on diameter; a

high voltage leads to increased rates of polymer ejection from the spinneret and thus facilitates the formation of fibers of larger diameter. However, due to the higher electric field strength at higher voltages the electrostatic repulsive forces on the polymeric fluid jet increase which favours the narrowing of the fiber diameter.²²⁰ Higher voltages also result in faster evaporation of the solvent which produces narrower fibers.²¹⁰

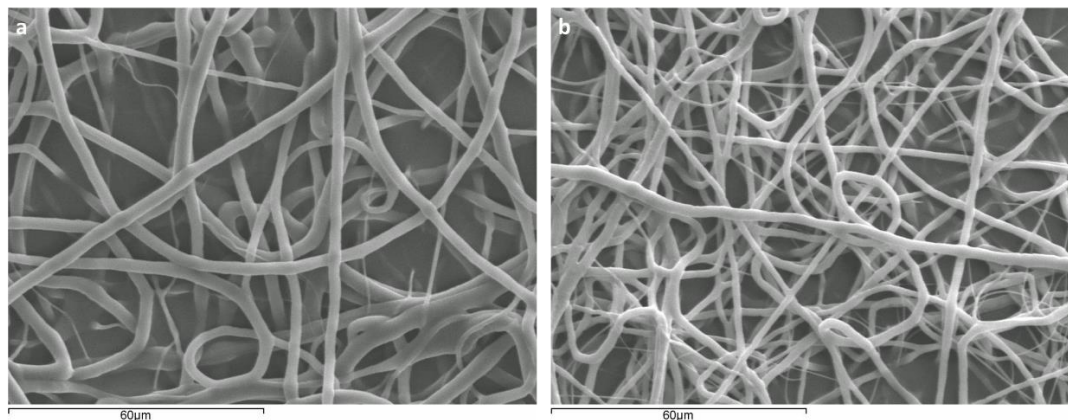


Figure 5.28: SEM images of 10% w/v polycaprolactone (PCL) in CHCl_3 :EtOH (3:1, v/v) electrospun with a distance of 10 cm between the spinneret and the collector plate at a feed rate of 1 mL/hr at an applied voltage of; **a)** 15 kV and **b)** 20 kV.

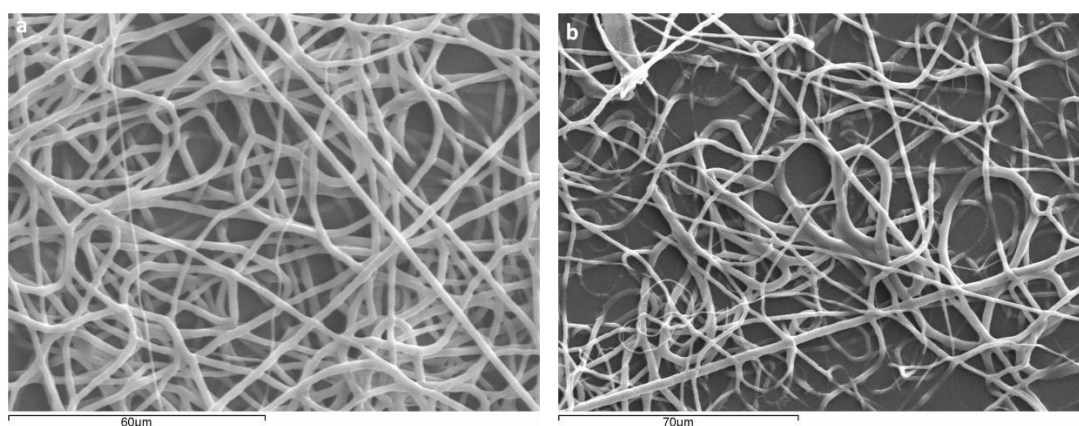
Following the successful production of supporting microfibers from electrospinning a PCL solution, a second solution was prepared incorporating the fluorescent calixarene **PIC**. The addition of any material to the spinning solution may cause changes to its properties including conductivity, viscosity, elastic strength and viscoelasticity, these changes can thus alter the structure and morphology of the resultant fibers.²²¹ Thus, electrospinning of a solution of PCL containing **PIC** could have been expected to produce fibers displaying a different morphology to that of the polymer alone.

PIC (20 mg) was dissolved in the PCL 10% w/v solution (5 mL) to produce a solution with 4% w/w **PIC** *in situ* w.r.t. the polymer in CHCl_3 :EtOH (3:1, v/v). Two samples of this **PIC** doped PCL solution were electrospun according to the parameters developed for spinning the polymer alone, **Table 5.13** and allowed to dry overnight at rt in a vacuum desiccator at 833.3 mbar.

Table 5.13: Electrospinning parameters applied to a 10% w/v polycaprolactone (PCL) solution with 4% w/w **PIC** *in situ* w.r.t. the polymer in CHCl₃:EtOH (3:1, v/v).

Sample No.	Applied Voltage (kV)	Spinneret-Copper Plate Distance (cm)	Solution Feed Rate (mL/hr)
1	15	10	1
2	20	10	1

The samples were visually examined under a UV lamp ($\lambda_{\text{ex}} = 365 \text{ nm}$) and appeared uniformly fluorescent. Further examination by optical and scanning electron microscopy showed the formation of pure microfibers with average diameters of 2.47 μM at 15 kV and 3.74 μM at 20 kV ($n=10$), **Figure 5.29**.

**Figure 5.29:** SEM images of 10% w/v polycaprolactone (PCL) with 4% w/w **PIC** *in situ* w.r.t. the polymer in CHCl₃:EtOH (3:1, v/v) electrospun with a distance of 10 cm between the spinneret and the collector plate and 1 mL/hr as the feed rate at an applied voltage of; **a)** 15 kV and **b)** 20 kV.

Examination of the average diameters of the PCL and **PIC**-PCL microfibers (**PIC**/PCL MFs) electrospun at 15 and 20 kV were approximately the same for samples prepared at 20 kV, **Table 5.14**, but at 15kV, the average diameter of the doped MFs is approximately half that of the polymer MFs. The variation could be attributed to a change in solution viscosity, conductivity or surface tension at this different voltage.²²⁰

Table 5.14: Average diameters of PCL and PIC/PCL MFs at applied voltages of 15 and 20 kV.

	Diameter of PCL MFs (μM)	Diameter of PIC/PCL MFs (μM)
15 kV	5.19	3.51
20 kV	2.47	3.74

Fluorescence microscopy was considered as a tool for further characterisation of the PIC/PCL MFs, however the shortest laser line excitation wavelength on the Olympus FluoView1000 Laser Scanning Confocal Microscope available for use within the biology department at Maynooth University was 405 nm. This was deemed unsuitable for studying a sample of PIC, as there is no significant absorption at this wavelength, **Figure 5.11**.

Following identification of appropriate parameters for production of PIC doped PCL microfibers, the experiment was repeated under the same conditions (15 kV) and the fibers collected on a glass slide (0.13-0.17 mm thick) placed on the grounded copper plate.

As discussed for the drop-casted solutions of PIC, reproducibility of the samples prepared by electrospinning is difficult, and thus the effective concentration of PIC was expected to vary slightly between samples. To obtain a reference fluorescence spectrum for further studies of PIC/PCL MFs as a copper sensing material, the glass slide was placed diagonally to touch opposite corners of a cuvette with the surface bearing the microfibers facing the excitation light source, **Figure 5.23**. The cuvette was filled with water and the sample excited ($\lambda_{\text{ex}} = 343 \text{ nm}$), blue plot in **Figure 5.30**. The emission profile of the fresh sample displayed both monomer (387, 408 and 433 nm) and excimer (488 nm) bands. The ratio of the intensity of the excimer to the first monomer (387 nm) band was ~ 0.93 . A second spectrum was obtained following 10 mins standing in the aqueous medium, orange plot in **Figure 5.30**, displayed a reduction in the intensity of both bands. Three further spectra, obtained at 20, 90 and 100 mins showed a continued decrease in signal intensity with the decline in the excimer signal being rather sharp.

To allay concerns that **PIC** may have leached from the microfibers into the water, the glass slide was removed and a fluorescence spectrum of the solvent was recorded. No emission was observed suggesting there was no **PIC** in the solution. However, due to the insolubility of **PIC** in water it was deemed possible that leached **PIC** may have fallen as particulate matter to the bottom of the cuvette. This possibility was ruled out following spectroscopic analysis of a solution prepared by replacing the “top” 1500 μL from the cuvette with the same quantity of MeCN and agitating the solution. No emission was observed following excitation at $\lambda_{\text{ex}}=343$ nm of this 50% v/v aq. MeCN solution, confirming that, under the conditions of the experiment, no **PIC** had leached from the **PIC**/PCL MFs into the water.

As **PIC** was shown to remain incorporated into the **PIC**/PCL MFs in the aqueous medium, the reduction in emission intensity over time was considered to be a result of surface aggregate formation between the **PIC** moieties likely driven by realignment following exposure to the water.

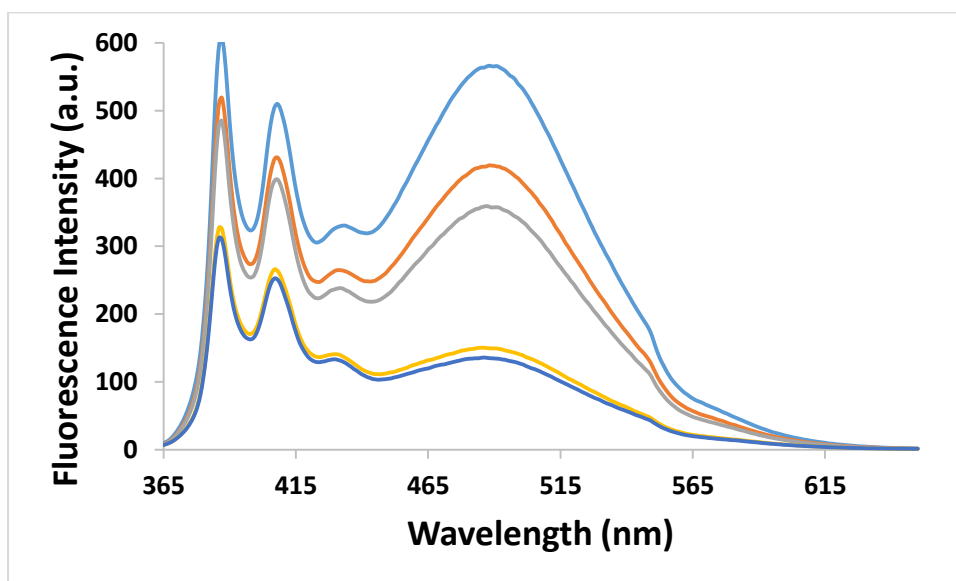


Figure 5.30: Emission spectra of **PIC**/PCL MFs deposited on a glass slide and placed in a cuvette of water, $\lambda_{\text{ex}} = 343$ nm at $t = 0$ mins (blue), 10 mins (orange), 20 mins (grey), 90 mins (yellow), 100 mins (dark blue).

The initial fluorescence study of the glass slide supported **PIC**/PCL MFs indicated an instability in the emission intensity in an aqueous environment, possibly influenced by the presentation of **PIC** within the microfibers, aggregation of **PIC** in the 100% aqueous medium or the use of the glass slide as a solid support.

In order to investigate the effect of the medium, a second sample was analysed in a solvent free environment. The surface of the slide carrying the microfibers was orientated facing the excitation light source, as shown in **Figure 5.23**.

The emission spectrum of the second glass slide in the empty cuvette was recorded, both monomer (388 and 410 nm) and excimer (487 nm) bands were displayed, blue plot in **Figure 5.31**. In contrast to the sample recorded standing in water, the ratio of intensity of the excimer to the first monomer band was calculated to be 1.05. The slight difference in excimer to monomer ratio of the two samples (0.93 and 1.05) reinforces the issue with sample reproducibility. Thus, the presentation and quantity of the fluorescent **PIC** in each sample was crucial to the resultant fluorescence emission profile.

Emission spectra obtained following 10 and 20 mins and 24 hr intervals, showed 23%, 38% and 46% reduction in the intensity at the λ_{\max} of the excimer peak. To ascertain if atmospheric moisture contributed to the changing profile, the glass slide was placed in a vacuum desiccator at rt (833.3 mbar) for 3 days. The fluorescence emission spectrum was re-recorded. The intensity at the λ_{\max} of the excimer peak had reduced by a further 8%. This trend indicated that the **PIC/PCL** MFs deposited onto glass slides were unstable and potential as a sensing system would be limited.

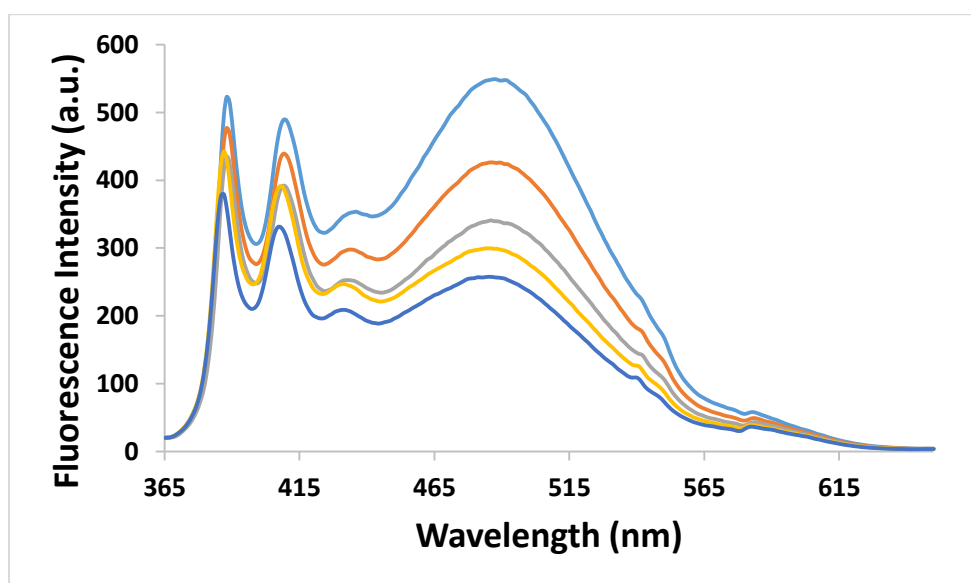


Figure 5.31: Emission spectra of **PIC/PCL** MFs deposited on a glass slide and placed into a cuvette with no solvent medium; $\lambda_{\text{ex}} = 343$ nm at $t = 0$ mins (blue), 10 mins

(orange), 20 mins (grey), 24 hrs (yellow) and following three days storage at rt in a vacuum desiccator at 833.3 mbar (dark blue).

5.5.2.2 Electrospinning of Polysulfone (PSF)

Since PIC/PCL MFs were unstable a second polymeric support was explored. In one interesting report, Min *et al.*, describe an efficient fluorescence sensor suited to Cu^{2+} ion detection from aqueous media. A polymer belonging to the polysulfone family incorporated with a functionalised rhodamine dye was electrospun.²⁰⁹ Polysulfones are a class of thermoplastic polymers, which are rigid, transparent and stable at high temperatures. The rhodamine dye doped polysulfone solution was electrospun onto a rotating drum and the resulting material cut into rectangular slices and placed directly inside a cuvette. The material was sufficiently rigid to remove the requirement for a glass slide support. The rigid sensor, following an extensive washing (MeOH and H_2O) and drying (under nitrogen for 1 hr) procedure could detect copper from aqueous solutions. Thus it was decided to explore polysulfone (PSF), **Figure 5.32**, for subsequent electrospinning experiments with PIC.

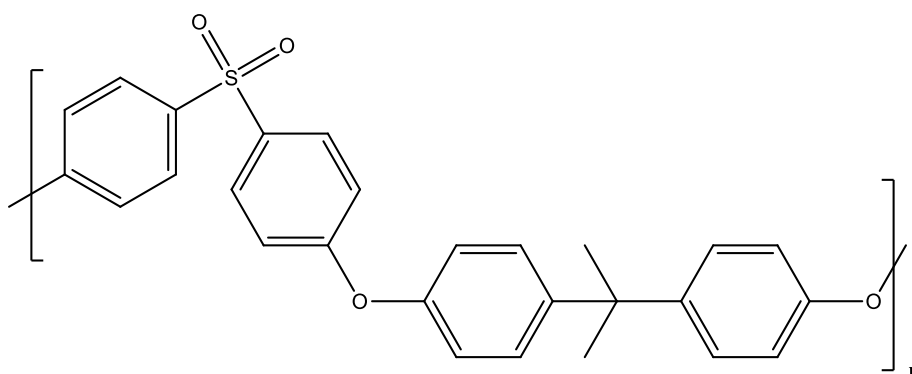


Figure 5.32: Structure of polysulfone (PSF).

Literature reports involving electrospinning of the polysulfone family relied heavily on DMF, DMAc or DMSO as either pure or cosolvents. These solvents have associated health and safety issues so a different solvent system was explored. A 20% w/v solution of PSF was prepared in chloroform, this involved dissolving PSF (2 g) in CHCl_3 (10 mL) by portion-wise addition of the polymer to a rapidly stirring solution of CHCl_3 . Three samples of this solution were electrospun according to the parameters shown in **Table 5.15** and allowed to dry at rt overnight in a vacuum desiccator at 833.3 mbar.

Table 5.15: Electrospinning parameters applied to a 20% w/v solution of PSF in CHCl_3 .

Sample No.	Applied Voltage (kV)	Spinneret-Copper Plate Distance (cm)	Solution Feed Rate (mL/hr)
1	15	10	2
2	15	10	1
3	20	10	1

All three electrospun samples were examined by optical and SEM microscopy and were shown to comprise electrospayed PSF clusters with little evidence of fibers between the clusters, **Figure 5.33**.

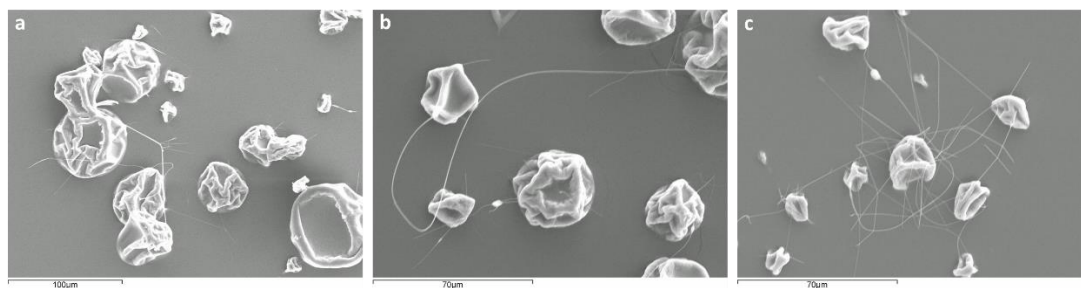


Figure 5.33: SEM images of 20% w/v polysulfone (PSF) in CHCl_3 electrospun with a distance of 10 cm between the spinneret and the collector plate; **a)** 15 kV and 2 mL/hr, **b)** 15 kV and 1 mL/hr and **c)** 20 kV and 1 mL/hr.

One of the undesired features of nanofibers produced from electrospinning is beading since it leads to a reduced surface area. To overcome beading effects high molecular weight polymers and high solution concentrations can be used, this is because entanglements and overlapping between polymer chains plays a crucial role for producing bead-free, uniform nanofibers.²²² Thus three samples were electrospun from a solution of 30% w/v PSF in CHCl_3 according to the parameters shown in **Table 5.16** and allowed to dry overnight at rt in a vacuum desiccator at 833.3 mbar.

Table 5.16: Electrospinning parameters applied to a 30% w/v solution of PSF in CHCl₃.

Sample No.	Applied Voltage (kV)	Spinneret-Copper Plate Distance (cm)	Solution Feed Rate (mL/hr)
1	10	10	1
2	15	10	1
3	20	10	1

No spinning was observed at 10 kV, and only drops of the solution fell from the electrified syringe needle. However, bead-free microfibers formed at 15 and 20 kV, **Figure 5.34**. They had a flat appearance with average diameters of 6.54 μM at 15 kV and 5.86 μM at 20 kV (n=10).

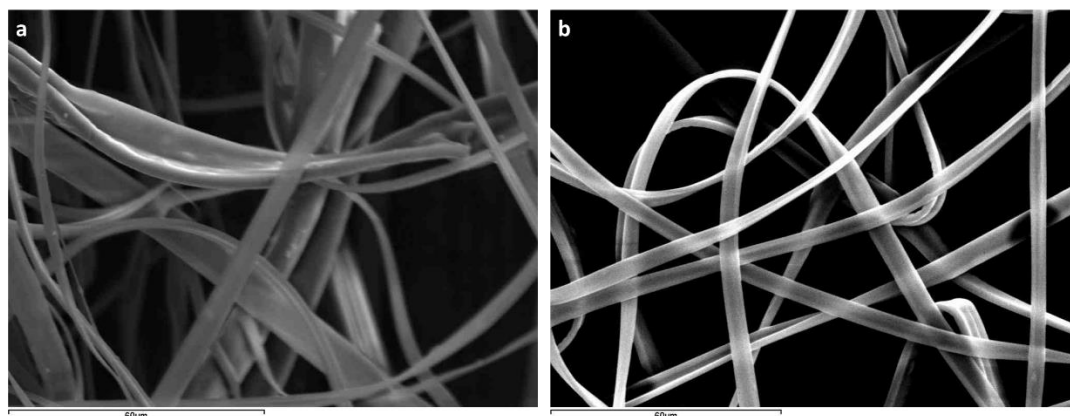
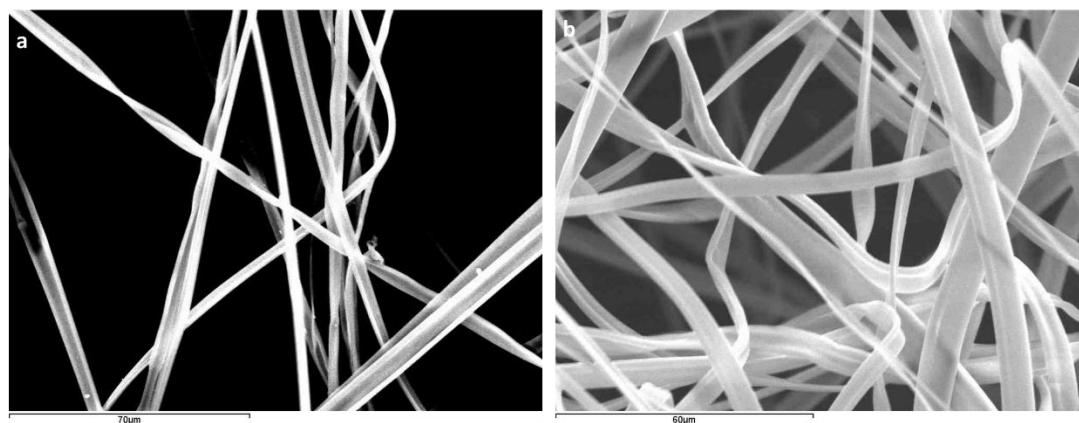


Figure 5.34: SEM images of 30% w/v polysulfone (PSF) in CHCl₃ electrospun with a distance of 10 cm between the spinneret and the collector plate and 1 mL/hr as the feed rate at an applied voltage of; **a)** 15 kV and **b)** 20 kV.

Following the successful production of bead-free microfibers from a 30% w/v solution of PSF in CHCl₃, **PIC** (20 mg) was dissolved in the PSF solution (10 mL) to produce a solution with 0.67% w/w **PIC** *in situ* w.r.t. the polymer in CHCl₃. This **PIC** doped PSF solution was electrospun according to the parameters shown in **Table 5.17** and allowed to dry overnight at rt in a vacuum desiccator at 833.3 mbar. All electrospun samples were examined by optical and SEM microscopy and were shown to be pure microfibers with an average diameter of 8.99 μM at 15 kV and 9.74 μM at 20 kV (n=10), **Figure 5.35**. The fibers appeared fluorescent following visual examination under a UV lamp (365 nm).

Table 5.17: Electrospinning parameters applied to a 30% w/v polysulfone (PSF) solution with 0.67% w/w PIC w.r.t. the polymer in CHCl₃.

Sample No.	Applied Voltage (kV)	Spinneret-Copper Plate Distance (cm)	Solution Feed Rate (mL/hr)
1	15	10	1
2	20	10	1

**Figure 5.35:** SEM images of 30% w/v polysulfone (PSF) and 0.67% w/w PIC w.r.t. the polymer in CHCl₃ electrospun with a distance of 10 cm between the spinneret and the collector plate and 1 mL/hr as the feed rate at an applied voltage of; **a)** 15 kV and **b)** 20 kV.

Unlike the rigid material formed by Min and co-workers,²⁰⁹ the electrospun PIC doped PSF microfibers (PIC/PSF MFs) after several hours of electrospinning of the solution were insufficiently rigid to allow them to be cut into uniform strips. As a compromise, a hollow glass tube was selected as a solid support. An initial investigation of the fluorescence behaviour of the glass tube standing in a solvent free cuvette revealed a low level of background emission with a maximum of ~6 a.u., **Figure 5.36**. Thus, it was deemed appropriate to measure the emission spectra of MFs supported on the glass tube.

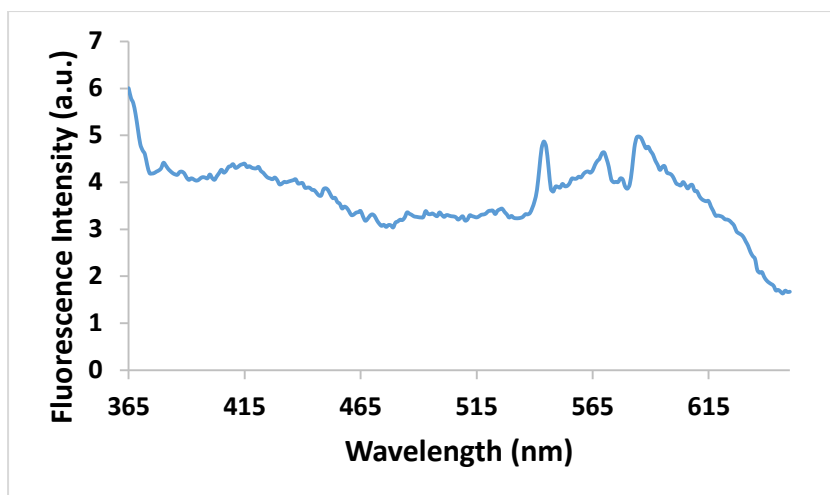


Figure 5.36: Emission spectrum of the hollow glass tube ($\lambda_{\text{ex}}=343$ nm) in a solvent free cuvette.

Small portions of the PSF microfibers with and without incorporated **PIC** were wrapped around a hollow glass tube and the emission spectra of both samples were recorded with $\lambda_{\text{ex}} = 343$ nm. Significantly the scaffolding PSF microfibers were themselves fluorescent, **Figure 5.37a**, grey plot.

In order to identify excitation wavelengths that may produce fluorescence emission from **PIC** but not from PSF the absorbance spectrum of **PIC** was re-examined. **PIC** absorbs in three main regions with λ_{max} at 237, 280 and 343 nm. PSF and **PIC** solutions, in chloroform, were excited at all three wavelengths and the emission spectra recorded, **Figure 5.37a** and **b**. The data showed that PSF in solution only emitted fluorescence with 343 nm as the excitation wavelength. **PIC** emitted strong fluorescence when excited at 280 and 343 nm, with a profile indistinguishable from that recorded in MeCN, weaker signals were observed upon excitation at $\lambda_{\text{ex}} = 237$ nm. Thus it was hypothesised that excitation of the **PIC/PSF** MFs at 237 or 280 nm may produce emission that could be solely attributed to the incorporated **PIC** and not the polymer.

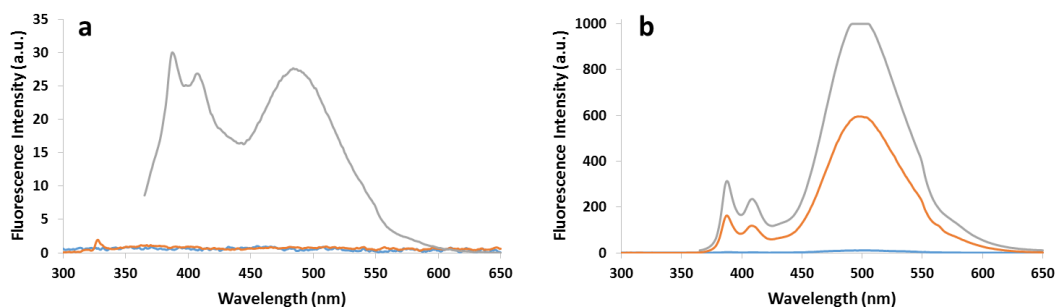


Figure 5.37: Emission spectra of solutions of **a)** PSF (10 mg/mL) and **b)** PIC (20 μ M) in CHCl_3 following excitation at $\lambda_{\text{ex}} = 237$ nm (blue), 280 nm (orange) or 343 nm (grey).

Small portions of the PSF microfibers and the **PIC/PSF** MFs were wrapped around a hollow glass tube and placed in a cuvette with no solvent. Emission spectra were recorded for both samples at $\lambda_{\text{ex}} = 237$ and 280 nm. The data, summarised in **Figure 5.38** show significant fluorescence emission in all cases.

Large sharp bands were observed at 475 nm ($\lambda_{\text{ex}} = 237$ nm) and 562 nm ($\lambda_{\text{ex}} = 280$ nm), which were attributed to an overtone of the excitation frequencies. These occur at exactly twice the wavelength of the excitation wavelength.

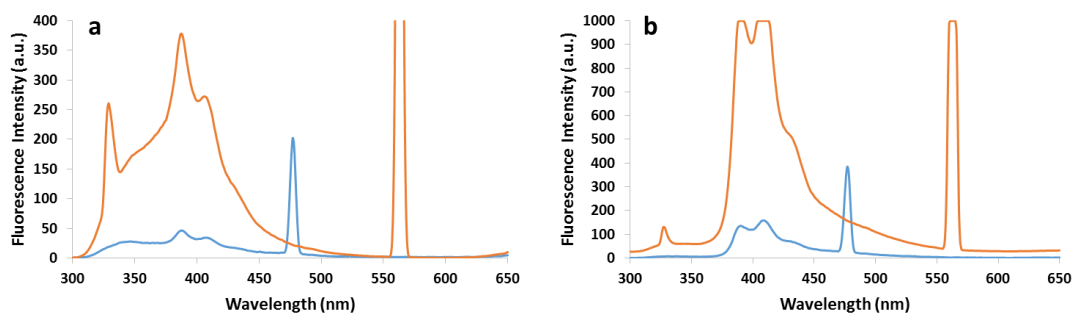


Figure 5.38: Emission spectra of **a)** PSF microfibers and **b)** **PIC/PSF** MFs wrapped around a hollow glass tube solid support in a solvent free cuvette; $\lambda_{\text{ex}} = 237$ nm (blue) and 280 nm (orange).

Emission spectra were also recorded for small portions of the PSF and the **PIC/PSF** MFs in the absence of a solid support at $\lambda_{\text{ex}} = 237$ and 280 nm. The spun fibers were carefully placed in the middle of an empty quartz cuvette. The spectrum of the PSF microfibers showed little fluorescence activity, **Figure 5.39a**, while the **PIC/PSF** MFs emitted a distinct fluorescence profile at both excitation wavelengths, **Figure 5.39b**. Emission occurred predominantly between 375 and 450 nm, attributed to pyrene monomer emission. Excimer emission was not evident, this was attributed to the

immobilisation of **PIC** within the polymeric microfibers which would make diffusional encounters between an excited and ground state pyrene unlikely.

The dramatic difference between the emission profiles of the glass tube supported, **Figure 5.38a** and the unsupported samples of PSF, **Figure 5.39a**, suggest that the glass tube is contributing to the observed fluorescence of PSF and it should be avoided in any further investigations.

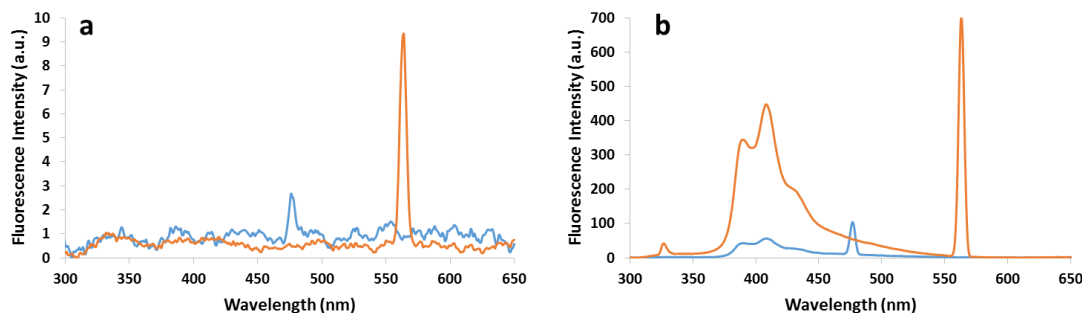


Figure 5.39: Emission spectra of **a)** PSF microfibers and **b)** PIC/PSF MFs with no hollow glass tube solid support in a solvent free cuvette; $\lambda_{\text{ex}} = 237$ nm (blue) and 280 nm (orange).

Small portions of the **PIC/PSF** MFs were immersed in millipore water, patted dry and placed in a quartz cuvette and their emission spectra recorded at $\lambda_{\text{ex}} = 237$ and 280 nm, blue plots in **Figure 5.40a** and **b**. The same material samples were then immediately immersed in an aqueous solution of copper perchlorate, patted dry and a second set of spectra acquired, orange plots in **Figure 5.40a** and **b**. Fluorescence quenching occurred in both cases indicating that the Cu^{2+} ion was being detected from aqueous solutions.

The low intensity of the emission signals w.r.t. the **PIC/PSF** NF sample studied in **Figure 5.39b** reiterates the previously stated expectation that difficulty in reproducibility of the emission intensities would be encountered, however, as a proof of concept the **PIC/PSF** MFs were effective as Cu^{2+} indicators from aqueous samples.

In the experimental design the extensive washing of the fibers in the protocol of Min and co-workers,²⁰⁹ was avoided in the fluorescence experiments involving the **PIC/PSF** MFs, in order to create a robust, widely applicable copper ion sensing tool

for environmental applications within field studies. However, it is possible that a more definitive response could have been found with their procedure.

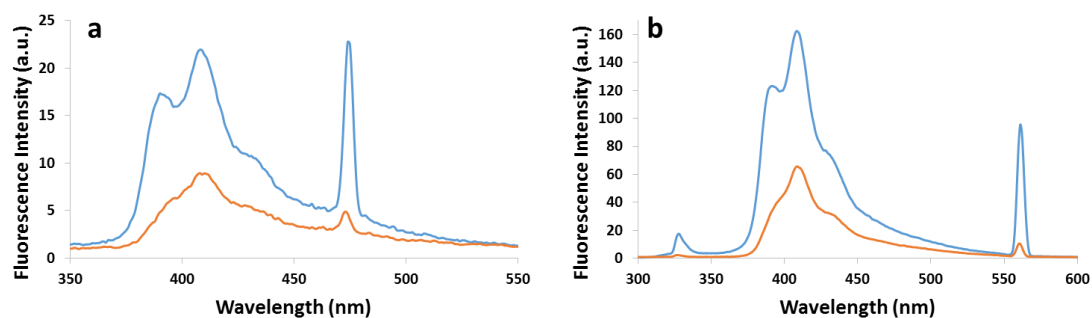


Figure 5.40: Emission spectra of PIC/PSF MFs after exposure to water (blue) and then immediately to an aqueous copper perchlorate solution (orange) at $\lambda_{\text{ex}} =$ **a)** 237 nm and **b)** 280 nm.

In order to further probe the sensing potential of the PIC/PSF MFs a competitive metal ion study was conducted. This involved measuring the fluorescence emission spectra of damp microfibers at excitation wavelengths of 237 and 280 nm, then immersing the same portion of microfibers into an aqueous solution of a competitive metal ion ($\text{Ca}(\text{ClO}_4)_2$, $\text{Pb}(\text{ClO}_4)_2$, $\text{Mn}(\text{ClO}_4)_2$, $\text{Zn}(\text{ClO}_4)_2$, $\text{Hg}(\text{ClO}_4)_2$, $\text{Ni}(\text{ClO}_4)_2$, $\text{Co}(\text{ClO}_4)_2$ and AgClO_4), measuring the emission spectra of these microfibers and finally immersing the same portion of microfibers into an aqueous copper perchlorate solution and measuring the emission spectrum, **Figure 5.41A** ($\lambda_{\text{ex}} = 237$ nm) and **Figure 5.41B** ($\lambda_{\text{ex}} = 280$ nm). A fresh portion of microfibers was used for each competitive metal ion, thus each sample is not identical and each set of spectra displayed are only internally comparable. Since the host samples are not quantifiable, the effective number of eqs of each metal salt in solution w.r.t. the portion of PIC/PSF MFs is not ascertainable. Thus, data obtained from the initial experiments could provide qualitative but not quantitative information about the metal ions present in solution.

In the cases of exposure of the damp microfibers to aqueous solutions of $\text{Ca}(\text{ClO}_4)_2$, $\text{Ni}(\text{ClO}_4)_2$ and AgClO_4 fluorescence quenching occurred, while all other metal perchlorates induced an enhancement of the emission profile at both excitation wavelengths. However, regardless of the nature of the metal perchlorate, the “portion size” of microfiber samples, and whether an initial quenching or

enhancement of the emission profile had occurred, the subsequent introduction of aqueous copper perchlorate solutions to the metal contaminated microfibers caused quenching in all cases. Thus it may be concluded that the **PIC/PSF** MFs have potential as a fluorescent indicator for the Cu^{2+} ion in water samples, with minimal interference from other competitive metal ions.

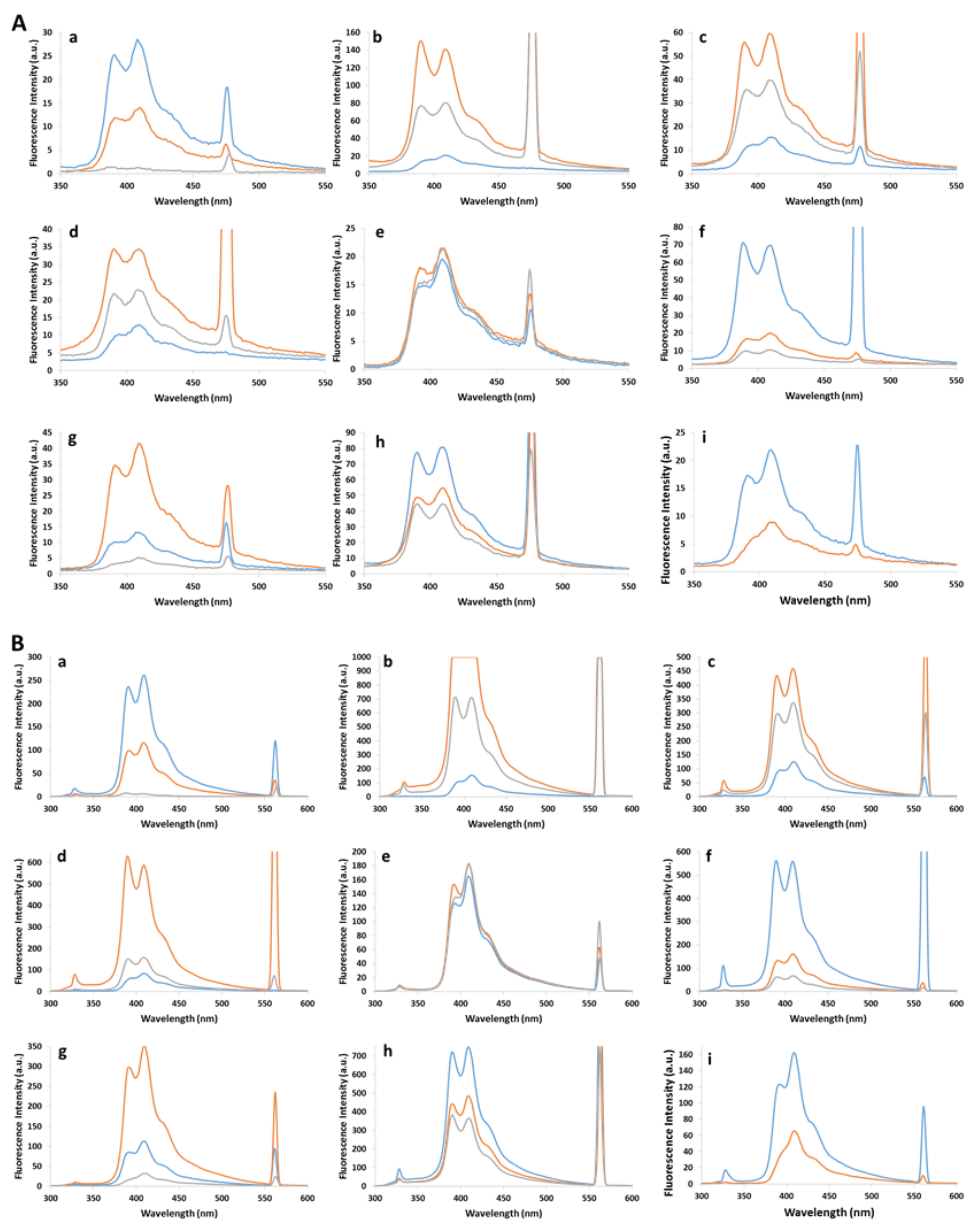


Figure 5.41: Emission spectra of **PIC/PSF** MFs $\lambda_{\text{ex}} =$ **A)** 237 nm and **B)** 280 nm; after exposure to water (blue); followed by exposure to an aqueous $\text{M}^{n+}(\text{ClO}_4^-)_n$ solution (orange); and subsequent exposure to an aqueous copper perchlorate solution (grey); where $\text{M}^{n+} =$ **a)** Ca^{2+} , **b)** Pb^{2+} , **c)** Mn^{2+} , **d)** Zn^{2+} , **e)** Hg^{2+} , **f)** Ni^{2+} , **g)** Co^{2+} , **h)** Ag^+ ; and **i)** after exposure to water (blue) and then immediately to an aqueous copper perchlorate solution (orange).

5.6 Solid Supports Study - Conclusions

- Glass slide drop-casted samples of **PIC** from DCM and MeCN were prepared. The sample from MeCN failed to adhere to the support and that from the DCM solution failed to show an *equilibrated* fluorescence profile in an air or water medium and was deemed unsuitable for further studies.
- Electrospun microfiber samples of **PIC** were prepared, supported on glass slides for sensor applications in aqueous systems.
- Electrospun PCL and **PIC**/PCL producing bead-free microfibers were analysed by optical and scanning electron microscopy.
- Fluorescence emission spectra of glass supported **PIC** doped PCL microfibers were recorded in aqueous and solvent-free environments. In both cases the fluorescence emission intensity was unstable over extended periods of time, limiting their potential utility as Cu^{2+} ion sensors.
- PSF and **PIC**/PSF MFs were successfully electrospun into bead-free microfibers. These microfibers proved effective as fluorescent indicators of the Cu^{2+} ion in aqueous solutions when used in small portions in a solvent-free medium.

Chapter 6

Conclusions and Future Work

A novel calix[4]arene chemosensor, **PIC**, equipped with distal isoxazole units as potential metal binding sites and pyrene units as aryl fluorophores was synthesised by catalyst-free nitrile oxide/alkyne cycloaddition (NOAC), it represents one of the first examples of an isoxazole functionalised calix[4]arene.

PIC presented in the cone conformation in the solution and solid state, as evidenced by ^1H NMR spectroscopy and x-ray crystallography, respectively. Intramolecular π - π interaction of the pyrene moieties in the solution state was indicated by excimer emission in the fluorescence spectrum. No such interactions were evident in the solid state structures.

Excimer quenching occurred in the presence of Cu^{2+} ions only over a range of other divalent transition metal cations, introduced as perchlorate salts. A ^1H NMR spectroscopic study suggested the Cu^{2+} ion binding site involved the isoxazole-pyrene region. Stern-Volmer analysis indicated that the quenching mechanism was purely static up to two eqs of Cu^{2+} . The binding constant (K_a) between **PIC** and copper perchlorate in MeCN, calculated using the Benesi-Hildebrand method, was found to be $47,000 \text{ M}^{-1}$. The detection limit of **PIC** for Cu^{2+} ions in MeCN was $0.3 \mu\text{M}$.

Three novel calixarenes structurally related to **PIC**; were synthesised to study the relationship between host structure and ion sensing ability. **EPIC**, incorporated an ethylene linker between the lower rim of the calixarene and the isoxazole heterocycle, **PPIC** introduced an alkyl chain between the isoxazole rings and the pyrene units and **MPIC** had methoxy groups in place of the hydroxyl groups of **PIC**.

EPIC and **PPIC** presented as cone conformers in solution while **MPIC** was conformationally mobile in solution over the temperature range - 50 to 45°C . NMR spectroscopic data, showed it to present as cone and paco conformers in a 1:2.8 ratio at -30°C . The paco conformer was dominant at all temperatures in the range -30 to 25°C . An x-ray crystal structure of **MPIC** showed that it presented as the paco conformer in the solid state structure, with no evidence of inter- or intramolecular π - π stacking between pyrene moieties. All three molecules displayed monomer and excimer bands in their fluorescence emission spectra.

At the outset of the work presented in this thesis, it was hypothesised that the structural changes incorporated to **EPIC**, **PPIC** and **MPIC** may result in significantly different sensitivities to the Cu^{2+} ion from that observed with **PIC**. As such the new hosts could provide direct information on the functionalities of pyrene appended isoxazole functionalised calixarenes **PIC** necessary for detection of Cu^{2+} . However, in all three cases significant fluorescence quenching occurred in the presence of Cu^{2+} ions with good to reasonable selectivity for copper. Job's plot analysis indicated that **EPIC**, **PPIC** and **MPIC** like **PIC** formed 1:1 complexes with Cu^{2+} . Stern-Volmer analysis showed that the Cu^{2+} induced quenching mechanism of the three pyrene functionalised calixarenes was purely static up to two eqs of $\text{Cu}(\text{ClO}_4)_2$ in MeCN. At higher guest levels a combination of static and dynamic quenching in all three calixarene hosts, **EPIC**, **PPIC** and **MPIC** was observed.

The binding constants (K_a) of **EPIC**, **PPIC** and **MPIC** for copper perchlorate in MeCN, calculated using the Benesi-Hildebrand method, were found to be 29,000, 33,000 and 6,000 M^{-1} , respectively, **Table 4.15**. These values were all lower than the K_a value of 47,000 M^{-1} calculated for **PIC** and Cu^{2+} (Section 2.5.5) which suggested that the structural changes between these and **PIC** had a negative impact on the host:guest complexation. The detection limits calculated indicated that **EPIC**, **PPIC** and **MPIC** accurately detected Cu^{2+} ions in MeCN solution to the lowest concentrations of 0.9, 2.2 and 3.6 μM respectively. Whilst still low, these values indicate that the new molecules are less sensitive to Cu^{2+} than **PIC**.

^1H NMR spectroscopic studies of the effect of the Cu^{2+} ion on all three new functional calixarenes were carried out. In all three cases signals in the pyrene region became broad and unresolved at high concentrations of $\text{Cu}(\text{ClO}_4)_2$ which indicated that the pyrene moiety was in close proximity to the Cu^{2+} cation during the binding event.

The potential for the detection of metal ions in real-world applications was probed by examining the sensing ability of **PIC** for Cu^{2+} ions in aqueous media. The intensity of the excimer band of **PIC** in 5-60% v/v aq. MeCN was found to vary over time until an *equilibration* point was reached. This trend was attributed to ACQ and AIE effects caused by random alignment of the hydrophobic calixarene core and pyrene moieties of **PIC** forming a variety of supramolecular structures.

The existence of **PIC** aggregates in aq. MeCN was supported by SEM and UV-Vis analysis. No evidence of aggregation was observed in samples prepared from 100% MeCN, while irregular aggregates were observed in samples prepared from aq. media. Aggregation was also supported by comparison of the absorbance spectra of **PIC** (4-8 μM) in 100% MeCN and 60% v/v aq. MeCN. P_A values greater than 2.97 measured in the former and less than 2.07 in the latter suggested that aggregation occurred in the aqueous solution.

When the guests were introduced as MeCN solutions, **PIC** in 50% v/v aq. MeCN showed an impressive but not complete selectivity for the Cu^{2+} ion, 92% excimer quenching was observed with 10 eqs of copper, however, Ag^+ ions also caused 22% quenching of the same signal.

PIC, in 5-60% v/v aq. MeCN, showed a wide range of responses with various levels of enhancement or quenching of the excimer band, with copper perchlorate introduced as an aqueous sample. In 50% v/v aq. MeCN, 85% quenching of the excimer band occurred following exposure to 10 eqs of aqueous copper perchlorate. This compares very favourably to the >90% quenching observed in 100% MeCN under the same experimental conditions.

In 60% v/v aq. MeCN, some degree of quenching of the excimer band of **PIC** occurred following exposure to 50 eqs of aqueous metal perchlorates. Significant quenching levels, >25% with zinc, lead, silver, copper and mercury perchlorates, suggested that in the aqueous environment the water solvated metal ions have a wider range of binding opportunities than are available in MeCN solutions as a consequence of the formation/disruption of **PIC** aggregates in the aqueous media.

SEM analysis of a drop-casted and vacuum dried 50% v/v aq. MeCN solution containing **PIC**: $\text{Cu}(\text{ClO}_4)_2$ (1:1) revealed a lower density of non-uniform aggregates compared to a similarly prepared sample of the host-alone. An area of high density well-structured honeycomb like aggregates formed, supporting the hypothesis that the metal ions can influence the type of aggregates formed.

Solid state emission properties were investigated by drop-casting of solutions of **PIC**, in DCM and MeCN, onto a glass slide. The dried MeCN sample did not show a strong

affinity for the solid support and fell off gradually just by movement of the slide. The sample from the DCM solution failed to *equilibrate* when measured in an air or water medium and was deemed unsuitable for further studies.

Electrospinning was successfully used to incorporate **PIC** into polymeric microfibers supported on a glass slide. Polycaprolactone polymer solutions were electrospun in the absence and presence of **PIC**, producing bead-free microfibers, confirmed by optical and scanning electron microscopy. Fluorescence spectra of **PIC** doped PCL microfibers were recorded water and solvent free environments. In both cases the emission intensity continued to decrease over extended periods of time, limiting the utility of the **PIC**/PCL MFs as Cu^{2+} ion sensors in aqueous solutions.

Polysulfone had the potential to form a rigid material of overlapping microfibers and it was electrospun into bead-free microfibers in the absence and presence of **PIC**. However, these microfibers spun for several hours were insufficiently rigid to allow them to be cut into slices. When used in small portions in a solvent free cuvette with no solid support they proved effective as fluorescent indicators of the Cu^{2+} ion in aqueous solutions.

Structural changes to enhance the aqueous solubility of calixarenes are often adopted, amongst these the introduction of polar groups on the upper rim, remote from the binding site, is an attractive possibility and one which could be considered to adapt **PIC** for aqueous applications. However, on the basis of the foundation studies reported in Chapter 5, the author is attracted to the material based development of a **PIC** based metal sensor in aqueous media.

Electrospinning proved useful for accessing **PIC** doped polymeric microfibers showing potential as indicators of the presence of Cu^{2+} ions in water. An important parameter in electrospinning of functional microfibers is the ratio of polymer to the molecule of interest. In the future, a range of polymeric solutions with different **PIC**:polymer ratios could be electrospun and their morphological and emission properties studied. This could result in **PIC** doped microfibers that could be tuned for the detection of various analytes of interest.

The **PIC**/PSF MFs did not rigidify sufficiently to produce material samples capable of being cut into reproducible units. Thus future work could entail the use of different solvents, such as DMF, DMSO and DMAc, to produce a rigid mat of fibers which could be cut into slices for direct use in a cuvette. Advantages of this approach include the possibility that the effective concentration of **PIC** in the slices could be ascertained from the mass of each slice. Thus, the potential exists for a qualitative and quantitative sensor for the Cu^{2+} ion from an aqueous medium.

Chapter 7

Experimental

7.1 Instrumentation and Reagents

Standard reagents were supplied by Alfa Aesar, TCI Europe or Sigma Aldrich and were used without further purification. HPLC grade solvents were used as received.

Analytical TLC was performed on pre-coated silica gel 60 F₂₅₄ plates from Merck. All plates were visualised by UV irradiation. Flash chromatography was performed using silica gel 40-63 μM , 60 Å.

Electrospray (ESI) mass spectra were carried out on an Agilent Technologies 6410 Time of Flight LC/MS.

NMR spectra were recorded on a Bruker Avance spectrometer at 25°C except where otherwise stated. NMR spectra were recorded in CDCl₃ unless otherwise stated. Chemical shifts are reported in ppm downfield from TMS as standard. ¹H and ¹³C NMR were recorded at 500 and 125 MHz respectively unless otherwise stated.

UV-Vis spectra were recorded with on a UNICAM UV500 UV-Visible Spectrometer at 25°C driven by a PC on which the data were saved as text (.txt) files of absorbance intensity versus wavelength.

Fluorescence spectra were recorded with a Jasco FP-6300 spectrofluorometer operating in emission mode. Excitation and emission bandwidths were set at 2.5 nm.

All fluorescence experiments were carried out in triplicate. The fluorescence spectrometer was driven by a PC on which the data were saved as text (.txt) files of fluorescence intensity versus wavelength.

Absorbance and emission spectra were analysed and presented using Microsoft Excel 2013.

Infrared spectra were recorded as KBr discs using a Perkin Elmer system 2000 FT-IR spectrophotometer.

Mercury 3.5.1 software was used for the analysis of x-ray structures.

Melting point analyses were carried out using a Stewart Scientific SMP 11 melting point apparatus.

Perchlorate salts of metal ions are potentially explosive and were manipulated with care and used only in small quantities.

Sodium hydride (NaH) was obtained as a 60% dispersion in mineral oil from Sigma Aldrich; immediately prior to use the mineral oil covering was removed using petroleum ether under a N₂ atmosphere. The stripped NaH was retained in an inert atmosphere and used immediately.

Electrospray (ESI) mass spectra were collected on an Agilent Technologies 6410 Time of Flight LC/MS. Mass spectra were interpreted using were obtained using 'Agilent Masshunter Workstation Software'. The molecular ions found were analysed by subtracting the mass of the proton or adduct (*e.g.* sodium ion or potassium ion) and adding the mass of an electron (0.00055 amu). This value was then compared to the exact mass of the target compound, the observed mass was subtracted from the target mass and this value was then divided by the target mass and multiplied by 1,000,000. This gave the mass error in ppm which was considered acceptable once it was within +/- 5 ppm range.

SEM analysis was carried out using a Hitachi S-3200-N with a tungsten filament, which possessed a maximum magnification of x200,000 with a resolution of 3.5 nm.

Light microscopy was performed using an Olympus BX51M optical microscope and images were analysed using Olympus DP-Soft CVI software version 3.2.

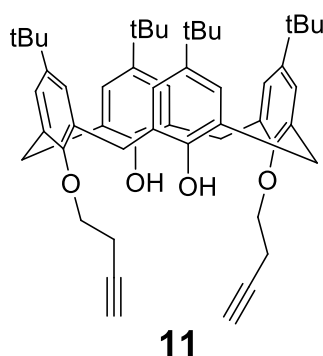
Gilson pipettes were calibrated annually, and their accuracy was confirmed weekly by measurement of the mass of titrated samples of pure water on a 3 decimal place balance.

7.2 5,11,17,23-tetra-tert-Butyl-25,27-bis(but-3-ynyloxy)-26,28-dihydroxycalix [4]arene, 12¹⁰⁴

4-Tert-butylcalix[4]arene (1.000 g, 1.54 mmol, 1 eq) was dissolved in anhydrous acetonitrile (30 mL), potassium carbonate (1.064 g, 7.70 mmol, 5 eq) was added and the solution was allowed to stir for 1 hr at rt to allow for deprotonation. 4-Bromo-1-butyne (0.860 g, 6.47 mmol, 4.2 eq) in anhydrous acetonitrile (10 mL) was added dropwise over 30 min and the resulting solution was heated to reflux for 24 hrs. The

solution was then allowed to cool, filtered over celite to remove any insoluble impurities and the filtrate was concentrated under vacuum. 2 M HCl (20 mL) was added and the mixture was extracted with DCM, washed with water (30 mL x 2), brine (30 mL), dried over MgSO₄ and the solvent removed under reduced pressure to yield a white solid. The crude product was purified by flash column chromatography (SiO₂, Pet. Ether:EtOAc, 10:0.5, v/v) to give the pure product as a bright white solid.

Yield: 36%, m.p. = 232 - 234 °C

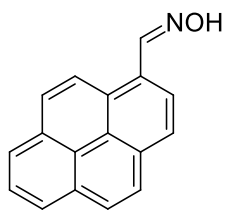


¹H NMR spectroscopic data corresponded to that found in the literature.¹⁰⁴

7.3 1-Pyrenecarbaldoxime, **12**⁸⁸

1-Pyrenecarbaldehyde (200 mg, 0.86 mmol, 1 eq) was dissolved in EtOH (8 mL), hydroxylamine hydrochloride (180 mg, 2.50 mmol, 3 eq) was added along with sodium acetate trihydrate (476 mg, 3.50 mmol, 4 eq) in distilled water (4 mL). The resulting solution was heated to reflux for 1 hr. After cooling, distilled water (10 mL) was added and the mixture was extracted with EtOAc (10 mL x 3). The organic layers were combined, washed with 5% aqueous NaOH (20 mL) and dried over anhydrous magnesium sulphate. The solvent was removed under reduced pressure to yield a yellow solid.

Yield: 95%, m.p. = 190 - 192 °C

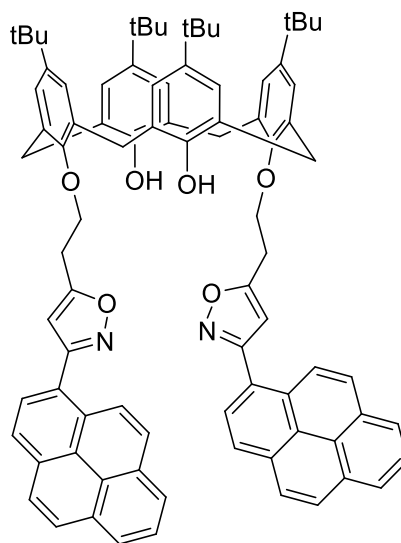
**12**

^1H NMR spectroscopic data corresponded to that found in the literature.⁸⁸

7.4 5,11,17,23-*tetra-tert*-Butyl-25,27-bis[(3-(pyren-1-yl)isoxazol-5-yl)ethyl]- 26,28-dihydroxycalix[4]arene (EPIC), **14**

The alkyne **11** (100 mg, 0.13 mmol, 1 eq) was dissolved in EtOH (40 mL), oxime **12** (130 mg, 0.53 mmol, 4 eq) and Ch-T (65 mg, 0.27 mmol, 2 eq) were added and the solution was allowed to stir at reflux. Further portions of Ch-T (65 mg, 0.27 mmol, 2 eq) were added at $t = 3$ and $t = 6$ hrs. The resulting solution was then allowed to stir for 18 hrs at reflux. Following cooling, water (20 mL) was added to the solution. The organic layer was extracted with chloroform (40 mL), washed with 5% NaOH (30 mL), dried over anhydrous magnesium sulphate and the solvent removed under reduced pressure to yield the crude product which was purified by flash column chromatography (SiO_2 , DCM; 100%). The pure product was obtained as a white solid by crystallisation from EtOH:DCM (2:1, v/v).

Yield: 49%, m.p. = 162 - 165 °C

**14**

^1H NMR: δ 8.45 (d, $J = 9.5$ Hz, 2H, ArH), 8.17 – 8.11 (m, 4H, ArH), 8.09 – 8.02 (m, 8H, ArH), 7.97 – 7.92 (m, 2H, ArH), 7.58 (d, $J = 9.5$ Hz, 2H, ArH), 7.13 (s, 4H, calix-ArH), 6.88 (s, 2H, isox-H), 6.78 (s, 2H, OH), 6.73 (s, 4H, calix-ArH), 4.03 (d, $J = 13.0$ Hz, 4H, calix-CH methylene bridge), 3.95 (t, $J = 6.1$ Hz, 4H, OCH₂), 3.25 (d, $J = 13.0$ Hz, 4H, calix-CH methylene bridge), 2.76 (t, $J = 6.2$ Hz, 4H, OCH₂CH₂), 1.38 (s, 18H, *t*-butyl CH₃), 0.90 (s, 18H, *t*-butyl CH₃).

^{13}C NMR: δ 169.4, 163.2, 150.6, 149.4, 147.3, 141.7, 132.1, 132.0, 131.2, 130.8, 129.0, 128.3, 128.3, 127.7, 127.4, 127.3, 126.0, 125.6, 125.4, 125.3, 125.2, 124.9, 124.7, 124.6, 124.4, 124.2, 105.1 (isox-CH), 72.7 (OCH₂), 33.94 (*t*-butyl qC), 33.89 (*t*-butyl qC), 31.8 (*t*-butyl CH₃), 31.5 (calix-CH₂ methylene bridge), 30.9 (*t*-butyl CH₃), 27.2 (OCH₂CH₂).

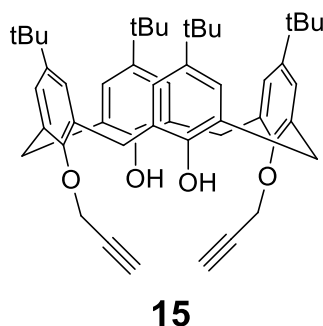
IR (cm⁻¹): 3416, 2959, 1603, 1485, 1202, 848.

HRMS (ESI): calcd for C₈₆H₈₂N₂NaO₆ 1261.6065 [M + Na]⁺, found 1261.6039 (diff ppm -2.06).

7.5 5,11,17,23-*tetra-tert*-Butyl-25,27-dipropargyloxy-26,28-dihydroxycalix[4] arene, 15¹⁸

4-*Tert*-butylcalix[4]arene (2.000 g, 3.08 mmol, 1 eq) was dissolved in dry acetone (30 mL), potassium carbonate (1.023 g, 7.40 mmol, 2.4 eq) was added and the solution was allowed to stir for 1 hour to allow for deprotonation. Propargyl bromide (1.262 g, 10.61 mmol, 3.44 eq) in acetone (10 mL) was added dropwise over 30 min and the resulting solution was heated to reflux for 24 hrs. The solution was then allowed to cool, filtered over celite to remove any insoluble impurities. The filtrate was concentrated under vacuum. 2M aqueous HCl (20 mL) was added to the residue and the product was extracted with DCM. The organic extracts were washed with water and brine, dried over anhydrous Na₂SO₄ and evaporated to dryness *in vacuo* to yield an off-white solid. The pure product was obtained by crystallisation from DCM:MeOH (3:1, v/v) to yield a white crystalline solid.

Yield: 74%, m.p. = 210 – 212 °C

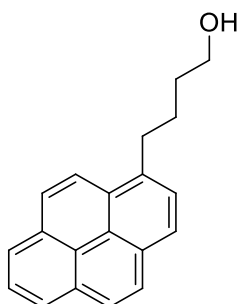


^1H NMR spectroscopic data corresponded to that found in the literature.¹⁸

7.6 1-Pyrenebutanol, **16**²²³

1-Pyrenebutyric acid (1.000 g, 3.47 mmol, 1 eq) was dissolved in anhydrous THF (30 mL), LAH (197 mg, 5.20 mmol, 1.5 eq) was added portion-wise at 0 °C. The resulting solution was stirred at rt for 1 hour. The remaining LAH was quenched with 3% KOH, EtOAc (30 mL) was added and the solution was washed with brine. The organic extracts were dried over anhydrous MgSO_4 . The solvent was removed under reduced pressure to yield the pure product as a dark yellow oil which required no further purification.

Yield: 95%



16

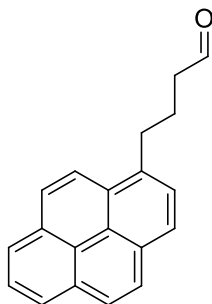
^1H NMR spectroscopic data corresponded to that found in the literature.²²³

7.7 1-Pyrenebutanal, **17**¹²¹

1-Pyrenebutanol **16** (2.044 g, 7.46 mmol, 1 eq) was dissolved in anhydrous DCM (30 mL), 3 Å molecular sieves (20.000 g) were added to the solution along with pyridinium chlorochromate (2.410 g, 11.18 mmol, 1.5 eq). The resulting solution was

allowed to stir at room temperature for 3 hrs. After which the solution was filtered over silica and the solvent removed under reduced pressure to yield the pure aldehyde as a pale yellow solid.

Yield: 85%, m.p. = 66 - 68 °C



17

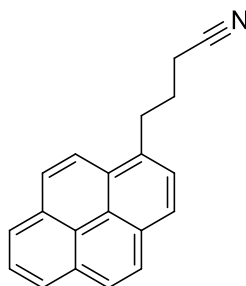
¹H NMR spectroscopic data corresponded to that found in the literature.¹²¹

7.8 1-Pyrenebutanaldoxime, **18**

Approach (i)

1-Pyrenebutanal **17** (694 mg, 2.55 mmol, 1 eq) was dissolved in EtOH (20 mL) in a scientific MW vessel. Hydroxylamine hydrochloride (266 mg, 3.82 mmol, 1.5 eq) and pyridine (302 mg, 3.82 mmol, 1.5 eq) were added. The resulting mixture was heated to 125°C in a scientific MW (t = 1 hr, P_{max} = 300 W). Following cooling, water (10 mL) was added to the solution. The organic layer was extracted with chloroform (30 mL), dried over anhydrous magnesium sulphate and the solvent removed under reduced pressure to yield the crude product as a dark yellow solid which was purified by flash column chromatography (SiO₂, petroleum ether:DCM; 6:4, v/v) to produce 1-pyrenebutanenitrile, **19** and 1-pyrenebutanaldoxime, **18**.

Yield: 46%, m.p. = 90 -93 °C

**19**

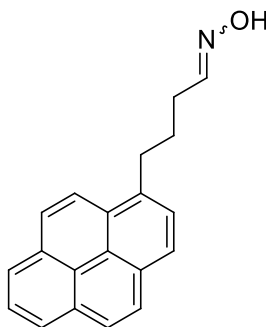
$^1\text{H NMR}$: δ 8.24 (d, $J = 9.3$ Hz, 1H, ArH), 8.22 – 8.17 (m, 2H, ArH), 8.17 – 8.11 (m, 2H, ArH), 8.08 – 7.99 (m, 3H, ArH), 7.88 (d, $J = 7.8$ Hz, 1H, ArH), 3.53 (t, $J = 7.5$ Hz, 2H, pyr- CH_2), 2.41 (t, $J = 7.0$ Hz, 2H, CH_2CN), 2.27 – 2.19 (m, 2H, pyr- CH_2CH_2).

$^{13}\text{C NMR}$: δ 133.7 (1-pyr-qC), 131.4, 130.8, 130.4, 128.7 (4 x qC), 127.8, 127.4, 127.3, 127.1, 126.0, 125.2 (6 x CH), 125.2 (qC), 125.0, 124.9 (2 x CH), 124.9 (qC), 122.7 (CH), 119.6 (CN), 32.0 (pyr- CH_2), 27.2 (CH_2CN), 16.8 ($\text{CH}_2\text{CH}_2\text{CN}$).

IR (cm^{-1}): 3049, 2246, 1601, 1433, 843.

HRMS (ESI): calcd for $\text{C}_{20}\text{H}_{15}\text{NNa}$ 292.1097 [$\text{M} + \text{Na}$] $^+$, found 292.1102 (diff ppm -1.71).

Yield: 43%, m.p. = 114 - 117 °C

**18**

Presented in solution in CDCl_3 as a 2:3 ratio of *E*:-*Z*-isomers.

$^1\text{H NMR}$: δ 8.29 – 8.24 (m, 1H, ArH), 8.20 – 8.15 (m, 2H, ArH), 8.15-8.09 (m, 2H, ArH), 8.07-7.96 (m, 3H, ArH), 7.90 – 7.85 (m, 1H, ArH), 7.52 (t, $J = 5.9$ Hz, 0.4 H, CHNOH *E*-isomer), 7.37 (br s, 0.6 H, NOH *Z*-isomer), 7.07 (br s, 0.4 H, NOH *E*-isomer), 6.81 (t, $J = 5.5$ Hz, 0.6 H, CHNOH *Z*-isomer), 3.44 – 3.38 (m, 2H, pyr- CH_2), 2.60 – 2.53 (m, 1.2H,

CH_2CHNOH *Z*-isomer), 2.41 – 2.34 (m, 0.8H, CH_2CHNOH , *E*-isomer), 2.12 – 2.04 (m, 2H, pyr- CH_2CH_2).

^{13}C NMR: δ 152.0 (C_{HNOH}), 135.8, 135.8, 131.4, 130.9, 130.0, 128.7, 128.6 (7 x qC), 127.5, 127.4, 127.4, 127.3, 127.3, 126.7, 125.9 (7 x C_{H}), 125.1, 125.0 (2 x qC), 125.0 (C_{H}), 125.0 (qC), 124.8, 124.8, 124.8, 123.3, 123.2 (5 x C_{H}), 33.2, 32.8, 29.3, 28.4, 28.2, 24.9 (6 x C_{H_2}).

IR (cm^{-1}): 3397, 3210, 2928, 2858, 1663, 1435, 844.

HRMS (ESI): calcd for $\text{C}_{20}\text{H}_{17}\text{NNaO}$ 310.1202 [$\text{M} + \text{Na}$] $^+$, found 310.1207 (diff ppm - 1.61).

Approach (ii)

1-Pyrenebutanal (688 mg, 2.53 mmol, 1 eq) was dissolved in MeOH:H₂O (60 mL, 11:1, v/v), hydroxylamine hydrochloride (351 mg, 5.06 mmol, 2 eq) and sodium acetate trihydrate (688 mg, 5.06 mmol, 2 eq) were added. The resulting solution was heated to reflux for 3 hrs. Following cooling, addition of water (50 mL) to the solution induced formation of a pale yellow ppt which was collected and dried to yield the pure oximes in a 1:1.8 mixture of *E*- and *Z*-isomers. Data corresponded to that recorded above.

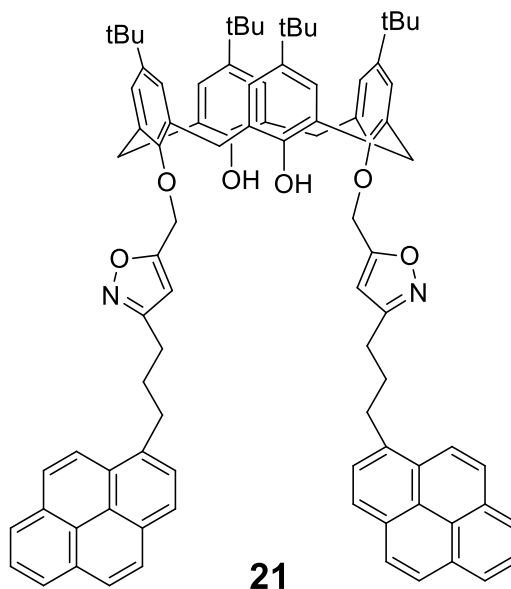
Yield: 92%

7.9 5,11,17,23-tetra-*tert*-Butyl-25,27-bis[(3-(3-(pyren-1-yl)propyl)isoxazol-5-yl)methyl]-26,28-dihydroxycalix[4]arene (PPIC), 21

The oxime **18** (476 mg, 1.66 mmol, 6 eq) was dissolved in DCM (60 mL), NCS (332 mg, 2.49 mmol, 9 eq) was added and the solution was allowed to stir at rt for 1 hr. The alkyne **15** (200 mg, 0.28 mmol, 1 eq) was added and the resulting solution was heated to reflux. NEt₃ (502 mg, 694 μL , 4.96 mmol, 18 eq), dissolved in DCM (306 μL) was added to the refluxing solution over 17 hrs using a syringe pump operating at 1 $\mu\text{L}/\text{min}$. Following cooling, the organic extracts were washed with water (2 x 30 mL), dried over anhydrous sodium sulphate and the solvent removed under reduced

pressure to yield the crude product which was purified by flash column chromatography (SiO₂, DCM; 100%) to yield the pure product as an off-white solid.

Yield: 49%, m.p. = 117 – 120 °C



¹H NMR: δ 8.18 (d, J = 9.2 Hz, 2H, ArH), 8.13 – 8.09 (m, 2H, ArH), 8.08 – 8.05 (m, 2H, ArH), 8.03 – 7.98 (m, 4H, ArH), 7.98 – 7.91 (m, 6H, ArH), 7.78 (d, J = 7.7 Hz, 2H, ArH), 7.03 (s, 4H, calix-ArH), 6.72 (s, 4H, calix-ArH), 6.62 (s, 2H, 2 x OH), 6.32 (s, 2H, 2 x isox-H), 4.97 (s, 4H, OCH₂), 4.15 (d, J = 13.3 Hz, 4H, calix-CH methylene bridge), 3.34 (t, J = 6.9 Hz, 4H, pyr-CH₂), 3.24 (d, J = 13.3 Hz, 4H, calix-CH methylene bridge), 2.75 (t, J = 7.2 Hz, 4H, pyr-CH₂CH₂CH₂), 2.22 – 2.12 (m, 4H, pyr-CH₂CH₂), 1.27 (s, 18H, t-butyl CH₃), 0.89 (s, 18H, t-butyl CH₃).

¹³C NMR: δ 167.5, 163.7, 150.4, 149.5, 147.6, 141.8, 135.8, 132.2, 131.4, 130.9, 129.9, 128.7, 127.7, 127.7 (13 x qC), 127.5, 127.4, 127.3, 126.6, 125.8, 125.7, 125.2 (7 x CH), 125.1, 125.0 (2 x qC), 124.8, 124.8, 123.3 (3 x CH), 103.5 (isox-CH), 68.3 (OCH₂), 33.9 (t-butyl qC), 33.8 (t-butyl qC), 32.8 (pyr-CH₂), 31.7 (t-butyl CH₃), 31.5 (calix-CH₂ methylene bridge), 30.9 (t-butyl CH₃), 30.0 (isox-CH₂CH₂), 25.9 (isox-CH₂).

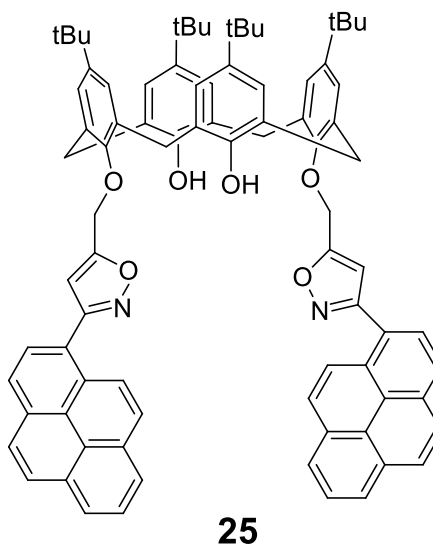
IR (cm⁻¹): 3416, 2959, 1603, 1485, 1202, 1018, 848.

HRMS (ESI): calcd for C₉₀H₉₀KN₂O₆ 1333.643 [M + K]⁺, found 1333.6435 (diff ppm - 0.37).

7.10 5,11,17,23-tetra-tert-Butyl-25,27-bis[(3-(pyren-1-yl)isoxazol-5-yl)methyl]-26,28-dihydroxycalix[4]arene (PIC), 25⁸⁸

The alkyne **15** (100 mg, 0.14 mmol, 1 eq) was dissolved in EtOH (40 mL), oxime **12** (135 mg, 0.55 mmol, 4 eq) and Ch-T (68 mg, 0.28 mmol, 2 eq) were added and the solution was allowed to stir at 40 °C. Ch-T, the same portion was added again at t = 3 and t = 6 hrs. The resulting solution was allowed to stir for 18 hrs at 40 °C. Following cooling, water (20 mL) was added. The organic layer was extracted with chloroform (30 mL), washed with 5% NaOH (20 mL) and dried over anhydrous magnesium sulphate. The solvent removed under reduced pressure to yield the crude product which was purified by flash column chromatography (SiO₂, DCM; 100%). The pure product was obtained as a white solid following crystallisation from EtOH:DCM (2:1, v/v).

Yield: 53%, m.p. = 224 - 228 °C



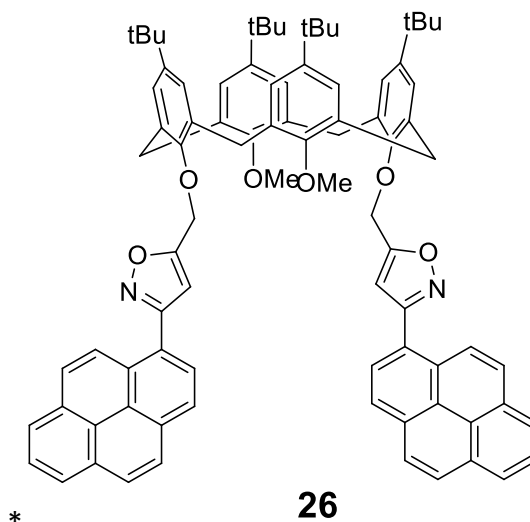
¹H NMR spectroscopic data corresponded to that found in the literature.⁸⁸

7.11 5,11,17,23-tetra-tert-Butyl-25,27-bis[(3-(pyren-1-yl)isoxazol-5-yl)methyl]-26,28-dimethoxycalix[4]arene (MPIC), 27**Approach (i)**

PIC (50 mg, 0.04 mmol, 1 eq) was dissolved in DMF (5 mL), NaH (30 mg, 1.23 mmol, 30 eq) was added and the resulting solution was stirred at rt for 15 mins. MeI (117

mg, 0.83 mmol, 20 eq) was added and the mixture allowed to stir at rt for 24 hrs. H₂O (10 mL) was added and the organic layer was extracted with DCM (20 mL), dried over anhydrous MgSO₄ and the solvent removed under reduced pressure to yield an off-white solid which was triturated with MeOH to yield the pure product as a bright white solid.

Yield: 62%, m.p. = 273 - 276 °C



MPIC presented in a 1:2.78 ratio of cone and paco conformers at 240 K.

¹H NMR (240 K) - paco conformer: δ 8.55 (d, J = 9.3 Hz, 2H, pyr-H), 8.17 – 7.80 (m, 16H, pyr-H)*, 7.30 (s, 2H, calix-ArH), 7.14 (br s, 2H, calix-ArH)*, 7.00 (br d, J = 2.4 Hz, 2H, calix-ArH), 6.82 (s, 2H, isox-H), 6.60 (br d, J = 2.4 Hz, 2H, calix-ArH), 5.12 (d, J = 12.4 Hz, 2H, OCH), 4.88 (d, J = 12.3 Hz, 2H, OCH), 4.23 (d, J = 12.9 Hz, 2H, calix-CH methylene bridge), 3.86 (d, J = 14.1 Hz, 2H, calix-CH methylene bridge), 3.79 (d, J = 14.1 Hz, 2H, calix-CH methylene bridge), 3.37 (s, 3H, OCH₃), 3.34 (s, 3H, OCH₃), 3.20 (d, J = 13.2 Hz, 2H, calix-CH methylene bridge), 1.34 (s, 9H, t-butyl CH₃), 1.11 (s, 9H, t-butyl CH₃), 1.07 (s, 18H, t-butyl CH₃).

¹H NMR (240 K) – cone conformer: δ 8.33 (d, J = 9.3 Hz, 2H, cone pyr-H), 8.17 – 7.80 (m, 14H, pyr-H)*, 7.69 (d, J = 8.9 Hz, 2H, cone pyr-H), 7.14 (br s, 4H, calix-ArH)*, 6.90 (s, 2H, isox-H), 6.57 (s, 4H, calix-ArH), 5.11 (s, 4H, OCH₂), 4.43 (d, J = 12.6 Hz, 4H, calix-CH methylene bridge), 4.00 (s, 6H, OCH₃), 3.27 (d, J = 12.7 Hz, 4H, calix-CH methylene bridge), 1.31 (s, 18H, t-butyl CH₃), 0.87 (s, 18H, t-butyl CH₃).

*denotes overlapping pacoc and cone ^1H NMR signals.

^{13}C NMR (240 K): δ 169.1, 168.4, 162.9, 155.2, 155.0, 154.7, 152.8, 151.8, 145.4, 145.1, 144.8, 143.7, 135.3, 135.3, 133.0, 132.5, 132.4, 131.9, 131.8, 131.5, 130.7, 130.5, 130.2, 129.9, 128.7, 128.5, 128.3, 128.3, 128.0, 127.7, 127.0, 126.8, 126.7, 126.0, 125.8, 125.5, 125.4, 125.3, 125.1, 125.1, 124.6, 124.5, 124.4, 124.4, 124.3, 124.0, 123.6, 123.0, 122.7, 105.7, 105.2, 65.4, 60.5, 60.0, 57.9, 37.6, 34.1, 33.7, 33.7, 33.6, 31.6, 31.2, 30.9.

IR (cm^{-1}): 2953, 1604, 1479, 1361, 1202, 1019, 845.

HRMS (ESI): calcd for $\text{C}_{86}\text{H}_{82}\text{N}_2\text{NaO}_6$ 1261.6065 $[\text{M} + \text{Na}]^+$, found 1261.6105 (diff ppm -3.17).

Approach (ii)

PIC (80 mg, 0.06 mmol, 1 eq) was dissolved in acetone (25 mL), Cs_2CO_3 (645 mg, 1.98 mmol, 30 eq) was added and the resulting mixture was stirred at rt for 15 mins. MeI (187 mg, 1.32 mmol, 20 eq) was added and the mixture heated at reflux for 17 hrs. Following cooling, H_2O (20 mL) was added and the organic layer was extracted with DCM (volume), dried over anhydrous MgSO_4 . The solvent removed under reduced pressure to yield an off-white solid which was triturated with MeOH to yield the pure product as a bright white solid.

Yield: 71%, m.p. = 273 - 276 °C

Data corresponded to that recorded above.

Bibliography

- (1) von Baeyer, A. *Ber. Dtsch. Chem. Ges.*, **1872**, 5, 1094.
- (2) Mercelis, J. *Technology and Culture*, **2012**, 53, 366-400.
- (3) Zinke, A.; Ziegler, E. *Ber. Dtsch. Chem. Ges.*, **1944**, 77, 264-272.
- (4) Niederl, J. B.; Vogel, H. J. *J Am Chem Soc* **1940**, 62, 2512-2514.
- (5) Gutsche, C. D.; Muthukrishnan, R. *J. Org. Chem.*, **1978**, 43, 4905-4906.
- (6) Emert, J.; Breslow, R. *J Am Chem Soc* **1975**, 97, 670-672.
- (7) Pedersen, C. J. *J Am Chem Soc* **1967**, 89, 7017-7036.
- (8) Nimse, S. B.; Kim, T. *Chem. Soc. Rev.*, **2013**, 42, 366-386.
- (9) Bandela, A. K.; Hinge, V. K.; Yarramala, D. S.; Rao, C. P. *ACS Appl. Mater. Interfaces*, **2015**, 7, 11555-11566.
- (10) Tzadka, E.; Goldberg, I.; Vigalok, A. *Chem. Commun.*, **2009**, 2041-2043.
- (11) Rawat, V.; Press, K.; Goldberg, I.; Vigalok, A. *Org. Biomol. Chem.*, **2015**, 13, 11189-11193.
- (12) Zeng, X. F.; Ma, J. K.; Luo, L.; Yang, L. L.; Cao, X. L.; Tian, D. M.; Li, H. B. *Org. Lett.*, **2015**, 17, 2976-2979.
- (13) In <https://www.shu.ac.uk/research/meri/contact-angle-measurement>
Accessed 14/03/2016.
- (14) Boonkitpatarakul, K.; Yodta, Y.; Niamnontc, N.; Sukwattanasinitt, M. *RSC Adv.*, **2015**, 5, 33306-33311.
- (15) Maity, D.; Bhatt, M.; Paul, P. *Microchim. Acta*, **2015**, 182, 377-384.
- (16) Menon, S. K.; Sewani, M. *Reviews in Analytical Chemistry*, **2006**, 25, 49-82.
- (17) Creaven, B. S.; Donlon, D. F.; McGinley, J. *Coord. Chem. Rev.*, **2009**, 253, 893-962.
- (18) Mummidivarapu, V. V.; Hinge, V. K.; Tabbasum, K.; Gonnade, R. G.; Rao, C. P. *J. Org. Chem.*, **2013**, 78, 3570-3576.
- (19) Alfieri, C.; Dradi, E.; Pochini, A.; Ungaro, R.; Andreetti, G. D. *J. Chem. Soc., Chem. Commun.*, **1983**, 1075-1077.
- (20) Sahin, O. *J. Mol. Struct.*, **2013**, 1041, 175-182.
- (21) Lavendomme, R.; Leroy, A.; Luhmer, M.; Jabin, I. *J. Org. Chem.*, **2014**, 79, 6563-6570.
- (22) Balazs, B.; Toth, G.; Horvath, G.; Grün, A.; Csokai, V.; Toke, L.; Bitter, I. *Eur. J. Org. Chem.*, **2001**, 61-71.

- (23) Ocak, U.; Ocak, M.; Shen, X.; Surowiec, K.; Bartsch, R. A. *J. Fluoresc.*, **2009**, *19*, 997-1008.
- (24) Callan, J. F.; de Silva, A. P.; Magri, D. C. *Tetrahedron*, **2005**, *61*, 8551-8588.
- (25) Galbraith, E.; James, T. D. *Chem. Soc. Rev.*, **2010**, *39*, 3831-3842.
- (26) Suresh, P.; Azath, I. A.; Pitchumani, K. *Sens. Actuators B Chem.*, **2010**, *146*, 273-277.
- (27) Ghosh, P.; Bharadwaj, P. K.; Roy, J.; Ghosh, S. *J Am Chem Soc* **1997**, *119*, 11903-11909.
- (28) Tang, W. S.; Lu, X. X.; Wong, K. M. C.; Yam, V. W. W. *J. Mater. Chem.*, **2005**, *15*, 2714-2720.
- (29) Wieser, C.; Dieleman, C. B.; Matt, D. *Coord. Chem. Rev.*, **1997**, *165*, 93-161.
- (30) Sliwa, W.; Deska, M. *Arkivoc*, **2008**, 87-127.
- (31) Roundhill, D. M. *Prog. Inorg. Chem.*, **2007**, *43*, 533-592.
- (32) Beer, P. D.; Drew, M. G. B.; Heseck, D.; Kan, M.; Nicholson, G.; Schmitt, P.; Sheen, P. D.; Williams, G. J. *Chem. Soc., Dalton Trans.*, **1998**, 2783-2785.
- (33) Brindley, G. D.; Fox, O. D.; Beer, P. D. *J. Chem. Soc., Dalton Trans.*, **2000**, 4354-4359.
- (34) Schazmann, B.; O'Mally, S.; Nolan, K.; Diamond, D. *Supramol. Chem.*, **2006**, *18*, 515-522.
- (35) Benounis, M.; Jaffrezic-Renault, N.; Halouani, H.; Lamartine, R.; Dumazet-Bonnamour, I. *Mater. Sci. Eng. C.*, **2006**, *26*, 364-368.
- (36) In http://www.pci.tu-bs.de/aqgericke/PC4/Kap_1/jablonsk.htm Accessed 14/03/2016.
- (37) In <http://electronicdesign.com/displays/master-fundamentals-led-illumination> Accessed 11/02/2016.
- (38) Valeur, B. *Molecular Fluorescence Principles and Applications*; Wiley-VCH: Germany, 2002.
- (39) In <http://www.cyberphysics.co.uk/topics/radioact/Radio/EMSpectrumcolor.jpg> Accessed 12/02/2016.
- (40) Sun, M.; Zhang, D.; Li, Y.; Wang, J.; Gao, Y.; Yang, W. *J. Lumin.*, **2014**, *148*, 55-59.
- (41) Agarwal, N.; Patil, M.; Patil, M. *RSC Adv.*, **2015**, *5*, 98447-98455.

- (42) Huang, J.; Su, J.-H.; Tian, H. *J. Mater. Chem.*, **2012**, *22*, 10977-10989.
- (43) Robertson, T. A.; Bunel, F.; Roberts, M. S. *Cells*, **2013**, *2*, 591-606.
- (44) Ono, A.; Togashi, H. *Angew. Chem. Int. Ed. Engl.*, **2004**, *43*, 4300-4302.
- (45) Birks, J. B. *Rep. Prog. Phys.*, **1975**, *38*, 903-974.
- (46) Ghosh, K.; Sena, T.; Patra, A. *New J. Chem.*, **2010**, *34*, 1387-1393.
- (47) de Silva, A. P.; Gunaratne, H. Q. N.; Habib-Jiwan, J. L.; McCoy, C. P.; Rice, T. E.; Soumillion, J. P. *Angew. Chem. Int. Ed. Engl.*, **1995**, *34*, 1728-1731.
- (48) Olson, E. J.; Buhlmann, P. *J. Org. Chem.*, **2011**, *76*, 8406-8412.
- (49) Job, P. *Anal. Chim.*, **1928**, *9*, 113-203.
- (50) Sayago, A.; Boccio, M.; Asuero, A. G. *Int. J. Pharm.*, **2005**, *295*, 29-34.
- (51) Renny, J. S.; Tomasevich, L. L.; Tallmadge, E. H.; Collum, D. B. *Angew. Chem. Int. Ed. Engl.*, **2013**, *52*, 11998-12013.
- (52) Bell, J. H.; Pratt, R. F. *Inorg. Chem.*, **2002**, *41*, 2747-2753.
- (53) Stern, O.; Volmer, M. *Physik. Z.*, **1919**, *20*, 183-188.
- (54) Lakowicz, J. R. *Principles of Fluorescence Spectroscopy*; Springer: USA, 2006.
- (55) Kavitha, S. R.; Umadevi, M.; Vanelle, P.; Terme, T.; Khoumeri, O. *Eur. Phys. J. D*, **2014**, *68*, 308-316.
- (56) Benesi, H. A.; Hildebrand, J. H. *J Am Chem Soc* **1949**, *71*, 2703-2707.
- (57) Xu, Z.; Singh, N. J.; Lim, J.; Pan, J.; Kim, H. N.; Park, S.; Kim, K. S.; Yoon, J. *J Am Chem Soc* **2009**, *131*, 15528-15533.
- (58) Ratte, H. T. *Environ. Toxicol. Chem.*, **1999**, *18*, 89-108.
- (59) Wang, F.; Nandhakumar, R.; Moon, J. H.; Kim, K. M.; Lee, J. Y.; Yoon, J. *Inorg. Chem.*, **2011**, *50*, 2240-2245.
- (60) Watanabe, M.; Suliman, M. E.; Qureshi, A. R.; Garcia-Lopez, E.; Barany, P.; Heimburger, O.; Stenvinkel, P.; Lindholm, B. *Am. J. Clin. Nutr.*, **2008**, *87*, 1860-1866.
- (61) Sutariya, P. G.; Pandya, A.; Lodha, A.; Menon, S. K. *Analyst*, **2014**, *139*, 4794-4798.
- (62) Kolb, H. C.; Finn, M. G.; Sharpless, K. B. *Angew. Chem. Int. Ed. Engl.*, **2001**, *40*, 2004-2021.
- (63) Buchner, E. *Ber. Dtsch. Chem. Ges.*, **1888**, *21*, 2637.
- (64) Huisgen, R. *Angew. Chem. Int. Ed. Engl.*, **1963**, *2*, 565-598.

- (65) Dondoni, A.; Mangini, A.; Ghersetti, S. *Tetrahedron Lett.*, **1966**, *39*, 4789-4791.
- (66) Kelly, D. R.; C., B. S.; King, D. S.; de Silva, D. S.; Lord, G.; Taylor, J. P. *Org. Biomol. Chem.*, **2008**, *6*, 787-796.
- (67) Mukaiyama, T.; Hoshino, T. *J Am Chem Soc* **1960**, *82*, 5339-5342.
- (68) Padwa, A.; Pearson, W. H. *Synthetic Applications of 1,3-Dipolar Cycloaddition Chemistry Toward Heterocycles and Natural Products*; 2nd ed.; John Wiley and Sons, 2002.
- (69) Singh, I.; Zarafshani, Z.; Heaney, F.; Lutz, J.-F. *Polym. Chem.*, **2011**, *2*, 372-375.
- (70) Clayden, J.; Greeves, N.; Warren, S.; Wothers, P. *Organic Chemistry*; Oxford University Press Inc.: New York, 2008.
- (71) Padmavathi, V.; Reddy, K. V.; Padmaja, A.; Venugopalan, P. *J. Org. Chem.*, **2003**, *68*, 1567-1570.
- (72) Heaney, F. *Eur. J. Org. Chem.*, **2012**, *2012*, 3043-3058.
- (73) Hamama, W. S.; Ibrahim, M. E.; Zoorob, H. H. *J. Heterocycl. Chem.*, **2016**, *Ahead of Print*.
- (74) Wakefield, B. J.; Wright, D. J. *Adv. Heterocycl. Chem.*, **1979**, *25*, 147-204.
- (75) Munsey, M. S.; Natale, N. R. *Coord. Chem. Rev.*, **1991**, *109*, 251-281.
- (76) Watson, A. A.; House, D. A.; Steel, P. J. *Aust. J. Chem.*, **1995**, *48*, 1549-1572.
- (77) Pinna, R.; Ponticelli, G.; Preti, C. *J. Inorg. Nucl. Chem.*, **1975**, *37*, 1681-1684.
- (78) Chen, Z.; Wu, Y.; He, C.; Wang, B.; Gu, D.; Gan, F. *Synt. Met.* **2010**, *160*, 2581-2586.
- (79) Potkin, V. I.; Bumagin, N. A.; Petkevich, S. K.; Lyakhov, A. S.; Rudakov, D. A.; Livantsov, M. V.; Golantsov, N. E. *Synthesis* **2012**, *44*, 151-157.
- (80) Chang, K.-C.; Luo, L.-Y.; Diao, E. W.-G.; Chung, W.-S. *Tetrahedron Lett.*, **2008**, *49*, 5013-5016.
- (81) Senthilvelan, A.; Ho, I. T.; Chang, K. C.; Lee, G. H.; Liu, Y. H.; Chung, W. S. *Chem. Eur. J.*, **2009**, *15*, 6152-6160.
- (82) Sahin, O.; Yilmaz, M. *Tetrahedron*, **2011**, *67*, 3501-3508.
- (83) Wang, N. J.; Sun, C. M.; Chung, W. S. *Sens. Actuators B Chem.*, **2012**, *171*, 984-993.
- (84) Lee, J. Y.; Kim, S. K.; Jung, J. H.; Kim, J. S. *J. Org. Chem.*, **2005**, *70*, 1463-1466.

- (85) Jin, T.; Ichikawa, K.; Koyama, T. *J. Chem. Soc., Chem. Commun.*, **1992**, 499-501.
- (86) Diao, H. *M.Sc. Thesis*, **2012**, *M. Sc.*, 137.
- (87) Maher, N. J. *Ph.D. Thesis*, **2013**, 274.
- (88) Maher, N. J.; Diao, H. W.; O'Sullivan, J.; Fadda, E.; Heaney, F.; McGinley, J. *Tetrahedron* **2015**, *71*, 9223-9233.
- (89) Ho, I. T.; Haung, K. C.; Chung, W. S. *Chem. Asian. J.*, **2011**, *6*, 2738-2736.
- (90) Park, S. Y.; Yoon, J. H.; Hong, C. S.; Souane, R.; Kim, J. S.; Matthews, S. E.; Vicens, J. *J. Org. Chem.*, **2008**, *73*, 8212-8218.
- (91) Kim, J. S.; Park, S. Y.; Kim, S. H.; Thuery, P.; Souane, R.; Matthews, S. E.; Vicens, J. *Bull. Korean Chem. Soc.*, **2010**, *31*, 624-629.
- (92) Pathak, R. K.; Hinge, V. K.; Mondal, P.; Rao, C. P. *Dalton Trans.*, **2012**, *41*, 10652-10660.
- (93) Wajid, A.; Mohod, R. B. *J. Applicable Chem.*, **2015**, *4*, 609-614.
- (94) Pasa, S.; Ocak, Y. S.; Temel, H.; Kilicoglu, T. *Inorg. Chim. Acta*, **2013**, *405*, 493-504.
- (95) Al-Noor, T. H.; Lateef, S. M.; Rhayma, M. H. *J. Chem. Pharm. Res.*, **2012**, *4*, 4141-4148.
- (96) Asfari, Z.; Bilyk, A.; Bond, C.; Harrowfield, J. M.; Koutsantonis, G. A.; Lengkeek, N.; Mocerino, M.; Skelton, B. W.; Sobolev, A. N.; Strano, S.; Vicens, J.; White, A. H. *Org. Biomol. Chem.*, **2004**, *2*, 387-396.
- (97) Dupont, N.; Navaza, A.; Coleman, A. W.; Shkurenko, O.; Suwinska, K. *J. Mol. Struct.*, **2011**, *991*, 50-59.
- (98) Roach, P. L.; Clifton, I. J.; Hensgens, C. M. H.; Shibata, N.; Long, A. J.; Strange, R. W.; Hasnain, S. S.; Schofield, C. J.; Baldwin, J. E.; Hajdu, J. *Eur. J. Biochem.* **1996**, *242*, 736-740.
- (99) Buser, H. J.; Scharwarzenbach, D.; D., P.; Ludi, A. *Inorg. Chem.*, **1977**, *16*, 2704-2710.
- (100) Ajayakumar, G.; Sreenath, K.; Gopidas, K. R. *Dalton Trans.*, **2009**, *7*, 1180-1186.
- (101) Kratochvil, B.; Zatko, D. A.; Markuszewshi, R. *Anal. Chem.*, **1966**, *38*, 770-772.
- (102) Armbruster, D. A.; Pry, T. *Clin. Biochem. Rev.*, **2008**, *29*, 49-52.
- (103) Chawla, H. M.; Goel, P.; Shukla, R. *Tetrahedron Lett.*, **2014**, *55*, 2173-2176.

- (104) Bois, J.; Espinas, J.; Darbost, U.; Felix, C.; Duchamp, C.; Bouchu, D.; Taoufik, M.; Bonnamour, I. *J. Org. Chem.*, **2010**, *75*, 7550-7558.
- (105) Bianchini, R.; Catelani, G.; Cecconi, R.; D'Andrea, F.; Guazzelli, L.; Isaad, J.; Rolla, M. *Eur. J. Org. Chem.*, **2008**, 444-454.
- (106) Kovalev, I. S.; Slovesnova, N. V.; Kopchuk, D. S.; Zyryanov, G. V.; Taniya, O. S.; Rusinov, V. L.; Chupakhin, O. N. *Russ. Chem. B.* **2014**, *63*, 1312-1316.
- (107) Rosen, C. B.; Hansen, D. J.; Gothelf, K. V. *Org. Biomol. Chem.*, **2013**, *11*, 7916-7922.
- (108) Freeman, C.; Vyle, J. S.; Heaney, F. *RSC Adv.*, **2013**, *3*, 1652-1655.
- (109) Gutsche, C. D. *Calixarenes An Introduction*; 2nd ed.; RSC Publishing, 2008.
- (110) Algay, V.; O'Sullivan, J.; Heaney, F. *European Journal of Organic Chemistry* **2014**, *2014*, 2522-2532.
- (111) Mahon, M. F.; McGinley, J.; Rooney, D. A.; Walsh, J. M. D. *Tetrahedron* **2008**, *64*, 11058-11066.
- (112) McGinley, J.; McKee, V.; Walsh, J. M. D. *Inorg. Chim. Acta*, **2011**, *375*, 57-62.
- (113) Bond, A. D.; Creaven, B. S.; Donlon, D. F.; Gernon, T. L.; McGinley, J.; Toftlund, H. *Eur. J. Inorg. Chem.*, **2007**, 749-756.
- (114) Yan, B.; Wang, Q.-M.; Ma, D.-J. *Inorg. Chem.*, **2009**, *48*, 36-44.
- (115) Arce, R.; Pino, E. F.; Valle, C.; Negrón-Encarnación, I.; Morel, M. *J. Phys. Chem. A*, **2011**, *115*, 152-160.
- (116) Halasinski, T. M.; Salama, F.; Allamandola, L. J. *Astrophys. J.*, **2005**, *628*, 555-566.
- (117) Duhamel, J. *Polymers*, **2012**, *4*, 211-239.
- (118) Kim, J. S.; Quang, D. T. *Chem. Rev.*, **2007**, *107*, 3780-3799.
- (119) Leray, I.; Valeur, B. *Eur. J. Inorg. Chem.*, **2009**, 3525-3535.
- (120) O'Driscoll, L. J.; Frampton, H.; Welsh, D. J.; Bryce, M. R.; Bailey, S. W. D.; Lambert, C. J. *Chem. Eur. J.*, **2015**, *21*, 3891-3894.
- (121) Bi, B.; Maurer, K.; Moeller, K. D. *Angew. Chem. Int. Ed. Engl.*, **2009**, *48*, 5872-5874.
- (122) Crandall, J. K.; Reix, T. *J. Org. Chem.*, **1992**, *57*, 6759-6764.
- (123) Zhu, J.; Song, G.; Yao, G.; Chen, G. *Synth. Commun.* **2012**, *42*, 1934-1940.

- (124) Parghi, K. D.; Satam, J. R.; Jayaram, R. V. *Green Chem. Lett. Rev.*, **2011**, *4*, 143-149.
- (125) Chan, A. S. C.; Chen, C. C.; Lin, C. W.; Lin, Y. C.; Cheng, M. C.; Peng, S. M. *J. Chem. Soc., Chem. Commun.*, **1995**, 1767-1768.
- (126) Boucher, J. L.; Delaforge, M.; Mansuy, D. *Biochemistry*, **1994**, *33*, 7811-7818.
- (127) Singh, M. K.; Lakshman, M. K. *J. Org. Chem.*, **2009**, *74*, 3079-3084.
- (128) Browder, C. C.; Moss, C. B.; Kraft, M. B.; Petrucka, P. L.; Morey, T. S.; Leach, C. W.; Gearhart, N. C. *Lett. Org. Chem.* **2011**, *8*, 229-233.
- (129) Ohno, H.; Aso, A.; Kadoh, Y.; Fujii, N.; Tanaka, T. *Angew. Chem. Int. Ed.*, **2007**, *46*, 6325-6328.
- (130) Tønder, J. E.; Hansen, J. B.; Begtrup, M.; Pettersson, I.; Rimvall, K.; Christensen, B.; Ehrbar, U.; Olesen, P. H. *J. Med. Chem.*, **1999**, *42*, 4970-4980.
- (131) Churykau, D. H.; Zinovich, V. G.; Kulinkovich, O. G. *Synlett* **2004**, *11*, 1949-1952.
- (132) Aicher, T. D.; Balkan, B.; Bell, P. A.; Brand, L. J.; Cheon, S. H.; Deems, R. O.; Fell, J. B.; Fillers, W. S.; Fraser, J. D.; Gao, J.; Knorr, D. C.; Kahle, G. G.; Leone, C. L.; Nadelson, J.; Simpson, R.; Smith, H. C. *J. Med. Chem.*, **1998**, *41*, 4556-4566.
- (133) Wang, N. J.; Sun, C. M.; Chung, W. S. *Tetrahedron*, **2011**, *67*, 8131-8139.
- (134) Bodenant, B.; Weil, T.; Businelli-Pourcel, M.; Fages, F.; Barbe, B.; Pianet, I.; Laguerre, M. *J. Org. Chem.*, **1999**, *64*, 7034-7039.
- (135) Gruber, T.; Fischer, C.; Felsmann, M.; Seichter, W.; Weber, E. *Org. Biomol. Chem.*, **2009**, *7*, 4904-4917.
- (136) Talanova, G. G.; Elkarim, N. S. A.; Talanov, V. S.; Bartsch, R. A. *Anal. Chem.*, **1999**, *71*, 3106-3109.
- (137) Metivier, R.; Leray, I.; Valeur, B. *Chem. Eur. J.*, **2004**, *10*, 4480-4490.
- (138) Ocak, U.; Ocak, M.; Surowiec, K.; Bartsch, R. A.; Gorbunova, M. G.; Tu, C.; Surowiec, M. A. *J. Incl. Phenom. Macrocycl. Chem.*, **2009**, *63*, 131-139.
- (139) Jaime, C.; De Mendoza, J.; Prados, P.; Nieto, P. M.; Sanchez, C. *J. Org. Chem.*, **1991**, *56*, 3372-3376.
- (140) Aoki, I.; Kawabata, H.; Nakashima, K.; Shinkai, S. *J. Chem. Soc., Chem. Commun.*, **1991**, 1771-1773.

- (141) Lee, S. H.; Kim, S. K.; Bok, J. H.; Lee, S. H.; Yoon, J.; Lee, K.; Kim, J. S. *Tetrahedron Lett.*, **2005**, *46*, 8163-8167.
- (142) Korbakov, N.; Timmerman, P.; Lidich, N.; Urbach, B.; Sa'ar, A.; Yitzchaik, S. *Langmuir*, **2008**, *24*, 2580-2587.
- (143) Baruah, M.; Qin, W.; Vallee, R. A. L.; Beljonne, D.; Rohand, T.; Dehaen, W.; Boens, N. *Org. Lett.*, **2005**, *7*, 4377-4380.
- (144) Henary, M. M.; Wu, Y.; Fahrni, C. J. *Chem. Eur. J.*, **2004**, *10*, 3015-3025.
- (145) Bhatt, K. D.; Gupte, H. S.; Makwana, B. A.; Vyas, D. J.; Maity, D.; Jain, V. K. *J. Fluoresc.*, **2012**, *22*, 1493-1500.
- (146) Tumambac, G. E.; Rosencrance, C. M.; Wolf, C. *Tetrahedron*, **2004**, *60*, 11293-11297.
- (147) Depauw, A.; Kumar, N.; Ha-Thi, M. H.; Leray, I. *J. Phys. Chem. A*, **2015**, *119*, 6065-6073.
- (148) McClure, D. S. *J. Chem. Phys.*, **1952**, *20*, 682-686.
- (149) Varnes, A. W.; Dodson, R. B.; Wehry, E. L. *J Am Chem Soc* **1972**, *94*, 946-950.
- (150) Irving, H.; Williams, J. P. *Nature*, **1948**, *162*, 746-747.
- (151) Ramakrishnan, S.; Rajendiran, V.; Palaniandavar, M.; Periasamy, V. S.; Srinag, B. S.; Krishnamurthy, H.; Akbarsha, M. A. *Inorg. Chem.*, **2009**, *48*, 1309-1322.
- (152) Alcón, M. J.; Iglesias, M.; Sanchez, F. *Inorg. Chim. Acta*, **2002**, *333*, 83-92.
- (153) Wang, J.-G.; Qin, J.-H.; Hu, P. Z. *Acta Cryst.*, **2009**, *65*, 415.
- (154) Grasdalen, H.; Svare, I. *Acta Chem. Scand.* **1971**, *25*, 1089-1102.
- (155) Hathaway, B. J.; Underhill, A. E. *J. Chem. Soc.*, **1960**, 3705-3711.
- (156) Inamo, M.; Kohagura, T.; Kaljurand, I.; Leito, I. *Inorg. Chim. Acta*, **2002**, *340*, 87-96.
- (157) Becker, S.; Dürr, M.; Miska, A.; Becker, J.; Gawlig, C.; Behrens, U.; Ivanović-Burmazović, I.; Schindler, S. *Inorg. Chem.*, **2016**, *55*, 3759-3766.
- (158) Chawla, H. M.; Shukla, R.; Pandey, S. *Tetrahedron Lett.*, **2013**, *54*, 2063-2066.
- (159) Pathak, R. K.; Hinge, V. K.; Rai, A.; Panda, D.; Rao, C. P. *Inorg. Chem.*, **2012**, *51*, 4994-5005.
- (160) Joseph, R.; Ramanujam, B.; Acharya, A.; Rao, C. P. *Tetrahedron Lett.*, **2009**, *50*, 2735-2739.

- (161) Zhu, M.; Yuan, M.; Liu, X.; Xu, J.; Lv, J.; Huang, C.; Liu, H.; Li, Y.; Wang, S.; Zhu, D. *Org. Lett.*, **2008**, *10*, 1481-1484.
- (162) Goswami, S.; Chakraborty, S.; Paul, S.; Halder, S.; Panja, S.; Mukhopadhyay, S. K. *Org. Biomol. Chem.*, **2014**, *12*, 3037-3044.
- (163) Bott, S. G.; Coleman, A. W.; Atwood, J. L. *J Am Chem Soc* **1986**, *108*, 1709-1710.
- (164) Dijkstra, P. J.; Brunink, J. A. J.; Bugge, K. E.; Reinhoudt, D. N.; Harkema, S.; Ungaro, R.; Ugozzoli, F.; Ghidini, E. *J Am Chem Soc* **1989**, *111*, 7567-7575.
- (165) Iwamoto, K.; Ikeda, A.; Araki, K.; Haradaa, T.; Shinkai, S. *Tetrahedron*, **1993**, *49*, 9937-9946.
- (166) Casnati, A.; Pochini, A.; Ungaro, R.; Ugozzoli, J. F.; Arnaud, F.; Fanni, S.; Schwing, M. J.; Egberink, R. J. M.; de Jong, F.; Reinhoudt, D. N. *J Am Chem Soc* **1995**, *117*, 2767-2777.
- (167) Montavon, G.; Duplatre, G.; Barakat, N.; Burgard, N.; Asfari, Z.; Vicens, J. *J. Incl. Phenom. Mol. Recogn. Chem.*, **1997**, *27*, 155-168.
- (168) van der Veen, N. J.; Egberink, R. J. M.; Engbersen, J. F. J.; van Veggel, F. J. C. M.; Reinhoudt, D. N. *Chem. Commun.*, **1999**, 681-682.
- (169) Oueslati, I.; Abidi, R.; Amri, H.; Thue'ry, P.; Nierlich, M.; Asfari, Z.; Harrowfield, J.; Vicens, J. *Tetrahedron Lett.*, **2000**, *41*, 8439-8443.
- (170) Talanov, V. S.; Hwang, H. S.; Bartsch, R. A. *J. Chem. Soc., Perkin Trans.*, **2001**, 1103-1108.
- (171) Talanova, G. G.; Talanov, V. S.; Hwang, H. S.; Park, C.; Surowiec, K.; Bartsch, R. A. *Org. Biomol. Chem.*, **2004**, *2*, 2585-2592.
- (172) Desai, V.; Kaler, S. G. *Am. J. Clin. Nutr.*, **2008**, *88*, 855-858.
- (173) Barnham, K. J.; Masters, C. L.; Bush, A. I. *Nat. Rev. Drug Discov.*, **2004**, *3*, 205-214.
- (174) Hahn, S. H.; Tanner, M. S.; Danke, D. M.; Gahl, W. A. *Biochem. Mol. Med.*, **1995**, *54*, 142-145.
- (175) Waggoner, D. J.; Bartnikas, T. B.; Gitlin, J. D. *Neurobiology of Disease*, **1999**, *6*, 221-230.
- (176) Kadirvelu, K.; Thamaraiselvi, K.; Namasivayam, C. *Bioresour. Technol.*, **2001**, *76*, 63-65.

- (177) Miller, M. M.; Wasik, S. P.; Huang, G.-L.; Shiu, W.-Y.; Mackay, D. *Environ. Sci. Technol.* **1985**, *19*, 522-529.
- (178) Burdick; Laboratories, J. *Solvent Guide*; Burdick and Jackson Laboratories, 1984.
- (179) Reynders, P.; Kuhnle, W.; Zachariasse, K. A. *J Am Chem Soc* **1990**, *112*, 3929-3939.
- (180) Siu, H.; Duhamel, J. *Macromolecules*, **2005**, *38*, 7184-7186.
- (181) Li, Y.; Zhou, H.; Chen, J.; Shahzad, S. A.; Yu, C. *Biosensors and Bioelectronics*, **2016**, *76*, 38-53.
- (182) Mei, J.; Leung, N. L. C.; Kwok, R. T. K.; Lam, J. W. Y.; Tang, B. Z. *Chem. Rev.*, **2015**, *115*, 11718-11940.
- (183) Zhao, Z.; Chen, S.; Lam, J. W. Y.; Wang, Z.; Lu, P.; Mahtab, F.; Sung, H. H. Y.; Williams, I. D. W.; Ma, Y.; Kwok, H. S.; Tang, B. Z. *J. Mater. Chem.*, **2011**, *21*, 7210-7216.
- (184) Shyamal, M.; Mazumdar, P.; Maity, S.; Sahoo, G. P.; Salgado-Morán, G.; Misra, A. *J. Phys. Chem. A*, **2016**, *120*, 210-220.
- (185) Diwan, U.; Kumar, V.; Mishra, R. K.; Rana, N. K.; Koch, B.; Singh, M. K.; Upadhyay, K. K. *Anal. Chim. Acta*, **2016**, *929*, 39-48.
- (186) Kim, J. H.; Hwang, A. R.; Chang, S. K. *Tetrahedron Lett.*, **2004**, *45*, 7557-7561.
- (187) Chan, K. L.; Lim, J. P. F.; Yang, X.; Dodabalapur, A.; Jabbour, G. E.; Sellinger, A. *Chem. Commun.*, **2012**, *48*, 5106-5108.
- (188) Winnik, F. M. *Chem. Rev.*, **1993**, *93*, 587-614.
- (189) Guo, D.-S.; Liu, Y. *Acc. Chem. Res.*, **2014**, *47*, 1925-1934.
- (190) Siu, H.; Duhamel, J. *J. Phys. Chem. B*, **2008**, *112*, 15301-15312.
- (191) Sellers, K.; Alsop, W.; Clough, S.; Hoyt, M.; Pugh, B.; Robb, J.; Weeks, K. *Perchlorate: Environmental Problems and Solutions*; CRC Press, 2006.
- (192) Banks, W. H.; Righellato, E. C.; Davies, C. W. *Trans. Faraday Soc.*, **1931**, *27*, 621-627.
- (193) Hayashi, S.; Takigami, A.; Koizumi, T. *ChemPlusChem*, **2016**, *81*, 930-934.
- (194) Chang, Y.-T.; Schutz, P. G. *Bioorg. Med. Chem. Lett.*, **1999**, *9*, 2479-2482.
- (195) Roice, M.; Johannsen, I.; Meldal, M. *QSAR Comb. Sci.*, **2004**, *23*, 662-673.
- (196) Gill, I. *Chem. Mater.*, **2001**, *13*, 3404-3421.

- (197) Li, A.; Lu, R.-F.; Wang, Y.; Wang, X.; Han, K.-L.; Deng, W.-Q. *Angew. Chem. Int. Ed.*, **2010**, *49*, 3330-3333.
- (198) Chen, M.-M.; Li, H.-X.; Lang, J.-P. *Eur. J. Inorg. Chem.*, **2016**, 2508-2515.
- (199) Kumar, S. S.; Mathiyarasu, J.; Lakshminarasimha Phani, K. *J. Electroanal. Chem.*, **2005**, *578*, 95-103.
- (200) Wang, H.; Bai, F.-Q.; Liu, H.; Bai, B.; Ran, X.; Qu, S.; Shi, J.; Xie, D.; Li, H.-Y.; Li, M.; Zhang, H.-Z. *Phys. Chem. Chem. Phys.*, **2011**, *13*, 9697-9705.
- (201) de Almeida, A. K. A.; Dias, J. M. M.; Silva, A. J. C.; Navarro, M.; Junior, S. A.; Tonholo, J.; Ribeiro, A. S. *Synth. Met.* **2013**, *171*, 45-50.
- (202) Takazawa, K. *Chem. Mater.*, **2007**, *19*, 5293-5301.
- (203) Yoon, K.; Hsiao, B. S.; Chu, B. J. *Membr. Sci.*, **2009**, *326*, 484-492.
- (204) Agarwal, S.; Wendorff, J. H.; Greiner, A. *Adv. Mater.*, **2009**, *21*, 3343-3351.
- (205) Kuo, C. C.; Wang, C. T.; Chen, W. C. *Macromol. Mater. Eng.*, **2008**, *293*, 999-1008.
- (206) Lee, S.; Obendorf, S. K. *J. Appl. Polym. Sci.*, **2006**, *102*, 3430-3437.
- (207) Canbolat, M. F.; Celebioglu, A.; Uyar, T. *Colloids Surf., B*, **2014**, *115*, 15-21.
- (208) Min, M.; Shen, L.; Hong, G.; Zhu, M.; Zhang, Y.; Wang, X.; Chen, Y.; Hsiao, B. S. *Chem. Eng. J.*, **2012**, *197*, 88-100.
- (209) Min, M.; Wang, X.; Chen, Y.; Wang, L.; Huang, H.; Shi, J. *Sens. Actuators, B*, **2013**, *188*, 360-366.
- (210) Athira, K. S.; Sanpui, P.; Chatterjee, K. *Journal of Polymer and Biopolymer Physics Chemistry*, **2014**, *2*, 62-66.
- (211) Li, D.; Xia, Y. *Adv. Mater.*, **2004**, *16*, 1151-1170.
- (212) Huang, Z. M.; Zhang, Y. Z.; Kotaki, M.; Ramakrishna, S. *Compos. Sci. Technol.*, **2003**, *63*, 2223-2253.
- (213) Greiner, A.; Wendorff, J. H. *Angew. Chem. Int. Ed.*, **2007**, *46*, 5670-5703.
- (214) Chen, T.; Cai, T.; Jin, Q.; Ji, J. *e-Polymers*, **2015**, *15*, 3-13.
- (215) Ghasemi-Mobarakeh, L.; Prabhakarana, M. P.; Morshedc, M.; Nasr-Esfahani, M.-H.; Ramakrishna, S. *Biomaterials*, **2008**, *29*, 4532-4539.
- (216) Kwon, I. K.; Kidoaki, S.; Matsuda, T. *Biomaterials*, **2005**, *26*, 3929-3939.
- (217) He, X.; Tan, L.; Wu, X.; Yan, C.; Chen, D.; Meng, X.; Tang, F. *J. Mater. Chem.*, **2012**, *22*, 18471-18478.

- (218) Ramos, J.; Velasco-Torrijos, T. *Unpublished Results*.
- (219) Kia, C. S.; Baeka, D. H.; Ganga, K. D.; Leea, K. H.; Umb, I. C.; Park, Y. H. *Polymer*, **2005**, *46*, 5094-5102.
- (220) Zhang, C.; Yuan, X.; Wu, L.; Han, Y.; Sheng, J. *Eur. Polym. J.* **2005**, *41*, 423-432.
- (221) Drew, C.; Wang, X.; Samuelson, L. A.; Kumar, J. *J. Macromol. Sci., Pure Appl. Chem.*, **2003**, *A40*, 1415-1422.
- (222) McKee, M. G.; Wilkes, G. L.; Colby, R. H.; Long, T. E. *Macromolecules*, **2004**, *37*, 1760-1767.
- (223) Bogani, L.; Danieli, C.; Biavardi, E.; Bendiab, N.; Barra, A. L.; Dalcanale, E.; Wernsdorfer, W.; Cornia, A. *Angew. Chem. Int. Ed. Engl.*, **2009**, *48*, 746-750.

Appendix

Publication List

Algay, V.; O'Sullivan, J.; Heaney, F. 2014, C-3 β -Tethered Functional Cholesterol Conjugates by Nitrile Oxide Alkyne Cycloaddition (NOAC), *Eur. J. Org. Chem.*, 2522-2532.

Maher, N. J.; Diao, H.; O'Sullivan, J.; Fadda, E.; Heaney, F.; McGinley, J. 2015, Lower rim isoxazole-calix[4]arene derivatives as fluorescence sensors for copper(II) ions, *Tetrahedron*, 71, 9223-9233.

Oral Presentations

O'Sullivan, J., *Pyrene Functionalised Calixarenes as Metal Sensors*, 67th Irish Universities Chemistry Research Colloquium, **Maynooth University**, (June 2015).

Poster Presentations

O'Sullivan, J.; Heaney, F. *Calixarene Molecules - Delivery Drivers of the Chemical World*, Irish Research Council Annual Symposium, **Dublin Convention Centre**, (September 2013).

O'Sullivan, J.; Heaney, F. *Synthesis of Functional Calixarenes for the Selective Detection of Metal Ions*, 66th Irish Universities Chemistry Research Colloquium, **NUI Galway**, (June 2014).

O'Sullivan, J.; Heaney, F. *Synthesis of Functional Calixarenes for the Selective Detection of Metal Ions*, 3rd RSC Younger Members Symposium, **University of Birmingham**, (June 2014).

O'Sullivan, J.; Heaney, F. *Synthesis of Functional Calixarenes for the Selective Detection of Metal Ions*, Postgraduate Research Day 2014, **Maynooth University**, (September 2014).

O'Sullivan, J.; Heaney, F. *Calix[4]arenes as Metal Sensors: baskets or scaffolds?*, 13th International Conference on Calixarenes "Calix 2015", **Giardini Naxos, Sicily**, (July 2015).

Graduate Modules

Chemistry Specific Modules:

CH801	Core Skills and Research Techniques in Chemistry.
CH803	Teaching Skills in Chemistry.
CH807	Review of Research Papers.
CH808	Research Supervision Training.
BI834	Introduction to Computational Drug Design.

Generic/Transferable Modules:

CTL1	Professional Certificate in Postgraduate Teaching & Learning: Tutors & Demonstrators
GSE1	Information, Literacy & Communications
BI810	Beyond Ph.D. – What Next?

Crystal Structure Report for PIC.2DCM

A specimen of $C_8H_8Cl_4N_2O_6$, approximate dimensions 0.040 mm x 0.100 mm x 0.500 mm, was used for the X-ray crystallographic analysis. The X-ray intensity data were measured. The X-ray intensity data were measured at 100(2)K using an Oxford Cryosystems Cobra low temperature device using a MiTeGen micromount. See Table 1 for collection parameters and exposure time. Bruker APEX software was used to correct for Lorentz and polarization effects.

A total of 2982 frames were collected. The total exposure time was 17.39 hours. The frames were integrated with the Bruker SAINT software package using a wide-frame algorithm. The integration of the data using a monoclinic unit cell yielded a total of 101901 reflections to a maximum θ angle of 59.49° (0.89 Å resolution), of which 10376 were independent (average redundancy 9.821, completeness = 95.6%, $R_{int} = 13.42\%$, $R_{sig} = 8.18\%$) and 8193 (78.96%) were greater than $2\sigma(F^2)$. The final cell constants of $a = 23.5559(19)$ Å, $b = 12.2149(10)$ Å, $c = 24.8863(19)$ Å, $\beta = 91.135(5)^\circ$, volume = $7159.2(10)$ Å³, are based upon the refinement of the XYZ-centroids of 7855 reflections above $20\sigma(I)$ with $7.104^\circ < 2\theta < 101.5^\circ$. Data were corrected for absorption effects using the Multi-Scan method (SADABS). The ratio of minimum to maximum apparent transmission was 0.673. The calculated minimum and maximum transmission coefficients (based on crystal size) are 0.5062 and 0.7522.

The structure was solved and refined using the Bruker SHELXTL and OLEX2 Software Packages, using the space group $P2_1/c$, with $Z = 4$ for the formula unit, $C_8H_8Cl_4N_2O_6$. The final anisotropic full-matrix least-squares refinement on F^2 with 898 variables converged at $R1 = 19.43\%$, for the observed data and $wR2 = 51.20\%$ for all data. The goodness-of-fit was 2.207. The largest peak in the final difference electron density synthesis was $0.850 e^-/\text{Å}^3$ and the largest hole was $-1.225 e^-/\text{Å}^3$ with an RMS deviation of $0.154 e^-/\text{Å}^3$. On the basis of the final model, the calculated density was 1.281 g/cm^3 and $F(000)$, 2908 e^- .

Refinement Note: Data truncated to $D = 0.89\text{Å}$. Poor diffraction. Modelled as a twin (-1 0 0 0 -1 0 0 0 1, BASF = 0.126(3)). Restraints necessary for one CH_2Cl_2 model.

References: see CIF.

Table 1: Data collection details for TCD392_pl.

Axis	dx/mm	2 θ / $^{\circ}$	ω / $^{\circ}$	φ / $^{\circ}$	χ / $^{\circ}$	Width/ $^{\circ}$	Frames	Time/s	Wavelength/ \AA	Voltage/kV	Current/mA	Temperature/K
Omega	50.039	-76.00	161.65	33.17	57.00	1.40	97	21.00	1.54184	45	0.6	100
Omega	50.039	94.41	81.02	297.45	-55.35	1.40	96	21.00	1.54184	45	0.6	100
Omega	50.039	93.31	80.38	162.00	-54.74	1.40	95	21.00	1.54184	45	0.6	100
Omega	50.039	89.30	75.93	254.13	-57.20	1.40	97	21.00	1.54184	45	0.6	100
Omega	50.039	-33.71	206.22	135.00	54.74	1.40	95	21.00	1.54184	45	0.6	100
Omega	50.039	93.31	338.50	360.00	64.88	1.40	90	21.00	1.54184	45	0.6	100
Omega	50.039	-33.71	314.99	0.00	-64.88	1.40	69	21.00	1.54184	45	0.6	100
Omega	50.039	-63.31	175.93	360.00	54.74	1.40	96	21.00	1.54184	45	0.6	100
Phi	50.039	93.31	61.64	0.10	-23.00	1.40	257	21.00	1.54184	45	0.6	100
Omega	50.039	-48.31	190.92	90.00	54.74	1.40	96	21.00	1.54184	45	0.6	100
Phi	50.039	93.31	348.14	193.60	23.00	1.40	192	21.00	1.54184	45	0.6	100
Phi	50.039	93.31	79.77	0.10	-57.06	1.40	257	21.00	1.54184	45	0.6	100
Omega	50.039	-26.89	213.04	0.00	54.74	1.40	95	21.00	1.54184	45	0.6	100
Phi	50.039	78.31	64.77	0.10	-57.06	1.40	257	21.00	1.54184	45	0.6	100
Omega	50.039	-33.71	314.99	270.00	-64.88	1.40	69	21.00	1.54184	45	0.6	100
Omega	50.039	93.31	338.50	27.00	64.87	1.40	90	21.00	1.54184	45	0.6	100
Omega	50.039	-70.02	168.90	12.80	55.55	1.40	96	21.00	1.54184	45	0.6	100
Omega	50.039	93.31	80.38	135.00	-54.74	1.40	95	21.00	1.54184	45	0.6	100
Omega	50.039	-33.71	206.22	90.00	54.74	1.40	95	21.00	1.54184	45	0.6	100
Omega	50.039	-69.88	167.48	26.90	57.76	1.40	97	21.00	1.54184	45	0.6	100
Omega	50.039	93.31	80.37	243.00	-54.74	1.40	95	21.00	1.54184	45	0.6	100
Omega	50.039	-33.71	314.99	45.00	-64.88	1.40	69	21.00	1.54184	45	0.6	100
Omega	50.039	-63.31	175.92	90.00	54.74	1.40	96	21.00	1.54184	45	0.6	100
Omega	50.039	-76.00	161.79	21.25	56.66	1.40	97	21.00	1.54184	45	0.6	100
Omega	50.039	-76.00	161.74	358.26	56.79	1.40	97	21.00	1.54184	45	0.6	100
Omega	50.039	-76.00	161.70	352.23	56.87	1.40	97	21.00	1.54184	45	0.6	100

Table 2. Crystal data and structure refinement for tcd392_pl.

Identification code	tcd392_pl	
Empirical formula	$C_{86}H_{81}Cl_4N_2O_6$	
Formula weight	1380.32	
Temperature	100.15 K	
Wavelength	1.54178 Å	
Crystal system	Monoclinic	
Space group	$P2_1/c$	
Unit cell dimensions	$a = 23.5559(19)$ Å	$\alpha = 90^\circ$.
	$b = 12.2149(10)$ Å	$\beta = 91.135(5)^\circ$.
	$c = 24.8863(19)$ Å	$\gamma = 90^\circ$.
Volume	$7159.2(10)$ Å ³	
Z	4	
Density (calculated)	1.281 Mg/m ³	
Absorption coefficient	1.951 mm ⁻¹	
F(000)	2908	
Crystal size	0.5 x 0.1 x 0.04 mm ³	
Theta range for data collection	1.775 to 59.495°.	
Index ranges	$-26 \leq h \leq 26$, $-13 \leq k \leq 13$, $-27 \leq l \leq 27$	
Reflections collected	101901	
Independent reflections	10376 [R(int) = 0.1342]	
Completeness to theta = 59.495°	99.6 %	
Absorption correction	Semi-empirical from equivalents	
Max. and min. transmission	0.7522 and 0.5062	
Refinement method	Full-matrix least-squares on F ²	
Data / restraints / parameters	10376 / 7 / 898	
Goodness-of-fit on F ²	2.207	
Final R indices [I > 2σ(I)]	R1 = 0.1943, wR2 = 0.4923	
R indices (all data)	R1 = 0.2146, wR2 = 0.5120	
Largest diff. peak and hole	0.850 and -1.225 e.Å ⁻³	

Table 3. Atomic coordinates ($\times 10^4$) and equivalent isotropic displacement parameters ($\text{\AA}^2 \times 10^3$) for tcd392_pl. $U(\text{eq})$ is defined as one third of the trace of the orthogonalized U^{ij} tensor.

	x	y	z	U(eq)
O(00H)	3060(3)	5650(7)	3088(3)	45(2)
O(00K)	4304(4)	3663(7)	3222(4)	56(2)
O(00N)	3054(3)	2931(7)	3831(3)	41(2)
O(002)	3096(3)	5229(6)	4148(3)	38(2)
C(010)	3882(4)	4985(9)	4757(4)	35(2)
C(017)	1485(10)	9059(13)	1827(7)	91(6)
C(003)	2308(4)	6456(9)	4214(4)	32(2)
C(005)	2569(5)	7255(8)	3813(4)	35(2)
C(00A)	2421(5)	4175(9)	2124(4)	42(3)
C(00B)	2625(5)	3362(10)	2477(4)	42(3)
O(00C)	3720(3)	4909(6)	5264(3)	38(2)
C(00F)	2569(4)	5492(9)	4362(4)	31(2)
C(00M)	2529(5)	2495(8)	3915(4)	36(2)
C(00O)	7540(6)	1186(12)	4809(6)	60(4)
C(00T)	2364(5)	7089(8)	3241(4)	34(2)
C(00U)	2306(5)	2447(9)	2570(4)	38(3)
C(00W)	6679(6)	-1165(10)	4287(5)	48(3)
C(00Y)	1161(7)	2177(13)	1120(7)	79(5)
C(011)	2293(4)	4729(8)	4693(4)	32(2)
C(016)	2706(5)	5263(9)	2027(5)	41(3)
C(019)	6066(5)	623(9)	3859(4)	37(2)
C(01A)	946(5)	6301(10)	5002(5)	43(3)
C(01C)	1782(5)	6699(8)	4423(4)	35(2)
C(01D)	5883(5)	-457(9)	3750(4)	37(2)
O(01I)	3141(3)	3454(7)	2759(3)	43(2)
C(01K)	586(7)	2256(18)	1980(9)	99(7)
C(01L)	2269(5)	1778(8)	3534(4)	31(2)
C(01N)	5218(5)	1320(10)	3377(4)	41(3)
C(01R)	2437(5)	6145(9)	2383(4)	36(2)
N(01T)	4750(5)	3085(8)	3480(4)	52(3)
C(01U)	5731(5)	1538(9)	3677(5)	39(3)
C(01X)	2540(5)	3574(9)	4789(5)	43(3)
C(01Y)	7372(6)	101(12)	4721(6)	60(4)

C(022)	1008(6)	2871(10)	1632(5)	52(3)
C(023)	5955(5)	2624(9)	3776(5)	45(3)
C(024)	6218(5)	-1376(10)	3983(5)	49(3)
C(027)	686(5)	5432(11)	5339(5)	46(3)
N(02C)	4059(4)	4112(8)	5537(3)	43(2)
C(02D)	5400(5)	-652(10)	3433(5)	48(3)
C(02F)	451(5)	1378(13)	3820(7)	65(4)
C(02N)	7259(5)	2054(11)	4585(5)	50(3)
C(02Q)	1904(5)	3976(9)	1844(4)	44(3)
C(02X)	1741(5)	2264(9)	4522(4)	39(3)
C(02Z)	6446(5)	2755(10)	4046(5)	44(3)
C(030)	658(8)	1390(15)	4810(7)	81(5)
C(036)	6769(5)	1900(10)	4282(5)	48(3)
C(038)	4811(6)	2160(12)	3211(5)	53(3)
C(03D)	4339(5)	4270(11)	4676(5)	46(3)
C(03I)	2615(5)	6280(9)	2908(4)	40(3)
C(03J)	6889(5)	-76(10)	4397(5)	48(3)
C(03S)	5072(5)	235(10)	3254(5)	43(3)
C(03Z)	1468(5)	1554(9)	4152(5)	44(3)
C(045)	4128(5)	3070(12)	2798(4)	53(3)
C(047)	1020(6)	7351(10)	5330(5)	52(3)
C(048)	2276(5)	2734(8)	4400(4)	34(2)
C(049)	3647(6)	3534(17)	2466(6)	80(5)
C(04A)	1991(5)	6797(9)	2186(4)	40(3)
C(04C)	890(5)	1038(10)	4262(5)	50(3)
C(04E)	6572(5)	791(9)	4192(4)	38(3)
C(04F)	1907(5)	7686(8)	3021(4)	34(2)
C(04H)	506(5)	6586(12)	4529(5)	57(4)
C(04I)	4418(6)	2101(12)	2768(5)	57(3)
C(04J)	955(7)	-205(11)	4266(8)	69(4)
C(04L)	1510(5)	5991(9)	4766(4)	37(2)
C(04S)	741(7)	3926(10)	1445(7)	67(4)
C(04U)	1575(5)	3065(9)	1934(4)	41(3)
C(04V)	3584(5)	5743(10)	4401(5)	43(3)
C(04X)	2489(5)	1580(9)	3002(4)	41(3)
C(04Z)	1732(5)	1351(9)	3671(5)	42(3)
C(050)	1790(5)	2295(9)	2308(5)	41(3)
C(004)	4427(5)	3781(9)	5180(5)	41(3)

C(007)	1773(4)	5006(8)	4890(4)	34(2)
C(009)	5849(5)	1854(9)	6385(5)	44(3)
C(01S)	6018(6)	284(10)	5583(5)	55(3)
C(02P)	5530(5)	1966(9)	5886(4)	38(3)
C(02T)	4937(6)	2117(9)	4907(5)	46(3)
C(02W)	5769(5)	2663(9)	6797(4)	42(3)
C(034)	5135(5)	2835(8)	5794(4)	36(2)
C(03A)	5613(5)	1162(9)	5473(4)	42(3)
C(03F)	5318(6)	1263(9)	5003(5)	46(3)
C(03T)	4848(5)	2912(9)	5299(4)	41(3)
C(040)	5372(5)	3533(9)	6702(4)	38(3)
C(041)	5085(5)	3627(10)	6225(4)	42(3)
C(046)	6238(5)	993(9)	6471(4)	44(3)
C(04G)	6074(5)	2538(9)	7283(5)	46(3)
C(04W)	6526(6)	903(11)	6973(5)	54(3)
C(012)	6299(6)	200(11)	6057(6)	57(3)
C(01M)	6446(6)	1671(11)	7360(5)	51(3)
C(00L)	1730(5)	7578(8)	2499(4)	37(3)
C(02E)	924(8)	8923(13)	2673(7)	79(5)
C(03R)	1208(7)	8242(9)	2263(5)	59(4)
C(03N)	791(7)	7525(13)	1971(8)	81(5)
CI(00)	1431(3)	4161(5)	3510(2)	124(2)
C(02K)	1190(9)	5100(13)	3072(7)	81(5)
CI(02)	2475(3)	4803(6)	6211(4)	150(3)
C(03U)	2930(7)	3785(15)	6360(7)	87(5)
CI(1)	3459(5)	4146(7)	6834(3)	166(4)
CI(01)	425(2)	5078(6)	3036(3)	139(3)

Table 4. Bond lengths [\AA] and angles [$^\circ$] for tcd392_pl.

O(00H)-H(00H)	0.8400	C(00U)-C(050)	1.379(16)
O(00H)-C(03I)	1.368(14)	C(00W)-H(00W)	0.9500
O(00K)-N(01T)	1.410(13)	C(00W)-C(024)	1.337(18)
O(00K)-C(045)	1.339(16)	C(00W)-C(03J)	1.444(18)
O(00N)-H(00N)	0.8400	C(00Y)-H(00C)	0.9800
O(00N)-C(00M)	1.366(14)	C(00Y)-H(00D)	0.9800
O(002)-C(00F)	1.397(13)	C(00Y)-H(00E)	0.9800
O(002)-C(04V)	1.443(13)	C(00Y)-C(022)	1.58(2)
C(010)-O(00C)	1.329(13)	C(011)-C(01X)	1.543(15)
C(010)-C(03D)	1.405(17)	C(011)-C(007)	1.372(16)
C(010)-C(04V)	1.454(16)	C(016)-H(01D)	0.9900
C(017)-H(01A)	0.9800	C(016)-H(01E)	0.9900
C(017)-H(01B)	0.9800	C(016)-C(01R)	1.540(16)
C(017)-H(01C)	0.9800	C(019)-C(01D)	1.412(16)
C(017)-C(03R)	1.62(2)	C(019)-C(01U)	1.435(16)
C(003)-C(005)	1.532(14)	C(019)-C(04E)	1.454(16)
C(003)-C(00F)	1.375(15)	C(01A)-C(027)	1.492(17)
C(003)-C(01C)	1.386(15)	C(01A)-C(047)	1.528(17)
C(005)-H(00A)	0.9900	C(01A)-C(04H)	1.591(16)
C(005)-H(00B)	0.9900	C(01A)-C(04L)	1.511(16)
C(005)-C(00T)	1.509(14)	C(01C)-H(01F)	0.9500
C(00A)-C(00B)	1.404(17)	C(01C)-C(04L)	1.381(15)
C(00A)-C(016)	1.511(16)	C(01D)-C(024)	1.484(17)
C(00A)-C(02Q)	1.411(17)	C(01D)-C(02D)	1.391(17)
C(00B)-C(00U)	1.370(17)	O(01I)-C(049)	1.413(17)
C(00B)-O(01I)	1.396(14)	C(01K)-H(01G)	0.9800
O(00C)-N(02C)	1.422(12)	C(01K)-H(01H)	0.9800
C(00F)-C(011)	1.411(15)	C(01K)-H(01I)	0.9800
C(00M)-C(01L)	1.421(15)	C(01K)-C(022)	1.53(2)
C(00M)-C(048)	1.388(15)	C(01L)-C(04X)	1.451(15)
C(00O)-H(00O)	0.9500	C(01L)-C(04Z)	1.415(16)
C(00O)-C(01Y)	1.40(2)	C(01N)-C(01U)	1.433(16)
C(00O)-C(02N)	1.363(19)	C(01N)-C(038)	1.459(18)
C(00T)-C(03I)	1.425(15)	C(01N)-C(03S)	1.402(17)
C(00T)-C(04F)	1.403(16)	C(01R)-C(03I)	1.374(16)
C(00U)-C(04X)	1.563(15)	C(01R)-C(04A)	1.398(16)

N(01T)-C(038)	1.323(17)	C(03D)-C(004)	1.402(17)
C(01U)-C(023)	1.447(17)	C(03J)-C(04E)	1.387(17)
C(01X)-H(01J)	0.9900	C(03S)-H(03S)	0.9500
C(01X)-H(01K)	0.9900	C(03Z)-C(04C)	1.530(18)
C(01X)-C(048)	1.534(15)	C(03Z)-C(04Z)	1.383(17)
C(01Y)-H(01Y)	0.9500	C(045)-C(049)	1.501(18)
C(01Y)-C(03J)	1.40(2)	C(045)-C(04I)	1.369(19)
C(022)-C(04S)	1.503(18)	C(047)-H(04A)	0.9800
C(022)-C(04U)	1.537(17)	C(047)-H(04B)	0.9800
C(023)-H(023)	0.9500	C(047)-H(04C)	0.9800
C(023)-C(02Z)	1.335(17)	C(049)-H(049)	0.9500
C(024)-H(024)	0.9500	C(04A)-H(04D)	0.9500
C(027)-H(02A)	0.9800	C(04A)-C(00L)	1.383(16)
C(027)-H(02B)	0.9800	C(04C)-C(04J)	1.526(18)
C(027)-H(02C)	0.9800	C(04F)-H(04F)	0.9500
N(02C)-C(004)	1.316(15)	C(04F)-C(00L)	1.362(15)
C(02D)-H(02D)	0.9500	C(04H)-H(04E)	0.9800
C(02D)-C(03S)	1.398(18)	C(04H)-H(04G)	0.9800
C(02F)-H(02E)	0.9800	C(04H)-H(04H)	0.9800
C(02F)-H(02F)	0.9800	C(04I)-H(04I)	0.9500
C(02F)-H(02G)	0.9800	C(04J)-H(04J)	0.9800
C(02F)-C(04C)	1.55(2)	C(04J)-H(04K)	0.9800
C(02N)-H(02N)	0.9500	C(04J)-H(04L)	0.9800
C(02N)-C(036)	1.381(18)	C(04L)-C(007)	1.385(15)
C(02Q)-H(02Q)	0.9500	C(04S)-H(04M)	0.9800
C(02Q)-C(04U)	1.378(17)	C(04S)-H(04N)	0.9800
C(02X)-H(02X)	0.9500	C(04S)-H(04O)	0.9800
C(02X)-C(03Z)	1.410(16)	C(04U)-C(050)	1.410(16)
C(02X)-C(048)	1.423(16)	C(04V)-H(04P)	0.9900
C(02Z)-H(02Z)	0.9500	C(04V)-H(04Q)	0.9900
C(02Z)-C(036)	1.413(18)	C(04X)-H(04R)	0.9900
C(030)-H(03A)	0.9800	C(04X)-H(04S)	0.9900
C(030)-H(03B)	0.9800	C(04Z)-H(04Z)	0.9500
C(030)-H(03C)	0.9800	C(050)-H(050)	0.9500
C(030)-C(04C)	1.54(2)	C(004)-C(03T)	1.478(17)
C(036)-C(04E)	1.448(17)	C(007)-H(007)	0.9500
C(038)-C(04I)	1.427(19)	C(009)-C(02P)	1.444(17)
C(03D)-H(03D)	0.9500	C(009)-C(02W)	1.439(16)

C(009)-C(046)	1.408(17)	C(02K)-Cl(01)	1.80(2)
C(01S)-H(01S)	0.9500	Cl(02)-C(03U)	1.679(15)
C(01S)-C(03A)	1.456(18)	C(03U)-H(03I)	0.9900
C(01S)-C(012)	1.35(2)	C(03U)-H(03J)	0.9900
C(02P)-C(034)	1.426(16)	C(03U)-Cl(1)	1.754(15)
C(02P)-C(03A)	1.438(16)		
C(02T)-H(02T)	0.9500	C(03I)-O(00H)-H(00H)	109.5
C(02T)-C(03F)	1.395(18)	C(045)-O(00K)-N(01T)	107.7(9)
C(02T)-C(03T)	1.394(16)	C(00M)-O(00N)-H(00N)	109.5
C(02W)-C(040)	1.432(17)	C(00F)-O(002)-C(04V)	116.1(8)
C(02W)-C(04G)	1.403(17)	O(00C)-C(010)-C(03D)	109.2(9)
C(034)-C(03T)	1.398(16)	O(00C)-C(010)-C(04V)	118.7(10)
C(034)-C(041)	1.451(16)	C(03D)-C(010)-C(04V)	132.1(10)
C(03A)-C(03F)	1.355(17)	H(01A)-C(017)-H(01B)	109.5
C(03F)-H(03F)	0.9500	H(01A)-C(017)-H(01C)	109.5
C(040)-H(040)	0.9500	H(01B)-C(017)-H(01C)	109.5
C(040)-C(041)	1.359(16)	C(03R)-C(017)-H(01A)	109.5
C(041)-H(041)	0.9500	C(03R)-C(017)-H(01B)	109.5
C(046)-C(04W)	1.413(19)	C(03R)-C(017)-H(01C)	109.5
C(046)-C(012)	1.423(19)	C(00F)-C(003)-C(005)	122.5(9)
C(04G)-H(04T)	0.9500	C(00F)-C(003)-C(01C)	118.7(9)
C(04G)-C(01M)	1.387(18)	C(01C)-C(003)-C(005)	118.8(10)
C(04W)-H(04W)	0.9500	C(003)-C(005)-H(00A)	108.8
C(04W)-C(01M)	1.360(19)	C(003)-C(005)-H(00B)	108.8
C(012)-H(012)	0.9500	H(00A)-C(005)-H(00B)	107.7
C(01M)-H(01M)	0.9500	C(00T)-C(005)-C(003)	113.8(8)
C(00L)-C(03R)	1.579(16)	C(00T)-C(005)-H(00A)	108.8
C(02E)-H(02H)	0.9800	C(00T)-C(005)-H(00B)	108.8
C(02E)-H(02I)	0.9800	C(00B)-C(00A)-C(016)	125.0(11)
C(02E)-H(02J)	0.9800	C(00B)-C(00A)-C(02Q)	117.9(11)
C(02E)-C(03R)	1.49(2)	C(02Q)-C(00A)-C(016)	117.1(10)
C(03R)-C(03N)	1.49(2)	C(00U)-C(00B)-C(00A)	120.1(11)
C(03N)-H(03E)	0.9800	C(00U)-C(00B)-O(01I)	117.1(10)
C(03N)-H(03G)	0.9800	O(01I)-C(00B)-C(00A)	122.8(11)
C(03N)-H(03H)	0.9800	C(010)-O(00C)-N(02C)	109.4(8)
Cl(00)-C(02K)	1.674(18)	O(002)-C(00F)-C(011)	119.5(9)
C(02K)-H(02K)	0.9900	C(003)-C(00F)-O(002)	119.3(9)
C(02K)-H(02L)	0.9900	C(003)-C(00F)-C(011)	120.9(9)

O(00N)-C(00M)-C(01L)	121.3(9)	C(04L)-C(01A)-C(04H)	109.4(9)
O(00N)-C(00M)-C(048)	117.1(9)	C(003)-C(01C)-H(01F)	119.0
C(048)-C(00M)-C(01L)	121.5(10)	C(04L)-C(01C)-C(003)	121.9(10)
C(01Y)-C(00O)-H(00O)	118.7	C(04L)-C(01C)-H(01F)	119.0
C(02N)-C(00O)-H(00O)	118.7	C(019)-C(01D)-C(024)	118.3(10)
C(02N)-C(00O)-C(01Y)	122.6(12)	C(02D)-C(01D)-C(019)	120.7(10)
C(03I)-C(00T)-C(005)	120.9(10)	C(02D)-C(01D)-C(024)	121.0(10)
C(04F)-C(00T)-C(005)	121.8(9)	C(00B)-O(01I)-C(049)	118.8(9)
C(04F)-C(00T)-C(03I)	117.3(9)	H(01G)-C(01K)-H(01H)	109.5
C(00B)-C(00U)-C(04X)	121.6(10)	H(01G)-C(01K)-H(01I)	109.5
C(00B)-C(00U)-C(050)	120.6(10)	H(01H)-C(01K)-H(01I)	109.5
C(050)-C(00U)-C(04X)	117.6(10)	C(022)-C(01K)-H(01G)	109.5
C(024)-C(00W)-H(00W)	118.1	C(022)-C(01K)-H(01H)	109.5
C(024)-C(00W)-C(03J)	123.8(11)	C(022)-C(01K)-H(01I)	109.5
C(03J)-C(00W)-H(00W)	118.1	C(00M)-C(01L)-C(04X)	123.6(10)
H(00C)-C(00Y)-H(00D)	109.5	C(04Z)-C(01L)-C(00M)	116.2(9)
H(00C)-C(00Y)-H(00E)	109.5	C(04Z)-C(01L)-C(04X)	119.7(10)
H(00D)-C(00Y)-H(00E)	109.5	C(01U)-C(01N)-C(038)	124.1(11)
C(022)-C(00Y)-H(00C)	109.5	C(03S)-C(01N)-C(01U)	119.3(10)
C(022)-C(00Y)-H(00D)	109.5	C(03S)-C(01N)-C(038)	116.5(11)
C(022)-C(00Y)-H(00E)	109.5	C(03I)-C(01R)-C(016)	120.5(10)
C(00F)-C(011)-C(01X)	121.2(10)	C(03I)-C(01R)-C(04A)	118.6(10)
C(007)-C(011)-C(00F)	118.1(9)	C(04A)-C(01R)-C(016)	120.8(9)
C(007)-C(011)-C(01X)	120.5(9)	C(038)-N(01T)-O(00K)	106.5(10)
C(00A)-C(016)-H(01D)	109.8	C(019)-C(01U)-C(023)	117.7(10)
C(00A)-C(016)-H(01E)	109.8	C(01N)-C(01U)-C(019)	118.1(10)
C(00A)-C(016)-C(01R)	109.6(9)	C(01N)-C(01U)-C(023)	124.0(10)
H(01D)-C(016)-H(01E)	108.2	C(011)-C(01X)-H(01J)	109.3
C(01R)-C(016)-H(01D)	109.8	C(011)-C(01X)-H(01K)	109.3
C(01R)-C(016)-H(01E)	109.8	H(01J)-C(01X)-H(01K)	108.0
C(01D)-C(019)-C(01U)	120.2(10)	C(048)-C(01X)-C(011)	111.6(9)
C(01D)-C(019)-C(04E)	119.0(10)	C(048)-C(01X)-H(01J)	109.3
C(01U)-C(019)-C(04E)	120.5(9)	C(048)-C(01X)-H(01K)	109.3
C(027)-C(01A)-C(047)	109.9(10)	C(00O)-C(01Y)-H(01Y)	121.3
C(027)-C(01A)-C(04H)	107.6(10)	C(03J)-C(01Y)-C(00O)	117.4(12)
C(027)-C(01A)-C(04L)	114.4(10)	C(03J)-C(01Y)-H(01Y)	121.3
C(047)-C(01A)-C(04H)	106.2(10)	C(01K)-C(022)-C(00Y)	110.8(14)
C(04L)-C(01A)-C(047)	109.0(10)	C(01K)-C(022)-C(04U)	111.5(11)

C(04S)-C(022)-C(00Y)	108.2(12)	H(03A)-C(030)-H(03B)	109.5
C(04S)-C(022)-C(01K)	108.9(14)	H(03A)-C(030)-H(03C)	109.5
C(04S)-C(022)-C(04U)	111.9(10)	H(03B)-C(030)-H(03C)	109.5
C(04U)-C(022)-C(00Y)	105.5(11)	C(04C)-C(030)-H(03A)	109.5
C(01U)-C(023)-H(023)	119.9	C(04C)-C(030)-H(03B)	109.5
C(02Z)-C(023)-C(01U)	120.3(11)	C(04C)-C(030)-H(03C)	109.5
C(02Z)-C(023)-H(023)	119.9	C(02N)-C(036)-C(02Z)	124.4(11)
C(00W)-C(024)-C(01D)	119.7(11)	C(02N)-C(036)-C(04E)	118.3(11)
C(00W)-C(024)-H(024)	120.1	C(02Z)-C(036)-C(04E)	117.3(11)
C(01D)-C(024)-H(024)	120.1	N(01T)-C(038)-C(01N)	122.3(12)
C(01A)-C(027)-H(02A)	109.5	N(01T)-C(038)-C(04I)	111.0(12)
C(01A)-C(027)-H(02B)	109.5	C(04I)-C(038)-C(01N)	126.6(12)
C(01A)-C(027)-H(02C)	109.5	C(010)-C(03D)-H(03D)	128.2
H(02A)-C(027)-H(02B)	109.5	C(004)-C(03D)-C(010)	103.6(10)
H(02A)-C(027)-H(02C)	109.5	C(004)-C(03D)-H(03D)	128.2
H(02B)-C(027)-H(02C)	109.5	O(00H)-C(03I)-C(00T)	121.6(10)
C(004)-N(02C)-O(00C)	105.1(8)	O(00H)-C(03I)-C(01R)	117.5(10)
C(01D)-C(02D)-H(02D)	120.4	C(01R)-C(03I)-C(00T)	120.8(10)
C(01D)-C(02D)-C(03S)	119.2(11)	C(01Y)-C(03J)-C(00W)	121.5(12)
C(03S)-C(02D)-H(02D)	120.4	C(04E)-C(03J)-C(00W)	117.0(11)
H(02E)-C(02F)-H(02F)	109.5	C(04E)-C(03J)-C(01Y)	121.4(12)
H(02E)-C(02F)-H(02G)	109.5	C(01N)-C(03S)-H(03S)	118.9
H(02F)-C(02F)-H(02G)	109.5	C(02D)-C(03S)-C(01N)	122.1(11)
C(04C)-C(02F)-H(02E)	109.5	C(02D)-C(03S)-H(03S)	118.9
C(04C)-C(02F)-H(02F)	109.5	C(02X)-C(03Z)-C(04C)	122.2(11)
C(04C)-C(02F)-H(02G)	109.5	C(04Z)-C(03Z)-C(02X)	118.0(11)
C(00O)-C(02N)-H(02N)	119.6	C(04Z)-C(03Z)-C(04C)	119.9(10)
C(00O)-C(02N)-C(036)	120.8(12)	O(00K)-C(045)-C(049)	116.5(12)
C(036)-C(02N)-H(02N)	119.6	O(00K)-C(045)-C(04I)	111.4(10)
C(00A)-C(02Q)-H(02Q)	118.6	C(04I)-C(045)-C(049)	132.0(14)
C(04U)-C(02Q)-C(00A)	122.8(10)	C(01A)-C(047)-H(04A)	109.5
C(04U)-C(02Q)-H(02Q)	118.6	C(01A)-C(047)-H(04B)	109.5
C(03Z)-C(02X)-H(02X)	119.9	C(01A)-C(047)-H(04C)	109.5
C(03Z)-C(02X)-C(048)	120.2(10)	H(04A)-C(047)-H(04B)	109.5
C(048)-C(02X)-H(02X)	119.9	H(04A)-C(047)-H(04C)	109.5
C(023)-C(02Z)-H(02Z)	117.5	H(04B)-C(047)-H(04C)	109.5
C(023)-C(02Z)-C(036)	125.1(11)	C(00M)-C(048)-C(01X)	121.0(10)
C(036)-C(02Z)-H(02Z)	117.5	C(00M)-C(048)-C(02X)	119.9(9)

C(02X)-C(048)-C(01X)	119.0(10)	C(022)-C(04S)-H(04N)	109.5
O(01I)-C(049)-C(045)	109.1(12)	C(022)-C(04S)-H(04O)	109.5
O(01I)-C(049)-H(049)	125.5	H(04M)-C(04S)-H(04N)	109.5
C(045)-C(049)-H(049)	125.5	H(04M)-C(04S)-H(04O)	109.5
C(01R)-C(04A)-H(04D)	118.9	H(04N)-C(04S)-H(04O)	109.5
C(00L)-C(04A)-C(01R)	122.2(10)	C(02Q)-C(04U)-C(022)	122.1(10)
C(00L)-C(04A)-H(04D)	118.9	C(02Q)-C(04U)-C(050)	116.6(10)
C(030)-C(04C)-C(02F)	108.0(12)	C(050)-C(04U)-C(022)	121.2(11)
C(03Z)-C(04C)-C(02F)	110.2(11)	O(002)-C(04V)-C(010)	111.1(9)
C(03Z)-C(04C)-C(030)	112.2(10)	O(002)-C(04V)-H(04P)	109.4
C(04J)-C(04C)-C(02F)	109.7(12)	O(002)-C(04V)-H(04Q)	109.4
C(04J)-C(04C)-C(030)	108.0(13)	C(010)-C(04V)-H(04P)	109.4
C(04J)-C(04C)-C(03Z)	108.8(10)	C(010)-C(04V)-H(04Q)	109.4
C(036)-C(04E)-C(019)	118.5(10)	H(04P)-C(04V)-H(04Q)	108.0
C(03J)-C(04E)-C(019)	122.1(10)	C(00U)-C(04X)-H(04R)	108.6
C(03J)-C(04E)-C(036)	119.2(11)	C(00U)-C(04X)-H(04S)	108.6
C(00T)-C(04F)-H(04F)	118.7	C(01L)-C(04X)-C(00U)	114.6(9)
C(00L)-C(04F)-C(00T)	122.6(10)	C(01L)-C(04X)-H(04R)	108.6
C(00L)-C(04F)-H(04F)	118.7	C(01L)-C(04X)-H(04S)	108.6
C(01A)-C(04H)-H(04E)	109.5	H(04R)-C(04X)-H(04S)	107.6
C(01A)-C(04H)-H(04G)	109.5	C(01L)-C(04Z)-H(04Z)	117.9
C(01A)-C(04H)-H(04H)	109.5	C(03Z)-C(04Z)-C(01L)	124.2(10)
H(04E)-C(04H)-H(04G)	109.5	C(03Z)-C(04Z)-H(04Z)	117.9
H(04E)-C(04H)-H(04H)	109.5	C(00U)-C(050)-C(04U)	121.7(11)
H(04G)-C(04H)-H(04H)	109.5	C(00U)-C(050)-H(050)	119.1
C(038)-C(04I)-H(04I)	128.3	C(04U)-C(050)-H(050)	119.1
C(045)-C(04I)-C(038)	103.3(12)	N(02C)-C(004)-C(03D)	112.7(11)
C(045)-C(04I)-H(04I)	128.3	N(02C)-C(004)-C(03T)	122.3(10)
C(04C)-C(04J)-H(04J)	109.5	C(03D)-C(004)-C(03T)	124.8(11)
C(04C)-C(04J)-H(04K)	109.5	C(011)-C(007)-C(04L)	122.2(10)
C(04C)-C(04J)-H(04L)	109.5	C(011)-C(007)-H(007)	118.9
H(04J)-C(04J)-H(04K)	109.5	C(04L)-C(007)-H(007)	118.9
H(04J)-C(04J)-H(04L)	109.5	C(02W)-C(009)-C(02P)	118.3(10)
H(04K)-C(04J)-H(04L)	109.5	C(046)-C(009)-C(02P)	121.9(11)
C(01C)-C(04L)-C(01A)	120.4(10)	C(046)-C(009)-C(02W)	119.8(11)
C(01C)-C(04L)-C(007)	118.0(10)	C(03A)-C(01S)-H(01S)	119.0
C(007)-C(04L)-C(01A)	121.6(10)	C(012)-C(01S)-H(01S)	119.0
C(022)-C(04S)-H(04M)	109.5	C(012)-C(01S)-C(03A)	122.0(12)

C(034)-C(02P)-C(009)	122.4(10)	C(046)-C(012)-H(012)	119.1
C(034)-C(02P)-C(03A)	119.4(10)	C(04G)-C(01M)-H(01M)	119.2
C(03A)-C(02P)-C(009)	118.2(10)	C(04W)-C(01M)-C(04G)	121.6(11)
C(03F)-C(02T)-H(02T)	119.8	C(04W)-C(01M)-H(01M)	119.2
C(03T)-C(02T)-H(02T)	119.8	C(04A)-C(00L)-C(03R)	119.7(9)
C(03T)-C(02T)-C(03F)	120.4(11)	C(04F)-C(00L)-C(04A)	118.3(9)
C(040)-C(02W)-C(009)	119.1(10)	C(04F)-C(00L)-C(03R)	121.8(10)
C(04G)-C(02W)-C(009)	118.0(11)	H(02H)-C(02E)-H(02I)	109.5
C(04G)-C(02W)-C(040)	122.9(10)	H(02H)-C(02E)-H(02J)	109.5
C(02P)-C(034)-C(041)	116.1(10)	H(02I)-C(02E)-H(02J)	109.5
C(03T)-C(034)-C(02P)	119.6(10)	C(03R)-C(02E)-H(02H)	109.5
C(03T)-C(034)-C(041)	124.2(11)	C(03R)-C(02E)-H(02I)	109.5
C(02P)-C(03A)-C(01S)	117.8(11)	C(03R)-C(02E)-H(02J)	109.5
C(03F)-C(03A)-C(01S)	123.4(11)	C(00L)-C(03R)-C(017)	104.1(13)
C(03F)-C(03A)-C(02P)	118.7(11)	C(02E)-C(03R)-C(017)	107.9(12)
C(02T)-C(03F)-H(03F)	118.9	C(02E)-C(03R)-C(00L)	113.0(10)
C(03A)-C(03F)-C(02T)	122.2(11)	C(02E)-C(03R)-C(03N)	111.2(15)
C(03A)-C(03F)-H(03F)	118.9	C(03N)-C(03R)-C(017)	107.8(13)
C(02T)-C(03T)-C(004)	118.0(10)	C(03N)-C(03R)-C(00L)	112.4(10)
C(02T)-C(03T)-C(034)	119.5(11)	C(03R)-C(03N)-H(03E)	109.5
C(034)-C(03T)-C(004)	122.4(10)	C(03R)-C(03N)-H(03G)	109.5
C(02W)-C(040)-H(040)	119.4	C(03R)-C(03N)-H(03H)	109.5
C(041)-C(040)-C(02W)	121.3(10)	H(03E)-C(03N)-H(03G)	109.5
C(041)-C(040)-H(040)	119.4	H(03E)-C(03N)-H(03H)	109.5
C(034)-C(041)-H(041)	118.6	H(03G)-C(03N)-H(03H)	109.5
C(040)-C(041)-C(034)	122.8(12)	Cl(00)-C(02K)-H(02K)	109.6
C(040)-C(041)-H(041)	118.6	Cl(00)-C(02K)-H(02L)	109.6
C(009)-C(046)-C(04W)	119.5(11)	Cl(00)-C(02K)-Cl(01)	110.4(10)
C(009)-C(046)-C(012)	118.2(11)	H(02K)-C(02K)-H(02L)	108.1
C(04W)-C(046)-C(012)	122.2(12)	Cl(01)-C(02K)-H(02K)	109.6
C(02W)-C(04G)-H(04T)	119.6	Cl(01)-C(02K)-H(02L)	109.6
C(01M)-C(04G)-C(02W)	120.9(11)	Cl(02)-C(03U)-H(03I)	108.8
C(01M)-C(04G)-H(04T)	119.6	Cl(02)-C(03U)-H(03J)	108.8
C(046)-C(04W)-H(04W)	119.9	Cl(02)-C(03U)-Cl(1)	113.8(11)
C(01M)-C(04W)-C(046)	120.1(12)	H(03I)-C(03U)-H(03J)	107.7
C(01M)-C(04W)-H(04W)	119.9	Cl(1)-C(03U)-H(03I)	108.8
C(01S)-C(012)-C(046)	121.8(12)	Cl(1)-C(03U)-H(03J)	108.8
C(01S)-C(012)-H(012)	119.1		

Table 5. Anisotropic displacement parameters ($\text{\AA}^2 \times 10^3$) for tcd392_pl. The anisotropic displacement factor exponent takes the form: $-2\pi^2[h^2 a^{*2}U^{11} + \dots + 2 h k a^* b^* U^{12}]$

	U^{11}	U^{22}	U^{33}	U^{23}	U^{13}	U^{12}
O(00H)	37(4)	66(5)	32(4)	1(4)	5(3)	9(4)
O(00K)	45(5)	52(5)	70(6)	3(4)	7(4)	12(4)
O(00N)	32(4)	64(5)	29(4)	-3(3)	5(3)	-4(3)
O(002)	27(4)	59(5)	30(4)	-2(3)	4(3)	3(3)
C(010)	28(6)	44(6)	32(6)	5(4)	-1(5)	-3(5)
C(017)	151(18)	49(9)	72(10)	23(7)	-22(11)	5(10)
C(003)	28(6)	46(6)	21(5)	-2(4)	0(4)	-10(4)
C(005)	43(6)	30(5)	33(6)	-2(4)	2(5)	-10(4)
C(00A)	48(7)	47(6)	32(6)	5(5)	8(5)	4(5)
C(00B)	32(6)	59(7)	35(6)	-7(5)	12(5)	5(5)
O(00C)	36(4)	48(4)	29(4)	3(3)	-1(3)	9(3)
C(00F)	27(5)	46(6)	20(5)	-6(4)	-2(4)	-2(5)
C(00M)	36(6)	37(6)	34(6)	-2(4)	-2(5)	4(5)
C(00O)	47(8)	65(9)	68(9)	-7(6)	-16(7)	6(6)
C(00T)	39(6)	39(6)	24(5)	-1(4)	15(5)	-8(5)
C(00U)	45(7)	48(6)	21(5)	0(4)	2(5)	9(5)
C(00W)	49(8)	50(7)	43(7)	1(5)	4(6)	4(6)
C(00Y)	79(11)	69(10)	88(11)	-38(8)	-49(9)	28(8)
C(011)	35(6)	32(5)	29(5)	5(4)	-9(5)	-3(4)
C(016)	37(6)	45(6)	41(6)	0(5)	4(5)	-4(5)
C(019)	33(6)	35(6)	44(6)	0(5)	0(5)	-3(4)
C(01A)	32(6)	55(7)	43(6)	4(5)	4(5)	3(5)
C(01C)	40(6)	33(5)	33(5)	0(4)	-2(5)	2(5)
C(01D)	42(6)	38(6)	32(6)	-9(4)	10(5)	4(5)
O(01I)	28(4)	61(5)	40(4)	-1(3)	3(3)	1(3)
C(01K)	50(10)	112(15)	133(16)	34(12)	-32(10)	-27(9)
C(01L)	40(6)	38(5)	15(5)	7(4)	-2(4)	3(4)
C(01N)	35(6)	52(7)	36(6)	-2(5)	8(5)	8(5)
C(01R)	40(6)	42(6)	27(5)	-3(4)	2(5)	-4(5)
N(01T)	48(6)	52(6)	56(6)	-4(5)	-5(5)	13(5)
C(01U)	35(6)	36(6)	46(6)	-6(4)	3(5)	-3(5)
C(01X)	39(6)	31(6)	57(7)	0(5)	-5(5)	4(5)
C(01Y)	58(9)	62(9)	62(9)	-7(6)	-6(7)	7(7)

Appendix

C(022)	53(8)	47(7)	55(8)	0(5)	-16(6)	1(6)
C(023)	52(8)	40(6)	45(7)	3(5)	7(6)	9(5)
C(024)	46(7)	38(6)	65(8)	1(5)	11(6)	1(5)
C(027)	34(6)	59(7)	47(7)	16(5)	11(5)	3(5)
N(02C)	48(6)	55(6)	28(5)	5(4)	6(4)	13(4)
C(02D)	48(7)	40(6)	56(7)	-4(5)	11(6)	-2(5)
C(02F)	29(7)	69(9)	96(11)	14(8)	1(7)	0(6)
C(02N)	36(7)	54(7)	61(8)	-11(6)	-5(6)	-3(5)
C(02Q)	54(7)	39(6)	38(6)	-5(5)	-7(6)	5(5)
C(02X)	40(6)	48(6)	28(5)	-2(4)	-2(5)	0(5)
C(02Z)	41(7)	43(6)	47(7)	-10(5)	4(6)	2(5)
C(030)	75(11)	94(12)	75(10)	-32(8)	27(9)	-44(9)
C(036)	50(7)	44(7)	51(7)	-14(5)	5(6)	2(5)
C(038)	47(8)	76(9)	37(7)	4(6)	20(6)	4(6)
C(03D)	37(7)	70(8)	32(6)	6(5)	7(5)	-7(6)
C(03I)	37(6)	44(6)	40(6)	6(5)	10(5)	7(5)
C(03J)	43(7)	56(7)	45(7)	0(5)	6(6)	5(6)
C(03S)	32(6)	53(7)	43(7)	-5(5)	14(5)	-10(5)
C(03Z)	41(7)	36(6)	55(7)	-4(5)	5(6)	-1(5)
C(045)	43(7)	89(9)	28(6)	3(6)	5(5)	27(7)
C(047)	61(8)	52(7)	43(7)	-2(5)	24(6)	8(6)
C(048)	43(6)	33(5)	25(5)	1(4)	-4(5)	-4(4)
C(049)	38(8)	149(16)	54(8)	14(9)	3(7)	35(9)
C(04A)	39(6)	48(6)	34(6)	13(5)	-7(5)	3(5)
C(04C)	43(7)	45(7)	62(8)	-6(5)	3(6)	0(5)
C(04E)	39(6)	38(6)	38(6)	-6(4)	10(5)	5(5)
C(04F)	38(6)	28(5)	37(6)	5(4)	7(5)	-1(4)
C(04H)	31(6)	83(9)	55(8)	35(7)	-3(6)	1(6)
C(04I)	50(8)	84(10)	38(7)	-2(6)	12(6)	7(7)
C(04J)	55(9)	39(7)	112(13)	8(7)	9(8)	-2(6)
C(04L)	30(6)	41(6)	39(6)	3(4)	0(5)	-5(5)
C(04S)	67(9)	38(7)	95(11)	-2(6)	-37(8)	8(6)
C(04U)	45(7)	47(7)	30(6)	-8(5)	-7(5)	5(5)
C(04V)	32(6)	56(7)	41(6)	20(5)	-3(5)	-14(5)
C(04X)	52(7)	34(6)	37(6)	-3(4)	-4(5)	7(5)
C(04Z)	44(7)	37(6)	45(7)	-7(5)	-9(5)	-2(5)
C(050)	32(6)	38(6)	54(7)	-6(5)	3(5)	10(5)
C(004)	36(6)	45(6)	44(6)	1(5)	7(5)	-8(5)

C(007)	30(6)	27(5)	44(6)	-2(4)	1(5)	-4(4)
C(009)	43(7)	37(6)	51(7)	5(5)	12(6)	-3(5)
C(01S)	69(9)	46(7)	50(8)	0(5)	13(7)	7(6)
C(02P)	40(6)	40(6)	35(6)	8(4)	11(5)	-6(5)
C(02T)	59(8)	42(6)	39(6)	-6(5)	11(6)	3(5)
C(02W)	58(7)	42(6)	27(6)	-1(4)	16(5)	0(5)
C(034)	46(6)	38(6)	24(5)	-3(4)	6(5)	-9(5)
C(03A)	42(7)	46(7)	38(6)	-2(5)	12(5)	-2(5)
C(03F)	63(8)	39(6)	38(6)	0(5)	9(6)	-1(5)
C(03T)	53(7)	40(6)	30(6)	5(4)	8(5)	1(5)
C(040)	46(7)	48(6)	19(5)	1(4)	10(5)	-6(5)
C(041)	50(7)	51(7)	27(6)	0(4)	3(5)	-13(5)
C(046)	53(7)	42(6)	37(6)	13(5)	8(5)	-3(5)
C(04G)	51(7)	37(6)	49(7)	3(5)	0(6)	1(5)
C(04W)	47(7)	54(8)	62(8)	9(6)	14(6)	-2(6)
C(012)	55(8)	46(7)	71(9)	-4(6)	7(7)	2(6)
C(01M)	54(8)	69(8)	29(6)	8(5)	-9(5)	-3(6)
C(00L)	52(7)	31(5)	29(5)	9(4)	-5(5)	7(5)
C(02E)	82(11)	61(9)	93(11)	-18(8)	-31(9)	39(8)
C(03R)	92(11)	32(6)	51(7)	-9(5)	-33(7)	27(6)
C(03N)	67(10)	63(9)	111(13)	-29(8)	-49(9)	28(8)
CI(00)	173(6)	90(3)	109(4)	7(3)	-34(4)	52(4)
C(02K)	103(13)	59(9)	81(11)	12(7)	0(10)	-34(9)
CI(02)	106(5)	125(5)	219(8)	13(5)	-7(5)	8(4)
C(03U)	93(7)	85(6)	84(6)	-3(4)	12(5)	-3(5)
CI(1)	241(10)	129(5)	126(5)	-2(4)	-48(6)	-50(6)
CI(01)	66(3)	169(6)	181(7)	-30(5)	-29(4)	21(3)

Table 6. Hydrogen coordinates ($\times 10^4$) and isotropic displacement parameters ($\text{\AA}^2 \times 10^{-3}$) for tcd392_pl.

	x	y	z	U(eq)
H(00H)	3038	5561	3422	68
H(00N)	3095	3041	3501	62
H(01A)	1710	9621	2015	136
H(01B)	1182	9411	1614	136
H(01C)	1731	8641	1589	136
H(00A)	2479	8013	3924	42
H(00B)	2988	7173	3829	42
H(00O)	7863	1323	5034	73
H(00W)	6881	-1767	4440	57
H(00C)	1330	1480	1234	119
H(00D)	1433	2584	904	119
H(00E)	815	2037	906	119
H(01D)	2661	5470	1644	49
H(01E)	3117	5204	2114	49
H(01F)	1604	7371	4329	42
H(01G)	243	2089	1766	149
H(01H)	486	2712	2288	149
H(01I)	759	1573	2109	149
H(01J)	2956	3593	4741	51
H(01K)	2467	3347	5163	51
H(01Y)	7578	-493	4876	73
H(023)	5753	3247	3647	54
H(024)	6106	-2111	3917	59
H(02A)	909	5347	5673	70
H(02B)	683	4738	5141	70
H(02C)	296	5640	5424	70
H(02D)	5295	-1379	3340	58
H(02E)	77	1083	3907	97
H(02F)	569	1088	3472	97
H(02G)	431	2179	3801	97
H(02N)	7403	2773	4639	60
H(02Q)	1778	4493	1583	52

H(02X)	1567	2429	4853	46
H(02Z)	6589	3479	4083	52
H(03A)	598	2184	4811	121
H(03B)	931	1192	5096	121
H(03C)	296	1018	4871	121
H(03D)	4542	4147	4355	56
H(03S)	4740	97	3043	51
H(04A)	675	7490	5533	77
H(04B)	1090	7967	5088	77
H(04C)	1344	7268	5581	77
H(049)	3677	3834	2116	96
H(04D)	1862	6699	1825	49
H(04F)	1712	8185	3245	41
H(04E)	441	5934	4306	85
H(04G)	660	7175	4308	85
H(04H)	146	6823	4682	85
H(04I)	4369	1526	2514	68
H(04J)	580	-546	4295	103
H(04K)	1195	-425	4574	103
H(04L)	1132	-443	3933	103
H(04M)	942	4199	1131	101
H(04N)	767	4468	1735	101
H(04O)	341	3798	1348	101
H(04P)	3459	6388	4609	52
H(04Q)	3845	6001	4121	52
H(04R)	2360	849	2879	49
H(04S)	2909	1565	3028	49
H(04Z)	1541	896	3416	50
H(050)	1575	1656	2381	50
H(007)	1586	4505	5119	41
H(01S)	6085	-245	5312	66
H(02T)	4736	2158	4573	56
H(03F)	5373	733	4729	55
H(040)	5309	4054	6978	45
H(041)	4840	4237	6172	51
H(04T)	6024	3055	7564	55
H(04W)	6775	306	7039	65
H(012)	6546	-405	6117	69

H(01M)	6651	1611	7691	61
H(02H)	1189	9481	2808	119
H(02I)	805	8457	2971	119
H(02J)	590	9280	2510	119
H(03E)	528	7980	1758	122
H(03G)	577	7097	2231	122
H(03H)	993	7028	1732	122
H(02K)	1343	4948	2713	97
H(02L)	1321	5835	3186	97
H(03I)	3114	3545	6026	105
H(03J)	2714	3155	6500	105

Table 7. Torsion angles [°] for tcd392_pl.

O(00K)-N(01T)-C(038)-C(01N)	-176.9(11)	C(00B)-O(01I)-C(049)-C(045)	-151.8(12)
O(00K)-N(01T)-C(038)-C(04I)	0.6(14)	O(00C)-C(010)-C(03D)-C(004)	-0.2(12)
O(00K)-C(045)-C(049)-O(01I)	-71.7(18)	O(00C)-C(010)-C(04V)-O(002)	-87.9(12)
O(00K)-C(045)-C(04I)-C(038)	-2.0(15)	O(00C)-N(02C)-C(004)-C(03D)	-2.8(13)
O(00N)-C(00M)-C(01L)-C(04X)	-9.5(15)	O(00C)-N(02C)-C(004)-C(03T)	-177.6(10)
O(00N)-C(00M)-C(01L)-C(04Z)	178.1(9)	C(00F)-O(002)-C(04V)-C(010)	102.2(11)
O(00N)-C(00M)-C(048)-C(01X)	8.1(14)	C(00F)-C(003)-C(005)-C(00T)	94.0(12)
O(00N)-C(00M)-C(048)-C(02X)	-177.1(9)	C(00F)-C(003)-C(01C)-C(04L)	-1.4(15)
O(002)-C(00F)-C(011)-C(01X)	-4.8(13)	C(00F)-C(011)-C(01X)-C(048)	-94.9(11)
O(002)-C(00F)-C(011)-C(007)	-179.0(8)	C(00F)-C(011)-C(007)-C(04L)	1.2(15)
C(010)-O(00C)-N(02C)-C(004)	2.7(11)	C(00M)-C(01L)-C(04X)-C(00U)	-84.0(13)
C(010)-C(03D)-C(004)-N(02C)	2.0(13)	C(00M)-C(01L)-C(04Z)-C(03Z)	-2.8(16)
C(010)-C(03D)-C(004)-C(03T)	176.6(10)	C(00O)-C(01Y)-C(03J)-C(00W)	-179.4(13)
C(003)-C(005)-C(00T)-C(03I)	-83.1(13)	C(00O)-C(01Y)-C(03J)-C(04E)	-3(2)
C(003)-C(005)-C(00T)-C(04F)	94.2(12)	C(00O)-C(02N)-C(036)-C(02Z)	178.5(13)
C(003)-C(00F)-C(011)-C(01X)	170.3(9)	C(00O)-C(02N)-C(036)-C(04E)	-2.1(19)
C(003)-C(00F)-C(011)-C(007)	-4.0(14)	C(00T)-C(04F)-C(00L)-C(04A)	4.3(16)
C(003)-C(01C)-C(04L)-C(01A)	177.8(9)	C(00T)-C(04F)-C(00L)-C(03R)	178.9(11)
C(003)-C(01C)-C(04L)-C(007)	-1.3(15)	C(00U)-C(00B)-O(01I)-C(049)	120.5(13)
C(005)-C(003)-C(00F)-O(002)	0.9(13)	C(00W)-C(03J)-C(04E)-C(019)	-2.9(17)
C(005)-C(003)-C(00F)-C(011)	-174.2(9)	C(00W)-C(03J)-C(04E)-C(036)	-178.8(11)
C(005)-C(003)-C(01C)-C(04L)	176.9(9)	C(00Y)-C(022)-C(04U)-C(02Q)	91.6(14)
C(005)-C(00T)-C(03I)-O(00H)	-2.1(16)	C(00Y)-C(022)-C(04U)-C(050)	-86.6(14)
C(005)-C(00T)-C(03I)-C(01R)	-178.6(10)	C(011)-C(01X)-C(048)-C(00M)	92.5(12)
C(005)-C(00T)-C(04F)-C(00L)	177.3(10)	C(011)-C(01X)-C(048)-C(02X)	-82.3(12)
C(00A)-C(00B)-C(00U)-C(04X)	-173.8(10)	C(016)-C(00A)-C(00B)-C(00U)	174.0(10)
C(00A)-C(00B)-C(00U)-C(050)	2.0(16)	C(016)-C(00A)-C(00B)-O(01I)	-3.8(17)
C(00A)-C(00B)-O(01I)-C(049)	-61.6(16)	C(016)-C(00A)-C(02Q)-C(04U)	-173.7(10)
C(00A)-C(016)-C(01R)-C(03I)	83.8(13)	C(016)-C(01R)-C(03I)-O(00H)	3.9(16)
C(00A)-C(016)-C(01R)-C(04A)	-93.6(12)	C(016)-C(01R)-C(03I)-C(00T)	-179.5(10)
C(00A)-C(02Q)-C(04U)-C(022)	179.0(11)	C(016)-C(01R)-C(04A)-C(00L)	178.4(10)
C(00A)-C(02Q)-C(04U)-C(050)	-2.7(17)	C(019)-C(01D)-C(024)-C(00W)	0.2(17)
C(00B)-C(00A)-C(016)-C(01R)	-96.2(13)	C(019)-C(01D)-C(02D)-C(03S)	-4.7(17)
C(00B)-C(00A)-C(02Q)-C(04U)	5.1(17)	C(019)-C(01U)-C(023)-C(02Z)	-2.7(17)
C(00B)-C(00U)-C(04X)-C(01L)	90.6(13)	C(01A)-C(04L)-C(007)-C(011)	-177.8(10)
C(00B)-C(00U)-C(050)-C(04U)	0.4(16)	C(01C)-C(003)-C(005)-C(00T)	-84.1(12)

C(01C)-C(003)-C(00F)-O(002)	179.1(8)	C(024)-C(01D)-C(02D)-C(03S)	175.3(10)
C(01C)-C(003)-C(00F)-C(011)	4.0(14)	C(027)-C(01A)-C(04L)-C(01C)	176.6(10)
C(01C)-C(04L)-C(007)-C(011)	1.3(15)	C(027)-C(01A)-C(04L)-C(007)	-4.3(15)
C(01D)-C(019)-C(01U)-C(01N)	-1.2(16)	N(02C)-C(004)-C(03T)-C(02T)	136.8(12)
C(01D)-C(019)-C(01U)-C(023)	-176.8(10)	N(02C)-C(004)-C(03T)-C(034)	-40.2(17)
C(01D)-C(019)-C(04E)-C(036)	177.5(10)	C(02D)-C(01D)-C(024)-C(00W)	-179.9(11)
C(01D)-C(019)-C(04E)-C(03J)	1.6(16)	C(02N)-C(00O)-C(01Y)-C(03J)	-1(2)
C(01D)-C(02D)-C(03S)-C(01N)	0.9(17)	C(02N)-C(036)-C(04E)-C(019)	-178.1(11)
O(01I)-C(00B)-C(00U)-C(04X)	4.1(15)	C(02N)-C(036)-C(04E)-C(03J)	-2.1(17)
O(01I)-C(00B)-C(00U)-C(050)	180.0(9)	C(02Q)-C(00A)-C(00B)-C(00U)	-4.6(16)
C(01K)-C(022)-C(04U)-C(02Q)	-148.0(14)	C(02Q)-C(00A)-C(00B)-O(01I)	177.6(10)
C(01K)-C(022)-C(04U)-C(050)	33.8(17)	C(02Q)-C(00A)-C(016)-C(01R)	82.5(12)
C(01L)-C(00M)-C(048)-C(01X)	-175.4(9)	C(02Q)-C(04U)-C(050)-C(00U)	-0.1(16)
C(01L)-C(00M)-C(048)-C(02X)	-0.6(15)	C(02X)-C(03Z)-C(04C)-C(02F)	120.5(13)
C(01N)-C(01U)-C(023)-C(02Z)	-178.0(11)	C(02X)-C(03Z)-C(04C)-C(030)	0.1(18)
C(01N)-C(038)-C(04I)-C(045)	178.1(12)	C(02X)-C(03Z)-C(04C)-C(04J)	-119.3(13)
C(01R)-C(04A)-C(00L)-C(04F)	-2.0(17)	C(02X)-C(03Z)-C(04Z)-C(01L)	2.5(17)
C(01R)-C(04A)-C(00L)-C(03R)	-176.7(11)	C(02Z)-C(036)-C(04E)-C(019)	1.3(16)
N(01T)-O(00K)-C(045)-C(049)	179.4(12)	C(02Z)-C(036)-C(04E)-C(03J)	177.4(11)
N(01T)-O(00K)-C(045)-C(04I)	2.4(15)	C(038)-C(01N)-C(01U)-C(019)	174.2(10)
N(01T)-C(038)-C(04I)-C(045)	0.8(15)	C(038)-C(01N)-C(01U)-C(023)	-10.5(18)
C(01U)-C(019)-C(01D)-C(024)	-175.1(10)	C(038)-C(01N)-C(03S)-C(02D)	-174.2(10)
C(01U)-C(019)-C(01D)-C(02D)	4.9(16)	C(03D)-C(010)-O(00C)-N(02C)	-1.5(12)
C(01U)-C(019)-C(04E)-C(036)	-7.5(16)	C(03D)-C(010)-C(04V)-O(002)	92.7(14)
C(01U)-C(019)-C(04E)-C(03J)	176.6(11)	C(03D)-C(004)-C(03T)-C(02T)	-37.4(17)
C(01U)-C(01N)-C(038)-N(01T)	-27.3(18)	C(03D)-C(004)-C(03T)-C(034)	145.7(12)
C(01U)-C(01N)-C(038)-C(04I)	155.6(12)	C(03I)-C(00T)-C(04F)-C(00L)	-5.3(15)
C(01U)-C(01N)-C(03S)-C(02D)	2.6(17)	C(03I)-C(01R)-C(04A)-C(00L)	0.9(17)
C(01U)-C(023)-C(02Z)-C(036)	-3.7(19)	C(03J)-C(00W)-C(024)-C(01D)	-1.7(19)
C(01X)-C(011)-C(007)-C(04L)	-173.1(10)	C(03S)-C(01N)-C(01U)-C(019)	-2.4(16)
C(01Y)-C(00O)-C(02N)-C(036)	4(2)	C(03S)-C(01N)-C(01U)-C(023)	172.9(11)
C(01Y)-C(03J)-C(04E)-C(019)	-179.4(12)	C(03S)-C(01N)-C(038)-N(01T)	149.4(12)
C(01Y)-C(03J)-C(04E)-C(036)	4.7(18)	C(03S)-C(01N)-C(038)-C(04I)	-27.7(18)
C(022)-C(04U)-C(050)-C(00U)	178.2(11)	C(03Z)-C(02X)-C(048)-C(00M)	0.2(16)
C(023)-C(02Z)-C(036)-C(02N)	-176.2(13)	C(03Z)-C(02X)-C(048)-C(01X)	175.1(10)
C(023)-C(02Z)-C(036)-C(04E)	4.4(18)	C(045)-O(00K)-N(01T)-C(038)	-1.8(13)
C(024)-C(00W)-C(03J)-C(01Y)	179.6(13)	C(047)-C(01A)-C(04L)-C(01C)	-59.9(13)
C(024)-C(00W)-C(03J)-C(04E)	3.1(19)	C(047)-C(01A)-C(04L)-C(007)	119.2(11)

C(048)-C(00M)-C(01L)-C(04X)	174.1(10)	C(009)-C(02P)-C(034)-C(041)	1.9(15)
C(048)-C(00M)-C(01L)-C(04Z)	1.8(15)	C(009)-C(02P)-C(03A)-C(01S)	-0.3(15)
C(048)-C(02X)-C(03Z)-C(04C)	-179.4(10)	C(009)-C(02P)-C(03A)-C(03F)	-179.6(11)
C(048)-C(02X)-C(03Z)-C(04Z)	-1.1(16)	C(009)-C(02W)-C(040)-C(041)	-2.2(17)
C(049)-C(045)-C(04I)-C(038)	-178.3(15)	C(009)-C(02W)-C(04G)-C(01M)	1.0(17)
C(04A)-C(01R)-C(03I)-O(00H)	-178.6(10)	C(009)-C(046)-C(04W)-C(01M)	-2.9(18)
C(04A)-C(01R)-C(03I)-C(00T)	-2.0(16)	C(009)-C(046)-C(012)-C(01S)	3.2(19)
C(04A)-C(00L)-C(03R)-C(017)	-71.9(14)	C(01S)-C(03A)-C(03F)-C(02T)	-179.4(12)
C(04A)-C(00L)-C(03R)-C(02E)	171.3(13)	C(02P)-C(009)-C(02W)-C(040)	1.1(16)
C(04A)-C(00L)-C(03R)-C(03N)	44.5(18)	C(02P)-C(009)-C(02W)-C(04G)	178.9(10)
C(04C)-C(03Z)-C(04Z)-C(01L)	-179.2(10)	C(02P)-C(009)-C(046)-C(04W)	-178.0(11)
C(04E)-C(019)-C(01D)-C(024)	-0.1(15)	C(02P)-C(009)-C(046)-C(012)	-2.0(17)
C(04E)-C(019)-C(01D)-C(02D)	179.9(10)	C(02P)-C(034)-C(03T)-C(004)	178.9(10)
C(04E)-C(019)-C(01U)-C(01N)	-176.2(10)	C(02P)-C(034)-C(03T)-C(02T)	2.0(16)
C(04E)-C(019)-C(01U)-C(023)	8.1(16)	C(02P)-C(034)-C(041)-C(040)	-3.0(16)
C(04F)-C(00T)-C(03I)-O(00H)	-179.4(9)	C(02P)-C(03A)-C(03F)-C(02T)	-0.1(18)
C(04F)-C(00T)-C(03I)-C(01R)	4.1(16)	C(02W)-C(009)-C(02P)-C(034)	-1.0(16)
C(04F)-C(00L)-C(03R)-C(017)	113.6(12)	C(02W)-C(009)-C(02P)-C(03A)	179.5(10)
C(04F)-C(00L)-C(03R)-C(02E)	-3.2(19)	C(02W)-C(009)-C(046)-C(04W)	3.1(17)
C(04F)-C(00L)-C(03R)-C(03N)	-130.0(14)	C(02W)-C(009)-C(046)-C(012)	179.2(11)
C(04H)-C(01A)-C(04L)-C(01C)	55.8(14)	C(02W)-C(040)-C(041)-C(034)	3.3(17)
C(04H)-C(01A)-C(04L)-C(007)	-125.1(11)	C(02W)-C(04G)-C(01M)-C(04W)	-0.9(19)
C(04I)-C(045)-C(049)-O(01I)	104.5(17)	C(034)-C(02P)-C(03A)-C(01S)	-179.8(10)
C(04S)-C(022)-C(04U)-C(02Q)	-25.8(17)	C(034)-C(02P)-C(03A)-C(03F)	0.8(16)
C(04S)-C(022)-C(04U)-C(050)	156.0(12)	C(03A)-C(01S)-C(012)-C(046)	-3(2)
C(04V)-O(002)-C(00F)-C(003)	81.0(11)	C(03A)-C(02P)-C(034)-C(03T)	-1.8(15)
C(04V)-O(002)-C(00F)-C(011)	-103.9(10)	C(03A)-C(02P)-C(034)-C(041)	-178.6(10)
C(04V)-C(010)-O(00C)-N(02C)	178.9(9)	C(03F)-C(02T)-C(03T)-C(004)	-178.4(11)
C(04V)-C(010)-C(03D)-C(004)	179.3(11)	C(03F)-C(02T)-C(03T)-C(034)	-1.3(18)
C(04X)-C(00U)-C(050)-C(04U)	176.4(10)	C(03T)-C(02T)-C(03F)-C(03A)	0.3(19)
C(04X)-C(01L)-C(04Z)-C(03Z)	-175.5(10)	C(03T)-C(034)-C(041)-C(040)	-179.7(11)
C(04Z)-C(01L)-C(04X)-C(00U)	88.1(12)	C(040)-C(02W)-C(04G)-C(01M)	178.8(11)
C(04Z)-C(03Z)-C(04C)-C(02F)	-57.8(15)	C(041)-C(034)-C(03T)-C(004)	-4.5(17)
C(04Z)-C(03Z)-C(04C)-C(030)	-178.1(13)	C(041)-C(034)-C(03T)-C(02T)	178.6(11)
C(04Z)-C(03Z)-C(04C)-C(04J)	62.5(15)	C(046)-C(009)-C(02P)-C(034)	-179.9(10)
C(050)-C(00U)-C(04X)-C(01L)	-85.3(12)	C(046)-C(009)-C(02P)-C(03A)	0.6(16)
C(007)-C(011)-C(01X)-C(048)	79.2(13)	C(046)-C(009)-C(02W)-C(040)	180.0(10)
C(009)-C(02P)-C(034)-C(03T)	178.7(10)	C(046)-C(009)-C(02W)-C(04G)	-2.2(16)

C(046)-C(04W)-C(01M)-C(04G)	2(2)
C(04G)-C(02W)-C(040)-C(041)	-180.0(11)
C(04W)-C(046)-C(012)-C(01S)	179.1(13)
C(012)-C(01S)-C(03A)-C(02P)	1.4(19)
C(012)-C(01S)-C(03A)-C(03F)	-179.2(13)
C(012)-C(046)-C(04W)-C(01M)	-178.8(12)

Crystal Structure Report for EPIC.2DCM

A specimen of $C_{88}H_{86}Cl_4N_2O_6$, approximate dimensions 0.050 mm x 0.050 mm x 0.450 mm, was used for the X-ray crystallographic analysis. The X-ray intensity data were measured at 100(2)K using an Oxford Cryosystems Cobra low temperature device using a MiTeGen micromount. See Table 1 for collection parameters and exposure time. Bruker APEX software was used to correct for Lorentz and polarization effects.

A total of 2307 frames were collected. The total exposure time was 48.70 hours. The frames were integrated with the Bruker SAINT software package using a narrow-frame algorithm. The integration of the data using a monoclinic unit cell yielded a total of 95410 reflections to a maximum θ angle of 68.41° (0.83 Å resolution), of which 13552 were independent (average redundancy 7.040, completeness = 99.7%, $R_{int} = 6.89\%$, $R_{sig} = 4.33\%$) and 10118 (74.66%) were greater than $2\sigma(F^2)$. The final cell constants of $a = 20.6668(8)$ Å, $b = 18.8882(7)$ Å, $c = 21.5171(8)$ Å, $\beta = 118.2830(17)^\circ$, volume = $7396.7(5)$ Å³, are based upon the refinement of the XYZ-centroids of 9955 reflections above $20\sigma(I)$ with $6.607^\circ < 2\theta < 136.5^\circ$. Data were corrected for absorption effects using the multi-scan method (SADABS). The ratio of minimum to maximum apparent transmission was 0.712. The calculated minimum and maximum transmission coefficients (based on crystal size) are 0.5361 and 0.7531.

The structure was solved and refined using the Bruker SHELXTL Software Package, using the space group $P2_1/c$, with $Z = 4$ for the formula unit, $C_{88}H_{86}Cl_4N_2O_6$. The final anisotropic full-matrix least-squares refinement on F^2 with 983 variables converged at $R1 = 8.87\%$, for the observed data and $wR2 = 28.35\%$ for all data. The goodness-of-fit was 1.034. The largest peak in the final difference electron density synthesis was $0.751 e^-/\text{Å}^3$ and the largest hole was $-1.527 e^-/\text{Å}^3$ with an RMS deviation of $0.093 e^-/\text{Å}^3$. On the basis of the final model, the calculated density was $1.266 g/cm^3$ and $F(000)$, 2976 e^- .

Refinement Note: Two tBu groups with libration were modelled as disordered in two positions with occupancies of (1) 78/22% and (2) 61/39% (1 = C31, C32, C33; 2 = C39, C40, C41). Restraints (ISOR, SADI) and constraints (EADP) were used and the

model refined to convergence. Two CH₂Cl₂ molecules were also modelled as disordered with restrained C-Cl distances and occupancies of 72% and 88% for the major moieties.

Bruker APEX v2014.11-0, Bruker AXS Inc., Madison, Wisconsin, USA.

SADABS (2014/5) Bruker AXS Inc., Madison, Wisconsin, USA; Sheldrick, G. M. University of Göttingen, Germany.

SHELXL-2014, (2014), Bruker AXS Inc., Madison, Wisconsin, USA; Sheldrick, G. M. University of Göttingen, Germany.

Acknowledgement:

Facility funded by PRTL I and ERDF.

Table 1: Data collection details for TCD218.

Axis	dx/mm	2 θ / $^{\circ}$	ω / $^{\circ}$	φ / $^{\circ}$	χ / $^{\circ}$	Width/ $^{\circ}$	Frames	Time/s	Wavelength/ \AA	Voltage/kV	Current/mA	Temperature/K
Omega	50.027	-49.35	190.58	180.00	54.74	1.90	70	76.00	1.54184	45	0.6	100
Omega	50.027	108.96	343.00	300.00	64.88	1.90	72	76.00	1.54184	45	0.6	100
Omega	50.027	109.17	3.49	124.18	24.60	1.90	71	76.00	1.54184	45	0.6	100
Omega	50.027	108.96	343.00	125.00	64.88	1.90	72	76.00	1.54184	45	0.6	100
Omega	50.027	-49.35	299.42	180.00	-64.88	1.90	59	76.00	1.54184	45	0.6	100
Omega	50.027	108.96	96.03	75.00	-54.74	1.90	70	76.00	1.54184	45	0.6	100
Phi	50.027	-47.74	343.92	308.80	23.00	1.90	96	76.00	1.54184	45	0.6	100
Omega	50.027	91.76	352.97	181.80	81.27	1.90	38	76.00	1.54184	45	0.6	100
Omega	50.027	108.96	96.03	125.00	-54.74	1.90	70	76.00	1.54184	45	0.6	100
Omega	50.027	-49.35	190.58	36.00	54.74	1.90	70	76.00	1.54184	45	0.6	100
Omega	50.027	108.96	96.03	175.00	-54.74	1.90	70	76.00	1.54184	45	0.6	100
Omega	50.027	-11.25	337.47	60.00	-64.88	1.90	39	76.00	1.54184	45	0.6	100
Omega	50.027	108.96	96.03	50.00	-54.74	1.90	70	76.00	1.54184	45	0.6	100
Omega	50.027	108.96	96.03	100.00	-54.74	1.90	70	76.00	1.54184	45	0.6	100
Omega	50.027	108.96	343.00	50.00	64.87	1.90	72	76.00	1.54184	45	0.6	100
Omega	50.027	-49.35	190.58	216.00	54.74	1.90	70	76.00	1.54184	45	0.6	100
Omega	50.027	-11.25	228.68	60.00	54.74	1.90	70	76.00	1.54184	45	0.6	100
Omega	50.027	108.96	343.00	175.00	64.87	1.90	72	76.00	1.54184	45	0.6	100
Omega	50.027	91.76	353.06	23.78	80.96	1.90	38	76.00	1.54184	45	0.6	100
Omega	50.027	108.96	96.03	200.00	-54.74	1.90	70	76.00	1.54184	45	0.6	100
Omega	50.027	108.96	96.03	150.00	-54.74	1.90	70	76.00	1.54184	45	0.6	100
Phi	50.027	-64.35	58.14	0.45	-57.06	1.90	189	76.00	1.54184	45	0.6	100
Phi	50.027	-47.74	325.81	269.65	57.06	1.90	133	76.00	1.54184	45	0.6	100
Omega	50.027	108.96	343.00	250.00	64.87	1.90	72	76.00	1.54184	45	0.6	100
Omega	50.027	108.96	96.03	225.00	-54.74	1.90	70	76.00	1.54184	45	0.6	100
Omega	50.027	108.96	343.00	360.00	64.88	1.90	72	76.00	1.54184	45	0.6	100
Omega	50.027	-11.25	337.47	240.00	-64.87	1.90	39	76.00	1.54184	45	0.6	100
Phi	50.027	-49.35	73.14	0.45	-57.06	1.90	189	76.00	1.54184	45	0.6	100
Omega	50.027	108.96	343.00	75.00	64.87	1.90	72	76.00	1.54184	45	0.6	100
Omega	50.027	108.96	343.00	325.00	64.87	1.90	72	76.00	1.54184	45	0.6	100

Table 2. Crystal data and structure refinement for TCD218.

Identification code	tcd218	
Empirical formula	$C_{88}H_{86}Cl_4N_2O_6$	
Formula weight	1409.38	
Temperature	100(2) K	
Wavelength	1.54178 Å	
Crystal system	Monoclinic	
Space group	$P2_1/c$	
Unit cell dimensions	$a = 20.6668(8)$ Å	$\alpha = 90^\circ$.
	$b = 18.8882(7)$ Å	$\beta =$
	$c = 21.5171(8)$ Å	$\gamma = 90^\circ$.
Volume	$7396.6(5)$ Å ³	
Z	4	
Density (calculated)	1.266 Mg/m ³	
Absorption coefficient	1.898 mm ⁻¹	
F(000)	2976	
Crystal size	0.450 x 0.050 x 0.050 mm ³	
Theta range for data collection	2.428 to 68.407°.	
Index ranges	$-24 \leq h \leq 24, -22 \leq k \leq 22, -25 \leq l \leq 21$	
Reflections collected	95410	
Independent reflections	13552 [R(int) = 0.0689]	
Completeness to theta = 67.679°	99.9 %	
Absorption correction	Semi-empirical from equivalents	
Max. and min. transmission	0.7531 and 0.5361	
Refinement method	Full-matrix least-squares on F ²	
Data / restraints / parameters	13552 / 114 / 983	
Goodness-of-fit on F ²	1.034	
Final R indices [I > 2σ(I)]	R1 = 0.0887, wR2 = 0.2551	
R indices (all data)	R1 = 0.1125, wR2 = 0.2835	
Largest diff. peak and hole	0.751 and -1.527 e.Å ⁻³	

Table 3. Atomic coordinates ($\times 10^4$) and equivalent isotropic displacement parameters ($\text{\AA}^2 \times 10^3$) for TCD218. $U(\text{eq})$ is defined as one third of the trace of the orthogonalized U^{ij} tensor.

	x	y	z	U(eq)
C(2)	7206(2)	3880(2)	7917(2)	29(1)
C(3)	7121(2)	4439(2)	8296(2)	28(1)
C(4)	7481(2)	5068(2)	8344(2)	36(1)
C(5)	7938(2)	5167(2)	8032(2)	39(1)
C(6)	8011(2)	4595(2)	7667(2)	37(1)
C(7)	7658(2)	3950(2)	7602(2)	32(1)
C(8)	7768(2)	3346(2)	7199(2)	38(1)
C(9)	8300(2)	2781(2)	7667(2)	30(1)
C(10)	8053(2)	2151(2)	7816(2)	30(1)
C(11)	8533(2)	1673(2)	8313(2)	30(1)
C(12)	9278(2)	1815(2)	8620(2)	30(1)
C(13)	9560(2)	2418(2)	8456(2)	30(1)
C(14)	9051(2)	2895(2)	7984(2)	32(1)
C(15)	8256(3)	1038(2)	8553(2)	39(1)
C(16)	8319(2)	1166(2)	9277(2)	32(1)
C(17)	7796(2)	1569(2)	9350(2)	28(1)
C(18)	7842(2)	1671(2)	10012(2)	27(1)
C(19)	8434(2)	1378(2)	10599(2)	32(1)
C(20)	8974(2)	982(2)	10550(2)	36(1)
C(21)	8897(2)	884(2)	9876(2)	33(1)
C(22)	7259(2)	2092(2)	10094(2)	29(1)
C(23)	7337(2)	2888(2)	10044(2)	26(1)
C(24)	6904(2)	3261(2)	9421(2)	26(1)
C(25)	7030(2)	3975(2)	9351(2)	29(1)
C(26)	7563(2)	4323(2)	9942(2)	34(1)
C(27)	7987(2)	3982(2)	10589(2)	34(1)
C(28)	7864(2)	3258(2)	10616(2)	31(1)
C(29)	6639(2)	4361(2)	8648(2)	34(1)
C(30)	8332(2)	5876(3)	8109(3)	56(1)
C(31)	7763(5)	6467(4)	7827(6)	97(3)
C(32)	8811(5)	5873(4)	7760(5)	85(3)
C(33)	8812(5)	6023(5)	8905(4)	81(3)
C(34)	10391(2)	2525(2)	8775(2)	41(1)

C(35)	10658(3)	2077(4)	8362(5)	105(3)
C(36)	10781(3)	2326(4)	9562(3)	93(2)
C(37)	10588(3)	3293(3)	8739(3)	68(2)
C(38)	9633(2)	689(2)	11205(2)	54(1)
C(39)	9385(6)	354(7)	11703(6)	82(3)
C(40)	10092(5)	1327(5)	11660(5)	86(4)
C(41)	10142(5)	203(5)	11098(4)	60(3)
C(42)	8549(3)	4402(2)	11220(2)	46(1)
C(43)	8145(4)	4954(3)	11424(3)	70(2)
C(44)	9080(3)	4780(3)	11020(2)	56(1)
C(45)	9007(3)	3920(3)	11853(2)	59(1)
C(31B)	8054(14)	6200(13)	7375(7)	74(8)
C(32B)	9137(6)	5733(12)	8329(13)	61(7)
C(33B)	8273(17)	6463(12)	8559(14)	81(9)
C(39B)	9636(8)	836(9)	11886(5)	58(4)
C(40B)	10330(5)	895(8)	11169(7)	59(4)
C(41B)	9615(8)	-121(4)	11077(6)	52(3)
C(46)	5678(2)	2847(2)	8894(2)	37(1)
C(47)	5190(2)	2328(3)	8335(2)	49(1)
C(48)	4897(2)	2613(3)	7609(2)	46(1)
O(49)	4617(2)	2128(2)	7090(2)	63(1)
N(50)	4323(2)	2489(3)	6439(2)	66(1)
C(51)	4447(2)	3165(3)	6591(2)	50(1)
C(52)	4796(2)	3262(3)	7329(2)	46(1)
C(53)	4167(3)	3693(3)	6011(2)	54(1)
C(54)	4573(2)	4294(3)	6031(2)	47(1)
C(55)	5316(2)	4431(3)	6572(2)	47(1)
C(56)	5683(3)	5015(3)	6579(2)	50(1)
C(57)	5367(3)	5544(3)	6034(2)	52(1)
C(58)	5738(3)	6145(3)	6019(3)	61(1)
C(59)	5419(4)	6634(3)	5469(3)	69(2)
C(60)	4733(4)	6518(3)	4932(3)	69(2)
C(61)	4322(3)	5922(3)	4912(2)	66(2)
C(62)	3607(4)	5769(4)	4355(3)	71(2)
C(63)	3232(3)	5197(4)	4342(3)	70(2)
C(64)	3533(3)	4675(3)	4898(2)	62(2)
C(65)	3165(3)	4068(4)	4896(3)	72(2)
C(66)	3464(3)	3578(3)	5446(3)	65(1)

C(67)	4253(3)	4808(3)	5468(2)	54(1)
C(68)	4643(3)	5419(3)	5478(2)	51(1)
C(69)	6959(2)	1702(3)	6830(2)	44(1)
C(70)	6146(2)	1791(3)	6569(2)	44(1)
C(71)	5672(2)	1510(2)	5847(2)	43(1)
O(72)	4960(2)	1664(2)	5593(2)	59(1)
N(73)	4574(2)	1355(3)	4921(2)	60(1)
C(74)	5064(2)	1039(2)	4799(2)	41(1)
C(75)	5773(2)	1122(2)	5379(2)	46(1)
C(76)	4838(2)	636(2)	4127(2)	44(1)
C(77)	4199(2)	802(2)	3495(2)	46(1)
C(78)	3715(3)	1381(3)	3404(3)	60(1)
C(79)	3110(3)	1508(3)	2781(3)	70(2)
C(80)	2931(3)	1079(3)	2171(3)	64(1)
C(81)	2296(3)	1214(4)	1515(3)	75(2)
C(82)	2153(3)	792(4)	951(3)	72(2)
C(83)	2630(3)	255(3)	990(3)	70(2)
C(84)	3253(3)	104(3)	1605(2)	56(1)
C(85)	3754(3)	-425(3)	1677(3)	60(1)
C(86)	4364(3)	-565(3)	2296(3)	61(1)
C(87)	4521(3)	-165(2)	2914(3)	50(1)
C(88)	5141(3)	-301(2)	3559(3)	52(1)
C(89)	5288(3)	95(2)	4141(3)	49(1)
C(90)	4036(3)	388(2)	2876(2)	48(1)
C(91)	3405(3)	533(3)	2224(2)	53(1)
C(92)	8856(2)	3253(3)	9561(2)	47(1)
C(93)	3144(4)	1651(4)	4966(4)	88(2)
CI(1)	9442(1)	2801(1)	10339(1)	53(1)
CI(2)	9218(13)	4053(7)	9452(7)	53(2)
CI(2B)	9345(14)	3990(10)	9500(15)	53(2)
CI(3)	2674(1)	2171(1)	4195(1)	93(1)
CI(4)	2603(1)	1468(1)	5359(1)	79(1)
CI(4B)	3202(7)	1247(7)	5700(6)	79(1)
O(1)	6817(1)	3267(1)	7832(1)	32(1)
O(2)	6353(1)	2904(1)	8849(1)	31(1)
O(3)	7219(1)	1845(1)	8763(1)	32(1)
O(4)	7297(1)	2030(2)	7508(1)	42(1)

Table 4. Bond lengths [\AA] and angles [$^\circ$] for TCD218.

C(2)-O(1)	1.371(4)	C(19)-H(19A)	0.9500
C(2)-C(7)	1.396(5)	C(20)-C(21)	1.393(5)
C(2)-C(3)	1.395(5)	C(20)-C(38)	1.526(6)
C(3)-C(4)	1.380(5)	C(21)-H(21A)	0.9500
C(3)-C(29)	1.517(5)	C(22)-C(23)	1.521(5)
C(4)-C(5)	1.408(6)	C(22)-H(22A)	0.9900
C(4)-H(4A)	0.9500	C(22)-H(22B)	0.9900
C(5)-C(6)	1.384(6)	C(23)-C(28)	1.386(5)
C(5)-C(30)	1.535(6)	C(23)-C(24)	1.400(5)
C(6)-C(7)	1.394(6)	C(24)-O(2)	1.392(4)
C(6)-H(6A)	0.9500	C(24)-C(25)	1.394(5)
C(7)-C(8)	1.514(5)	C(25)-C(26)	1.391(5)
C(8)-C(9)	1.519(5)	C(25)-C(29)	1.522(5)
C(8)-H(8A)	0.9900	C(26)-C(27)	1.402(5)
C(8)-H(8B)	0.9900	C(26)-H(26A)	0.9500
C(9)-C(14)	1.386(5)	C(27)-C(28)	1.396(5)
C(9)-C(10)	1.391(5)	C(27)-C(42)	1.526(5)
C(10)-C(11)	1.392(5)	C(28)-H(28A)	0.9500
C(10)-O(4)	1.396(4)	C(29)-H(29A)	0.9900
C(11)-C(12)	1.385(5)	C(29)-H(29B)	0.9900
C(11)-C(15)	1.519(5)	C(30)-C(32)	1.498(7)
C(12)-C(13)	1.397(5)	C(30)-C(33B)	1.515(9)
C(12)-H(12A)	0.9500	C(30)-C(31)	1.523(7)
C(13)-C(14)	1.392(5)	C(30)-C(32B)	1.523(9)
C(13)-C(34)	1.533(5)	C(30)-C(31B)	1.528(9)
C(14)-H(14A)	0.9500	C(30)-C(33)	1.545(9)
C(15)-C(16)	1.521(5)	C(31)-H(31A)	0.9800
C(15)-H(15A)	0.9900	C(31)-H(31B)	0.9800
C(15)-H(15B)	0.9900	C(31)-H(31C)	0.9800
C(16)-C(21)	1.383(5)	C(32)-H(32A)	0.9800
C(16)-C(17)	1.390(5)	C(32)-H(32B)	0.9800
C(17)-O(3)	1.364(4)	C(32)-H(32C)	0.9800
C(17)-C(18)	1.396(5)	C(33)-H(33A)	0.9800
C(18)-C(19)	1.391(5)	C(33)-H(33B)	0.9800
C(18)-C(22)	1.522(5)	C(33)-H(33C)	0.9800
C(19)-C(20)	1.389(5)	C(34)-C(35)	1.508(7)

C(34)-C(37)	1.517(7)	C(31B)-H(31D)	0.9800
C(34)-C(36)	1.538(7)	C(31B)-H(31E)	0.9800
C(35)-H(35A)	0.9800	C(31B)-H(31F)	0.9800
C(35)-H(35B)	0.9800	C(32B)-H(32D)	0.9800
C(35)-H(35C)	0.9800	C(32B)-H(32E)	0.9800
C(36)-H(36A)	0.9800	C(32B)-H(32F)	0.9800
C(36)-H(36B)	0.9800	C(33B)-H(33D)	0.9800
C(36)-H(36C)	0.9800	C(33B)-H(33E)	0.9800
C(37)-H(37A)	0.9800	C(33B)-H(33F)	0.9800
C(37)-H(37B)	0.9800	C(39B)-H(39D)	0.9800
C(37)-H(37C)	0.9800	C(39B)-H(39E)	0.9800
C(38)-C(39B)	1.488(8)	C(39B)-H(39F)	0.9800
C(38)-C(41)	1.493(6)	C(40B)-H(40D)	0.9800
C(38)-C(39)	1.528(7)	C(40B)-H(40E)	0.9800
C(38)-C(40B)	1.529(8)	C(40B)-H(40F)	0.9800
C(38)-C(41B)	1.551(7)	C(41B)-H(41D)	0.9800
C(38)-C(40)	1.559(7)	C(41B)-H(41E)	0.9800
C(39)-H(39A)	0.9800	C(41B)-H(41F)	0.9800
C(39)-H(39B)	0.9800	C(46)-O(2)	1.447(4)
C(39)-H(39C)	0.9800	C(46)-C(47)	1.508(6)
C(40)-H(40A)	0.9800	C(46)-H(46A)	0.9900
C(40)-H(40B)	0.9800	C(46)-H(46B)	0.9900
C(40)-H(40C)	0.9800	C(47)-C(48)	1.483(6)
C(41)-H(41A)	0.9800	C(47)-H(47A)	0.9900
C(41)-H(41B)	0.9800	C(47)-H(47B)	0.9900
C(41)-H(41C)	0.9800	C(48)-C(52)	1.338(7)
C(42)-C(43)	1.525(7)	C(48)-O(49)	1.344(5)
C(42)-C(44)	1.530(6)	O(49)-N(50)	1.410(5)
C(42)-C(45)	1.536(7)	N(50)-C(51)	1.314(7)
C(43)-H(43A)	0.9800	C(51)-C(52)	1.410(6)
C(43)-H(43B)	0.9800	C(51)-C(53)	1.485(7)
C(43)-H(43C)	0.9800	C(52)-H(52A)	0.9500
C(44)-H(44A)	0.9800	C(53)-C(66)	1.400(7)
C(44)-H(44B)	0.9800	C(53)-C(54)	1.399(8)
C(44)-H(44C)	0.9800	C(54)-C(55)	1.444(6)
C(45)-H(45A)	0.9800	C(54)-C(67)	1.446(6)
C(45)-H(45B)	0.9800	C(55)-C(56)	1.336(7)
C(45)-H(45C)	0.9800	C(55)-H(55A)	0.9500

C(56)-C(57)	1.439(6)	C(77)-C(78)	1.432(7)
C(56)-H(56A)	0.9500	C(77)-C(90)	1.440(6)
C(57)-C(58)	1.380(8)	C(78)-C(79)	1.353(7)
C(57)-C(68)	1.426(7)	C(78)-H(78A)	0.9500
C(58)-C(59)	1.397(7)	C(79)-C(80)	1.432(8)
C(58)-H(58A)	0.9500	C(79)-H(79A)	0.9500
C(59)-C(60)	1.356(9)	C(80)-C(91)	1.390(8)
C(59)-H(59A)	0.9500	C(80)-C(81)	1.423(8)
C(60)-C(61)	1.399(9)	C(81)-C(82)	1.363(9)
C(60)-H(60A)	0.9500	C(81)-H(81A)	0.9500
C(61)-C(62)	1.423(9)	C(82)-C(83)	1.390(9)
C(61)-C(68)	1.435(6)	C(82)-H(82A)	0.9500
C(62)-C(63)	1.322(9)	C(83)-C(84)	1.370(8)
C(62)-H(62A)	0.9500	C(83)-H(83A)	0.9500
C(63)-C(64)	1.445(8)	C(84)-C(85)	1.393(8)
C(63)-H(63A)	0.9500	C(84)-C(91)	1.460(7)
C(64)-C(65)	1.376(9)	C(85)-C(86)	1.357(8)
C(64)-C(67)	1.432(7)	C(85)-H(85A)	0.9500
C(65)-C(66)	1.394(8)	C(86)-C(87)	1.427(7)
C(65)-H(65A)	0.9500	C(86)-H(86A)	0.9500
C(66)-H(66A)	0.9500	C(87)-C(88)	1.396(7)
C(67)-C(68)	1.402(8)	C(87)-C(90)	1.423(7)
C(69)-O(4)	1.426(4)	C(88)-C(89)	1.364(7)
C(69)-C(70)	1.508(6)	C(88)-H(88A)	0.9500
C(69)-H(69A)	0.9900	C(89)-H(89A)	0.9500
C(69)-H(69B)	0.9900	C(90)-C(91)	1.418(7)
C(70)-C(71)	1.488(6)	C(92)-Cl(2)	1.750(6)
C(70)-H(70A)	0.9900	C(92)-Cl(1)	1.754(5)
C(70)-H(70B)	0.9900	C(92)-Cl(2B)	1.761(9)
C(71)-O(72)	1.336(5)	C(92)-H(92C)	0.9900
C(71)-C(75)	1.340(6)	C(92)-H(92D)	0.9900
O(72)-N(73)	1.407(5)	C(92)-H(92A)	0.9900
N(73)-C(74)	1.306(6)	C(92)-H(92B)	0.9900
C(74)-C(75)	1.413(6)	C(93)-Cl(4B)	1.707(11)
C(74)-C(76)	1.499(6)	C(93)-Cl(4)	1.727(7)
C(75)-H(75A)	0.9500	C(93)-Cl(3)	1.770(7)
C(76)-C(89)	1.372(7)	C(93)-H(93C)	0.9900
C(76)-C(77)	1.410(6)	C(93)-H(93D)	0.9900

C(93)-H(93A)	0.9900	C(11)-C(12)-C(13)	122.7(3)
C(93)-H(93B)	0.9900	C(11)-C(12)-H(12A)	118.6
O(1)-H(1)	0.8496	C(13)-C(12)-H(12A)	118.6
O(3)-H(3)	0.8501	C(14)-C(13)-C(12)	116.8(3)
		C(14)-C(13)-C(34)	122.6(3)
O(1)-C(2)-C(7)	120.0(3)	C(12)-C(13)-C(34)	120.5(3)
O(1)-C(2)-C(3)	119.2(3)	C(9)-C(14)-C(13)	122.7(3)
C(7)-C(2)-C(3)	120.7(3)	C(9)-C(14)-H(14A)	118.6
C(4)-C(3)-C(2)	118.9(3)	C(13)-C(14)-H(14A)	118.6
C(4)-C(3)-C(29)	120.3(3)	C(11)-C(15)-C(16)	111.0(3)
C(2)-C(3)-C(29)	120.9(3)	C(11)-C(15)-H(15A)	109.4
C(3)-C(4)-C(5)	122.5(4)	C(16)-C(15)-H(15A)	109.4
C(3)-C(4)-H(4A)	118.7	C(11)-C(15)-H(15B)	109.4
C(5)-C(4)-H(4A)	118.7	C(16)-C(15)-H(15B)	109.4
C(6)-C(5)-C(4)	116.5(4)	H(15A)-C(15)-H(15B)	108.0
C(6)-C(5)-C(30)	123.2(4)	C(21)-C(16)-C(17)	118.7(3)
C(4)-C(5)-C(30)	120.3(4)	C(21)-C(16)-C(15)	120.8(3)
C(5)-C(6)-C(7)	123.1(3)	C(17)-C(16)-C(15)	120.6(3)
C(5)-C(6)-H(6A)	118.4	O(3)-C(17)-C(16)	119.4(3)
C(7)-C(6)-H(6A)	118.4	O(3)-C(17)-C(18)	119.8(3)
C(6)-C(7)-C(2)	118.2(4)	C(16)-C(17)-C(18)	120.7(3)
C(6)-C(7)-C(8)	120.2(3)	C(19)-C(18)-C(17)	118.4(3)
C(2)-C(7)-C(8)	121.6(3)	C(19)-C(18)-C(22)	120.4(3)
C(7)-C(8)-C(9)	113.9(3)	C(17)-C(18)-C(22)	121.1(3)
C(7)-C(8)-H(8A)	108.8	C(20)-C(19)-C(18)	122.6(3)
C(9)-C(8)-H(8A)	108.8	C(20)-C(19)-H(19A)	118.7
C(7)-C(8)-H(8B)	108.8	C(18)-C(19)-H(19A)	118.7
C(9)-C(8)-H(8B)	108.8	C(19)-C(20)-C(21)	116.7(3)
H(8A)-C(8)-H(8B)	107.7	C(19)-C(20)-C(38)	121.6(3)
C(14)-C(9)-C(10)	117.9(3)	C(21)-C(20)-C(38)	121.6(3)
C(14)-C(9)-C(8)	120.4(3)	C(16)-C(21)-C(20)	122.8(3)
C(10)-C(9)-C(8)	121.6(3)	C(16)-C(21)-H(21A)	118.6
C(11)-C(10)-C(9)	121.8(3)	C(20)-C(21)-H(21A)	118.6
C(11)-C(10)-O(4)	119.2(3)	C(23)-C(22)-C(18)	113.1(3)
C(9)-C(10)-O(4)	118.7(3)	C(23)-C(22)-H(22A)	109.0
C(12)-C(11)-C(10)	117.8(3)	C(18)-C(22)-H(22A)	109.0
C(12)-C(11)-C(15)	120.2(3)	C(23)-C(22)-H(22B)	109.0
C(10)-C(11)-C(15)	121.8(3)	C(18)-C(22)-H(22B)	109.0

H(22A)-C(22)-H(22B)	107.8	C(30)-C(31)-H(31B)	109.5
C(28)-C(23)-C(24)	118.2(3)	H(31A)-C(31)-H(31B)	109.5
C(28)-C(23)-C(22)	120.1(3)	C(30)-C(31)-H(31C)	109.5
C(24)-C(23)-C(22)	121.7(3)	H(31A)-C(31)-H(31C)	109.5
O(2)-C(24)-C(25)	119.4(3)	H(31B)-C(31)-H(31C)	109.5
O(2)-C(24)-C(23)	119.0(3)	C(30)-C(32)-H(32A)	109.5
C(25)-C(24)-C(23)	121.5(3)	C(30)-C(32)-H(32B)	109.5
C(26)-C(25)-C(24)	117.8(3)	H(32A)-C(32)-H(32B)	109.5
C(26)-C(25)-C(29)	120.0(3)	C(30)-C(32)-H(32C)	109.5
C(24)-C(25)-C(29)	122.1(3)	H(32A)-C(32)-H(32C)	109.5
C(25)-C(26)-C(27)	122.8(3)	H(32B)-C(32)-H(32C)	109.5
C(25)-C(26)-H(26A)	118.6	C(30)-C(33)-H(33A)	109.5
C(27)-C(26)-H(26A)	118.6	C(30)-C(33)-H(33B)	109.5
C(28)-C(27)-C(26)	116.9(3)	H(33A)-C(33)-H(33B)	109.5
C(28)-C(27)-C(42)	123.3(3)	C(30)-C(33)-H(33C)	109.5
C(26)-C(27)-C(42)	119.9(3)	H(33A)-C(33)-H(33C)	109.5
C(23)-C(28)-C(27)	122.6(3)	H(33B)-C(33)-H(33C)	109.5
C(23)-C(28)-H(28A)	118.7	C(35)-C(34)-C(37)	108.9(5)
C(27)-C(28)-H(28A)	118.7	C(35)-C(34)-C(13)	107.9(4)
C(3)-C(29)-C(25)	112.1(3)	C(37)-C(34)-C(13)	112.0(4)
C(3)-C(29)-H(29A)	109.2	C(35)-C(34)-C(36)	111.4(6)
C(25)-C(29)-H(29A)	109.2	C(37)-C(34)-C(36)	106.1(4)
C(3)-C(29)-H(29B)	109.2	C(13)-C(34)-C(36)	110.5(4)
C(25)-C(29)-H(29B)	109.2	C(34)-C(35)-H(35A)	109.5
H(29A)-C(29)-H(29B)	107.9	C(34)-C(35)-H(35B)	109.5
C(32)-C(30)-C(31)	111.9(6)	H(35A)-C(35)-H(35B)	109.5
C(33B)-C(30)-C(32B)	109.8(14)	C(34)-C(35)-H(35C)	109.5
C(33B)-C(30)-C(31B)	105.2(15)	H(35A)-C(35)-H(35C)	109.5
C(32B)-C(30)-C(31B)	102.3(14)	H(35B)-C(35)-H(35C)	109.5
C(32)-C(30)-C(5)	112.6(5)	C(34)-C(36)-H(36A)	109.5
C(33B)-C(30)-C(5)	120.6(12)	C(34)-C(36)-H(36B)	109.5
C(31)-C(30)-C(5)	109.1(4)	H(36A)-C(36)-H(36B)	109.5
C(32B)-C(30)-C(5)	108.9(9)	C(34)-C(36)-H(36C)	109.5
C(31B)-C(30)-C(5)	108.5(9)	H(36A)-C(36)-H(36C)	109.5
C(32)-C(30)-C(33)	109.1(6)	H(36B)-C(36)-H(36C)	109.5
C(31)-C(30)-C(33)	106.1(6)	C(34)-C(37)-H(37A)	109.5
C(5)-C(30)-C(33)	107.8(4)	C(34)-C(37)-H(37B)	109.5
C(30)-C(31)-H(31A)	109.5	H(37A)-C(37)-H(37B)	109.5

C(34)-C(37)-H(37C)	109.5	C(44)-C(42)-C(45)	107.7(4)
H(37A)-C(37)-H(37C)	109.5	C(42)-C(43)-H(43A)	109.5
H(37B)-C(37)-H(37C)	109.5	C(42)-C(43)-H(43B)	109.5
C(41)-C(38)-C(39)	110.4(6)	H(43A)-C(43)-H(43B)	109.5
C(39B)-C(38)-C(20)	115.2(6)	C(42)-C(43)-H(43C)	109.5
C(41)-C(38)-C(20)	117.8(4)	H(43A)-C(43)-H(43C)	109.5
C(39)-C(38)-C(20)	110.4(5)	H(43B)-C(43)-H(43C)	109.5
C(39B)-C(38)-C(40B)	116.0(9)	C(42)-C(44)-H(44A)	109.5
C(20)-C(38)-C(40B)	108.1(6)	C(42)-C(44)-H(44B)	109.5
C(39B)-C(38)-C(41B)	110.3(8)	H(44A)-C(44)-H(44B)	109.5
C(20)-C(38)-C(41B)	105.0(5)	C(42)-C(44)-H(44C)	109.5
C(40B)-C(38)-C(41B)	100.7(8)	H(44A)-C(44)-H(44C)	109.5
C(41)-C(38)-C(40)	108.0(6)	H(44B)-C(44)-H(44C)	109.5
C(39)-C(38)-C(40)	100.7(8)	C(42)-C(45)-H(45A)	109.5
C(20)-C(38)-C(40)	108.1(4)	C(42)-C(45)-H(45B)	109.5
C(38)-C(39)-H(39A)	109.5	H(45A)-C(45)-H(45B)	109.5
C(38)-C(39)-H(39B)	109.5	C(42)-C(45)-H(45C)	109.5
H(39A)-C(39)-H(39B)	109.5	H(45A)-C(45)-H(45C)	109.5
C(38)-C(39)-H(39C)	109.5	H(45B)-C(45)-H(45C)	109.5
H(39A)-C(39)-H(39C)	109.5	C(30)-C(31B)-H(31D)	109.5
H(39B)-C(39)-H(39C)	109.5	C(30)-C(31B)-H(31E)	109.5
C(38)-C(40)-H(40A)	109.5	H(31D)-C(31B)-H(31E)	109.5
C(38)-C(40)-H(40B)	109.5	C(30)-C(31B)-H(31F)	109.5
H(40A)-C(40)-H(40B)	109.5	H(31D)-C(31B)-H(31F)	109.5
C(38)-C(40)-H(40C)	109.5	H(31E)-C(31B)-H(31F)	109.5
H(40A)-C(40)-H(40C)	109.5	C(30)-C(32B)-H(32D)	109.5
H(40B)-C(40)-H(40C)	109.5	C(30)-C(32B)-H(32E)	109.5
C(38)-C(41)-H(41A)	109.5	H(32D)-C(32B)-H(32E)	109.5
C(38)-C(41)-H(41B)	109.5	C(30)-C(32B)-H(32F)	109.5
H(41A)-C(41)-H(41B)	109.5	H(32D)-C(32B)-H(32F)	109.5
C(38)-C(41)-H(41C)	109.5	H(32E)-C(32B)-H(32F)	109.5
H(41A)-C(41)-H(41C)	109.5	C(30)-C(33B)-H(33D)	109.5
H(41B)-C(41)-H(41C)	109.5	C(30)-C(33B)-H(33E)	109.5
C(43)-C(42)-C(27)	108.8(4)	H(33D)-C(33B)-H(33E)	109.5
C(43)-C(42)-C(44)	109.0(4)	C(30)-C(33B)-H(33F)	109.5
C(27)-C(42)-C(44)	109.8(3)	H(33D)-C(33B)-H(33F)	109.5
C(43)-C(42)-C(45)	109.9(4)	H(33E)-C(33B)-H(33F)	109.5
C(27)-C(42)-C(45)	111.7(4)	C(38)-C(39B)-H(39D)	109.5

C(38)-C(39B)-H(39E)	109.5	C(48)-C(52)-H(52A)	127.0
H(39D)-C(39B)-H(39E)	109.5	C(51)-C(52)-H(52A)	127.0
C(38)-C(39B)-H(39F)	109.5	C(66)-C(53)-C(54)	120.9(5)
H(39D)-C(39B)-H(39F)	109.5	C(66)-C(53)-C(51)	117.2(5)
H(39E)-C(39B)-H(39F)	109.5	C(54)-C(53)-C(51)	121.9(4)
C(38)-C(40B)-H(40D)	109.5	C(53)-C(54)-C(55)	124.3(4)
C(38)-C(40B)-H(40E)	109.5	C(53)-C(54)-C(67)	119.3(4)
H(40D)-C(40B)-H(40E)	109.5	C(55)-C(54)-C(67)	116.4(5)
C(38)-C(40B)-H(40F)	109.5	C(56)-C(55)-C(54)	122.6(4)
H(40D)-C(40B)-H(40F)	109.5	C(56)-C(55)-H(55A)	118.7
H(40E)-C(40B)-H(40F)	109.5	C(54)-C(55)-H(55A)	118.7
C(38)-C(41B)-H(41D)	109.5	C(55)-C(56)-C(57)	121.9(4)
C(38)-C(41B)-H(41E)	109.5	C(55)-C(56)-H(56A)	119.1
H(41D)-C(41B)-H(41E)	109.5	C(57)-C(56)-H(56A)	119.1
C(38)-C(41B)-H(41F)	109.5	C(58)-C(57)-C(68)	119.4(4)
H(41D)-C(41B)-H(41F)	109.5	C(58)-C(57)-C(56)	123.2(5)
H(41E)-C(41B)-H(41F)	109.5	C(68)-C(57)-C(56)	117.4(5)
O(2)-C(46)-C(47)	107.2(3)	C(57)-C(58)-C(59)	121.3(6)
O(2)-C(46)-H(46A)	110.3	C(57)-C(58)-H(58A)	119.3
C(47)-C(46)-H(46A)	110.3	C(59)-C(58)-H(58A)	119.3
O(2)-C(46)-H(46B)	110.3	C(60)-C(59)-C(58)	120.0(6)
C(47)-C(46)-H(46B)	110.3	C(60)-C(59)-H(59A)	120.0
H(46A)-C(46)-H(46B)	108.5	C(58)-C(59)-H(59A)	120.0
C(48)-C(47)-C(46)	112.9(4)	C(59)-C(60)-C(61)	122.0(5)
C(48)-C(47)-H(47A)	109.0	C(59)-C(60)-H(60A)	119.0
C(46)-C(47)-H(47A)	109.0	C(61)-C(60)-H(60A)	119.0
C(48)-C(47)-H(47B)	109.0	C(60)-C(61)-C(62)	124.3(5)
C(46)-C(47)-H(47B)	109.0	C(60)-C(61)-C(68)	118.6(5)
H(47A)-C(47)-H(47B)	107.8	C(62)-C(61)-C(68)	117.2(6)
C(52)-C(48)-O(49)	109.6(4)	C(63)-C(62)-C(61)	123.3(5)
C(52)-C(48)-C(47)	134.9(4)	C(63)-C(62)-H(62A)	118.3
O(49)-C(48)-C(47)	115.4(4)	C(61)-C(62)-H(62A)	118.3
C(48)-O(49)-N(50)	108.0(4)	C(62)-C(63)-C(64)	121.4(5)
C(51)-N(50)-O(49)	106.3(4)	C(62)-C(63)-H(63A)	119.3
N(50)-C(51)-C(52)	110.0(4)	C(64)-C(63)-H(63A)	119.3
N(50)-C(51)-C(53)	119.4(4)	C(65)-C(64)-C(67)	119.9(5)
C(52)-C(51)-C(53)	130.3(4)	C(65)-C(64)-C(63)	123.1(5)
C(48)-C(52)-C(51)	106.0(4)	C(67)-C(64)-C(63)	117.1(6)

C(64)-C(65)-C(66)	121.9(5)	C(76)-C(77)-C(78)	125.2(4)
C(64)-C(65)-H(65A)	119.1	C(76)-C(77)-C(90)	118.2(4)
C(66)-C(65)-H(65A)	119.1	C(78)-C(77)-C(90)	116.4(4)
C(65)-C(66)-C(53)	119.6(6)	C(79)-C(78)-C(77)	122.0(5)
C(65)-C(66)-H(66A)	120.2	C(79)-C(78)-H(78A)	119.0
C(53)-C(66)-H(66A)	120.2	C(77)-C(78)-H(78A)	119.0
C(68)-C(67)-C(64)	120.9(4)	C(78)-C(79)-C(80)	121.5(5)
C(68)-C(67)-C(54)	120.7(4)	C(78)-C(79)-H(79A)	119.2
C(64)-C(67)-C(54)	118.5(5)	C(80)-C(79)-H(79A)	119.2
C(67)-C(68)-C(57)	121.0(4)	C(91)-C(80)-C(81)	119.8(5)
C(67)-C(68)-C(61)	120.1(5)	C(91)-C(80)-C(79)	118.7(5)
C(57)-C(68)-C(61)	118.8(5)	C(81)-C(80)-C(79)	121.5(6)
O(4)-C(69)-C(70)	104.6(3)	C(82)-C(81)-C(80)	119.2(6)
O(4)-C(69)-H(69A)	110.8	C(82)-C(81)-H(81A)	120.4
C(70)-C(69)-H(69A)	110.8	C(80)-C(81)-H(81A)	120.4
O(4)-C(69)-H(69B)	110.8	C(81)-C(82)-C(83)	121.6(5)
C(70)-C(69)-H(69B)	110.8	C(81)-C(82)-H(82A)	119.2
H(69A)-C(69)-H(69B)	108.9	C(83)-C(82)-H(82A)	119.2
C(71)-C(70)-C(69)	114.6(4)	C(84)-C(83)-C(82)	121.8(5)
C(71)-C(70)-H(70A)	108.6	C(84)-C(83)-H(83A)	119.1
C(69)-C(70)-H(70A)	108.6	C(82)-C(83)-H(83A)	119.1
C(71)-C(70)-H(70B)	108.6	C(83)-C(84)-C(85)	124.4(5)
C(69)-C(70)-H(70B)	108.6	C(83)-C(84)-C(91)	117.6(6)
H(70A)-C(70)-H(70B)	107.6	C(85)-C(84)-C(91)	118.0(5)
O(72)-C(71)-C(75)	110.3(4)	C(86)-C(85)-C(84)	123.0(5)
O(72)-C(71)-C(70)	113.6(4)	C(86)-C(85)-H(85A)	118.5
C(75)-C(71)-C(70)	136.1(4)	C(84)-C(85)-H(85A)	118.5
C(71)-O(72)-N(73)	107.9(3)	C(85)-C(86)-C(87)	120.5(6)
C(74)-N(73)-O(72)	106.2(4)	C(85)-C(86)-H(86A)	119.8
N(73)-C(74)-C(75)	110.6(4)	C(87)-C(86)-H(86A)	119.8
N(73)-C(74)-C(76)	120.6(4)	C(88)-C(87)-C(90)	118.7(4)
C(75)-C(74)-C(76)	128.8(4)	C(88)-C(87)-C(86)	121.8(5)
C(71)-C(75)-C(74)	104.9(4)	C(90)-C(87)-C(86)	119.5(5)
C(71)-C(75)-H(75A)	127.5	C(89)-C(88)-C(87)	120.9(5)
C(74)-C(75)-H(75A)	127.5	C(89)-C(88)-H(88A)	119.6
C(89)-C(76)-C(77)	120.1(4)	C(87)-C(88)-H(88A)	119.6
C(89)-C(76)-C(74)	117.3(4)	C(88)-C(89)-C(76)	122.3(5)
C(77)-C(76)-C(74)	122.6(4)	C(88)-C(89)-H(89A)	118.9

C(76)-C(89)-H(89A)	118.9	H(92A)-C(92)-H(92B)	107.7
C(91)-C(90)-C(87)	119.3(4)	Cl(4B)-C(93)-Cl(3)	151.9(6)
C(91)-C(90)-C(77)	120.9(5)	Cl(4)-C(93)-Cl(3)	112.0(4)
C(87)-C(90)-C(77)	119.7(4)	Cl(4B)-C(93)-H(93C)	98.6
C(80)-C(91)-C(90)	120.3(5)	Cl(3)-C(93)-H(93C)	98.6
C(80)-C(91)-C(84)	119.9(5)	Cl(4B)-C(93)-H(93D)	98.6
C(90)-C(91)-C(84)	119.7(5)	Cl(3)-C(93)-H(93D)	98.6
Cl(2)-C(92)-Cl(1)	113.7(7)	H(93C)-C(93)-H(93D)	103.8
Cl(1)-C(92)-Cl(2B)	107.1(10)	Cl(4)-C(93)-H(93A)	109.2
Cl(1)-C(92)-H(92C)	110.3	Cl(3)-C(93)-H(93A)	109.2
Cl(2B)-C(92)-H(92C)	110.3	Cl(4)-C(93)-H(93B)	109.2
Cl(1)-C(92)-H(92D)	110.3	Cl(3)-C(93)-H(93B)	109.2
Cl(2B)-C(92)-H(92D)	110.3	H(93A)-C(93)-H(93B)	107.9
H(92C)-C(92)-H(92D)	108.6	C(2)-O(1)-H(1)	103.6
Cl(2)-C(92)-H(92A)	108.8	C(24)-O(2)-C(46)	112.9(3)
Cl(1)-C(92)-H(92A)	108.8	C(17)-O(3)-H(3)	116.2
Cl(2)-C(92)-H(92B)	108.8	C(10)-O(4)-C(69)	116.9(3)
Cl(1)-C(92)-H(92B)	108.8		

Table 5. Anisotropic displacement parameters ($\text{\AA}^2 \times 10^3$) for TCD218. The anisotropic displacement factor exponent takes the form: $-2\pi^2 [h^2 a^{*2} U^{11} + \dots + 2 h k a^* b^* U^{12}]$

	U^{11}	U^{22}	U^{33}	U^{23}	U^{13}	U^{12}
C(2)	25(2)	35(2)	22(2)	9(1)	8(1)	5(1)
C(3)	27(2)	31(2)	22(2)	8(1)	9(1)	7(1)
C(4)	38(2)	36(2)	26(2)	4(1)	9(2)	2(2)
C(5)	36(2)	43(2)	32(2)	9(2)	11(2)	-5(2)
C(6)	31(2)	49(2)	31(2)	16(2)	15(2)	4(2)
C(7)	29(2)	43(2)	20(2)	12(1)	8(1)	8(2)
C(8)	40(2)	52(2)	21(2)	8(2)	14(2)	11(2)
C(9)	33(2)	41(2)	18(2)	4(1)	15(1)	7(2)
C(10)	30(2)	42(2)	21(2)	-6(1)	14(1)	-1(2)
C(11)	43(2)	32(2)	22(2)	-4(1)	21(2)	0(2)
C(12)	39(2)	33(2)	21(2)	3(1)	17(2)	9(2)
C(13)	29(2)	39(2)	23(2)	-1(1)	14(1)	2(2)
C(14)	37(2)	39(2)	26(2)	5(1)	21(2)	3(2)
C(15)	63(3)	31(2)	33(2)	-4(2)	32(2)	-4(2)
C(16)	47(2)	24(2)	33(2)	-2(1)	27(2)	-2(2)
C(17)	37(2)	24(2)	24(2)	1(1)	17(2)	-3(1)
C(18)	37(2)	23(2)	28(2)	4(1)	20(2)	0(1)
C(19)	45(2)	29(2)	27(2)	5(1)	23(2)	9(2)
C(20)	46(2)	32(2)	35(2)	9(2)	25(2)	14(2)
C(21)	42(2)	30(2)	36(2)	4(2)	26(2)	7(2)
C(22)	36(2)	27(2)	29(2)	6(1)	20(2)	5(1)
C(23)	31(2)	27(2)	27(2)	3(1)	19(1)	6(1)
C(24)	29(2)	31(2)	22(2)	-1(1)	15(1)	3(1)
C(25)	37(2)	28(2)	27(2)	5(1)	20(2)	7(1)
C(26)	51(2)	28(2)	32(2)	1(1)	26(2)	2(2)
C(27)	47(2)	33(2)	26(2)	-3(1)	20(2)	-5(2)
C(28)	38(2)	36(2)	22(2)	4(1)	16(2)	4(2)
C(29)	38(2)	35(2)	33(2)	11(2)	21(2)	13(2)
C(30)	48(3)	52(3)	60(3)	11(2)	18(2)	-13(2)
C(31)	85(5)	45(4)	135(7)	29(4)	31(5)	-10(4)
C(32)	93(5)	81(5)	89(5)	14(4)	49(4)	-40(4)
C(33)	77(5)	80(5)	73(5)	-16(4)	26(4)	-52(5)
C(34)	31(2)	49(2)	42(2)	-7(2)	17(2)	0(2)

C(35)	45(3)	135(5)	144(6)	-76(5)	51(3)	-10(3)
C(36)	42(3)	119(5)	73(4)	44(4)	-9(3)	-13(3)
C(37)	38(3)	82(4)	71(3)	8(3)	14(2)	-14(2)
C(38)	55(2)	63(3)	45(2)	15(2)	25(2)	28(2)
C(39)	95(6)	113(7)	62(5)	42(5)	56(5)	59(6)
C(40)	76(6)	100(7)	54(5)	-2(4)	7(4)	47(5)
C(41)	62(5)	73(5)	49(4)	17(4)	31(4)	38(4)
C(42)	60(3)	51(2)	28(2)	-10(2)	21(2)	-16(2)
C(43)	94(4)	64(3)	58(3)	-33(3)	40(3)	-20(3)
C(44)	70(3)	56(3)	37(2)	-7(2)	21(2)	-27(2)
C(45)	70(3)	75(3)	23(2)	-4(2)	14(2)	-27(3)
C(31B)	78(11)	60(10)	71(11)	20(8)	25(8)	-30(8)
C(32B)	62(10)	56(10)	66(10)	3(7)	30(8)	-13(7)
C(33B)	85(12)	78(12)	86(12)	-4(8)	47(9)	-8(8)
C(39B)	63(7)	60(7)	37(5)	5(5)	11(5)	26(6)
C(40B)	46(6)	71(7)	49(6)	7(5)	14(5)	9(5)
C(41B)	64(7)	44(6)	39(5)	5(4)	17(5)	25(5)
C(46)	31(2)	47(2)	37(2)	3(2)	19(2)	3(2)
C(47)	43(2)	57(3)	45(2)	-1(2)	19(2)	-8(2)
C(48)	30(2)	60(3)	39(2)	-9(2)	10(2)	-5(2)
O(49)	64(2)	61(2)	44(2)	-10(2)	9(2)	2(2)
N(50)	61(3)	81(3)	38(2)	-6(2)	7(2)	12(2)
C(51)	41(2)	59(3)	40(2)	-6(2)	12(2)	10(2)
C(52)	40(2)	59(3)	36(2)	-2(2)	18(2)	4(2)
C(53)	45(2)	78(3)	31(2)	-1(2)	10(2)	23(2)
C(54)	47(2)	63(3)	29(2)	2(2)	16(2)	24(2)
C(55)	46(2)	64(3)	25(2)	6(2)	12(2)	25(2)
C(56)	55(3)	61(3)	29(2)	6(2)	18(2)	21(2)
C(57)	70(3)	60(3)	32(2)	4(2)	28(2)	26(2)
C(58)	88(4)	57(3)	44(3)	4(2)	35(3)	20(3)
C(59)	109(5)	57(3)	51(3)	7(2)	46(3)	31(3)
C(60)	112(5)	58(3)	48(3)	17(2)	47(3)	44(3)
C(61)	83(4)	81(4)	36(2)	11(2)	31(2)	55(3)
C(62)	82(4)	88(4)	36(2)	18(3)	23(3)	58(4)
C(63)	61(3)	102(5)	35(2)	9(3)	12(2)	49(3)
C(64)	54(3)	90(4)	35(2)	6(2)	15(2)	35(3)
C(65)	51(3)	111(5)	34(2)	-2(3)	4(2)	27(3)
C(66)	48(3)	89(4)	42(3)	-5(2)	9(2)	14(3)

C(67)	55(3)	79(3)	27(2)	8(2)	18(2)	38(3)
C(68)	63(3)	61(3)	32(2)	9(2)	25(2)	36(2)
C(69)	43(2)	60(3)	27(2)	-12(2)	15(2)	-6(2)
C(70)	43(2)	56(3)	37(2)	-2(2)	22(2)	-8(2)
C(71)	38(2)	55(3)	40(2)	1(2)	21(2)	-11(2)
O(72)	50(2)	79(2)	45(2)	-11(2)	19(2)	-1(2)
N(73)	49(2)	82(3)	40(2)	-9(2)	13(2)	-3(2)
C(74)	42(2)	41(2)	42(2)	-1(2)	22(2)	-8(2)
C(75)	47(2)	47(2)	47(2)	-3(2)	25(2)	-9(2)
C(76)	43(2)	48(2)	43(2)	-2(2)	21(2)	-17(2)
C(77)	44(2)	41(2)	44(2)	-6(2)	15(2)	-14(2)
C(78)	59(3)	58(3)	50(3)	-13(2)	14(2)	-4(2)
C(79)	67(3)	68(3)	59(3)	1(3)	17(3)	13(3)
C(80)	53(3)	80(4)	47(3)	-8(3)	12(2)	-17(3)
C(81)	66(3)	89(4)	58(3)	4(3)	19(3)	-11(3)
C(82)	62(3)	83(4)	50(3)	-3(3)	10(3)	-27(3)
C(83)	82(4)	75(4)	50(3)	-9(3)	29(3)	-38(3)
C(84)	66(3)	58(3)	43(2)	-2(2)	24(2)	-36(3)
C(85)	75(3)	55(3)	57(3)	-10(2)	37(3)	-29(3)
C(86)	76(3)	54(3)	66(3)	-12(2)	43(3)	-25(3)
C(87)	70(3)	38(2)	58(3)	-10(2)	43(3)	-27(2)
C(88)	51(3)	45(2)	68(3)	-4(2)	36(2)	-16(2)
C(89)	48(2)	42(2)	58(3)	-3(2)	27(2)	-14(2)
C(90)	52(3)	47(2)	43(2)	-5(2)	20(2)	-23(2)
C(91)	54(3)	52(3)	48(2)	-4(2)	19(2)	-23(2)
C(92)	36(2)	68(3)	34(2)	-8(2)	15(2)	2(2)
C(93)	72(4)	106(5)	79(4)	-11(4)	31(3)	11(4)
Cl(1)	50(1)	51(1)	53(1)	5(1)	20(1)	-5(1)
Cl(2)	69(4)	51(1)	35(2)	10(1)	20(2)	19(2)
Cl(2B)	69(4)	51(1)	35(2)	10(1)	20(2)	19(2)
Cl(3)	64(1)	134(2)	77(1)	0(1)	31(1)	2(1)
Cl(4)	69(1)	85(1)	88(1)	11(1)	40(1)	2(1)
Cl(4B)	69(1)	85(1)	88(1)	11(1)	40(1)	2(1)
O(1)	36(1)	34(1)	31(1)	3(1)	21(1)	1(1)
O(2)	26(1)	40(1)	26(1)	-1(1)	12(1)	3(1)
O(3)	37(1)	36(1)	25(1)	0(1)	16(1)	4(1)
O(4)	31(1)	66(2)	30(1)	-18(1)	16(1)	-8(1)

Table 6. Hydrogen coordinates ($\times 10^4$) and isotropic displacement parameters ($\text{\AA}^2 \times 10^{-3}$) for TCD218.

	x	y	z	U(eq)
H(4A)	7417	5450	8597	43
H(6A)	8317	4646	7451	44
H(8A)	7953	3540	6886	45
H(8B)	7287	3122	6896	45
H(12A)	9612	1490	8955	36
H(14A)	9227	3317	7875	38
H(15A)	8547	614	8570	46
H(15B)	7736	946	8207	46
H(19A)	8470	1451	11051	38
H(21A)	9256	611	9827	40
H(22A)	6767	1944	9723	35
H(22B)	7291	1980	10557	35
H(26A)	7644	4813	9905	41
H(28A)	8154	3010	11044	37
H(29A)	6189	4097	8329	41
H(29B)	6489	4837	8725	41
H(31A)	7423	6382	7327	146
H(31B)	8011	6922	7880	146
H(31C)	7488	6476	8094	146
H(32A)	8506	5805	7250	127
H(32B)	9168	5486	7953	127
H(32C)	9071	6326	7848	127
H(33A)	8500	6033	9135	121
H(33B)	9058	6482	8969	121
H(33C)	9181	5649	9116	121
H(35A)	10358	2172	7857	158
H(35B)	10619	1575	8455	158
H(35C)	11173	2192	8507	158
H(36A)	11302	2453	9771	139
H(36B)	10735	1815	9612	139
H(36C)	10553	2582	9805	139
H(37A)	10368	3442	8244	102

H(37B)	11123	3341	8959	102
H(37C)	10399	3590	8990	102
H(39A)	9046	-37	11462	123
H(39B)	9136	710	11844	123
H(39C)	9814	173	12123	123
H(40A)	9774	1643	11756	130
H(40B)	10302	1587	11404	130
H(40C)	10490	1152	12107	130
H(41A)	9868	-211	10825	89
H(41B)	10533	48	11558	89
H(41C)	10358	452	10841	89
H(43A)	7890	5285	11032	105
H(43B)	8500	5215	11841	105
H(43C)	7788	4718	11531	105
H(44A)	8804	5101	10624	85
H(44B)	9338	4429	10883	85
H(44C)	9438	5051	11426	85
H(45A)	9280	3579	11724	89
H(45B)	8680	3666	11989	89
H(45C)	9353	4209	12251	89
H(31D)	8094	5850	7059	111
H(31E)	8351	6617	7407	111
H(31F)	7539	6341	7190	111
H(32D)	9175	5317	8076	92
H(32E)	9405	5645	8838	92
H(32F)	9349	6145	8213	92
H(33D)	7754	6553	8415	121
H(33E)	8527	6321	9056	121
H(33F)	8498	6895	8496	121
H(39D)	9205	617	11882	87
H(39E)	9622	1349	11948	87
H(39F)	10084	640	12275	87
H(40D)	10267	789	10697	89
H(40E)	10748	625	11522	89
H(40F)	10423	1402	11264	89
H(41D)	9169	-322	11058	78
H(41E)	10048	-342	11464	78
H(41F)	9618	-211	10630	78

H(46A)	5435	3315	8812	44
H(46B)	5782	2676	9367	44
H(47A)	5474	1892	8376	59
H(47B)	4774	2198	8419	59
H(52A)	4931	3699	7576	55
H(55A)	5552	4092	6938	56
H(56A)	6166	5084	6954	60
H(58A)	6221	6228	6390	73
H(59A)	5681	7048	5471	83
H(60A)	4526	6852	4557	83
H(62A)	3388	6094	3974	85
H(63A)	2753	5128	3958	84
H(65A)	2693	3980	4509	86
H(66A)	3193	3168	5437	78
H(69A)	7092	1194	6868	52
H(69B)	7111	1937	6509	52
H(70A)	6013	1550	6901	53
H(70B)	6039	2302	6573	53
H(75A)	6224	942	5427	55
H(78A)	3822	1685	3792	72
H(79A)	2796	1890	2746	84
H(81A)	1976	1594	1471	90
H(82A)	1716	868	519	86
H(83A)	2522	-14	579	84
H(85A)	3664	-700	1274	72
H(86A)	4688	-933	2318	73
H(88A)	5464	-674	3593	62
H(89A)	5717	-7	4571	58
H(92C)	8407	3409	9577	57
H(92D)	8710	2939	9147	57
H(92A)	8749	2942	9152	57
H(92B)	8385	3349	9562	57
H(93C)	3262	1239	4754	105
H(93D)	3610	1922	5193	105
H(93A)	3301	1201	4843	105
H(93B)	3591	1906	5306	105
H(1)	6688	3292	8152	48
H(3)	7220	1773	8374	90(20)

Table 7. Torsion angles [°] for TCD218.

O(1)-C(2)-C(3)-C(4)	-176.2(3)	C(12)-C(11)-C(15)-C(16)	73.0(4)
C(7)-C(2)-C(3)-C(4)	1.4(5)	C(10)-C(11)-C(15)-C(16)	-103.1(4)
O(1)-C(2)-C(3)-C(29)	3.3(5)	C(11)-C(15)-C(16)-C(21)	-100.1(4)
C(7)-C(2)-C(3)-C(29)	-179.1(3)	C(11)-C(15)-C(16)-C(17)	80.0(5)
C(2)-C(3)-C(4)-C(5)	-0.9(5)	C(21)-C(16)-C(17)-O(3)	-179.3(3)
C(29)-C(3)-C(4)-C(5)	179.6(3)	C(15)-C(16)-C(17)-O(3)	0.7(5)
C(3)-C(4)-C(5)-C(6)	0.2(5)	C(21)-C(16)-C(17)-C(18)	-1.7(5)
C(3)-C(4)-C(5)-C(30)	-179.3(3)	C(15)-C(16)-C(17)-C(18)	178.2(3)
C(4)-C(5)-C(6)-C(7)	0.0(5)	O(3)-C(17)-C(18)-C(19)	179.4(3)
C(30)-C(5)-C(6)-C(7)	179.5(3)	C(16)-C(17)-C(18)-C(19)	1.9(5)
C(5)-C(6)-C(7)-C(2)	0.5(5)	O(3)-C(17)-C(18)-C(22)	-0.5(5)
C(5)-C(6)-C(7)-C(8)	-179.6(3)	C(16)-C(17)-C(18)-C(22)	-178.1(3)
O(1)-C(2)-C(7)-C(6)	176.4(3)	C(17)-C(18)-C(19)-C(20)	-0.8(6)
C(3)-C(2)-C(7)-C(6)	-1.2(5)	C(22)-C(18)-C(19)-C(20)	179.2(3)
O(1)-C(2)-C(7)-C(8)	-3.5(5)	C(18)-C(19)-C(20)-C(21)	-0.5(6)
C(3)-C(2)-C(7)-C(8)	178.9(3)	C(18)-C(19)-C(20)-C(38)	177.8(4)
C(6)-C(7)-C(8)-C(9)	102.0(4)	C(17)-C(16)-C(21)-C(20)	0.4(6)
C(2)-C(7)-C(8)-C(9)	-78.1(4)	C(15)-C(16)-C(21)-C(20)	-179.5(4)
C(7)-C(8)-C(9)-C(14)	-77.8(4)	C(19)-C(20)-C(21)-C(16)	0.6(6)
C(7)-C(8)-C(9)-C(10)	99.6(4)	C(38)-C(20)-C(21)-C(16)	-177.6(4)
C(14)-C(9)-C(10)-C(11)	5.7(5)	C(19)-C(18)-C(22)-C(23)	103.3(4)
C(8)-C(9)-C(10)-C(11)	-171.7(3)	C(17)-C(18)-C(22)-C(23)	-76.8(4)
C(14)-C(9)-C(10)-O(4)	179.3(3)	C(18)-C(22)-C(23)-C(28)	-78.2(4)
C(8)-C(9)-C(10)-O(4)	1.8(5)	C(18)-C(22)-C(23)-C(24)	99.4(4)
C(9)-C(10)-C(11)-C(12)	-5.2(5)	C(28)-C(23)-C(24)-O(2)	-177.6(3)
O(4)-C(10)-C(11)-C(12)	-178.7(3)	C(22)-C(23)-C(24)-O(2)	4.8(5)
C(9)-C(10)-C(11)-C(15)	171.1(3)	C(28)-C(23)-C(24)-C(25)	4.8(5)
O(4)-C(10)-C(11)-C(15)	-2.4(5)	C(22)-C(23)-C(24)-C(25)	-172.9(3)
C(10)-C(11)-C(12)-C(13)	0.9(5)	O(2)-C(24)-C(25)-C(26)	177.3(3)
C(15)-C(11)-C(12)-C(13)	-175.4(3)	C(23)-C(24)-C(25)-C(26)	-5.1(5)
C(11)-C(12)-C(13)-C(14)	2.5(5)	O(2)-C(24)-C(25)-C(29)	-6.4(5)
C(11)-C(12)-C(13)-C(34)	-176.0(3)	C(23)-C(24)-C(25)-C(29)	171.2(3)
C(10)-C(9)-C(14)-C(13)	-2.1(5)	C(24)-C(25)-C(26)-C(27)	1.9(5)
C(8)-C(9)-C(14)-C(13)	175.4(3)	C(29)-C(25)-C(26)-C(27)	-174.5(3)
C(12)-C(13)-C(14)-C(9)	-1.9(5)	C(25)-C(26)-C(27)-C(28)	1.6(6)
C(34)-C(13)-C(14)-C(9)	176.6(3)	C(25)-C(26)-C(27)-C(42)	-178.6(4)

C(24)-C(23)-C(28)-C(27)	-1.1(5)	C(28)-C(27)-C(42)-C(43)	-116.0(5)
C(22)-C(23)-C(28)-C(27)	176.6(3)	C(26)-C(27)-C(42)-C(43)	64.2(5)
C(26)-C(27)-C(28)-C(23)	-2.0(5)	C(28)-C(27)-C(42)-C(44)	124.9(4)
C(42)-C(27)-C(28)-C(23)	178.2(4)	C(26)-C(27)-C(42)-C(44)	-54.9(5)
C(4)-C(3)-C(29)-C(25)	-99.8(4)	C(28)-C(27)-C(42)-C(45)	5.5(6)
C(2)-C(3)-C(29)-C(25)	80.7(4)	C(26)-C(27)-C(42)-C(45)	-174.3(4)
C(26)-C(25)-C(29)-C(3)	75.5(4)	O(2)-C(46)-C(47)-C(48)	-71.0(4)
C(24)-C(25)-C(29)-C(3)	-100.8(4)	C(46)-C(47)-C(48)-C(52)	-21.3(7)
C(6)-C(5)-C(30)-C(32)	-1.1(7)	C(46)-C(47)-C(48)-O(49)	164.0(4)
C(4)-C(5)-C(30)-C(32)	178.3(5)	C(52)-C(48)-O(49)-N(50)	0.3(5)
C(6)-C(5)-C(30)-C(33B)	-175.6(14)	C(47)-C(48)-O(49)-N(50)	176.4(4)
C(4)-C(5)-C(30)-C(33B)	3.9(15)	C(48)-O(49)-N(50)-C(51)	1.0(5)
C(6)-C(5)-C(30)-C(31)	123.7(6)	O(49)-N(50)-C(51)-C(52)	-1.9(5)
C(4)-C(5)-C(30)-C(31)	-56.9(7)	O(49)-N(50)-C(51)-C(53)	-176.9(4)
C(6)-C(5)-C(30)-C(32B)	-47.4(11)	O(49)-C(48)-C(52)-C(51)	-1.4(5)
C(4)-C(5)-C(30)-C(32B)	132.0(11)	C(47)-C(48)-C(52)-C(51)	-176.4(5)
C(6)-C(5)-C(30)-C(31B)	63.2(13)	N(50)-C(51)-C(52)-C(48)	2.1(5)
C(4)-C(5)-C(30)-C(31B)	-117.3(13)	C(53)-C(51)-C(52)-C(48)	176.4(5)
C(6)-C(5)-C(30)-C(33)	-121.6(6)	N(50)-C(51)-C(53)-C(66)	40.2(7)
C(4)-C(5)-C(30)-C(33)	57.9(6)	C(52)-C(51)-C(53)-C(66)	-133.7(5)
C(14)-C(13)-C(34)-C(35)	-99.2(6)	N(50)-C(51)-C(53)-C(54)	-141.7(5)
C(12)-C(13)-C(34)-C(35)	79.3(6)	C(52)-C(51)-C(53)-C(54)	44.5(7)
C(14)-C(13)-C(34)-C(37)	20.7(5)	C(66)-C(53)-C(54)-C(55)	-176.2(4)
C(12)-C(13)-C(34)-C(37)	-160.8(4)	C(51)-C(53)-C(54)-C(55)	5.7(7)
C(14)-C(13)-C(34)-C(36)	138.7(5)	C(66)-C(53)-C(54)-C(67)	1.4(7)
C(12)-C(13)-C(34)-C(36)	-42.8(6)	C(51)-C(53)-C(54)-C(67)	-176.7(4)
C(19)-C(20)-C(38)-C(39B)	2.0(10)	C(53)-C(54)-C(55)-C(56)	-179.1(4)
C(21)-C(20)-C(38)-C(39B)	-179.8(8)	C(67)-C(54)-C(55)-C(56)	3.2(6)
C(19)-C(20)-C(38)-C(41)	173.2(6)	C(54)-C(55)-C(56)-C(57)	-1.6(7)
C(21)-C(20)-C(38)-C(41)	-8.6(8)	C(55)-C(56)-C(57)-C(58)	-178.6(4)
C(19)-C(20)-C(38)-C(39)	45.2(8)	C(55)-C(56)-C(57)-C(68)	-0.5(6)
C(21)-C(20)-C(38)-C(39)	-136.7(7)	C(68)-C(57)-C(58)-C(59)	0.0(7)
C(19)-C(20)-C(38)-C(40B)	-129.5(7)	C(56)-C(57)-C(58)-C(59)	178.1(4)
C(21)-C(20)-C(38)-C(40B)	48.6(8)	C(57)-C(58)-C(59)-C(60)	-0.7(7)
C(19)-C(20)-C(38)-C(41B)	123.6(7)	C(58)-C(59)-C(60)-C(61)	1.0(7)
C(21)-C(20)-C(38)-C(41B)	-58.2(7)	C(59)-C(60)-C(61)-C(62)	-178.8(5)
C(19)-C(20)-C(38)-C(40)	-64.1(6)	C(59)-C(60)-C(61)-C(68)	-0.4(7)
C(21)-C(20)-C(38)-C(40)	114.1(6)	C(60)-C(61)-C(62)-C(63)	179.0(5)

C(68)-C(61)-C(62)-C(63)	0.6(7)	C(70)-C(71)-C(75)-C(74)	178.6(5)
C(61)-C(62)-C(63)-C(64)	-0.8(8)	N(73)-C(74)-C(75)-C(71)	-0.4(5)
C(62)-C(63)-C(64)-C(65)	-178.8(5)	C(76)-C(74)-C(75)-C(71)	-178.2(4)
C(62)-C(63)-C(64)-C(67)	0.5(7)	N(73)-C(74)-C(76)-C(89)	-153.6(4)
C(67)-C(64)-C(65)-C(66)	1.7(8)	C(75)-C(74)-C(76)-C(89)	24.0(6)
C(63)-C(64)-C(65)-C(66)	-179.0(5)	N(73)-C(74)-C(76)-C(77)	27.4(6)
C(64)-C(65)-C(66)-C(53)	-1.5(8)	C(75)-C(74)-C(76)-C(77)	-155.0(4)
C(54)-C(53)-C(66)-C(65)	-0.1(7)	C(89)-C(76)-C(77)-C(78)	-175.7(4)
C(51)-C(53)-C(66)-C(65)	178.1(5)	C(74)-C(76)-C(77)-C(78)	3.3(7)
C(65)-C(64)-C(67)-C(68)	179.3(4)	C(89)-C(76)-C(77)-C(90)	0.2(6)
C(63)-C(64)-C(67)-C(68)	-0.1(6)	C(74)-C(76)-C(77)-C(90)	179.2(4)
C(65)-C(64)-C(67)-C(54)	-0.3(7)	C(76)-C(77)-C(78)-C(79)	-180.0(5)
C(63)-C(64)-C(67)-C(54)	-179.6(4)	C(90)-C(77)-C(78)-C(79)	4.0(8)
C(53)-C(54)-C(67)-C(68)	179.2(4)	C(77)-C(78)-C(79)-C(80)	-1.8(9)
C(55)-C(54)-C(67)-C(68)	-3.0(6)	C(78)-C(79)-C(80)-C(91)	-1.7(9)
C(53)-C(54)-C(67)-C(64)	-1.2(6)	C(78)-C(79)-C(80)-C(81)	-179.7(6)
C(55)-C(54)-C(67)-C(64)	176.6(4)	C(91)-C(80)-C(81)-C(82)	1.6(9)
C(64)-C(67)-C(68)-C(57)	-178.4(4)	C(79)-C(80)-C(81)-C(82)	179.7(6)
C(54)-C(67)-C(68)-C(57)	1.2(6)	C(80)-C(81)-C(82)-C(83)	-3.2(9)
C(64)-C(67)-C(68)-C(61)	-0.1(6)	C(81)-C(82)-C(83)-C(84)	2.7(9)
C(54)-C(67)-C(68)-C(61)	179.4(4)	C(82)-C(83)-C(84)-C(85)	-179.7(5)
C(58)-C(57)-C(68)-C(67)	178.8(4)	C(82)-C(83)-C(84)-C(91)	-0.5(7)
C(56)-C(57)-C(68)-C(67)	0.6(6)	C(83)-C(84)-C(85)-C(86)	-179.5(5)
C(58)-C(57)-C(68)-C(61)	0.6(6)	C(91)-C(84)-C(85)-C(86)	1.4(7)
C(56)-C(57)-C(68)-C(61)	-177.7(4)	C(84)-C(85)-C(86)-C(87)	-0.2(7)
C(60)-C(61)-C(68)-C(67)	-178.6(4)	C(85)-C(86)-C(87)-C(88)	179.5(4)
C(62)-C(61)-C(68)-C(67)	-0.1(6)	C(85)-C(86)-C(87)-C(90)	-0.4(6)
C(60)-C(61)-C(68)-C(57)	-0.3(6)	C(90)-C(87)-C(88)-C(89)	-1.1(6)
C(62)-C(61)-C(68)-C(57)	178.2(4)	C(86)-C(87)-C(88)-C(89)	178.9(4)
O(4)-C(69)-C(70)-C(71)	177.8(4)	C(87)-C(88)-C(89)-C(76)	0.7(7)
C(69)-C(70)-C(71)-O(72)	-172.8(4)	C(77)-C(76)-C(89)-C(88)	-0.2(6)
C(69)-C(70)-C(71)-C(75)	8.6(7)	C(74)-C(76)-C(89)-C(88)	-179.2(4)
C(75)-C(71)-O(72)-N(73)	0.4(5)	C(88)-C(87)-C(90)-C(91)	179.8(4)
C(70)-C(71)-O(72)-N(73)	-178.5(4)	C(86)-C(87)-C(90)-C(91)	-0.3(6)
C(71)-O(72)-N(73)-C(74)	-0.7(5)	C(88)-C(87)-C(90)-C(77)	1.2(6)
O(72)-N(73)-C(74)-C(75)	0.6(5)	C(86)-C(87)-C(90)-C(77)	-178.9(4)
O(72)-N(73)-C(74)-C(76)	178.7(4)	C(76)-C(77)-C(90)-C(91)	-179.4(4)
O(72)-C(71)-C(75)-C(74)	0.0(5)	C(78)-C(77)-C(90)-C(91)	-3.1(6)

C(76)-C(77)-C(90)-C(87)	-0.7(6)	C(83)-C(84)-C(91)-C(80)	-1.0(7)
C(78)-C(77)-C(90)-C(87)	175.5(4)	C(85)-C(84)-C(91)-C(80)	178.2(4)
C(81)-C(80)-C(91)-C(90)	-179.3(5)	C(83)-C(84)-C(91)-C(90)	178.8(4)
C(79)-C(80)-C(91)-C(90)	2.6(8)	C(85)-C(84)-C(91)-C(90)	-2.0(6)
C(81)-C(80)-C(91)-C(84)	0.4(8)	C(25)-C(24)-O(2)-C(46)	-98.9(4)
C(79)-C(80)-C(91)-C(84)	-177.7(5)	C(23)-C(24)-O(2)-C(46)	83.5(4)
C(87)-C(90)-C(91)-C(80)	-178.8(4)	C(47)-C(46)-O(2)-C(24)	-168.6(3)
C(77)-C(90)-C(91)-C(80)	-0.1(7)	C(11)-C(10)-O(4)-C(69)	-98.1(4)
C(87)-C(90)-C(91)-C(84)	1.5(6)	C(9)-C(10)-O(4)-C(69)	88.2(4)
C(77)-C(90)-C(91)-C(84)	-179.9(4)	C(70)-C(69)-O(4)-C(10)	-167.6(3)

Table 8. Hydrogen bonds for TCD218 [\AA and $^\circ$].

D-H...A	d(D-H)	d(H...A)	d(D...A)	$\angle(\text{DHA})$
C(93)-H(93B)...N(50)	0.99	2.44	3.341(8)	151
C(93)-H(93D)...O(72)	0.99	2.55	3.332(7)	136
C(93)-H(93D)...N(73)	0.99	2.56	3.053(8)	111
C(93)-H(93B)...N(50)	0.99	2.44	3.341(8)	151
C(93)-H(93D)...O(72)	0.99	2.55	3.332(7)	136
O(1)-H(1)...O(2)	0.85	2.06	2.859(3)	156
O(3)-H(3)...O(4)	0.85	2.00	2.803(4)	157

Crystal Structure Report for MPIC.2DCM

A specimen of $C_{86}H_{82}N_2O_6$, approximate dimensions 0.020 mm x 0.090 mm x 0.310 mm, was used for the X-ray crystallographic analysis. The X-ray intensity data were measured at 100(2)K using an Oxford Cryosystems Cobra low temperature device using a MiTeGen micromount. See Table 1 for collection parameters and exposure time. Bruker APEX software was used to correct for Lorentz and polarization effects.

A total of 2984 frames were collected. The total exposure time was 33.16 hours. The integration of the data using a **monoclinic** unit cell yielded a total of 39795 reflections to a maximum θ angle of 68.43° (0.83 Å resolution), of which 11481 were independent (average redundancy 3.466, completeness = 99.8%, $R_{int} = 7.82\%$, $R_{sig} = 6.99\%$) and 9245 (80.52%) were greater than $2\sigma(F^2)$. The final cell constants of $a = 33.9554(11)$ Å, $b = 20.6101(7)$ Å, $c = 9.7933(3)$ Å, $\beta = 101.069(2)^\circ$, volume = $6726.1(4)$ Å³, are based upon the refinement of the XYZ-centroids of reflections above $20\sigma(I)$. Data were corrected for absorption effects using the Multi-Scan method (SADABS). The ratio of minimum to maximum apparent transmission was 0.812. The calculated minimum and maximum transmission coefficients (based on crystal size) are 0.6112 and 0.7531.

The structure was solved and refined using Bruker XT, XL and OLEX2 software, using the space group **Cc**, with $Z = 4$ for the formula unit, $C_{86}H_{82}N_2O_6$. The final anisotropic full-matrix least-squares refinement on F^2 with 862 variables converged at $R1 = 4.89\%$, for the observed data and $wR2 = 12.39\%$ for all data. The goodness-of-fit was 1.038. The largest peak in the final difference electron density synthesis was $0.303 e^-/\text{Å}^3$ and the largest hole was $-0.330 e^-/\text{Å}^3$ with an RMS deviation of $0.039 e^-/\text{Å}^3$. On the basis of the final model, the calculated density was $1.224 g/cm^3$ and $F(000)$, 2640 e^- .

Refinement Note: One t-butyl group is disordered and was modelled with constraints and restraints (SADI, EADP) with refined occupancies of 70:30%.

References:

Bruker APEX v2014.11-0, Bruker AXS Inc., Madison, Wisconsin, USA.

OLEX2; Dolomanov, O.V., Bourhis, L.J., Gildea, R.J., Howard, J.A.K. & Puschmann, H.

(2009), J. Appl. Cryst. 42, 339-341.

SADABS (2014/5) Bruker AXS Inc., Madison, Wisconsin, USA; Sheldrick, G. M. University of Göttingen, Germany.

XT, XL (2014), Bruker AXS Inc., Madison, Wisconsin, USA; Sheldrick, G.M. (2008). Acta Cryst. A64, 112-122; Sheldrick, G.M. (2015). Acta Cryst. A71, 3-8.

Table 1: Data collection details for TCD388.

Axis	dx/mm	2 θ / $^{\circ}$	ω / $^{\circ}$	ϕ / $^{\circ}$	χ / $^{\circ}$	Width/ $^{\circ}$	Frames	Time/s	Wavelength/ \AA	Voltage/kV	Current/mA	Temperature/K
Omega	50.000	108.96	342.40	360.00	64.87	1.20	115	40.00	1.54184	45	0.6	100
Omega	50.000	109.69	353.03	181.34	72.84	1.20	65	40.00	1.54184	45	0.6	100
Omega	50.000	-76.00	268.34	266.35	-46.61	1.20	110	40.00	1.54184	45	0.6	100
Phi	50.000	109.35	77.69	340.40	-23.00	1.20	166	40.00	1.54184	45	0.6	100
Omega	50.000	-49.35	191.08	36.00	54.74	1.20	110	40.00	1.54184	45	0.6	100
Omega	50.000	107.97	3.12	346.41	23.30	1.20	113	40.00	1.54184	45	0.6	100
Omega	50.000	-49.35	191.08	252.00	54.74	1.20	110	40.00	1.54184	45	0.6	100
Omega	50.000	108.96	342.40	150.00	64.87	1.20	115	40.00	1.54184	45	0.6	100
Omega	50.000	-49.35	299.67	0.00	-64.88	1.20	93	40.00	1.54184	45	0.6	100
Omega	50.000	108.96	96.53	250.00	-54.74	1.20	110	40.00	1.54184	45	0.6	100
Omega	50.000	108.96	96.53	75.00	-54.74	1.20	110	40.00	1.54184	45	0.6	100
Omega	50.000	-49.35	299.67	180.00	-64.88	1.20	93	40.00	1.54184	45	0.6	100
Omega	50.000	100.71	353.17	9.26	79.14	1.20	61	40.00	1.54184	45	0.6	100
Omega	50.000	108.96	96.53	150.00	-54.74	1.20	110	40.00	1.54184	45	0.6	100
Omega	50.000	-11.25	229.18	360.00	54.74	1.20	110	40.00	1.54184	45	0.6	100
Omega	50.000	108.96	342.40	250.00	64.87	1.20	115	40.00	1.54184	45	0.6	100
Omega	50.000	-49.35	191.08	180.00	54.74	1.20	110	40.00	1.54184	45	0.6	100
Omega	50.000	108.96	96.53	125.00	-54.74	1.20	110	40.00	1.54184	45	0.6	100
Omega	50.000	108.96	96.53	50.00	-54.74	1.20	110	40.00	1.54184	45	0.6	100
Phi	50.000	94.35	80.80	360.00	-57.06	1.20	300	40.00	1.54184	45	0.6	100
Phi	50.000	-64.35	58.15	360.00	-57.06	1.20	300	40.00	1.54184	45	0.6	100
Omega	50.000	108.96	342.40	100.00	64.87	1.20	115	40.00	1.54184	45	0.6	100
Omega	50.000	108.96	96.53	100.00	-54.74	1.20	110	40.00	1.54184	45	0.6	100
Omega	50.000	100.88	352.45	183.14	81.35	1.20	61	40.00	1.54184	45	0.6	100
Omega	50.000	-11.25	337.32	0.00	-64.87	1.20	62	40.00	1.54184	45	0.6	100

Table 2. Crystal data and structure refinement for tcd388.

Identification code	tcd388	
Empirical formula	$C_{86}H_{82}N_2O_6$	
Formula weight	1239.53	
Temperature	99.98 K	
Wavelength	1.54178 Å	
Crystal system	Monoclinic	
Space group	Cc	
Unit cell dimensions	$a = 33.9554(11)$ Å	$\alpha = 90^\circ$.
	$b = 20.6101(7)$ Å	$\beta = 101.069(2)^\circ$.
	$c = 9.7933(3)$ Å	$\gamma = 90^\circ$.
Volume	$6726.1(4)$ Å ³	
Z	4	
Density (calculated)	1.224 Mg/m ³	
Absorption coefficient	0.592 mm ⁻¹	
F(000)	2640	
Crystal size	0.31 x 0.09 x 0.02 mm ³	
Theta range for data collection	2.521 to 68.426°.	
Index ranges	$-40 \leq h \leq 40$, $-24 \leq k \leq 24$, $-11 \leq l \leq 10$	
Reflections collected	39795	
Independent reflections	11481 [R(int) = 0.0782]	
Completeness to theta = 67.679°	100.0 %	
Absorption correction	Semi-empirical from equivalents	
Max. and min. transmission	0.7531 and 0.6112	
Refinement method	Full-matrix least-squares on F ²	
Data / restraints / parameters	11481 / 38 / 862	
Goodness-of-fit on F ²	1.038	
Final R indices [I > 2σ(I)]	R1 = 0.0489, wR2 = 0.1144	
R indices (all data)	R1 = 0.0670, wR2 = 0.1239	
Absolute structure parameter	-0.03(18)	
Largest diff. peak and hole	0.303 and -0.330 e.Å ⁻³	

Table 3. Atomic coordinates ($\times 10^4$) and equivalent isotropic displacement parameters ($\text{\AA}^2 \times 10^3$) for tcd388. $U(\text{eq})$ is defined as one third of the trace of the orthogonalized U^{ij} tensor.

	x	y	z	U(eq)
C(1)	5884(1)	6106(2)	8000(4)	29(1)
O(1)	5770(1)	7422(1)	6632(3)	30(1)
C(2)	6067(1)	6128(2)	6710(4)	32(1)
O(2)	5391(1)	8785(1)	6451(3)	28(1)
C(3)	6332(1)	6718(2)	6656(4)	31(1)
O(3)	5192(1)	7537(1)	10057(3)	30(1)
C(4)	6737(1)	6649(2)	6650(4)	35(1)
O(4)	5217(1)	6144(1)	6593(3)	30(1)
C(5)	6992(1)	7177(2)	6602(4)	35(1)
C(6)	6821(1)	7794(2)	6616(4)	34(1)
C(7)	6415(1)	7889(2)	6635(4)	28(1)
C(8)	6240(1)	8567(2)	6649(4)	30(1)
C(9)	6050(1)	8702(2)	7903(4)	26(1)
C(10)	6286(1)	8724(2)	9234(4)	30(1)
C(11)	6121(1)	8807(2)	10424(4)	27(1)
C(12)	5706(1)	8832(2)	10243(4)	28(1)
C(13)	5457(1)	8806(2)	8931(4)	27(1)
C(14)	5007(1)	8783(2)	8784(4)	27(1)
C(15)	4814(1)	8154(2)	8171(4)	25(1)
C(16)	4546(1)	8165(2)	6909(4)	27(1)
C(17)	4365(1)	7604(2)	6284(4)	27(1)
C(18)	4466(1)	7020(2)	6989(4)	28(1)
C(19)	4736(1)	6985(2)	8245(4)	27(1)
C(20)	4854(1)	6328(2)	8921(4)	30(1)
C(21)	5296(1)	6188(2)	9075(4)	27(1)
C(22)	5550(1)	6156(2)	10374(4)	28(1)
C(23)	5965(1)	6102(2)	10525(4)	30(1)
C(24)	6122(1)	6087(2)	9312(4)	31(1)
C(25)	5470(1)	6135(2)	7893(4)	26(1)
C(26)	4907(1)	7561(2)	8836(4)	26(1)
C(27)	5637(1)	8774(2)	7768(4)	26(1)
C(28)	6171(1)	7345(2)	6623(4)	29(1)
C(29)	5041(2)	7539(2)	11308(4)	36(1)

C(30)	5517(1)	7425(2)	5283(5)	35(1)
C(31)	7435(1)	7090(2)	6504(5)	45(1)
C(32)	7711(2)	7468(4)	7530(10)	63(1)
C(33)	7473(2)	7311(5)	5005(9)	63(1)
C(34)	7558(3)	6351(4)	6564(11)	63(1)
C(35)	6390(1)	8879(2)	11862(4)	35(1)
C(36)	6176(2)	8657(4)	13013(5)	63(2)
C(37)	6506(2)	9599(3)	12048(6)	58(2)
C(38)	6773(1)	8474(2)	12000(5)	41(1)
C(39)	4112(1)	7627(2)	4802(4)	29(1)
C(40)	4402(1)	7603(2)	3778(4)	34(1)
C(41)	3820(1)	7055(2)	4502(4)	34(1)
C(42)	3864(1)	8253(2)	4536(4)	34(1)
C(43)	6229(1)	6120(2)	11984(5)	38(1)
C(44)	6066(2)	5684(3)	12997(5)	45(1)
C(45)	6656(2)	5914(5)	11972(6)	93(3)
C(46)	6224(2)	6815(3)	12525(6)	69(2)
C(47)	5339(1)	9433(2)	5903(4)	32(1)
C(48)	5036(1)	9424(2)	4603(4)	28(1)
O(49)	5151(1)	9164(1)	3468(3)	32(1)
N(50)	4827(1)	9196(2)	2334(3)	31(1)
C(51)	4532(1)	9465(2)	2820(4)	27(1)
C(52)	4652(1)	9616(2)	4258(4)	29(1)
C(53)	4138(1)	9601(2)	1923(4)	27(1)
C(54)	3939(1)	9173(2)	883(4)	27(1)
C(55)	4107(1)	8568(2)	541(4)	28(1)
C(56)	3909(1)	8174(2)	-458(4)	31(1)
C(57)	3521(1)	8334(2)	-1228(4)	29(1)
C(58)	3316(1)	7940(2)	-2284(5)	35(1)
C(59)	2939(1)	8116(2)	-3023(4)	35(1)
C(60)	2762(1)	8689(2)	-2726(4)	35(1)
C(61)	2961(1)	9108(2)	-1687(4)	32(1)
C(62)	2792(1)	9720(2)	-1416(5)	35(1)
C(63)	2995(1)	10123(2)	-447(4)	34(1)
C(64)	3380(1)	9955(2)	361(4)	31(1)
C(65)	3590(1)	10368(2)	1369(4)	32(1)
C(66)	3959(1)	10190(2)	2141(4)	30(1)
C(67)	3552(1)	9346(2)	119(4)	27(1)

C(68)	3341(1)	8925(2)	-919(4)	29(1)
C(69)	5125(1)	5507(2)	6041(4)	35(1)
C(70)	4852(1)	5587(2)	4672(4)	30(1)
O(71)	5014(1)	5856(2)	3645(3)	35(1)
N(72)	4709(1)	5930(2)	2462(4)	33(1)
C(73)	4382(1)	5706(2)	2807(4)	30(1)
C(74)	4456(1)	5480(2)	4209(4)	31(1)
C(75)	3997(1)	5762(2)	1805(4)	30(1)
C(76)	3725(1)	5241(2)	1541(4)	30(1)
C(77)	3808(1)	4608(2)	2139(4)	32(1)
C(78)	3545(1)	4115(2)	1816(5)	34(1)
C(79)	3174(1)	4191(2)	873(5)	33(1)
C(80)	2896(1)	3687(2)	524(5)	40(1)
C(81)	2537(2)	3783(2)	-393(5)	44(1)
C(82)	2448(1)	4379(2)	-1000(5)	45(1)
C(83)	2712(1)	4902(2)	-682(5)	39(1)
C(84)	2626(2)	5529(3)	-1300(5)	47(1)
C(85)	2882(2)	6029(2)	-975(5)	41(1)
C(86)	3261(1)	5950(2)	-30(5)	35(1)
C(87)	3538(1)	6449(2)	255(4)	37(1)
C(88)	3904(1)	6357(2)	1143(4)	35(1)
C(89)	3356(1)	5338(2)	596(4)	32(1)
C(90)	3079(1)	4809(2)	259(5)	32(1)
C(32A)	7645(5)	7734(8)	6280(20)	63(1)
C(34A)	7640(5)	6975(10)	8113(16)	63(1)
C(33A)	7515(6)	6473(9)	5820(20)	63(1)

Table 4. Bond lengths [\AA] and angles [$^\circ$] for tcd388.

C(1)-C(2)	1.512(5)
C(1)-C(24)	1.382(6)
C(1)-C(25)	1.392(6)
O(1)-C(28)	1.374(5)
O(1)-C(30)	1.431(5)
C(2)-H(2A)	0.9900
C(2)-H(2B)	0.9900
C(2)-C(3)	1.521(6)
O(2)-C(27)	1.396(4)
O(2)-C(47)	1.439(5)
C(3)-C(4)	1.383(6)
C(3)-C(28)	1.401(6)
O(3)-C(26)	1.387(5)
O(3)-C(29)	1.415(5)
C(4)-H(4)	0.9500
C(4)-C(5)	1.398(7)
O(4)-C(25)	1.392(5)
O(4)-C(69)	1.431(5)
C(5)-C(6)	1.400(6)
C(5)-C(31)	1.535(6)
C(6)-H(6)	0.9500
C(6)-C(7)	1.399(6)
C(7)-C(8)	1.519(6)
C(7)-C(28)	1.392(6)
C(8)-H(8A)	0.9900
C(8)-H(8B)	0.9900
C(8)-C(9)	1.519(5)
C(9)-C(10)	1.393(6)
C(9)-C(27)	1.392(6)
C(10)-H(10)	0.9500
C(10)-C(11)	1.395(6)
C(11)-C(12)	1.388(6)
C(11)-C(35)	1.532(5)
C(12)-H(12)	0.9500
C(12)-C(13)	1.396(5)
C(13)-C(14)	1.506(6)

C(13)-C(27)	1.394(6)
C(14)-H(14A)	0.9900
C(14)-H(14B)	0.9900
C(14)-C(15)	1.524(5)
C(15)-C(16)	1.386(5)
C(15)-C(26)	1.392(6)
C(16)-H(16)	0.9500
C(16)-C(17)	1.396(6)
C(17)-C(18)	1.397(6)
C(17)-C(39)	1.538(5)
C(18)-H(18)	0.9500
C(18)-C(19)	1.388(6)
C(19)-C(20)	1.527(5)
C(19)-C(26)	1.396(6)
C(20)-H(20A)	0.9900
C(20)-H(20B)	0.9900
C(20)-C(21)	1.510(6)
C(21)-C(22)	1.393(6)
C(21)-C(25)	1.400(6)
C(22)-H(22)	0.9500
C(22)-C(23)	1.393(6)
C(23)-C(24)	1.393(6)
C(23)-C(43)	1.535(6)
C(24)-H(24)	0.9500
C(29)-H(29A)	0.9800
C(29)-H(29B)	0.9800
C(29)-H(29C)	0.9800
C(30)-H(30A)	0.9800
C(30)-H(30B)	0.9800
C(30)-H(30C)	0.9800
C(31)-C(32)	1.461(9)
C(31)-C(33)	1.566(9)
C(31)-C(34)	1.578(9)
C(31)-C(32A)	1.542(15)
C(31)-C(34A)	1.613(15)
C(31)-C(33A)	1.483(15)
C(32)-H(32A)	0.9800
C(32)-H(32B)	0.9800

C(32)-H(32C)	0.9800
C(33)-H(33A)	0.9800
C(33)-H(33B)	0.9800
C(33)-H(33C)	0.9800
C(34)-H(34A)	0.9800
C(34)-H(34B)	0.9800
C(34)-H(34C)	0.9800
C(35)-C(36)	1.523(7)
C(35)-C(37)	1.538(7)
C(35)-C(38)	1.530(7)
C(36)-H(36A)	0.9800
C(36)-H(36B)	0.9800
C(36)-H(36C)	0.9800
C(37)-H(37A)	0.9800
C(37)-H(37B)	0.9800
C(37)-H(37C)	0.9800
C(38)-H(38A)	0.9800
C(38)-H(38B)	0.9800
C(38)-H(38C)	0.9800
C(39)-C(40)	1.537(6)
C(39)-C(41)	1.532(6)
C(39)-C(42)	1.536(6)
C(40)-H(40A)	0.9800
C(40)-H(40B)	0.9800
C(40)-H(40C)	0.9800
C(41)-H(41A)	0.9800
C(41)-H(41B)	0.9800
C(41)-H(41C)	0.9800
C(42)-H(42A)	0.9800
C(42)-H(42B)	0.9800
C(42)-H(42C)	0.9800
C(43)-C(44)	1.521(7)
C(43)-C(45)	1.514(7)
C(43)-C(46)	1.529(7)
C(44)-H(44A)	0.9800
C(44)-H(44B)	0.9800
C(44)-H(44C)	0.9800
C(45)-H(45A)	0.9800

C(45)-H(45B)	0.9800
C(45)-H(45C)	0.9800
C(46)-H(46A)	0.9800
C(46)-H(46B)	0.9800
C(46)-H(46C)	0.9800
C(47)-H(47A)	0.9900
C(47)-H(47B)	0.9900
C(47)-C(48)	1.474(5)
C(48)-O(49)	1.356(5)
C(48)-C(52)	1.345(6)
O(49)-N(50)	1.406(4)
N(50)-C(51)	1.314(6)
C(51)-C(52)	1.423(6)
C(51)-C(53)	1.480(6)
C(52)-H(52)	0.9500
C(53)-C(54)	1.417(6)
C(53)-C(66)	1.392(6)
C(54)-C(55)	1.438(6)
C(54)-C(67)	1.425(6)
C(55)-H(55)	0.9500
C(55)-C(56)	1.347(6)
C(56)-H(56)	0.9500
C(56)-C(57)	1.427(6)
C(57)-C(58)	1.392(6)
C(57)-C(68)	1.421(6)
C(58)-H(58)	0.9500
C(58)-C(59)	1.393(6)
C(59)-H(59)	0.9500
C(59)-C(60)	1.381(6)
C(60)-H(60)	0.9500
C(60)-C(61)	1.403(6)
C(61)-C(62)	1.431(6)
C(61)-C(68)	1.416(6)
C(62)-H(62)	0.9500
C(62)-C(63)	1.347(6)
C(63)-H(63)	0.9500
C(63)-C(64)	1.435(6)
C(64)-C(65)	1.393(6)

C(64)-C(67)	1.423(6)
C(65)-H(65)	0.9500
C(65)-C(66)	1.382(6)
C(66)-H(66)	0.9500
C(67)-C(68)	1.422(5)
C(69)-H(69A)	0.9900
C(69)-H(69B)	0.9900
C(69)-C(70)	1.485(6)
C(70)-O(71)	1.355(5)
C(70)-C(74)	1.351(6)
O(71)-N(72)	1.406(4)
N(72)-C(73)	1.305(6)
C(73)-C(74)	1.425(6)
C(73)-C(75)	1.481(6)
C(74)-H(74)	0.9500
C(75)-C(76)	1.407(6)
C(75)-C(88)	1.395(6)
C(76)-C(77)	1.437(6)
C(76)-C(89)	1.423(6)
C(77)-H(77)	0.9500
C(77)-C(78)	1.350(6)
C(78)-H(78)	0.9500
C(78)-C(79)	1.421(6)
C(79)-C(80)	1.401(6)
C(79)-C(90)	1.417(6)
C(80)-H(80)	0.9500
C(80)-C(81)	1.384(7)
C(81)-H(81)	0.9500
C(81)-C(82)	1.371(7)
C(82)-H(82)	0.9500
C(82)-C(83)	1.399(7)
C(83)-C(84)	1.435(7)
C(83)-C(90)	1.414(6)
C(84)-H(84)	0.9500
C(84)-C(85)	1.347(7)
C(85)-H(85)	0.9500
C(85)-C(86)	1.445(6)
C(86)-C(87)	1.386(6)

C(86)-C(89)	1.412(6)
C(87)-H(87)	0.9500
C(87)-C(88)	1.385(6)
C(88)-H(88)	0.9500
C(89)-C(90)	1.436(6)
C(32A)-H(32D)	0.9800
C(32A)-H(32E)	0.9800
C(32A)-H(32F)	0.9800
C(34A)-H(34D)	0.9800
C(34A)-H(34E)	0.9800
C(34A)-H(34F)	0.9800
C(33A)-H(33D)	0.9800
C(33A)-H(33E)	0.9800
C(33A)-H(33F)	0.9800
C(24)-C(1)-C(2)	121.1(4)
C(24)-C(1)-C(25)	118.3(4)
C(25)-C(1)-C(2)	120.6(4)
C(28)-O(1)-C(30)	114.5(3)
C(1)-C(2)-H(2A)	108.9
C(1)-C(2)-H(2B)	108.9
C(1)-C(2)-C(3)	113.2(3)
H(2A)-C(2)-H(2B)	107.7
C(3)-C(2)-H(2A)	108.9
C(3)-C(2)-H(2B)	108.9
C(27)-O(2)-C(47)	111.6(3)
C(4)-C(3)-C(2)	120.8(4)
C(4)-C(3)-C(28)	118.7(4)
C(28)-C(3)-C(2)	120.5(4)
C(26)-O(3)-C(29)	116.0(3)
C(3)-C(4)-H(4)	118.6
C(3)-C(4)-C(5)	122.8(4)
C(5)-C(4)-H(4)	118.6
C(25)-O(4)-C(69)	112.7(3)
C(4)-C(5)-C(6)	116.6(4)
C(4)-C(5)-C(31)	122.1(4)
C(6)-C(5)-C(31)	121.3(4)
C(5)-C(6)-H(6)	118.7

C(7)-C(6)-C(5)	122.6(4)
C(7)-C(6)-H(6)	118.7
C(6)-C(7)-C(8)	121.1(4)
C(28)-C(7)-C(6)	118.3(4)
C(28)-C(7)-C(8)	120.6(4)
C(7)-C(8)-H(8A)	108.8
C(7)-C(8)-H(8B)	108.8
H(8A)-C(8)-H(8B)	107.7
C(9)-C(8)-C(7)	113.7(3)
C(9)-C(8)-H(8A)	108.8
C(9)-C(8)-H(8B)	108.8
C(10)-C(9)-C(8)	120.4(4)
C(27)-C(9)-C(8)	121.3(3)
C(27)-C(9)-C(10)	118.2(4)
C(9)-C(10)-H(10)	118.8
C(9)-C(10)-C(11)	122.4(4)
C(11)-C(10)-H(10)	118.8
C(10)-C(11)-C(35)	121.1(4)
C(12)-C(11)-C(10)	117.2(4)
C(12)-C(11)-C(35)	121.7(4)
C(11)-C(12)-H(12)	118.8
C(11)-C(12)-C(13)	122.5(4)
C(13)-C(12)-H(12)	118.8
C(12)-C(13)-C(14)	120.9(4)
C(27)-C(13)-C(12)	118.0(4)
C(27)-C(13)-C(14)	121.1(3)
C(13)-C(14)-H(14A)	108.6
C(13)-C(14)-H(14B)	108.6
C(13)-C(14)-C(15)	114.6(3)
H(14A)-C(14)-H(14B)	107.6
C(15)-C(14)-H(14A)	108.6
C(15)-C(14)-H(14B)	108.6
C(16)-C(15)-C(14)	119.7(4)
C(16)-C(15)-C(26)	118.9(4)
C(26)-C(15)-C(14)	121.4(4)
C(15)-C(16)-H(16)	118.8
C(15)-C(16)-C(17)	122.4(4)
C(17)-C(16)-H(16)	118.8

C(16)-C(17)-C(18)	116.9(4)
C(16)-C(17)-C(39)	120.5(4)
C(18)-C(17)-C(39)	122.1(4)
C(17)-C(18)-H(18)	118.7
C(19)-C(18)-C(17)	122.7(4)
C(19)-C(18)-H(18)	118.7
C(18)-C(19)-C(20)	120.2(4)
C(18)-C(19)-C(26)	118.3(4)
C(26)-C(19)-C(20)	121.4(4)
C(19)-C(20)-H(20A)	109.1
C(19)-C(20)-H(20B)	109.1
H(20A)-C(20)-H(20B)	107.8
C(21)-C(20)-C(19)	112.6(3)
C(21)-C(20)-H(20A)	109.1
C(21)-C(20)-H(20B)	109.1
C(22)-C(21)-C(20)	121.9(4)
C(22)-C(21)-C(25)	117.9(4)
C(25)-C(21)-C(20)	120.0(4)
C(21)-C(22)-H(22)	118.8
C(21)-C(22)-C(23)	122.4(4)
C(23)-C(22)-H(22)	118.8
C(22)-C(23)-C(24)	117.2(4)
C(22)-C(23)-C(43)	119.8(4)
C(24)-C(23)-C(43)	122.8(4)
C(1)-C(24)-C(23)	122.7(4)
C(1)-C(24)-H(24)	118.6
C(23)-C(24)-H(24)	118.6
C(1)-C(25)-O(4)	120.3(4)
C(1)-C(25)-C(21)	121.4(4)
O(4)-C(25)-C(21)	118.2(4)
O(3)-C(26)-C(15)	119.5(4)
O(3)-C(26)-C(19)	119.5(3)
C(15)-C(26)-C(19)	120.9(4)
C(9)-C(27)-O(2)	120.2(3)
C(9)-C(27)-C(13)	121.3(3)
C(13)-C(27)-O(2)	118.4(3)
O(1)-C(28)-C(3)	119.4(4)
O(1)-C(28)-C(7)	119.7(4)

C(7)-C(28)-C(3)	120.9(4)
O(3)-C(29)-H(29A)	109.5
O(3)-C(29)-H(29B)	109.5
O(3)-C(29)-H(29C)	109.5
H(29A)-C(29)-H(29B)	109.5
H(29A)-C(29)-H(29C)	109.5
H(29B)-C(29)-H(29C)	109.5
O(1)-C(30)-H(30A)	109.5
O(1)-C(30)-H(30B)	109.5
O(1)-C(30)-H(30C)	109.5
H(30A)-C(30)-H(30B)	109.5
H(30A)-C(30)-H(30C)	109.5
H(30B)-C(30)-H(30C)	109.5
C(5)-C(31)-C(33)	106.4(5)
C(5)-C(31)-C(34)	111.5(5)
C(5)-C(31)-C(32A)	113.2(8)
C(5)-C(31)-C(34A)	101.6(7)
C(32)-C(31)-C(5)	113.7(5)
C(32)-C(31)-C(33)	109.4(6)
C(32)-C(31)-C(34)	111.0(6)
C(33)-C(31)-C(34)	104.3(6)
C(32A)-C(31)-C(34A)	98.1(11)
C(33A)-C(31)-C(5)	113.1(9)
C(33A)-C(31)-C(32A)	122.9(12)
C(33A)-C(31)-C(34A)	103.3(11)
C(31)-C(32)-H(32A)	109.5
C(31)-C(32)-H(32B)	109.5
C(31)-C(32)-H(32C)	109.5
H(32A)-C(32)-H(32B)	109.5
H(32A)-C(32)-H(32C)	109.5
H(32B)-C(32)-H(32C)	109.5
C(31)-C(33)-H(33A)	109.5
C(31)-C(33)-H(33B)	109.5
C(31)-C(33)-H(33C)	109.5
H(33A)-C(33)-H(33B)	109.5
H(33A)-C(33)-H(33C)	109.5
H(33B)-C(33)-H(33C)	109.5
C(31)-C(34)-H(34A)	109.5

C(31)-C(34)-H(34B)	109.5
C(31)-C(34)-H(34C)	109.5
H(34A)-C(34)-H(34B)	109.5
H(34A)-C(34)-H(34C)	109.5
H(34B)-C(34)-H(34C)	109.5
C(11)-C(35)-C(37)	107.2(4)
C(36)-C(35)-C(11)	111.5(4)
C(36)-C(35)-C(37)	110.5(5)
C(36)-C(35)-C(38)	106.8(4)
C(38)-C(35)-C(11)	112.0(4)
C(38)-C(35)-C(37)	108.8(4)
C(35)-C(36)-H(36A)	109.5
C(35)-C(36)-H(36B)	109.5
C(35)-C(36)-H(36C)	109.5
H(36A)-C(36)-H(36B)	109.5
H(36A)-C(36)-H(36C)	109.5
H(36B)-C(36)-H(36C)	109.5
C(35)-C(37)-H(37A)	109.5
C(35)-C(37)-H(37B)	109.5
C(35)-C(37)-H(37C)	109.5
H(37A)-C(37)-H(37B)	109.5
H(37A)-C(37)-H(37C)	109.5
H(37B)-C(37)-H(37C)	109.5
C(35)-C(38)-H(38A)	109.5
C(35)-C(38)-H(38B)	109.5
C(35)-C(38)-H(38C)	109.5
H(38A)-C(38)-H(38B)	109.5
H(38A)-C(38)-H(38C)	109.5
H(38B)-C(38)-H(38C)	109.5
C(40)-C(39)-C(17)	107.6(3)
C(41)-C(39)-C(17)	112.4(3)
C(41)-C(39)-C(40)	108.8(3)
C(41)-C(39)-C(42)	107.5(4)
C(42)-C(39)-C(17)	112.0(3)
C(42)-C(39)-C(40)	108.4(3)
C(39)-C(40)-H(40A)	109.5
C(39)-C(40)-H(40B)	109.5
C(39)-C(40)-H(40C)	109.5

H(40A)-C(40)-H(40B)	109.5
H(40A)-C(40)-H(40C)	109.5
H(40B)-C(40)-H(40C)	109.5
C(39)-C(41)-H(41A)	109.5
C(39)-C(41)-H(41B)	109.5
C(39)-C(41)-H(41C)	109.5
H(41A)-C(41)-H(41B)	109.5
H(41A)-C(41)-H(41C)	109.5
H(41B)-C(41)-H(41C)	109.5
C(39)-C(42)-H(42A)	109.5
C(39)-C(42)-H(42B)	109.5
C(39)-C(42)-H(42C)	109.5
H(42A)-C(42)-H(42B)	109.5
H(42A)-C(42)-H(42C)	109.5
H(42B)-C(42)-H(42C)	109.5
C(44)-C(43)-C(23)	111.8(4)
C(44)-C(43)-C(46)	107.3(4)
C(45)-C(43)-C(23)	112.1(4)
C(45)-C(43)-C(44)	108.0(5)
C(45)-C(43)-C(46)	110.0(5)
C(46)-C(43)-C(23)	107.6(4)
C(43)-C(44)-H(44A)	109.5
C(43)-C(44)-H(44B)	109.5
C(43)-C(44)-H(44C)	109.5
H(44A)-C(44)-H(44B)	109.5
H(44A)-C(44)-H(44C)	109.5
H(44B)-C(44)-H(44C)	109.5
C(43)-C(45)-H(45A)	109.5
C(43)-C(45)-H(45B)	109.5
C(43)-C(45)-H(45C)	109.5
H(45A)-C(45)-H(45B)	109.5
H(45A)-C(45)-H(45C)	109.5
H(45B)-C(45)-H(45C)	109.5
C(43)-C(46)-H(46A)	109.5
C(43)-C(46)-H(46B)	109.5
C(43)-C(46)-H(46C)	109.5
H(46A)-C(46)-H(46B)	109.5
H(46A)-C(46)-H(46C)	109.5

H(46B)-C(46)-H(46C)	109.5
O(2)-C(47)-H(47A)	109.9
O(2)-C(47)-H(47B)	109.9
O(2)-C(47)-C(48)	109.0(3)
H(47A)-C(47)-H(47B)	108.3
C(48)-C(47)-H(47A)	109.9
C(48)-C(47)-H(47B)	109.9
O(49)-C(48)-C(47)	116.8(4)
C(52)-C(48)-C(47)	134.0(4)
C(52)-C(48)-O(49)	109.1(4)
C(48)-O(49)-N(50)	109.0(3)
C(51)-N(50)-O(49)	105.6(3)
N(50)-C(51)-C(52)	110.9(4)
N(50)-C(51)-C(53)	122.2(4)
C(52)-C(51)-C(53)	126.9(4)
C(48)-C(52)-C(51)	105.3(4)
C(48)-C(52)-H(52)	127.3
C(51)-C(52)-H(52)	127.3
C(54)-C(53)-C(51)	124.0(4)
C(66)-C(53)-C(51)	116.5(4)
C(66)-C(53)-C(54)	119.4(4)
C(53)-C(54)-C(55)	123.5(4)
C(53)-C(54)-C(67)	119.0(4)
C(67)-C(54)-C(55)	117.5(4)
C(54)-C(55)-H(55)	119.1
C(56)-C(55)-C(54)	121.8(4)
C(56)-C(55)-H(55)	119.1
C(55)-C(56)-H(56)	119.1
C(55)-C(56)-C(57)	121.7(4)
C(57)-C(56)-H(56)	119.1
C(58)-C(57)-C(56)	122.5(4)
C(58)-C(57)-C(68)	119.0(4)
C(68)-C(57)-C(56)	118.5(4)
C(57)-C(58)-H(58)	119.6
C(57)-C(58)-C(59)	120.9(4)
C(59)-C(58)-H(58)	119.6
C(58)-C(59)-H(59)	119.8
C(60)-C(59)-C(58)	120.4(4)

C(60)-C(59)-H(59)	119.8
C(59)-C(60)-H(60)	119.6
C(59)-C(60)-C(61)	120.8(4)
C(61)-C(60)-H(60)	119.6
C(60)-C(61)-C(62)	121.6(4)
C(60)-C(61)-C(68)	118.9(4)
C(68)-C(61)-C(62)	119.5(4)
C(61)-C(62)-H(62)	119.8
C(63)-C(62)-C(61)	120.5(4)
C(63)-C(62)-H(62)	119.8
C(62)-C(63)-H(63)	119.1
C(62)-C(63)-C(64)	121.8(4)
C(64)-C(63)-H(63)	119.1
C(65)-C(64)-C(63)	122.1(4)
C(65)-C(64)-C(67)	119.1(4)
C(67)-C(64)-C(63)	118.8(4)
C(64)-C(65)-H(65)	119.6
C(66)-C(65)-C(64)	120.8(4)
C(66)-C(65)-H(65)	119.6
C(53)-C(66)-H(66)	119.2
C(65)-C(66)-C(53)	121.6(4)
C(65)-C(66)-H(66)	119.2
C(64)-C(67)-C(54)	120.0(4)
C(68)-C(67)-C(54)	120.6(4)
C(68)-C(67)-C(64)	119.3(4)
C(57)-C(68)-C(67)	119.8(4)
C(61)-C(68)-C(57)	120.0(4)
C(61)-C(68)-C(67)	120.1(4)
O(4)-C(69)-H(69A)	110.3
O(4)-C(69)-H(69B)	110.3
O(4)-C(69)-C(70)	107.0(3)
H(69A)-C(69)-H(69B)	108.6
C(70)-C(69)-H(69A)	110.3
C(70)-C(69)-H(69B)	110.3
O(71)-C(70)-C(69)	116.4(4)
C(74)-C(70)-C(69)	133.9(4)
C(74)-C(70)-O(71)	109.6(4)
C(70)-O(71)-N(72)	108.5(3)

C(73)-N(72)-O(71)	106.1(3)
N(72)-C(73)-C(74)	111.3(4)
N(72)-C(73)-C(75)	119.2(4)
C(74)-C(73)-C(75)	129.4(4)
C(70)-C(74)-C(73)	104.5(4)
C(70)-C(74)-H(74)	127.7
C(73)-C(74)-H(74)	127.7
C(76)-C(75)-C(73)	121.8(4)
C(88)-C(75)-C(73)	118.0(4)
C(88)-C(75)-C(76)	120.2(4)
C(75)-C(76)-C(77)	123.2(4)
C(75)-C(76)-C(89)	118.6(4)
C(89)-C(76)-C(77)	118.2(4)
C(76)-C(77)-H(77)	119.4
C(78)-C(77)-C(76)	121.2(4)
C(78)-C(77)-H(77)	119.4
C(77)-C(78)-H(78)	118.8
C(77)-C(78)-C(79)	122.3(4)
C(79)-C(78)-H(78)	118.8
C(80)-C(79)-C(78)	123.2(4)
C(80)-C(79)-C(90)	118.4(4)
C(90)-C(79)-C(78)	118.4(4)
C(79)-C(80)-H(80)	119.3
C(81)-C(80)-C(79)	121.4(4)
C(81)-C(80)-H(80)	119.3
C(80)-C(81)-H(81)	119.9
C(82)-C(81)-C(80)	120.2(5)
C(82)-C(81)-H(81)	119.9
C(81)-C(82)-H(82)	119.5
C(81)-C(82)-C(83)	121.0(5)
C(83)-C(82)-H(82)	119.5
C(82)-C(83)-C(84)	122.0(4)
C(82)-C(83)-C(90)	119.2(4)
C(90)-C(83)-C(84)	118.8(4)
C(83)-C(84)-H(84)	119.4
C(85)-C(84)-C(83)	121.3(4)
C(85)-C(84)-H(84)	119.4
C(84)-C(85)-H(85)	119.3

C(84)-C(85)-C(86)	121.4(4)
C(86)-C(85)-H(85)	119.3
C(87)-C(86)-C(85)	122.1(4)
C(87)-C(86)-C(89)	119.2(4)
C(89)-C(86)-C(85)	118.7(4)
C(86)-C(87)-H(87)	119.5
C(88)-C(87)-C(86)	121.0(4)
C(88)-C(87)-H(87)	119.5
C(75)-C(88)-H(88)	119.7
C(87)-C(88)-C(75)	120.7(4)
C(87)-C(88)-H(88)	119.7
C(76)-C(89)-C(90)	120.0(4)
C(86)-C(89)-C(76)	120.4(4)
C(86)-C(89)-C(90)	119.6(4)
C(79)-C(90)-C(89)	119.9(4)
C(83)-C(90)-C(79)	119.9(4)
C(83)-C(90)-C(89)	120.2(4)
C(31)-C(32A)-H(32D)	109.5
C(31)-C(32A)-H(32E)	109.5
C(31)-C(32A)-H(32F)	109.5
H(32D)-C(32A)-H(32E)	109.5
H(32D)-C(32A)-H(32F)	109.5
H(32E)-C(32A)-H(32F)	109.5
C(31)-C(34A)-H(34D)	109.5
C(31)-C(34A)-H(34E)	109.5
C(31)-C(34A)-H(34F)	109.5
H(34D)-C(34A)-H(34E)	109.5
H(34D)-C(34A)-H(34F)	109.5
H(34E)-C(34A)-H(34F)	109.5
C(31)-C(33A)-H(33D)	109.5
C(31)-C(33A)-H(33E)	109.5
C(31)-C(33A)-H(33F)	109.5
H(33D)-C(33A)-H(33E)	109.5
H(33D)-C(33A)-H(33F)	109.5
H(33E)-C(33A)-H(33F)	109.5

Table 5. Anisotropic displacement parameters ($\text{\AA}^2 \times 10^3$) for tcd388. The anisotropic displacement factor exponent takes the form: $-2\pi^2 [h^2 a^{*2} U^{11} + \dots + 2 h k a^* b^* U^{12}]$

	U ¹¹	U ²²	U ³³	U ²³	U ¹³	U ¹²
C(1)	38(2)	19(2)	28(2)	-1(2)	5(2)	-1(2)
O(1)	27(2)	32(2)	30(2)	1(1)	3(1)	2(1)
C(2)	39(3)	28(2)	30(2)	-2(2)	8(2)	0(2)
O(2)	33(2)	27(2)	22(1)	1(1)	0(1)	-1(1)
C(3)	34(2)	37(2)	21(2)	-1(2)	4(2)	5(2)
O(3)	31(2)	34(2)	24(2)	1(1)	1(1)	-1(1)
C(4)	38(2)	42(3)	25(2)	4(2)	6(2)	7(2)
O(4)	36(2)	28(2)	24(2)	-1(1)	-1(1)	0(1)
C(5)	32(2)	48(3)	24(2)	3(2)	4(2)	4(2)
C(6)	32(2)	42(3)	26(2)	0(2)	5(2)	-6(2)
C(7)	30(2)	37(2)	18(2)	1(2)	4(2)	0(2)
C(8)	31(2)	35(2)	24(2)	2(2)	6(2)	-5(2)
C(9)	32(2)	22(2)	23(2)	1(1)	3(2)	-3(2)
C(10)	28(2)	28(2)	32(2)	2(2)	4(2)	-2(2)
C(11)	32(2)	25(2)	24(2)	1(2)	2(2)	-2(2)
C(12)	34(2)	27(2)	24(2)	0(2)	6(2)	-1(2)
C(13)	30(2)	24(2)	26(2)	-2(2)	2(2)	-1(2)
C(14)	27(2)	28(2)	26(2)	-2(2)	5(2)	2(2)
C(15)	23(2)	28(2)	24(2)	0(2)	5(2)	2(2)
C(16)	31(2)	24(2)	27(2)	4(2)	9(2)	3(2)
C(17)	26(2)	31(2)	25(2)	0(2)	6(2)	-1(2)
C(18)	29(2)	30(2)	28(2)	0(2)	8(2)	0(2)
C(19)	27(2)	29(2)	26(2)	0(2)	7(2)	-1(2)
C(20)	33(2)	31(2)	26(2)	2(2)	4(2)	-4(2)
C(21)	32(2)	21(2)	26(2)	4(2)	3(2)	-4(2)
C(22)	31(2)	25(2)	27(2)	2(2)	5(2)	-4(2)
C(23)	33(2)	24(2)	30(2)	2(2)	2(2)	-1(2)
C(24)	29(2)	27(2)	36(2)	2(2)	4(2)	4(2)
C(25)	33(2)	20(2)	24(2)	1(1)	2(2)	-1(2)
C(26)	24(2)	32(2)	22(2)	1(2)	4(2)	4(2)
C(27)	30(2)	21(2)	24(2)	0(1)	-1(2)	-2(2)
C(28)	29(2)	38(2)	19(2)	2(2)	4(2)	2(2)
C(29)	42(3)	42(3)	23(2)	1(2)	3(2)	6(2)

C(30)	33(2)	33(2)	34(2)	-2(2)	-2(2)	-1(2)
C(31)	28(2)	53(3)	54(3)	-3(2)	8(2)	2(2)
C(32)	41(2)	80(3)	71(3)	2(2)	19(2)	14(2)
C(33)	41(2)	80(3)	71(3)	2(2)	19(2)	14(2)
C(34)	41(2)	80(3)	71(3)	2(2)	19(2)	14(2)
C(35)	34(2)	44(3)	25(2)	-1(2)	0(2)	-2(2)
C(36)	45(3)	116(5)	26(2)	3(3)	3(2)	3(3)
C(37)	56(3)	48(3)	58(3)	-19(3)	-19(3)	9(3)
C(38)	43(3)	38(3)	38(3)	0(2)	-4(2)	-3(2)
C(39)	33(2)	27(2)	27(2)	1(2)	5(2)	2(2)
C(40)	38(2)	41(3)	24(2)	0(2)	4(2)	-4(2)
C(41)	33(2)	36(2)	30(2)	0(2)	1(2)	1(2)
C(42)	35(2)	35(2)	27(2)	-1(2)	-4(2)	1(2)
C(43)	38(3)	42(3)	30(2)	2(2)	-2(2)	-3(2)
C(44)	49(3)	52(3)	29(2)	3(2)	-1(2)	1(2)
C(45)	34(3)	212(9)	31(3)	7(4)	0(2)	17(4)
C(46)	98(5)	51(3)	45(3)	-1(2)	-18(3)	-24(3)
C(47)	41(3)	26(2)	26(2)	1(2)	2(2)	3(2)
C(48)	34(2)	26(2)	25(2)	0(2)	8(2)	-3(2)
O(49)	29(2)	38(2)	28(2)	-2(1)	2(1)	3(1)
N(50)	29(2)	38(2)	24(2)	-1(1)	0(1)	1(2)
C(51)	32(2)	26(2)	23(2)	4(2)	6(2)	-1(2)
C(52)	34(2)	28(2)	25(2)	0(2)	8(2)	2(2)
C(53)	28(2)	29(2)	26(2)	3(2)	6(2)	-1(2)
C(54)	28(2)	29(2)	24(2)	4(2)	8(2)	1(2)
C(55)	28(2)	29(2)	29(2)	4(2)	5(2)	0(2)
C(56)	36(2)	28(2)	31(2)	0(2)	10(2)	2(2)
C(57)	35(2)	29(2)	24(2)	4(2)	6(2)	-2(2)
C(58)	39(3)	31(2)	34(2)	1(2)	11(2)	-1(2)
C(59)	36(2)	37(3)	31(2)	-2(2)	4(2)	-7(2)
C(60)	33(2)	40(3)	32(2)	2(2)	2(2)	-1(2)
C(61)	32(2)	39(3)	26(2)	2(2)	6(2)	-2(2)
C(62)	29(2)	41(3)	35(2)	3(2)	2(2)	6(2)
C(63)	36(2)	32(2)	35(2)	0(2)	4(2)	7(2)
C(64)	36(2)	31(2)	26(2)	3(2)	8(2)	5(2)
C(65)	36(2)	30(2)	30(2)	-1(2)	10(2)	4(2)
C(66)	35(2)	31(2)	23(2)	-1(2)	5(2)	-5(2)
C(67)	30(2)	29(2)	23(2)	3(2)	6(2)	-1(2)

C(68)	29(2)	34(2)	23(2)	3(2)	5(2)	-3(2)
C(69)	41(3)	31(2)	29(2)	-2(2)	-2(2)	-4(2)
C(70)	39(2)	22(2)	28(2)	-1(2)	8(2)	1(2)
O(71)	33(2)	42(2)	29(2)	1(1)	4(1)	-4(1)
N(72)	33(2)	38(2)	28(2)	-3(1)	5(2)	-2(2)
C(73)	34(2)	27(2)	29(2)	-7(2)	4(2)	-1(2)
C(74)	34(2)	29(2)	28(2)	0(2)	6(2)	-2(2)
C(75)	34(2)	33(2)	25(2)	-4(2)	6(2)	2(2)
C(76)	34(2)	32(2)	23(2)	-5(2)	7(2)	2(2)
C(77)	33(2)	32(2)	31(2)	-3(2)	3(2)	2(2)
C(78)	37(2)	32(2)	34(2)	0(2)	7(2)	2(2)
C(79)	33(2)	31(2)	35(2)	-7(2)	6(2)	1(2)
C(80)	38(3)	32(3)	46(3)	-6(2)	2(2)	-2(2)
C(81)	37(3)	41(3)	53(3)	-11(2)	4(2)	-6(2)
C(82)	34(3)	43(3)	53(3)	-5(2)	-3(2)	4(2)
C(83)	35(2)	41(3)	39(3)	-1(2)	2(2)	5(2)
C(84)	37(3)	51(3)	48(3)	1(2)	-6(2)	7(2)
C(85)	43(3)	37(3)	39(3)	3(2)	-3(2)	7(2)
C(86)	39(2)	34(2)	32(2)	-1(2)	4(2)	4(2)
C(87)	47(3)	33(2)	30(2)	6(2)	6(2)	4(2)
C(88)	45(3)	29(2)	31(2)	1(2)	9(2)	-6(2)
C(89)	36(2)	32(2)	27(2)	0(2)	4(2)	4(2)
C(90)	30(2)	33(2)	33(2)	-2(2)	5(2)	2(2)
C(32A)	41(2)	80(3)	71(3)	2(2)	19(2)	14(2)
C(34A)	41(2)	80(3)	71(3)	2(2)	19(2)	14(2)
C(33A)	41(2)	80(3)	71(3)	2(2)	19(2)	14(2)

Table 6. Hydrogen coordinates ($\times 10^4$) and isotropic displacement parameters ($\text{\AA}^2 \times 10^{-3}$) for tcd388.

	x	y	z	U(eq)
H(2A)	5849	6128	5878	39
H(2B)	6229	5731	6676	39
H(4)	6846	6223	6680	42
H(6)	6989	8164	6612	40
H(8A)	6456	8888	6631	36
H(8B)	6035	8628	5793	36
H(10)	6568	8681	9336	36
H(12)	5586	8869	11041	34
H(14A)	4890	9148	8185	32
H(14B)	4939	8849	9713	32
H(16)	4484	8570	6455	32
H(18)	4344	6631	6593	34
H(20A)	4780	6318	9851	37
H(20B)	4700	5983	8349	37
H(22)	5435	6170	11185	34
H(24)	6405	6062	9391	37
H(29A)	4978	7985	11539	54
H(29B)	5244	7360	12062	54
H(29C)	4797	7273	11190	54
H(30A)	5589	7791	4743	52
H(30B)	5236	7468	5381	52
H(30C)	5551	7018	4803	52
H(32A)	7668	7364	8466	95
H(32B)	7663	7932	7349	95
H(32C)	7988	7362	7463	95
H(33A)	7377	7758	4851	95
H(33B)	7311	7025	4317	95
H(33C)	7754	7288	4909	95
H(34A)	7832	6309	6398	95
H(34B)	7374	6111	5847	95
H(34C)	7544	6174	7482	95
H(36A)	5957	8958	13076	94

H(36B)	6367	8651	13901	94
H(36C)	6067	8220	12801	94
H(37A)	6647	9733	11309	87
H(37B)	6682	9663	12956	87
H(37C)	6263	9862	11997	87
H(38A)	6703	8025	11730	62
H(38B)	6918	8485	12967	62
H(38C)	6944	8653	11391	62
H(40A)	4557	7199	3914	52
H(40B)	4586	7974	3945	52
H(40C)	4250	7620	2822	52
H(41A)	3675	7079	3536	51
H(41B)	3628	7074	5131	51
H(41C)	3970	6647	4646	51
H(42A)	3709	8250	3584	50
H(42B)	4045	8629	4660	50
H(42C)	3681	8281	5195	50
H(44A)	6046	5238	12643	67
H(44B)	5799	5836	13094	67
H(44C)	6247	5696	13905	67
H(45A)	6655	5486	11533	140
H(45B)	6808	5891	12930	140
H(45C)	6783	6230	11446	140
H(46A)	6392	6843	13457	104
H(46B)	5948	6938	12571	104
H(46C)	6328	7111	11896	104
H(47A)	5597	9600	5717	38
H(47B)	5249	9723	6589	38
H(52)	4494	9811	4848	35
H(55)	4364	8442	1035	34
H(56)	4032	7780	-656	37
H(58)	3435	7545	-2502	42
H(59)	2802	7840	-3737	42
H(60)	2504	8802	-3231	42
H(62)	2536	9842	-1923	43
H(63)	2879	10530	-294	41
H(65)	3479	10778	1528	38
H(66)	4094	10477	2836	36

H(69A)	4992	5249	6677	42
H(69B)	5374	5280	5926	42
H(74)	4270	5296	4706	37
H(77)	4053	4534	2774	39
H(78)	3610	3703	2234	41
H(80)	2956	3270	925	48
H(81)	2351	3436	-604	53
H(82)	2203	4437	-1645	54
H(84)	2383	5594	-1952	56
H(85)	2811	6443	-1375	49
H(87)	3476	6862	-166	44
H(88)	4092	6702	1303	42
H(32D)	7543	8081	6800	95
H(32E)	7591	7841	5286	95
H(32F)	7935	7688	6607	95
H(34D)	7926	6879	8182	95
H(34E)	7509	6610	8485	95
H(34F)	7610	7367	8650	95
H(33D)	7517	6554	4840	95
H(33E)	7304	6159	5903	95
H(33F)	7775	6300	6283	95

Table 7. Torsion angles [°] for tcd388.

C(1)-C(2)-C(3)-C(4)	117.8(4)
C(1)-C(2)-C(3)-C(28)	-61.7(5)
C(2)-C(1)-C(24)-C(23)	176.3(4)
C(2)-C(1)-C(25)-O(4)	4.1(6)
C(2)-C(1)-C(25)-C(21)	-172.8(4)
C(2)-C(3)-C(4)-C(5)	-180.0(4)
C(2)-C(3)-C(28)-O(1)	-0.4(5)
C(2)-C(3)-C(28)-C(7)	177.2(4)
O(2)-C(47)-C(48)-O(49)	-73.4(4)
O(2)-C(47)-C(48)-C(52)	105.9(5)
C(3)-C(4)-C(5)-C(6)	2.5(6)
C(3)-C(4)-C(5)-C(31)	-176.1(4)
C(4)-C(3)-C(28)-O(1)	-179.9(4)
C(4)-C(3)-C(28)-C(7)	-2.3(6)
C(4)-C(5)-C(6)-C(7)	-1.8(6)
C(4)-C(5)-C(31)-C(32)	-130.0(6)
C(4)-C(5)-C(31)-C(33)	109.5(6)
C(4)-C(5)-C(31)-C(34)	-3.6(7)
C(4)-C(5)-C(31)-C(32A)	172.7(10)
C(4)-C(5)-C(31)-C(34A)	-83.1(9)
C(4)-C(5)-C(31)-C(33A)	27.0(12)
O(4)-C(69)-C(70)-O(71)	68.4(5)
O(4)-C(69)-C(70)-C(74)	-107.2(5)
C(5)-C(6)-C(7)-C(8)	-179.9(4)
C(5)-C(6)-C(7)-C(28)	-0.8(6)
C(6)-C(5)-C(31)-C(32)	51.4(7)
C(6)-C(5)-C(31)-C(33)	-69.1(6)
C(6)-C(5)-C(31)-C(34)	177.9(5)
C(6)-C(5)-C(31)-C(32A)	-5.8(11)
C(6)-C(5)-C(31)-C(34A)	98.4(9)
C(6)-C(5)-C(31)-C(33A)	-151.5(10)
C(6)-C(7)-C(8)-C(9)	-120.9(4)
C(6)-C(7)-C(28)-O(1)	-179.5(3)
C(6)-C(7)-C(28)-C(3)	2.9(5)
C(7)-C(8)-C(9)-C(10)	66.1(5)
C(7)-C(8)-C(9)-C(27)	-110.7(4)

C(8)-C(7)-C(28)-O(1)	-0.4(5)
C(8)-C(7)-C(28)-C(3)	-177.9(3)
C(8)-C(9)-C(10)-C(11)	-176.0(4)
C(8)-C(9)-C(27)-O(2)	-6.1(6)
C(8)-C(9)-C(27)-C(13)	170.9(4)
C(9)-C(10)-C(11)-C(12)	3.4(6)
C(9)-C(10)-C(11)-C(35)	-175.5(4)
C(10)-C(9)-C(27)-O(2)	177.1(3)
C(10)-C(9)-C(27)-C(13)	-6.0(6)
C(10)-C(11)-C(12)-C(13)	-2.8(6)
C(10)-C(11)-C(35)-C(36)	-153.9(4)
C(10)-C(11)-C(35)-C(37)	85.1(5)
C(10)-C(11)-C(35)-C(38)	-34.2(6)
C(11)-C(12)-C(13)-C(14)	175.2(4)
C(11)-C(12)-C(13)-C(27)	-2.0(6)
C(12)-C(11)-C(35)-C(36)	27.2(6)
C(12)-C(11)-C(35)-C(37)	-93.8(5)
C(12)-C(11)-C(35)-C(38)	146.9(4)
C(12)-C(13)-C(14)-C(15)	-114.3(4)
C(12)-C(13)-C(27)-O(2)	-176.5(3)
C(12)-C(13)-C(27)-C(9)	6.6(6)
C(13)-C(14)-C(15)-C(16)	-116.9(4)
C(13)-C(14)-C(15)-C(26)	61.7(5)
C(14)-C(13)-C(27)-O(2)	6.3(6)
C(14)-C(13)-C(27)-C(9)	-170.7(4)
C(14)-C(15)-C(16)-C(17)	178.8(4)
C(14)-C(15)-C(26)-O(3)	-2.3(6)
C(14)-C(15)-C(26)-C(19)	-178.2(4)
C(15)-C(16)-C(17)-C(18)	0.0(6)
C(15)-C(16)-C(17)-C(39)	-172.3(4)
C(16)-C(15)-C(26)-O(3)	176.3(3)
C(16)-C(15)-C(26)-C(19)	0.4(6)
C(16)-C(17)-C(18)-C(19)	-0.9(6)
C(16)-C(17)-C(39)-C(40)	81.4(5)
C(16)-C(17)-C(39)-C(41)	-158.8(4)
C(16)-C(17)-C(39)-C(42)	-37.7(5)
C(17)-C(18)-C(19)-C(20)	-176.2(4)
C(17)-C(18)-C(19)-C(26)	1.5(6)

C(18)-C(17)-C(39)-C(40)	-90.6(5)
C(18)-C(17)-C(39)-C(41)	29.3(5)
C(18)-C(17)-C(39)-C(42)	150.4(4)
C(18)-C(19)-C(20)-C(21)	118.6(4)
C(18)-C(19)-C(26)-O(3)	-177.1(4)
C(18)-C(19)-C(26)-C(15)	-1.2(6)
C(19)-C(20)-C(21)-C(22)	112.5(4)
C(19)-C(20)-C(21)-C(25)	-62.8(5)
C(20)-C(19)-C(26)-O(3)	0.5(5)
C(20)-C(19)-C(26)-C(15)	176.5(4)
C(20)-C(21)-C(22)-C(23)	-172.4(4)
C(20)-C(21)-C(25)-C(1)	170.1(4)
C(20)-C(21)-C(25)-O(4)	-6.8(5)
C(21)-C(22)-C(23)-C(24)	0.4(6)
C(21)-C(22)-C(23)-C(43)	175.4(4)
C(22)-C(21)-C(25)-C(1)	-5.4(6)
C(22)-C(21)-C(25)-O(4)	177.7(3)
C(22)-C(23)-C(24)-C(1)	-1.6(6)
C(22)-C(23)-C(43)-C(44)	46.3(6)
C(22)-C(23)-C(43)-C(45)	167.7(5)
C(22)-C(23)-C(43)-C(46)	-71.3(5)
C(24)-C(1)-C(2)-C(3)	-60.1(5)
C(24)-C(1)-C(25)-O(4)	-178.9(4)
C(24)-C(1)-C(25)-C(21)	4.3(6)
C(24)-C(23)-C(43)-C(44)	-139.0(4)
C(24)-C(23)-C(43)-C(45)	-17.6(7)
C(24)-C(23)-C(43)-C(46)	103.4(5)
C(25)-C(1)-C(2)-C(3)	116.9(4)
C(25)-C(1)-C(24)-C(23)	-0.7(6)
C(25)-O(4)-C(69)-C(70)	179.4(3)
C(25)-C(21)-C(22)-C(23)	3.0(6)
C(26)-C(15)-C(16)-C(17)	0.2(6)
C(26)-C(19)-C(20)-C(21)	-59.0(5)
C(27)-O(2)-C(47)-C(48)	-172.7(3)
C(27)-C(9)-C(10)-C(11)	0.9(6)
C(27)-C(13)-C(14)-C(15)	63.0(5)
C(28)-C(3)-C(4)-C(5)	-0.5(6)
C(28)-C(7)-C(8)-C(9)	60.0(5)

C(29)-O(3)-C(26)-C(15)	97.4(4)
C(29)-O(3)-C(26)-C(19)	-86.7(4)
C(30)-O(1)-C(28)-C(3)	-88.8(4)
C(30)-O(1)-C(28)-C(7)	93.6(4)
C(31)-C(5)-C(6)-C(7)	176.8(4)
C(35)-C(11)-C(12)-C(13)	176.1(4)
C(39)-C(17)-C(18)-C(19)	171.3(4)
C(43)-C(23)-C(24)-C(1)	-176.4(4)
C(47)-O(2)-C(27)-C(9)	-90.0(4)
C(47)-O(2)-C(27)-C(13)	93.0(4)
C(47)-C(48)-O(49)-N(50)	-180.0(3)
C(47)-C(48)-C(52)-C(51)	-179.7(4)
C(48)-O(49)-N(50)-C(51)	-0.5(4)
O(49)-C(48)-C(52)-C(51)	-0.4(4)
O(49)-N(50)-C(51)-C(52)	0.2(4)
O(49)-N(50)-C(51)-C(53)	178.1(3)
N(50)-C(51)-C(52)-C(48)	0.1(5)
N(50)-C(51)-C(53)-C(54)	41.0(6)
N(50)-C(51)-C(53)-C(66)	-139.0(4)
C(51)-C(53)-C(54)-C(55)	-2.7(6)
C(51)-C(53)-C(54)-C(67)	177.5(4)
C(51)-C(53)-C(66)-C(65)	-179.7(4)
C(52)-C(48)-O(49)-N(50)	0.6(4)
C(52)-C(51)-C(53)-C(54)	-141.5(4)
C(52)-C(51)-C(53)-C(66)	38.5(6)
C(53)-C(51)-C(52)-C(48)	-177.6(4)
C(53)-C(54)-C(55)-C(56)	-179.8(4)
C(53)-C(54)-C(67)-C(64)	3.0(6)
C(53)-C(54)-C(67)-C(68)	-179.0(4)
C(54)-C(53)-C(66)-C(65)	0.3(6)
C(54)-C(55)-C(56)-C(57)	-0.5(6)
C(54)-C(67)-C(68)-C(57)	-1.8(6)
C(54)-C(67)-C(68)-C(61)	-178.9(4)
C(55)-C(54)-C(67)-C(64)	-176.8(4)
C(55)-C(54)-C(67)-C(68)	1.2(5)
C(55)-C(56)-C(57)-C(58)	178.7(4)
C(55)-C(56)-C(57)-C(68)	-0.1(6)
C(56)-C(57)-C(58)-C(59)	-179.2(4)

C(56)-C(57)-C(68)-C(61)	178.3(4)
C(56)-C(57)-C(68)-C(67)	1.2(6)
C(57)-C(58)-C(59)-C(60)	0.4(7)
C(58)-C(57)-C(68)-C(61)	-0.5(6)
C(58)-C(57)-C(68)-C(67)	-177.6(4)
C(58)-C(59)-C(60)-C(61)	0.7(7)
C(59)-C(60)-C(61)-C(62)	176.6(4)
C(59)-C(60)-C(61)-C(68)	-1.7(6)
C(60)-C(61)-C(62)-C(63)	-177.6(4)
C(60)-C(61)-C(68)-C(57)	1.6(6)
C(60)-C(61)-C(68)-C(67)	178.6(4)
C(61)-C(62)-C(63)-C(64)	-1.0(7)
C(62)-C(61)-C(68)-C(57)	-176.7(4)
C(62)-C(61)-C(68)-C(67)	0.3(6)
C(62)-C(63)-C(64)-C(65)	-179.7(4)
C(62)-C(63)-C(64)-C(67)	0.5(7)
C(63)-C(64)-C(65)-C(66)	179.4(4)
C(63)-C(64)-C(67)-C(54)	178.5(4)
C(63)-C(64)-C(67)-C(68)	0.4(6)
C(64)-C(65)-C(66)-C(53)	1.4(6)
C(64)-C(67)-C(68)-C(57)	176.2(4)
C(64)-C(67)-C(68)-C(61)	-0.8(6)
C(65)-C(64)-C(67)-C(54)	-1.3(6)
C(65)-C(64)-C(67)-C(68)	-179.3(4)
C(66)-C(53)-C(54)-C(55)	177.2(4)
C(66)-C(53)-C(54)-C(67)	-2.5(6)
C(67)-C(54)-C(55)-C(56)	-0.1(6)
C(67)-C(64)-C(65)-C(66)	-0.8(6)
C(68)-C(57)-C(58)-C(59)	-0.5(6)
C(68)-C(61)-C(62)-C(63)	0.6(6)
C(69)-O(4)-C(25)-C(1)	85.5(4)
C(69)-O(4)-C(25)-C(21)	-97.5(4)
C(69)-C(70)-O(71)-N(72)	-176.4(3)
C(69)-C(70)-C(74)-C(73)	175.7(4)
C(70)-O(71)-N(72)-C(73)	-0.2(4)
O(71)-C(70)-C(74)-C(73)	-0.1(5)
O(71)-N(72)-C(73)-C(74)	0.1(4)
O(71)-N(72)-C(73)-C(75)	175.4(3)

N(72)-C(73)-C(74)-C(70)	0.0(5)
N(72)-C(73)-C(75)-C(76)	135.1(4)
N(72)-C(73)-C(75)-C(88)	-46.5(5)
C(73)-C(75)-C(76)-C(77)	-4.3(6)
C(73)-C(75)-C(76)-C(89)	178.1(4)
C(73)-C(75)-C(88)-C(87)	-176.4(4)
C(74)-C(70)-O(71)-N(72)	0.2(4)
C(74)-C(73)-C(75)-C(76)	-50.5(6)
C(74)-C(73)-C(75)-C(88)	127.9(5)
C(75)-C(73)-C(74)-C(70)	-174.7(4)
C(75)-C(76)-C(77)-C(78)	-177.5(4)
C(75)-C(76)-C(89)-C(86)	-1.7(6)
C(75)-C(76)-C(89)-C(90)	177.4(4)
C(76)-C(75)-C(88)-C(87)	2.0(6)
C(76)-C(77)-C(78)-C(79)	0.1(7)
C(76)-C(89)-C(90)-C(79)	0.3(6)
C(76)-C(89)-C(90)-C(83)	-179.9(4)
C(77)-C(76)-C(89)-C(86)	-179.4(4)
C(77)-C(76)-C(89)-C(90)	-0.3(6)
C(77)-C(78)-C(79)-C(80)	-180.0(4)
C(77)-C(78)-C(79)-C(90)	-0.2(7)
C(78)-C(79)-C(80)-C(81)	179.6(5)
C(78)-C(79)-C(90)-C(83)	-179.9(4)
C(78)-C(79)-C(90)-C(89)	0.0(6)
C(79)-C(80)-C(81)-C(82)	1.0(8)
C(80)-C(79)-C(90)-C(83)	-0.1(6)
C(80)-C(79)-C(90)-C(89)	179.8(4)
C(80)-C(81)-C(82)-C(83)	-1.5(8)
C(81)-C(82)-C(83)-C(84)	-179.9(5)
C(81)-C(82)-C(83)-C(90)	1.2(7)
C(82)-C(83)-C(84)-C(85)	179.5(5)
C(82)-C(83)-C(90)-C(79)	-0.4(7)
C(82)-C(83)-C(90)-C(89)	179.7(4)
C(83)-C(84)-C(85)-C(86)	2.4(8)
C(84)-C(83)-C(90)-C(79)	-179.3(4)
C(84)-C(83)-C(90)-C(89)	0.8(7)
C(84)-C(85)-C(86)-C(87)	176.3(5)
C(84)-C(85)-C(86)-C(89)	-2.3(7)

C(85)-C(86)-C(87)-C(88)	-178.7(4)
C(85)-C(86)-C(89)-C(76)	-179.5(4)
C(85)-C(86)-C(89)-C(90)	1.5(6)
C(86)-C(87)-C(88)-C(75)	-1.9(7)
C(86)-C(89)-C(90)-C(79)	179.4(4)
C(86)-C(89)-C(90)-C(83)	-0.8(6)
C(87)-C(86)-C(89)-C(76)	1.9(6)
C(87)-C(86)-C(89)-C(90)	-177.2(4)
C(88)-C(75)-C(76)-C(77)	177.3(4)
C(88)-C(75)-C(76)-C(89)	-0.2(6)
C(89)-C(76)-C(77)-C(78)	0.1(6)
C(89)-C(86)-C(87)-C(88)	-0.1(7)
C(90)-C(79)-C(80)-C(81)	-0.2(7)
C(90)-C(83)-C(84)-C(85)	-1.6(8)

Table 8. Hydrogen bonds for tcd388 [\AA and $^\circ$].

D-H...A	d(D-H)	d(H...A)	d(D...A)	$\angle(\text{DHA})$
C(29)-H(29A)...N(50)#1	0.98	2.69	3.671(6)	177

Symmetry transformations used to generate equivalent atoms:

#1 x,y,z+1